

UNIVERSITAT POLITÈCNICA DE VALÈNCIA
CENTRO DE INVESTIGACION PRINCIPE FELIPE



UNIVERSITAT
POLITÈCNICA
DE VALÈNCIA



PRINCIPE FELIPE
CENTRO DE INVESTIGACION

DEVELOPMENT OF ANALYTICAL PROCEDURES FOR THE CHARACTERIZATION OF POLYPEPTIDE-BASED NANOCONJUGATES

Doctoral Thesis
Snežana Đorđević

Supervisor
Prof. María J. Vicent

Tutor
Prof. Ramon Martínez-Máñez

April 2023

"That is the trouble with many scientists and inventors; they lack patience. They lack the willingness to work things out slowly, clearly, and sharply in their mind so they can actually feel it work. They want to try their first idea right off, and the result is that they use up lots of money and lots of good material only to find eventually that they were working in the wrong direction. We all make mistakes, and it is better to make them before we begin."

Nikola Tesla

ABSTRACT

Due to the (poly)ionic and proteinic nature of polypeptide-drug conjugates (PDCs), their translation "from bench to bedside" represents a complex and expensive undertaking, requiring reproducible and scalable polymerization techniques, the implementation of sophisticated analytical tools, exhaustive characterization steps, and the collection of detailed safety and efficacy data.

Classical techniques, such as liquid chromatography (LC) – UV/Vis and size exclusion chromatography (SEC) implemented in the quality control of PDCs during and after synthesis, cannot always support a qualitative and quantitative analysis of degradation products and metabolites. As an alternative, mass spectrometry (MS) and asymmetric flow field flow fractionation (AF4) have grown in influence on polypeptide and PDC characterization. The analysis of drug and degradation products/metabolites can take advantage of LC when coupled to MS. Meanwhile, AF4-mediated separation does not suffer from problems related to the interaction of the analyte with the column like in SEC; instead, AF4 applies a cross flow in an empty channel, which supports the "tailor-made" separation of molecules according to size and molecular weight.

The research included in this Ph.D. thesis focuses on developing new analytical procedures that will aid the selection of PDC candidates for further preclinical studies. We implemented an artificial intelligence tool (design of experiments) to develop analytical methods and optimize the synthesis of genipin-crosslinked PDCs. Moreover, we explored relatively new techniques, such as AF4 and mass spectrometry imaging, in developing novel single and combination PDCs and studying their biological fate in the search for efficient therapies for a range of diseases (advanced solid tumors, including triple negative breast, prostate, and pancreatic cancer, as well as spinal cord injury).

RESUMEN

Debido a la naturaleza (poli)iónica de los conjugados polipéptido-fármaco (PDC), su traslado a clínica puede ser una tarea complicada y costosa, que requiere técnicas de polimerización reproducibles y escalables, la implementación de herramientas analíticas sofisticadas, pasos de caracterización exhaustivos y la recopilación de datos detallados de seguridad y eficacia.

Algunas técnicas clásicas implementadas en el control de calidad de los PDC no se pueden utilizar para el análisis cualitativo y cuantitativo de productos de degradación y metabolitos. Como alternativa, la espectrometría de masas (MS) y el análisis de fraccionamiento de flujo de campo de flujo asimétrico (AF4) se han posicionado de forma relevante en dicha caracterización de polipéptidos y PDC. Mediante el uso de métodos de LC-MS, se puede realizar el análisis tanto de fármacos como de productos o metabolitos de degradación. Además, dado que la separación en AF4 no se basa en la interacción del analito con la columna, como ocurre en SEC, sino aplicando el flujo cruzado en un canal vacío; en AF4 es posible una separación de moléculas "a medida" según su tamaño y peso molecular dando lugar a la mejora selectiva de la separación.

Teniendo en cuenta lo descrito anteriormente con respecto al diseño de PDC y su caracterización, la investigación incluida en esta tesis se centra en el desarrollo de nuevos procedimientos analíticos que ayuden a la selección de candidatos PDC con las características adecuadas que les permitirán avanzar a su evaluación preclínica. Implementaremos una herramienta de inteligencia artificial, diseño de experimentos, para desarrollar métodos analíticos adecuados y determinar las condiciones óptimas en la síntesis de nanoconjugados polipeptídicos. Además, exploraremos técnicas relativamente nuevas, como AF4 para desarrollar nuevos nanoconjugados polipeptídicos simples y de combinación y además, generaremos imágenes de espectrometría de masas, para entender su

comportamiento en modelos preclínicos relevantes, lo que nos permitirá identificar terapias eficaces para una gran variedad de patologías (tumores sólidos avanzados incluyendo cáncer de mama triple negativo, cáncer de próstata y cáncer de páncreas, así como, lesión medular).

RESUM

A causa de la naturalesa (poli)iònica i, de vegades, proteica dels conjugats polipèptid-fàrmac (PDC), el seu trasllat a clínica pot ser una tasca complicada i costosa, que requereix tècniques de polimerització reproduïbles i escalables, la implementació d'eines analítiques sofisticades, passos de caracterització exhaustius i la recopilació de dades detallades de seguretat i eficàcia.

Algunes tècniques clàssiques implementades en el control de qualitat dels PDC no es poden utilitzar per l'anàlisi qualitativa i quantitativa de productes de degradació i metabòlits. Com a alternativa, l'espectrometria de masses (MS) i l'anàlisi del fraccionament de flux de camp de flux asimètric (AF4) han trobat el seu camí en la caracterització de PDC. Mitjançant l'ús de mètodes LC-MS, es pot realitzar l'anàlisi tant de fàrmacs com de productes/metabòlits de degradació. A més, atès que la separació en AF4 no es basa en la interacció de l'analit amb la columna com en SEC sinó aplicant el flux creuat en un canal buit, una separació de molècules "a mesura" segons la seua grandària i pes molecular i la millora selectiva de la separació és possible en l'instrument AF4.

Tenint en compte tot el descrit anteriorment respecte al disseny de PDC i la seua caracterització, la investigació inclosa en aquest projecte es centra en el desenvolupament de nous procediments analítics que ajuden a la selecció de candidats PDC per als seu estudi preclínic posterior. Implementarem una eina d'intel·ligència artificial, disseny d'experiments, per a desenvolupar mètodes analítics i la síntesi de nanoconjugats basats en polipèptids de manera adequada. A més, explorarem tècniques relativament noves, com AF4, i generarem imatges d'espectrometria de masses, per a desenvolupar nous conjugats a la recerca de teràpies eficaces per a tractar una varietat de malalties (càncer de mama triple negatiu, càncer de pròstata, càncer de pàncrees, així com en la lesió de medul·la espinal).

ACKNOWLEDGMENTS

“What does the Ph.D. degree mean to you?” a question I received at one of the many conferences I attended, got me thinking. Honestly, a Ph.D. has never been just a degree for me, but instead, a journey where I learned a lot about myself as a person and as a scientist! Like everyone else, I started on my PhD project as a newbie in a research lab and I have gained many technical skills. However, it was also a period where I started questioning myself, think more about everything and anything, gave me power to learn logic, and how to work in a boundary-less environment. This endeavor would not have been possible without my supervisor Maria Jesus Vicent who had faith in me and my skills, who generously supported me during the whole period of my Ph.D. project, and who shaped me as a researcher I am today. I am also very grateful to my non-official mentors, Maria and Inma who have made a huge mark in my heart during my time at CIPF. I could not have undertaken this journey and successfully finished it if you two have not listened patiently to all my ideas, answered all my questions, or gave me “a push” when I needed it. Next on the gratitude list is Stu, my English teacher, my science counterpart, my debate partner, my beer and football partner, and one of my best friends. Thank you, Stu, for all the debates that we had, for the “tough love”, for the immense editing help and for any-time feedback sessions. I am also grateful to all my lab mates who were there for me at any experimental or life (read visa) crisis and for bearing with me acting too creative, imaginative, and bossy.

Lastly, I would like to dedicate my thesis to my family: to my dad who has been a role model of how being brave and hard work take you long way; to my mom who has been so supportive even though she would prefer for her daughter to be closer to home; to my sisters for celebrating every small step forward that I take like if it was theirs; and finally to my Una, for every smile, hug, and every out of the blue “I love you so much, Auntie Nena”.

ZAHVALNICA

Generalno nije praksa pisati zahvalnice ili dodati nešto na drugom jeziku sem engleskom. Ali ja ne bih bila ja kada ne bih nešto specijalno uradila, zar ne sestrice slatke?

I tako, došao je i taj dan kada je vaša Nena napokon završila sa studijama. Mader, možeš sada da budeš mirna, nema šta više da mi kida živce jer sada sve ostalo što radim zavisice samo od mene i ni od koga više.

Želela sam samo da i osobe koje su za mene veoma važne znaju koliko sam im zahvalna na svemu, ne samo u ovih četiri godine doktorata nego od trenutka kada sam odlučila da idem svojim putem (neobičnim ali mojim) i napustim Beograd i Srbiju. Da, to si ti fader, hvala što si bio jedan od prvih koji mi je dao podršku da idem svojim putem i onda kada je izgledalo nemoguće, za svako čekanje na aerodromu, za svaki poziv i komentarisanje o sportu. Da, to si ti mader, hvala što si izdržala svih ovih godina da budeš daleko do mene iako znam da bi najviše volela kad bi ti sva deca bila tu pored tebe, hvala za svaku skuvanu čorbicu i kafu i onu iseckanu bananu koju nikad neću da zaboravim. Da, to ste i vas dve moje sestrice slatke, hvala za svako vaše radovanje za moje uspehe kao da je vaše, hvala za svaku poruku iz grupe Tetke 2, svaku podršku ali i „tough love“ kad je trebalo. I da, to je i moja Una, koja će kad nauči da čita saznati koliko mi je značio njen osmeh, zagrljaj i ono njeno „Teta Neno, ja te volim, puuuuno!“ da prebrodim teške dane doktorata. Pogodite šta, i ja vas volim puno!

LIST OF ABBREVIATIONS

2D	Two-dimensional
3D	Three-dimensional
9AA	9-aminoacridine
ACN	Acetonitrile
AF4-UV	Asymmetric field flow fractionation-ultraviolet
AFM	Atomic force microscopy
AGM	Aminoglutethimide
ANOVA	Analysis of variances
APCI	Atmospheric pressure chemical ionization
Apo	Apolipoprotein
Arg	Arginine
Asp	Aspartic acid
ATR-FTIR	Attenuated total reflection - Fourier transform infrared spectroscopy
AU	Arbitrary units
AUC	Analytical ultracentrifugation
BDC	Bisdemethoxycurcumin
BME	Basement membrane extract
BSA	Bovine-serum albumin
CA4	Combrestatin A4
CD	Circular dichroism
CE	Collision energy
CER	Ceritinib
CHCA	α -cyano-4-hydroxycinnamic acid
COVID 19	Coronavirus disease 2019
Cryo-TEM	Cryogenic transmission electron microscopy
CSF	Cerebrospinal fluid
CURC	Curcumin
CXP	Collision cell exit potential
D ₂ O	Deuterated water
DCFH-DA	2',7'-Dichlorofluorescin diacetate
DCM	Dichloromethane
DDS	Drug delivery system
DESI	Desorption electrospray ionization
DG	Diacylglycerol

DHB	2.5-dihydroxybenzoic acid
DIN	Dinaciclib
DLS	Dynamic light scattering
DMF	Dimethylformamide
DMSO	Dimethyl sulfoxide
DMTMM	Dimethoxy-1,3,5-triazin-2-yl)-4-methyl morpholinium
DoE	Design of experiments
DOX	Doxorubicin
DP	Declustering potential
dPBS	Dulbecco's phosphate-buffered saline
DTT	Dithiothreitol
ELISA	Enzyme-linked immunoassay.
EM	Electron microscopy
EMA	European Medicines Agency
EP	Entrance potential
EPR	Enhanced permeability and retention effect
ESI	Electrospray ionization
Et-SS	Ethyl disulfide
EXEM	Exemestane
FA	Formic acid
FAS	Fasudil
F_{cross}	Crossflow
FCS	Fluorescence correlation spectroscopy
FD	Free drug
FDA	Food and Drug Administration
F_{det}	Detector flow
FDR	False discovery rate
FFF	Field flow fractionation
F_{focus}	Focus flow
F_{in}	Inlet flow
F_{inj}	Injection flow
F_{out}	Outlet flow
FRET	Fluorescence resonance energy transfer
F_{slot}	Slot flow
GC-MS	Gas chromatography-mass spectrometry
G-CSF	Granulocyte colony-stimulating factor
GFLG	Glycyl-phenylalanyl-leucyl-glycine

GILT	Gama-interferon-inducible lysosomal thiol
Glu	Glutamic acid
Gly	Glycine
GPL	Glycerophospholipids
GSH	Glutathione
H&E	Hematoxylin and eosin
HPLC-UV	High-performance liquid chromatography – ultraviolet
HPMA	N-(2-Hydroxypropyl)methacrylamide
HPMC	Hydroxypropyl methylcellulose
HSA	Human serum albumin
ICH	International Council for Harmonisation
ICP-MS	Inductively coupled plasma–mass spectrometer
IR	Infrared
ITO	Indium tin oxide
k	Retention factor
LAL	Limulus ameocyte lysate assay
LAPA	Lapatinib
LC-MS/MS	liquid chromatography-mass spectrometry
Leu	Leucine
LLE	Liquid-liquid extraction
LOD	Limit of detection
LONI	Lonidamine
LOQ	Limit of quantification
LORLA	Lorlatinib
Lys	Lysine
MALDI-TOF	Matrix-assisted laser desorption ionization – time-of-flight
MALS	Multi-angle light scattering
MDR	Multidrug resistance
MDS	Molecular dynamics simulation
MeOH	Methanol
MMAE	Monomethyl auristin E
MMAF	Monomethyl auristatin F
MRM	Multiple reaction monitoring
MS	Mass spectrometry
MSI	Mass spectrometry imaging
Mw	Molecular weight
NCA-ROP	N-carboxy anhydride ring-opening polymerization

NCL	Nanotechnology Characterization Laboratory
NEDC	N-naphthyl-ethylenediamine-dihydrochloride
NIRA	Niraparib
NMR	Nuclear magnetic resonance
NOESY-NMR	Nuclear Overhauser effect spectroscopy-nuclear magnetic resonance
NP-HPLC	Normal-phase-HPLC
NVTX	Navitoclax
OFAT	One factor at a time
PArg	Poly-arginine
PBS	Phosphate-buffered saline
PC	Phosphatidylcholine
PCA	Principal component analysis
PD	Pharmacodynamic
PDCs	Polypeptide-drug conjugates
PDI	Polydispersity index
PEG	Poly(ethylene glycol)
PES	Polyethersulfone
PGA	Linear-poly-L-glutamic acid
PGA	Poly-L-glutamic acid
Phe	Phenylalanine
Ph-SS	Phenyl disulfide
PK	Pharmacokinetic
PLGA	Poly(lactic-co-glycolic acid)
PLL	Poly-L-lysine
PLO	Poly-L-ornithine
Pro	Proline
PSar	Polysarcosine
PT	Potentiometry
PTA	particle tracking analysis
PTX	Paclitaxel
PVP	Polyvinylpyrrolidone
Q2	Quadrupole 2
Q3	Quadrupole 3
QTRAP	Quadrupole ion trap
RC	Regenerative cellulose
RES	Resiquimod
RI	Refractive index

ROSCO	Roscovitine
RP-HPLC	Reversed-phased-HPLC
RS	Remote sensing
Rt	Retention time
RUCA	Rucaparib
S/N	Signal-to-noise ratio
SANS	Small-angle neutron scattering
SAS	Small-angle scattering
SAXS	Small-angle x-ray scattering
SCI	Spinal cord injury
SEC	Size-exclusion chromatography
SEM	Scanning electron microscopy
Ser	Serine
SS-SIL	Redox-responsive self-immolating linkers bearing disulfide moieties
StPGA	Star-shaped poly-L-glutamic acid
TDL	Total drug loading
TEA	Triethanolamine
TEM	transmission electron microscopy
TFA	Trifluoroacetic acid
TLC	Thin-layer chromatography
TME	Tumor microenvironment
Tyr	Tyrosine
UK	United Kingdom
USA	United States of America
Vis-FLD	Visible-fluorescence detector
W	Peak width at 10% of its height

TABLE OF CONTENTS

ABSTRACT	5
RESUMEN	7
RESUM.....	9
ACKNOWLEDGMENTS	11
ZAHVALNICA.....	12
LIST OF ABBREVIATIONS.....	13
OBJECTIVES	23

CHAPTER I

INTRODUCTION.....	25
1.1 Nanomedicine.....	26
1.2 Polymer Therapeutics.....	31
1.3 Rational design of Polypeptide-Drug Conjugates	36
1.4 Molecular tale of PDCs, as narrated by analytical chemistry	50
1.4.1 Insight into the bioanalysis of PDCs.....	53
1.4.2 The Interaction of PDCs with Biological Constituents.....	54
1.4.3 Pharmacokinetics	56
1.4.4 Sample preparation	58
1.4.5 Sample analysis.....	60
1.5 Aims	63
1.6 Liquid Chromatography- Mass Spectrometry – The gold standard for quantitative and qualitative analyses	64
1.6.1 The theoretical principle of LC-MS.....	64
1.7 Design of Experiment – a robust tool for method development ...	67
1.8 Asymmetric-Flow Field-Flow Fractionation – a powerful tool for the physico-chemical characterization of PDCs	70
1.8.1 The theoretical principle of AF4.....	77

1.9	Matrix-Assisted Laser Desorption Ionization Mass Spectrometry Imaging	79
1.9.1	Mass Spectrometry Imaging	79
1.9.2	The theoretical principle of MSI.....	82
1.9.3	MALDI-MSI.....	83

CHAPTER II

A ROBUST AND PREDICTIVE PLATFORM FOR THE CHARACTERIZATION OF NEXT-GENERATION POLYPEPTIDE-DRUG NANOCONJUGATES..... 89

2.1	Introduction	90
2.2	Results	91
2.2.1	DoE in LC-MS/MS Method Development for the Quantitative Determination of Fasudil	91
2.2.2	Tailor-made LC-MS/MS methods for the quantitative determination of anticancer drugs as a component of PDC characterization studies	105
2.3	Discussion	112
2.4	Conclusion.....	114
2.5	Experimental materials and methods	115
2.5.1	Materials.....	115
2.5.2	Methods.....	116
2.6	Supplementary material.....	117

CHAPTER III

DESIGN OF GENIPIN-ASSEMBLED POLYPEPTIDE-BASED NANOCONJUGATES FOR COMBINATION THERAPY..... 130

3.1	Introduction	131
3.2	Results	135
3.2.1	Evaluating the behavior of PGA within the AF4 separation module.....	135

3.2.2	DoE implementation in the synthesis of genipin-crosslinked StPGA-based combination conjugates.....	149
3.3	Discussion	161
3.4	Conclusions	163
3.5	Experimental materials and methods	164
3.5.1	Materials.....	164
3.5.2	PDCs synthesis.....	165
3.5.3	Methods.....	166

CHAPTER IV

EVALUATING THE BIOLOGICAL FATE AND PHARMACOLOGICAL EFFECT OF PDCs BY MASS SPECTROMETRY IMAGING		169
4.1	Introduction	170
4.2	Results	173
4.2.1	Synthesis, Characterization, and Evaluation of <i>in vitro</i> Toxicity of Single and Combination PGA-based Conjugates	173
4.2.2	Development of a MALDI-MSI Method for Fasudil and Dinaciclib Detection	177
4.2.3	Evaluation of Drug Release and Spatial Localization in Spheroids/Mammospheres Following Exposure of MDA-MB-231 TNBC Cells to PDCs	183
4.2.4	Metabolic Alterations Induced in 3D TNBC models after Treatment with Single and Combination PDCs.....	189
4.3	Discussion	193
4.4	Conclusion.....	197
4.5	Experimental material and methods	198
4.5.1	Materials.....	198
4.5.2	PDCs synthesis.....	199
4.5.3	Physicochemical-Characterization of PGA-drug conjugates.....	200
4.5.4	<i>In vitro</i> cell viability assay - MBE embedded spheroids	202

4.5.5	<i>In vitro</i> cell viability assay – mammospheres	203
4.5.6	Sample embedding	203
4.5.7	Sample sectioning and matrix application	204
4.5.8	Image acquisition and data processing.....	204
4.5.9	Histological analysis	205
4.6	Supplementary material.....	206

CHAPTER V

CRITICAL STRATEGIES FOR CRAFTING POLYMER-DRUG CONJUGATES POSSESSING ON-DEMAND DRUG RELEASE	208	
5.1	Introduction	209
5.2	Results	212
5.2.1	Drug-Et-SS synthesis and their characterization with accurate and robust LC-MS/MS platform	212
5.2.2	Drug Release from Individual Drug-Et-SS Depends on Drug Structural Features	215
5.2.3	Ph-SS as a Robust Substitute for Et-SS	221
5.2.4	Synthesis and Characterization of Polypeptide-based Fasudil Conjugates with Optimized Linkers	226
5.2.5	<i>In vitro</i> Anti-Cancer Activity of PDCs Depends on Variables Other Than Drug Release.....	229
5.2.6	Biological Environment and Carrier Architecture as Essential Factors Influencing the Design of Polypeptide-based Drug Conjugates.....	239
5.3	Discussion	243
5.4	Conclusion.....	247
5.5	Experimental material and methods	249
5.5.1	Materials.....	249
5.5.2	Synthesis and Characterization of Drug-Linkers	250
5.5.3	Synthesis and Characterization of PGA-drug conjugates	250

5.5.4	Drug release from Drug-linkers and PGA-drug conjugates with DTT.....	252
5.5.5	Fasudil Release from PGA Conjugates in Cell Medium and MBA-231-TNBC Cells.....	252
5.5.6	Direct mass spectrometry scan.....	253
5.5.7	LC-MS/MS for determination of FAS, DIN, NIRA, RUCA, and RES.....	254
5.5.8	Asymmetric flow field flow fractionation for size determination	254
5.5.9	Protocol optimization for fasudil extraction from cell medium 255	
5.5.10	Cell culture conditions	255
5.5.11	<i>In vitro</i> cell viability assay	255
5.5.12	GSH/GSSG assay.....	256
5.6	Supplementary Material	257

CHAPTER VI

GENERAL DISCUSSION AND FINAL REMARKS.....	269
--	------------

REFERENCES.....	284
------------------------	------------

OBJECTIVES

The central work presented in this proposal involves developing adequate physicochemical techniques to validate the effectiveness and understand the fate of polypeptide-drug conjugates in relevant physiological fluids.

Objective 1. Synthesis and full characterization of polypeptide-drug conjugates as therapeutic moieties for spinal cord injury and cancer

1.1. Synthesis and characterization of polypeptide-drug conjugates carrying fasudil for the treatment of spinal cord injury

1.2. Synthesis, characterization, and the *in vitro* toxicity evaluation of single and combination polypeptide-drug conjugates carrying fasudil and dinaciclib on the same polypeptide chain for the treatment of triple negative breast cancer

Objective 2. Development of a robust and predictive platform for the characterization of next-generation polypeptide-drug conjugates implementing a design of experiments approach

2.1. LC-MS/MS method development for the quantitative determination of FAS as part of the characterization of the PGA-SS-FAS used to promote neuroregeneration after spinal cord injury

2.2. Tailor-made gradient LC method optimization for the quantitative determination of the free forms of sixteen anticancer drugs

Objective 3. Design of a genipin-assembled star-shaped polypeptide-drug conjugate-based combination therapy

3.1. Evaluation of the PGA behavior within the AF4 separation module

3.2. Implementation of design of experiments in the synthesis of genipin-assembled star-shaped polypeptide-drug conjugate-based combination therapies

Objective 4. Evaluation of biological fate and pharmacological effect of polypeptide-drug conjugates by mass spectrometry imaging

4.1. Development of MALDI-MSI method to detect FAS and DIN in a 3D TNBC *in vitro* model

4.2. Evaluation of drug release, spatial localization, and metabolite formation following exposure of 3D TNBC models to single and combination PDCs carrying FAS and DIN

4.3 Analysis of metabolomic fingerprint of 3D TNBC model and its alterations induced by combination PDC treatment

Objective 5. Evaluation of drug/linker chemical structures and the type of chemical group available for conjugation on drug release from PDCs

5.1. Evaluation of how the chemical group nature in the drug available for conjugation influences drug release kinetics

5.2. Validation of drug release kinetics by directly analyzing resultant metabolites in preclinically relevant cell models to improve *in vitro* and *in vivo* correlations

5.3. Report the critical strategies under consideration when rationally designing PDCs with optimized biological output

CHAPTER I

INTRODUCTION

1.1 NANOMEDICINE

Nanomedicine has emerged from the interaction of nanoengineering and nanotechnology with life sciences, resulting in a system with at least two components – an appropriate nanocarrier and an active pharmaceutical ingredient.^{1,2} The interdisciplinary field of nanomedicine involves conventional therapeutics, such as small molecule drugs, and nanosized materials intending to improve diagnosis, treatment, and prevention of disease or injury and with the final goal of preserving and improving human health.³

Since their first appearance in the early 80s, nanomedicines have fundamentally changed how we address unmet medical needs, including, but not limited to, treating cardiovascular⁴, lung⁵ and kidney disease⁶, neurodegenerative disorders⁷, primary and metastatic tumors⁸, diabetes⁹, infections and inflammation-based diseases¹⁰⁻¹², autoimmune disorders¹³ and modulating intestinal barrier functions or gut microbiome composition¹⁴. Some nanotechnology-based strategies aim to improve the water solubility and stability of associated active payloads in the bloodstream, promote transport across biological barriers, and prolong circulation times, thus, leading to increased safety and efficacy of active moieties.^{15,16} Currently, there exists around a hundred nanomedicines approved by regulatory agencies worldwide (European Medicine Agency – EMA, Food and Drug Administration – FDA), with more than 550 in advanced pre-clinical and clinical studies (Table 1.1).¹⁷

Table 1.1 Nanomedicines approved by the FDA and EMA from 2016-2022 (See Sainz et al. for nanomedicines approved before 2016¹⁸)

Tradename/Year of Approval	Nanoconstruct and Active Moiety	Application	Company
Paigebin® 2016	Polymer-drug/protein conjugate; A recombinant Y-shaped PEG (40kDa) interferon alfa 2b	Chronic hepatitis B and C	Xiamen Amytop Biotech
Luxturna® 2017	Viral vector; Encoding human retinal pigment epithelium-specific kDa protein (RPE65)	Blindness; Leber congenital amaurosis; retinal dystrophy	Applied Genetic Technologies
Sublocade® 2017	PLGA nanoparticles/ buprenorphine	Opioid use disorder	Indivior
Vyxeos® 2017	Liposomes with cytarabine: daunorubicin combination therapy (5:1 mol ratio)	Acute myeloid leukemia	Jazz Pharmaceuticals
Adynovate®/ Adynovi® 2017	Recombinant anti-hemophilic factor modified with PEG	Hemophilia	Takeda
Zilretta® 2017	PLGA hydrogel with triamcinolone acetonide	Knee osteoarthritis	Flexion Therapeutics
Doxophos® 2017	Doxorubicin micellar	Cancer	Oasmia Pharmaceuticals
Besponsa® 2017	Recombinant humanized IgG4 targeting CD22; calicheamicin derivative	Acute lymphocytic leukemia	UCB Celltech

Mylotarg® 2017	Humanized IgG4 targeting CD33; calicheamicin derivative	Acute myeloid leukemia	Pfizer; UCB Celltech
Besponsa® 2017	Recombinant humanized IgG4 targeting CD22; calicheamicin derivative	Acute lymphocytic leukemia	UCB Celltech
Rebiny® 2017	Polymer-protein conjugate; GlycoPEGylated human blood coagulation factor IX	Coagulation factor IX deficiency (Hemophilia B)	Neose
Onpatro® 2018	Lipid nanoparticle for siRNA targeting TTR protein	TTR-mediated amyloidosis	Alnylam Pharmaceuticals
Asparlas® 2018	Polyethyleneglycol-L-asparaginase isoenzyme II	Acute lymphocytic leukemia	Servier Pharmaceuticals
Inveltys® 2018	Nanosuspension of loteprednol etabonate	Post-operative ophthalmic inflammation	KALA pharmaceutical
Arikace® 2018	Liposome; amikacin	Bronchiectasis	Insmed
VivaGel® 2018	Dendrimer	Bacterial vaginosis	Starpharma;
Jivi® 2018	Polymer-protein conjugate; Pegylated recombinant human blood coagulation factor VIII	Coagulation factor VIII deficiency (Hemophilia A)	Bayer
Sebacia Microparticle® 2018	Inorganic nanoparticle (gold-coated silica particle)	Acne vulgaris	Sebacia
Cequa® 2018	Micelles; Cyclosporine	Dru eye; immunosuppression	Auven Therapeutics

Hensify® 2019	Core-Shell nanoparticle (a crystalline hafnium oxide core and an amorphous thin biocompatible coating)	Cancer, esophagus cancer, head, and neck (squamous cell carcinoma)	Nanobiotix
Givosiran® 2019	GalNAc-siRNA conjugate	Acute hepatic porphyria	Alnylam Pharmaceuticals
Polivy® 2019	An anti-CD79b monoclonal Antibody; MMAE	Chronic lymphocytic leukemia	Chugai Pharmaceutical Genentech; Roche
Padcev® 2019	A monoclonal antibody targeting Nectin-4; MMAE	Cancer, breast; gastrointestinal; head and neck	Astellas Pharma
CharisMA® 2019	Viral vector (adeno-associated viral vectors); Encoding the survival motor neuron 2 gene	Motor function disorders; Spinal muscular atrophy	Avexis (Novartis);
Fulaimei® 2019	Polymer-protein (GLP-1) conjugate; PEG-loxanatide	Diabetes type 2	Jiangsu Pharmaceutical
Enhertu® 2020	Humanized anti-HER2 antibody; Exatecan	Cancer, breast; bile duct	Daiichi Sankyo
Blenrep® 2020	An anti-BCMA fucosylated humanized monoclonal Ab (J6M0); MMAF	Multiple myeloma	GlaxoSmithKline
Trodely® 2020	Humanized anti-EGP-1 monoclonal antibody, hRS7; Maleimidocaproyl-Phe-Lys-p-aminobenzyl- CO-20-O- SN-38 (MC-Phe-Lys-PABO-CO-20-O-SN-38)	Cancer, breast metastatic	Gilead

Zynlonta® 2021	Humanized monoclonal IgG1-kappa antibody targeting CD19 antigen	B-cell acute lymphocytic leukemia	ADC Therapeutics
Delytact® 2021	Vaccine; Conditionally replicating ICP34.5 and ICP47 gene-deleted oncolytic Herpes simplex virus	Cancer, Breast metastatic	Daiichi Sankyo
Inclisiran® 2021	Liposome; double-stranded small interfering RNA targeting human proprotein convertase subtilisin/Kexin type 9	Atherosclerosis; dyslipidemia	Alnylam Pharmaceutical
mRNA-1273® 2022	Lipid nanoparticle loaded with full spike mRNA	Vaccine for COVID-19 (prevention)	Moderna
Tozinameran® 2022	The lipid nanoparticle loaded with complete spike mRNA	Vaccine for COVID-19 (prevention)	Pfizer and BioNTech SE

PEG – polyethylene glycol; COVID-19 – coronavirus disease 2019; PLGA - poly(lactic-co-glycolic acid); MMAE - Monomethyl auristatin E; MMAF - Monomethyl auristatin F; Phe- phenylalanine; Lys- lysine

Regardless of the immense progress made, many challenges associated with the clinical translation of nanomedicine persist, including, but not limited to, reliability and repeatability of production, safety, clinical trial design, market approval, and sustainability as an alternative strategy for clinical application.^{19–21} After the tremendous success of vaccines in coronavirus disease 2019 (COVID-19) prevention, scientific society and regulatory agencies have recognized the importance of fast-tracking/rapid approval with minimal bureaucracy while

maintaining the highest safety standards. Thus, the responses to the COVID-19 pandemic may have accelerated many translational pathways and provided hope for nanomedicine's future.²² Moreover, the post-COVID era of medicine and medicinal products has seen an increased interest in immunotherapy and gene delivery employing non-viral vectors such as liposomes.¹⁷

Nanomedicine with demonstrated clinical benefits include liposomes, lipid nanoparticles, polymeric micelles, polymer therapeutics, nanogels, nanoparticles, and nanocrystals.^{23,24} Applications may differ on a case-by-case basis, and every group offers specific advantages and suffers from various disadvantages; however, we will focus specifically on polymer-drug conjugates from the polymer therapeutics family.

1.2 POLYMER THERAPEUTICS

Coined by Prof. Ruth Duncan²⁵, the term “polymer therapeutics” defines a family of nanomedicines considered new chemical entities encompassing polymeric drugs (polymeric macromolecules with inherent activity), polymer-drug conjugates, polymer-protein conjugates, polymeric micelles with a covalently-bound drug, and polymeric non-viral vectors for gene delivery. As the field evolves, additional self-assembling polymeric systems have been included together with an increasing number of hybrid nanosystems that include inorganic components or lipidic moieties (Figure 1.1).²⁶

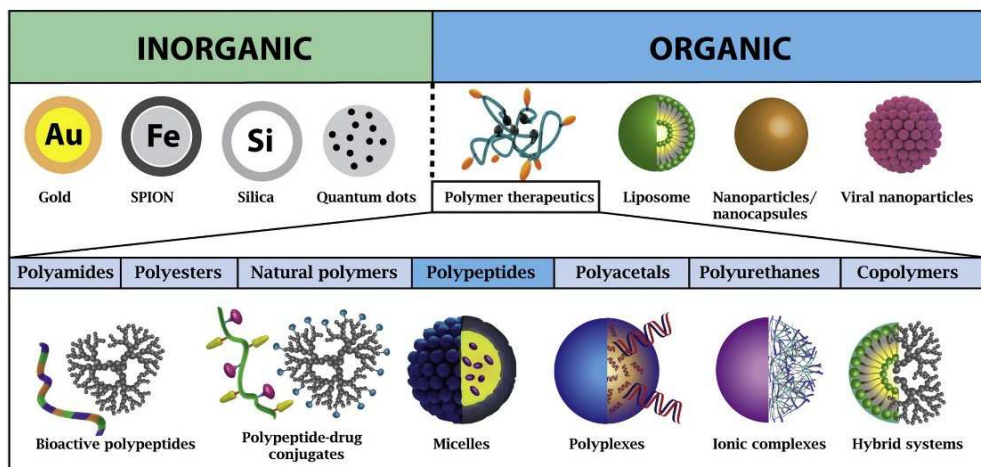


Figure 1.1. Types of nanomedicines and the position of polymer therapeutics in the field. Reproduced from T.Melnik and S.Đorđević et al.²⁷

As a successful class of nanomedicines, polymer therapeutics offer advantages that include disease-specific targeting, controlled drug release, convenient administration routes (e.g., intravenous, transdermal, and pulmonary), and the ability to reach difficult-to-access sites such as the brain. The presence of a rationally designed bioresponsive linker, which offers an additional point for pharmacokinetics control and allows an adequate safety:benefit ratio, represents a differential feature of this class. The presence of more than thirty examples in the market demonstrates the clinical benefits of polymer therapeutics; said examples include two top-selling-drugs in the USA in the last decade: Copaxone® - a polypeptide-based drug for multiple sclerosis treatment^{27,28} and Neulasta®, a poly(ethylene glycol) (PEG) conjugate of recombinant granulocyte colony-stimulating factor (G-CSF) used to treat the symptoms of prevent neutropenia (lack of specific white blood cells) caused by chemotherapy.²⁹ Meanwhile, many other examples currently find themselves in early and advanced clinical trials.^{27,30}

1.2.1 Polymer-Drug Conjugates

Poor bioavailability and stability under physiological conditions and rapid metabolism/clearance significantly influence the therapeutic efficacy of small-molecule drugs. The conjugation of drugs to water-soluble polymers (forming polymer-drug conjugates) modulates their physicochemical properties to enhance biological output. Since the first reports of drug conjugation to synthetic/natural macromolecules such as polymers^{31,32}, over twenty-five polymer conjugates have met market approval³³. Of note, only Movantik® (PEG-Naloxone), approved in 2014 for opioid-derived constipation, is considered a polymer-drug conjugate.

Benefits that derive from the conjugation of a small molecule drug as a single moiety or in combination with a water-soluble polymeric carrier include i) tailored drug loading and the improvement of drug pharmacokinetic and pharmacodynamic profiles by rational polymer selection³⁴, ii) passive targeting and accumulation in pathological sites (tumor or inflammation sites) owing to the enhanced permeability and retention effect (EPR)^{35–37}, iii) lower off-target toxicity and higher on-target efficacy of the conjugated drug^{38,39}, iv) extended circulation time in the bloodstream and altered pharmacokinetics⁴⁰, v) control release of the drug(s) at the site of action; vi) the potential to bypass mechanisms of drug resistance, including *p*-glycoprotein-mediated multidrug resistance (MDR)^{39,41}, vii) enhanced efficacy in treating cancer and other diseases^{42–44} and prevention of metastasis^{45,46}, and ii) modulation of cellular signaling and apoptotic pathways^{47,48}. The conjugation of drug combinations to the same multivalent polymeric carrier can ensure the delivery to the target site and support optimal therapeutic activity. Moreover, optimized drug ratios combined with the rational choice of linking moieties can strictly control drug release and bioavailability to improve therapeutic outcomes.^{27,49} While the application of drug combinations represents a critical

advantage of polymer-drug conjugates, the enhanced complexity of the systems brings new challenges.²²

Ringsdorf first described the four main features for consideration when rationally designing polymer-drug conjugates.⁵⁰ Although they now represent a more versatile platform, the general basis remains: (i) a hydrophilic polymeric carrier (to enable water solubility of low molecular hydrophobic drugs), ideally biodegradable (to achieve the elimination from the body), multivalent (for a high loading capacity), and biocompatible (to achieve appropriate host response)⁵¹, (ii) adequate selection of drug(s) with appropriate efficacy and structural features that allow conjugation to a polymeric carrier, (iii) bioresponsive linkers that under selected endogenous or exogenous triggers allow for the controlled drug release at the site of action, and (iv) the possibility of implementing targeting moieties to enhance accumulation and bioavailability at a desired site of action.⁵² With these four features in mind, rationally-designed polymer-based drug conjugates have gained much attention. Novel approaches include the development of polypeptide-based drug-conjugates, which implement synthetic poly-amino acids as the multivalent, biodegradable polymeric carrier component.^{23,53}

1.2.2 Polypeptide-Drug Conjugates

Among the existing polymer classes, synthetic polypeptides hold much promise for biomedical applications as they mimic natural proteins and demonstrate substantial biocompatibility (safety, low immunogenicity), multivalency, and biodegradability. Polypeptides display high levels of biocompatibility due to their amino-acid composition (specific endogenous proteases known as cathepsins or carboxypeptidases degrade polypeptides) - a

property that provides significant advantages over other polymers used in drug delivery.²⁷ Additionally, the development of polymerization techniques (mainly N-carboxy anhydride ring-opening polymerization or NCA-ROP)⁵⁴ and synthetic chemistry have permitted the production of polypeptides with narrow polydispersity, minimal side product formation, high reproducibility, and precise functionalization of the polypeptide backbone.

The feasibility and simplicity of polypeptide chain modification that allows the desired bioresponsive conjugation of a therapeutic moiety, targeting moiety and/or imaging moiety, represents the main requirement when developing polypeptide-drug conjugates (which we designate as “PDCs” in this thesis). Seven naturally-occurring amino acids possess characteristics that have fostered their implementation as building blocks for PDC – the positive charged amino acids arginine (Arg) and lysine (Lys), the uncharged polar amino acid serine (Ser), the uncharged hydrophobic amino acid tyrosine (Tyr), and finally, the negatively charged amino acids glutamic acid (Glu) and aspartic acid (Asp).

The appearance of more than eleven examples in advanced phases of clinical trials has demonstrated the clinical benefit of polypeptide-based materials. Two polypeptidic drugs have reached the market: *Copaxone*[®], a random copolymer of L-Glu, L-Ala, L-Lys, and L-Tyr for the treatment of multiple sclerosis^{29,55,56}, and *Vivagel*[®], a topically administered poly-lysine-based dendrimer device employed as an antiviral moiety (HIV-1 and HSV-2).⁵⁷ Given the common use of the Glu, Asp, and Lys amino acids in PDCs, our laboratory addressed their recent implementation as single and combination therapies or as imaging moieties in a review published by T. Melnyk and S. Đorđević et al. - “*Therapeutic Potential of Polypeptide-Based Conjugates: Rational Design and Analytical Tools That Can Boost Clinical Translation.*”²⁷

The synthetic chemistry involved and the ability to incorporate bioresponsive linking moieties and other biomimetic features greatly enhance the scope of PDCs compared to other types of nanomedicine⁵³; however, said nanomedicines must meet defined and exact prerequisites, which we will discuss in the forthcoming chapters.

1.3 RATIONAL DESIGN OF POLYPEPTIDE-DRUG CONJUGATES

The optimization of physicochemical properties supports the generation of PDCs with unique pharmacokinetic features that impact clinical safety and efficacy and vary depending on the polypeptide nature, route of administration (biological barriers to bypass), and desired application.⁵⁸ Strategic choices during PDC synthesis include the design of bioresponsive covalent linking moieties connecting the drug(s)/active moiety(s) to a polypeptide-based carrier, which should display stability during blood circulation but degradability in the targeted tissues/cells to allow for controlled drug(s) release. We possess considerable evidence that nanomedicines (including PDCs) present unique behaviors at the bio-nano interface controlled by their specific physico-chemical characteristics.⁵⁹ A complex system of simultaneous interactions drives the interaction of a PDC with the bio-nano interface; therefore, we require the step-wise design of experiments in relevant physiological environments to explore PDC performance in a biological milieu.⁵⁸ The importance of a material property depends on the experiment performed; however, several crucial features of PDCs have effects across a wide range of biological systems, and we will discuss each in the following sections (Figure 1.2).

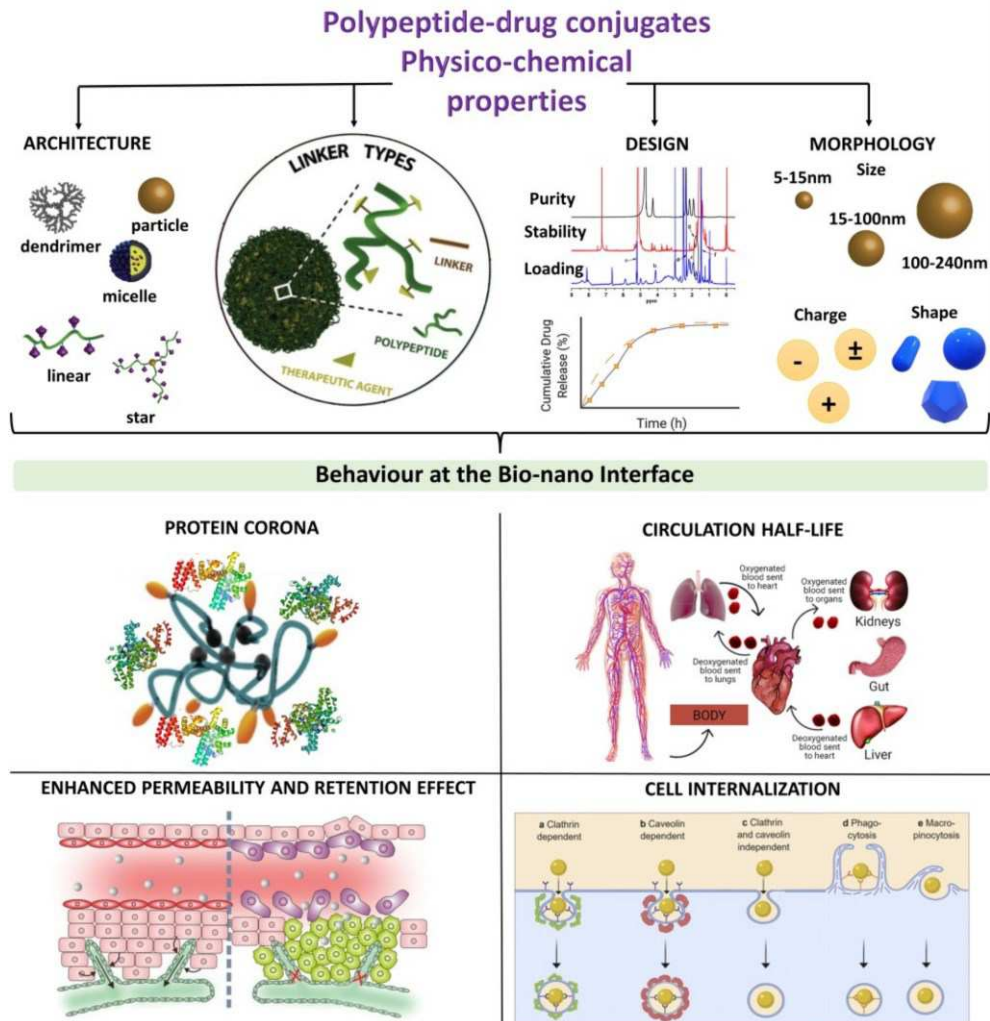


Figure 1.2. The physico-chemical properties of polypeptide-drug conjugates. The impact of polypeptide-drug conjugates physico-chemical properties (e.g., architecture, linking chemistry, stability, purity, morphology, size, shape, solution conformation, and net charge) on the bio-nano interface influences different biological processes such as protein corona formation, degradation, clearance, targeting, cell trafficking, and biodistribution.

1.3.1 Synthesis, Identification, and Purity

The scalability and robustness of PDC synthesis and the final manufacturing process remain essential considerations regarding clinical translation. Carrier and polypeptide architecture selection highly depend on the cargo, release mechanism, and intended site of action; thus, these factors deserve consideration during the early stages of rational design.

The final polypeptide carrier's properties may differ depending on the synthetic strategy applied. Peptide bond formation via coupling two amino acids with N- and C-terminal protecting groups or recombinant techniques expressing an amino acid sequence in *E.coli* suffer from poor process scalability.^{60,61} On the contrary, recent achievements in polymerization techniques such as NCA-ROP-based strategies^{62,63} have enabled the controlled synthesis of complex polypeptide carriers with various structures (linear, star, micelles, dendrimers, nanoparticles), sizes, and molecular weights.^{64–68} NCA-ROP requires amino acid derivatives (NCAs with protected side-chain chemical groups) to generate a final compound that contains an already modified side chain or that can undergo post-synthetic modification.⁶⁹ The choice of (macro)initiator remains critical to the NCA-ROP process, determining the polydispersity index (PDI) of the resultant polypeptides⁷⁰ and their final topology.^{71,72} The incorporation of PEG as a macroinitiator grants amphiphilicity to the resulting polypeptide chain and allows for the generation of polymeric micelles.⁷³ PEGylation increases circulation times by increasing size⁷⁴ and impeding recognition/clearance by the immune system (through opsonization, phagocytosis, and elimination).⁷⁵ Of note, PEG can produce toxic carboxylic metabolites resulting in acidosis and hypercalcemia⁷⁶ that, together with reported hypersensitivity reactions^{77,78}, has raised doubts regarding the safety of PEG (the “PEG dilemma”). Thus, alternatives to PEG, such as polysarcosine (PSar, N-

methylglycine), have emerged, which grants water-solubility, immune evasion, flexibility, and a lack of immunogenicity without adverse effects.⁷⁹ So far, several PSar-polypeptide micelles have displayed promising preclinical activity in targeted drug delivery or as non-viral vectors.⁸⁰

As mentioned above, formulation complexity and final PDC composition play vital roles in their interactions with biological components.⁸¹ Therefore, tight control over the entire synthetic process remains of utmost importance to ensure scalability and repeatability and provide a detailed description of new products. Encouragingly, Buriak et al. recently documented examples of best practices when reporting synthetic processes.⁸² All newly published materials must be provided with a detailed description of composition and details regarding sensitive or challenging synthetic steps. Additionally, purification methods and purity analysis also deserve attention, as any impurity (e.g., precursors, residual solvents, or endotoxin contamination) may alter the biological response or induce a non-specific immune response.^{83,84} Furthermore, beyond the toxicity of the active moiety and PDCs as a whole product, the multiple components may cause unexpected toxicities. Therefore, we must also consider the drug-free nanocarrier and the whole nanoconstruct in preclinical pharmacokinetic (PK) and pharmacodynamic (PD) studies at different doses if they remain unstudied/unapproved.

1.3.2 Effect of size, molecular weight and net charge on EPR, cellular uptake, and clearance

The enhanced permeability and retention (EPR) effect, which relates to the anatomical architecture and pathophysiological processes in tumor tissues

applicable to cancer and inflammatory/infectious diseases, represents the primary rationale behind the development of nanomedicines such as PDCs.^{37,85} A recent publication by Wu et al. described the advantages and pitfalls of EPR and highlighted those tumor characteristics significantly influencing the EPR effect's efficacy, including the overexpression of inflammatory factors, irregular vascularization, and disruptive vascularization of tumor blood vessels, and the lack of lymphatic drainage.⁸⁶ Of note, the results of recent studies have created doubt surrounding the importance of the EPR effect, primarily based on the gap between preclinical development and clinical studies.⁸⁷⁻⁹⁰ When discussing the EPR effect, heterogeneity relates to the accumulation and retention, which varies depending on the solid tumor type and tissue environment. More specifically, macromolecule accumulation in solid tumors depends on more than simple extravasation through disrupted blood vessels⁹¹; furthermore, immune cells such as macrophages in the tumor microenvironment (TME) play an essential role in nanomedicine accumulation in the tumor.^{92,93} Moreover, the EPR effect is more pronounced in studies using *in vivo* xenograft models than in clinical scenarios.⁹⁴ Therefore, we need to improve our understanding of EPR-associated mechanisms, the dependence on pathophysiology, nanomedicine interactions with TME-associated factors, and the influence of nanomedicine properties on biological fate to move forward.⁹⁵

The overall molecular weight, size, shape, and net charge of a given nanomedicine (which includes PDCs) all represent essential parameters that govern their resistance to elimination by the hepatic, reticuloendothelial, or renal systems and therefore modulate blood circulation times.

40-50 kDa (a threshold for renal clearance) represents the lower Mw limit for a given DDS to take advantage of the EPR effect.³⁷ DDSs above this size generally

possess prolonged circulation time, gradually permeating, accumulating, and retaining in tumor tissue longer than small drugs.

The design of DDSs in a size range between 10–100 nm favors their accumulation in well-vascularized pathological sites;^{96,97} however, an efficient therapeutic response after exposure to a DDS/PDC also requires adequate tissue diffusion and cellular uptake in addition to accumulation in the affected target tissue. Notably, the size represents another critical factor in determining cell uptake - small DDS (from a few to hundred nanometers) enter the cells via pino- or micropinocytosis, DDSs of 120-200 nm usually become internalized via caveolin- or clathrin-mediated endocytosis, while larger particle (in general) (250 nm to 3 μ m) become phagocytosed, leading to an increased clearance rate.⁹⁸ The uptake rate and efficiency of smaller (15-30 nm) and larger (70-240 nm) particles remain low, while optimum uptake occurs for particles of 30-50 nm in size. Moreover, a size of about 50 nm leads to a more efficient interaction of particles with cell receptors leading to internalization through receptor-mediated endocytosis.^{99,100}

While we can therapeutically apply unmodified PDCs, their relatively small size (below 50 kDa and \approx 5 nm in hydrodynamic size) prompts short circulation half-time and/or non-specific biodistribution profiles; however, we can take advantage of the tendency of PDCs/polypeptide carriers to self-assemble due to their intrinsic properties into “aggregates” of larger sizes.¹⁰¹ The stability of self-assembled PDCs under physiological conditions depends on forces including hydrophobic/hydrophilic balance, π - π stacking, and dipole interactions.¹⁰² Increasing stability and size by implementing different crosslinking strategies, which include so-called "click" reactions^{101,103–106} or cross-linking reactions based on genipin¹⁰⁷, bioresponsive disulfides^{4,108,109}, boronic acid^{110,111}, and aldehyde/amine derivatives¹¹² can increase the serum half-life of a PDC and support EPR-mediated accumulation. Crosslinking of polypeptidic chains with biodegradable/non-

biodegradable linkers supports the generation of stabilized and flexible structures displaying controlled drug release and tunable size. Several studies have demonstrated the advantages of cross-linked systems for PGA^{101,113} and poly-L-lysine (PLL)⁴, with a significant increase in blood circulation times demonstrated *in vivo*.

Net charge significantly affects *in vivo* fate and represents another physical parameter to consider when designing PDCs. Negatively-charged PDCs offer a longer half-life but tend to face uptake by the reticulo-endothelial system (RES) in the liver and spleen; however, using slightly negative or neutral charges reduces non-specific cellular uptake and opsonization. A positive charge supports PDC binding to the negatively-charged vascular endothelial surface of the blood vessels resulting in a rapid decrease in plasma concentration and reduced drug accumulation at the site of action by the EPR effect.¹¹⁴ Neutralizing positively-charged molecules during synthesis can benefit *in vivo* activity by modulating the cell trafficking and uptake mechanism.

After adequate positive charge shielding approaches, PLL, poly-L-ornithine (PLO), or poly-arginine (PArg) may represent suitable materials for developing PDCs or non-viral vectors for systemic delivery.^{115–119} Chemical alterations such as amide formation can compensate for the positive charge of amino groups. For instance, the modification of lysine into a β -carboxylic amide created pH-sensitive negatively-charged micelles (based on PLL-poly(L-leucine) diblock copolymers) that regain their positive charge upon hydrolysis to assist in internalization at the site of action.¹²⁰ PEGylation, as in the case of DEP[®] technology^{121,122}, and dendrimeric PEG-PLL modification in phase I-II clinical trials⁷⁵, have been employed to shield positive charges. Qi et al. developed a multilayered system with PEG-PGA layer-by-layer assembly that quenches the positive charge of PEG-PLL-poly-aspartame bearing monomethyl auristatin E (MMAE) to prevent premature opsonization and minimize

non-specific biological adhesion.¹²³ The resulting multilayered DDS disintegrated at low pH in the TME, improving cell internalization through exposure to the amine's positive charges. Nevertheless, even with the existence of shielding processes, PLL and PArg have found their application mainly as carriers for topical application, such as in the case of Vivagel® virucide.⁵⁷

Ultimately, charge combined with size and deformability may allow for different organ tropism. For instance, murine macrophages phagocytize molecules with high surface charge and large particle sizes more efficiently.¹²⁴ Additionally, particles' negative charge, large size, and deformability favor lymphatic uptake.¹²⁵ These properties may serve as guidelines for PDC rational design with maximized therapeutic efficacy, predictable *in vivo* behavior, and targeting, in which the size and surface charge control possess significance.

1.3.3 Polypeptide-drug Linking Chemistries

Implementing optimal linking moieties in PDCs allows for prolonged plasma stability followed by efficient and controlled release kinetics under the desired conditions. Linking moiety selection relies on the target's available functional groups (e.g., drug), the required administration route and associated microenvironmental conditions, and the biological barriers faced on the "journey" to the targeted tissue/cellular compartment. The first generation of PDCs employed simple one-step conjugation using ester, disulfide, amide, thioether, and triazole bonds;^{126,127} however, the slow release and relatively low stability of ester bonds in the bloodstream exhibited by these systems have limited the implementation of amide and ester-linking strategies.¹¹⁴ More structurally advanced linkers provide site-specific drug conjugation and sensitivity to physiological gradients (e.g.,

temperature, pH, redox potential, hypoxia, presence of specific enzymes) or external stimuli (e.g., magnetic fields, photoirradiation, ultrasound, electric fields, temperature) (Figure 1.3).¹²⁸

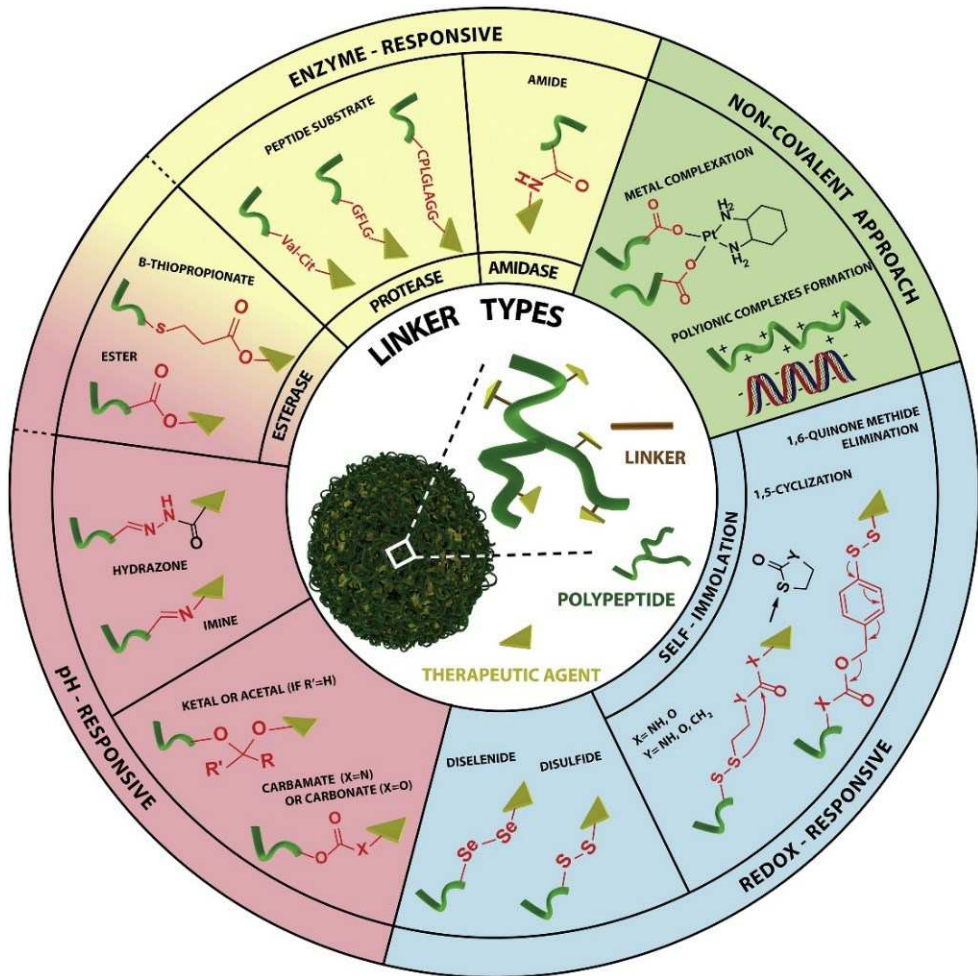


Figure 1.3. Advanced linking strategies employed in the rational design of polypeptide-drug conjugates. Reproduced from T.Melnik and S.Đorđević et al.²⁷

pH-sensitive linkers take advantage of low pH within the TME, inflammatory sites, and intracellular organelles involved in uptake represent the

most broadly implemented linking moieties.¹²⁹ Pyruvate and lactate produced by anaerobic glycolysis in the TME due to the hypoxic conditions result in a slightly acidic pH (< 6.7) compared to plasma and normal tissues (pH = 7.4)¹³⁰; however, insufficient pH differences between tumor and normal tissue may not permit targeted drug release leading to limited application of pH-responsive PDCs.¹²⁹ pH-cleavable linkers include hydrazone, orthoester, imine, acetal/ketal, and cis-aconityl bonds.^{131,132}

Second most common used linkers, disulfide linkers, provide redox sensitivity of PDCs, allowing stability in circulation where glutathione (GSH) levels are approximately 5-10 μM and cleavage in the cytosol of tumor cells or endosomes, where GSH levels may rise to 10 mM.¹³³ The incorporation of redox-responsive functionalities in the absence of thiol groups employs synthetic strategies that may involve using self-immolative linkers that undergo degradation in response to a reductive environment resulting in drug release.

Proteolytic enzymes play critical roles in the early and progressive stages of cancer and degenerative disease.^{134,135} For instance, the TME of certain cancers possesses high levels of lysosomal cysteine proteases such as Cathepsin B,¹³⁶ which efficiently triggers the cleavage of sequences such as glycyl-penylalanyl-leucyl-glycine (GFLG), valine-citrulline, or biotin-avidin¹³⁷, and papain, which digests substrates as glycine-glycine-leucine (Gly-Gly-Leu)¹³⁸. Overexpression of the cysteine-related protease cathepsin K in bone tissue resorption sites suggests a potential implementation in therapeutics for the treatment of osteoporosis, prostate or breast cancer bone metastases, and other bone-related pathologies.¹³⁹⁻
¹⁴¹ Pan et al. explored the potential of cathepsin K mediated cleavage of a Gly-Gly-Pro-Nle peptide linker in polymer-drug conjugates¹³⁹; however, Cathepsin K remains unutilized as the trigger in PDC design.

Strong ionic bonding between metals and carboxylic group-bearing polymeric chains have been widely employed in nanomedicine design as a part of linking chemistry. Metal complexation represents the most straightforward method to obtain platinum-based drugs, with examples in clinics such as PDCs.¹⁴² PGA and PAsp possess innate and substantially more robust complexation capabilities than traditional encapsulation and display a higher degree of responsiveness at lower pH due to the protonation of carboxylic groups involved in Pt-based drug release.

1.3.4 Stability

Nanomedicine instability can lead to significant clinical consequences, such as agglomerations following intravenous administration, which may lead to an embolism within the pulmonary microvasculature and low therapeutic efficacy due to the altered homogeneous distribution of the active moiety.¹⁴³ Therefore, stability over time represents an essential parameter for PDCs and any nanomedicine from two aspects – i) chemical stability (stability against chemical degradation after freeze/thaw cycles and under storage conditions) and ii) physical stability, which refers to agglomeration and aggregation.

Factors that negatively affect the chemical stability of PDCs during synthesis, under storage conditions (e.g., alterations in pH, humidity, temperature, oxygen concentration, the addition of electrolytes, and light exposure), or in plasma require identification and control. Low plasma chemical stability leads to drug release in the bloodstream due to carrier degradation or linker between the drug

and a carrier and requires the quantification of the free drug *versus* the bound drug.^{144–146}

Ideally, the final product formulation must maintain physical stability after incorporating an active, targeting, and/or imaging moiety into a carrier.¹⁴⁷ The evaluation of physical stability involves the determination of the radius, size distribution, surface charge, and morphology under storage conditions or in biological fluids. Recent FDA guidelines reported the importance of “protein corona” characterization, the absorbed plasma proteins to the surface of nanomedicines that may lead to destabilization or an increase in size.¹⁴⁸ Therefore, size stability in biological media may affect the efficacy and safety of PDCs due to the protein corona formation and/or aggregation; therefore, this factor represents a crucial quality parameter.

The protein corona can affect biodistribution by negatively impacting targeting. Thus a detailed analysis and/or careful engineering of the protein corona may improve parameters affecting therapeutic outcomes, including targeting, toxicity, biocompatibility, disease detection, and payload capacity.¹⁴⁹ Exploiting hydrophilic polymers such as PSar, which increases biocompatibility by reducing the non-specific interactions with biological components, represents a common means to control protein corona composition.^{150–152} Additionally, the protein corona formed around intravenously injected DDSs becomes enriched with disease-specific proteins, which conventional proteomics cannot detect. Studies have provided evidence of disease detection through protein corona molecular fingerprinting and biomarker discovery.¹⁵³ The detection of disease-specific proteins represents a promising step in discovering novel diagnostic biomarkers, as demonstrated by Kostarelos et al..¹⁵⁴ They evaluated the ability of proteins to bind to amphotericin B-containing liposomes (AmBisome®) used to treat fungal infections and discovered 67 potential biomarker proteins to differentiate non-

infectious acute systemic inflammation from sepsis. Apart from a large number of inert plasma proteins binding to the PDCs, functional proteins can undergo adsorption to the PDC surface to provide targeting functionalities. Said proteins include apolipoproteins (e.g., ApoA, C, and E) that direct the transport through lymphatic and circulatory systems^{155,156} or those (e.g., ApoE, ApoJ, and ApoA1) that direct brain targeting^{157,158}.

1.3.5 Drug loading

The polypeptide carriers of PDCs should provide minimum toxicity, biocompatibility and biodegradability, and high drug-loading capacity. Drug loading capacity mostly depends on i) the polypeptide carrier type, ii) the PDC synthetic process, iii) the interaction between the carrier and the drug (the linker type used or the charge effect between the carrier and the drug), iv) the carrier Mw and architecture, and v) the choice of active moiety.^{159,160} Therefore, each drug/active moiety requires a custom carrier with specific and optimized physicochemical features and a specific synthesis approach to obtain efficient and optimized loading.

While the covalent attachment of drugs to a polypeptide backbone usually represents a random process that influences heterogeneity¹⁶¹, the accurate determination of drug loading represents, alongside free drug content, a parameter of utmost importance. The progression to biological characterization for a given PDC requires a free drug content of less than 2 wt% of total drug loading.³⁹ At the same time, the determination and close control of loading capacity influence drug release and, consequently, the effect of PDCs.¹⁶²

1.3.6 Drug Release Kinetics

The when, where, and how of active moiety release from PDCs represents another critical issue in the rational design of PDCs. In the case of plasma instability and drug release in circulation, the effect of PDCs may approach the effect of small drugs due to the loss of the EPR effect. At the same time, high levels of stability lead to altered drug release at the site of action and low antitumor activity. The required drug release rate will differ depending on the target. For instance, PDCs used for hematological malignancy treatment demands prolonged circulation times and release in lymph nodes, bone marrow, and spleen. The successful treatment of solid tumors also requires homogenous tumor distribution, adequate accumulation, and retention to provide a drug depot at the site of action.¹⁶³

Drug release behavior from PDCs depends on physicochemical parameters such as linker type, size, conformation, and accessibility of the trigger to the linker and requires investigation on a case-by-case basis. Nevertheless, we generally consider that the effective treatment of any disease by PDCs occurs through a prolonged release mechanism that maintains the therapeutic concentration longer while minimizing the risk of toxicity from high local dose.¹⁶⁴

Drug release from PDCs may follow various release kinetics profiles. Zero-order kinetics represent the most favorable situation, leading to a constant drug concentration between minimum effective and maximum tolerant concentration. The initial burst release often observed with pH-sensitive linkers of unpredictable and uncontrollable nature may lead to initial toxicity related to the high local concentration.¹⁶⁵

Biosensitive drug-release studies aim to analyze the free fraction of drug released within complex scenarios - from a simple mixture of enzymes, cell

medium, or pH buffers (150 mM Cl and pH 7.4 to mimic blood and the TME; 20 mM Cl and pH 6.9 to mimic intracellular medium like early endosomes; 70 mM Cl and pH 5.5 to mimic late endosomes and lysosomes¹⁶⁶) to biological fluids such as plasma, cerebrospinal fluid (CSF), or urine.¹⁶⁷ These studies can monitor polypeptide chain degradation¹⁶⁷ and metabolite identification resulting from nanomedicine degradation to determine suitable administration routes and dose schedules.^{168,169}

1.4 MOLECULAR TALE OF PDCs, AS NARRATED BY ANALYTICAL CHEMISTRY

Due to the (poly)ionic and often proteinic nature of PDCs, their translation "from bench to bedside" can represent a complicated and expensive undertaking, requiring reproducible and scalable polymerization techniques, the implementation of sophisticated analytical tools, exhaustive characterization steps, and the collection of detailed safety and efficacy data. The variety of materials implemented and the complexity of synthetic techniques in designing PDCs require distinct methodological approaches to characterize the physico-chemical properties. Furthermore, the physico-chemical features require evaluation in relevant biological fluids (depending on the route of administration), where the presence of various molecules can modify a given nanomedicine and lead to degradation, agglomeration, or protein corona formation.¹⁷⁰ Ultimately, we require novel approaches to address the significant limitations found by regulatory agencies regarding the lack of pure, homogeneous, and well-characterized PDCs. Encouragingly, the Nanotechnology Characterization Laboratory (NCL - a resource and knowledge base for all cancer researchers in academia, industry, and

government to facilitate the development and clinical translation of nanotechnologies intended as cancer therapeutics and diagnostics)¹⁷¹ has issued a nanomedicine-relevant roadmap by establishing a trans-disciplinary evaluation infrastructure covering preclinical characterization procedures (chemical, physical, in-vitro, and in-vivo studies). We provide an overview of analytical techniques used for the physicochemical characterization of nanomedicines (including PDCs), highlighting NCL-approved techniques for the routine evaluation of critical parameters in Figure 1.4.

Analytical chemistry encompasses the simple qualitative or quantitative determination of a single constituent and finds use in situations that require a fully detailed description of the chemical constitution of complex and highly heterogeneous objects or situations involving multiply related but non-identical analytes (e.g., drug dimers and the identification of metabolites in release studies)^{172,173}. These situations further complicate methodology choice and development for PDC characterization, which may require combining two or more techniques to allow progression to biological evaluation.

Before moving into clinical trials, all nanomedicine candidates require characterization using straightforward, robust, and affordable analytical methods to ensure a high-quality product and control the physico-chemical characteristics (and other factors) that influence efficacy and safety. The integration of analytical techniques throughout PDC development supports pharmaceutical analysis, which involves measurements of "clean" sample solutions during the multistep synthesis and manufacturing process, and bioanalysis, which includes biological sample analysis through *in vitro*, *in vivo* studies, and clinical trials.¹⁷⁴

In the following sections, we will discuss the utility of recently reported analytical techniques for assessing PDC quality, physicochemical and biological characterization techniques, and the obstacles we currently face. We will discuss

considerations when implementing the mentioned techniques, the questions/problems arising during analysis, and how to rapidly and efficiently overcome these obstacles to foster rapid translation.

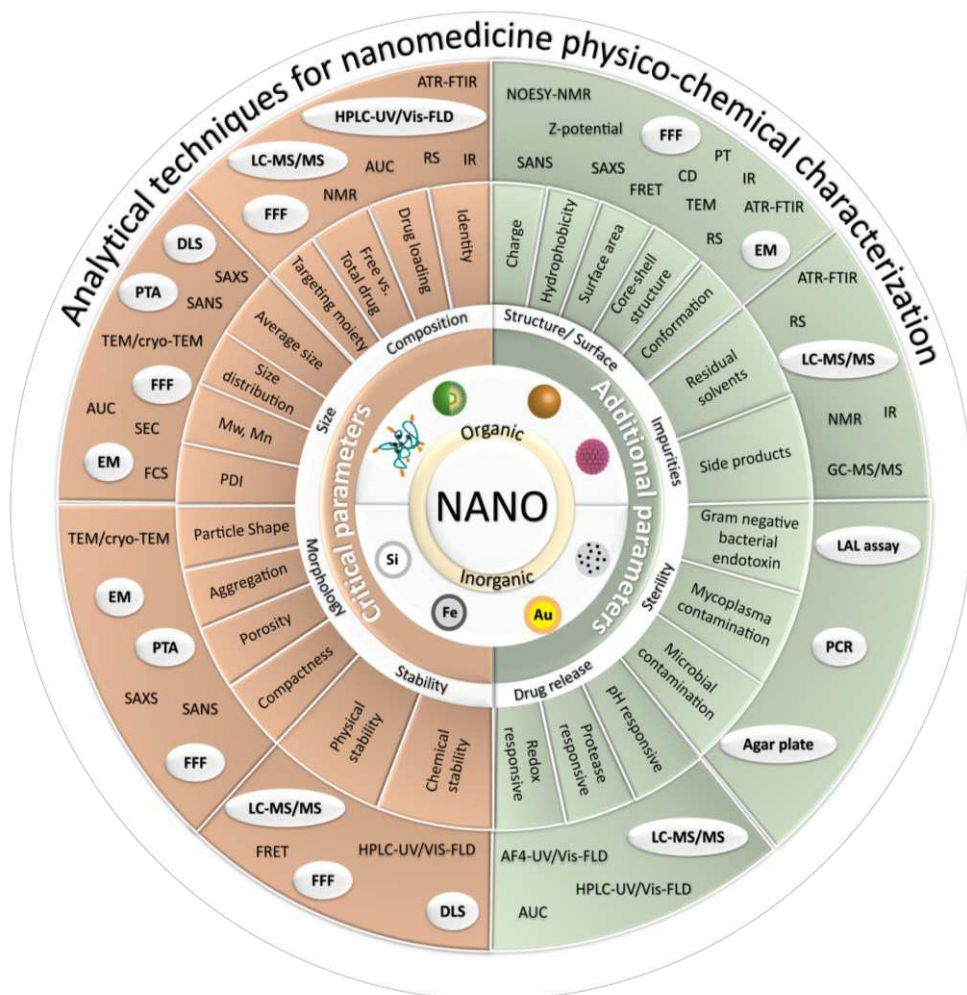


Figure 1.4. Critical nanomedicine parameters and corresponding analytical techniques for their characterization with highlighting NCL-approved techniques. (NCL – nanotechnology characterization laboratory; LC-MS/MS = liquid chromatography–mass spectrometry; Vis-FLD = visible-fluorescence detector; FFF = field flow fractionation; NMR = nuclear magnetic resonance; NOESY-NMR = nuclear Overhauser effect spectroscopy - nuclear magnetic

resonance; AUC = analytical ultracentrifugation; IR = infrared; RS = remote sensing; HPLC-UV = high-performance liquid chromatography – ultraviolet; ATR-FTIR = attenuated total reflection - Fourier transform infrared spectroscopy; SAXS = small angle x-ray scattering; SANS = small angle neutron scattering; CD = circular dichroism; FRET = fluorescence resonance energy transfer; EM = electron microscopy; TEM = transmission electron microscopy; Cryo-TEM = cryogenic transmission electron microscopy; PT = potentiometry; GC-MS/MS = gas chromatography–mass spectrometry; DLS = dynamic light scattering; SEC = size-exclusion chromatography; AF4-UV = asymmetric field flow fractionation-ultraviolet; PTA = particle tracking analysis; FCS = fluorescence correlation spectroscopy; PCR = polymerase chain reaction; LAL assay = limulus amoebocyte lysate assay; Si = Silicon; Fe = Iron; Au = gold). Reproduced from S.Đorđević et al.²²

1.4.1 Insight into the bioanalysis of PDCs

The adequate design of bioanalytical studies can support the robust evaluation of a PDC's ability to reach the intended target tissue/cell. Bioanalyses as a part of PK and PD studies tackle cell viability, stability in biological fluids and the interaction with biological components, drug release studies, hemocompatibility, immunogenicity, cell-specificity, and *in vivo* efficacy and can even provide an understanding of the molecular pathways responsible for the pharmacological output. We will now discuss recent advances regarding emerging techniques and versatile bioanalytical methods that will provide valuable future insight during the biological characterization of PDCs.

1.4.2 The Interaction of PDCs with Biological Constituents

The charge represents the primary influence on the interaction of plasma proteins with PDCs, with a more pronounced effect observed for strong positive charges.^{175,176} Protein corona characterization usually employs sample incubation with bovine serum albumin (BSA) under physiological conditions or direct incubation in plasma. The BSA adsorbed to PDCs can be analyzed after precipitation and centrifugation, while bicinchoninic acid protein assay kits can determine free BSA (the fraction left in the supernatant). The protein precipitation method is relatively straightforward but suffers from disadvantages such as protein corona disruption and the loss of “real” information regarding adsorbed proteins. Thus, the experimental characterization of the protein corona remains challenging due to the system complexity and weak interactions between plasma proteins and PDCs.

Alternatively, field flow fractionation (FFF) may represent a robust option for analyzing nanomedicine-protein complexes without prior sample preparation, as the complex remains intact in the FFF channel. Multi-angle light scattering (MALS) detector coupled with asymmetric flow FFF (AF4) and proteomics analysis by mass spectrometry (MS) has been implemented in the analysis of the size and PDI of three core-crosslinked polymeric nanoparticles with long circulation times (N-(2-Hydroxypropyl)methacrylamide - HPMA, PSar, and PEG) to study their interactions with plasma proteins.¹⁷⁷ The implementation of fluorescence correlation spectroscopy represents another option; this approach facilitates size monitoring in complex biological matrices and can evaluate the impact on serum protein adsorption by determination of hydrodynamic size.¹⁷⁸ Nevertheless, this technique requires the labeling of molecules with a fluorophore.

A supplementary *in silico* method, molecular dynamics simulation (MDS), has emerged as an alternative method to assess the interaction of albumin with hydrophilic polymers. MDS is based on the approximations of the underlying interactions between the atoms of two molecules¹⁷⁹, where atom velocities and their position in the simulated system derive from Newton's equations of motion¹⁸⁰ and an empirical force field¹⁸¹. MDS represents a valuable tool for the design and optimization of drug candidates and polymeric structures and has been employed, for instance, to evaluate the impact of surface modifications of mannosamine-conjugated multifunctional PGA-dendrimers as nanocarriers of the MART-1, gp100:44, and gp100:209 tumor-associated antigens and their dynamic interactions with target receptors.¹⁸² Additionally, researchers implemented MDS to study the adsorption dynamics and the effect of protein adsorption on the conformation of PEG¹⁸³ and polypeptides such as PSar and PAla¹⁸⁴. These studies reported that PEG and PSar developed a similar interaction pattern with the protein surface regarding the interaction's affinity and intensity. PAla and a polymer isomer of PSar known to self-aggregate and induce protein aggregation displayed a greater affinity for the protein surface than PEG and PSar, which they attributed to how the polymer interacts with water and, in particular, to the tendency of the polymer to reduce the surface exposed to water by self-aggregating or adsorbing to the protein surface.¹⁸⁴ These examples demonstrate MDS's ability to predict the protein corona's composition and influence on polymer targeting and efficacy.

Interestingly, the binding of plasma proteins to polypeptides supports prolonged survival times in human serum without having to use initial polypeptides with increased molecular weight. Human serum albumin (HSA) binding to a set of polypeptides of varying charge, size, and hydrophobicity, covalently linked to 3,5-bis [[bis(2pyridylmethyl)amino] methyl] benzoic acid, a zinc chelator, increased due to the targeting of zinc-binding sites on HAS.¹⁸⁵ Binding affinity evaluation used

surface plasmon resonance with HSA covalently immobilized on a sensor chip, according to observed uptake and off-rates on sensorgrams. The results indicated that Zn²⁺ ion chelating agents might provide a general route to increased survival times of peptides in serum in therapeutic and diagnostic applications.¹⁸⁵

Apart from serum proteins, studies have also evaluated interactions of PDCs with GSH.¹⁸⁶ GSH, an endogenous sulfur-containing molecule, can bind to and detoxify many heavy-metal ions, including Pt-based drugs.¹⁸⁷ For example, the Pt-S bonds formed upon the reaction of free cisplatin (CDDP) with GSH increase absorption at 260 nm, thereby making UV spectroscopy an easy and effective technique for monitoring time-dependent absorption and reaction degree.¹⁸⁸ He et al. revealed that a PGA-CDDP conjugate reacted with GSH to a lesser extent when compared to free CDDP, possibly because the conjugation of CDDP to PGA slows the substitution kinetics of the Pt-S complex. Additionally, the authors stated that the spherical structure of PGA-CDDP acted as a shield against GSH detoxification.

1.4.3 Pharmacokinetics

Determining the bioactive moiety and carrier concentration in biological fluids represents an essential part of PK studies; however, detecting the active moiety and polypeptide as a single entity remains challenging. Thus, the determination of free/released active moiety levels often occurs in bodily fluids. The separation of “free” from “bound” drug fractions usually employs solid-phase extraction, liquid-liquid extraction, size exclusion, ultrafiltration with a molecular weight cut-off centrifugal filter, AF4, and liquid chromatography.^{189–195} After the separation, the NCL recommends the LC-MS/MS method to quantify free drug amounts by implementing reference standards in the European pharmacopeia

monographs specific to the individual drug. Recent PK profiles research of a range of PEGylated polypeptides conjugated to therapeutic protein granulocyte colony-stimulating factor (G-CSF)¹⁹⁶ or doxorubicin (DOX)¹²² during *in vivo* studies highlighted the use of UV-Vis, fluorescence, charge aerosol detectors, and ELISA kits as an alternative for the determination of free drug concentration in biological fluids. After intravenous administration of PEG-PGA conjugates, the authors quantified G-CSF concentration in serum using a Human G-CSF ELISA Kit; the derived PK data established a comparable/slightly better bioavailability and bioactivity between two PGA-PEG20G-CSF conjugates (with different PGA block length) compared to the commercial Pegfilgrastim (PEG-G-CSF). Finally, as expected, the study demonstrated that a negatively-charged PGA block prolonged the half-life of G-CSF. In another related study, Kaminskis et al. used HPLC and SEC for the PK evaluation of DOX or a dendrimeric PEG-PLL-DOX administered to the lungs via liquid instillation.¹²² Fluorescence HPLC determined total DOX concentration in plasma, bronchoalveolar lavage fluid, and lung tissue, while the implementation of SEC in degradation studies detected dendrimer scaffolds and low Mw breakdown products in plasma and urine. These studies revealed a two-fold more rapid clearance of DOX-PEG-PLL dendrimer conjugate compared to the free dendrimer, suggesting that DOX becomes gradually liberated from the PEG-PLL dendrimer scaffold and eliminated. Low Mw breakdown products formed a significant part of dendrimer excreted in the urine, although the authors detected small amounts in six- and seven-day plasma samples and in lung tissue homogenate supernatant. Furthermore, recent research has emphasized analytical ultracentrifugation as a straightforward and rapid method for the separation and determination of free and bound drug fractions in a single measurement.¹⁹⁷

We can exploit the ability of the matrix-assisted laser desorption ionization–time-of-flight (MALDI-TOF) technique to detect polypeptides in

metabolomics-based analysis and the detection of degradation products and has already been applied to the quantification of drug metabolites in paclitaxel conjugated to PGA (PGA-PTX) and HPMA-PTX conjugate drug release studies.¹⁹⁸ While matrix effects from amino acids present in biological fluids deserve consideration during the analysis of polypeptide metabolites, we generally lack information on this type of analysis, which opens opportunities for new analytical methods and data analysis to eliminate the naturally present amino acids that may interfere. NMR in metabolomics has become a relevant tool for understanding the molecular mechanisms involved in responses to anticancer therapies; however, no examples currently exist for PDCs. During the *in vitro* and *in vivo* studies of DOX/HPMA-DOX, Armiñán et al. employed NMR-based metabolic profiling to evaluate the biochemical pathways involved.⁴⁷ Experiments in MCF7 cells revealed metabolic changes in response to the altered cellular trafficking of free DOX (diffusion) and the HPMA-DOX (lysosomotropic drug release and endocytosis).⁴⁷ NMR metabolomics in combination with other qualitative techniques (such as MALDI/TOF imaging, MS with separation techniques such as LC, GC, supercritical fluid chromatography, and capillary electrophoresis)¹⁹⁹ may represent the first step forward to a rapid, effective, and non-destructive means to characterize the efficacy and toxicity of PDCs.

1.4.4 Sample preparation

Biological samples contain organic molecules (e.g., proteins, enzymes, hormones, and cytokines) and inorganic salts (e.g., phosphate and bicarbonate buffer, sodium chloride, potassium chloride, or ion complexes with organic molecules).²⁰⁰ The implementation of one or more analytical procedures in preparing these complex biological samples occurs for one purpose – to recover the highest amount of analyte while simplifying the sample matrix (the constituents of

sample excluding the analyte of interest). The complexity of the process represents a significant source of errors that influence sensitivity and accuracy.²⁰¹ The uncertainty of measurement devices, the precision of the analytical chemist, and the inter-lab, inter-day, and intra-day repeatability and carry-over effects contribute to these errors, and they require detection and evaluation in any bioanalysis.²⁰²

The typical implementation of HPLC coupled with various detectors supports quantitative and qualitative analyses. As LC columns cannot handle high matrix complexity and detectors remain incompatible with some matrix components (e.g., salts and mass spectrometer), analytes become extracted from the matrix and often concentrated.²⁰³ Liquid-liquid extraction and solid-phase extraction in manual sample preparation before analysis can remove possible interfering compounds that coelute with the analyte under analysis and minimize matrix effects. Notably, we require alternative sample preparation methods, given the labor-intensive and expensive nature of those currently used. Herodes et al. proposed a simple protein precipitation method in methanol to prepare plasma samples and the chromatographic separation of metanephrine and normetanephrine.²⁰⁴ The authors minimized matrix effects derived from plasma constituents and achieved necessary quantitation limits through simple protein precipitation and sample extract dilution.

Implementing an on-line automated sample preparation known as the “column switching” technique (involving the hyphenation of two or more columns) represents an exciting alternative to support sample clean-up acceleration and eliminate human error during sample preparation.²⁰⁵ This strategy has been implemented in the determination of drug levels in biological samples and has found use in simultaneous analyte enrichment and analysis for antidepressants, anticonvulsants, anxiolytics, and antipsychotics in plasma samples from

schizophrenic patients²⁰⁶, antihypertensive drugs of different pharmacological classes and their metabolites in human serum²⁰⁷, nucleoside drugs such as lamivudine, zidovudine, didanosine and emtricitabine in human plasma²⁰⁸, psychotropic drugs²⁰⁹, and for pharmacokinetic evaluations of absolute bioavailability and dose proportionality of bavachinin²¹⁰.

1.4.5 Sample analysis

Chromatographic methods with high selectivity, significant separation efficacy, and rapid analysis represent an irreplaceable and most widely applied technique in bioanalysis.²¹¹ Chromatography has undergone a century of development and represents the most effective and standard method for analyzing a range of analytes in a complex mixture. The careful consideration of column (e.g., silica purity, pore diameter, column length, and separation surface), mobile phase composition, and additives support successful separation. Metal ion impurities in silica columns cause peak tailing and loss of resolution, which entails the use of high-purity silica columns or high concentrations of ion-pairing agents (trifluoroacetic acid - TFA - or triethanolamine). Nevertheless, elevated levels of TFA can cause a signal reduction in the negative ion mode of MS detection, thereby requiring the use of a column with high purity or a lower TFA concentration (0.05% or lower). Absorption in the low UV region and the resultant upward baseline drift represents another concern when using TFA or other additives in the mobile phase, especially in the low concentration region when using a gradient. In this case, adding an ion-pairing agent in the organic phase and using a flat baseline are recommended. Using a small pore diameter (100 angstroms) results in the inferior separation of molecules with low Mw; in contrast, wide pore silica columns can help to analyze higher molecular weight compounds (more than 3 kDa). For example,

the simultaneous analysis of drugs, targeting moieties, and PDC metabolites in release studies require a column with a higher pore diameter (300 angstroms). Two or more analytes in the sample generally require the use of longer columns; however, longer columns will not induce better polypeptide retention as they do for small drugs, as the peptides will only interact with the silica surface at the top of the column.²¹²

In addition to sample preparation, the calibration solutions used in the quantitative analysis represent critical factors in method development. In which concentration range and how are the standard solutions prepared? What type of matrix is used? Was standard addition or the internal standard method used? Interestingly, many articles that calculate recovery (R) do not specify the mode of implementation of these values in the study. An adequate recovery value (70% or more) remains insufficient; instead, one must take the R-value in calculating concentration or use a matrix-matched calibration solution. Obtaining a matrix-matched calibration solution (e.g., CSF or tissue extraction) can represent a challenging task; in this case, a surrogate matrix that mimics the composition of the real matrix (instead of using a simple matrix such as MilliQ water) is recommended.²⁰²

The analyte characteristics, sample preparation, and method optimization determine sensitivity; however, method sensitivity may remain insufficient to detect analytes in biological samples. For example, the concentration range may not support stability studies in plasma that aim to determine free drug content, with detector choice as an essential factor. The interference of coeluting components from the biological matrix represents another cause for reduced sensitivity, which remains critical to the recovery of the analyte while removing matrix components efficiently. Other challenges include inadequate detector response to different compounds (e.g., weak ionization in MS) or matrix effects.

Aubry et al. suggested optimizing three key factors to resolve these problems and develop a sensitive method: i) proper sample preparation, ii) adequate column choice for a specific molecule to obtain an excellent chromatographic separation, and iii) improvement of detector signal.²¹³

The low concentrations of analytes common to bioanalysis can exacerbate the above-noted problems; therefore, the combination of chromatography with MS increases sensitivity and provides qualitative analysis. The sensitivity of analytical methods employed in determining TDL, free drug, release kinetics, and stability testing remains crucial in nanomedicine and PDCs analysis. The method development, sample preparation, and detector choice represent crucial factors for said studies. The International Council for Harmonisation (ICH) of Technical Requirements for Pharmaceuticals for Human Use has recognized the significance of method sensitivity and prompted the development of the “Q14 Analytical Procedure Development Guideline”.²¹⁴ The ICHQ14 guidelines aim to harmonize scientific approaches and facilitate efficient analytical procedures. Furthermore, ICH quality guidelines represent an excellent starting point to foster more reliable pre-clinical results. Careful quality control of complex PDCs with fit-for-purpose analytical methodologies can improve the repeatability and quality of pre-clinical studies and the reproducibility of clinical efficacy.

Analytical data validation, especially from biological sample analysis, fundamentally supports the subsequent safety and efficacy of either active moiety, or PDCs. While sophisticated techniques such as LC-MS offer a range of mass scanning and analysis, they often suffer from high complexity and a lack of robustness. Therefore, we must demonstrate that the developed method fits a specific purpose. The “Guideline on Bioanalytical Method Validation, 2008” by the EMA and “Guidance for Industry, Bioanalytical Method Validation, 2001”, by the FDA provide generally accepted criteria that guide the validation of bioanalytical

studies. Nevertheless, these guides are not mandatory in preclinical studies, and the parameters that must undergo evaluation can differ depending on the analytical method employed or the requirement for qualitative or quantitative analysis.²⁰² The determination of free and total combretastatin A4 (CA4) from a PEG-g-PGA-CA4 conjugate in plasma and tissue homogenate represents an excellent example of method validation for PDCs.²¹⁵ Zeng et al. developed and applied a simple, sensitive, accurate method with an intra- and inter-day variability of less than 15% to study PK and tissue distribution of the PEG-g-PGA-CA4 PDC in tumor-bearing nude mice.

1.5 AIMS

Considering all the above-described factors regarding PDC design and characterization, the research included in this Ph.D. thesis focuses on developing new analytical procedures that aid the selection of PDC candidates for further preclinical studies moving always towards a future clinical translation. We will implement an artificial intelligence tool (DoE) to develop appropriate analytical methods and optimize PDC synthesis. Moreover, we will explore relatively new techniques, such as AF4 and MSI, in developing new single and combination PGA-based PDCs and studying their biological fate as part of a search for efficient therapies in treating a range of unmet clinical needs such as metastatic tumors or spinal cord injury.

1.6 LIQUID CHROMATOGRAPHY- MASS SPECTROMETRY – THE GOLD STANDARD FOR QUANTITATIVE AND QUALITATIVE ANALYSES

Over 100 years since the development of the first mass spectrometer by Francis Aston (University of Cambridge, UK), the MS technique remains a vital research tool throughout the multifaceted life-sciences field.²¹⁶ The modern-day spectrometer exists in a form that Aston would be unlikely to recognize and performs tasks that surpass the wildest aspirations of the technology's pioneer. Developments in ionization, flight path, and analysis protocols in MS have helped to keep the spectrometer relevant. Key examples of these developments include electrospray ionization, which has enabled the conversion of analytes from solution into the gas phase without disrupting the molecule's natural conformation, which has led to an increase in the importance of MS in the pharmaceutical field.

Classical techniques, such as HPLC-UV or spectrophotometers (used in free drug determination, drug release, or total drug loading (TDL) determination), often cannot qualitatively and quantitatively analyze degradation products or metabolites. LC-MS methods may represent the solution to previously noted problems, as analyzing drugs, degradation products, or metabolites depends on fragmentation patterns and it offers apart from quantitative, the qualitative analysis as well.

1.6.1 The theoretical principle of LC-MS

Liquid chromatography-mass spectrometry (LC-MS) combines the separating power of HPLC with the detection potency of MS (Figure 1.5.). Differential interactions of molecules with a liquid mobile phase and the stationary phase (usually hydrophobic materials chemically bonded to a solid support)

represent the basic principle of HPLC. This analytical approach can be used in liquid-solid adsorption or liquid-liquid partition chromatography mode. In adsorption chromatography, the solute becomes separated between two phases according to the adsorption affinity to the solid stationary phase. In contrast, solute separation occurs according to the partition coefficient between two liquid phases (one mobile and one stationary phase carried on a solid surface) in partition chromatography. Adsorption chromatography represents the most commonly used technique and can employ a non-polar stationary phase (reversed-phase chromatography– RP-HPLC) or polar stationary phase (normal-phase chromatography – NP-HPLC). The choice of RP-HPLC or NP-HPLC depends on the analyte of interest’s chemical characteristics and the necessary degree of separation of two or more compounds.

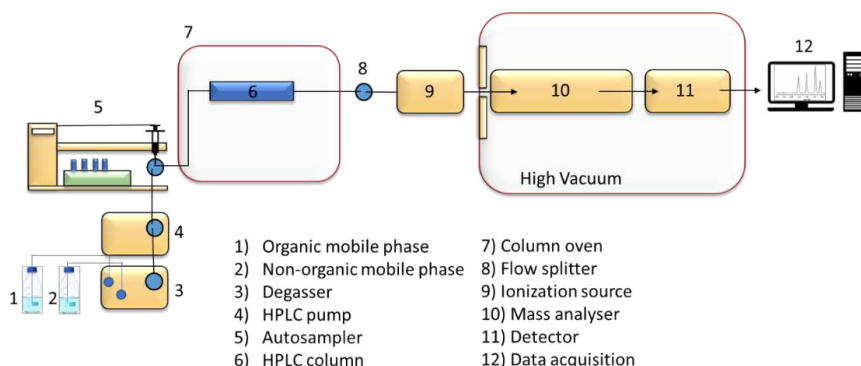


Figure 1.5. The working principle of liquid chromatography-mass spectrometry

As the analytes elute from the LC column, they arrive at a detector - an MS in the case of LC-MS, which supports the study of the masses of atoms, molecules, or molecular fragments. Generally, interfacing a liquid chromatograph with a mass spectrometer provides more significant challenges than other detectors (e.g., refractive index or UV-VIS detector). The relatively high amount of mobile phase eluting from the column requires using a flow splitter in the LC-MS instrument,

which takes only one part of the mobile phase and introduces it into the MS. The mobile phase and analytes must be volatile to perform MS analysis and avoid instrument contamination, with only volatile solvents (e.g., acetonitrile, methanol, or isopropanol) and buffers allowed as part of the aqueous mobile phase (e.g., formate or ammonium-hydrogen carbonate). There currently exist several types of interfaces (ionization sources) such as electrospray ionization (ESI - Figure 1.6A), atmospheric pressure chemical ionization (APCI- Figure 1.6.B) and MALDI (Figure 1.6.C) that can solve previously noted problems and make the combination of HPLC and MS techniques possible.

After ionization, the ions introduced into the mass analyzer become accelerated and separated according to their mass-to-charge ratio (m/z) by an electric field. Types of mass analyzers include quadrupole, ion trap, time-of-flight, triple quadrupole, orbitrap, and their combinations. The compact quadrupole ion trap (QTRAP) device, a widely used mass separator, is well suited as a chromatography detector. The principle of the QTRAP analyzer is based on the filtration of ions using electrostatic potentials applied to the mass analyzer elements that select ions according to their mass-to-charge (m/z) ratio. Removing non-selected ions from the mass analyzer means they remain undetected.²¹⁷

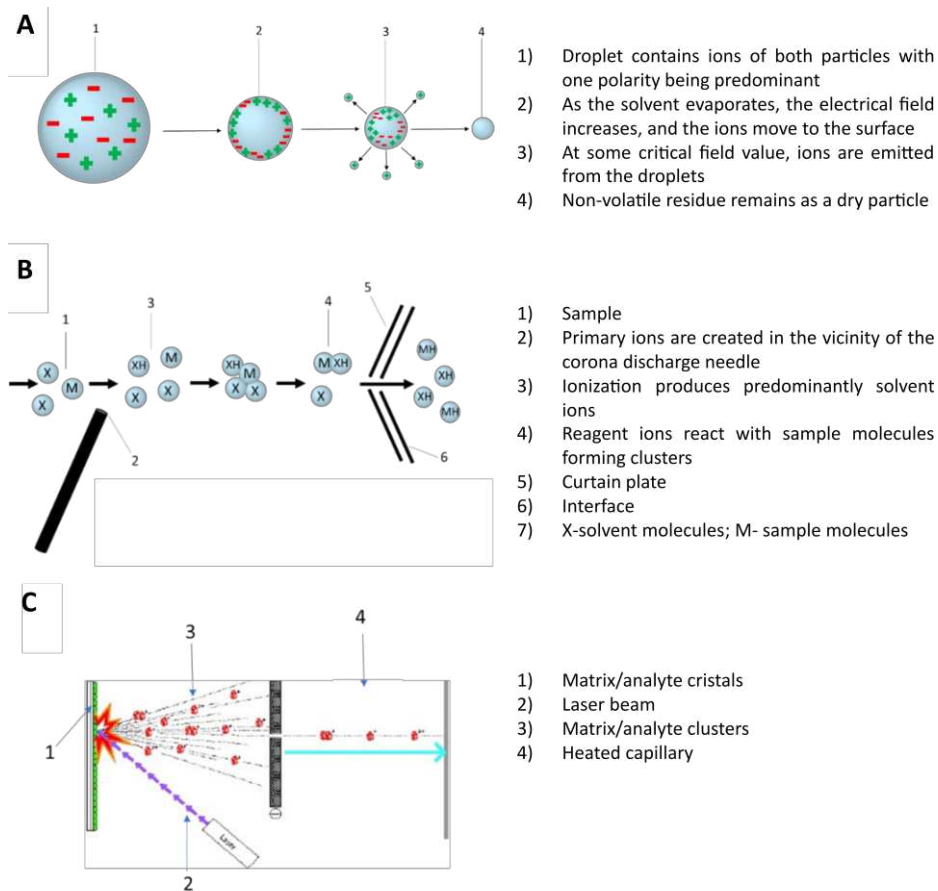


Figure 1.6. The working principle of ionization processes in MS (A) electrospray ionization, (B) atmospheric pressure chemical ionization, and (C) matrix-assisted laser/desorption ionization. Adapted from ABSciex Handbook²¹⁸

1.7 DESIGN OF EXPERIMENT – A ROBUST TOOL FOR METHOD DEVELOPMENT

The characterization of any analyte requires adequate method development to meet significant chemical and biological needs. Method development involves obtaining more rapid, sensitive, simple, informative, and

environmentally sustainable analytical methods.²¹⁹ Experimental planning, method validation, quality control, multivariate data analysis, and interpretation of results can foster better understanding and higher confidence in the obtained results.

The analytical protocols for PDC characterization involve numerous steps, from method development, sample preparation, sample analysis, and method validation to data analysis.²⁰³ Most often, scientists choose the most straightforward approach for the method development – (auto)tuning or the “one factor at a time” (OFAT). Autotuning (implemented using the manufacturer software) can help in cases that do not require high sensitivity, while the OFAT approach aids analysis when method parameters do not influence each other. Nevertheless, (auto)tuning and the OFAT approach remain insufficient, with the latter providing local knowledge (only about the performed experiment) and does not consider the interactions between variables.²²⁰ Using a design of experiment (DoE) approach to identify those factors that influence the results represents the most advisable and generally acceptable means to evaluate and optimize method variables; this strategy minimizes uncontrolled effects and uses statistical analysis to evaluate their impact.²²¹

The DoE term originated in the 1920s when the statistician Ronald Fisher emphasized the need to consider statistical analyses during research planning phases rather than final experimental stages. As he highlighted: “to consult the statistician after an experiment is finished is often merely to ask him to conduct a postmortem examination. He/she can perhaps say what the experiment died of.” DoE involves statistical analyses during the entire experimental process and can define the measurement outputs to improve, the process variable factors to change, the experimental procedures, the actual experimental performance, and the interpretation of results.²²² By this approach, we can adapt a process average in the desired direction, obtain a robust process (to make the outputs resistant to

uncontrollable process changes), obtain essential variables and control their effect on the process, and finally learn of and discard non-essential variables/factors from the optimization process.

Overall, DoE represents a structured, organized method for the determination of the relationships between variable factors affecting the process outputs and requires seven distinct stages according to National Institute of Standards and Technology Handbook²²³:

- I. Setting solid objectives – using a base derived from personal technical experience and scientific literature, set a clear quality target product profile, and define the goal (screening, characterization, or optimization of a specific process)
- II. Selecting process variable factors and outputs – based on the first step (definition of DoE objective) and must ensure the selection of factors (either categorical or numerical) and their levels accordingly (design space)
- III. Selecting an experimental design – based on the defined DoE objectives (screening, characterization, or optimization of a specific process), choose between several Doe design types (e.g., factorial, response surface, or a combined) and generate a design matrix (list of experiments with variable levels of factors)
- IV. Executing the design– the generated design matrix should be random, executed accurately, and ensure the identification of factors not included in DoE
- V. Confirming data consistency with experimental assumptions – identify and remove outliers or repeat DoE
- VI. Analyzing data – use ANOVA and graphical tools to identify the main effect of significant factors and their interactions
- VII. Interpreting results – execution of confirmation runs, augmenting the design space, or proceeding with scale-up or technology transfer

Although some researchers remain relatively unaware of DoE's power, there exists a body of literature resources implementing DoE-based approaches to the optimization of related procedures²²⁰, especially in LC-MS²²⁴. Kurve et al. optimized their LC-MS methodology and minimized matrix effects by implementing DoE to achieve high sensitivity, low detection limits, and acceptable accuracy in the analysis of thiabendazole, aldicarb, and imazalil levels.²²⁵ Adjustment of the electrospray ionization source and mass spectrometer parameters reduced (but did not eliminate) matrix effects, while factorial design provided a means to define optimal conditions for the lowest matrix effects.²²⁵

1.8 ASYMMETRIC-FLOW FIELD-FLOW FRACTIONATION – A POWERFUL TOOL FOR THE PHYSICO-CHEMICAL CHARACTERIZATION OF PDCs

Asymmetric FFF (AF4) represents a promising method for nanomedicine characterization due to the gentle and sample-tailored separation inside the empty channel that maintains weak complexes such as nanoparticles and proteins. A broad literature base has reported affinity studies of nanomedicines with long circulation times to proteins by AF4.^{226–232} These examples, and existing AF4 standard operation procedures from the NCL²³³, demonstrate that coupling AF4 to MALS or DLS represents a powerful and robust analytical technique for characterizing nanomedicines (including PDCs) that may overcome limitations associated with traditional techniques.

Techniques such as dynamic light scattering (DLS), size exclusion chromatography (SEC) or gel permeation chromatography (GPC), small-angle neutron (SANS), X-ray (SAXS), and light (SALS) scattering, MALDI-TOF MS, scanning/transmission electron microscopy (SEM/TEM and cryo-TEM), or atomic force microscopy (AFM) provide information regarding size, average Mw, or conformation (Figure 1.7A). These features determine the biodistribution, clearance route, cellular uptake, and biological performance of PDCs.^{162,234–236} The size range for successful targeting and adequate half-life time differs depending on the administration route; however, we understand less about the influence of conformation, which also modulates final output.²³⁴

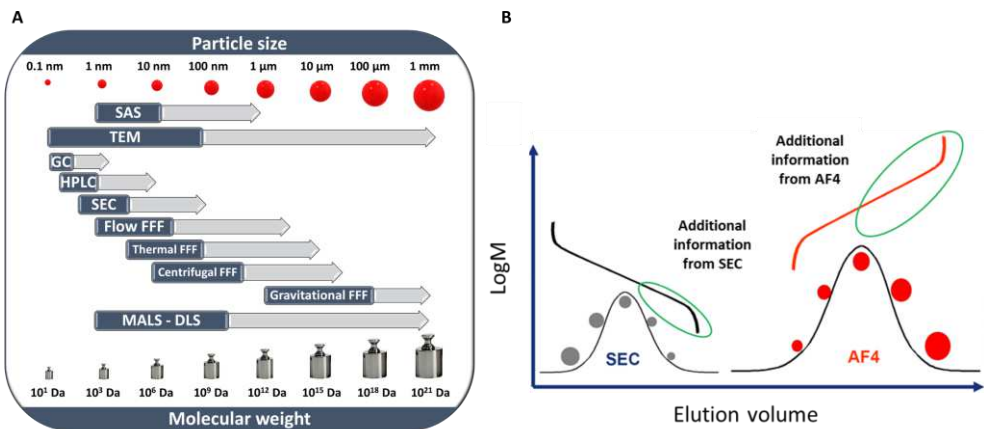


Figure 1.7. The comparison of AF4 with other techniques for size and Mw determination.

(A) Available techniques for analyzing size and Mw – the limits in Mw and size for each technique (B) Comparison of AF4 fractogram with SEC chromatogram (Reproduced with permission from Postnova Analytics GmbH). (SAS-small angle scattering, TEM-transmission electron microscopy, GC- gas chromatography, HPLC- high-performance liquid chromatography, SEC-size exclusion chromatography, FFF- field flow fractionation, MALS-multi-angle light scattering, DLS- dynamic light scattering, Mw- molecular weight). Used with minimal alterations from Melnyk T. and Đorđević et.al²⁷

While DLS represents a straightforward and rapid technique to implement, findings from complementary methods must support the results due to problems related to light absorption, large aggregates, mathematical calculations, and the available amount of the sample. DLS is generally employed for stability studies in biological fluids or phosphate-buffered saline (PBS) by following aggregate size and appearance.^{237–239} Nevertheless, free drug content assessed by HPLC coupled with different detectors represents an optimal indicator of PDC stability.²⁴⁰

Electron microscopy, particularly transmission electron microscopy (TEM), can directly image and characterize polypeptide-based systems of different sizes and shapes, including rod-like PGAs,²⁴¹ vesicular PEG-*b*-PGA-Dox conjugates,²⁴² polypeptide polyplexes,²⁴³ star-shaped PGAs (star-PGAs)²⁴⁴ or crosslinked self-assembled star-shaped PGAs.²⁴⁴ Depending on instrument potency, size can represent a limitation, while the low contrast of polypeptides can make TEM a tricky technique to implement. The need for sample preparation procedures that require the addition of conducting agents for imaging non-conductive materials and drying, diluting, and freezing, which can affect sample morphology, represents a drawback of microscopy-associated techniques.²⁴⁵

In this context, small-angle scattering techniques (SAS) represent highly complementary tools that support the study of the conformation of polypeptide-based systems in solutions that mimic physiological media. The possibility of sample analysis without prior sample preparation remains essential, given the intended use of such systems for biomedical purposes. Moreover, specific surface interactions in microscopic analysis can lead to surface-induced morphological changes, as exemplified by Miller et al..²⁴⁶ The authors demonstrated fiber formation in TEM analysis of an octapeptide, although SAS failed to provide evidence of self-assembly in solution.²⁴⁷ SAS allows the investigation of objects and features in the 10 to 500 nm scale and is particularly well suited to studying protein and polypeptide self-

assembly. For example, Zagorodko et al. established the presence of nanorod-shaped supramolecular species formed by StPGAs with benzene-tri carboxamide-based cores of different hydrophobicity using SAXS and SANS.²⁴¹ The obtained profiles demonstrated that StPGAs with hydrophobic cores behaved as typical polyelectrolytes at low concentrations but assembled into one dimensional-nanorods upon an increase in concentration due to supramolecular interactions in the molecule center. SAXS has also been successfully employed in analyzing the self-assembly of PLL into micelles in a study that investigated the influence of the degree of ϵ -PLL modification with octenyl succinic anhydride.²⁴⁸ Results suggested that the increased degree of substitution promoted micelle aggregation to form the larger particles previously seen by DLS. SAS can also provide information regarding how drug/linker conjugation influences the structure of PDCs in solution. Conejos-Sánchez et al. employed SANS to explore the formation of PGA-DOX conjugates with varying drug loadings.²⁴⁰ SANS revealed that differences in drug loading non-significantly influenced conjugate solution conformation, with all conjugates exhibiting similar *in vitro* activities; however, drug conjugation significantly changed PGA conformation. Arroyo-Crespo et al. used scattering data to investigate the structures of PGA-based combination-drug conjugates with fixed DOX content, and a varied amount of aminoglutethimide (AGM) conjugated through a glycine linker.²⁴⁹ While low AGM loading permitted sufficient flexibility to retain a helical conformation similar to unmodified PGA, high AGM loading prompted the formation of smaller, more globular structures with increased *in vivo* antitumor efficacy.

While sophisticated SAS techniques can provide valuable information regarding PDCs, the associated expense only permits analysis for selected candidates. Alternatively, techniques such as circular dichroism (CD)^{248,250}, SEC, or FFF coupled with light scattering detectors provide more manageable and more

accessible options to study secondary structures and may represent a valuable easy-to-implement alternative at the industrial scale.

Alongside MALDI-TOF^{251–253}, SEC and gel permeation chromatography (GPC) have been used for decades to estimate Mw, PDI, size, and purity of polymers produced for cells or living organisms and by chemical synthesis.²⁵⁴ While these techniques represent the method of choice for the characterization of polypeptides, including PSar and hybrid polypeptide materials^{196,249,255–259}, FFF has emerged as a complementary characterization technique given numerous advantages over SEC (Figures 1.7A and 1.7B), which include i) enhanced separation of high Mw molecules, ii) a lack of shear degradation and interaction with columns, iii) no requirement for calibrations curve obtained from standard materials not matching the analyte, iv) “tailor-made” separation by cross-flow adjustment, v) the adjustment of separation according to the unique requirements of a given sample (implementing a gradient of any shape), and vi) the ability to analyze gels and complex systems.²⁶⁰ To our knowledge, any examples of FFF-based characterization of PDCs remain unreported; however, entities such as the NCL have named AF4 analysis as a first-line characterization tool for the analysis of complex nanosystems.²³¹ As an example of a PDC “adjacent” system, Rebolj et al. demonstrated the need for two SEC columns to obtain comparable data to AF4 analysis of a PEG-G-CSF with a protein component of 18 kDa.²⁶¹

FFF separates particles over a wide range (nanometer to several micron scale) (Figure 1.7A) in a channel that pumps carrier liquid from the inlet to the outlet to establish a parabolic flow. An additional force applied perpendicularly to the primary flow direction forces the sample to accumulate towards the channel back wall, thereby inducing separation. The separation mechanism depends on the force applied; accordingly, FFF can be divided into the flow, electrical, centrifugal, gravitational, and thermal FFF techniques that separate components by

hydrodynamic diffusion, behavior in an electric field, chemical composition, mass, and thermal diffusion, respectively. Sedimentation (SdFFF) and magnetic (MgFFF) FFF have also been described in the characterization of ligand-decorated DDSs. MgFFF represents a necessary means to optimize magnetic DDSs^{262–265}, while SdFFF has been implemented in separating poly(d,l-lactic-co-glycolic acid) microspheres of different sizes²⁶⁶ and in stability studies after lyophilization and storage²⁶⁷.

FFF can be coupled with a range of detectors such as UV-VIS, refraction detector, fluorescence detector, multi-angle light scattering (MALS), viscometer, inductively coupled plasma–mass spectrometer (ICP-MS), or DLS. Separation generally occurs under mild conditions and can be applied to delicate samples of biological origin, such as proteins, protein complexes, and nucleic acids.²⁶⁸ A single measurement yields the size and concentration of each component in a mixture at high resolution without the problem of discriminating smaller particles, as in batch DLS.²⁶⁹ FFF can also analyze neutral and charged particles, a clear advantage for PDCs given their polyelectrolyte identity. The relationship between R_g (geometric radius) and M_w obtained from FFF-MALS can provide information regarding shape, where the slope of the logarithmic dependency indicates a sphere, random coil, or rod-like shape.²⁷⁰ Of note, developing a suitable fractionation method can represent a time-consuming experience; however, the implementation of experimental design (Design of Experiments or “DoE” approach) (see Section 5.3) can make FFF more accessible by a combination with theoretical models.^{271–273} During the characterization of PDCs, FFF combined with UV-VIS or fluorescence detection can evaluate drug loading. The collection and further characterization of fractions allow the detection of chain degradation metabolites, the visualization of particles and aggregates in different solutions, and the determination of total drug loading and release kinetics after separation. Adding a UV-VIS or fluorescence detector coupled to a waste line of cross-flow can allow the determination of levels

of any “free” unconjugated drug/moiety.²⁷⁴ Nevertheless, free drug concentration may lie under the detection limit, and membrane adsorption deserves consideration. FFF also has a significant advantage when coupled with ICP-MS regarding the analysis of metal ionic components of DDSs, impurities, or metallic nanoparticles toxicity in physiological fluids.²⁷⁵

FFF has also contributed to the analysis of pharmaceuticals and polymeric compounds as a quality control technique. Engel et al. reported one of the few validated AF4-MALS methods in drug delivery in determining poly(D, L-lactide-coglycolide) content in solid dosage forms and the quantitative analysis of particles during the release in a dissolution test.²⁷⁶ Although examples of FFF implementation in PDC characterization remain scarce, this technique represents an exciting alternative to SEC, and the number of relevant studies will likely continue to grow. A recent focus on protein corona analysis may enhance our understanding of nanomedicine safety and efficacy. Techniques other than AF4, which include distinct microscopy techniques²⁷⁷, have been combined to provide a more detailed picture of the protein corona’s biological effects^{149,278}.

Overall, the detailed analysis of nanoparticles in complex biological media represents a challenge to low-resolution size determination methods such as batch DLS. Therefore, the urgent need for methods that assess changes in physico-chemical parameters when a nanomedicine enters systemic circulation has prompted using FFF techniques.

1.8.1 The theoretical principle of AF4

Comprehending the basic principles represents an essential step in implementing AF4, especially for a complex analyte such as a PDC. As mentioned previously, AF4 differs from SEC mainly in the use of an empty separation channel instead of the column and the use of three flows: injection flow (F_{inj}), focus flow (F_{focus}), and crossflow (F_{cross}) (Figure 1.8.). The injected sample is carried to the channel by the F_{inj} , while the simultaneous effect of F_{focus} (the flow opposite to the direction of F_{inj}) and F_{cross} (flow with a force perpendicular to the F_{inj}) analytes are focused on the membrane wall (frit wall covered with the molecular cut-off membrane). As we used Postnova instrument design, we set the F_{inj} , F_{cross} , and outlet flow (F_{out} – the flow that reaches the detectors) while the F_{focus} is automatically controlled as given by $F_{focus} = F_{cross} + F_{out} - F_{inj}$.

Sample injection and focusing represent the first step in AF4 analysis (Figure 1.8A), with the time necessary for this process specific for each analyte and estimated using the following formula^{279,280}:

$$t_{inj} = \left(\frac{V_o}{3F_{cross}} \right)^{\frac{2}{3}} * \left(\frac{w^2}{D_i} \right)^{\frac{1}{3}}$$

where t_{inj} is injection time, V_o is the channel volume, D_i is the analyte's intrinsic diffusion coefficient, and w is the channel thickness. The instrument parameters w , t_{inj} , F_{focus} , F_{inj} , and F_{cross} must undergo optimization for each analyte due to the difference in D_i .

The sample fractionation follows the focusing step by turning off the F_{focus} while keeping the F_{cross} and F_{inj} (referred to as inlet flow – F_{in} – in this phase) (Figure 1.8B). The fundamental principle of AF4 separation is based on the nature of the

laminar flow, where the mobile phase's laminar layers move slower near the AF4 channel's bottom and top wall than the middle layers. The created parabolic flow velocity profile carries the individual particles through the AF4 channel while the F_{cross} simultaneously pushes them toward the accumulation wall. Small particles with large D_i values travel with the faster-moving laminar layers, while big particles with smaller D_i values travel closer to the accumulation order. As a result, small particles elute first, followed by larger particles at the end of the separation phase. The AF4 channel can be coupled with concentration detectors (UV or refractive index – RI) and light scattering detectors (MALS) and determine both the concentration, Mw, and radius of gyration for eluted peaks.

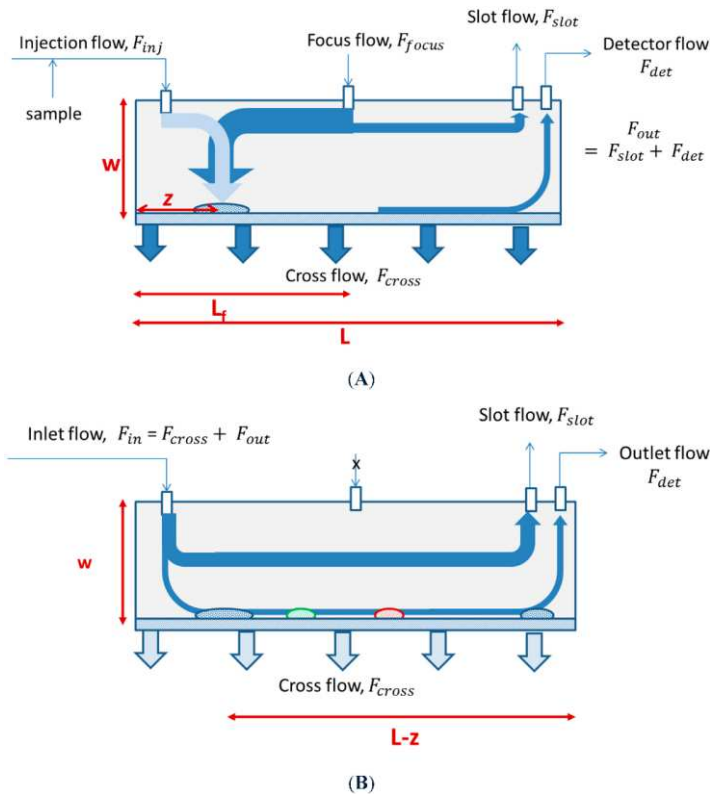


Figure 1.8. The working principle of asymmetric flow field flow fractionation during sample focusing (A) and separation (fractionation) (B). The injection flow (F_{inj}) leads the

injected sample from the autosampler into the separation channel. The focusing flow (F_{focus}) allows sample accumulation at the membrane wall (Mw cut-off membrane). The crossflow (F_{cross}) is pumped out through the accumulation wall leading to the sample fractionation. F_{out} becomes split at the end of the channel into a slot flow (F_{slot}) that removes the analyte-free upper laminar layers and the detector flow (F_{det}) that carries the analytes out of the channel to the detector and the fraction collector (if implemented in the instrument design)(L – channel length, z - the focusing point, w – the channel thickness). Used with minimal alterations from Kuklennyik et al.²⁷¹

1.9 MATRIX-ASSISTED LASER DESORPTION IONIZATION MASS SPECTROMETRY IMAGING

1.9.1 Mass Spectrometry Imaging

The biodistribution and the delivery of active moiety to target sites represent crucial issues for nanomedicine/DDSs, given that this property directly relates to their efficacy. Thus, one must undertake proof-of-principle studies early in development to demonstrate the delivery of the active drug at a necessary concentration.

The LC-MS/MS, an extremely sensitive and selective method, is considered a standard quantitative and qualitative analytical tool; however, the loss of information regarding the spatial distribution of the administered active moiety and metabolites in tissues represents a significant disadvantage of this approach. Alternatively, imaging technologies provide methods that compensate for the above disadvantage. Imaging with autoradiography often has been used classically in pharmacokinetic studies; however, this approach does suffer from problems,

including the need for radioisotope-labeled compounds and difficulties distinguishing the administered compound from metabolites.

While understanding the when, where, and how of drug delivery and release after PDC administration represents a complex task, this information guides design optimization and the choice of therapeutic dose and administration regimen.²⁸¹ Non-invasive imaging techniques require the conjugation of an additional moiety for monitoring purposes in tissues/cell compartments. Li et al. synthesized a macromolecular fluorophore by conjugating a small molecule NIR-II fluorophore (Flav7) to an amphiphilic polypeptide (poly[oligo(ethylene glycol) methyl ether methacrylate]- block-poly[2-amino-N₄-(2-diisopropylamine-ethyl)-l-aspartic acid] or P(OEGMA)₂₁-P(Asp)₁₆-iPr) that enabled visualization of tumor features by NIR-II fluorescence imaging.²⁸² Additionally, NIR-II fluorescence imaging monitored photothermal ablation on tumors in response to treatment. In a related study, Cheah et al. employed fluorescence in the *ex vivo* imaging of a zinc (II) phthalocyanine (ZnPc) derivative (Pc 1) conjugated to PGA (1-PG) in biodistribution studies.²⁸³ The authors semi-quantitatively analyzed the intensity of emitted fluorescence at different time points to establish that a large quantity of administered 1-PG and Pc 1 accumulated within the tumor, liver, and lungs. Additionally, fluorescence imaging studies identified the time point associated with the highest tumor accumulation of Pc 1 and 1-PG to initiate the photodynamic therapy.

The confocal immunofluorescence technique has been widely employed to analyze intracellular uptake of conjugates²⁸⁴, and a novel methodology based on fluorescence correlation spectroscopy (FCS) has recently been described²⁸⁵. By NIR dye labeling, FCS allowed the direct determination of the stability and half-life of PSar-based core-crosslinked micelles in blood circulation. This technique that does not require the separation of solid (cells) and liquid (plasma) components of the

blood, thereby maintaining the properties and integrity of the DDS under review, can estimate the concentration of the fluorescent species in blood, and can distinguish between free drugs and those contained within DDS due to their difference in size.

Recently, MS imaging (MSI) has become increasingly prominent in pharmacokinetic studies as a technique that resolves the issues of previously mentioned imaging techniques. MSI, a label-free, non-destructive technology for bioimaging, can determine the spatial distribution of biomolecules, drugs, and other xenobiotics in tissue sections, organs, and whole animal body sections.²⁸⁶ Furthermore, the tissue sections used for histology can undergo further analysis using MSI and MS/MS to identify and quantify analytes directly. Nevertheless, sample preparation and complex data analysis make MSI handling more challenging than traditional techniques in routine analysis; thus, we require further method development and adjustment to PDC analysis to position MSI as the reference technique to understand PDC biological fate among other applications.

MSI has found applications in the analysis of drug and metabolite distribution studies in tumor tissues^{287,288} and 3D cell cultures²⁸⁹, tumor vascularization²⁹⁰, antibody imaging in 3D colon-cancer cell cultures²⁹¹, the determination of treatment schedule and the combination therapy optimization^{292,293}, metabolic alterations, and biomarker discovery^{294,295}, and 3D imaging of tumors²⁹⁶ among many other notable applications. *In vivo* distribution studies of a polypeptidic micelle (NK105 - PEG-PAsp encapsulating PTX) in a pancreatic cancer xenograft model demonstrated that NK105 delivered more PTX to the tumor and less to neural tissues when compared to the free drug, thereby supporting greater anti-tumor efficacy and lower neurotoxicity.²⁹⁷ In a related study of the aurora kinase inhibitor - AZD2811, poly-D, L-lactide (PLA) – PEG nanoparticles encapsulated with AZD2811, and AZD1152- a water-soluble prodrug of AZD2811

Ashton et al. demonstrated that MSI permitted the monitoring of the free drug, the polymeric carrier, and the prodrug throughout the adenocarcinoma tumor during *in vivo* studies with nude rats bearing human colon adenocarcinoma (SW620) xenografts.²⁹⁸ The authors treated nude rats with a single AZD2811 (25 mg/kg), AZD1152 (25 mg/kg), or AZD2811 (25 mg/kg) dose on days one and three; MSI detected the free drug released from AZD2811 nanoparticles for up to six days after the last administration, indicating a sustained drug delivery. For comparison, the authors detected the active moiety (AZD2811) in the tumor at 2 and 6 h but not 24 h after treatment with the AZD1152 prodrug and AZD2811. Additionally, these studies demonstrated that AZD2811 nanoparticles specifically accumulated in colon adenocarcinoma, had a minimal impact on bone marrow pathology, and provided enhanced efficacy in preclinical *in vitro* models. These examples highlight the potential uses of MSI in the bioanalysis of nanomedicines. We anticipate that MSI will revolutionize the characterization of PDC biodistribution and PK data collection.

1.9.2 The theoretical principle of MSI

A study by Caprioli (1997) represents the earliest implementation of MSI, more specifically matrix assisted laser desorption ionization MSI (MALDI MSI) to biological samples, specifically, the imaging protein in regions of the rat splenic pancreas.²⁹⁹ Since then, the applications of MSI have encompassed a wide range of pharmaceuticals in 3D *in vitro* models, tissue samples, or even whole animal sections. A typical MSI experiment accelerates an ionization beam (the type depending on the implemented ionization source) toward the sample's surface to generate single charged ions from analytes present in the sample and acquires the mass spectra at defined x and y coordinates. Image reconstruction employs software (usually

provided by the instrument supplier) in which each pixel comprises a complete mass spectrum, MS/MS spectrum, or selected ion transition(s).

Several ionization mechanisms can generate ions for MSI, including MALDI, desorption electrospray ionization (DESI), laser ablation electrospray ionization, secondary ion MS, laser desorption ionization, and nanostructure initiator MS. The ionization technique employed in MS determines the nature of analytes detected (e.g., small molecules or proteins, polar or non-polar), while the ionization choice in MSI will also influence the spatial resolution that can vary from 1-200 μm (10-50 μm in most instruments).³⁰⁰

Since the work in this thesis is based on the implementation of MALDI-MSI we will focus on introducing the main principles and considerations regarding MALDI as an ionization source for MSI.

1.9.3 MALDI-MSI

MALDI represents a widely applied ionization technique in MSI-mediated imaging of drugs and metabolites in biological samples, as the technique covers a wide range of possible analytes.^{301–306}

In a well-designed experiment MALDI-MSI usually contains three steps (Figure 1.9):

- (i) **sample preparation** - a sample is collected, sectioned and coated with a laser energy-absorbing chemical matrix (MALDI matrix).
- (ii) **mass spectra acquisition** - the MALDI-matrix coated section is irradiated by a laser beam to ionize the analytes present in the sample

and analyzed by a mass analyzer (in our case time-of-flight TOF analyzer).

- (iii) **data processing** - the intensities of specific mass-to-charge (m/z) values are processed and plotted with spatial information and with a color gradient to create a MALDI MS image.

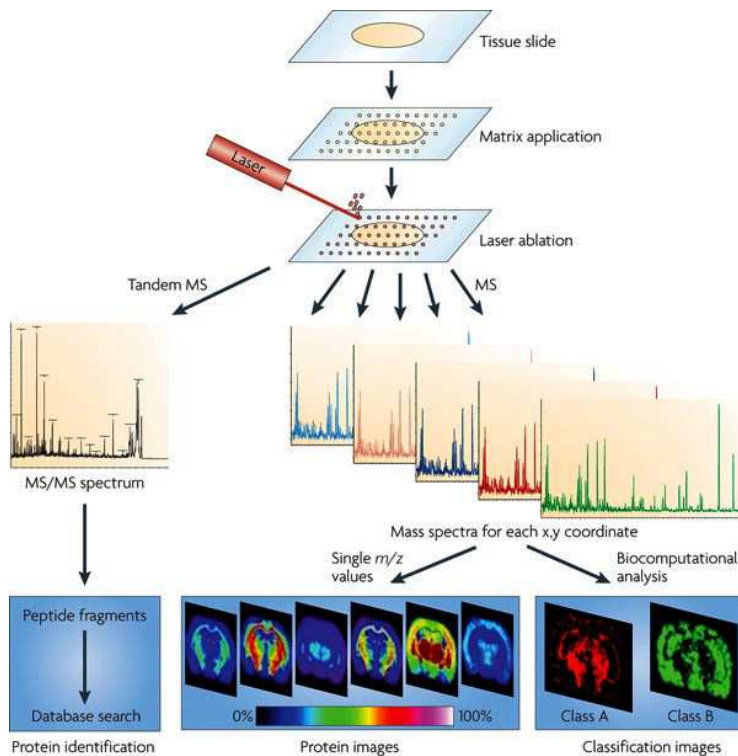


Figure 1.9. Schematic outline of typical MALDI-MSI workflow for fresh frozen tissue samples. The sample preparation process includes cryo-sectioning and mounting the tissues on a conductive slide, followed by matrix application. Mass spectra generated at each x and y coordinate for spatial analysis or fragmentation of MS spectra for identification. Further steps include the generation of MALDI-MS images displaying the distribution of a single analyte within the tissue as well as the biocomputational analysis for obtaining classification

images and database searching for analyte annotation. Used with minimal alterations from Schwamborn et al³⁰⁷

Sample preparation

Sample preparation is the first step to be considered and controlled to obtain a robust and accurate MALDI-MSI. The consistent sample collection and preparation and uniform sample coverage with the matrix are essential for the later MALDI-MSI analysis to be performed meaningfully.³⁰⁸ MALDI-MSI enables spatial molecular analysis in a broad range of samples, including spheroids in 3D cell cultures, tissue sections, whole body section, and even formalin-fixed and paraffin-embedded (FFPE) tissues.³⁰⁹ The sample preparation processes differ between these sample types, however some basic principles need to be considered in each case such as sample collection, sample sectioning, post-sectioning and ionization aiding treatments.

Generally, the rapid and consistent collection protocols are vital for all type of samples to prevent rapid delocalization or degradation of target compounds.^{286,310} MALDI-MSI is best performed on fresh, snap frozen tissue achieved by the implementation of different solvents depending on the sample type (its size and fragility). Snap freezing can be carried out in several different ways to ensure adequate maintenance of the tissue structure and minimal degradation. Essentially different solvent systems can be used to exert different temperatures on the tissue to ensure no tissue fracturing occurs. Typically, a snap frozen free-floating method in liquid nitrogen is performed for smaller samples and dry-ice chilled isopentane for bigger samples due to the faster cooling rate compared to liquid nitrogen. However, very fragile samples can be frozen in dry-ice chilled isopropyl alcohol to conserve sample integrity. Many other sample stabilization processes have been developed, such as dry-iced chilled hexane for freezing the

whole-body sections³¹¹ and FFPE samples³¹²; however, concerns are raised about the use of FFPE samples regarding delocalization of small m/z analytes due to the FFPE fixation process and the de-waxing before MALDI-MSI analysis. Post snap-freezing the samples are usually stored at -80°C and sectioned on the day of MALDI-MSI analyses.

Samples are usually sectioned at 10–20 µm, a thickness comparable to a mammalian cell. In this way, the majority of cells are cut open and MALDI matrix is allowed to co-crystallize with the content of the cells.³¹³ Usually, in histology experiments small samples are embedded with the polymer with an optimal cutting temperature (OCT polymer) that allows easier sample cryosectioning. However, the OCT may suppress the ion signal in MS experiments, thus either mounting the samples with a drop of water or gelatine may be implemented.³¹³ Recently, an alternative embedding procedure (especially for *in vitro* samples such as 3D spheroids) using hydroxypropyl methylcellulose and polyvinylpyrrolidone has been developed to permit precise cryosectioning and maintain sample integrity while offering ion suppression-free MALDI-MSI analysis.³¹⁴

As mentioned above, some steps may vary depending on analyte of interest in the MALDI-MSI such as the implementation of washing steps. So far, washing procedures of the mounted sections have been employed in the MALDI-MSI of proteins and peptides since the washing step will remove lipids and salts and consequently reduce peptide ions suppression that leads to higher method sensitivity. However, in the case when analytes such as lipids, metabolites and drugs are analyzed by MALDI-MSI, these washing steps should be avoided. The MALDI-MSI analysis of proteins and peptides are not the focus of this thesis but it is relevant to mention that native proteins can be detected with reasonable sensitivity up to around the 25–30 kDa mass range or larger by using on-tissue tryptic digestion. Moreover, a chemical derivatization prior matrix application may

be employed to increase the sensitivity of MALDI-MSI for the analysis of specific analyte such as drugs. For further information regarding, washing steps, tryptic digestion and chemical derivatization we refer the reader to the review by Diehl et al.³¹⁵, Cillero-Pastor et al.³¹⁶ and Zhou et al.³¹⁷.

Next step in the sample preparation process is application of the MALDI-matrix solution that usually consists of³¹³:

(i) a MALDI-matrix – an organic acid used to absorb laser energy in the MALDI source, leading to the explosive desorption of analytes held within matrix crystals.

(ii) an organic solvent (methanol or acetonitrile) to rapidly extract analytes of interest from the sample and allowing their co-crystallization within the growing MALDI-matrix crystals on the sample surface.

(iii) strong organic acid (e.g., trifluoroacetic acid when performing positive mode ionization) to increase the analyte ionization by enriching the surrounding media with protons.

These three components of MALDI-matrix solution together with MALDI-matrix application play a critical role in obtaining the high quality and high-resolution MALDI-MSI data. The most commonly used matrices for pharmaceutical applications are α -cyano-4-hydroxycinnamic acid (CHCA), 9-aminoacridine (9AA), 2,5-dihydroxybenzoic acid (DHB), and 1,5-diaminonaphthalene (DAN) due to their ability to extract and ionize well the drugs, small endogenous metabolites, and lipids.²⁸⁶ Matrix choice, matrix solvent and application process (spraying or sublimation) is mainly driven by the type of analyte needed to be imaged, reproducibility and homogeneity of crystallization and crystal size that directly influence the spatial resolution of MALDI-MSI images.³¹⁸ Matrices and their application methods are thoroughly reviewed by Perry et al.³¹⁸ and Calvano et al.³¹⁹.

Mass spectra acquisition

MALDI-MSI was conceived on TOF instrumentation but has since benefited from: high mass resolving power and less chemical matrix interference provided by Fourier transform mass spectrometry (FTMS);³²⁰ the separation of isobaric species by the addition of ion mobility;^{321,322} high spatial resolution with commercial sources now capable of 10 μm spatial resolution that can often be tuned further to near one micron;³⁰⁰ high spatial resolution without the expense of sensitivity by introducing the MALDI-2 laser (a secondary laser directed at the MALDI plume to increase sensitivity by ionizing the neutral ions in the MALDI plume)^{322,323}.

Data analysis

MALDI-MS images are large datasets that require data processing that converts raw dataset into a visualized form for analytes of interest. Data analysis is usually comprised of four steps³²⁴:

- (i) **data preprocessing** - baseline correction, noise reduction, normalization, spectra smoothing, and recalibration, which clean the spectra from baseline and background noise, facilitating the selection of peaks of interest.
- (ii) **data reduction** - peak picking or scale-space transformation
- (iii) **data representation** - univariate/multivariate statistics and clustering/classification algorithms to analyze and visualize the preprocessed data and to identify trends within the data.
- (iv) **postprocessing** - image magnification and coregistration with high-resolution microscopy images.

CHAPTER II

**A ROBUST AND PREDICTIVE PLATFORM
FOR THE CHARACTERIZATION OF NEXT-
GENERATION POLYPEPTIDE-DRUG
NANOCONJUGATES**

2.1 INTRODUCTION

Characterizing any analyte (including polypeptide-drug conjugates or PDCs) requires adequate method development to meet the associated chemical and biological demands. The control of PDC properties (e.g., structure, total drug loading (TDL), free drug (FD), drug release, and pharmacokinetics) requires multi-step analytical protocols involving method development, sample preparation/analysis, method validation, and data analysis.²⁷ Method development involves the acquisition of more rapid, sensitive, simple, informative, and environmentally sustainable analytical methods.³²⁵ Moreover, method validation, experimental planning, quality control, multivariate data analysis, and interpretation of results can foster a better understanding and provide higher confidence in the obtained results.

In this chapter, we explored the potential of the “design of experiments” (DoE) approach in simultaneously optimizing liquid chromatography–mass spectrometry (LC-MS/MS) methods for the quantitative determination of fasudil (FAS), a Rho-kinase inhibitor that can contribute to functional regeneration after spinal cord injury (SCI), as a free drug and a poly-L-glutamic acid (PGA) conjugate using a redox-responsive linker (PGA-SS-FAS).³²⁶ We also explored how DoE could optimize LC-MS/MS methods to quantitatively determine commonly used anticancer drugs. Our main aim involved screening LC-MS/MS methods to obtain an internal database from which users can select a single anticancer drug/combination of anticancer drugs and the LC-MS/MS conditions for their quantitative determination. This approach will provide confidence in obtained results, given that the best possible LC-MS/MS method supported data acquisition.

The specific objectives of this chapter aim:

Objective 1. LC-MS/MS method development for the quantitative determination of FAS as part of the characterization of the PGA-SS-FAS PDC used to promote neuroregeneration after spinal cord injury.

Objective 2. Tailor-made gradient LC method optimization for the quantitative determination of the free forms of sixteen anticancer drugs.

2.2 RESULTS

2.2.1 DoE in LC-MS/MS Method Development for the Quantitative Determination of Fasudil

LC-MS/MS method optimization by DoE first requires the optimization of LC conditions before MS factors due to their dependence on LC parameters. We performed multiple reaction monitoring scans following two fasudil (FAS) mass transitions ($292.4 \text{ m/z} \rightarrow 99.2 \text{ m/z}$ and $292.4 \text{ m/z} \rightarrow 129.0 \text{ m/z}$) with a 30 V collision energy in positive electrospray ionization mode to optimize chromatographic conditions (Figure 2.1.). We defined values for initial MS parameters - ion spray voltage (5500 V), temperature (750 °C), curtain gas (40 psi), nebulizer (gas 1 – 50 psi), and auxiliary gas (gas 2 – 70 psi) - to optimize LC parameters. Section 2.2.1.2 will describe the optimization of MS parameters.

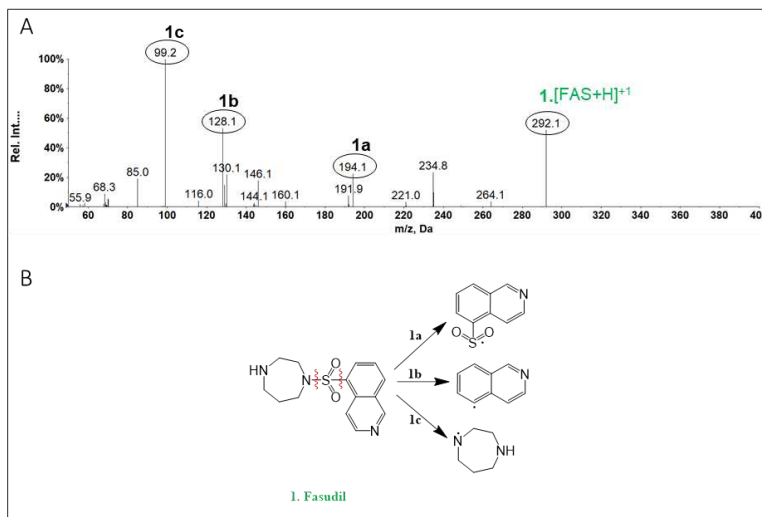


Figure 2.1. Qualitative analysis of a fasudil standard solution. (A) Direct MS/MS analysis for fasudil identified by matching molecular fragments with **(B)** the fragmentation mechanism.

Optimization of LC Parameters

We initiated the DoE study by performing a **Box-Behnken design**ⁱ to optimize three LC isocratic parameters: flow rate, acetonitrile (ACN) content in the mobile phase, and formic acid (FA) concentration in the mobile phase. We performed sixteen experiments from the design matrix developed by DoE with the design space defined by the maximum and minimum levels of LC factors (flow rate 0.1 – 0.5 ml/min; ACN content 60 – 80 %; FA concentration – 0.1-0.5 %; Table S2.1). We followed two system **outputs**ⁱⁱ: maximized FAS peak area and minimized total run time (by minimizing FAS retention time) while simultaneously optimizing the

ⁱa response surface methodology design that requires only three levels to run an experiment (-1, 0, 1)

ⁱⁱ chromatographic property used to characterize the quality of LC data

retention factorⁱⁱⁱ.³²⁷ Analysis of variance (ANOVA) confirmed the prediction power of our DoE response surface quadratic model: a significant p-value ($p < 0.0001$) and a predicted R^2 in reasonable agreement with the adjusted R^2 for both system outputs (0.9754/0.9668 for retention time and 0.9875/0.9648 for the peak area).

We examined the statistical significance of factor effects through p-values and **coefficient estimates**^{iv}. P-values less than 0.05 indicate the significance of the factor/interaction. A higher coefficient estimate signifies the more critical nature of the factor/interaction; meanwhile, the coefficient's positive and negative prefix indicates whether an increase in the factor leads to an increase or decrease in system output, respectively.

As shown in the results collected in Table 2.1, we observed an increase in the FAS peak area and hence the increase of method sensitivity when using a higher content of ACN (coefficient estimate $1.40E+06$). Meanwhile, increased FA content and flow rate decreased the FAS peak area (coefficient estimate $-3.29E+06$ and $-1.60E+06$, respectively). We expected to observe an increase in method sensitivity with increased ACN as the organic solvent content in the mobile phase decreases liquid surface tension to favor the formation of the **Taylor cone**^v and tiny charged droplets in the electrospray ionization source³²⁸. Adding FA to the mobile phase alters the charge supply to a certain extent; however, over-addition can lead to **overcharging**^{vi}, leading to instabilities in spraying and molecule fragmentation and a consequent reduction in method sensitivity³²⁹. In the case of retention time as the system output, the increased ACN % in the mobile phase and flow rate reduced the

ⁱⁱⁱ ratio of time retained in the stationary phase to the time retained in the mobile phase for an analyte - optimal values lie between 2 and 10 (non-complicated analyses use a range of 2-5 in practice)

^{iv} the expected change in response per unit change in the factor value when holding remaining factors constant

^v the cone shape of a conductive liquid formed in the electrospraying process

^{vi} an overly high charge location on one molecule

FAS retention time as expected (coefficient estimate -0.7514 and -0.4554, respectively). Finally, the FA % in the mobile phase non-significantly influenced retention time ($p = 0.8977$).

Table 2.1. Coefficient estimates and ANOVA results (p-values) for the response surface quadratic model obtained in the LC parameters optimization process

	Rt (min)		Peak area (counts)	
	p-value	Coefficient estimate	p-value	Coefficient estimate
Model	< 0.0001	-	< 0.0001	-
b₀ (intercept)	-	4.12	-	1.44E+07
b₁ (% acetonitrile)	< 0.0001	-0.74	0.0035	1.40E+06
b₂ (% formic acid)	0.89	0.0023	< 0.0001	-3.29E+06
b₃ (flow rate)	< 0.0001	-0.45	0.0017	-1.60E+06
b₁₂	0.87	-0.0042	0.53	2.47E+05
b₁₃	0.0031	0.064	0.87	-6.25E+04
b₂₃	0.501	-0.099	0.23	5.29E+05
b₁₁	0.0004	0.13	0.71	1.27E+05
b₂₂	0.81	0.0028	0.0038	-2.15E+06
b₃₃	0.016	0.042	0.76	1.17E+05
Lack of Fit	0.79	-	0.84	-
R²	-	0.97	-	0.98
Adj R²	-	0.96	-	0.96

P-values < 0.05 indicate the significance of the factor/interaction. A higher coefficient estimate signifies the more critical nature of the factor/interaction. The coefficient's positive and negative prefix indicates if the factor increases lead to an increase or decrease of the system output, respectively. Rt = retention time.

Next, we chose optimal LC conditions based on the desirability function, an objective numerical optimization function that ranges from a value of 0 outside the limits to 1 at the goal. The weight or importance of each output and factor can modify each goal^{vii}. For this purpose, we set the importance of system outputs at 4 for maximization of FAS peak area (maximum importance value as the primary goal of LC-MS/MS development = highest method sensitivity) and 2 for retention factor optimization (as the secondary goal = the basis of LC – sample retention on the column with the minimal total runtime). Thus, a higher desirability value brings us closer to our goals – a maximized peak area and minimized total runtime. The 3D response surface graph (Figure 2.2) represents how the desirability value changes with ACN % and FA % with a constant flow rate of 0.4 ml/min. The red and blue colors represent the highest and lowest desirability values; overall, Figure 2.1 demonstrates that higher FA % and ACN % allowed us to approach the goals for the LC-MS/MS method. Design expert software, using numerical optimization, reveals a point in the 3D response surface graph that maximizes the desirability value and offers us optimal factor levels for the LC-MS/MS method under development. This so-called **solution** has a desirability value of 0.92: FA 0.1%, ACN 80%, and a flow rate of 0.4 ml/min. Importantly, we must consider this last step of DoE development carefully - a DoE model quickly finding a desirability value of 1 would mean the choice of factor importance as easy-fitting, which would require the implementation of broader factor levels (more expansive design space) and stricter factor importance.

^{vii} the parameters/aspects of a process set or altered (LC parameters)

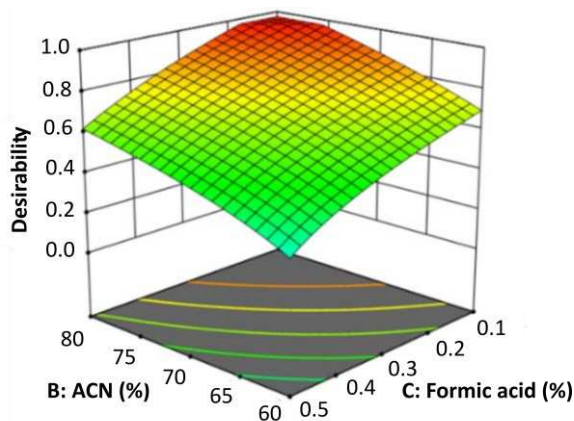


Figure 2.2. 3D response surface plot, representing desirability as a function of ACN % and FA % for a constant flow rate of 0.4 ml/min. (ACN-acetonitrile, FA-formic acid)

Overall, we determined optimal LC parameters for the quantitative determination of FAS by performing only sixteen DoE methods while predicting all other possibilities inside the design space; however, we continued with MS parameter optimization for the quantitative determination of FAS to fully take advantage of the potential power of DoE in LC-MS/MS method development. This additional step will provide faster method development and optimization independent of human deductive uncertainty and errors.

Optimization of MS Parameters

The design of a factor screen represents an essential first step to define significant factors, simplify DoE, and support parameter multivariate **optimization**^{viii}. We screened five MS parameters in a range that defined the design space: ion spray voltage (3000-5500 V), ion source temperature (300-750 °C), curtain gas pressure (20-40 psi), nebulizer (Gas 1) gas pressure (20-60 psi) and

^{viii} optimization process that depends on multiple variables

auxiliary (Gas 2) gas pressure (40-80 psi). We performed **fractional factorial design**^{ix} with sixteen duplicate random experiments, three replicates at the central point (point with the level of all factors set at middle value), and the average ratio of FAS peak area as the outcome (Table S2, 35 runs in total).

We must demonstrate a statistically significant prediction and accuracy obtained by several statistical tools (i.e., t-test, ANOVA, and individual control charts) for a reliable DoE prediction model. As all statistical tools require normally distributed data, we first performed diagnostics on the obtained system outputs for each experiment and analyzed the **plot of residuals**^x and the **Box-Cox plot**^{xi} (**Error! Reference source not found.2.3**).

Figure 2.3. Statistical tests to evaluate the data distribution A) Residuals vs. predicted values of peak area B) Box-Cox plot

The residual and Box-Cox plots indicate the need for data transformation to obtain a normal distribution. We observed data distribution on the residual plot

^{ix} a reduced version of full factorial design, with regards to the size of a test performed

^x a representation of how close each data point is vertically taken from the prediction equation graph from the model

^{xi} linearity plot of the correlation between Y and the transformed X for given values of lambda (usually used for assessing data distribution normality)

corresponding to the shape of a logarithmic function, suggesting that we must perform a logarithmic transformation of the FAS peak area (as a system output) (Figure 2.3A). The Box-Cox plot aided decision-making, given the ability to identify an appropriate exponent (Lambda) to use for data transformation into a "normal shape" (Figure 2.3B). Lambda indicates the power to which all data undergoes involution; in this case, a value of $\lambda = 0$ indicates the need for a logarithmic transformation. Nevertheless, Box-Cox-guided data transformation does not guarantee normal data distribution, as this approach only indicates the smallest standard deviation of the system outputs³³⁰. We assume that transformed data has the highest likelihood (not a guarantee) of being normally distributed in the case of the smallest standard deviation among all possible transformations with Lambda values between -5 and +5. Therefore, we must evaluate residual plots (Figure 2.4A) and the Box-Cox plot (Figure 2.4B) to confirm the normal distribution of the transformed data (in this case, after the logarithmic transformation of the FAS peak area obtained for all 35 experiments). We determined how the data follows the residual plot line from the residual plot (Figure 2.4.A) and how the calculated λ value (blue line) lies close to the predicted λ value (green line) from the Box-Cox plot. We concluded that data logarithmic transformation provides the normal data distribution required for further statistical analysis.

Next, we added a three-center point in the factorial design (three experiments with factors at their median value) and included the obtained system outputs in DoE to evaluate how well the model predicts system outputs in the design space center. The curvature test - in which we compare predicted system outputs to the experimentally obtained outputs - can determine how well a DoE model predicts in the design space center. A p-value of 0.2455 indicates insignificant model curvature (no significant difference between the experimentally obtained and predicted value of the FAS peak area). This finding suggests we can

remove center points to simplify analysis as the whole design space provides robust model prediction.

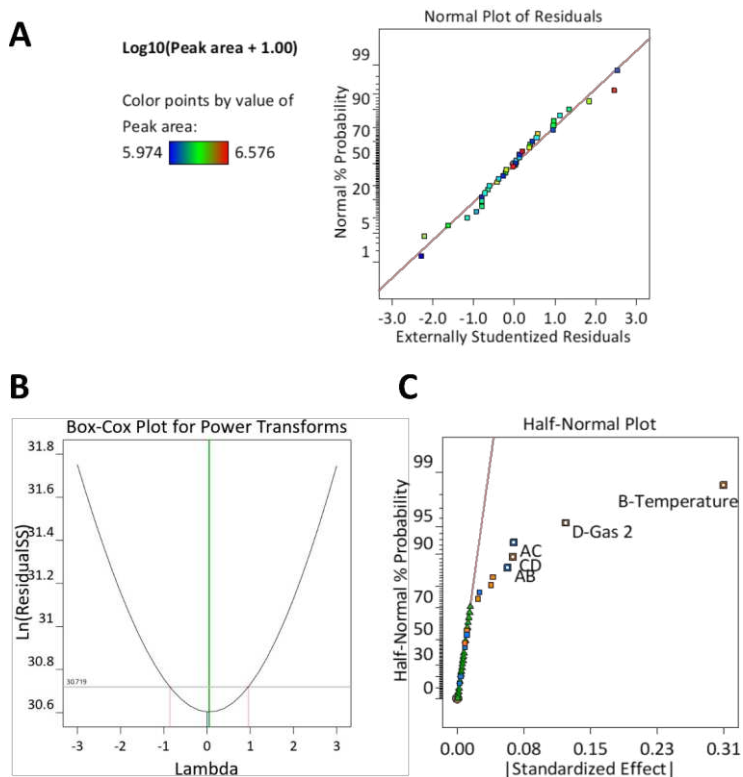


Figure 2.4. Statistical tests evaluating data distribution and determining significant MS parameters (A) normal plot of residuals, (B) Box-Cox plot, and (C) Half-normal probability plot of standardized effects.

After assuring normal data distribution and the non-essential nature of center points in model prediction, we continued our study to identify MS factors that significantly impact FAS peak area. For this purpose, we used a half-normal probability plot (Figure 2.4C) and ANOVA test to determine p-values and coefficient estimates for each factor (Table 2.2) and examine their influence on the FAS peak

area. A Lack-of-Fit F-value of 1.44 and a model F value of 41.9 (Table 2.2) imply that the designed model fits the desired purpose and predicts FAS peak area as the LC-MS/MS instrument response. The absolute value of the estimated effect for an unimportant factor typically positions close to a near-zero line in a half-normal probability plot (Figure 2.4C); meanwhile, the value becomes displaced off the line for a crucial factor. Additionally, p -values <0.05 indicates the factor's significance, with a larger coefficient estimate indicating the more critical nature of the factor's influence on the system output. Thus, with the estimated effects displaced off the line in a half-normal probability plot, with the most considerable coefficient estimates and $p < 0.05$, factors A ($p = 0.0125$), B ($p < 0.0001$), and D ($p < 0.0001$) corresponding to ion spray voltage, temperature, and auxiliary gas pressure, respectively, significantly influence MS instrument response (FAS peak area). The ion spray voltage is applied to the ion spray needle tip (where the analyte becomes ionized) and profoundly influences method sensitivity. Auxiliary gas pressure and temperature participate in spray droplet evaporation, which influences the quantity of lost/obtained ions for analysis - rapid evaporation can prompt analyte loss, which decreases method sensitivity.

After determining significant factors, we obtained optimum operating conditions using more complex experimental designs (such as the Box-Behnken design). We performed the experimental design according to a predefined experimental plan (fifteen experiments performed by changing the values of ion spray voltage, ion source temperature, and auxiliary gas pressure, as described in Table S3).

Table 2.2. P and F values obtained from the ANOVA test and coefficient estimate results for tested MS factors

Source	F-value	p-value	Coefficient Estimate
Model	41.90	< 0.0001	-
A-Ion spray voltage	7.62	0.013	0.029
B-TEM	468.55	< 0.0001	0.15
C-Gas 1	0.401	0.53	-0.0045
D-Gas 2	77.25	< 0.0001	0.062
E-Curtain gas	0.65	0.43	0.0057
AB	16.87	0.0006	-0.029
AC	0.21	0.76	0.0032
AD	0.0801	0.78	-0.002
AE	0.036	0.85	-0.0014
BC	0.408	0.53	0.0045
BD	20.44	0.0002	0.032
BE	0.65	0.43	-0.0057
CD	2.87	0.106	0.012
CE	3.28	0.086	-0.013
DE	8.37	0.093	0.021
Lack of Fit	1.44	0.24	

We can visualize the influence of factors by examining *contour plots*^{xii}, where red-colored regions have the highest desired responses (Figure 2.5). Based on the identified design space with the highest responses, we defined the optimal conditions for ion source parameters as an auxiliary gas pressure value of 65 psi, an ion spray voltage of 4000 V, and an ion source temperature of 750 °C.

^{xii} a graphical method for representing a 3-dimensional surface by plotting constant z slices, called contours, on a 2-dimensional format

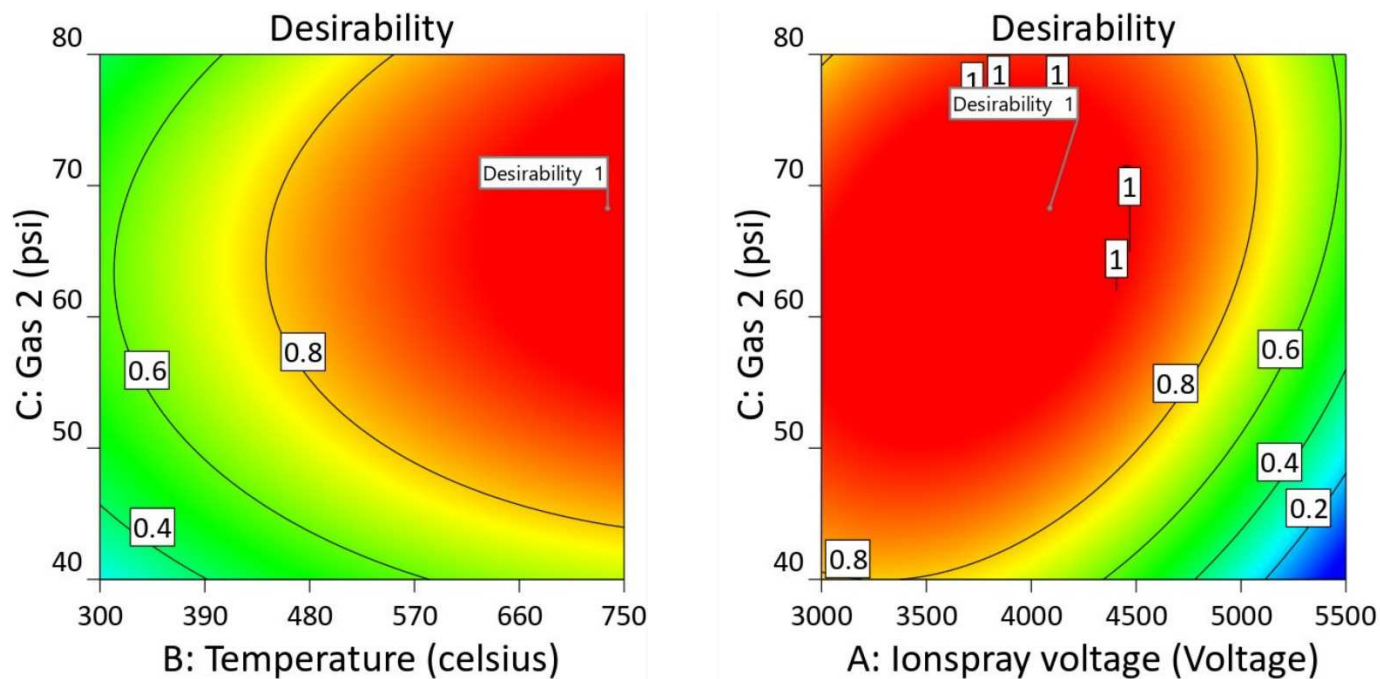


Figure 2.5. Contour plots defining optimal ion source conditions for an MS method to determine fasudil quantitatively. Desirability values of 1 and close to 1 represented in red; values of a combination of factors in the red zone considered optimal for MS parameters.

Optimization of Collision and Focusing Parameters

As the next step in LC-MS/MS method optimization, we studied the influence of ion source position, collision energy (CE), collision cell exit potential (CXP), entrance potential (EP), and declustering potential (DP) on the FAS peak area. In this case, we implemented the "one factor at a time" (OFAT) approach as these parameters do not interact.

We detected FAS with the MS/MS method by molecular ion fragmentation (292.4 m/z [M+H]⁺ ion) in the quadrupole 2 (Q2) part of the MS analyzer, filtering and detecting 99.2 m/z and 129.0 m/z masses in quadrupole 3 (Q3). Ionized molecules enter the mass analyzer where DP is applied, which helps prevent ion clustering. According to the manufacturer-recommended values for DP, we evaluated the influence on FAS peak area at three levels (100, 200, and 300 V)²¹⁸. Figure 2.6 demonstrates that 100 V of DP provided the highest peak area value compared to the other potentials (200 and 300 V). Next, we evaluated the EP at three levels (5, 10, and 15 V) (applying different EPs at Q0 guides and focusing ions into the MS instrument). An increase in EP negatively influences ion focusing and leads to their loss in the analyzer, which causes poor sensitivity of an MRM method. Thus, we chose 5 V as an optimal value for EP as this value provided the highest FAS peak area. We observed better FAS ion fragmentation at a CE value of 30 V compared to 15 V; however, any further increase reduced the peak area. The CE value describes the rate of ion acceleration in the entrance of quadrupole 2 (Q2). A higher CE leads to more significant fragmentation; however, too low CE values can prompt inefficient molecule fragmentation, while too high CE values can cause over-fragmentation. A poorly optimized CE value can drastically reduce MRM method sensitivity, and the results from Figure 2.6 confirm such an outcome. Further data analysis demonstrated that rising CXP values decrease MRM method sensitivity. These results are expected, as CXP focuses and accelerates ion exit from

Q2, and raising CXP to high levels leads to loss of the fragmented ions. Thus we chose 15 V as an optimal CXP value.

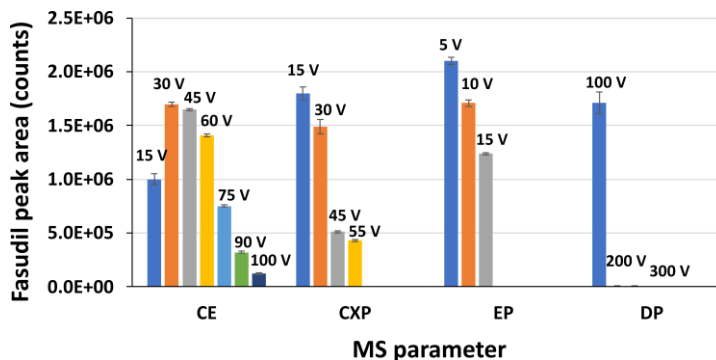


Figure 2.6. Fasudil peak area obtained during experiments for optimization of collision parameters. CE - collision energy, CXP - collision cell exit potential, EP - entrance potential, DP - declustering potential.

As a last step in LC-MS/MS method optimization, we evaluated sensitivity improvements by comparing the FAS peak area between three methods: 1) auto-tuned conditions, 2) optimized MS conditions only, and 3) optimized LC and MS conditions. We observed an 89% and 179% improvement in sensitivity from auto-tuned to optimized MS conditions only and optimized LC and MS conditions, respectively. These results confirmed that a DoE approach supports the definition of an effective LC-MS/MS method for FAS determination, which ensures the method's high sensitivity. Table 2.3 describes the method and the chosen values for different LC and MS parameters.

Table 2.3. Final LC and MS conditions for the quantitative determination of fasudil determined through a DoE approach

Parameter	Value	Parameter	Value
Horizontal position	6 mm	Declustering potential	100 V
Vertical position	4 mm	Entrance potential	5 V
Ion spray voltage	4000 V	Collision energy	30
Temperature	750 °C	Collision cell exit potential	15 V
Curtain gas	40 psi	Flow rate (ml/min)	0.4
Nebulizer (GS1)	40 psi	% Acetonitrile	80
Auxiliary gas (GS2)	65 psi	% Formic acid	0.1 %

2.2.2 Tailor-made LC-MS/MS methods for the quantitative determination of anticancer drugs as a component of PDC characterization studies

The advantages of DoE have prompted a rise in published articles on LC-MS methods (especially those optimizing isocratic LC methods)²²⁴; however, the power of DoE in gradient method development remains incompletely explored. Thus, we sought to evaluate the predictive power of DoE in a more complex gradient LC-MS method and simultaneously optimize LC-MS/MS methods for the determination of sixteen anticancer drugs from our internal library.

We initiated LC-MS/MS method development by DoE to optimize LC conditions. We performed an MRM scan following one mass transition for each drug (Table S4) in positive electrospray ionization (ESI) mode. We defined values for MS parameters such as ion spray voltage (5500 V), temperature (250 °C), curtain gas (20 V), nebulizer (45 V) and auxiliary gas (45 V), declustering potential (62 V),

entrance potential (2 V), exit potential (8 V) by system auto-tuning to optimize LC parameters.

We performed a Box-Behnken design to optimize seven LC parameters: ACN content in the eluent at the beginning (A) and end of the gradient (B), flow rate (C), FA 0.1% content in sample (D), column temperature (E), gradient time (F), and plateau time (G) (Table S5). To ensure a retention factor value of at least 1 and low detection limits, we added an on-column concentration step in each experiment, keeping the eluent starting conditions constant for *the dead time*^{xiii}.

All steps before defining optimal LC parameters parallel the DoE optimization process described in the previous sections – data transformation, normal distribution analysis, and important factor detection. We confirmed the predictive capacity of our DoE model with the ANOVA test, observing significant model p and F values for each system output. We chose optimal LC conditions according to the desirability graph, an objective function that ranges from 0 outside the limits to a value of 1 at the goal. Adjusting the importance of each response and factor and final optimization finds a point with maximized desirability function to alter goal characteristics. For this purpose, we selected suitable ranges for LC-MS/MS system response: analyte response maximization (signal-to-noise ratio – S/N), total run time minimization (by minimizing the retention time) but with simultaneous optimal retention factor (2-5), optimal tailing factor range (0.9-1.3) and optimal range for the peak width at 10% of its height (0.1-0.3)³²⁷. Optimizing with the desirability function identified a robust set of LC conditions that met the goals for each active moiety.

^{xiii} The time needed for the mobile phase to pass through the column.

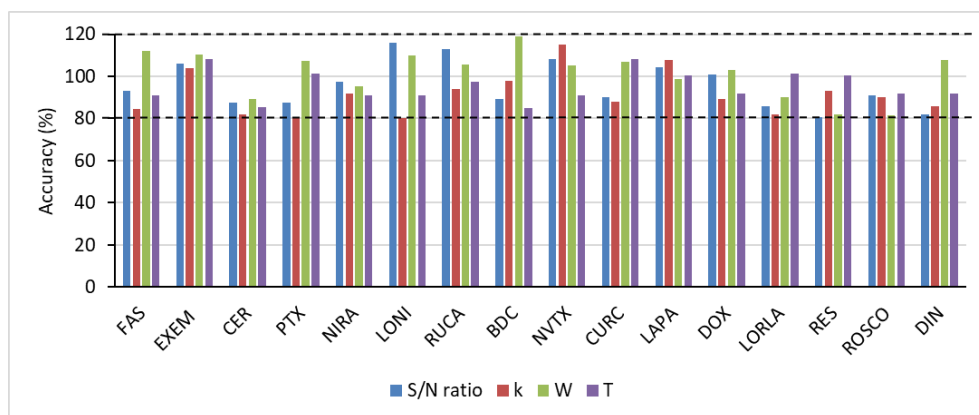


Figure 2.7. DoE prediction accuracy of LC outputs for each drug. S/N - signal-to-noise ratio, k - retention factor, W – peak width at 10% of its height, T - tailing factor, FAS - fasudil, EXEM – exemestane, CER – ceritinib, PTX – paclitaxel, NIRA – niraparib, LONI – lonidamine, RUCA – rucaparib, BDC – bisdemethoxycurcumin, NVTX – navitoclax, CURC – curcumin, LAPA – lapatinib, DOX – doxorubicin, LORLA – lorlatinib, RES – resiquimod, ROSCO – roscovitine, DIN - dinaciclib; black dotted lines- generally accepted limit within a $\pm 20\%$.

Finally, we performed a confirmation run to analyze the accuracy of the predicted outputs and validate our DoE model for LC-MS/MS method development (Figure 2.7). Accuracy values for predicted LC outputs all lay in a generally accepted limit (within a $\pm 20\%$, black dotted line on the graph), suggesting robust agreement with the measured values; however, peak width prediction displayed a lower level of accuracy than other LC outputs due to a high dependence on the Gaussian transformation of the chromatographic peak. We report the individual LC gradient method for each active moiety in Table 2.4 and Figure S2.1; however, the power of DoE lies in reanalyzing the data and finding tailor-made methods for a combination of drugs implemented as a combination therapy or using a single drug as an internal standard for another drug (e.g., using NIRA as an internal standard for RUCA and vice versa, or BDC and CURC combination).

Table 2.4. The final LC gradient method for the determination of fifteen anticancer drugs

Drug	LC Parameters						
	ACN % start	ACN % end	Flow, ml/min	Aq. phase %	Column temp. (°C)	Gradient time (min)	Plateau time (min)
RUCA	5.7	64.3	0.31	13.6	43	7.45	2.65
NIRA	14.0	100.0	0.24	0.5	45	6.66	2.47
DIN	5.0	6.8	91.6	11.8	54	1.74	6.74
FAS	5.0	41.4	0.26	20.0	30	1.16	4.40
CER	5.0	48.5	0.25	12.7	36	2.58	7.45
EXEM	40.9	100.0	0.50	2.3	35	7.42	1.80
ROSCO	5.0	48.5	0.35	17.1	45	8.1	7.49
LAPA	5.3	78.0	0.35	7.4	47	4.32	4.42
CURC	8.8	99.4	0.38	0.2	50	7.99	1.35
BDC	11.8	100.0	0.40	7.1	46	7.94	2.96
NVTX	5.2	100.0	0.33	1.1	48	4.71	3.75
DOX	5.1	45.0	0.20	1.7	58	7.99	3.47
PTX	37.4	100.0	0.2	0	51	1.03	4.49
LONI	21.5	60.1	0.27	10.6	30	4.33	6.27
LORLA	17.2	74.5	0.20	7.5	53	1.27	3.79
RES	5.0	89.0	0.48	10.1	45.8	2.01	2.10

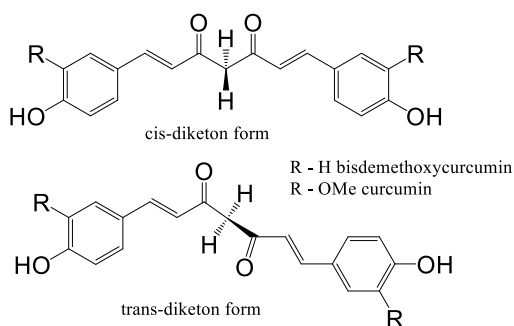
ACN - acetonitrile; Aq. - aqueous; Temp. - temperature; RUCA - rucaparib; NIRA - niraparib; DIN - dinaciclib; FAS - fasudil; CER - ceritinib; EXEM - exemestane; ROSCO - roscovitine; LAPA - lapatinib;

CURC - curcumin; BDC - bisdemethoxycurcumin; NVTX - navitoclax; DOX - doxorubicin; PTX - paclitaxel; LONI - lonidamine; LORLA - lorlatinib; RES - resiquimod

Interestingly, the developed LC-MS/MS methods for BDC and CURC uncovered two separate chromatographic peaks for each drug, indicating the

presence of structural conformers (Scheme 2.1 and Figure 2.8). We observed the presence of two conformer peaks for only one mass transition (369.9 – 177.2 m/z and 309.8 – 147.1 m/z, for CURC and BDC, respectively), indicating a different fragmentation mechanism for the two conformers.

Previous studies with well-studied BDC and CURC behavior in solution confirmed the detection of BDC and CURC structural conformers by our LC-MS/MS method^{331,332}, with BDC and CURC existing as *cis* and *trans* isomers in the solution. Two phenol-methoxy groups positioned on the opposite sides of the curcumin backbone define the *trans* form; meanwhile, the *cis* form contains the phenol-methoxy groups on the same side of the backbone.^{331,332} These results emphasize the importance of following more than one mass transition in the LC-MS/MS method and implementing modified C18 columns to provide better retention and separation of anticancer drugs. In our study, we implemented a Kinetex Biphenyl C18 column that, apart from hydrophobic interactions, provided the different π - π stacking of BDC and CURC conformers on the column packing modified with biphenyl groups, leading to their separation. The separation of structural conformers of CURC and analogs represents a crucial step, given their differing docking scores and critical interactions with epidermal growth factor receptor tyrosine kinase that may modulate their anticancer effect.^{333–335}



Scheme 2.1. Chemical structure of curcumin and bisdemethoxycurcumin structural conformers

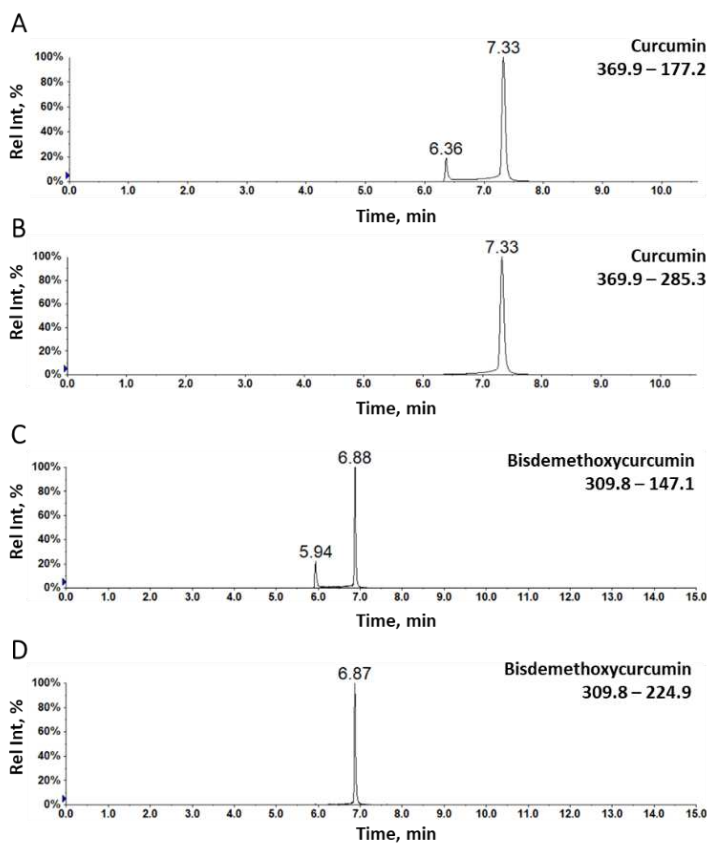


Figure 2.8. LC-MS chromatograms of two MRM scans for (A and B) curcumin and (C and D) bisdemethoxycurcumin

Ultimately, the superiority of DoE in method development lies in simultaneously mapping and modeling LC response behavior within a given design space across multiple variables by varying all factors at once according to a predefined DoE-obtained experimental matrix. For instance, by adjusting the ACN % at the gradient end (from Figure 2.9A to 2.9B), we simultaneously determine how the three factors influence the ceritinib retention factor (ACN % at the start and end of the gradient and the gradient time).

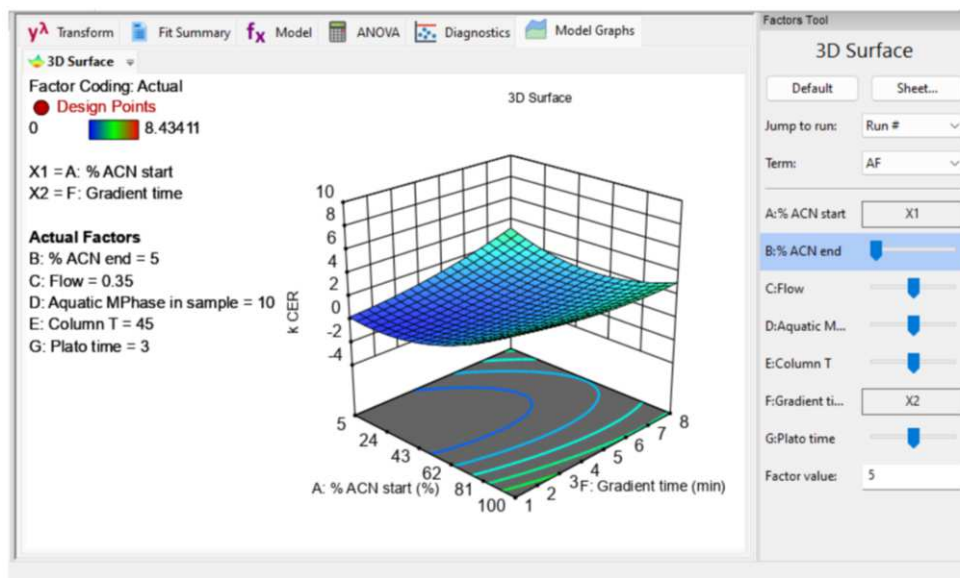
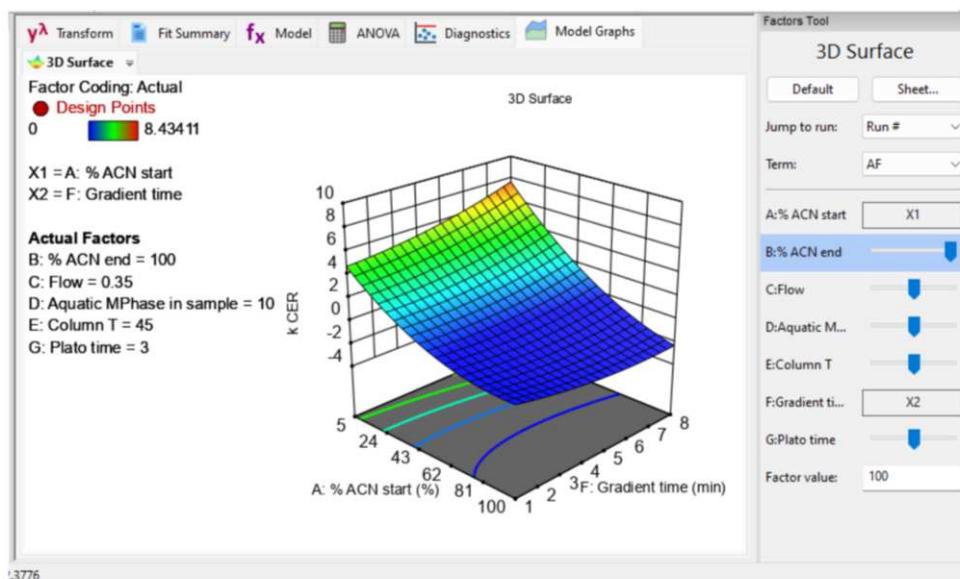
A**B**

Figure 2.9. 3D surface graph for the optimization of LC-MS/MS conditions in the quantitative determination of ceritinib. (A) ACN 0% at the gradient end and (B) ACN 100% at the gradient end.

2.3 DISCUSSION

The FDA and EMA promote the use of quality-by-design approaches (DoE, among others) for pharmaceutical product development. The International Conference on Harmonisation has already published ICH Q8, Q9, and Q10 guidelines to implement this approach to achieve high-quality pharmaceutical products^{214,336}.

Unlike traditional approaches such as auto-tuning or OFAT, which can prove helpful when not requiring high method sensitivity, DoE considers the interactions between variables, minimizes the uncontrolled effects, and evaluates their impact on analysis.^{220,221} Although the nanomedicine field has yet to fully take advantage of the associated advantages, DoE currently represents the most advisable way to optimize any method. The availability of literature resources that implement DoE to optimize related procedures has recently increased, especially in LC-MS/MS methodologies.²²⁴ Kostic et al. employed DoE to improve the LC-MS/MS-mediated analysis of zwitterionic antiepileptic drugs that improved peak areas and signal-to-noise ratios.³³⁷ Our results broadly agree with the study by Kostic et al. in that parameters such as scan time, ion source geometry, sheath, auxiliary gas pressure, capillary temperature, collision pressure, and mobile phase composition positively impact the sensitivity of LC-MS/MS methods. Krueve et al. optimized electrospray interface and quadrupole ion-trap mass spectrometer parameters (ESI-MS) on three pesticides (thiabendazole, aldicarb, and imazalil) to achieve high sensitivity, low detection limits, and acceptable accuracy.²²⁵

Approximately 80% of LC methods are based on **gradient**^{xiv} separation, a versatile approach with broad applications in quantitative studies. In **isocratic**^{xv}

^{xiv} constant change in the composition, and hence the polarity, of the mobile phase during the LC separation

^{xv} consistent mixture of mobile phase over the complete LC run

separations (such as the previously developed method for the quantitative determination of fasudil), the predetermined eluent composition remains constant throughout the method, leading to the constant strength of analyte and column interaction. Of note, the eluent's strength increases over gradient separation, meaning that the interaction of the analyte with the column decreases, which leads to final analyte elution. The theoretical background of gradient elution remains complex, and factors other than isocratic elution, which may act in the opposite direction or multiply the effect on system output, can affect the procedure. Thus, in the second part of our study, we evaluated the possibility of using DoE in the simultaneous development of LC gradient methods for the quantitative determination of sixteen anticancer drugs. DoE allowed us to obtain an accurate, specific, and sensitive LC-MS/MS method; moreover, we ensured the use of the developed LC-MS/MS methods in separating drug-linkers metabolites by obtaining the optimal retention factor (k) for each drug (higher than 2), a requisite for drug release result interpretation and metabolite identification (see Chapter V).

The technical and regulatory challenges associated with repeatability in chemistry, adaption, and control of manufacturing processes and scale-up of such complex products all represent obstacles to the translation of nanomedicines from bench to bedside.³³⁸ Implementing DoE to identify and classify critical nanomedicine properties and factors influencing manufacturing processes may lead to a deeper understanding of nanomedicine as a platform²². Puri et al. and Troiano et al. exemplified the use of quality-by-design approaches by implementing DoE to achieve optimized nanoparticles with a desired quality target product profile.^{339,340} DoE can find use in any complex optimization problem, from nanoparticle manufacturing to rapidly identifying dynamically optimized and actionable combination therapies.³⁴¹ With this in mind, we refer the reader to Chapter III, where we explored the application of DoE in the design of crosslinked PGA-based combination nanoconjugates.

2.4 CONCLUSION

In this chapter, we demonstrated how proper experimental planning, method validation, quality control, and multivariate data analysis could foster a better understanding and provide higher confidence in the obtained results. DoE implementation streamlines the optimization process and saves time and resources while providing information that guides decision-making during early process development.

Importantly, we implemented the developed LC-MS/MS method to characterize the synthesized PGA-SS-Et-FAS (fasudil conjugated to poly-L-glutamic acid through disulfide linker), plasma stability study and determination of free FAS in CSF, and the additional in vitro sample preparation optimization and method validation, with results published in the following manuscripts:

- "A rationally designed self-immolative linker enhances the synergism between a polymer-rock inhibitor conjugate and neural progenitor cells in the treatment of spinal cord injury," Giraldo et al. *Biomaterials* 2021³²⁶ (See **Appendix 1**). To note, Snežana was involved in the synthesis and the whole physico-chemical characterization of PGA-SS-Et-FAS, including the plasma stability study and the determination of free FAS in CSF.
- "Transplantation of Human Fetal Spinal cord-derived NPCs Primed with a Polyglutamate-conjugated Rho/Rock Inhibitor as a Therapy for Acute Spinal Cord Injury," Giraldo et al. *Cells* 2022³⁴² (See **Appendix 2**). To note, Snežana was involved in the synthesis and the whole physico-chemical characterization of PGA-SS-Et-FAS, and the additional in vitro sample preparation optimization and method validation.

Moreover, we implemented the developed LC-MS/MS method in the characterization of PGA-DOX-mUNO (doxorubicin conjugated to poly-L-glutamic acid), resulted in the following publication:

- "Depletion of Mannose Receptor-Positive Tumor-Associated Macrophages via a Peptide-Targeted Star-Shaped Polyglutamate Inhibits Breast Cancer Progression in Mice" Lepland et al. *Cancer Research Communications* 2022³⁴³ (See **Appendix 3**) To note, Snežana was involved in the physicochemical characterization of PGA-DOX-mUNO conjugate including the free drug determination, plasma stability study, stability in intraperitoneal fluid and the release kinetics

Additionally, we implemented a tailor-made gradient LC-MS/MS method for drug release experiments in a linker-based study described in Chapter V.

Over the next decade, we believe researchers from a range of backgrounds will begin to appreciate the utility of a systematic, accurate and rigorous physico-chemical characterization that entails the delineation of a robust LC-MS/MS method. Combining conceptual molecular-level understanding with computational tools such as artificial intelligence, including DoE and machine learning, will ultimately guide researchers toward a robust and predictive platform for developing next-generation nanomedicines.

2.5 EXPERIMENTAL MATERIALS AND METHODS

2.5.1 Materials

Material suppliers were as follows: dinaciclib (MedKoo Biosciences, US), fasudil (Xingcheng Chempharm Co. Ltd, China), and methanol (LC-MS grade) were

obtained from Sigma-Aldrich (St. Louis, United States). Water (LC-MS grade) and formic acid (LC-MS grade) were purchased from Fisher Scientific (Pittsburgh, US). All the drugs (were purchased from MedKoo Biosciences (Morrisville, US) except for fasudil hydrochloride (FAS), which was obtained from Xingcheng Chempharm Co. Ltd (Zhejiang, China).

2.5.2 Methods

LC-MS/MS method development with the implementation of DoE was performed by analysis of 5 µg/ml standard solution of all sixteen drugs in MeOH with the addition of aquatic mobile phase as stated in the DoE. On each analysis day, we added a control sample (1 µg/ml fasudil standard solution) and a blank sample (MeOH) at the sequence's beginning, middle, and end to control the instrument response. The data analysis for the DoE study was performed with the Design Expert 12 software package.

2.6 SUPPLEMENTARY MATERIAL

Table S2.1. Experimental design matrix table for optimization of LC parameters in the development of LC-MS/MS method for fasudil determination

Run	Flow rate (ml/min)	ACN %	FA %
1	0.3	70	0.3
2	0.3	70	0.3
3	0.3	70	0.3
4	0.5	70	0.1
5	0.1	70	0.5
6	0.3	60	0.5
7	0.5	60	0.3
8	0.5	80	0.3
9	0.3	80	0.5
10	0.3	60	0.1
11	0.1	70	0.1
12	0.3	70	0.3
13	0.3	80	0.1
14	0.5	70	0.5
15	0.1	60	0.3
16	0.1	80	0.3

ACN- acetonitrile, FA-formic acid

Table S2.2 Experimental design matrix table for MS parameters screening in the development of LC-MS/MS method for the quantitative determination of fasudil

Run	Factor A	Factor B	Factor C	Factor D	Factor E
1	3000	750	20	80	40
2	3000	300	60	80	40
3	4250	525	40	60	30
4	5500	300	20	40	20
5	3000	750	60	40	40
6	3000	300	60	40	20
7	3000	750	20	40	20
8	3000	300	60	80	40
9	3000	300	20	80	20
10	5500	750	20	80	20
11	5500	750	60	40	20
12	5500	750	20	40	40
13	5500	300	60	80	20
14	5500	750	20	80	20
15	3000	300	20	40	40
16	3000	750	60	80	20
17	5500	750	60	40	20
18	3000	750	60	80	20
19	3000	300	20	80	20
20	3000	750	60	40	40
21	4250	525	40	60	30
22	5500	300	60	80	20
23	4250	525	40	60	30
24	3000	300	20	40	40
25	5500	300	20	80	40
26	3000	750	20	40	20
27	5500	300	60	40	40
28	5500	300	20	40	20
29	5500	300	20	80	40

30	5500	750	20	40	40
31	5500	300	60	40	40
32	5500	750	60	80	40
33	5500	750	60	80	40
34	3000	750	20	80	40
35	3000	300	60	40	20

Factor A: Ion spray voltage, V; Factor B: Ion spray temperature, °C;
 Factor C: Gas 1, psi; Factor D: Gas 2, psi; Factor E: Curtain gas, psi

Table S2.3 Experimental design matrix table for MS parameters optimization in the development of LC-MS/MS method for the quantitative determination of fasudil

Run	Factor A	Factor B	Factor C
1	3000	750	60
2	4250	750	40
3	5500	525	40
4	4250	300	40
5	3000	300	60
6	4250	525	60
7	4250	750	80
8	4250	525	60
9	3000	525	40
10	3000	525	80
11	5500	750	60
12	5500	525	80
13	5500	300	60
14	4250	525	60
15	4250	300	80

Factor A: Ion spray voltage, V; Factor B: Ion spray temperature, °C;
 Factor C: Gas 2, psi

Table S2.4. MS/MS mass transitions followed in the MRM scan of the developed LC-MS/MS method in the determination of sixteen anticancer drugs

Drug	Mass transitions followed in MRM (m/z)	Collision energy (V)
Fasudil	292.2 – 99.0	35
Niraparib	321.2 – 304.2	30
Rucaparib	324.3 – 293.0	30
Dinaciclib	397.2 – 335.0	40
Resiquimod	315.2 – 251.0	30
Ceritinib	560.2 – 518.2 560.2 – 435.2	40
Exemestane	339.2 – 121.2 298.3 – 121.1	30
Roscovitine	356.1 – 233.1	40
Lapatinib	457.8 – 349.1	40
Curcumin	369.9 – 177.2 369.9 – 285.3	25
Bisdemethoxycurcumin	309.8 – 147.1 309.8 – 224.9	20
Navitoclax	487.3 – 177.1	30
Doxorubicin	544.1 – 397.1 544.1 – 379.1	20
Paclitaxel	855.4 – 286.1 855.4 – 240.1	30
Lonidamine	363.3 – 302.9	20
Lorlatinib	447.9 – 228.1	40

Table S2.5. Experimental design matrix table for optimization of LC-MS/MS method

ACN % start	ACN % end	Flow (ml/min)	% Aq phase*	Column temp. (°C)	Gradient time (min)	Plateau time (min)
52.5	100	0.2	10	45	1	6
52.5	5	0.5	10	45	1	6
100	100	0.35	20	45	4.5	6
52.5	52.5	0.35	20	60	1	6
52.5	52.5	0.5	0	45	4.5	9
52.5	5	0.35	10	60	4.5	9
52.5	52.5	0.5	20	45	4.5	9
52.5	52.5	0.35	10	45	4.5	6
100	52.5	0.5	10	60	4.5	6
52.5	52.5	0.2	0	45	4.5	3
100	52.5	0.35	10	45	8	3
100	5	0.35	0	45	4.5	6
52.5	100	0.35	10	30	4.5	3
52.5	5	0.35	10	30	4.5	3
52.5	100	0.5	10	45	1	6
100	100	0.35	0	45	4.5	6
52.5	52.5	0.35	10	45	4.5	6
52.5	100	0.35	10	30	4.5	9
5	52.5	0.5	10	30	4.5	6
5	52.5	0.2	10	30	4.5	6
100	52.5	0.5	10	30	4.5	6
52.5	100	0.2	10	45	8	6
100	5	0.35	20	45	4.5	6
52.5	52.5	0.35	0	30	1	6
52.5	52.5	0.2	20	45	4.5	9
52.5	52.5	0.35	20	30	1	6
5	52.5	0.5	10	60	4.5	6
52.5	5	0.35	10	60	4.5	3
5	52.5	0.35	10	45	1	3
100	52.5	0.35	10	45	8	9
52.5	52.5	0.35	0	30	8	6
52.5	52.5	0.5	0	45	4.5	3

100	52.5	0.2	10	30	4.5	6
5	5	0.35	0	45	4.5	6
52.5	5	0.2	10	45	8	6
52.5	100	0.5	10	45	8	6
52.5	5	0.5	10	45	8	6
52.5	52.5	0.35	10	45	4.5	6
5	52.5	0.35	10	45	8	3
52.5	52.5	0.5	20	45	4.5	3
52.5	52.5	0.35	10	45	4.5	6
52.5	52.5	0.35	10	45	4.5	6
5	5	0.35	20	45	4.5	6
100	52.5	0.35	10	45	1	3
5	52.5	0.2	10	60	4.5	6
5	52.5	0.35	10	45	1	9
100	52.5	0.35	10	45	1	9
52.5	52.5	0.35	0	60	1	6
52.5	52.5	0.2	0	45	4.5	9
52.5	5	0.35	10	30	4.5	9
52.5	5	0.2	10	45	1	6
52.5	52.5	0.35	20	30	8	6
100	52.5	0.2	10	60	4.5	6
52.5	52.5	0.35	10	45	4.5	6
5	100	0.35	0	45	4.5	6
5	52.5	0.35	10	45	8	9
52.5	100	0.35	10	60	4.5	3
5	100	0.35	20	45	4.5	6
52.5	52.5	0.35	20	60	8	6
52.5	52.5	0.35	0	60	8	6
52.5	52.5	0.35	10	45	4.5	6
52.5	52.5	0.2	20	45	4.5	3
52.5	100	0.35	10	60	4.5	9

ACN- acetonitrile; Aq.- aquatic phase with 0.1 % formic acid in the sample

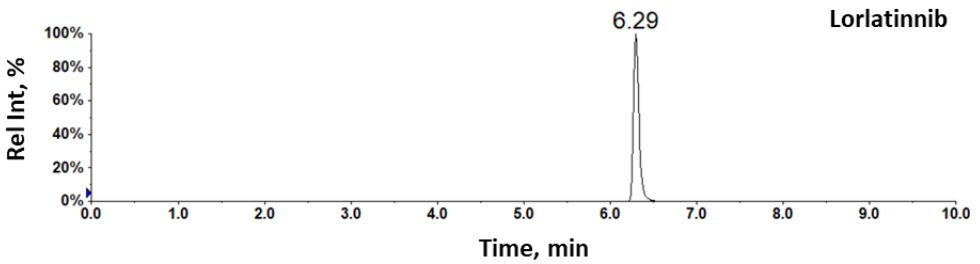
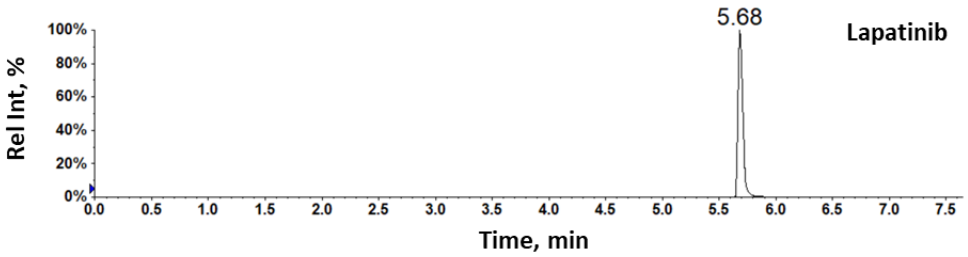
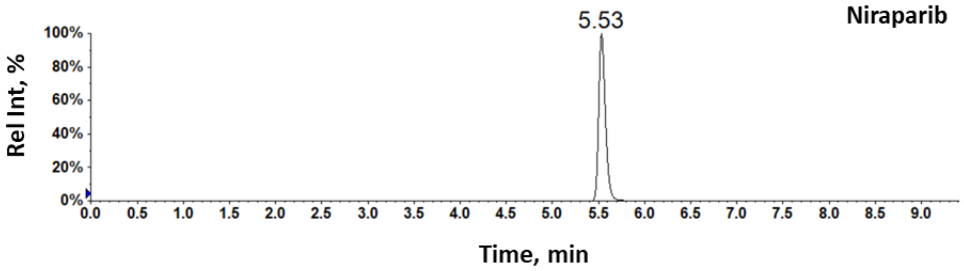
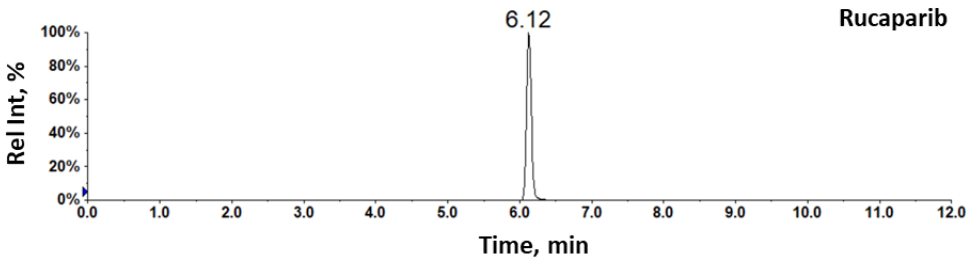
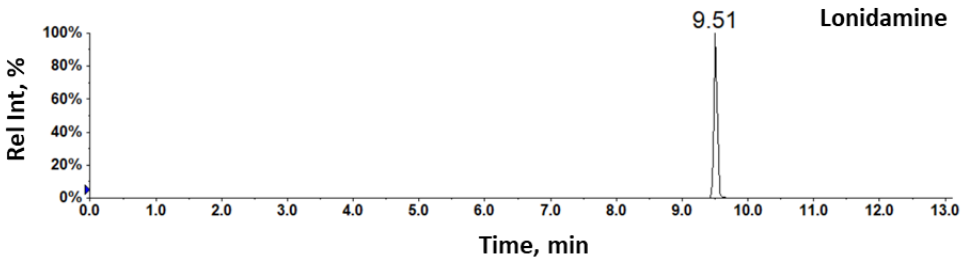
Table S2.6. Important LC factors and factor interactions for system outputs. The data transformation, type of prediction model, and P/F value indicate the good prediction of each model.

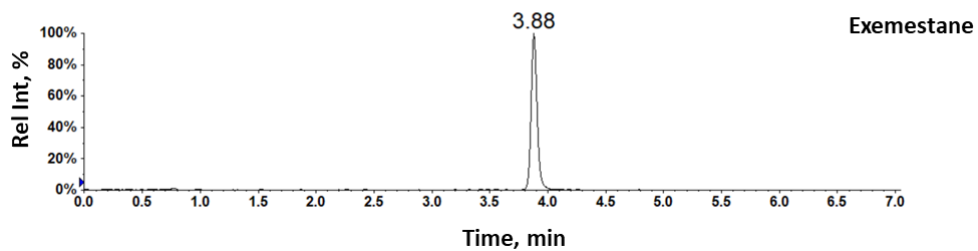
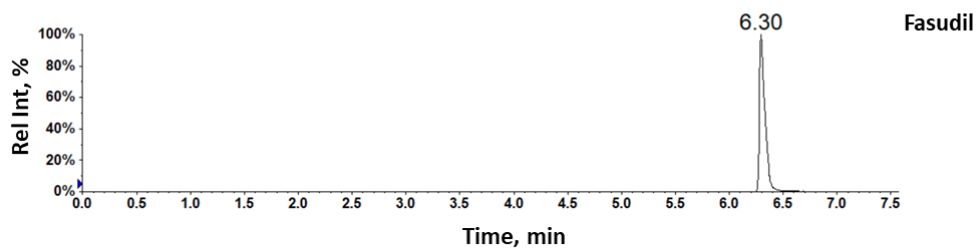
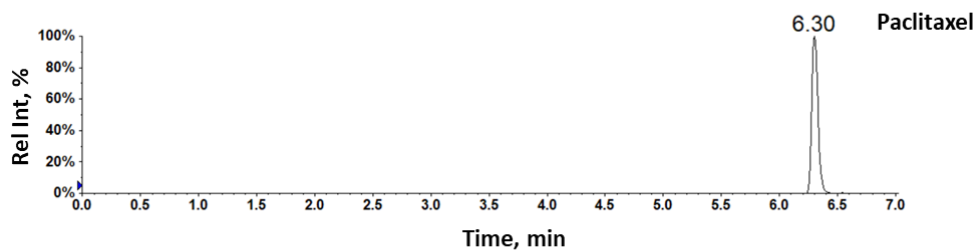
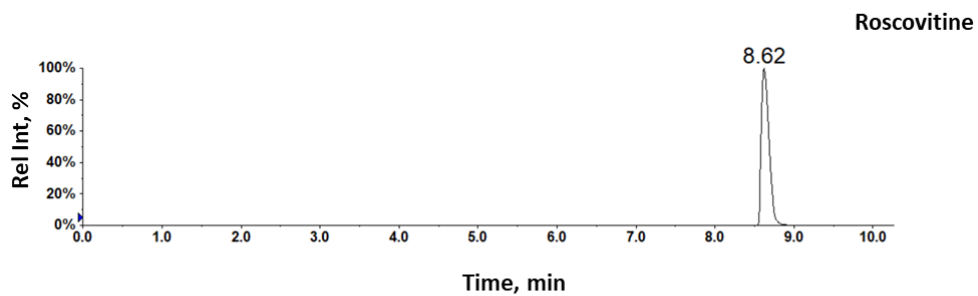
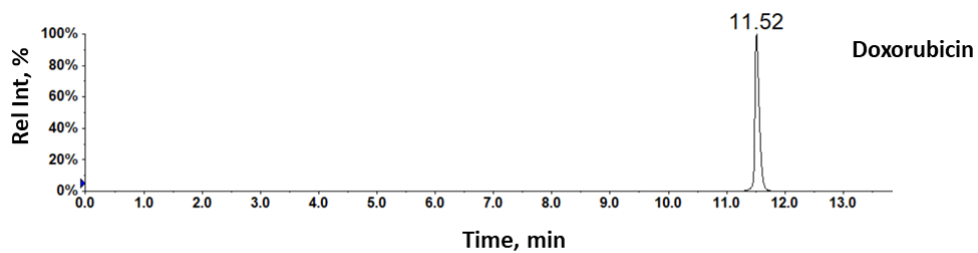
Drug	System output	Data transformation	Prediction model	P/F-value	Key factors
Rucaparib	S/N	Natural log	Quadratic	<0.0001/5.83	A, AB, E ² , G ²
	k	Square root	Quadratic	<0.0001/5.19	AB, A ² , B ² , D ²
	Peak width	Inverse	Quadratic	<0.0001/5.46	A, C, E, AB, AD, A ² , B ² , D ² , F ²
	T	None	Quadratic	0.0005/3.73	A, B, AB, A ² , B ² , E ² , F ²
Niraparib	S/N	Square root	Quadratic	0.0196/2.18	A, B, C, AB, A ² , B ²
	k	Square root	Quadratic	0.0011/3.26	A, F, AB, A ² , B ² , D ² , E ² , G ²
	Peak width	Inverse	Quadratic	<0.0001/7.76	A, B, C, AD, BE, C ² , E ² , F ² , G ²
	T	Square root	Quadratic	0.0002/4.28	A, B, AF, BE, BF, B ² , F ² , G ²
Fasudil	S/N	Square root	Quadratic	<0.001/3.61	A, C, A ²
	k	Square root	Quadratic	<0.0001/5.47	AB, A ² , B ² , D ² , F ² , G ²
	Peak width	Square root	Quadratic	<0.0001/4.39	A, C, AB, AC, AE, B ² , C ² , D ² , E ²
	T	None	Quadratic	<0.001/3.36	AB, A ² , B ²
Dinaciclib	S/N	Square root	Linear	<0.0001/6.41	A, C, E
	k	Power	2FI	<0.0001/2.43	AB, AD, A ² , B ² , C ² , D ² , E ² , F ² , G ²
	Peak width	Square root	Quadratic	<0.0001/8.82	A, C, D, AB, BD, A ² , B ² , C ² , D ²
	T	None	Quadratic	<0.0001/4.34	A, C, E, AB, AC, AE, BD, B ² , C ² , E ²
Resiquimod	S/N	Square root	Quadratic	<0.0001/4.21	A, C, E, AB
	k	Square root	Linear	<0.0001/2.16	A, AB, A ² , B ² , D ²
	Peak width	Square root	Quadratic	<0.0001/3.78	A, C, AB, BD, A ² , B ²
	T	Square root	Quadratic	<0.0001/4.11	A, B, C, AB, AC, BC, B ² , C ²

Ceritinib	S/N	Square root	Quadratic	0.0006/3.58	C, AB, AC, AE, C ² , D ²
	k	None	Quadratic	< 0.0001/6.02	A, F, AB, AF, A ² , B ² , C ² , D ² , E ² , F ² , G ²
	Peak width	Square root	Quadratic	< 0.0001/5.02	A, C, AB, AF, B ² , C ² , D ² , F ² , G ²
	T	None	Quadratic	< 0.0001/7.09	C, D, AB, AD, AF, BD, CE, A ² , B ² , C ² , F ²
Exemestane	S/N	Square root	Quadratic	< 0.0001/4.40	A, B, F; AB, A ²
	k	Square root	Linear	0.0012/4.07	A
	Peak width	Square root	Quadratic	< 0.0001/4.76	A, C, AB, AF, BF, FG, A ² , B ² , E ²
	T	Square root	Quadratic	< 0.0001/6.62	A, B, AB, A ² , B ² , E ²
Roscovitine	S/N	Square root	Linear	<0.0001/16.92	A, C
	k	Power	Quadratic	<0.0001/9.65	A, F, AC; AF, A ²
	Peak width	Square root	Quadratic	< 0.0001/5.68	A, C, D, F, AB, AD, AF, B ² , C ² , D ² , E ² , F ² , G ²
	T	None	Quadratic	0.0046/2.79	C, D, AF, A ² , D ²
Lapatinib	S/N	Inverse square root	Quadratic	<0.0001/20.81	A, C, E, AB, AC, AE, CE, A ² , B ² , C ² , D ² , E ² , F ² , G ²
	k	None	Quadratic	0.0085/2.48	A, B, AB, A ²
	Peak width	Square root	Quadratic	<0.0001/5.26	A, C, D, E, AB, A ² , E ²
	T	Natural log	Quadratic	<0.0001/6.44	C, D, E, AD, A ² , F ² , G ²
Curcumin	S/N	Natural log	Quadratic	<0.0001/14.12	A, C, F, AF, A ² , B ² , C ²
	k	Inverse square root	Linear	<0.0001/99.24	A, F
	Peak width	None	Quadratic	<0.0001/4.61	C, AB, AE, A ² , B ² , C ²
	T	Power	Quadratic	0.0006/3.49	A, B, D, AB, A ² , F ² , G ²
Bisdemethoxy curcumin	S/N	Square root	Quadratic	0.0056/2.63	A, F, AB, AF, A ² , C ² , D ²
	k	Power	Quadratic	<0.0001/17.30	A, F, AB, AC, AF, A ²
	Peak width	None	Quadratic	<0.0001/19.87	A, C, D, E, AC, AE, BD, CD, CE, A ² , C ² , D ²
	T	None	Quadratic	<0.0001/11.72	A, B, C, D, E, AE, AF, BG, DE, DG, A ² , B ² , C ² , D ² , G ²

Navitoclax	S/N	None	Quadratic	0.0014/3.21	A, C, F, AB, AD, D ²
	k	Power	Quadratic	<0.0001/5.91	A, F, AB, A ² , B ² , C ² , D ²
	Peak width	Square root	Quadratic	<0.0001/15.06	A, C, D, E, AB, AD, BD, A ² , B ² , C ² , D ² , F ² , G ²
	T	None	Quadratic	<0.0001/5.56	B, C, D, AB, BD, A ² , D ² , E ² , F ²
Doxorubicin	S/N	Square root	Linear	<0.0001/23.37	A, C
	k	Natural log	Quadratic	<0.0001/22.65	A, F, AB, AD, AF, A ² , B ² , C ² , D ² , E ² , F ² , G ²
	Peak width	Square root	Quadratic	<0.0001/8.98	A, C, AB, AD, B ² , D ²
	T	None	Quadratic	0.0001/4.27	A, D, AB, AD, AE, DE, B ²
Paclitaxel	S/N	Square root	Quadratic	<0.0001/5.27	A, B, AB, AG, BC, BF, CF, A ²
	k	Inverse square root	Linear	<0.0001/4.33	A, B
	Peak width	Natural log	Linear	0.0408/2.29	A, B
	T	Square root	Quadratic	<0.0001/6.73	A, B, AB, AG, BE, A ² , B ²
Lonidamine	S/N	Natural log	Quadratic	0.0133/2.73	AD, CE, CG, B ²
	k	Inverse square root	Linear	<0.0001/7.50	A, B, F
	Peak width	Square root	Quadratic	0.0005/3.58	A, B, F, AB, BE, BF, A ² , B ²
	T	Square root	Quadratic	<0.0001/5.97	A, B, F, AB, BE, BF, A ² , B ²
Lorlatinib	S/N	Square root	Quadratic	0.0425/2.91	A, E, AB, A ²
	k	None	Quadratic	<0.0001/11.81	A, F, AC, AF, A ²
	Peak width	Natural log	2FI	0.0011/3.12	A, C, E, AD; AF
	T	None	Quadratic	0.0012/2.57	D, A ² , D ² , E ²

S/N – signal-to-noise; k- retention factor; T- tailing factor; A- ACN % start; B- ACN % end; C- flow (ml/min); D- % Aq phase; E- Column temp. (°C); F- Gradient time (min); G- Plateau time (min)





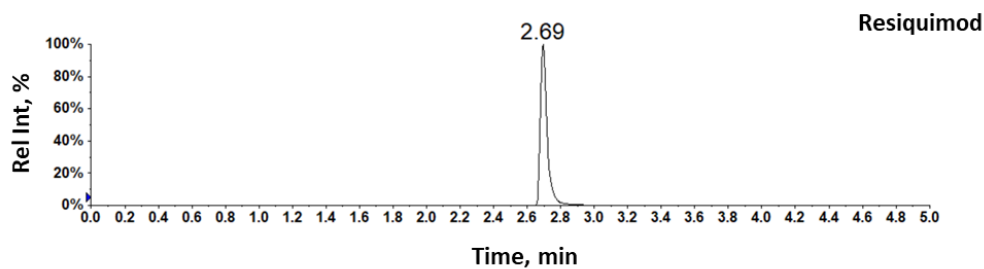
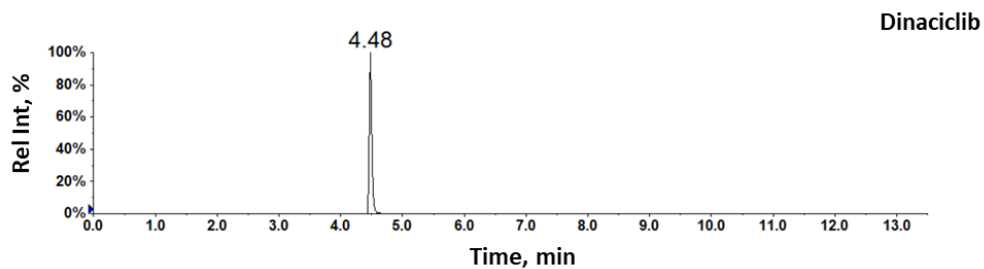
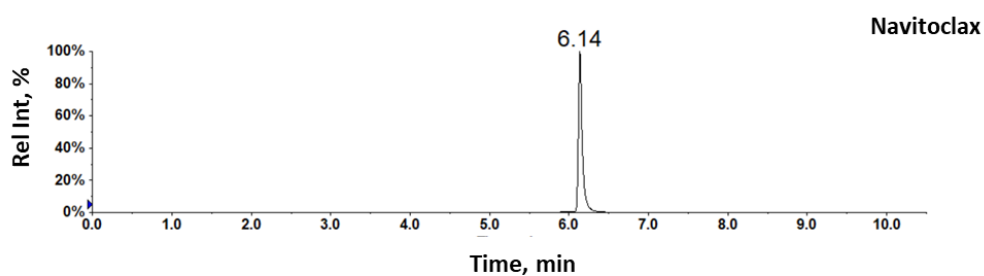
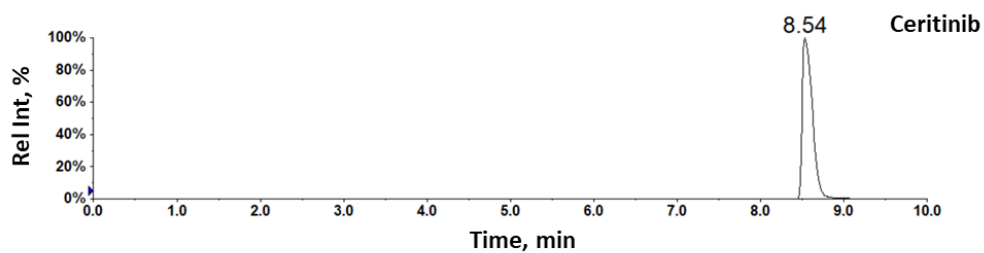


Figure S2.1. LC-MS/MS chromatograms of fourteen anticancer drugs obtained by DoE method development (Rel Int – relative intensity)

CHAPTER III

**DESIGN OF GENIPIN-ASSEMBLED
POLYPEPTIDE-BASED
NANOCONJUGATES FOR
COMBINATION THERAPY**

3.1 INTRODUCTION

Due to the molecular complexity of human pathologies, we require the simultaneous administration of multiple drugs to improve efficacy and decrease therapeutic resistance. Nanomedicine-based combination therapies represent an efficient means to treat pathologies such as triple negative breast cancer (TNBC),^{344,345} a complex heterogeneous disease with a high risk of metastasis and treatment resistance³⁴⁶. Relevant clinical milestones for combination nanomedicines include Combiplex® technology³⁴⁷, a liposome loaded with cytarabine and daunorubicin at a specific synergistic ratio (US Food and Drug Administration (FDA) approved Vyxeos, formerly CPX-351), which has improved all efficacy parameters, including overall survival, in Phase 3 clinical trial of high-risk acute myeloid leukemia patients.³⁴⁸

The multivalency of the polypeptidic carriers allows the conjugation of one or more active moieties (e.g., drugs in a specific ratio, imaging probe), ensuring the delivery of both drugs to the same cell at the same time following their site-specific release at the desired ratio and thereby potentiating synergism and therapeutic efficacy.

Polymer-based combination therapy design employs four broad types⁴⁹:

- I. polymer-drug conjugate + free drug(s) or a different type of therapy (e.g., radiotherapy)
- II. the combination of two single polymer-drug conjugates
- III. a single polymeric carrier carrying a combination of drugs
- IV. polymer-directed enzyme prodrug therapy (PDEPT) + polymer-enzyme liposome therapy (PELT)

While types I, II, and IV polymer combination therapies pose challenges in simultaneous drug combination delivery at the desired site of action, type III offers a robust means to address this issue. Using a single polymer to carry multiple drugs offers additional advantages, e.g., improved pharmacokinetics, co-delivery of drugs at a desired ratio, and specific release/activation at the site of action as a clear advantage compared with Combiplex® liposomal technology, as the presence of bioresponsive linkers may offer improved PK control.^{162,349} A possible reduction in loading capacity and the complexity associated with obtaining an optimal ratio and drug release necessary for a synergistic effect can impede the implementation of a single polymer chain as a carrier for two or more active moieties. Thus, we require novel, optimized protocols for developing polymer-based combination therapy including polypeptide-drug conjugates (PDCs).

The relatively small size (below 50 kDa and ≈5 nm in hydrodynamic size) of unmodified PDCs can prompt short circulation half-time and/or non-specific biodistribution profiles leading to low tumor accumulation. Increasing size can enhance the half-life of PDCs after intravenous administration and passive accumulation within pathological sites due to the enhanced permeation and retention effect.³⁷ Increasing the sizes of PDCs can employ bottom-up approaches such as supramolecular or self-assembly strategies and stabilization via crosslinking strategies. Interestingly, this strategy also supports the self-assembly and crosslinking of two different PDCs (e.g., carrying different drugs) at an adequate ratio to form a polypeptide-based combination PDC (Figure 3.1).

Our laboratory has explored various bottom-up approaches for the design of long-circulating PDCs, ranging from conventional supramolecular assembly^{241,350} to charge-like self-assembly²³⁴. In the latter, we utilized the “extraordinary” behavior of StPGA in non-salty aqueous solutions for assembly and stabilization employing click chemistry. As the harsh conditions used in click chemistry affect the stability of PDCs; therefore, we aimed to develop a new crosslinking method in water

starting from multiple single PDCs bearing selected drugs (Figure 3.1) to optimize and accelerate the generation of polypeptide-based combination conjugates with synergistic anticancer activity. For this purpose, we explored genipin, a natural water-soluble crosslinking agent well-known to interact with two amino groups to form covalent non-biodegradable linkages under mild conditions that do not affect any conjugated drugs or stimuli-responsive linking chemistries.³⁵¹ Star-shaped polyglutamates (StPGAs) present self-assembly activity in aqueous solutions, supporting the development of said crosslinked combinatorial treatment strategies.

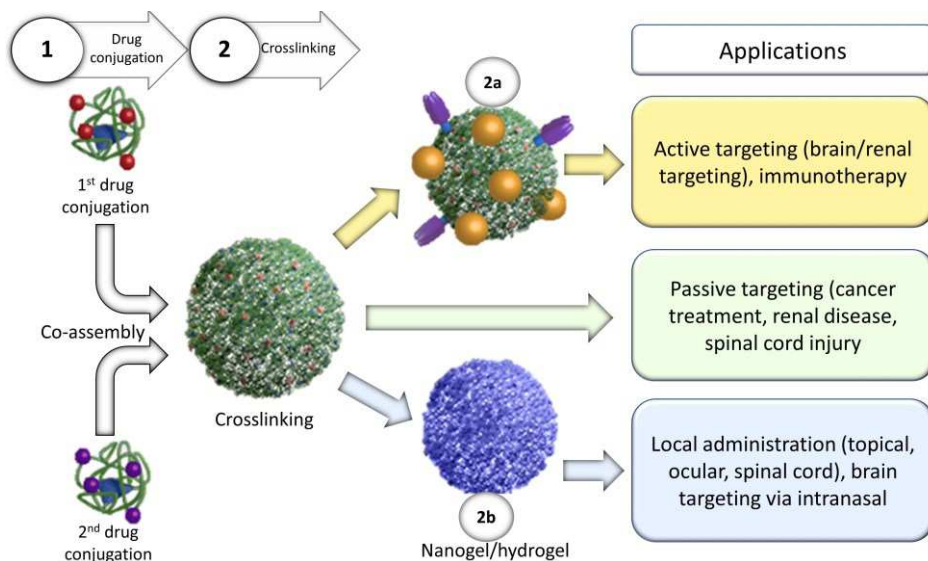


Figure 3.1. Rational design of crosslinked self-assembled PDCs functionalized with active moieties before assembly (1). Depending on the delivery need, surface modification with targeting moieties (2a) can enable active transport. Alternatively, gelation (2b) of the carrier and formation of nanogel/hydrogel represents another possibility of post-crosslinking modification (crucial for local delivery and brain targeting via intranasal administration).

Like any chemical reaction, crosslinking involves multiple modifiable steps and constituents to obtain the desired end-product. The optimization process frequently proceeds entirely via a trial-and-error approach involving the variation of one factor at a time (e.g., temperature, solvent, concentration, catalyst, or pH), which impedes the identification of optimal conditions for a particular process in the presence of interactions between two or more factors. Thus, we intended to explore and demonstrate the implementation of DoE in synthesizing anticancer therapeutics, particularly a genipin-crosslinked StPGA-based combination conjugate, which facilitates the identification of optimized experimental conditions.

As discussed in Chapter I, every drug delivery system must undergo characterization using a robust and fit-for-purpose analytical method. For size, molecular weight (Mw), polydispersity (PDI) determination, and conformation studies, we can implement techniques such as dynamic light scattering (DLS), small angle scattering (SAS), size exclusion chromatography (SEC), and asymmetric flow field flow fractionation (AF4). While DLS represents a straightforward and rapid technique, these results require the support of complementary methods due to problems related to light absorption, large aggregates, mathematical calculations, and the available sample amount. While sophisticated SAS techniques can provide valuable information regarding PDCs, the cost and general inaccessibility of such an approach preclude them from routine analysis; instead, only selected candidates generally undergo characterization by SAS. AF4 has emerged as a complementary characterization technique given numerous advantages over batch DLS, SAS, and SEC including i) enhanced separation of high molecular weight molecules, ii) a lack of shear degradation and interaction with columns, iii) no requirement for calibrations curve obtained from standard materials that do not match the analyte, iv) “tailor-made” separation by cross-flow adjustment, v) the adjustment of separation according to the unique requirements of a given sample (implementing

a gradient of any shape), and vi) the ability to analyze gels and complex nanosystems.²⁶⁰ AF4 has emerged as a powerful tool for macromolecule characterization³⁵²; however, a methodology to evaluate polyelectrolytes such as PGA by AF4 remains incompletely described. We also lack a complete understanding of how PGA behaves within the AF4 separation module - this information could foster an enhanced interpretation of experimental results.

Thus, we also aimed to evaluate the implementation of AF4 as a complementary method to small angle x-ray scattering (SAXS) for the exhaustive characterization of a genipin-crosslinked StPGA-based combination conjugate.

The specific objectives of this chapter aim are:

Objective 1. Evaluation of the behavior of PGA-based nanocarriers within the AF4 separation module

Objective 2. Implementation of DoE in the synthesis of genipin crosslinked self-assembled star-shaped polypeptide-based combination conjugates.

3.2 RESULTS

3.2.1 Evaluating the behavior of PGA within the AF4 separation module

The AF4 coupled with refractive index, ultraviolet and multi-angle light scattering detectors (AF4-RI-UV/Vis-MALS) represents a powerful tool for characterizing charged polypeptides such as PGA. Nevertheless, using an analytical tool with an elevated level of complexity to interpret and extrapolate results to

meaningful molecular parameters requires knowledge of the behavior of PGA in the AF4 channel and careful method optimization. Therefore, we evaluated the influence of crossflow, focusing time, carrier fluid composition, injected mass, and membrane type, specifically on regenerative cellulose (RC) and polyethersulfone (PES) on PGA retention. We evaluated each experimental condition by calculating the recovery of PGA according to the equation:

$$R(\%) = \frac{mass_{eluted}}{mass_{injected}}$$

To consider the day-to-day variability in instrument response and the efficacy of membrane after multiple injections, we analyzed a standard solution of bovine serum albumin (BSA, 1 mg/ml) at the beginning and the end of each sequence. We ensured that BSA recovery variability lay in the range of $\pm 5\%$ each day to allow the correct evaluation of the experimental results. Multiple and consecutive injections primarily affect the membrane's life expectancy; thus, we can exchange membranes if BSA recovery falls beyond the set limits. To ensure the repeatability of our results with a replacement membrane, and to condition the column we first covered the surface with BSA by analyzing the BSA standard solution until the BSA recovery reached a plateau.

We conducted our study with different molecular weight PGAs (12-25 kDa) of different architectures - linear (LinPGA) and StPGA to evaluate their interaction with the AF4 membrane and to evaluate the correlation of molecular weight and the recovery. First, we explored the influence of three different membranes (RC with a 10 kDa cut-off, RC with a 5 kDa cut-off, and PES with a 5 kDa cut-off) on PGA recovery. We hypothesized that the lower membrane cut-off would improve PGA recovery, given the lower level of elimination of PGAs of 12-25 kDa through the 5

kDa compared to the 10 kDa cut-off membrane. Interestingly, we obtained the opposite results – the PGA recovery of both LinPGA and StPGA became significantly reduced when implementing a lower cut-off membrane (Figure 3.2, $p = 0.0032$ for PGA(100), $p = 0.0001$ for PGA(150), $p = 0.0012$ for PGA(200), $p = 0.0014$ for StPGA(100), $p = 0.0021$ for StPGA(150), and $p = 0.0013$ for StPGA(200)). We attributed this phenomenon to the interactions between charged PGA and the charged membranes, as a smaller cut-off leads to a more positive membrane.³⁵³ In other words, a small pore radius (cut off) entails a higher membrane potential as the diffuse part of the membrane's double layer fills the entire pore; the counter ions from the carrier fluid become excluded, and consequently, the membrane becomes less charged. Thus, we found that 5 kDa RC displays a lower negative charge, leading to a weaker repulsion force between the membrane and the negatively charged PGAs and, consequently, smaller recoveries. Furthermore, our results suggest that PES 5 kDa allows for a significantly higher recovery during PGA analysis, as this membrane possesses a more negative zeta potential (-70) compared to RC 5 kDa membrane (-30) at physiological pH (obtained by Postnova), which induces more potent electrostatic repulsion and lower membrane adsorption (Figure 3.2, $p = 0.0012$ for PGA(100), $p = 0.003$ for PGA(150), $p = 0.0004$ for PGA(200), $p = 0.001$ for StPGA(100), $p = 0.0015$ for StPGA(150), and $p = 0.0015$ for StPGA(200)).

Interestingly, we also observed unexpected results when comparing PGAs of differing Mw values - increased Mw led to decreased recovery for both LinPGA (92.4% for LinPGA with 100 Glu units – LinPGA(100), 72.8% for LinPGA(150), and 62.5% for LinPGA(200)) and StPGA (94.4% for StPGA(100), 70.3% for StPGA(150) and 61.01% for StPGA(200)) when employing a 10 kDa RC membrane (Figure 3.2). To better understand this behavior, we calculated the Mw for each PGA sample and obtained lower values for 150 and 200 Glu units than expected. More specifically, for both LinPGA(150) and star PGA(150), we obtained Mw values in the range of

10-12 kDa instead of the expected 24 kDa: Meanwhile, for both LinPGA(200) and StPGA(200), we obtained Mw values in the range of 8-10 kDa instead of the expected 32 kDa. This difference derived from the highly acidic conditions used for deprotection after PGA polymerization, which induced peptide bond cleavage and lower-than-intended Mw values. Using milder conditions for deprotection ensured the synthesis of PGAs with expected Mw values. Thus, we implemented newly synthesized PGA and StPGA with a controlled synthesis that guaranteed the adequate physico-chemical characteristics of the polypeptide carrier.

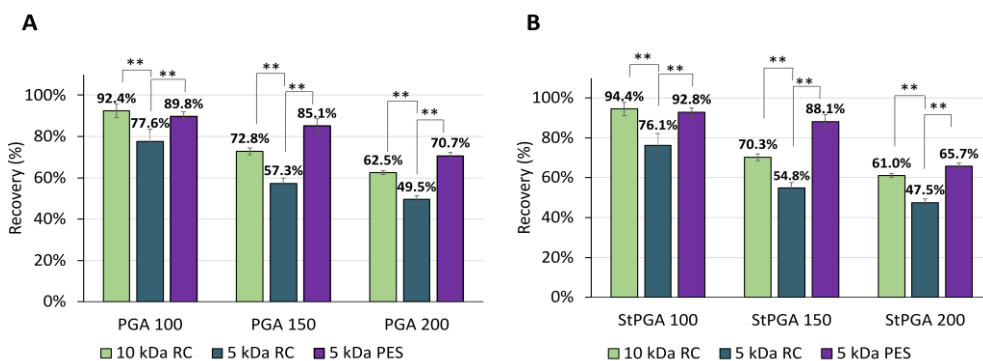


Figure 3.2. The influence of membrane on PGA analysis by AF4. Recovery values of (A) linear (Lin)PGA and (B) star-shaped (StPGA) analyzed with RC 10 kDa, RC 5 kDa, and PES 5 kDa membranes. Recovery values presented as average \pm SD, $n = 3$; ** $p < 0.005$.

Our new analysis of membrane influence demonstrated that increasing Mw leads to higher PGA recovery (Figure 3.3). Overall, we observed significantly lower recovery values for the RC 5 kDa membrane compared to the RC 10 kDa ($p = 0.0015$ for PGA(100), $p = 0.0003$ for PGA(150), $p = 0.012$ for PGA(200), $p = 0.0016$ for StPGA(100), $p = 0.0012$ for StPGA(150), and $p = 0.031$ for StPGA(200) and PES 5 kDa membranes ($p = 0.0002$ for PGA(100), $p = 0.0003$ for PGA(150), $p = 0.0012$ for PGA(200), $p = 0.0004$ for StPGA(100), $p = 0.0001$ for StPGA(150), and $p = 0.0013$ for

StPGA(200) (Figure 3.3). Thus, the RC 5 kDa membrane is an inappropriate choice for the PGA analysis due to the lowest recovery values. A comparison between the RC 10 kDa and PES 5 kDa membranes failed to reveal significantly different recovery values for PGAs of all Mw values; however, we employed the PES 5 kDa membrane in all subsequent relevant studies as we obtained 92-97% recovery even when implementing a low Mw cut-off (of benefit when analyzing low Mw samples).

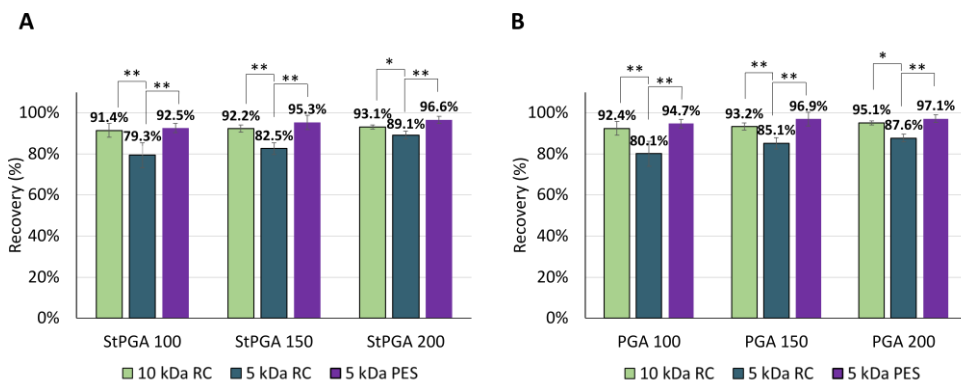


Figure 3.3. The new evaluation of membrane type influences the analysis of PGA by AF4. Recovery values of (A) linear PGA and (B) star PGA analyzed with RC 10 kDa, RC 5 kDa, and PES 5 kDa membrane. (Recovery values presented as average \pm SD, $n = 3$; * $p < 0.05$, ** $p < 0.005$)

Next, we implemented a DoE approach and performed twenty-nine experiments to explore the complex interactions between AF factors (Defined in Table 3.1). We evaluated each experimental condition by following StPGA(150) recovery as a system output, as the method under development uses StPGA(150) as a component of the genipin-crosslinked StPGA-based combination conjugate. AF4 parameters evaluated included: F_{cross} (0.1-3.5 ml/min, factor A), focusing time (1-5 min, factor B), carrier fluid composition (10-50 mM phosphate buffer [PB], factor C), and injected mass (10-62.5 μ g, factor D). We used $t_{run} = 45$ min and end $F_{cross} = 0$ ml/min for all twenty-nine experiments.

The ANOVA statistical analysis indicates that factors A (F_{cross}), B (focusing time), C (carrier fluid composition), A^2 , B^2 , C^2 and the interaction BD, CD, significantly influence StPGA150 recovery when analyzing with the AF4 (Table 3.2, $p < 0.05$). Additionally, the coefficient estimates for factor A (-13.5), B (-3.58), C (-6.58), and D (-1.33) indicate that an increase in value reduces StPGA recovery.

Table 3.1. Experimental matrix table defining the conditions for each experiment

Method	Factor A F_{cross} , ml/min	Factor B Focusing time, min	Factor C Carrier fluid composition, mM	Factor D Injected mass, mg
1	0.1	3	10	0.3175
2	1.8	3	30	0.3175
3	3.5	1	30	0.3175
4	1.8	1	30	0.625
5	1.8	5	10	0.3175
6	1.8	5	30	0.625
7	3.5	3	30	0.625
8	3.5	3	10	0.3175
9	3.5	3	30	0.01
10	1.8	3	30	0.3175
11	1.8	3	30	0.3175
12	0.1	3	30	0.625
13	0.1	3	50	0.3175
14	1.8	3	10	0.625
15	0.1	5	30	0.3175
16	1.8	1	10	0.3175
17	0.1	3	30	0.01
18	0.1	1	30	0.3175
19	1.8	3	50	0.625
20	1.8	1	30	0.01
21	1.8	3	50	0.01
22	1.8	1	50	0.3175
23	1.8	3	30	0.3175
24	3.5	5	30	0.3175

25	1.8	3	30	0.3175
26	3.5	3	50	0.3175
27	1.8	5	30	0.01
28	1.8	3	10	0.01
29	1.8	5	50	0.3175

Table 3.2. ANOVA statistical analysis of DoE Box-Behnken design implemented for determination of AF4 factors with significant influence on StPGA analysis.

Source	<i>p</i> -value
Model	< 0.0001
Factor A (Cross flow)	< 0.0001
Factor B (Focusing time)	0.0007
Factor C (Carrier fluid composition)	< 0.0001
Factor D (Injected mass)	0.1329
AB	0.7349
AC	0.3175
AD	0.1886
BC	0.6124
BD	0.0019
CD	< 0.0001
A²	0.0001
B²	0.0066
C²	0.0066
D²	0.6719

The model *p*-value implies that the DoE quadratic model can predict recovery values in the design space. *P*-values less than 0.05 indicate significant model terms.

These results agreed with our expectations - an increased crossflow (factor A) implemented in the fractionation channel will pull analytes closer to the accumulation wall, leading to a stronger interaction with the membrane. Longer focusing times (factor B) during the first step in AF4 analysis will increase the chance for the analyte to interact with the membrane, which will consequently lower recovery. We attributed the significant influence of salt content in the carrier fluid (factor C) on StPGA recovery to a reduction in the PES membrane's z-potential (a more positive membrane surface lowers the repulsion forces between StPGA and the PES membrane), leading to the sample loss and recovery decrease. The injected mass (Factor D) negatively influenced the recovery of StPGA with an overloading effect and retention time shift observed on the AF4 fractogram (Figure 3.4.) but with no significant influence on the StPGA recovery ($p = 0.1329$). However, factor D in combination with changes to focusing time (factor B), significantly influences StPGA recovery ($p = 0.0019$) due to the strong and significant interaction between these two factors. Increasing focusing time (factor B) and injected mass (factor D) will increase recovery values (coefficient estimated 5.50, Figure 3.5A) because the longer focusing time that leads to higher interaction of StPGA with the membrane becomes compensated by the higher mass injected into the channel. Similarly, the increased injected mass (factor D) compensates for the negative effect of higher salt content (factor C) on the recovery value (coefficient estimate for CD interaction = 8.0, Figure 3.5B). Nevertheless, the compensation of the StPGA injected mass (factor D) on the negative effect of high focusing time (factor B) and salt content (factor C) only occurs with a lower cross flow (factor A) as the high crossflow of 3.5 ml/min efficiently pushes even a high injected mass (0.0625 mg) towards the accumulation wall (Figure 3.6). These data, together with the p -value of term A^2 ($p=0.0001$) and the coefficient estimate of term A (-13.5), suggest that factor A (F_{cross}) exhibits the most significant effect on StPGA recovery.

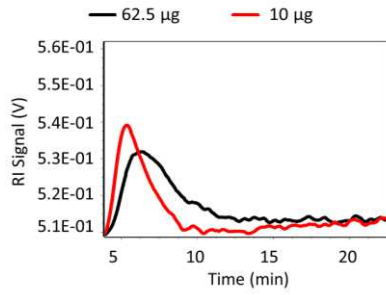
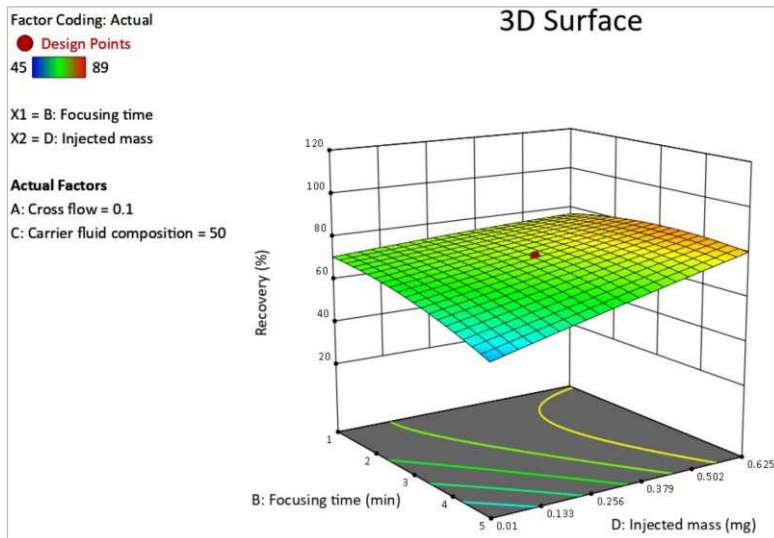


Figure 3.4. Overloading effect in PGA analysis by AF4. The AF4 fractogram obtained from the analysis of StPGA with 62.5 µg (black line) and 10 µg (red line) injected mass.

A



B

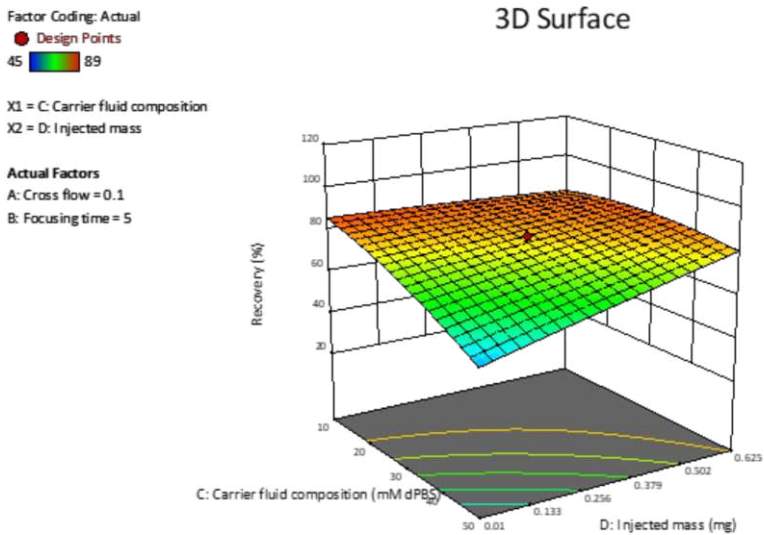


Figure 3.5. 3D response surface plot representing the dependence of StPGA recovery on (A) focusing time and injected mass, with the cross-flow and carrier fluid composition at a constant level (0.1 ml/min and 50 mM dPBS, respectively) and (B) carrier fluid composition and the injected mass, with the cross-flow and focusing time at a constant level (0.1 ml/min and 5 min, respectively).

A

Factor Coding: Actual

● Design Points

45 89

X1 = B: Focusing time

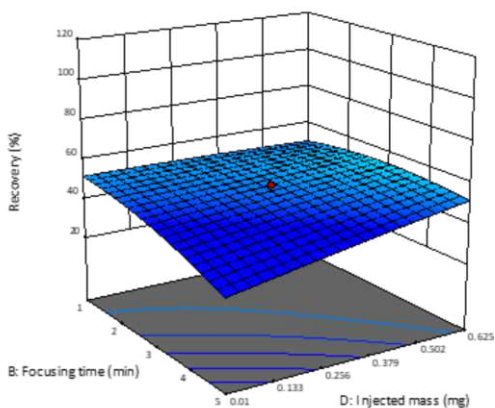
X2 = D: Injected mass

Actual Factors

A: Cross flow = 3.5

C: Carrier fluid composition = 50

3D Surface



B

Factor Coding: Actual

○ Design Points

45 89

X1 = C: Carrier fluid composition

X2 = D: Injected mass

Actual Factors

A: Cross flow = 3.5

B: Focusing time = 5

3D Surface

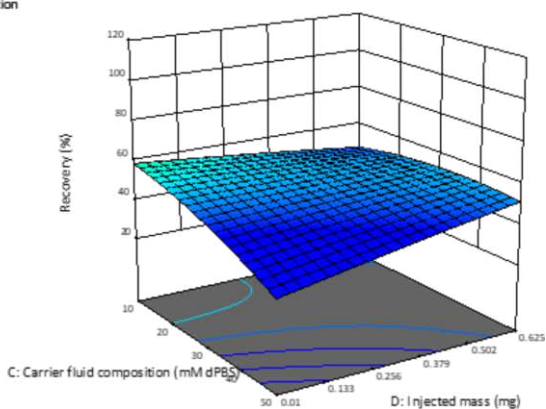
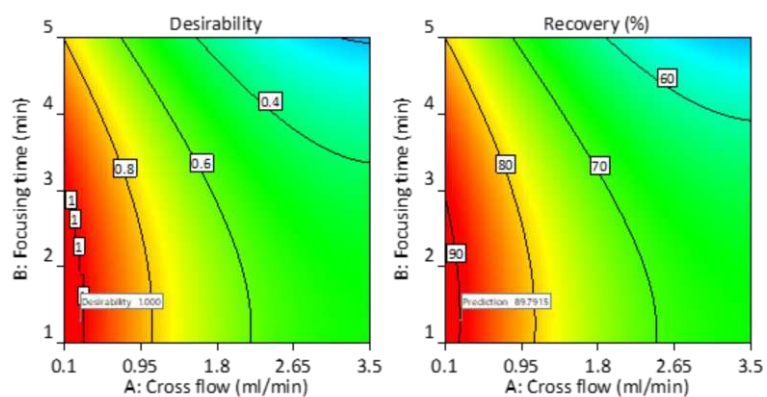
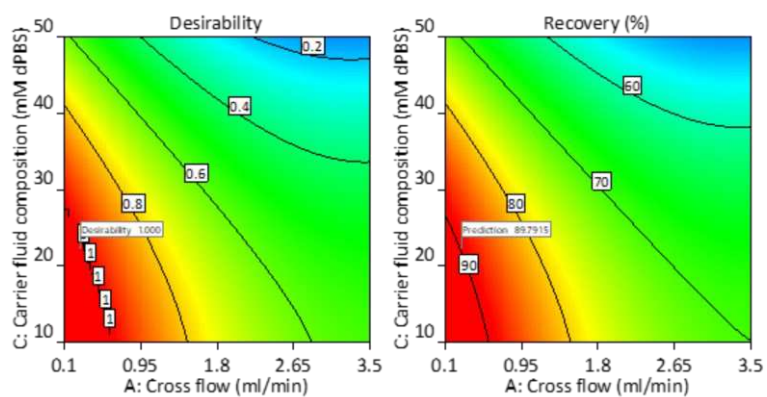
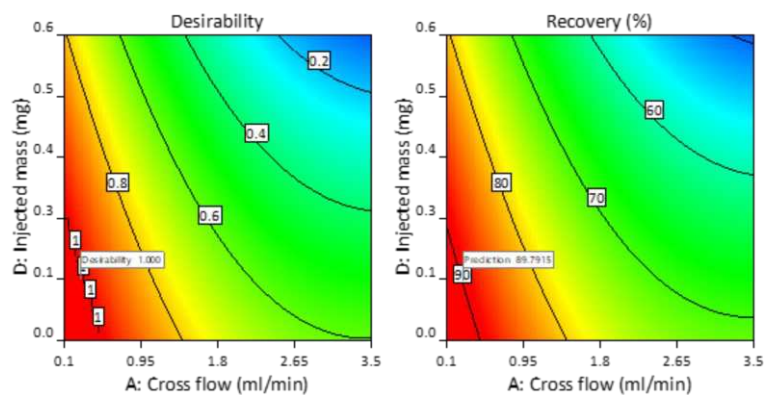


Figure 3.6. 3D Response surface plot representing the dependence of StPGA recovery on (A) focusing time (factor B) and injected mass (factor D), with the cross-flow (factor A) and carrier fluid composition (factor C) at a constant level (3.5 ml/min and 50 mM dPBS, respectively) and (B) carrier fluid composition (factor C) and the injected mass (factor D),

with the cross-flow (factor A) and focusing time (factor B) at a constant level (3.5 ml/min and 5 min, respectively).

Finally, we obtained the optimal conditions for each factor by analysis of desirability functions for each factor combinations to maximize StPGA recovery (Figure 3.7). The contour plots indicate that the optimal values for AF4 factors to obtain a desirability value >0.8 (red color, left graph) and recovery value higher than 80% (red color, right graph) were as follows: cross-flow < 1 ml/min, focusing time < 4.3 min, carrier fluid composition < 40 mM dPBS, and injection mass < 0.48 μ g.

Overall, we evaluated the influence of different AF4 factors on the behavior of StPGA(150) in the AF4 channel and obtained an optimal range for each examined factor that we subsequently implemented in the analysis of the size and Mw determination.

A**B****C**

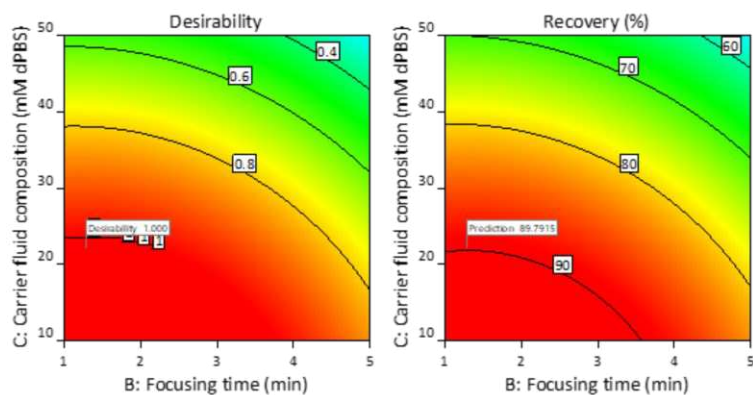
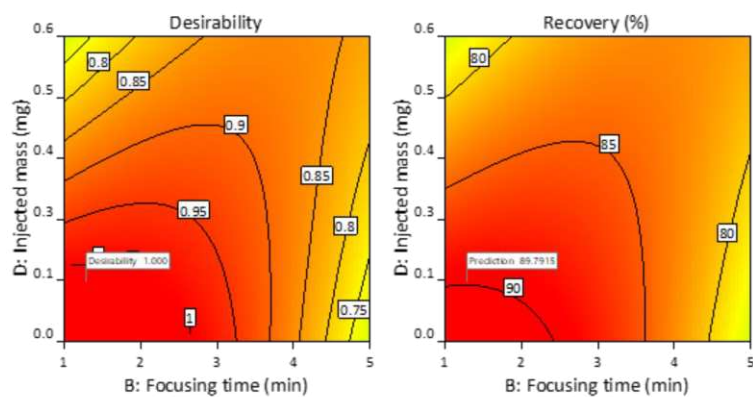
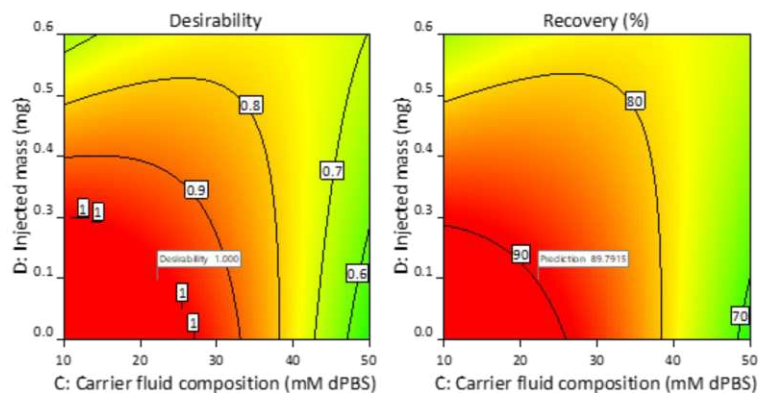
D**E****F**

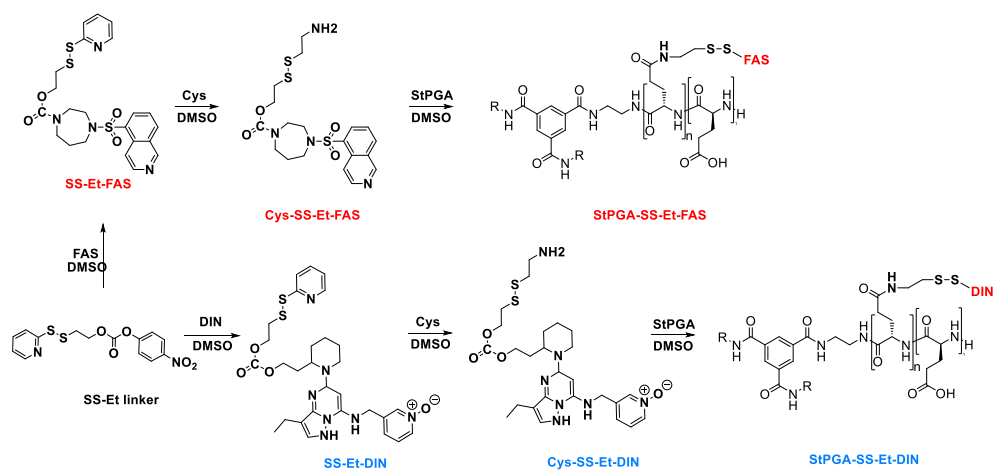
Figure 3.7. Contour plots obtained from the Box-Behnken design used to determine optimal AF4 conditions for StPGA analysis. Factor interactions between (A) factors A and B, (B) factors A and C, (C) factors A and D, (D) factors B and C, (E) factors B and D, (F) factors C and D, shown on the bases of desirability value (left graphs) and the recovery values (right graph). (A- cross flow, B- focusing time, C – carrier fluid composition, D- injection mass).

3.2.2 DoE implementation in the synthesis of genipin-crosslinked StPGA-based combination conjugates

We next used DoE to develop a new crosslinking method for PDCs in water to optimize and accelerate the generation of a genipin-crosslinked StPGA-based combination conjugate with synergistic anticancer activity. We selected fasudil (FAS) and dinaciclib (DIN) conjugated to StPGA (StPGA-SS-Et-FAS and StPGA-SS-Et-DIN), as model PDCs combination therapy for triple negative breast cancer (TNBC) as FAS and DIN synergistic effect was observed within the European Research Council project "*Towards the design of Personalized Polymer-based Combination Nanomedicines for Advanced Stage Breast Cancer Patients (MyNano)*" (see more details in Chapter IV). Additionally, different chemical properties of FAS and DIN offered us the possibility to examine the influence of drug type in the genipin crosslinking.

We synthesized single (StPGA-SS-Et-FAS and StPGA-SS-Et-DIN) PDCs that employed a self-immolating disulfide linker using an ethyl spacer between the drugs and StPGA carrier (Scheme 4.1) based on a protocol described in the Ph.D. thesis of Oleksandr Zagorodko and recently published with the difference in type of the carrier (StPGA instead of LinPGA).³²⁶ Briefly, to synthesize StPGA-SS-Et-FAS and StPGA-SS-Et-DIN, we first obtained disulfide-ethyl-fasudil (SS-Et-FAS) and disulfide-ethyl-dinaciclib (SS-Et-DIN) by using an SS-Et linker with an alcohol-

activated group (activation by p-nitrophenyl chloroformate) and free drugs. The final conjugation step comprised a thiol exchange with cysteamine hydrochloride and conjugation to StPGA through amide coupling (Scheme 3.1; see section 3.5.4 for more details on the synthesis). We obtained StPGA-SS-Et-FAS and StPGA-SS-Et-DIN with high yield and purity as shown by low free drug content (analyzed by LC-MS/MS), a hydrodynamic radius of 5-10 nm, and a z-potential of ≈ -20 mV (Table 3.3).



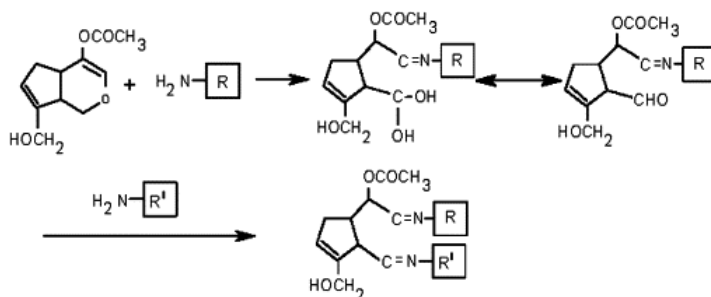
Scheme 3.1. Schematic representation of StPGA-SS-Et-FAS and StGA-SS-Et-DIN synthesis

Table 3.3. Physicochemical characterization of single StPGA-based PDCs

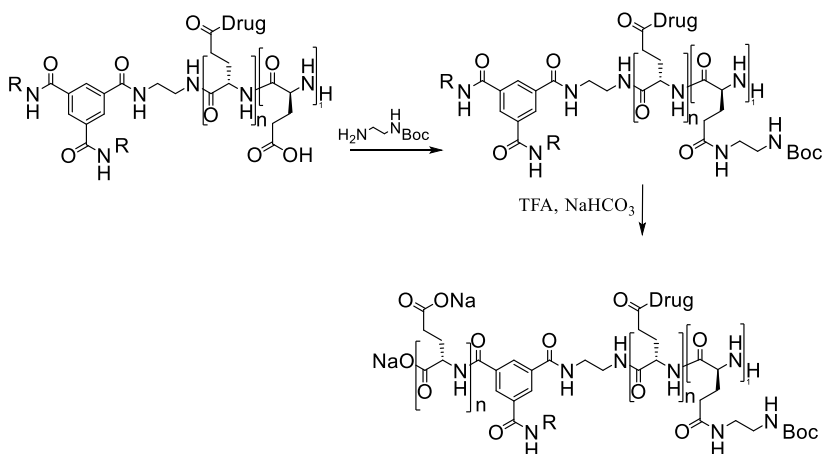
Compound	TDL (wt%) FAS/DIN	FD (wt% to TDL) FAS/DIN	Yield, %	Size, nm (average by number)	Z potential, mV
StPGA-SS-Et-FAS	12.58/-	< 0.005	82	5	-21.4
StPGA-SS-Et-DIN	-/6.55	0.008	78	5	-20.1

For the genipin crosslinking strategy (Scheme 3.2), we first modified the -COOH side-chain groups of StPGA-SS-Et-FAS and StPGA-SS-Et-DIN conjugates by 10 % (mol/mol) with an ethylenediamine derivative using a two-step synthesis (Scheme 3.3).

Next, we performed twenty-nine crosslinking reactions designed by DoE (Table 3.4) by simultaneously changing factors such as PDC concentration (1 - 5 mg/ml), genipin equivalence (0.25 – 1 eq), ionic strength (0 mM salt – Milli-Q, 10 mM dPBS, 240 mM dPBS), and PDCs ratio (ratio between StPGA-SS-Et-DIN and StPGA-SS-Et-FAS conjugates in the reaction solution, 0 = 1:15; 1 = 1:1000; -1 = 1:0). After 24 h, we removed unreacted genipin with glycine to avoid any additional crosslinking in the sample purification process. We analyzed the obtained blue products (Figure 3.8) by AF4-UV/Vis-MALS and SAXS to determine the size, PDI, and absorbance and used the obtained values in the DoE model to evaluate how the conditions of the chemical reaction influence genipin-crosslinked StPGA-based combination conjugate formation.



Scheme 3.2. Schematic representation of the genipin crosslinking mechanism proposed by Zhu and Park³⁵⁴



Scheme 3.3. Amino functionalization reaction scheme and salt transformation of StPGA-drug conjugates as the first step in the genipin crosslinking reaction

Table 3.4. Experimental design table for genipin crosslinking optimization

Exp N°	Conc (mg/ml)	Genipin equivalence	Ionic strength*	PDCs ratio**	Size (nm)	Abs	PDI
1	1	0.25	0	0	25.1	0.049	1.078
2	5	0.25	0	0	41	0.064	1.071
3	1	1	0	0	49.7	0.077	1.015
4	5	1	0	0	61.4	0.16	1.025
5	3	0.625	-1	-1	33.2	0.055	1.051
6	3	0.625	1	-1	46.3	0.045	1.068
7	3	0.625	-1	1	52.3	0.043	1.039
8	3	0.625	1	1	46.1	0.041	1.075
9	1	0.625	0	-1	5	0.018	0
10	5	0.625	0	-1	5	0.018	0
11	1	0.625	0	1	35.2	0.025	1.83
12	5	0.625	0	1	43.7	0.032	1.33
13	3	0.25	-1	0	36.8	0.029	1.27
14	3	1	-1	0	50.7	0.16	1.006
15	3	0.25	1	0	48.5	0.047	1.054
16	3	1	1	0	38.3	0.13	1.01
17	1	0.625	-1	0	43.4	0.056	1.02

18	5	0.625	-1	0	52.3	0.22	1.007
19	1	0.625	1	0	41.3	0.06	1.017
20	5	0.625	1	0	39.9	0.069	1.01
21	3	0.25	0	-1	32.7	0.036	1.14
22	3	1	0	-1	24.2	0.05	1.053
23	3	0.25	0	1	30	0.038	1.16
24	3	1	0	1	33.5	0.051	1.078
25	3	0.625	0	0	30.1	0.042	1.18
26	3	0.625	0	0	30.2	0.044	1.18
27	3	0.625	0	0	30.1	0.042	1.19
28	3	0.625	0	0	30.2	0.043	1.19
29	3	0.625	0	0	30.1	0.042	1.17

*0 = 10 mM dPBS; 1 = 240 mM dPBS; -1 = Milli-Q; **0 = StPGA_DIN: StPGA_FAS 1:15; 1 = StPGA_DIN: StPGA_FAS 1:1000; -1 = StPGA_DIN: StPGA_FAS 1:0; Exp – experiment, Abs- absorbance, PDI- polydispersity index

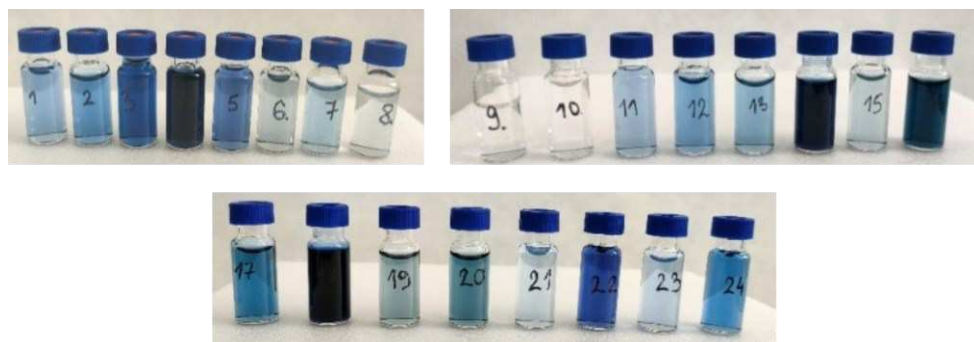


Figure 3.8. Genipin-crosslinked StPGA-based combination conjugate obtained by DoE. A more intense blue color correlates to a higher degree of genipin crosslinking (all solutions prepared at 2 mg/ml concentration in dPBS).

We accomplished the first step of multivariate optimization by Box-Behnken design to screen the factors studied and obtain the significant factors influencing each reaction output (i.e., UV absorbance signal, size average by number, and PDI). In this case, the UV absorbance signal signifies the degree of genipin-crosslinking – an increase in the genipin concentration in the reaction usually leads to a higher crosslinking degree demonstrated by a more intense blue color (Figure 3.8, see runs N° 4, 14, 16, and 18 with UV absorbance signals of 0.162, 0.163, 0.126, and 0.219). Interestingly, we obtained the highest absorbance value of run N°18 with a 0.625 eq. of genipin instead of the highest genipin equivalence (runs N°4, 14, and 16), indicating that the reaction degree depends on additional factors/possible factor interactions.


ANOVA analysis (Table 3.5) suggests factor A (polymer concentration, $p = 0.011$), factor B (genipin eq., $p = 0.0402$), and interactions between factors A and C (polymer concentration and ionic strength, $p = 0.048$) as statistically significant factors that impact crosslinking. We observed increased crosslinking with an increase of both genipin eq. and polymer concentrations (Figure 3.9A); however, we failed to observe the same behavior in the presence of a high ionic strength reaction solution (Figure 3.9B). Therefore, although ionic strength alone non-significantly influences crosslinking, we observed a significant interaction with polymer concentration. Of note, we can only obtain the dependence of crosslinking degree on factor interaction by DoE, which represents a significant advantage over the OFAT approach.

Table 3.5. ANOVA statistical analysis of DoE Box-Behnken design implemented for determination of reaction conditions with significant influence on the crosslinking degree.

Source	p-value
Model	0.039
Factor A - Polymer concentration	0.0402
Factor B - Genipin equivalent	0.011
Factor C - Ionic strength	0.17
Factor D – PDCs ratio	0.95
AB	0.33
AC	0.048
AD	0.92
BC	0.44
BD	0.99
CD	0.91
A²	0.016
B²	0.0093
C²	0.0044
D²	0.32

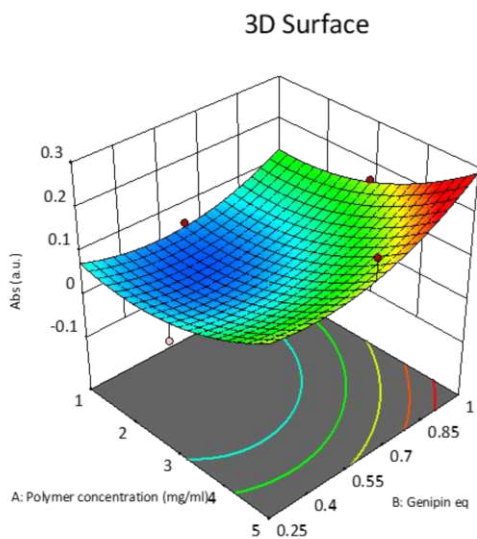
The model *p*-value implies that the DoE quadratic model can predict absorbance values in the designed space. *P*-values less than 0.05 indicate significant model terms.


A

Factor Coding: Actual
 Design Points:
 ● Above Surface
 ○ Below Surface
 0.0185  0.219

X1 = A: Polymer concentration
 X2 = B: Genipin eq

Actual Factors
 C: Ionic strength = -1
 D: Hydrophobicity = 0

**B**

Factor Coding: Actual
 Design Points:
 ● Above Surface
 ○ Below Surface
 0.0185  0.219

X1 = A: Polymer concentration
 X2 = B: Genipin eq

Actual Factors
 C: Ionic strength = 1
 D: Hydrophobicity = 0

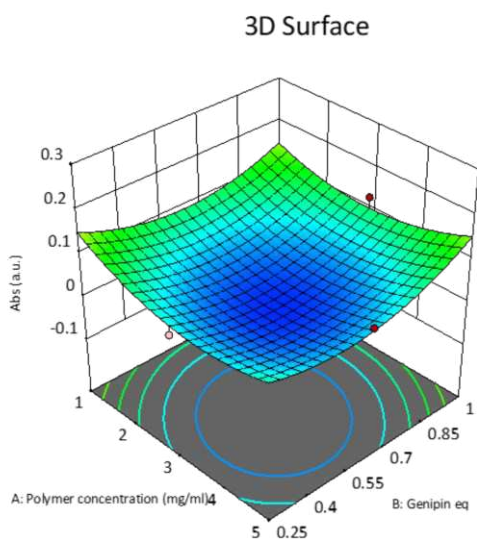


Figure 3.9. 3D Response surface plot describing the dependence of genipin crosslinking on genipin equivalence, polymer concentration, and ionic strength while PDCs ratio (hydrophobicity) remains constant (0 = StPGA-SS-Et-DIN: StPGA-SS-Et-FAS 1:1:15). (A) Level of ionic strength set at -1 (Milli-Q water), (B) Level of ionic strength set at 1 (240 mM dPBS)

Next, we evaluated the influence of reaction condition parameters on the obtained size of genipin crosslinked nanoconjugates. The model p-value of 0.0414, obtained from the ANOVA test, implies that the quadratic model fits the purpose and ensures that the model can predict the values. The p-values for factors A, B, and C (0.25, 0.25, and 0.82, respectively, Table 3.6.) indicate that polymer concentration, genipin equivalence, and ionic strength exhibit non-significant influence on the obtained size of genipin-crosslinked nanoconjugates. We hypothesized that an insufficiently wide design space (maximum and minimum levels of factors A, B, and C precluded the discovery of a significant difference. Only factor D (the PDCs ratio, $p = 0.022$) and the interaction between factors C and D (ionic strength and the PDCs ratio, $p = 0.038$) significantly influenced the size of the obtained nanoconjugates (Table 3.6). A coefficient estimate of 7.87 suggests that the increase in the StPGA-SS-Et-FAS % in the reaction lead to the formation of nanoconjugates with greater size; however, only at low ionic strength (Figure 3.10). We suggest that the presence of DIN as a more hydrophobic drug than FAS ($\log P$ 1.32 and 0.34, respectively) leads to the formation of more compact particles by shielding the DIN in the core of the particle and thus leading to smaller sizes. Additionally, the low ionic strength favors the observed extraordinary behaviour of StPGA in water solutions³⁵⁵.

The ANOVA analysis demonstrated that factors B (genipin equivalence, $p = 0.041$) and D (the PDCs ratio, $p = 0.048$) significantly influence the crosslinked nanoconjugate's PDI values (Table 3.7). PDI values closer to 1 indicate homogenous size distribution, a value obtained with genipin equivalence higher than 0.55 and the PDCs ratio lower than 0.5 (Figure 3.11, blue color).

Additionally, the transmission electron microscopy (TEM) analysis (Figure 3.12) confirmed the presence of small nanoconjugates (20-40 nm); however, we also observed aggregates when analyzing concentrated solution (2mg/ml), which we attributed to the sample preparation process during TEM analysis.

Nevertheless, this aggregation behavior requires further examination in biological fluids, given the potential influence on biological activity (part of our future studies).

Table 3.6. ANOVA statistical analysis of DoE Box-Behnken design implemented for determination of reaction conditions with significant influence on the obtained size of genipin-crosslinked nanoconjugates.

Source	p-value
Model	0.041
Factor A - Polymer concentration	0.25
Factor B - Genipin equivalent	0.25
Factor C - Ionic strength	0.82
Factor D - PDCs ratio	0.022
AB	0.84
AC	0.63
AD	0.69
BC	0.27
BD	0.58
CD	0.038
A²	0.61
B²	0.18
C²	0.0076
D²	0.27

P-values less than 0.05 indicate significant model terms. Values greater than 0.1 indicate non-significant model terms.

Factor Coding: Actual

● Design Points

5  61.4

X1 = D: Hydrophobicity

X2 = C: Ionic strength

Actual Factors

A: Polymer concentration = 5

B: Genipin eq = 1

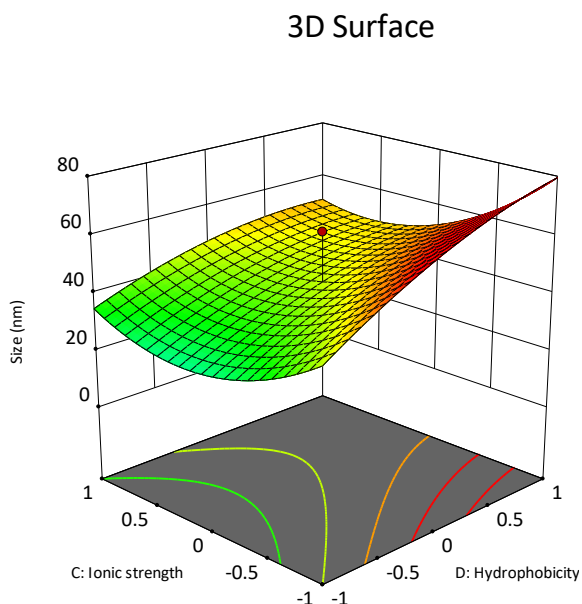


Figure 3.10. 3D Response surface plot representing the dependence of genipin crosslinked nanoconjugate's size on PDCs ratio (hydrophobicity degree) and ionic strength while keeping polymer concentration and genipin equivalence constant (5 mg/ml and 1 eq., respectively).

Table 3.7. ANOVA statistical analysis of DoE Box-Behnken design implemented for determination of reaction conditions with significant influence on the obtained PDI of genipin-crosslinked nanoconjugates.

Source	p-value
Model	0.041
Factor A - Polymer concentration	0.69
Factor B - Genipin equivalent	0.041
Factor C - Ionic strength	0.54
Factor D – PDCs ratio	0.048

P-values less than 0.05 indicate significant model terms. Values greater than 0.1 indicate non-significant model terms.

Factor Coding: Actual

○ Design Points

1  1.327

X1 = B: Genipin eq

X2 = D: Hydrophobicity

Actual Factors

A: Polymer concentration = 5

C: Ionic strength = -1

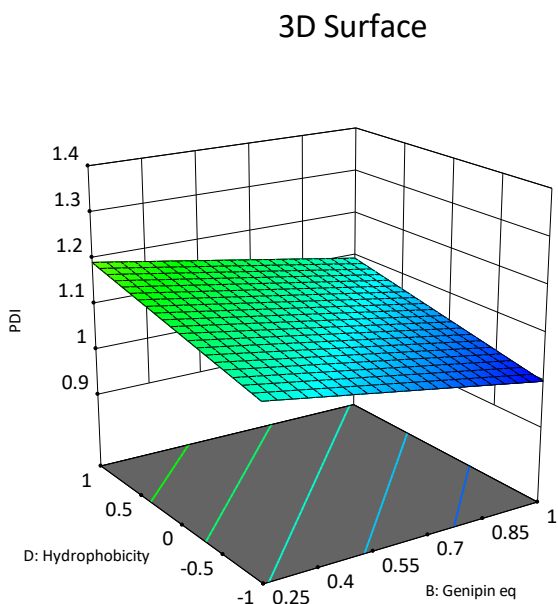


Figure 3.11. 3D Response surface plot representing the dependence of genipin crosslinked nanoconjugate's PDI on PDCs ratio (hydrophobicity degree) and genipin equivalence while keeping polymer concentration and ionic strength constant (5 mg/ml and -1, respectively).

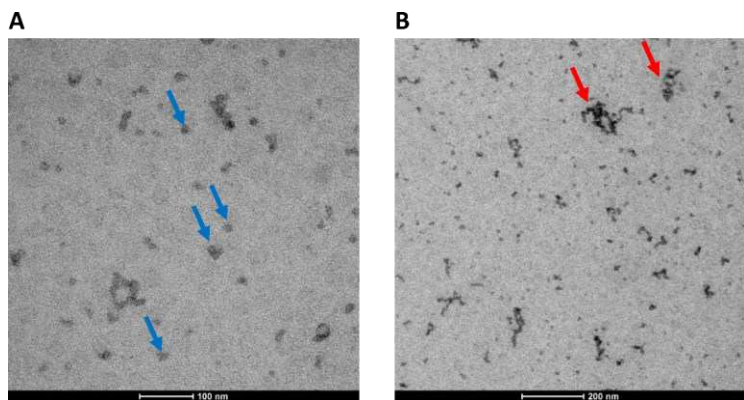


Figure 3.12. TEM images of genipin-crosslinked StPGA-drug conjugates (A) 0.5 mg/ml genipin crosslinked nanoconjugates - scale bar 100 nm - showing only small nanoconjugates (blue arrow); and (B) 2 mg/ml genipin crosslinked nanoconjugates - scale bar 200 nm - showing small nanoconjugates but also the aggregate formation (red arrow) during high concentration and sample preparation for TEM analysis

Ultimately, obtaining the nanoconjugates with a “tailor-made” size represents the real power of DoE, which we intend to demonstrate in this chapter. Due to the narrow design space implemented in our study, we obtained a size range of only between 20-60 nm. Therefore, to cover a broader range of nanoconjugates size and provide a complete understanding of genipin crosslinking reaction, we plan to continue this project to expand the levels of polymer concentration, ionic strength, and genipin equivalence.

3.3 DISCUSSION

AF4 remains among the most versatile and best-suited techniques for the fractionation of polyelectrolytes and with the increased implementation in the analysis of polymers with different origins.³⁵⁶ In practice, many factors that influence the elution behavior complicate the analysis of polymers and make the technique less robust. Moreover, the experimental parameter may differ depending on the instrument manufacturer; thus, a better understanding and proper data analysis require a careful evaluation on a case-by-case basis.

For sample recovery, we would expect that the high cross flow will lead to lower recovery values for StPGA, and indeed in our study, we obtained a decrease in StPGA recovery with the high cross flow; however, the sample peak may not resolve from the void peak with the decrease of crossflow. In contrast, the high cross flow may induce the formation of aggregates on the membrane that failed to elute entirely from the channel or elute at the end of the method when turning off the cross flow, thus, leading to low recovery values and consequently altering the determination of StPGA characteristics.

The behavior of charged polyelectrolytes, such as StPGA, in the AF4 channel, will depend significantly on the molecular volume leading to the

intermolecular and intramolecular repulsion and the repulsion force between the molecules and the AF4 membrane.^{356,357} Therefore, the salt content and, consequently, the carrier fluid's ionic strength will significantly influence the analysis of charged StPGA. For example, if the ionic strength remains insufficient to screen the StPGA-charged molecules, distinct factors may interfere with the elution, leading to the altered elution profile (elution with the void peak or during the focusing time) and interfering with the determination of Mw and size. Indeed, the ionic strength of carrier fluid significantly influenced the recovery value of StPGA with low ionic strength leading to higher recovery values due to the increased equilibrium height of StPGA in the AF4 channel and less interaction with the membrane. Of note, we must ensure that the high recovery value obtained by the low ionic strength does not induce early StPGA elution in the low resolution of the StPGA peak with the void peak.

In general, molecule retention (in our case StPGA) in AF4 depends on diffusion coefficients and not on the sample concentration and injected mass.²⁷⁹ A wide range of studies have reported peak distortion and variation in elution times with increased injected mass for various samples in practice.^{226,273,358–360} This effect (“overloading”) will depend on the sample characteristics (charge). Thus, the existence of overloading in the case of StPGA may derive from the molecules' negative charge. We have found the values of injected mass needed to obtain the optimal recovery value of StPGA; however, the amount of StPGA injected in the AF4 channel represents a tradeoff between the optimal recovery values and the requirements for a measurable MALS detection (mainly when analyzing molecules with low Mw).

The Nobel prize awards have recognized the significance of new synthetic methodologies in recent years; indeed, progress in organic synthesis represents a crucial part of academic research and applied science, focusing on discovering intrinsically novel reactions and identifying improved methodologies for existing

transformations.³⁶¹ Even though the pharmaceutical industry applies well-established statistical methods for reaction optimization^{362,363}, encouraging DoE methods in academia remains a more challenging task.³⁶⁴ In addition to analytical method development, as described in Chapter II, a DoE approach can also reduce the times and costs associated with the screening process³⁶⁴, as indicated by Hashiba et al. in their study that optimized mRNA encapsulation by lipid nanoparticles³⁶⁵. The application of DoE enabled a one-third reduction in the number of experiments and determined crucial factors affecting gene expression efficiency and tissue selectivity; however, the application of DoE to any complex optimization problem can aid undertakings such as nanoparticle manufacturing and the rapid identification of dynamically optimized and actionable combination therapies.³⁴¹

While we specifically investigated the use of DoE for optimizing the development of new crosslinked combination PDCs, we note the insufficiency of the design space to cover a more comprehensive range of nanoconjugate sizes. We suspect that the reason behind obtaining smaller nanoconjugates lies in the low PDC concentration in the solution. Thus, we next aim to expand the design space and better elucidate how distinct factors influence crosslinking and final nanoconjugates formation.

3.4 CONCLUSIONS

AF4 technique offers a unique power compared to other techniques, which includes the optimal sample fractionation purely by adjustment of instrument factors without relying on column packing characteristics like in SEC. Overall, we demonstrated how detailed knowledge of StPGA behavior inside the AF4 separation channel remains of primary importance for establishing the proper

experimental conditions and elucidating fractionation and detection dynamics to a greater degree.

In parallel, by using the example of genipin crosslinking of StPGA nanoconjugates to obtain combination therapeutics, we illustrated how DoE provides a detailed picture of the behavior of a particular process with high efficiency. Finally, we established how DoE determined each factor's contribution, modeled the effect of each factor on each response, and resolved factor interactions. In the near future, we intend to implement genipin crosslinking in tailor-made combination nanoconjugates (for the treatment of numerous disorders) and elucidate their biological fate with the help of the DoE approach.

3.5 EXPERIMENTAL MATERIALS AND METHODS

3.5.1 Materials

Material suppliers were as follows: sodium phosphate and sodium azide (Sigma Aldrich, USA), water LC-MS grade (Fisher Scientific, USA), StPGA, and linear PGA (Curapath, Spain), dinaciclib (MedKoo Biosciences, US), fasudil (Xingcheng Chempharm Co. Ltd, China), 4-nitrophenyl (2-(pyridine-2-yl)disulfanyl) ethyl carbonate (Fluorochem, UK), dichloromethane (DCM) (VWR chemicals, US), triethanolamine (TEA), methanol (MeOH) reagent grade and diethyl ether (Sharlab, Spain), LinPGA and SS-Et-FAS (Curapath S.L., Spain). Diisopropylethylamine (DIEA), DL-dithiothreitol (DTT), cysteamine hydrochloride, dimethyl sulfoxide (DMSO) anhydrous, ethyl acetate, and methanol (LC-MS grade) were obtained from Sigma-Aldrich (St. Louis, United States). Celite 545, diethyl ether, dichloromethane (DCM), and deuterated solvents such as deuterated oxide (D₂O) were purchased from VWR chemicals (Radnor, US). Silica 60A 20–45-micron, ammonium formate,

triethylamine (TEA), and formic acid (LC-MS grade) were purchased from Fisher Scientific (Pittsburgh, US). Vivaspin 10 kDa was obtained from Sartorius AG (Göttingen, Germany), and Sand 40-100 mesh was provided by ACROS organics (Geel, Belgium). Acetonitrile (ACN), chloroform, dimethylformamide (DMF), and methanol were purchased from Scharlab (Barcelona, Spain). 4-nitrophenyl-2-(pyridine-2-yl)disulfanyl ethyl carbonate and 4-nitrophenyl-4-(pyridine-2-yl)disulfanyl benzyl carbonate were purchased from Fluorochem (UK). Acetonitrile (LC-MS grade) was obtained from AppliChem GmbH. 4-dimethyl aminopyridine (DMAP) was obtained from Honeywell Fluka (Pittsburgh, US). 4-(4,6-Dimethoxy-1,3,5-triazin-2-yl)-4-methyl morpholinium (DMTMM) chloride (DMTMM·BF₄) was synthesized according to literature.³⁶⁶

3.5.2 PDCs synthesis

SS-Et-DIN/FAS Synthesis

DIN/FAS and DMAP were added to a solution of 4-nitrophenyl (2-(pyridine-2-yl)disulfanyl ethyl) carbonate (1:1:1 equivalence) in DCM, and the pH was adjusted to 8 with TEA. The reaction was left under inert conditions at room temperature overnight. The product was purified with column chromatography on silica gel (DCM-MeOH 95:5), the solvent evaporated, and a yellow viscous oil obtained was stored at -20°C until further use. The product identification was confirmed by a direct Q1 MS scan.

Cys-SS-Et-DIN/FAS Synthesis

Cysteamine hydrochloride was added to a solution of SS-Et-DIN/FAS (1:1 equivalence) at 15 mg/ml concentration in methanol and left to react at room

temperature for 3 h. The reaction was reprecipitated in ether two times, dried under vacuum, and analyzed with a Q1 MS scan to confirm the product formation.

Synthesis of StPGA-SS-Et-DIN, and StPGA-SS-Et-FAS

DMTMM BF₄ was added to a solution of StPGA in DMSO (dissolved by heating) and left for 30 min to activate the carboxylic groups of StPGA. Cys-SS-Et-DIN/FAS was added in the amount necessary to obtain the desired TDL; the pH was adjusted to 8.0 with TEA, and the solution was allowed to stir for 48 h at room temperature. The reaction was precipitated in ether, reprecipitated twice from methanol to ether, and the obtained white powder was dried under a vacuum. After drying, the conjugate was dissolved in Milli-Q and transformed into salt form by adding the 0.5 M NaHCO₃ until pH 8.0, purified through VivaSpin (3000 kDa cut off to remove extra salts and free drug) with approximately 100 ml Milli-Q and freeze-dried. The obtained white product was stored at -20°C and dissolved in Milli-Q water before each use.

3.5.3 Methods

TDL determination by UV-Vis

Fasudil and dinaciclib solutions in methanol were used as standard stock solutions, while the working standard solutions were obtained by dilution with Milli-Q water. The total conjugate drug loading was determined at three concentration levels (0.1 mg/ml, 0.25 mg/ml, and 0.5 mg/ml, in Milli-Q water) by measuring the absorbance at 323 nm (for fasudil) and 259 nm (for dinaciclib). StPGA water solution in the same concentration as the conjugates was used as a blank. UV-Vis measurements were performed using JASCO V-630 spectrophotometer at 25°C with a 1.0 cm quartz cell and a spectral bandwidth of 0.5 nm.

FD determination by LC-MS/MS

3 mg of conjugates were suspended in 500 μ l MeOH (LC-MS grade), vortexed for 5 min, centrifuged for 10 min at 11.000 rpm to remove the pellet, and the solution was subjected to LC-MS/MS analysis. The LC-MS/MS conditions and the validation parameters were described in Chapter II.

Direct mass spectrometry scan

All the samples monitored by mass spectrometry (MS) Q1 scan were analyzed by 20 μ l direct injection with ACN 50% and H₂O 50% (0.1% formic acid - FA) as mobile phase, and 0.5 ml/min flow rate, while the MS conditions were as follows: curtain gas 20 V, ion source temperature 250 °C, gas 1 45 V, gas 2 45 V, ion source voltage 5500 V, declustering potential 62 v, entrance potential 2 V.

Asymmetric flow field flow fractionation for size determination

The AF4 method was performed on the Postnova Analytics (Landsberg, Germany) fractionation channel equipped with a regenerative cellulose membrane with a 10 kDa cutoff and a 350 μ m spacer. Samples were dissolved in 10 mM sodium phosphate at 2 mg/ml concentration and analyzed with 10 mM sodium phosphate and 0.01% sodium azide as a mobile phase. The fractionation method consisted of a 40 μ l injection volume, 5 min injection time, 0.5 ml/min detector flow, 1 ml/min crossflow, and a total run time of 46.5 min. The detectors employed in the method were: a UV detector (280 nm), a refractometer, and a multi-angle light scattering detector. Data analysis for DoE was performed with Design Expert 13 software.

SAXS

The SAXS measurements were performed at the BL11 beamline of the Alba synchrotron (Barcelona, Spain). The observed q range was $4.24 \times 10^{-3} \text{ \AA}^{-1} \leq q \leq 3.52 \text{ \AA}^{-1}$, where q is the magnitude of the scattering vector $q = (4\pi/\lambda)\sin(\theta/2)$. Measurements were performed in Hilgenberg Mark-tubes made of glass N50

packed with green perforated plastic disk (length 80 mm, outer diameter 1.5 mm, wall thickness 0.01 mm). Samples were dissolved in 10 mM dPBS and equilibrated for 24 h before measurement, while 10 mM dPBS was implemented as blank. Analysis and fitting were performed with ATSAS software packages.

CHAPTER IV

**EVALUATING THE BIOLOGICAL FATE
AND PHARMACOLOGICAL EFFECT OF
PDCs BY MASS SPECTROMETRY
IMAGING**

4.1 INTRODUCTION

Matrix-assisted laser desorption/ionization-mass spectrometry imaging (MALDI-MSI) has begun to address the challenge of characterizing drug distribution within healthy and tumor tissues; therefore, this rapidly evolving technique may play an essential role in drug development. As discussed in the Introduction chapter, MALDI-MSI may guide/accelerate the progression of preclinical studies by helping to define/describe drug distribution and activity during early-stage preclinical development. Herein, we investigate MALDI-MSI's potential in elucidating the *in vitro* fate of novel polypeptide-drug conjugates (PDCs) in treating triple-negative breast cancer (TNBC).

TNBC, a complex and heterogeneous disease, has a high risk of metastasis and therapeutic resistance³⁴⁶; therefore, patients suffer from a poor clinical prognosis. While combining two or more therapeutic moieties that target cancer-associated pathways represents a keystone of current TNBC treatment strategies, advanced TNBC patients still exhibit inadequate responses.³⁶⁷ The low therapeutic effects and high incidence of side effects associated with many single and combination anticancer therapy has prompted the design of novel therapeutic approaches such as polymer-based combination conjugates. As opposed to drug encapsulation, the conjugation of single or combination drugs to a polymeric carrier (such as a polypeptide) offers numerous advantages, including an improved pharmacokinetic profile due to a site-specific drug release using bioresponsive linking chemistries, better chemical and physical stability, the ability to reach inaccessible disease sites, and differential cell fate as PDCs mainly follow a lysosomal delivery.^{37,368} Polymer based-combination therapies have emerged as a more efficient anti-tumor strategy (with promising preclinical data underlining the success of this approach^{39,161,369}), as this strategy alone can secure the simultaneous

delivery of more than one drug at the same site of action at a pre-set ratio, allowing drug synergism. Multivalency and high drug-loading capacity make poly-L-glutamic acid (PGA) the ideal carrier to secure synergistic effects.^{58,161,370,371}

We previously undertook a high-throughput combination screening of anticancer agents in a personalized manner (looking at four major breast cancer subtypes) within the European Research Council project "*Towards the design of Personalized Polymer-based Combination Nanomedicines for Advanced Stage Breast Cancer Patients (MyNano)*." For the TNBC subtype, we identified synergies between primaquine/fulvestrant, dinaciclib/fasudil, and exemestane/biscurcumin. While this chapter mainly focuses on developing MALDI-MSI for PDC characterization, we also synthesized single and combination PDCs for TNBC treatment as part of this goal.

We selected a combination of fasudil (FAS, a Rho-associated protein kinase) and dinaciclib (DIN, a cyclin-dependent kinase inhibitor) to conjugate to a linear PGA (LinPGA) given the availability of a single PGA-fasudil conjugate and the previous optimization of the synthetic and characterization conditions (see Appendix I and Chapter II). We then employed the resultant combination conjugate as a model PDC for MALDI-MSI study during a short research stay at Sheffield Hallam University (UK). Before the MSI study we first determined drug release, cell viability, and cellular fate in three-dimensional (3D) TNBC *in vitro* models that better mimic the physiological scenario than conventional two-dimensional cell monoculture-base models. We employed two different types of 3D TNBC models to evaluate toxicity and develop the MSI method for detecting free FAS and DIN – mammospheres generated using non-adherent plates (Figure 4.1A) and spheroids developed using an extracellular matrix-embedded approach reported by the Clevers laboratory³⁷² as this approach allows to mimic tumor heterogeneity as well as tumor-matrix interactions (Figure 4.1B).

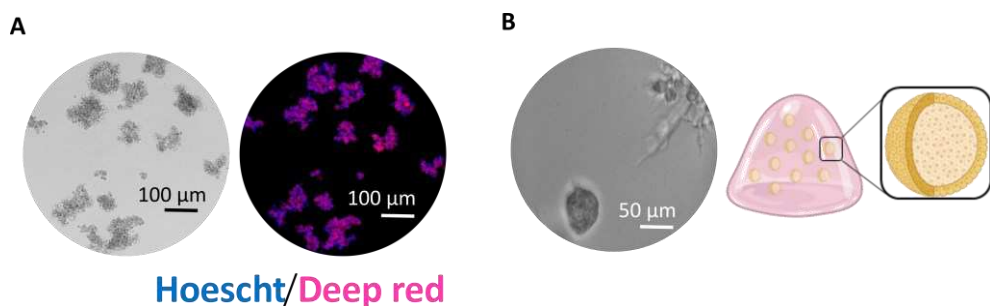


Figure 4.1. 3D TNBC spheroid models for the characterization of PDCs by MSI (A) Mammospheres (*Left*; microscopy, and *Right*; fluorescence images, Hoescht – nucleus and Deep red – cell membrane) **(B)** BME-embedded spheroids provided by Paz Boix at the Polymer Therapeutics Lab obtained following the protocol of Sachs et al.³⁷³.

MALDI-MSI provides simultaneous metabolomics and lipidomics data for drug detection in tissue; therefore, we analyzed the metabolomic fingerprint of the 3D TNBC models and the metabolomic alterations after the treatment with single and combination PDCs.

Specific objectives for this Chapter comprised:

Objective 1. Synthesis, characterization, and *in vitro* toxicity evaluation of single and combination PDCs carrying FAS and/or DIN

Objective 2. Development of MALDI-MSI method to detect FAS and DIN in a 3D TNBC *in vitro* model

Objective 3. The evaluation of drug release, spatial localization, and metabolite formation following exposure of 3D TNBC models to single and combination PDCs carrying FAS and DIN

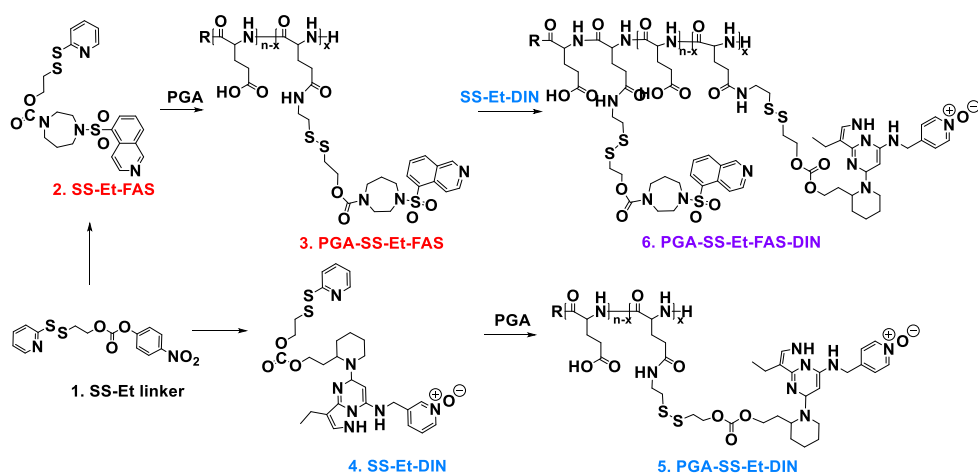
Objective 4. Analysis of metabolomic fingerprint of 3D TNBC model and its alterations induced by combination PDC treatment

4.2 RESULTS

4.2.1 Synthesis, Characterization, and Evaluation of *in vitro* Toxicity of Single and Combination PGA-based Conjugates

We synthesized single (PGA-SS-Et-FAS and PGA-SS-Et-DIN) and combination (PGA-SS-Et-FAS-DIN) PGA-based PDCs that employed a self-immolating disulfide linker using an ethyl spacer to conjugate the drugs to the PGA carrier (Scheme 4.1) based on a protocol described in the Ph.D. thesis of Oleksandr Zagorodko and recently published article³²⁶. Curapath S.L. (Valencia, Spain) kindly provided PGA-SS-Et-FAS, which was developed as part of a project awarded by La Marató TV3 as a conjugate selected for SCI treatment (Appendix 1); however, as the carrier deprotection process had been modified, we further optimized a protocol for synthesizing the single PGA-SS-Et-DIN and the combination PGA-SS-Et-FAS-DIN conjugates.

To synthesize PGA-SS-Et-DIN, we first obtained disulfide-ethyl-dinaciclib (SS-Et-DIN) using an SS-Et linker with an alcohol-activated group (activation by p-nitrophenyl chloroformate) (Scheme 4.1). The final conjugation step comprised of a thiol exchange with cysteamine hydrochloride and conjugation to PGA through amide coupling. Conjugating SS-Et-DIN to the PGA-SS-Et-FAS single conjugate generated the combination conjugate PGA-SS-Et-FAS-DIN. Section 4.5.2 provides a detailed description of the synthetic protocol. We obtained PGA-SS-Et-FAS, PGA-SS-Et-DIN, and PGA-SS-Et-FAS-DIN with high yield and purity as shown by low free drug content (analyzed by LC-MS/MS), a hydrodynamic radius of 5-10 nm indicating the unimeric conjugate composition, and a z-potential of ≈ -20 mV corresponding to the charge of PGA (Table 4.1 and Section 4.5.3).



Scheme 4.1. Scheme describing the synthesis of **PGA-SS-Et-FAS** (1-3) and **PGA-SS-Et-DIN** (1, 4, 5) and **PGA-SS-Et-FAS-DIN** (1-3, 5, 6).

Table 4.1. Physicochemical characterization of single and combination PGA-based PDCs

Compound	TDL (wt%) FAS/DIN	FD (wt% to TDL) FAS/DIN	Yield, %	Size, nm (average by number)	Z potential, mV
PGA-SS-Et-FAS	11.60/-	< 0.01	85	5	-23.4
PGA-SS-Et-DIN	-/3.93	0.0061	87	5	-26.1
PGA-SS-Et-FAS-DIN	11.60/1.54	< 0.0032/ < 0.0043	89	6	-26.6

PDC activity evaluation requires different model systems, ranging from analysis in traditional 2D cell cultures, advanced 3D cell models, patient-derived cell models, and cell co-cultures to *in vivo* testing in small and large animal models.³⁷⁴ For the MALDI-MSI study, we first evaluated the free drugs (FAS and DIN), PGA-SS-Et-FAS, PGA-SS-Et-DIN, and PGA-SS-Et-FAS-DIN in two different MDA-MB-231-cell line-based 3D TNBC models to ensure the toxicity of the studied PDCs: a 3D suspension model (mammospheres) and a basement membrane extract (BME)-embedded 3D model (spheroids) (Figure 4.1). We observed that free drugs, PGA-SS-Et-FAS, PGA-SS-Et-DIN, and PGA-SS-Et-FAS-DIN exhibited significantly higher

toxicity in mammospheres than spheroids in cell viability studies after 72 h treatment (Figure 4.2).

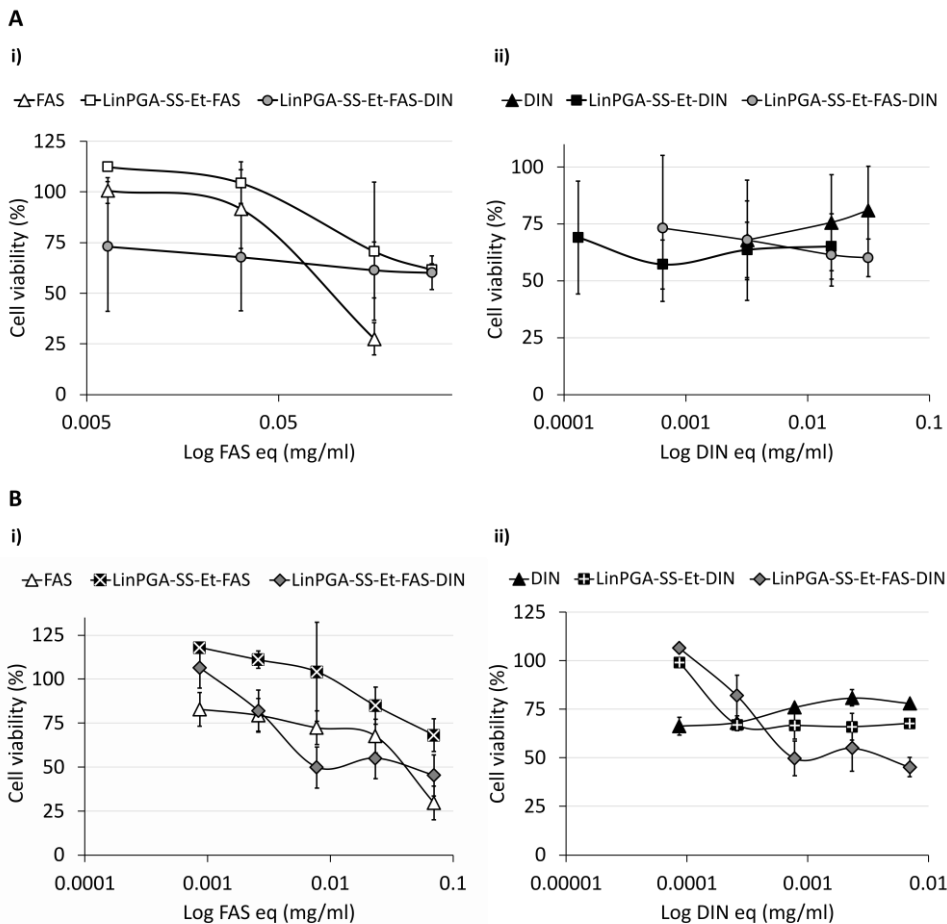


Figure 4.2. Cell toxicity studies of free drugs, PGA-SS-Et-FAS, PGA-SS-Et-DIN, and PGA-SS-Et-FAS-DIN in (A) spheroids^{xvi} and (B) mammospheres^{xvii} with i) FAS equivalent and ii) DIN equivalent concentrations.

^{xvi} Experiment performed by Paz Boix Montesinos

^{xvii} Experiment performed by Esther Masia

We hypothesized that free drugs and PDCs face more difficulty penetrating the complex matrix-embedded compact cell spheroids than the loose mammospheres formed in the suspension model. Moreover, differences in the toxicity of FAS and DIN between the two model systems (Table 4.2) may derive from the different expression levels of Rho kinase and CDKs (as the drug targets); however, we must confirm this hypothesis with experiments planned in the future.

Table 4.2. IC50 values of fasudil (FAS) and dinaciclib (DIN) determined in mammospheres and spheroid 3D TNBC *in vitro* cell models.

3D <i>in vitro</i> cell model	FAS IC50 (mg/ml)	DIN IC50 (mg/ml)
Mammospheres	0.057	0.007
Spheroids	0.085	0.016

The drug release studies with PDCs typically employ experimental protocols that mimic known tumor conditions (e.g., the presence of reducing agents such as dithiothreitol - DTT, acidic pH (i.e., 5.5), or high levels of cathepsin B). Therefore, we performed FAS and DIN release studies from PGA-SS-Et-FAS, PGA-SS-Et-DIN, and PGA-SS-Et-FAS-DIN in 5 mM DTT and 10 μ M DTT to mimic intracellular and extracellular GSH concentrations³⁷⁵. We employed a DoE-developed LC-MS/MS method (see Chapter II and Section 4.5.3) to quantitatively determine FAS and DIN release at defined time points over a 72-h period. In the presence of 5 mM DTT, we observed 25.3% FAS and 45.1% DIN cumulative release at 72 h from their respective PGA single drug conjugates (Figure 4.3). The drug release studies with PGA-SS-Et-FAS-DIN revealed a comparable level of FAS and DIN release under 5 mM DTT at 72 h (26.4% and 38.5%, respectively), indicating insignificant differences between FAS and DIN release from the combination conjugate compared to the single-drug conjugates. We failed to observe any FAS or DIN release from PGA-SS-Et-FAS, PGA-

SS-Et-DIN, or PGA-SS-Et-FAS-DIN in the presence of 10 μM DTT, which confirms the stability of these PDCs in the extracellular environment.

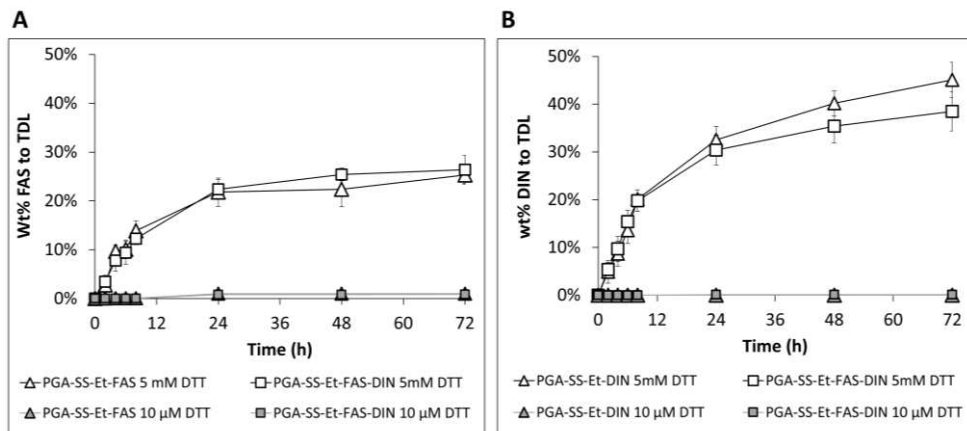


Figure 4.3. Drug release from single and combination PDCs. Release of (A) FAS and (B) DIN from PGA-SS-Et-FAS, PGA-SS-Et-DIN, and PGA-SS-Et-FAS-DIN under a reductive environment (5 mM DTT) with 10 μM DTT as a control sample (mimicking the extracellular environment). Data obtained from cumulative LC-MS/MS quantification of FAS and DIN at defined time points and presented as mean \pm SD ($n = 3$).

4.2.2 Development of a MALDI-MSI Method for Fasudil and Dinaciclib Detection

MALDI-MSI requires complex sample preparation with matrix choice and application as key aspects.³⁷⁶ Thus, as the first step in method optimization, we evaluated four available matrices dissolved in 70% acetonitrile (ACN) or 70% methanol (MeOH) for the detection of FAS and DIN by spotting the standard solution containing 10 $\mu\text{g}/\text{ml}$ FAS and 10 $\mu\text{g}/\text{ml}$ DIN on a MALDI plate, and applying on the dry spot the matrix solution: α -cyano-4-hydroxycinnamic acid (CHCA)

suitable for ion detection in positive mode, 2,5-dihydroxybenzoic acid (DHB) suitable for ion detection in both positive and negative mode, N-naphthyl-ethylenediamine-dihydrochloride (NEDC) suitable for ion detection with small Mw, or 9-aminoacridine (9AA) suitable for ion detection in negative mode (Experimental conditions described in detail in Table S4.1). Only the CHCA matrix enabled the detection of FAS and DIN m/z ions at 292.171 m/z and 397.249 m/z, respectively (Figure 4.4), while other matrices did not facilitate FAS and DIN detection (Blank MS spectra not shown); therefore, we continued method optimization by adjusting the CHCA matrix solution composition.

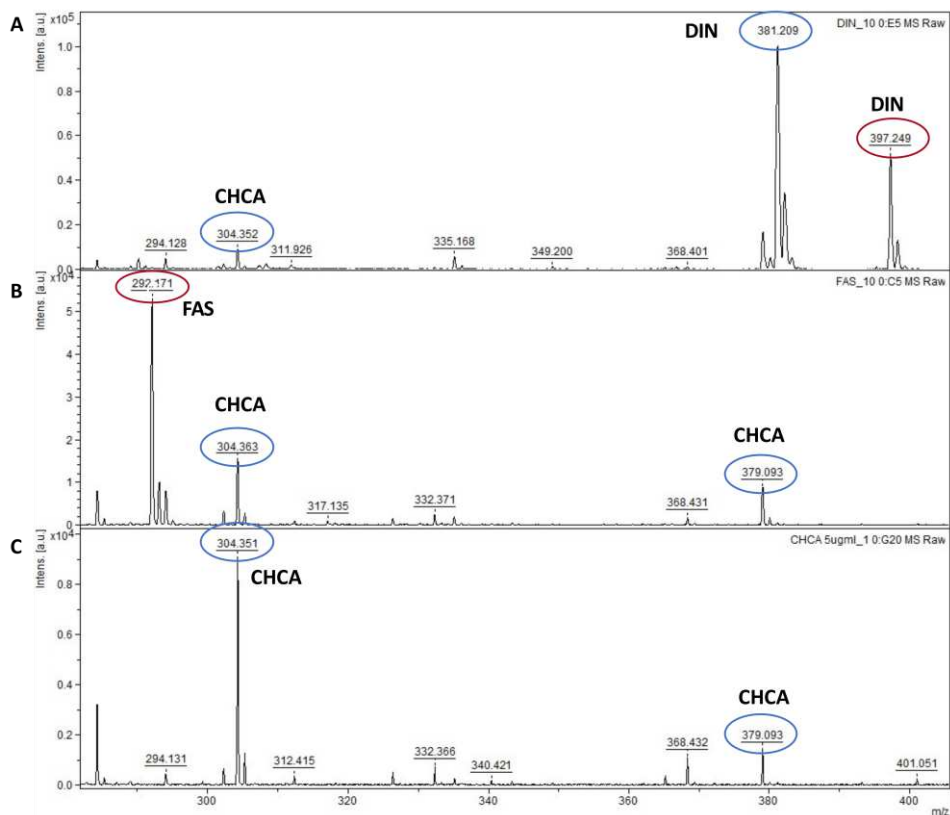


Figure 4.4. Evaluation of CHCA as a suitable matrix for dinaciclib (DIN) and Fasudil (FAS) detection by MALDI-TOF and implementing spotting method. (A) MALDI-TOF spectra of

DIN standard solution (10 µg/ml) with detected protonated molecular ion of DIN ($[\text{DIN}+\text{H}]^+$ = 397.249 m/z) and a DIN fragment 381.209 m/z. **(B)** MALDI-TOF spectra of FAS standard solution (10 µg/ml) with detected protonated molecular ion of FAS ($[\text{FAS}+\text{H}]^+$ = 292.171 m/z). **(C)** MALDI-TOF spectra of blank solution (5 µg/ml CHCA). Molecular ions at 304.351 m/z and 379.093 m/z correspond to the CHCA matrix.

We evaluated ACN and MeOH as organic solvents with high CHCA solubility and used a strong acid trifluoroacetic acid (TFA) and a relatively weak formic acid (FA) as acidic compounds to adjust the pH, improve ionization of basic compounds (DIN and FAS) thus increasing method sensitivity. To compare the results of FAS and DIN peak intensities, we calculated their relative intensities (dividing the intensity of the FAS and DIN peak by the intensity of the most abundant matrix peak – 190.05 m/z). We obtained the highest relative intensity of DIN and FAS with CHCA solution in 70% MeOH with 0.1% TFA due to the increased ability of the drug to ionize well at low pH and due to the better extraction of DIN and FAS with MeOH and better CHCA solubility in MeOH as opposed to the ACN (Figure 4.5A).

Next, to obtain high-sensitivity MALDI-MSI image acquisition, we optimized several MALDI parameters, including smartbeam laser properties (Figure 4.5B), laser power (Figure 4.5C), and detector gain (Figure 4.5D). We compared the signal-to-noise ratio (S/N) (left graphs, Figure 4.5A-C) and relative peak intensity (DIN and FAS peak intensity normalized with the most abundant matrix peak intensity - 190.05 m/z) (right graphs, Figure 4.5A-C) between the distinct levels of MALDI parameters to determine the optimal values for each parameter.

The Smartbeam laser used to generate MALDI ions from samples may hold different shapes and sizes depending on the instrument manufacturer; in the case of the Bruker Autoflex, six different smartbeam laser shapes/sizes exist: 1_minimum, 2_small, 3_medium, 4_large, 5_flat, and 6_ultra. We obtained the best S/N ratio with the 6_ultra smartbeam laser and the best relative intensity with

the 5_flat and 6_ultra smartbeam lasers; however, given the significant decrease in the S/N ratio when implementing the 5_flat smartbeam laser indicating higher background noise, we chose 6_ultra as the optimal smartbeam laser (Figure 4.5B).

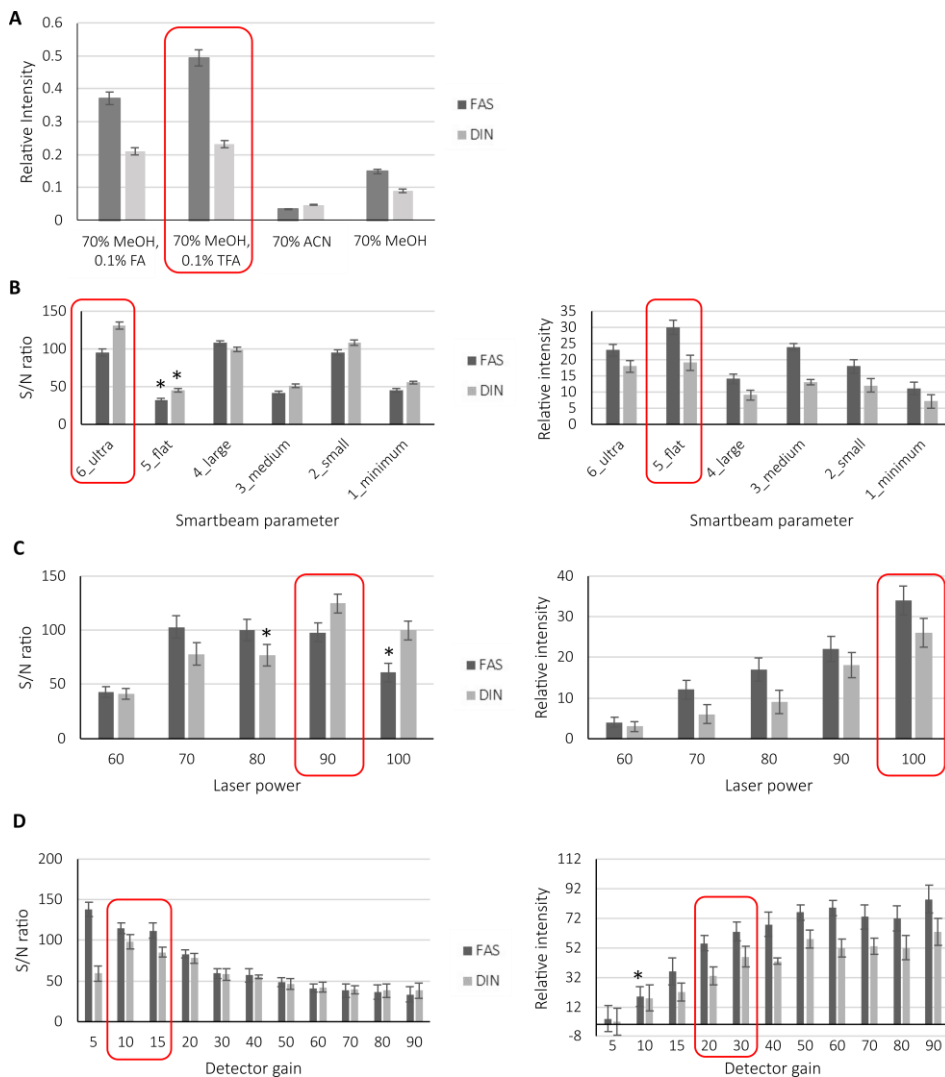


Figure 4.5. MALDI-MSI method development to obtain the optimal relative intensity of fasudil (FAS) and dinaciclib (DIN). (A) Evaluation of optimal CHCA matrix solution. Optimization of MS parameters such as (B) smartbeam laser, (C) laser power, and (D) detector gain performed by following the (left) signal-to-noise (S/N) ratio and (right) relative intensity of FAS and DIN to ensure that background noise does not affect the analysis. Red

boxes signify optimal parameter values. Data represented as average relative intensity (the ratio between FAS or DIN peak intensity and matrix ion 190.05 m/z) \pm SD, n = 3 (3 different spots on the same ITO slide, spotted on the left end, middle and right end of the slide); *p<0.05.

Next, we found that enhancing the laser power increased the relative peak intensity of DIN and FAS; however, increased laser power may lead to sample destruction and higher background noise. Therefore, we chose 90% as the optimal value for laser power, given the significantly higher S/N ratio compared to 100% for FAS and 80% for DIN (Figure 4.5C). We observed the gradual increase in relative intensity with higher detector gain as a higher number of ions reaches the detector; however, a higher relative intensity can lead to higher background noise and more ion interference (as in the case of laser power). Based on the generally acceptable S/N ratio value of at least 20 (arbitrary units, AU), we employed a detector gain of 20 AU as the optimal value, with 83 and 78 S/N ratios for FAS and DIN, respectively, and with better relative intensity compared to the gain of 15 and 10 AU (Figure 4.5D).

Maintaining sample integrity represents an essential part of MSI studies, preserving the localization and abundance of molecules in biological samples. The collection and sample handling must retain the samples close to their native state to obtain an accurate representation of the chemical processes. Given the small and fragile nature of both 3D TNBC models employed in this chapter, we required an optimized sample embedding process to permit enhanced sample handling prior to snap freezing in isopentane. Of the many universal MSI protocols developed so far³⁷⁷, we implemented the sample preparation protocol described by Dannhorn et al. (see Section 4.5.6) which demonstrated the compatibility of a hydrogel-embedding matrix across different MSI ionization techniques.³¹⁴ Moreover, the protocol described by Dannhorn et al was previously evaluated in the MSI center at

Sheffield Hallam university for metabolite imaging in 3D *in vitro* cell models. This study showed that the hydrogel embedding matrix composed of hydroxypropyl methylcellulose (HPMC) and polyvinylpyrrolidone (PVP) maintained the integrity of 3D *in vitro* cell models with minimal dislocation of metabolites compared to other embedding matrices.

Using the MALDI-MSI protocol currently under optimization, we first assessed possible ion interference from the HPMC and PVP components of the embedding hydrogel or basement membrane extract (BME) matrix by spraying a mixture of α -CHCA, FAS, and DIN standard solution onto cryosectioned spheroid samples (Section 4.5.7). Various colors describe the concentration gradient on the MSI images (Figure 4.6.) - black relates to a lack of detection of the specific ion, blue to the lowest concentration, and green, yellow, and red with increasing concentration. We detected both $[FAS+H]^+$ and $[DIN+H]^+$ ions on spiked samples (292.17 m/z and 397.25 m/z, respectively) (Figure 4.6.); however, we encountered ion interference for FAS, as shown by the presence of green, yellow, and red colors in the control samples without free drugs (Figure 4.6). We also detected ions at 381.21 m/z, 526.41 m/z, and 571.00 m/z in the spiked sample that were not present in the control samples (spheroid sample without spiking of FAS and DIN solution) that we ascribed to matrix-drug adduct ions formed in the matrix solution and during the spraying process (Figure 4.6. and Figure S4.1); however, we do not expect the detection of these matrix-drug adducts in real samples (spheroids treated with PDCs and collected over 72 h) as the *in vitro* models will undergo evaluation with PDCs and drugs released in the cells. We failed to identify ion signal interferences from HPMC, PVP, and BME within the targeted mass range (60-2000 m/z); therefore, we concluded that embedding media did not impact FAS and DIN detection within the spheroid model.

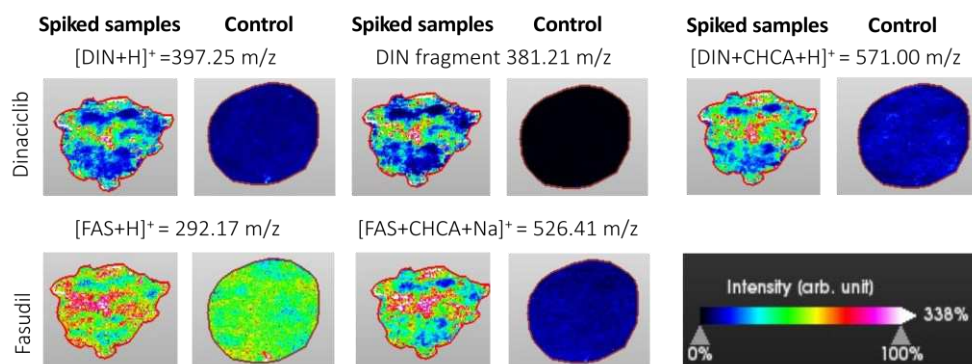


Figure 4.6. Dinaciclib and fasudil detection by MALDI-MSI in spiked and control 3D BME-embedded spheroids (without DIN and FAS spiking solution). The 397.25 m/z and 381.21 m/z corresponds to $[DIN+H]^+$ and DIN fragment ion, while 571.00 m/z DIN-matrix adduct ion $[DIN+CHCA+H]^+$. The 292.17 m/z and 526.41 m/z correspond to $[FAS+H]^+$ and FAS-matrix adduct ions $[FAS+CHCA+Na]^+$, respectively. Data normalized with the matrix peak intensity - 190.05 m/z. Intensity bar shown as an example for the color changes when the intensity of a specific m/z is increased.

Overall, we developed and optimized the MALDI-MSI method for detecting FAS and DIN in TNBC spheroids, securing that the matrix and the embedding medium do not interfere with the analysis; however, we must consider possible ion interferences for FAS.

4.2.3 Evaluation of Drug Release and Spatial Localization in Spheroids/Mammospheres Following Exposure of MDA-MB-231 TNBC Cells to PDCs

By implementing the sample embedding (preparation) protocol (see Section 4.5.6) and MALDI-MSI method optimized in the previous section (4.2.2), we performed MALDI-MSI analysis of the small molecules present in the TNBC

spheroids and mammospheres (Figure 4.7). Initially, we profiled sections from three biological replicates by MALDI-MSI in positive ion mode within the mass range of 60-2000 m/z to demonstrate the compatibility of the *in vitro* models with MSI by employing the MALDI-MSI to detect abundant molecules.

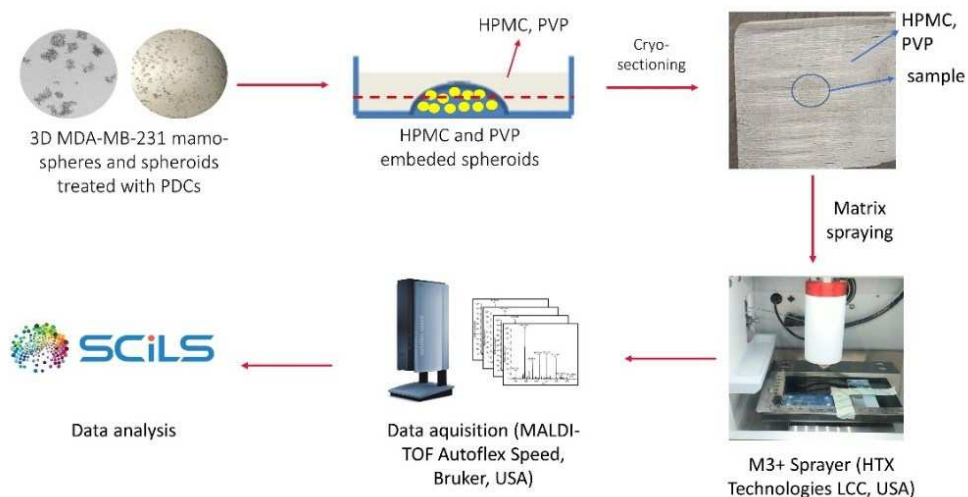


Figure 4.7. MALDI-MSI experimental protocol scheme used to image TNBC spheroids and mammospheres. 3D TNBC models were embedded in HPMC and PVP solution, sectioned with cryostat with 10 μm thickness and at -20°C , and analyzed by MALDI-TOF after matrix solution application (10 $\mu\text{g}/\text{ml}$ α -CHCA in 70% MeOH and 0.1% TFA). Data analysis performed with Scils software provided by Bruker (USA). HPMC – hydroxypropyl methylcellulose, PVP – polyvinyl pyrrolidone.

We performed metabolite annotation with the metaspaced2020.eu online platform and CoreMetabolome – v3, HMDB – v4, KEGG – v1, and LipidMaps – 2017-12-12 databases. Table 4.3 describes the identified metabolites and false discovery rate (FDR) value, indicating the confidence level for metabolite identification.

Table 4.3. Metabolite annotation with online platform metaspace2020.eu.

m/z	Annotation	FDR
148.06	Glutamate [M+H] ⁺	5%
184.49	Phosphorylcholine [M+H] ⁺	5%
86.002	Choline head [M+H] ⁺	5%
112.036	L-alanine/D-alanine/b-alanine/ [M+H] ⁺	5%
619.49	50 candidates TG [C ₃₆ H ₆₈ O ₆ + Na] ⁺	5%
636.45	PE 14:0/14:0 [C ₃₃ H ₆₆ NO ₈ P + H] ⁺	5%
664.49	6 candidates PE [C ₃₅ H ₇₀ NO ₈ P + H] ⁺	5%
782.54	11 candidates PC [C ₄₂ H ₈₂ NO ₇ P+K] ⁺	5%
827.44	41 candidates PE-NMe [C ₄₆ H ₈₄ NO ₈ P + NH ₄] ⁺	5%
76.08	Glycine [M+H] ⁺	5%
116.65	Proline [M+H] ⁺	5%
119.26	Threonine [M+H] ⁺	5%

MALDI-MSI detected the observed metabolites from spheroids and mammospheres control samples. The false discovery rate (FDR values) of 5% indicates the highest confidence of metabolite annotation.

We obtained MALDI-MSI images of spheroids (Figure 4.8A) and mammospheres (Figure 4.8F) with phosphorylcholine (184.49 m/z) and choline "head" (86.002 m/z) as primary metabolites. Phosphorylcholine and the choline head represent some of the most abundant lipid components of the cellular membrane, which can therefore serve as markers for cellular detection. We identified numerous peaks within the lipid range (600-850 m/z) in spheroids and mammospheres. The most abundant signals of 636.45 m/z, 664.49 m/z, 782.54 m/z, and 827.44 m/z corresponded to the phosphatidylcholine (PC) and phosphatidylethanolamine (PE) groups. The upregulation of choline metabolism in cancer cell lines results in elevated cellular total choline and PC levels, confirming the high abundance of PC ions in our MALDI-MSI study.³⁷⁸⁻³⁸⁰

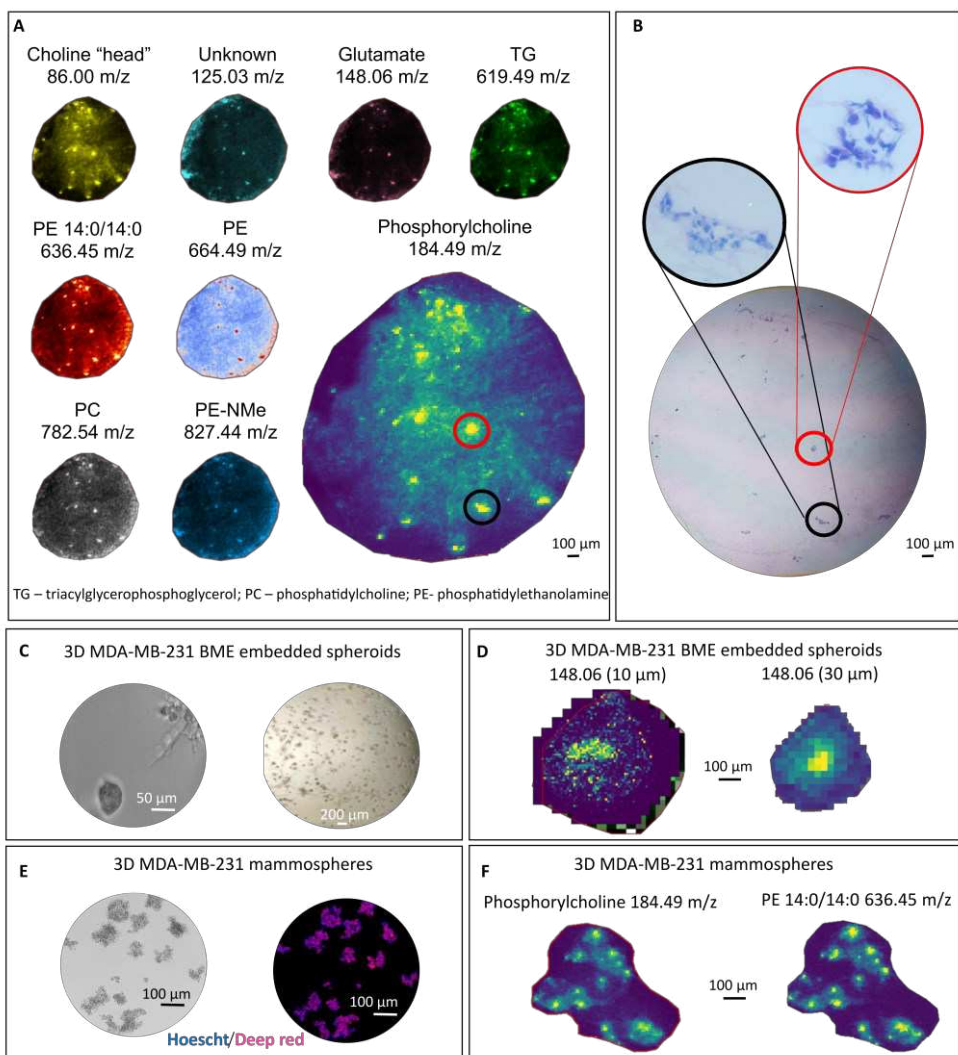


Figure 4.8. Mammospheres and spheroids distribution obtained by MALDI-MSI (A) 30 μm MALDI-MSI images with the most abundant metabolites used as markers for the detection of spheroids in BME matrix **(B)** H&E staining of untreated spheroids confirming the distribution of spheroids in BME detected by MALDI-MSI, **(C)** Microscopy images of BME-embedded spheroids obtained following the protocol of Sachs et al. **(D)** Glutamine spatial distribution in BME-spheroid at 10 and 30 μm spatial resolution. **(E)** Mammospheres (Left; microscopy, and Right; fluorescence images, Hoescht – nucleus and Deep red – cell

membrane). (F) 30 μm MALDI-MSI images with the most abundant metabolites in untreated mammospheres.

Cancer cells use metabolic reprogramming to perform glycolysis even in the presence of available oxygen. For instance, cancer cells rely on glutaminolysis to produce intermediary metabolites (e.g., α -ketoglutarate) for the tricarboxylic acid (TCA) cycle, which supports energy production for other pathways.³⁸¹ This fact may explain the identified amino acids in our untreated spheroids and mammospheres (Table 4.3). For example, studies have observed fluctuating alanine and aspartic acid levels in breast cancer due to the abnormal transport of ammonia to glutamine synthesis.³⁸¹

In breast cancer, highly proliferative cancer cells use glutamine as an essential energy source substrate (becoming transformed into glutamate) and for the generation of nucleotides, lipids, and proteins; hence, we used the elevated levels of glutamate as a marker for the cancer proliferation (Figure 4.8).³⁸² Glutamine represents a frequently mentioned amino acid among the proposed biomarkers of breast cancer; cancer cells consume glutamine to support self-sustained growth and aggressiveness.³⁸³ Yang et al. associated a decreased level of glutamine in serum and plasma with the accumulation of glutamic acid in the body, enhancing the proliferation of mammary epithelial cells.

Elevated levels of alanine most likely derive from increased alanine biosynthesis in response to the increased demand for alanine for the TCA cycle. The increased level of alanine may also come from muscle breakdown, as occurs in cachexia associated with advanced tumor stages.³⁸⁴ Muscles degrade amino acids for energy needs; as a result, the transamination of nitrogen to pyruvate forms alanine. Proline and amino acids related to proline metabolism may have a role in the development of gynecological and breast cancers.³⁸¹ Proline has been recently

controversially correlated with metastasis progression by interfering in collagen degradation processes, mitochondria energy-dependent mechanisms, and acting as a regulator of redox balance and a modulator of the urea, glutamine, and TCA cycles.^{385–387} Dipeptides containing proline at C-terminal, such as Gly-Pro, become cleaved by cytosolic prolydase, an enzyme specifically degrading X-proline dipeptide explaining the presence of Gly as a metabolite in our 3D models. Finally, although threonine has also been identified in breast cancer studies, patient cohort studies showed no clear correlation of the levels of this amino acid with patient prognosis.³⁸²

To confirm the spatial localization of spheroids/mammospheres in the samples, we correlated MALDI-MSI images with H&E staining (Figure 4.8B). We confirmed the distribution of BME-spheroids/mammospheres and verified the preservation of sample integrity during cryosectioning with minimal fracturing. Overall, we obtained MALDI-MSI images with 30 μm and 10 μm spatial resolution (Figure 4.8D and 4.8F) with a high correlation between spheroids/mammospheres shape and MALDI images.

Although we developed the method with FAS and DIN standard solutions matching the concentration of the drugs released from DTT release studies, we failed to detect drug distribution in the 3D cell models by MALDI-MSI, perhaps due to the MALDI-TOF instrument's high limit of detection (LOD). An increase in PDC concentration (from 80 to 240 μM , FAS equiv.) to treat spheroids and mammospheres failed to improve free drug detection at any time during 72 h of treatment; however, we identified metabolomic alterations in the 3D TNBC models upon PDC treatment (see Section 4.2.4) In the subsequent sections, we will discuss the potential reasons why we failed to detect drug release.

4.2.4 Metabolic Alterations Induced in 3D TNBC models after Treatment with Single and Combination PDCs

Since MALDI-MSI simultaneously provides us with metabolomic and lipidomic data for drug detection in tissue, we analyzed the metabolomic fingerprint of our TNBC models.

The exploration of metabolic signatures of tumor etiology and progression represents significant research efforts in cancer research within the past decade.³⁸⁸ To this end, NMR spectroscopy and MS represent valuable scientific tools for metabolomic analysis and can help to decipher differential metabolic patterns and identify driving factors.^{389,390} Advances in developing certain large-scale "omics" have MS as a core technology. MS-based metabolomics has undergone important developments in recent years with groundbreaking applications in cancer research by being implemented in investigating a substantial variety of chemical and biological molecules.³⁹¹ Therefore, we analyzed MALDI-MSI metabolomics data obtained from our TNBC models with principal component analysis (PCA).

We observed a clear metabolomic difference between untreated spheroids (green) and those treated with PGA-SS-Et-DIN (pink), free DIN (dark blue), and FAS (light blue) at 72 h, as shown by treatment group separations in the PCA plot (Figure 4.9A); however, PGA-SS-Et-FAS (yellow) and PGA-SS-Et-FAS-DIN (purple) demonstrated similar metabolomic signatures as the control sample at 72 h (green), confirming low conjugate toxicity and hence minimal impact on cell metabolism in spheroids (Figure 4.9A). Our PCA plots data also demonstrated differences in the metabolomic responses of control untreated mammospheres (green) and those treated with PGA-SS-Et-DIN (pink) and free FAS (light blue) and DIN (dark blue) at 72 h (Figure 4.9.B). Nevertheless, as opposed to spheroids, the PCA 3D plot of mammospheres clearly distinguishes metabolomics responses

between PGA-SS-Et-FAS (yellow) and PGA-SS-Et-FAS-DIN (purple) compared to the control samples (green) after 72 h of treatment. These results may correlate to higher conjugate toxicity in mammospheres compared to spheroids.

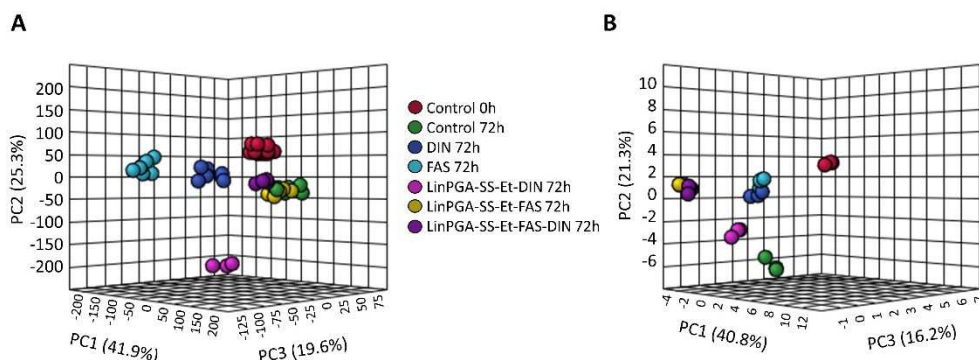


Figure 4.9. Treatment groups separated by metabolite signature. Synchronized 3D PCA plots of untreated and treated (A) spheroids and (B) mammospheres. Treatment group separations indicate the difference in metabolomic signature, while the conjunction of different groups in the same space of the 3D PCA plot suggests a similar metabolomic profile between groups (n=6, six spheroid/mammosphere replicates from one section and on the same ITO slide).

To allow the elucidation of specific metabolites responsible for the metabolomic difference between treatments, we evaluated feature (metabolite) loading plots obtained from PCA analysis (Figures 4.10 and 4.11).

Treatment of spheroids with free drugs significantly altered the levels of alanine, PC metabolites, and glutamate; more specifically, we observed an upregulation of alanine (112.04 m/z) and PC (619.49 and 636.45 m/z) and a downregulation of glutamate (148.06 m/z) compared to the control (untreated cells at 72 h) ($p < 0.005$; Figure 4.10). The downregulation of glutamate levels observed in our study only after the treatment with free drugs, as opposed to the

treatment with PDCs, correlates with the cytotoxicity profiles and the differential cell trafficking and the kinetics of drug release from the PDCs, as free drugs with a faster intracellular bioavailability, exhibited the highest toxicity and hence stopped cancer proliferation. Interestingly, we only observed a significant downregulation of 184.49 m/z (phosphorylcholine) after treatment with FAS, possibly due to the different metabolomic pathways affected compared to DIN.

The observed metabolomics patterns in mammospheres derived from differences in the levels of specific metabolites such as glycine (76.987 m/z), choline "head" (86.002 m/z, lipid fragment), proline (116.65 m/z), threonine (119.26 m/z) and phosphorylcholine (184.49 m/z) (Figure 4.11.). The alteration of distinct metabolites in mammospheres compared to the spheroid model demonstrates how the treatments may affect separate metabolomic pathways between models, thus, leading to the difference in toxicity.

Moreover, the metabolomic fingerprint change of control spheroids and mammospheres after 72h is expected due to the active metabolism of cells without the treatment.

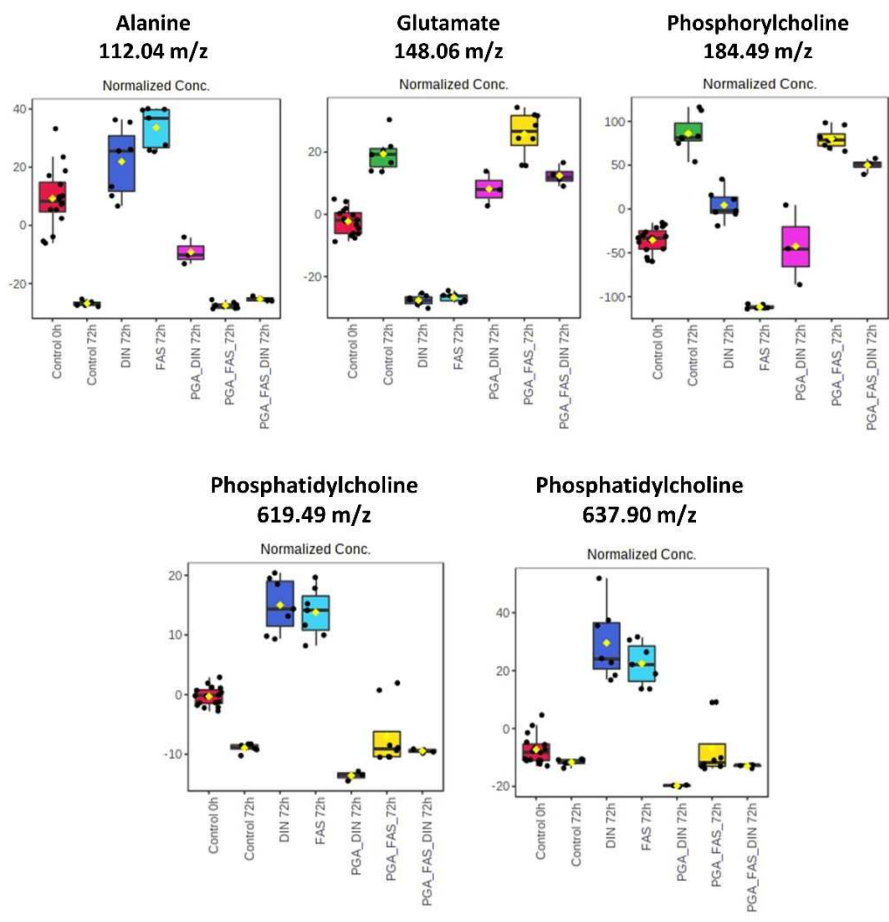


Figure 4.10. Feature loading plots comparing levels of specific metabolites between treatment groups in spheroids. Positive values indicate upregulation, while negative values indicate downregulation of specified metabolite in the treatment group compared to the control sample.

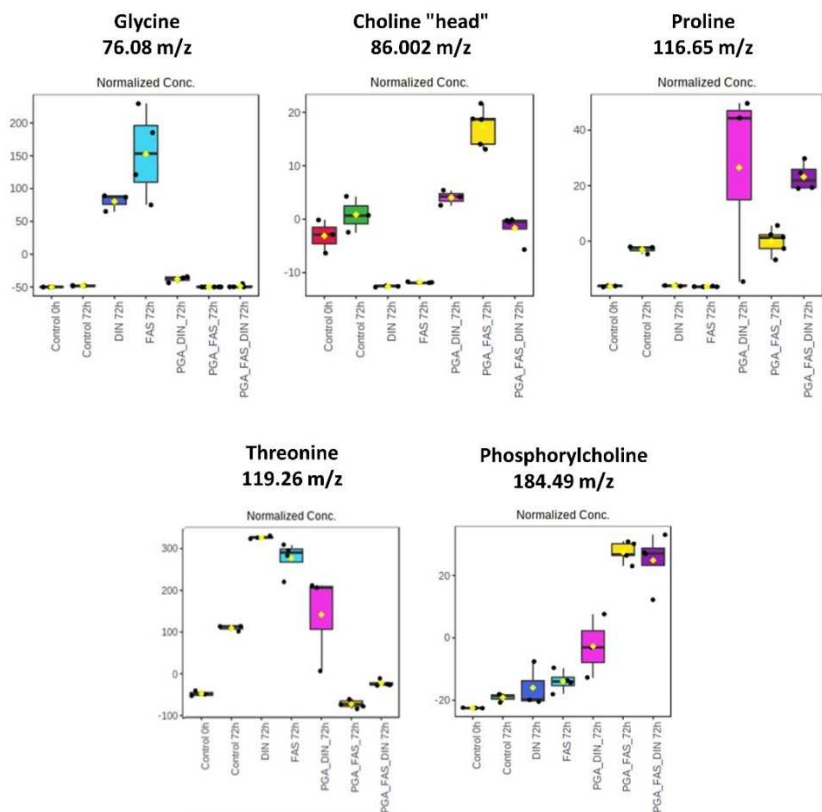


Figure 4.11. Feature loading plots comparing levels of specific metabolites between treatment groups in mammospheres. Positive values indicate upregulation, while negative values indicate downregulation of specified metabolite in the treatment group compared to the control sample.

4.3 DISCUSSION

Established methods that require labeling may alter drug properties and interactions, so they may not represent actual drug behavior in clinics. Moreover, traditional methods provide us with the spatial information of labeled molecules,

while unlabeled molecules remain undetected. Thus, the analytical tools for this purpose remained limited until recently.

After being introduced in 1997 in a study by Caprioli et al.²⁹⁹, MALDI-MSI has permitted the quantitative characterization of the spatial distribution of drugs within cells and tissues, thereby providing direct evidence that the drug has reached the target (or not). MSI, as a label-free imaging technique, enables the study of the pharmacological activity, quantification, the spatial distribution of drugs, and the evaluation of relevant metabolites following treatment with, for example, PDCs. MSI offers the unique ability to co-localize drug distribution signals and their metabolites with endogenous compounds as biological markers of therapeutic effect, disease progression, or toxicity. Moreover, current drug release studies of PDCs use experimental protocols (e.g., the presence of dithiothreitol, pH = 5.5, or cathepsin B) whose conditions mimic known tumor conditions; however, our previous research indicated a general lack of *in vitro-in vivo* correlations (Chapter V). Thus, we evaluated the possible implementation of MSI to study drug release in *in vitro* TNBC models while monitoring the spatial localization of drugs and metabolite formation.

In vitro cell-based screening assays remain vital for early preclinical phases and provide valuable information on cytotoxicity, effectiveness, and molecular cell biology.³⁹² As proof of potential, MALDI-MSI represented a crucial part of the analytical strategy for assessing 3D *in vitro* models by measuring drug penetration, distribution, and cellular response to drugs.^{289,291,393–396} The labor-intensive sample preparation process required for MS imaging presents a significant challenge. Transporting 3D aggregates such as mammospheres from well-plates to the sample embedding molds may lead to aggregate disruption, with the aggregates lost and consequently missing some information. Implementing our BME-embedded spheroid model in the *in vitro* toxicity studies of PDCs ensured homogenous

distribution and removed the sample transportation bottleneck required for mammospheres.

The conclusive identification and detection of drugs in biological samples proved problematic in our study due to the MALDI-TOF instrument's high LOD for FAS and DIN; however, we plan to explore other ionization sources available for MSI to solve the sensitivity issue. More specifically, a desorption electrospray ionization (DESI) source suitable for the analysis of pharmaceuticals has advantages such as no sample preparation and the use of ambient conditions for MSI.³⁹⁷ Moreover, a recently reported MSI instrument with a MALDI-2 ionization source uses a second laser parallel to the sample surface that fires into the evolving gas of ions. The charge transfer from post-ionized matrix molecules to neutral analyte molecules reduces ion suppression effects and significantly improves sensitivity.³⁹⁸ Thus, we intend to investigate the implementation of a high-resolution Select Series MRT (Waters, USA) MSI instrument equipped with DESI source (with lower LOD for small molecules) and TimsTOF Flex MALDI-2 (Bruker, USA) to detect released drugs in biological samples and obtain a multimodal MSI platform for PDC characterization. A tissue washing protocol with pH-adjusted aqueous buffer solution to enhance drug signals in tissue by removing endogenous salts and other suppressants may represent another solution for lowering the LOD of our MALDI-MSI method.³⁹⁹ This protocol, reported by Shariatgorji et al., also suggests the minimization of analyte delocalization by adjusting the pH to a level where drugs become insoluble.³⁹⁹

Interestingly, our linker study described in Chapter V (performed after MSI experiments) indicates lower FAS release from single PGA-SS-Et-FAS in TNBC mammospheres than in the DTT studies (0.32% and 26.4%, respectively). Additionally, we only observed ≈40% internalization of PGA-SS-Et-FAS in TNBC mammospheres; thus, we can also conclude the presence of insufficient drug release in the 3D TNBC models for detection by MALDI-MSI. Performing a similar

study in spheroids has been complicated by the presence of a matrix; however, we are currently optimizing the method.

Metabolomics, the study of small molecules, can provide a new perspective on the altered interactions between enzymes, small molecules, and the different biological pathways in tumor tissues. More specifically, the emergence of spatial metabolomics supports the spatial localization of molecules in addition to their relative intensities. Alterations of metabolites directly associate with cell anatomical features, provide a further understanding of diseases, and may lead to personalized treatment and/or faster diagnostic methods.⁴⁰⁰ Metabolites are generally accepted as a size ≤ 1500 Da and include lipids, small peptides, sugars, oligonucleotides, nucleosides, ketones, organic acids, amino acids, steroids, and others.⁴⁰¹ Among all metabolites, we mainly detected lipids as the most abundant metabolites and amino acids due to the implementation of CHCA, a matrix appropriate for peptide and amino acids analysis by MALDI. The spatial distribution of other types of metabolites lay outside the scope of our study as their detection requires a more specific sample preparation protocol; the timeframe of our study rendered the undertaking of such a protocol infeasible.

Reprogrammed cellular metabolism represents a well-established hallmark of cancer development.⁴⁰² The detection of choline metabolites in our 3D TNBC models with MALDI-MSI agrees with the literature as they associate with malignant transformation and have been proposed as biomarkers of tumor progression.⁴⁰³ Overall, the observed alteration of amino acid metabolism in TNBC models following treatment with PDCs indicates the significance of these studies in further elucidating their influence on metabolic reprogramming. Moreover, lipid metabolism alterations after PDC treatment correlate with GPL's role as a signaling molecule and regulator of migration, apoptosis, and neurotransmission in tumor tissues.⁴⁰⁴ Thus, we suggest implementing a metabolomics study to discover biomarkers that will support monitoring the *in vitro* response and possibly predict

therapeutic outcomes. Lastly, we suggest synthesizing C¹³-PGA-based PDCs and consequent LC-MS/MS metabolomics studies and MALDI-MSI to unravel the influence of glutamic acid (from PGA) on cell metabolism.

4.4 CONCLUSION

We synthesized and studied single and combination PDCs for treating TNBC; single conjugates of the ROCK-inhibitor (fasudil; FAS) and the CDK-inhibitor (dinaciclib; DIN) and a combination conjugate with both FAS and DIN conjugated on the same PGA carrier. We observed significantly higher anticancer activity in all treatment groups (free FAS and DIN, single and combination PDCs) in TNBC mammospheres compared to spheroids. The reason behind these differences may lie in the different mechanisms of internalization and the metabolomic pattern variability.

We analyzed *in vitro* TNBC models treated with free drugs and their corresponding PDC by MALDI-MSI, a method developed for detecting and imaging the spatial distribution of FAS and DIN in biological samples. The drugs remained undetectable due to the method's high LOD and insufficient release from PDCs; however, we obtained high-resolution MALDI-MSI images of both spheroids and mammospheres thanks to the controlled and carefully optimized sample preparation protocol. In the future, we will explore more sophisticated MSI tools for the exhaustive characterization of drug release studies using *in vitro* TNBC models.

Finally, our data confirms metabolomic profiling as a suitable technology to distinguish untreated and treated TNBC models; however, metabolite annotation only used an MS scan and did not include the MS/MS fragmentation spectra due to the restrictions in the instrument choice and the time frame. Thus, current studies

with more detailed LC-MS/MS metabolomics and proteomics studies and higher-resolution MSI data are underway to follow up on these initial findings; however, our MSI study opens the possibility of monitoring endogenous markers of TNBC progression or therapeutic response (via lipid, amino acid, protein, or metabolite imaging) directly at the site of action of PDCs. Lastly, we intend to perform a detailed comparative metabolomics study between TNBC spheroid and mammosphere models to better understand the different therapeutic responses and choose the best *in vivo* correlation model.

4.5 EXPERIMENTAL MATERIAL AND METHODS

4.5.1 Materials

Diisopropylethylamine (DIEA), DL-dithiothreitol (DTT), cysteamine hydrochloride, dimethyl sulfoxide (DMSO) anhydrous, ethyl acetate, methanol (LC-MS grade) and MALDI-matrices were obtained from Sigma-Aldrich (St. Louis, United States). Celite 545, diethyl ether, dichloromethane (DCM), and deuterated solvents such as deuterated oxide (D₂O) were purchased from VWR chemicals (Radnor, US). Silica 60A 20–45-micron, water (LC-MS grade), ammonium formate, triethylamine (TEA), and formic acid (LC-MS grade) were purchased from Fisher Scientific (Pittsburgh, US). Vivaspin 10 kDa was obtained from Sartorius AG (Göttingen, Germany), and Sand 40-100 mesh was provided by ACROS organics (Geel, Belgium). Acetonitrile (CAN), chloroform, dimethylformamide (DMF), and methanol were purchased from Scharlab (Barcelona, Spain). 4-nitrophenyl-2-(pyridine-2yldisulfanyl) ethyl carbonate and 4-nitrophenyl-4-(pyridine-2yldisulfanyl) benzyl carbonate were purchased from Fluorochem (UK). All the drugs (dinaciclib – DIN,

resiquimod – RES, niraparib – NIRA, and rucaparib – RUCA) were purchased from MedKoo Biosciences (Morrisville, US) except for fasudil hydrochloride (FAS) that was obtained from Xingcheng Chempharm Co. Ltd (Zhejiang, China). Poly-L-glutamic acid (PGA) and PGA-SS-Et-FAS were kindly provided by Polymer Therapeutic Solutions SL (Valencia, Spain). Acetonitrile (LC-MS grade) was obtained from AppliChem GmbH. 4-dimethyl aminopyridine (DMAP) was obtained from Honeywell Fluka (Pittsburgh, US). 4-(4,6-Dimethoxy-1,3,5-triazin-2-yl)-4-methylmorpholinium (DMTMM) chloride (DMTMM·BF₄) was synthesized according to literature.³⁶⁶

4.5.2 PDCs synthesis

SS-Et-DIN Synthesis

Dinaciclib and DMAP were added to a solution of 4-nitrophenyl (2-(pyridine-2-yl)disulfanyl) ethyl carbonate (1:1:1 equivalence) in DCM, and the pH was adjusted to 8 with TEA. The reaction was left under inert conditions at room temperature overnight. The product was purified with column chromatography on silica gel (DCM-MeOH 95:5), the solvent evaporated, and a yellow viscous oil obtained was stored at -20°C until further use. The product identification was confirmed by a direct Q1 MS scan.

Cys-SS-Et-DIN Synthesis

Cysteamine hydrochloride was added to a solution of SS-Et-DIN (1:1 equivalence) at 15 mg/ml concentration in methanol and left to react at room temperature for 3 h. The reaction was reprecipitated in ether two times, dried under vacuum, and analyzed with a Q1 MS scan to confirm the product formation.

Synthesis of LinPGA-SS-Et-DIN, and LinPGA-SS-Et-FAS-DIN

DMTMM BF₄ was added to a solution of LinPGA in DMSO (dissolved by heating) and left for 30 min to activate the carboxylic groups of LinPGA. Cys-SS-Et-DIN was added in the amount necessary to obtain the desired TDL; the pH was adjusted to 8.0 with TEA, and the solution was allowed to stir for 48 h at room temperature. The reaction was precipitated in ether, reprecipitated twice from methanol to ether, and the obtained white powder was dried under a vacuum. After drying, the conjugate was dissolved in Milli-Q and transformed into salt form by adding the 0.5 M NaHCO₃ until pH 8.0, purified through VivaSpin (3000 kDa cut off to remove extra salts and free drug) with approximately 100 ml Milli-Q and freeze-dried. The obtained white product was stored at -20°C and dissolved in Milli-Q water before each use.

Obtaining the LinPGA-SS-Et-FAS-DIN combination conjugate used an additional step of SS-Et-DIN conjugation. The reaction and purification processes were identical to the single LinPGA conjugates.

4.5.3 Physicochemical-Characterization of PGA-drug conjugates

TDL determination by UV-Vis

Fasudil and dinaciclib solutions in methanol were used as standard stock solutions, while the working standard solutions were obtained by dilution with Milli-Q water. The total conjugate drug loading was determined at three concentration levels (0.1 mg/ml, 0.25 mg/ml, and 0.5 mg/ml, in Milli-Q water) by measuring the absorbance at 323 nm (for fasudil) and 259 nm (for dinaciclib). LinPGA water solution in the same concentration as the conjugates was used as a blank. UV-Vis measurements were performed using JASCO V-630

spectrophotometer at 25°C with a 1.0 cm quartz cell and a spectral bandwidth of 0.5 nm.

FD determination by LC-MS/MS

3 mg of conjugates were suspended in 500 µl MeOH (LC-MS grade), vortexed for 5 min, centrifuged for 10 min at 11.000 rpm to remove the pellet, and the solution was subjected to LC-MS/MS analysis.

Fasudil and dinaciclib release studies

Release studies were performed in 5 mM (test sample) and 10 µM DTT (control sample) using three replicates for each sample group. 3 mg/ml conjugate solution was prepared in FA buffer solution (pH 5.5, LC-MS grade) and appropriate concentration of DTT and incubated at 37°C. At defined time points (0, 2, 4, 6, 24, 48, and 72 h), a 100 µl was aliquoted from the primary solution and subjected to the LC-MS/MS analysis.

LC-MS/MS method for quantitative determination of FAS and DIN

LC-MS/MS method development was performed by DoE with DesignExpert12 software (see Chapter II). The LC-MS/MS analysis was performed using an ExionLC system comprising a Pump, AC autosampler, AC Column oven, and AB Sciex QTRAP 4500 (all Sciex, Singapore). Eluent A was H₂O with FA 0.1%, and eluent B was CAN. All runs were performed using a Kinetex Biphenyl column (100 mm × 3.0 mm, 2.6 µm, 100 Å) from Phenomenex, USA, with a 20 µL injection volume. The drugs were detected in positive electrospray mode with multiple reaction monitoring scans (292.2 – 99.2 m/z for FAS with 35 CE and 397.3 – 335.1 m/z for DIN with 40 CE). The MS conditions implemented were as follows: curtain gas 20 V, ion source temperature 250 °C, gas 1 45 V, gas 2 45 V, ion source voltage 5500 V, declustering potential 62 v, entrance potential 2 V. The validation parameters evaluated were linearity, the limit of quantification (LOQ), the limit of

detection (LOD), and accuracy (Table S4.2). A low LOQ and a medium LOQ control standard solutions were analyzed each day before analyzing the sample to confirm the quality of LC-MS/MS response. Methanol with 0.1% FA was used as a blank control sample.

NMR spectroscopy

10 mg/ml sample solutions in deuterated water were analyzed at 27°C on a 300 Ultrashield™ spectrometer (Bruker, USA), and data were processed with the software TopSpin and Mestrenova.

Direct mass spectrometry scan

All the samples monitored by mass spectrometry (MS) Q1 scan were analyzed by 20 µl direct injection with ACN 50% and H₂O 50% (0.1% formic acid - FA) as mobile phase, and 0.5 ml/min flow rate, while the MS conditions were as follows: curtain gas 20 V, ion source temperature 250 °C, gas 1 45 V, gas 2 45 V, ion source voltage 5500 V, declustering potential 62 v, entrance potential 2 V.

4.5.4 *In vitro* cell viability assay - MBE embedded spheroids

We will employ BME-embedded spheroids, as this natural extracellular matrix-based hydrogel resembles the natural tumor extracellular matrix (ECM) (e.g., laminin, collagen IV, entactin, heparan sulfate proteoglycans), that thereby recapitulate a crucial physiological barrier that anti-tumor nanomedicines may face in a clinical setting.

We first seeded ten 40 µl-drops containing 1,000 cells and 10 mg/ml growth factor-reduced BME type II (R&D, 3533-010-02)) per well in a six-well suspension plate (Sigma, M9062) using low retention pipette tips (Sigma, Z740046). After incubating for 30 min at 37°C to solidify drops, we added 3 mL per well of DMEM/F12 (Gibco, 31330-038) supplemented with 10% fetal bovine serum. The

generated MDA-MB-231 spheroids were treated with single and combination PDCs to evaluate drug release, spatial localization, and metabolite formation at specified time points. Additionally, after 72 h (37°C, 5% CO₂), we measured cell viability using CellTiter Glo 3D following manufacturer's instructions.

4.5.5 *In vitro* cell viability assay – mammospheres

Cells were seeded on a 96-well plate at the density model 31250 cells/cm². After the confluency reached 80%, the cells were incubated for 24 h at 37 °C and treated with the solutions of free drug (in DMSO) and their single and combination conjugates in a determined concentration range. After 72 h, the cells were incubated for 6 h with a mixture of MTS and PMS (ratio 20:1) and measured directly at 490 nm on CLARIOstar multi-plate reader (BMG LABTECH). *In vitro* cell viability was expressed as the percentage difference between the viability of untreated control cells and cells treated with free drugs or conjugates.

4.5.6 Sample embedding

The procedure was followed by the previously developed method by Dannhorn et al. Briefly, matrix-embedded spheroids and aggregoids were washed twice with fresh dPBS solution and carefully transferred to embedding media-coated molds. A 7.5% HPMC and 2.5% PVP mixture was used as a sample embedding media. Additional embedding media was coated over the samples, frozen in isopropanol solution, conditioned under liquid nitrogen for approximately 2 min, and stored at -80°C before sectioning.

4.5.7 Sample sectioning and matrix application

To avoid sample storage and possible ion delocalization, samples were cryosectioned and analyzed on the same day. Embedded samples were cryosectioned on a CM1950 cryostat (Leica Biosystems, UK) with -24°C in the cryo-chamber and -20°C for the sample holder. Samples were attached onto metallic rings with ice and thermally equilibrated for 30 min. Sections with 10 µm thickness were thaw mounted onto Indium-Tin oxide (ITO)-coated slides, air dried, and desiccated with N₂ before matrix application. Eight layers of matrix solutions were deposited on the sample slides using M3+ Sprayer (HTX Technologies LCC, USA; with a flow rate of 200 µl/min, 80°C spray nozzle temperature, velocity 1000 mm/min, cick-cack pattern, 10 psi nitrogen pressure, 40 mm nozzle height, track spacing 3 mm), air dried, and directly analyzed with Autoflex Speed MALDI-TOF. For the method development and the sample spiking, matrix solution composed of 10 µg/ml α-CHCA, 70% MeOH, 0.1 % TFA and 10 µg/ml FAS and DIN was sprayed onto the 3D in vitro models sections and analyzed for the matrix interferences.

4.5.8 Image acquisition and data processing

Data acquisition was performed on Autoflex Speed (Bruker, Bremen, Germany) equipped with 2 kHz (kiloHertz) proprietary Smartbeam-II solid-state laser. MALDI-MSI images were acquired in positive ion full scan within 60-2000 m/z range using the FlexControl 3.4 software (Bruker Daltonik). Prior to analysis, the acquisition method was calibrated externally on the ITO slide using the α-CHCA matrix peaks (190.04987 m/z; 212.03240 m/z; 304.35121 m/z; 379.09246 m/z; 877.05400 m/z; and 1066.09660 m/z). MALDI-TOF imaging was performed using the FlexImaging software (Bruker Daltonik) by accumulating 500 laser shots per

measurement spot at a raster width of 30 or 10 μm as indicated. All raw data was processed using SCiLS™ Lab MVS Version 2019b (Bruker Daltonik, Germany) and normalized to the matrix ion (190.049 ± 0.05 m/z) was applied to all MALDI-TOF spectra. The formed peak list was used for co-localization of m/z images, spatial localization of m/z ions, and metabolomics analysis (metaspace2020.eu for metabolite annotation and metaboanalyst.ca for statistical analysis).

4.5.9 Histological analysis

After MALDI-MSI analysis, the slides were washed with 100% EtOH to remove the matrix's presence and stained with Mayer's hematoxylin and eosin (H&E) solutions. First, the sections were stained with hematoxylin for 1 min, then washed for 5 min with tap water before submerging in 100% EtOH twice for 3 min. Subsequently, the sections were stained with eosin for 1 min and then washed with 100% EtOH twice for 3 min. Finally, the sections were submerged in xylene substitute for 5 min and mounted using Pertex. Optical images were obtained by Olympus BX60 microscope (Olympus, UK) and QImaging Micropublisher 5.0 RTV camera and Capture-Pro software (QImaging, Canada).

4.6 SUPPLEMENTARY MATERIAL

Table S4.1. Matrix selection for MALDI-MSI detection of fasudil and dinaciclib

Solution	Matrix 10 µg/ml	ACN: H ₂ O (70:30)	MeOH: H ₂ O (70:30)	0.1% TFA	0.1% FA
A	CHCA	+	-	-	-
B	CHCA	-	+	-	-
C	CHCA	-	+	+	-
D	CHCA	-	+	-	+
E	DHB	+	-	-	-
F	DHB	-	+	-	-
G	NEDC	+	-	-	-
H	NEDC	-	+	-	-
I	9-AA	+	-	-	-
J	9-AA	-	+	-	-

CHCA – α -Cyano-4-hydroxycinnamic acid; DHB- 2,5-dihydroxybenzoic acid; NEDC - N-naphthyl-ethylenediamine-dihydrochloride; 9-AA- 9-aminoacridine; ACN- acetonitrile; MeOH- methanol; TFA- trifluoroacetic acid; FA- formic acid

Table S4.2. Validation parameters and MS/MS conditions for LC-MS/MS method implemented in the drug release studies for the quantification of drugs

Drug	Linearity				
	C range, µg/ml	R ²	Accuracy, %	LOQ, µg/ml	LOD, µg/ml
Fasudil	0.01 - 0.1	0.998	96.5 – 109.6	0.02	0.01
	0.1 - 0.5	0.997	97.6 – 102.2	0.10	0.03
	0.5 - 1.0	0.996	97.6 – 101.7	0.13	0.04
	1 - 5	0.999	98.7 – 100.8	0.39	0.12
Dinaciclib	0.02 – 0.1	0.998	96.5 – 101.4	0.02	0.01
	0.1 – 0.5	0.997	98.7 – 106.1	0.10	0.03
	0.5 – 1.0	0.997	98.7 – 101.6	0.11	0.03
	1.0 – 5.0	0.999	99.4 – 102.1	0.24	0.07

LOD – limit of detection, LOQ – limit of quantification, MRM-multiple reaction monitoring

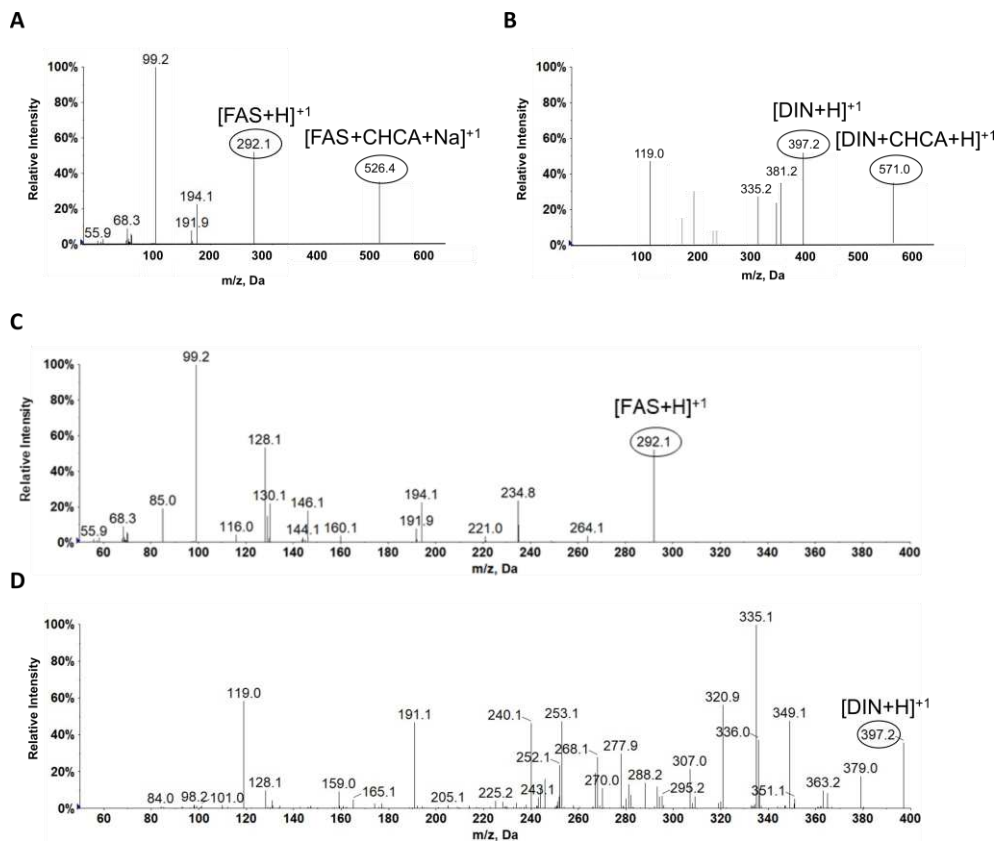


Figure S4.1. Qualitative analysis of FAS, DIN and their matrix adduct ions generated in the MALDI-TOF. (A) MS fragmentation spectra of 526.4 m/z confirming the presence of FAS ion 292.1 m/z (CE = 35 eV). **(B)** MS fragmentation spectra of 571.0 m/z confirming the presence of DIN ion 397.2 m/z (CE = 30 eV). **(C)** MS fragmentation spectra of FAS ion 292.1 m/z (CE = 35 eV). **(D)** MS fragmentation spectra of DIN ion 397.2 m/z (CE = 30 eV).

CHAPTER V

**CRITICAL STRATEGIES FOR CRAFTING
POLYMER-DRUG CONJUGATES
POSSESSING ON-DEMAND DRUG
RELEASE**

5.1 INTRODUCTION

Specificity, adequate potency, toxicity in a therapeutic range, and availability at the site of action represent essential attributes when selecting a lead compound for drug delivery research and development. Recent research in the anti-cancer nanomedicine field has underlined the importance of vascularization, macrophage populations, patient-specific tumor stroma, and patient-specific tissue morphology in selecting a candidate for clinical translation.^{21,405} These findings suggest the need for a disease-driven approach to the rational design of nanomedicine, which requires a robust understanding of the relationships between biology and technology, the techniques used to characterize nanomedicines, and the influence of disease pathophysiology on nanomedicine distribution, accumulation, and efficacy.²⁰

Among other capabilities, polymer-drug conjugates (PDCs)^{406–408} enable a therapeutic cargo to reach a desired site of action through passive (due to enhanced permeability and retention) and/or active targeting (by including targeting moieties).³⁷ Controlled drug release from PDCs supports bioavailability in the target tissue, cell, or subcellular compartment, which can be achieved by designing a linking moiety between the drug and the polymeric carrier for cleavage in the presence of endogenous or exogenous triggers.^{27,128} Redox-responsive self-immolative linkers bearing a disulfide moiety (SS-SIL) represent a powerful approach for intracellular drug delivery by PDCs.⁴⁰⁹ High levels of the reducing agent glutathione (GSH) in the endosomal compartment and the presence of specific reducing enzyme (gamma-interferon-inducible lysosomal thiol reductase or GILT) can trigger drug release from SS-SILs.^{410,411} The implementation of disulfide linkers remained limited to thiol-containing drugs until recently; now, novel

universal linking strategies have been developed to modify thiol-free drugs and allow conjugation to a suitable carrier.⁴¹²

The most prevalent SS-SILs use a cyclization elimination mechanism where drug release occurs through nucleophilic substitution-elimination – the so-called "thiol-disulfide interchange reaction."^{409,413} Importantly, disulfide linker stability can be easily tuned by introducing distinct spacers between the disulfide bond and the drug (e.g., methyl-disulfide or ethyl-disulfide [Et-SS]); however, the rate of linker self-immolation via the intramolecular cyclization mechanism of drug release can slow under acidic conditions, such as those present in the endosomal and lysosomal compartments and the tumor microenvironment (TME).^{414,415} This obstacle has prompted the development of alternative spacers for SS-SIL design, with phenyl-disulfide linkers (Ph-SS) as one potential alternative.

Multiple studies have sought to explore drug release mechanisms and fine-tune the activity of SS-SILs.^{416,417} Previous studies reported site-specific drug release from an Et-SS linker⁴¹⁸ and the influence of drug's structural features on the drug release.⁴¹⁹ Nevertheless, the authors of said studies failed to explain or investigate the reason behind these findings; thus, the possible intermediate metabolites remain unidentified and the influence of drug structural features on release kinetics remains unexplored.

To investigate the drug dependent release from SS-Et linkers and to improve the reproducibility of preclinical studies of PDCs, we designed robust analytical procedure required to meet the major chemical and biological needs. Herein, we implemented an artificial intelligence tool – design-of-experiments or DoE – to simultaneously optimize a liquid chromatography–tandem mass spectrometry (LC-MS/MS) method to quantitatively determine the presence of various active agents. Unlike traditional approaches such as auto-tuning or "one factor at a time", which remain helpful in the low method sensitivity setting, DoE

considers interactions between variables, minimizes uncontrolled effects, and evaluates their impact on the analysis.^{220,221}

We aimed to evaluate the impact of the chemical group of the drug used for conjugation (i.e., electronegativity, basicity, and ability to form resonance stabilized intermediates) on drug release kinetics. Importantly, we validated drug release kinetics by directly analyzing the resulting metabolites in preclinically relevant cell models, looking for a better theoretical and *in vitro* drug release correlation. Finally, we report on the critical strategies that must be considered when rationally designing PDCs to gain optimized biological output.

Specific objectives for this Chapter comprise:

Objective 1. Evaluate how the nature of the chemical group in the drug available for conjugation influences its release kinetics

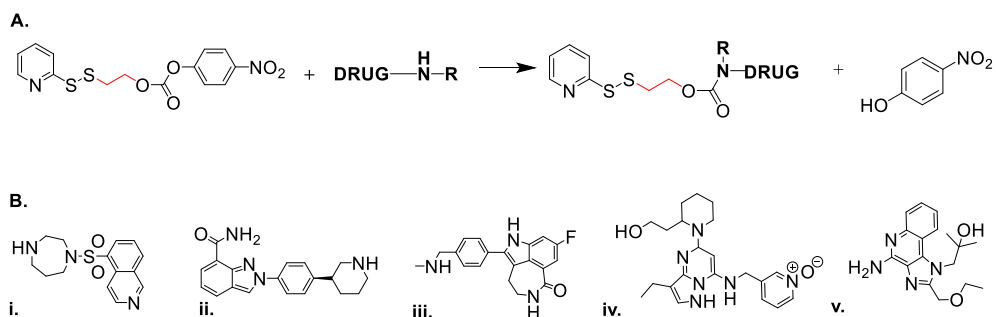
Objective 2. Validate drug release kinetics by directly analyzing resultant metabolites in preclinically relevant cell models to improve *in vitro* and *in vivo* correlations

Objective 3. Report the critical strategies under consideration when rationally designing PDCs with optimized biological output

5.2 RESULTS

5.2.1 Drug-Et-SS synthesis and their characterization with accurate and robust LC-MS/MS platform

To understand how the drug's chemical functionality influences release kinetics from corresponding "Drug-Et-SS," we synthesized five Drug-Et-SS formed using varying functional sites on different drugs. As model drugs, we chose fasudil (FAS), niraparib (NIRA), and rucaparib (RUCA), which each bear a secondary amino group (a chemical group with low electronegativity), dinaciclib (DIN), which bears a primary alcohol group, and resiquimod (RES), which bears a primary amino group that forms part of a resonance stabilized structure. We synthesized individual Drug-Et-SS by the reaction of each drug with the *p*-nitrophenyl chloroformate-activated alcohol group of the SS-Et linker (Scheme 5.1). We refer the reader to Section 3.5.2 and Table S5.1 for more detailed information regarding reaction conditions. We hypothesized that drugs bearing an amino group that forms part of resonance stabilized structure or a primary alcohol group (with higher electronegativity than the amino group) would provide the highest drug release rate.



Scheme 5.1. Synthetic scheme for drug-disulfide self-immolating drug-linker development. (A) Drug-Et-SS synthesis with the reaction conditions for each compound

presented in Table S5.1, and **(B)** chemical structures of the drugs implemented in this study bearing different chemical groups available for the attachment with Et-SS linker: i) fasudil, ii) niraparib, iii) rucaparib, with all three drugs bearing secondary amino group, then iv) dinaciclib with a hydroxyl group, and v) resiquimod with a secondary amino group as a part of resonance stabilized structure. Acknowledgement to Justine Hillaert, Dr Maria Medel and Dr Inmaculada Conejos Sanchez for the help in the synthesis process.

To better demonstrate our hypothesis, we reported the molecular ions ($[H^+]$) and/or sodium adduct ions ($[Na^+]$) for each synthesized Drug-Et-SS (FAS-Et-SS, NIRA-Et-SS, RUCA-Et-SS, DIN-Et-SS, and RES-Et-SS) obtained by a Q1 MS direct scan (Figure 5.1.); nevertheless, we also matched the MS/MS fingerprint spectra with their fragmentation mechanism to confirm the identity of Drug-Et-SS products and the success of chemical reaction (Figures S5.1-5.). Moreover, we determined the most abundant fragment of each drug and Drug-Et-SS from the MS/MS fingerprint spectra and used this data to form the multiple-reaction-monitoring (MRM) scan necessary for the LC-MS/MS method employed in the release studies (Table S5.2). The Q1 MS scan of RES-Et-SS and DIN-Et-SS demonstrated the product's higher susceptibility to MS in-source fragmentation when compared to other Drug-Et-SS, as shown by the presence of fragments such as $[DIN+H]^+$ and $[DIN-Et-S+H]^+$ in the DIN-Et-SS Q1 MS scan (Figure 5.1D) and $[RES+H]^+$ and $[RES-Et-S+H_2O]^+$ in the RES-Et-SS Q1 MS scan (Figure 5.1E). These results indicate lower stability and higher drug release associated with RES-Et-SS and DIN-Et-SS than the other Drug-Et-SS.

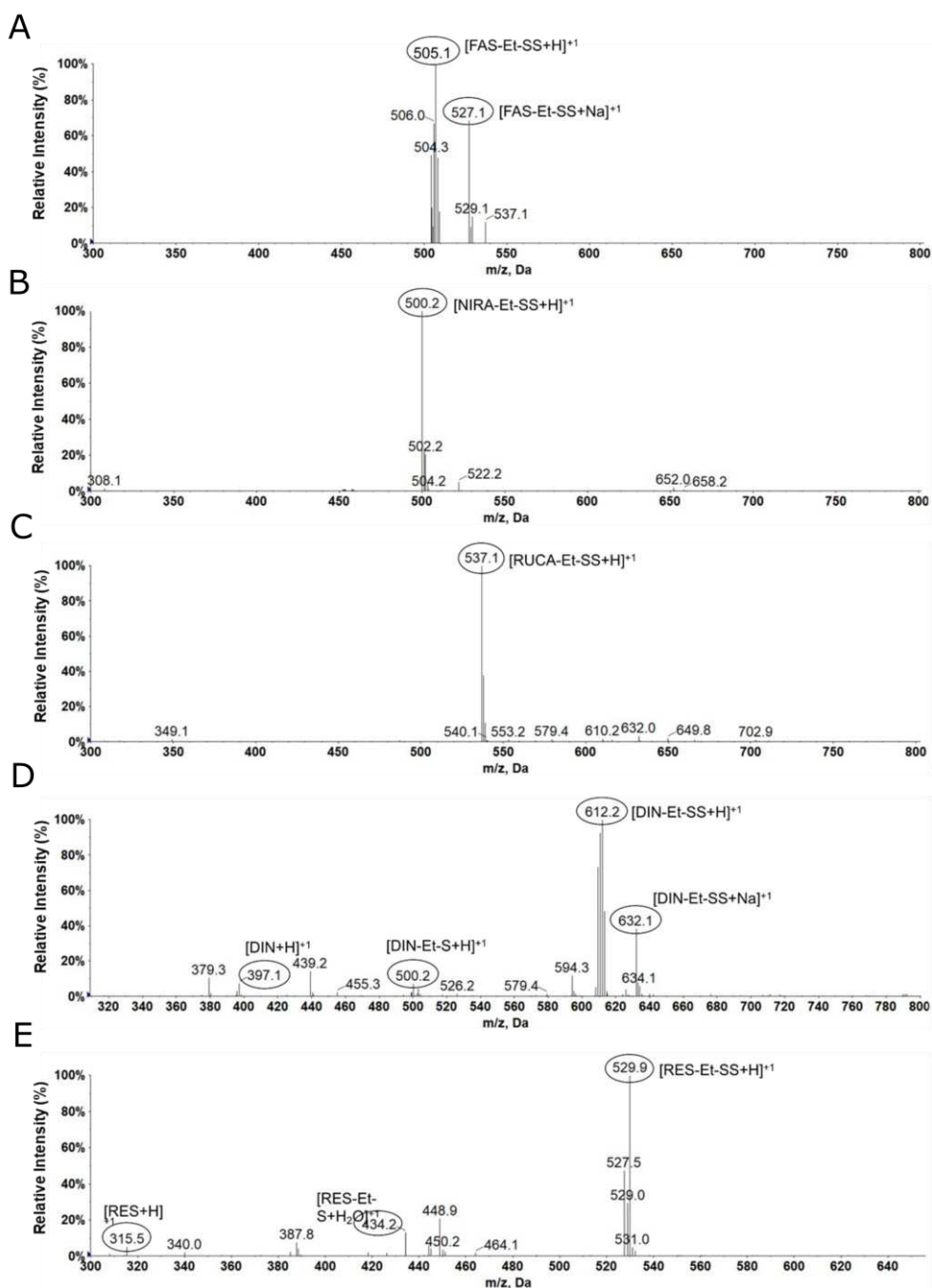


Figure 5.1. Q1 MS scans showing the identity of (A) fasudil-ethyl-disulfide (FAS-Et-SS), (B) niraparib-ethyl-disulfide (NIRA-Et-SS), (C) rucaparib-ethyl-disulfide (RUCA-Et-SS), (D) dinaciclib-ethyl-disulfide (DIN-Et-SS), and (E) resiquimod-ethyl-disulfide (RES-Et-SS).

5.2.2 Drug Release from Individual Drug-Et-SS Depends on Drug Structural Features

We then implemented the fit-for-purpose LC-MS/MS method developed in Chapter 2 (Figure S5.6) to perform drug release studies by quantifying the cumulative amount of drug released from the Et-SS spacer-linker at specific times over a total period of 144 h (six days) in the presence of 5 mM dithiothreitol (DTT), which provides a reductive environment (mimicking the lysosomal compartment) sufficient to induce SS-SIL cleavage. In agreement with our hypothesis, we found that DIN-Et-SS (with a primary -OH group) released a significantly higher cumulative amount of drug after a 144 h incubation in the presence of 5 mM DTT (63.8% of DIN) compared to FAS-Et-SS (39.7% of FAS, $p = 6.27\text{E-}05$), NIRA-Et-SS (42.8% of NIRA, $p = 0.00040$), and RUCA-Et-SS (24.08% of RUCA, $p = 1.72\text{E-}05$), bearing secondary amino groups (Figure 5.2A, empty squares). Additionally, we obtained significantly higher cumulative drug release from RES-Et-SS (with an amino group that forms part of resonance stabilized structure) after a 144 h incubation in the presence of 5 mM DTT (77.01% of RES) compared to FAS-Et-SS (39.7% of FAS, $p = 1.48\text{E-}05$), NIRA-Et-SS (42.8% of NIRA, $p = 6.66\text{E-}05$), and RUCA-Et-SS (24.08% of RUCA, $p = 6.40\text{E-}06$) (Figure 5.2A, empty diamonds). These data support our hypothesis that drug release from Drug-Et-SS under a reductive environment depends on drug structural features.

The 13.6% observed RES release at the 0 h time point under a reductive environment (5 mM DTT) combined with the low/negligible drug release from all other Drug-Et-SS (<0.41%, <0.52%, <0.45% corresponding to the limit of quantification (LOQ) of the LC-MS/MS method for FAS, NIRA, and RUCA, respectively) demonstrates how the capacity of drugs to form resonance-stabilized

structures prompts a rapid and initial “burst” release (Figure 5.2B – drug release over first 8 h). Interestingly, the incubation of RES-Et-SS with 10 μ M DTT prompted 12.8% and 15.3% RES release at 0 h and 144 h, respectively, indicating that much lower DTT concentrations suffice to support burst RES release from RES-Et-SS (Figure 5.2C); however, the highly significant difference between 144 h cumulative drug release values in the presence of 5 mM DTT and 10 μ M DTT for RES-Et-SS ($p = 1.28616E-06$) indicates the need for a highly reductive environment (such as that present in lysosomes) for complete RES release.

We did not observe any significant DIN release from DIN-Et-SS during 144 h incubation with 10 μ M DTT (0.002 to 0.03% DIN released from 0 to 144 h), confirming extracellular stability; however, DIN-Et-SS in the presence of 5 mM DTT provided significantly higher drug release when compared to 10 μ M DTT ($p = 2.42E-05$, Figure 5.2C) demonstrating its suitability to achieve site-specific release.

Interestingly, the LC-MS/MS chromatogram obtained from DIN-Et-SS and RES-Et-SS drug release studies with 5 mM DTT at 0 h provided proof of a rapid first step of DIN and RES release through the presence of the free drugs (DIN and RES) and intermediate products (DIN-Et-SH and RES-Et-SH) (Figures 5.3A and B). Via a Q1 MS scan, we confirmed the presence of RES-Et-SH and DIN-Et-SH intermediates eluting at retention times of 2.81 min and 2.89 min, respectively (Figures 5.3C and D). The presence of only RES-Et-SS and DIN-Et-SS in samples analyzed after incubation in the absence of DTT (Figures 5.3E and F) confirmed the DTT-specific release of RES and DIN; thus, findings at the 0 h time point in the presence of 5 mM DTT do not represent synthesis artifacts or indicate RES-Et-SS and DIN-Et-SS storage instability.

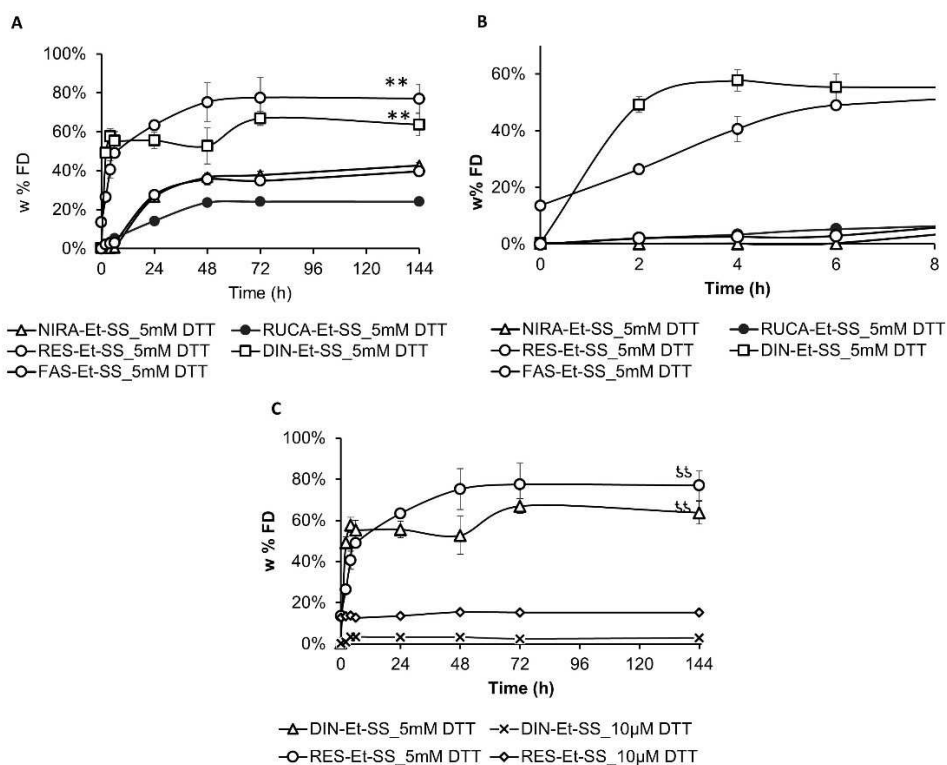


Figure 5.2. DTT-mediated drug release from Drug-Et-SS. Drug release over (A) 0-144 h and (B) 0-8 h in the presence of 5 mM DTT. (C) Comparison of DIN and RES release in response to 5 mM DTT and 10 μ M DTT. Niraparib-ethyl-disulfide (NIRA-Et-SS), fasudil-ethyl-disulfide (FAS-Et-SS) rucaparib-ethyl-disulfide (RUCA-Et-SS), resiquimod-ethyl-disulfide (RES-Et-SS) and dinaciclib-ethyl-disulfide (DIN-Et-SS) evaluated. Data presented as a cumulative weight percentage of free drug (w% FD) compared to the total drug amount in the drug-linker \pm SD ($n = 3$). ** $p < 0.005$ indicate a statistically significant difference between DIN-Et-SS and RES-Et-SS drug release compared to other Et-SS drug linkers. †† $p < 0.005$ indicate the statistically significant between drug release in the presence of 5 mM DTT and 10 μ M DTT for each Drug-Et-SS.

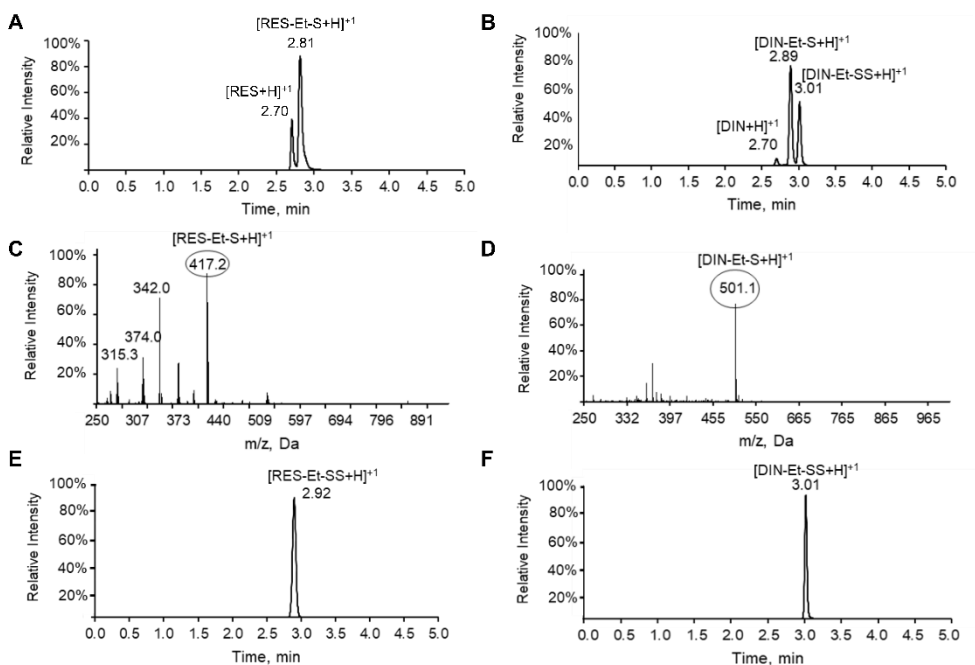


Figure 5.3. LC-MS/MS chromatograms obtained from (A) Resiquimod-ethyl-disulfide (RES-Et-SS) and (B) Dinaciclib-ethyl-disulfide (DIN-Et-SS) drug release studies in 5 mM DTT at 0 h showing the presence of intermediates (RES-Et-S-H and DIN-Et-S-H) and free drugs (resiquimod - RES, and dinaciclib – DIN. (C) Q1 MS scan at 2.81 min showing the intermediate product (RES-Et-S-H), and (D) Q1 MS scan at 2.89 min showing the intermediate product (DIN-Et-S-H). LC-MS/MS chromatogram of the blank sample (without DTT) indicating the presence of only peak for (E) RES-Et-SS and (F) only DIN-Et-SS.

The disappearance time of Drug-Et-SS compounds peaks from the LC-MS/MS chromatograms when incubated in the presence of 5 mM DTT (highly reducing environment) may represent the final indicator of the rapid nature of the first step of drug release. The absence of the RES-Et-SS peak and the presence of both free RES $[RES+H]^+$ and intermediate $[RES-Et-S+H]^+$ peaks at 0 h in the LC-MS/MS chromatogram indicates an immediate reduction of the -SS- bond when exposed to 5 mM DTT (Figure 5.4A). Next, we detected the last DIN-Et-SS peak in

the LC-MS/MS chromatogram at a 2 h time point (Figure 5.4.B), NIRA-Et-SS at 6 h (Figure 5.4.C), and FAS-Et-SS at 24 h (Figure 5.4.D), while the RUCA-Et-SS peak remained in the LC-MS/MS chromatogram even after 144 h incubation with 5 mM DTT (Figure 5.4.E). The LC-MS/MS chromatograms indicate the fastest first step of drug release from Et-SS linkers for RES-Et-SS, followed by DIN-Et-SS, NIRA-Et-SS, FAS-Et-SS and finally RUCA-Et-SS as the slowest and incomplete first step release during the 144 h of our study. With these results, we provided evidence for our theory that drug release from the Et-SS linker depends on the nature of the chemical group available for attachment of the drug to the Et-SS linker.

To support higher FAS, NIRA, and RUCA release, we proposed the implementation of a disulfide-modified linker using a phenyl instead of an ethyl spacer between the disulfide bond and the drug. The drug release mechanism from Ph-SS drug-linkers occurs through the 1,6-elimination (pDTB-dithiobenzyl) after disulfide bond reduction; thus, the second step of drug release does not depend on the drug's structural features as pDTB elimination occurs through the thioquinone methide cascade (Scheme 5.2B).⁴²⁰

Of note, the burst release obtained with RES-Et-SS represents a drug release phenomenon commonly observed in delivery systems with different forms and compositions. Specific indications include targeted delivery, wound treatment, pulsatile release, or encapsulated favor burst release. Nevertheless, this drug release mode may cause "side effects" such as short *in vivo* half-lives and shortened release profiles that require more frequent dosing and prompt local or systemic toxicity.⁴²¹ The influence of burst RES and DIN release from Et-SS on the therapeutic effect of their corresponding PDCs remains outside the scope of our study. Instead, we next focused on providing solutions for low FAS, NIRA, and RUCA release.

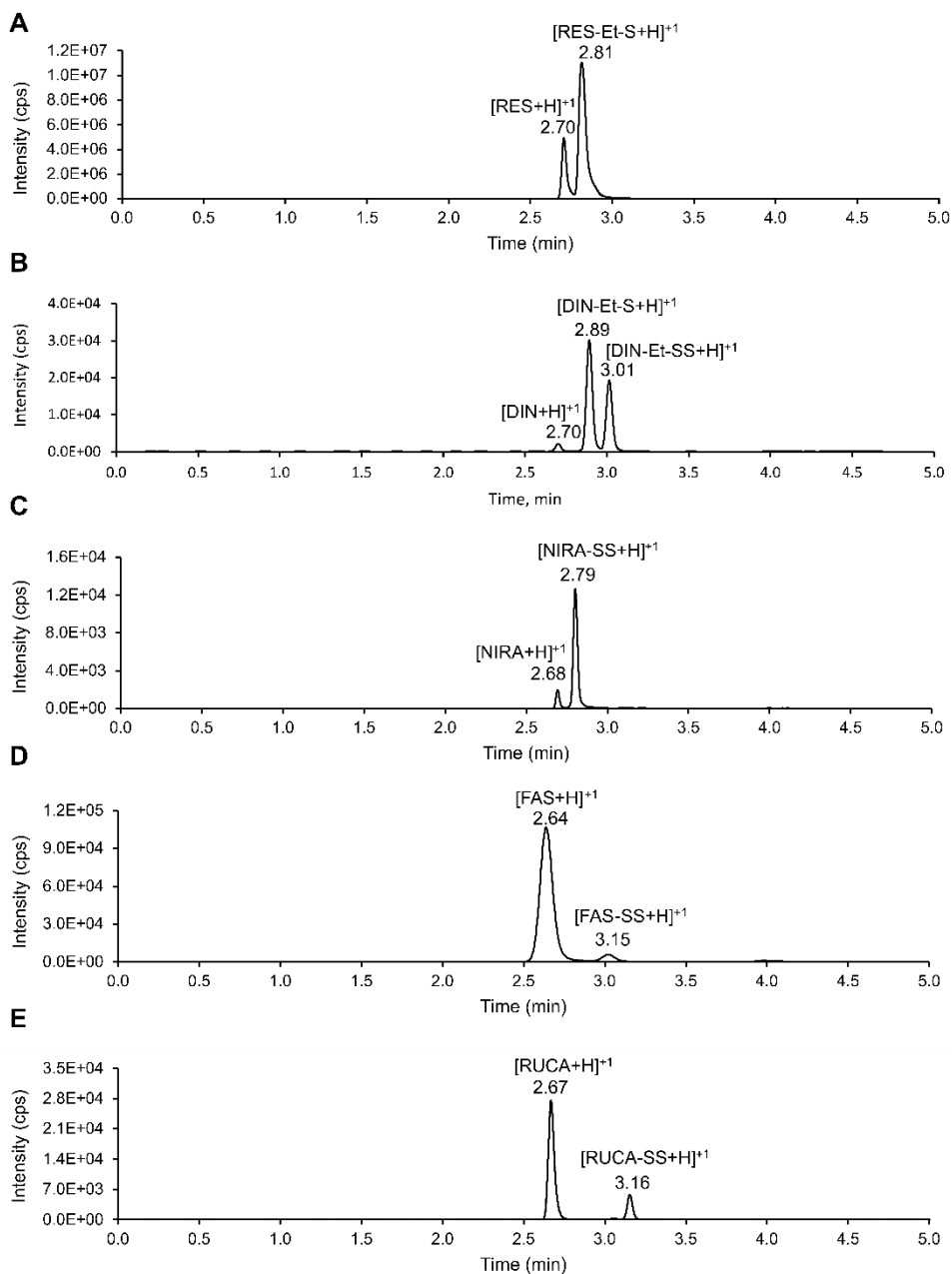
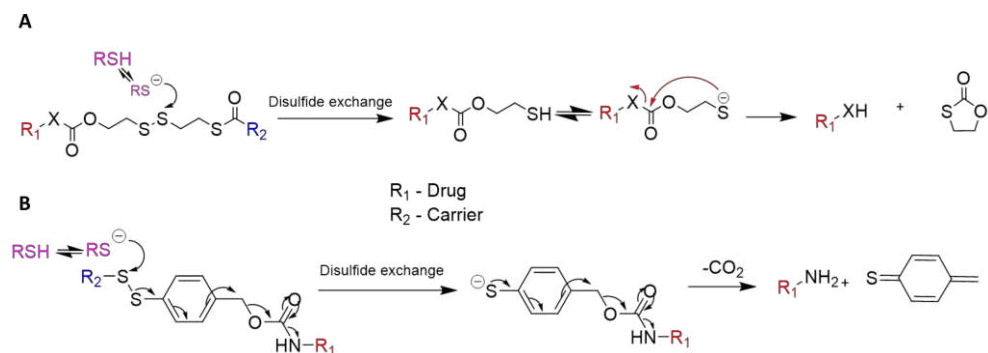


Figure 5.4. LC-MS/MS chromatograms from the last time point of drug release studies where the drug-linkers were detectable for (A) resiquimod-ethyl-disulfide (RES-Et-SS), with free RES [RES+H]⁺ and intermediate [RES-Et-S+H]⁺ detected at 0 h time point, (B) dinaciclib-ethyl-disulfide (DIN-Et-SS), with [DIN-Et-SS+H]⁺ lastly detected at 2 h, (C) niraparib-ethyl-

disulfide (NIRA-Et-SS), with [NIRA-Et-SS+H]⁺ last detected at 6 h, (D) fasudil-ethyl-disulfide (FAS-Et-SS), with [FAS-Et-SS+H]⁺ last detected at 24 h, and (E) rucaparib-ethyl-disulfide (RUCA-Et-SS), with [RUCA-Et-SS+H]⁺ still detected at 144 h.

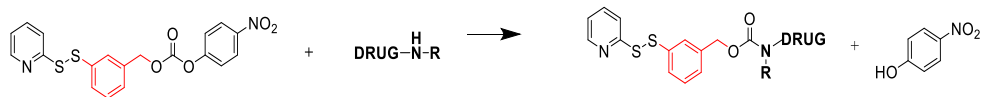


Scheme 5.2. Drug release mechanisms of (A) Drug-ethyl-disulfides by intramolecular cyclization and (B) Drug-phenyl-disulfides by thioquinone methide cascade. Adapted from Wang et al.⁴⁰⁹

5.2.3 Ph-SS as a Robust Substitute for Et-SS

Following the drug release results observed for the Drug-Et-SS, we aimed to enhance the drug release rate from FAS-Et-SS, NIRA-Et-SS, and RUCA-Et-SS by synthesizing counterparts that carried a Ph-SS, which displays increased hydrophobicity, instead of an Et-SS linker. We synthesized Drug-Ph-SS by reacting each drug with the p-nitrophenyl chloroformate-activated alcohol group of Ph-SS, resulting in “Drug-Ph-SS” product formation (Scheme 5.3). We refer the reader to Section 3.5.2 and Table S5.1 for more detailed information regarding reaction conditions. We confirmed the identity of Drug-Ph-SS by reporting the molecular ions ([H⁺]), sodium adduct ions ([Na⁺]), and/or potassium adduct ions ([K⁺]) in a Q1 MS scan for FAS-Ph-SS, NIRA-Ph-SS, and RUCA-Ph-SS (Figure 5.5.A-C) and matching

the fragmentation mechanism for each Drug-Ph-SS product to the MS/MS scan (Figure S5.7-9).



Scheme 5.3. Drug-phenyl-disulfide synthetic scheme. The reaction conditions, including the solvent, the temperature, and the additives, differ between the Drug-Ph-SS; See Table S5.1. for more details. Acknowledgement to Justine Hillaert, Dr Maria Medel and Dr Inmaculada Conejos Sanchez for the help in the synthesis process.

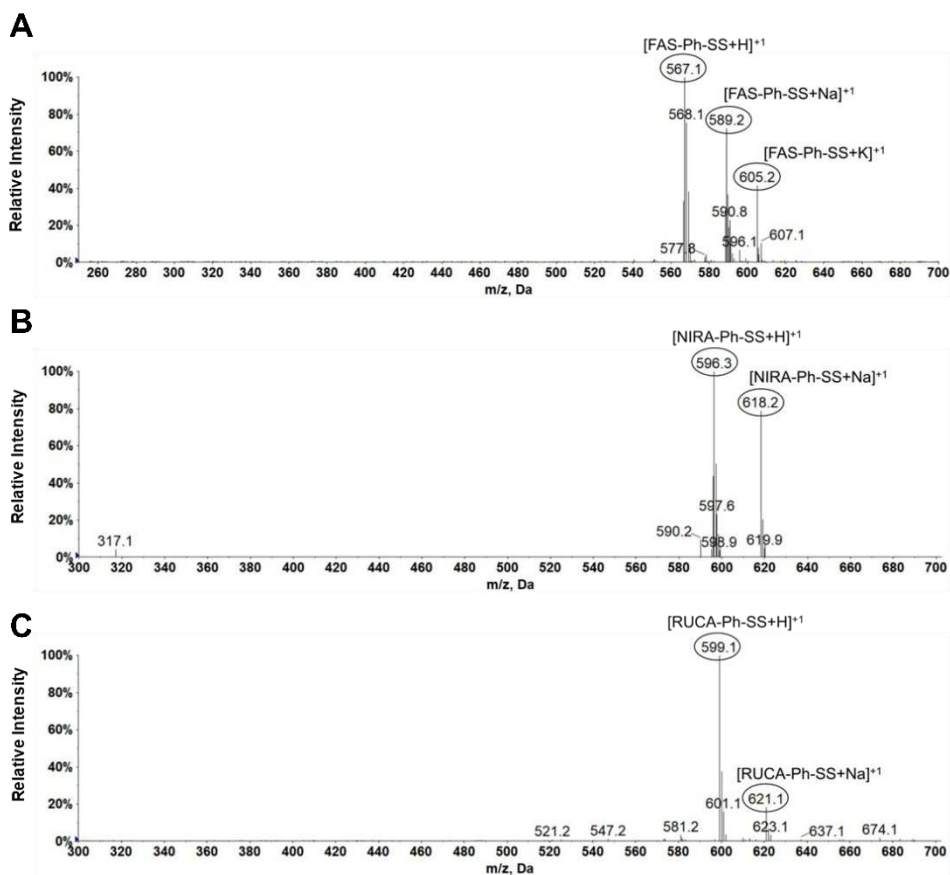


Figure 5.5. Q1 MS scans showing the identity of (A) fasudil-phenyl-disulfide (FAS-Ph-SS), (B) niraparib-phenyl-disulfide (NIRA-Ph-SS), and (C) rucaparib-phenyl-disulfide (RUCA-Ph-SS)

Encouragingly, the implementation of Ph-SS enabled a significantly higher release of NIRA (76.7%, $p = 0.00029$, Figure 5.6.A), FAS (82.3%, $p = 5.53E-06$, Figure 5.6.B), and RUCA (86.7%, $p = 7.064E-06$, Figure 5.6.C,) from their corresponding Drug-Ph-SS when compared to release from Et-SS drug linkers (39.7%, 42.8%, and 24.08%, respectively) in the presence of a highly reductive environment (5 mM DTT). The Ph-SS linker has yet to be implemented to a high degree for drug conjugation, as studies suggested low stability and specificity for intracellular drug release.⁴²² Of note, the negligible drug release data (<0.41%, <0.52%, <0.45% corresponding to the LOQ of the LC-MS/MS method for FAS, NIRA, and RUCA, respectively) of synthesized Drug-Ph-SS products under 10 μ M DTT (mimicking low reductive environment) indicates their extracellular stability, and that Ph-SS may represent a stable option for drugs with a secondary amino group.

We next confirmed one-step drug release from Drug-Ph-SS when we failed to detect the presence of any intermediates in the chromatograms obtained from drug release studies in the presence of 5 mM DTT (Figure 5.7). Additionally, we observed only the peak associated with the free drug (FAS, NIRA, and RUCA) at the last time point in the drug release studies (144 h), suggesting the complete degradation of each Drug-Ph-SS.

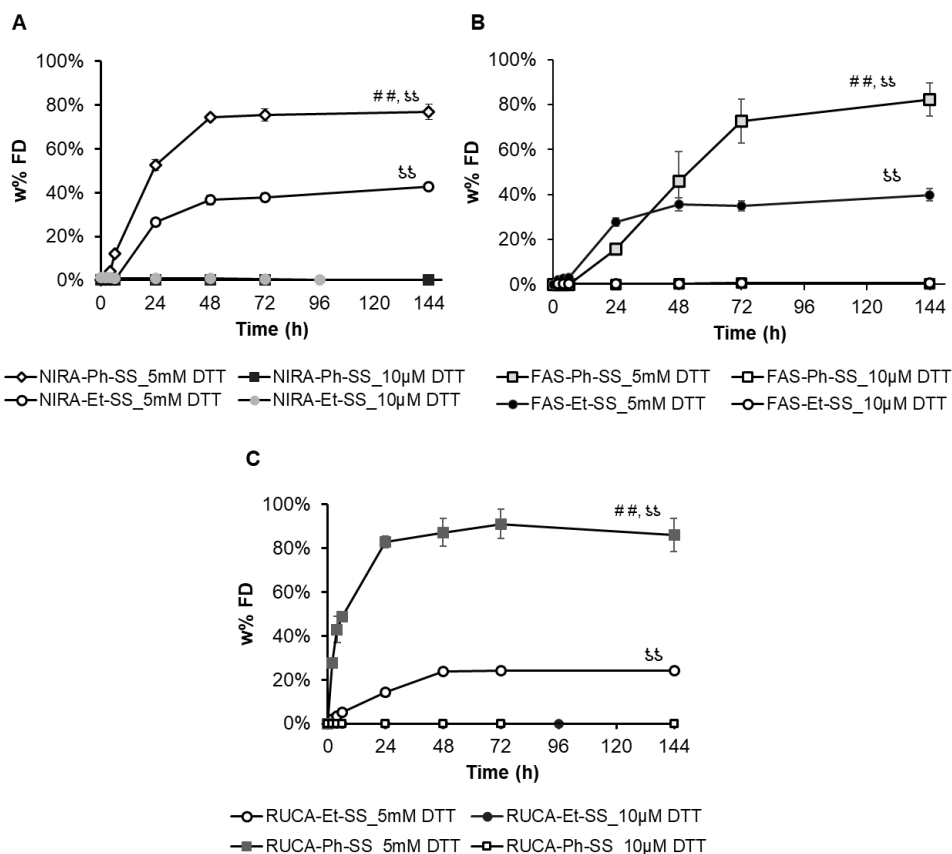


Figure 5.6. DTT-mediated drug release from Drug-Et-SS compared to Drug-Ph-SS.

Evaluation of drug release over 0-144 h in the presence of 5 mM DTT (highly reductive environment) or 10 μ M DTT (mimicking extracellular reductive conditions) from (A) niraparib-ethyl-disulfide (NIRA-Et-SS) and niraparib-phenyl-disulfide (NIRA-Ph-SS), (B) fasudil-ethyl-disulfide (FAS-Et-SS) and fasudil-phenyl-disulfide (FAS-Ph-SS), and (C) rucaparib-ethyl-disulfide (RUCA-Et-SS) and rucaparib-phenyl-disulfide (RUCA-Ph-SS). Data presented as the cumulative weight percentage of free drug (w% FD) compared to the total drug amount in the drug-linker \pm SD (n = 3). ##p<0.005 indicates statistically significant differences between drug release of each Drug-Ph-SS compared to their corresponding Drug-Et-SS. ‡‡ p<0.005 indicates statistically significant differences between drug release at 5 mM DTT and 10 μ M DTT.

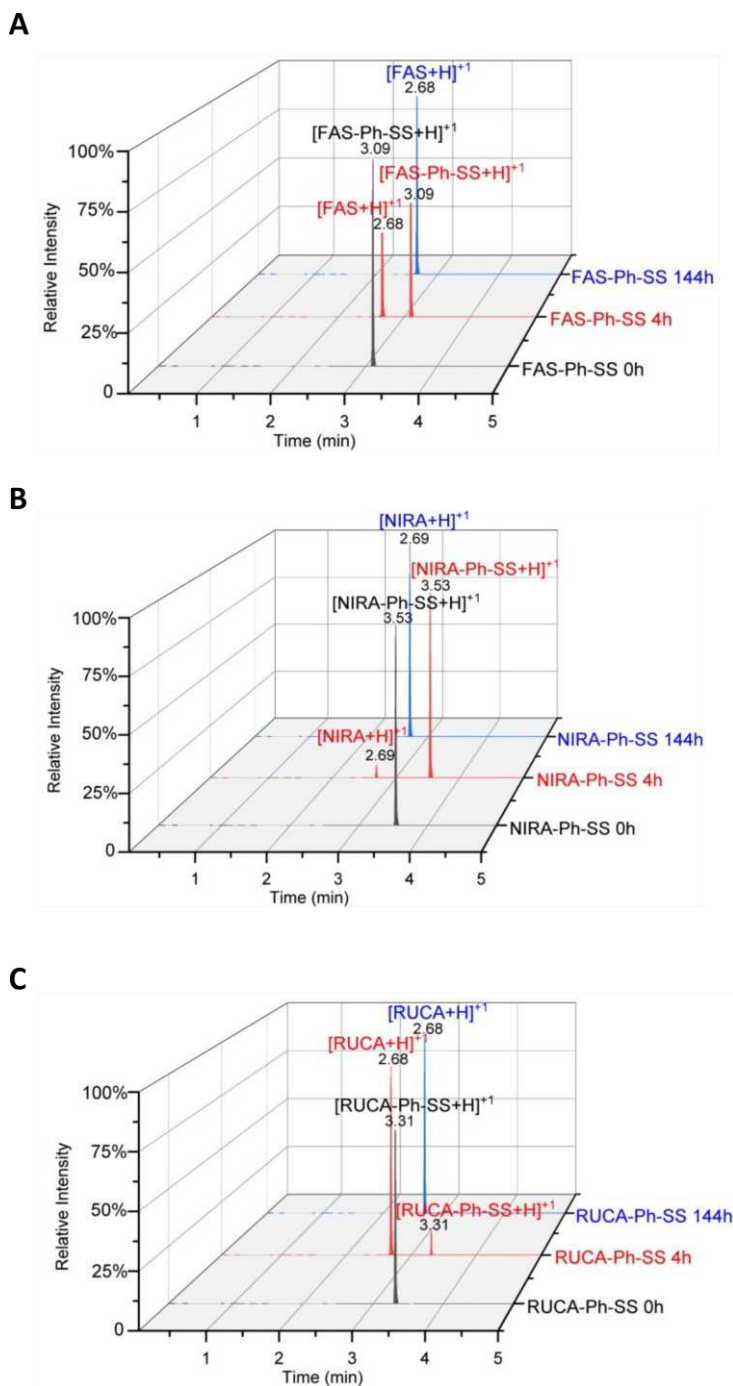


Figure 5.7. LC-MS/MS chromatogram at 0h, 4h, and 144h after the addition of 5 mM DTT to (A) FAS-Ph-SS, (B) NIRA-Ph-SS, and (C) RUCA-Ph-SS.

Overall, we provide evidence that implementing the Ph-SS linker offers significantly higher drug release than the Et-SS under a reductive environment and thereby represents a robust option for the attachment of drugs with secondary amino groups displaying low electronegativity. In this case, drug release did not significantly depend on drug structural features since the drug release relied on the thioquinone methide cascade and not cyclization (as in the case of Et-SS).^{422–424} Given this success, we then moved to the next level of complexity, which entails Drug-Et/Ph-SS conjugation to a polypeptide carrier, to explore whether we can quickly transfer the identified behavior at a small molecular weight scale to the rational design of PDCs.

5.2.4 Synthesis and Characterization of Polypeptide-based Fasudil Conjugates with Optimized Linkers

Studies of polymer-drug conjugates have underscored the importance of linking moieties to the tightly controlled release of drugs at the desired site of action.¹⁶⁵ Here, we chose FAS as a representative of drugs bearing a low electronegative -NR₂ group and a polyglutamate (PGA)-based polymer as a carrier, which displays biocompatibility, biodegradability, and multivalency and allows high drug loading.³⁴ We conjugated FAS to PGA using both Et-SS and Ph-SS and used the resultant PDCs - PGA-SS-Et-FAS and PGA-SS-Ph-FAS - as model PDCs to study drug release and efficacy in treating triple-negative breast cancer (TNBC) using *in vitro* models (Figure 5.8A).

We obtained PGA-SS-Et-FAS and PGA-SS-Ph-FAS with high purity and high yield (79.5 – 83.7%). UV/Vis analysis allowed the determination of total drug loading (TDL) in a range of 11.6±0.04 w% for PGA-SS-Et-FAS and 7.2±0.02 w% for PGA-SS-Ph-FAS (representing high loading of PGA); meanwhile, LC-MS/MS analysis

established a free drug content of below 0.02 w% (compared to TDL) for both conjugates, which lies under the generally accepted limits for designed PDCs (below 2 w% of TDL).^{58,425}

Dynamic light scattering (DLS) analysis demonstrated a hydrodynamic radius \approx of 5 nm in 10 mM phosphate buffer (PB) for PGA-SS-Et-FAS, which agrees well with the presence of unimeric PDC entities (Figure 5.8C). Meanwhile, the addition of the phenyl group as a hydrophobic spacer in PGA-SS-Ph-FAS led to the formation of micelles with a hydrodynamic radius of 99.2 nm (as determined by DLS – Figure 5.8D) and a radius of gyration of 63.7 nm (determined by asymmetric flow field flow fractionation – UV/Vis – multi-angle light scattering [AF4-UV/Vis-MALS] – Figure 5.8E). We then performed a DLS analysis of PGA-SS-Et-FAS and PGA-SS-Ph-FAS at the highest and lowest active dose concentrations (200 μ M and 80 μ M FAS eq.) used in *in vitro* toxicity evaluations. The sizes remained unchanged for PGA-SS-Et-FAS (5.7 ± 1.2 nm) and PGA-SS-Ph-FAS (99.2 ± 3.6 nm), ensuring the presence of unimers or micelles, respectively, for subsequent studies. Moreover, initial critical micellar concentration (CMC) studies of PGA-SS-Et-FAS and PGA-SS-Ph-FAS in Dulbecco's phosphate-buffered saline (dPBS, pH 7.4) confirmed the formation of particles by PGA-SS-Ph-FAS at a concentration >80 μ M FAS eq., but not for PGA-SS-Et-FAS and the stability of PGA-SS-Ph-FAS micelles after 24 h at 4°C (Figure 5.8F). Overall, the addition of phenyl spacer increases the hydrophobicity of the FAS-Ph-SS linker (logP 4.17, calculated in ChemDraw) compared to the FAS-Et-SS linker (logP 2.73, calculated in ChemDraw), leading to the formation of stable micelles with higher hydrodynamic radius triggered by π - π stacking at concentration >80 μ M FAS eq.

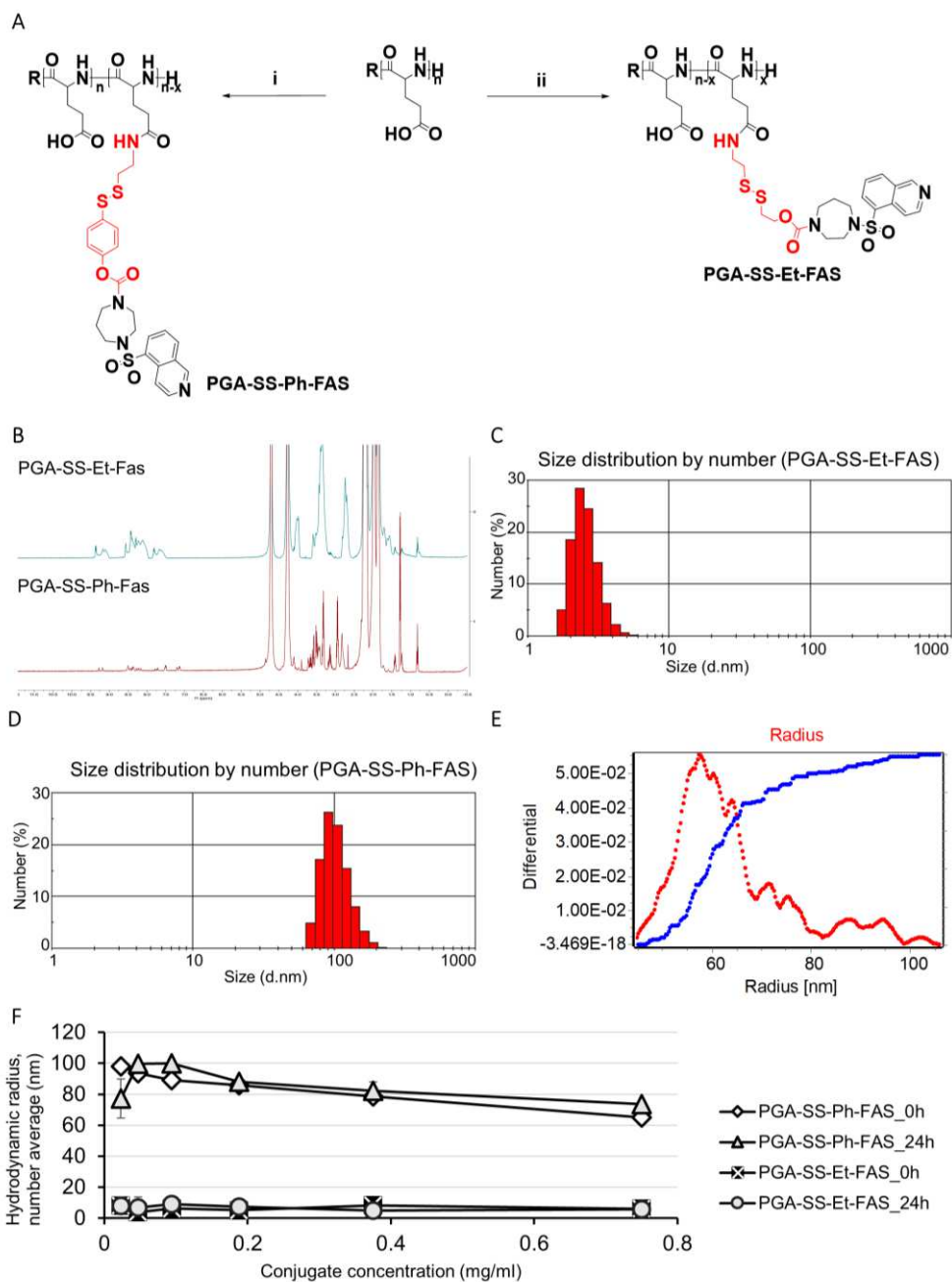


Figure 5.8. Synthesis and Characterization of PGA-SS-Et-FAS and PGA-SS-Ph-FAS. (A) Synthetic route for preparing PGA-SS-Et-FAS and PGA-SS-Ph-FAS (B) Chemical identity and purity of PGA-SS-Et-FAS and PGA-SS-Ph-FAS assessed via $^1\text{H-NMR}$ spectroscopy. (C) DLS

hydrodynamic radius determination of PGA-SS-Et-FAS, (D) DLS hydrodynamic radius determination of PGA-SS-Ph-FAS, (E) Asymmetric flow field flow fractionation – UV/Vis – multi-angle light scattering determination of the PGA-SS-Ph-FAS radius of gyration. (F) Size stability studies of PGA-SS-Et-FAS and PGA-SS-Ph-FAS in dPBS.

5.2.5 *In vitro* Anti-Cancer Activity of PDCs Depends on Variables Other Than Drug Release

Previous studies have reported significantly higher levels of the Rho-associated protein kinases (ROCK1 and ROCK2) in TNBC; therefore, these aggressive cancer cells may display a higher sensitivity to ROCK inhibitors such as fasudil.⁴²⁶ Thus, to understand the biological implications of different linking chemistries, we evaluated the toxicity of PGA-SS-Et-FAS and PGA-SS-Ph-FAS using the MDA-MB-231 TNBC cell line cultured as a traditional two-dimensional (2D) cell monolayer. Moreover, we also evaluated PGA-SS-Et-FAS and PGA-SS-Ph-FAS in advanced three-dimensional (3D) culture models (mammospheres), which have gained attention for their ability to better mimic *vivo* tumor features. We expect different cellular trafficking in the 3D models, with diffusion rates throughout these models (influenced by nanoconstruct size, shape, and even deformability) representing another potential parameter for consideration concerning our rational design of PDCs.⁴²⁷

We performed cell viability studies by MTS assay 72 h post-treatment with PGA-SS-Et-FAS and PGA-SS-Ph-FAS. Compared with free FAS, PGA-SS-Et-FAS and PGA-SS-Ph-FAS displayed significantly greater cytotoxicity at concentrations lower than 150 μ M FAS eq in the 2D model (Figure 5.9A). On the contrary, we failed to observe the increased toxicity of PGA-SS-Et-FAS and PGA-SS-Ph-FAS compared to free FAS in the 3D model (Figure 5.9B). As expected, comparisons using 200 μ M FAS

eq. between 2D and 3D TNBC models for PGA-SS-Et-FAS and PGA-SS-Ph-FAS ($p = 0.0013$ and $1.56E-6$, respectively) indicated that both conjugates exhibited more significant toxicity under 2D compared to 3D growth conditions (Figure 5.9C). To ensure that the cytotoxicity levels observed from PGA-SS-Et-FAS and PGA-SS-Ph-FAS arise from the FAS and not the PGA carrier, we introduced linear PGA as a control (PGA); as expected, we failed to observe any significant toxicity associated with control PGA.

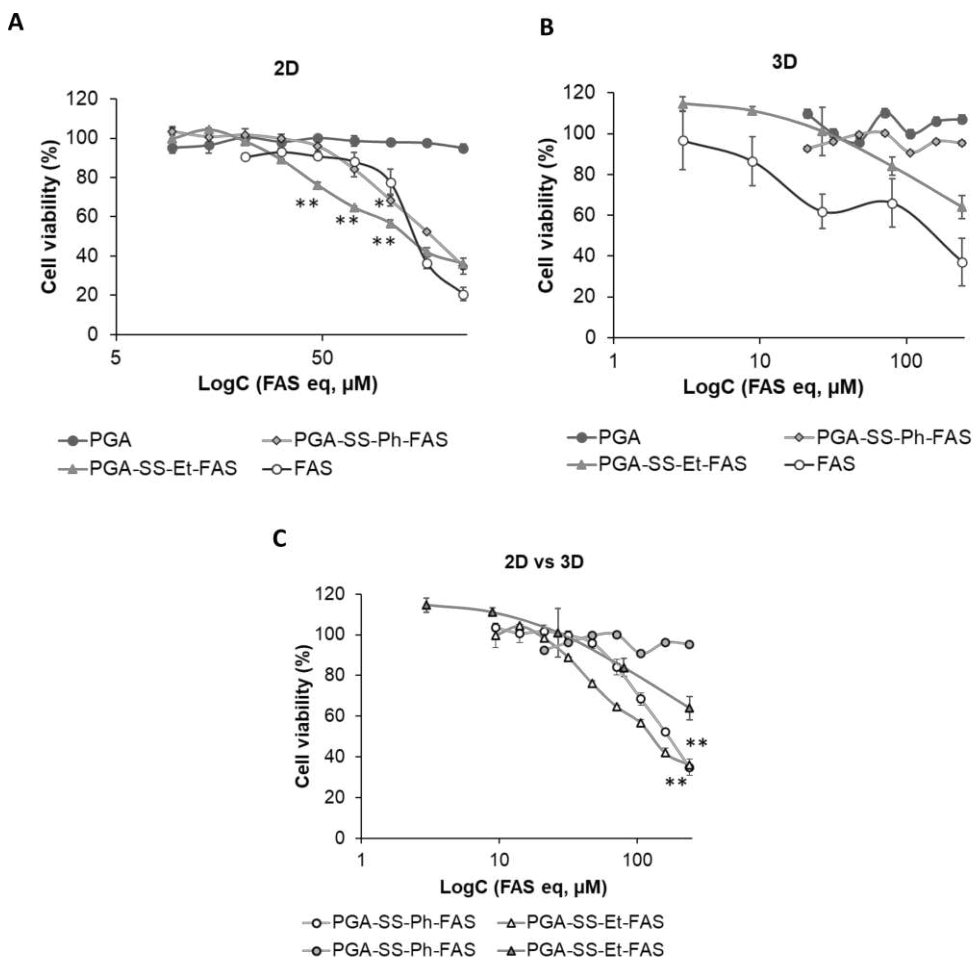


Figure 5.9. PGA-fasudil conjugates toxicity profiles in MBA-MB 231 TNBC cells cultured as (A) 2D monolayers and (B) 3D spheroids. $*p < 0.05$ and $**p < 0.005$ indicate significant differences between the toxicity of PGA-SS-Et-FAS and PGA-SS-Ph-FAS and free FAS;

$p < 0.005$ indicates a significant difference in the cytotoxicity of PGA-FAS conjugates between 2D and 3D models. Experiment performed by Esther Masia

Two reasons may lie behind the differential cytotoxicity of PGA-SS-Et-FAS and PGA-SS-Ph-FAS in 2D and 3D models. First, the more significant internalization of PGA-SS-Et-FAS and PGA-SS-Ph-FAS in the 2D monolayer than in 3D mammospheres, and second, a significant difference in drug release caused by distinct intracellular GSH levels. To be able to evaluate these two hypotheses we needed to quantify FAS released from PDCs in in vitro models for which we first optimized the sample preparation process (See Figure S5.5 and Sections 3.5.5 and 3.5.9 for more details).

To explore the first hypothesis (differences in internalization rate), we determined the level of internalized PGA-SS-Et-FAS and PGA-SS-Ph-FAS in 2D vs. 3D models by quantifying the levels of total FAS in cells and cell medium 72 h post-treatment (total FAS = free FAS + conjugated FAS, quantified after sample incubation with 50 mM DTT to ensure complete FAS release). We obtained significantly higher levels of total FAS internalized in the 2D model treated with PGA-SS-Et-FAS (53%, 69%, and 61%) compared to the 3D model (34%, 48%, and 33%) at all therapeutic concentrations tested (the lowest - 20 μM , $p = 0.00012$; medium - 80 μM , $p = 0.00057$; and the highest - 200 μM , $p = 0.00026$, respectively) (Figure 5.10A); thereby confirming the internalization variability of PGA-SS-Et-FAS in the two models. Meanwhile, PGA-SS-Ph-FAS internalization remained similar between the two models (Figure 5.10B) but with a significantly higher percentage of internalization at all three concentrations compared to PGA-SS-Et-FAS in 2D (83%, $p = 0.00027$; 93%, $p = 0.0011$; 90%, $p = 0.001$; Figure 5.10C) and in the 3D model (81%, $p = 3.60\text{E-}05$; 89%, $p = 0.00045$; 91%, $p = 1.51\text{E-}05$; Figure 5.10D). We suggest that the larger size and probably the more globular conformation of PGA-

SS-Ph-FAS facilitates the internalization in the *in vitro* models due to better fluidity and diffusion capacity as opposed to the unimolecular form of PGA-SS-Et-FAS.

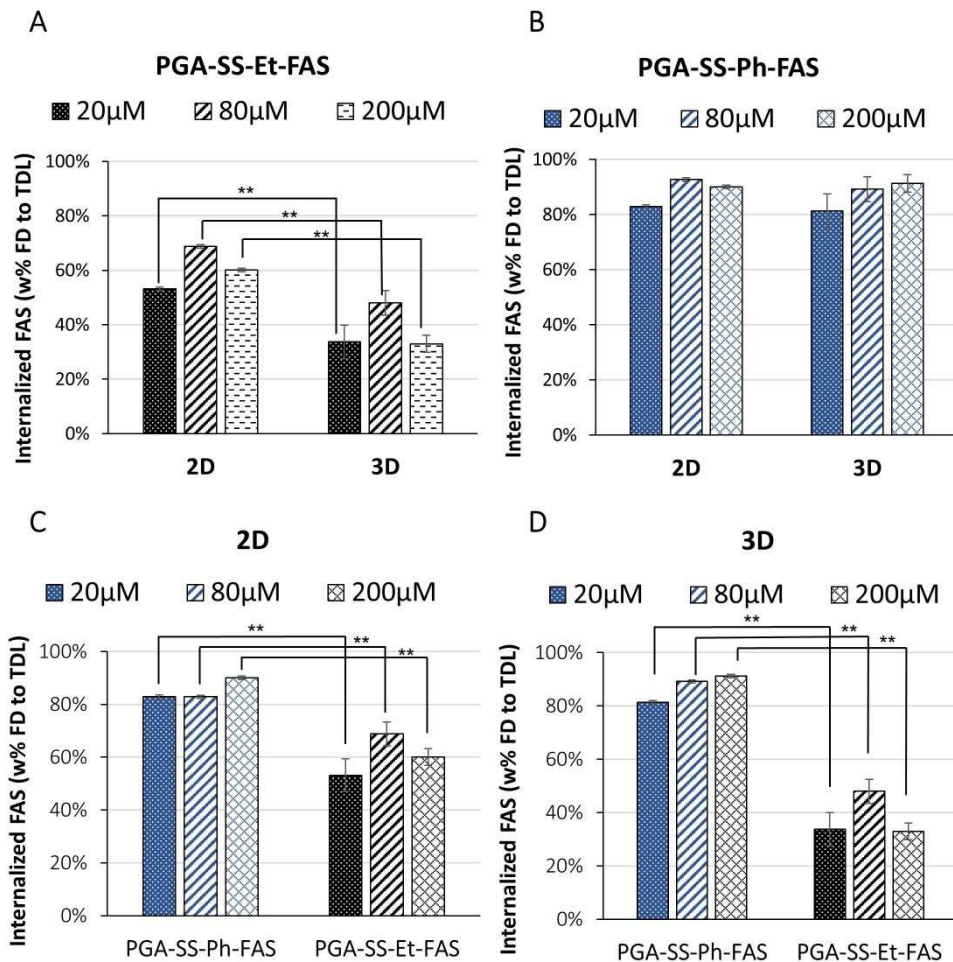


Figure 5.10. Internalization profiles showing significant differences in FAS w% internalized with (A) PGA-SS-Et-FAS between 2D and 3D TNBC *in vitro* models. (B) FAS w% internalized with PGA-SS-Ph-FAS conjugates in 2D and 3D TNBC cell models. FAS w% internalized with PGA-SS-Ph-FAS compared to PGA-SS-Et-FAS in (C) 2D and (D) 3D TNBC cell models. Data presented as average \pm SD (n = 3). ** $p < 0.005$ indicating the significant difference

Next, we sought to explore our second hypothesis for the difference observed in relation to *in vitro* cytotoxicity between models by evaluating drug release efficiency and intracellular GSH levels. Instead of performing drug release studies with DTT, we employed a more realistic scenario and directly quantified FAS released after the exposure of the *in vitro* TNBC models to PGA-SS-Et-FAS and PGA-SS-Ph-FAS for 72 h at three FAS eq concentrations (20, 80, and 200 μ M). We subsequently determined the w% of FAS released in cells and represented it as the percentage of free FAS compared to the total internalized FAS. We found significantly higher levels of FAS released from PGA-SS-Et-FAS (Figure 5.11A) and PGA-SS-Ph-FAS conjugates (Figure 5.11B) in the 2D model compared to the 3D mammospheres correlating with the observed activity (Figure 5.9).

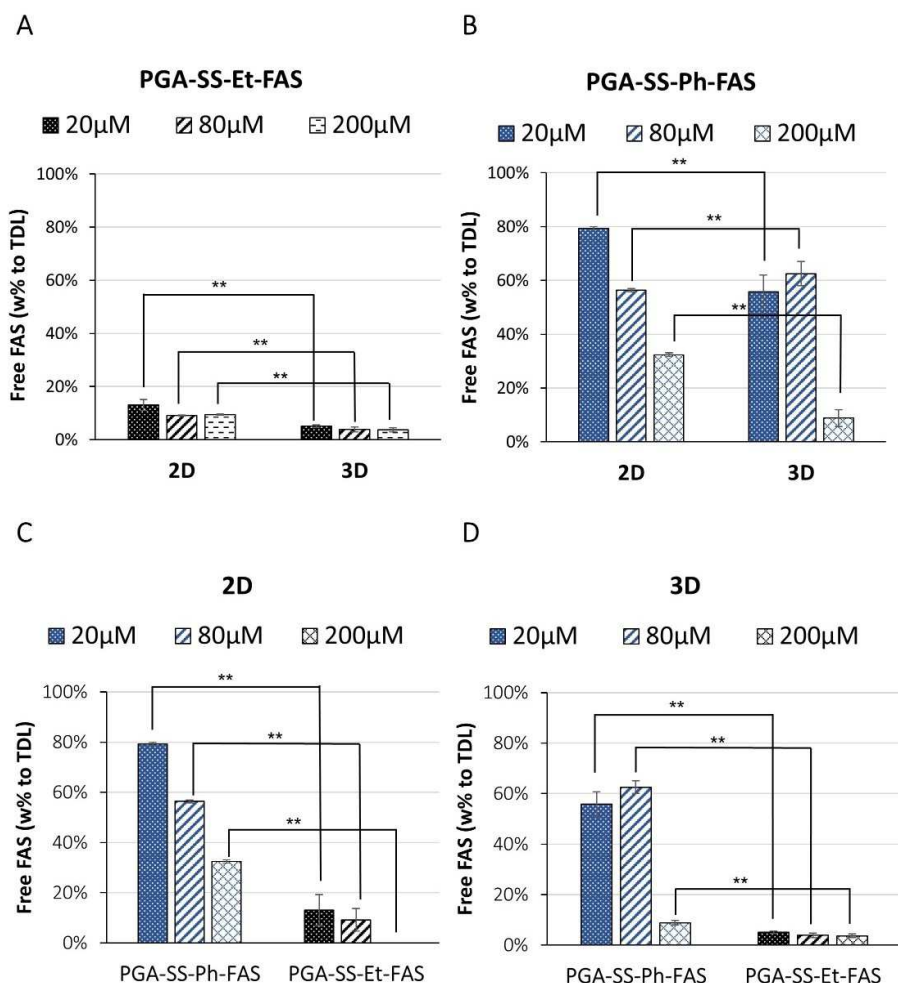


Figure 5.11. Fasudil (FAS) release studies of PGA-FAS conjugates in TNBC 2D and 3D cell models. (A) Free FAS detected in cells released from the internalized PGA-SS-Et-FAS **(B)** Free FAS detected in cells released from the internalized PGA-SS-Ph-FAS. Free FAS w% released from the internalized PGA-SS-Ph-FAS compared to PGA-SS-Et-FAS in **(C)** 2D and **(D)** 3D TNBC cell models. Data presented as average \pm SD (n = 3). ****** $p < 0.005$ indicating the significant difference

The *in vitro* drug release study and the cell viability data obtained from PGA-SS-Et-FAS and PGA-SS-Ph-FAS in the 2D and 3D TNBC models also correlated

with GSH and GSH/GSSG levels: the significantly higher values present in the 2D model (25.89 ± 0.39 mM GSH, and 16.76 ± 1.99 GSH/GSSG) compared to 3D model (13.40 ± 0.59 mM GSH, and 3.45 ± 0.22 GSH/GSSG) indicate a higher reducing environment, which prompts more significant FAS release and cytotoxicity ($p = 0.001$ for GSH and $p=0.0003$ for GSH/GSSG). The decreased levels of GSH/GSSG in 3D cell models indicate more significant levels of oxidative stress, possibly due to the hypoxia in the center of relatively large, compact 3D mammospheres (see Fig 4.1 in Chapter IV).

Finally, we confirmed that PGA-SS-Ph-FAS provided significantly higher FAS release intracellularly at all concentrations and in both 2D (Figure 5.11C) and 3D models (Figure 5.11D) compared to PGA-SS-Et-FAS via drug release studies using *in vitro* models. Thus, we provided the evidence that SS-Ph linker act as a good substitute for SS-Et linker in the design of PDCs with higher release of drugs bearing low electronegative amine group. Interestingly, from the drug release data in both models, we observed the lowering trend of FAS release in cells with increased treatment doses, indicating a limitation on the reductive capacity for -SS- bond cleavage inside cells due to a possible conformational impediment to the S-S moiety upon increase concentration and subsequent conjugate lysosomal accumulation (Figure 5.11). This concentration dependent release is mostly observed in the 2D and 3D model for PGA-SS-Ph-FAS and only in 2D model for PGA-SS-Et-FAS, since the release of FAS is sufficient enough for the differences between different concentrations to be detected.

The low amount of free FAS quantified in the cell medium (<10%) after 72 h PGA-SS-Et-FAS and PGA-SS-Ph-FAS in both *in vitro* models suggests the predominantly intracellular release of FAS (Figure 5.12); however, we cannot conclude from our study if the quantified amount of FAS in the cell medium derives from the extracellular release of FAS from PGA-SS-Et-FAS and PGA-SS-Ph-FAS or the efflux of intracellular FAS).

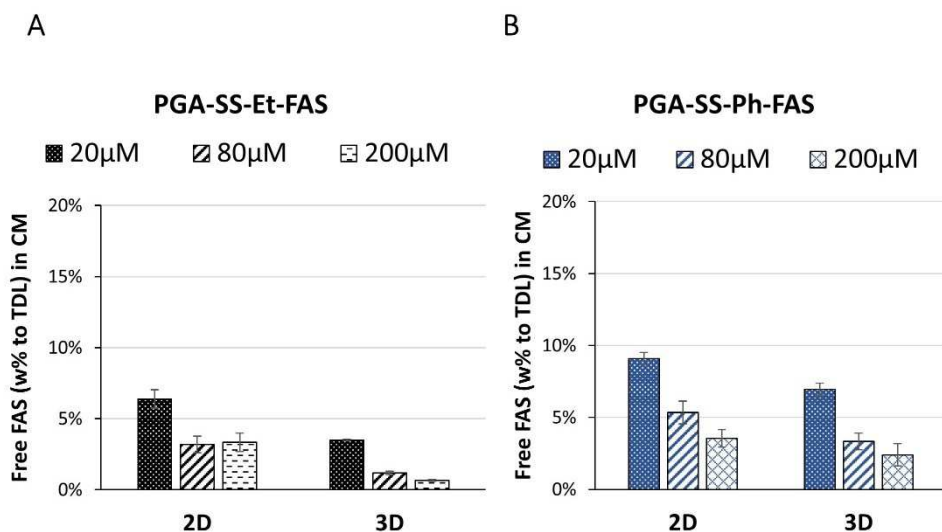


Figure 5.12. Free fasudil (FAS) detected in cell medium (CM) of 2D and 3D *in vitro* cell models 72 h after the treatment with (A) PGA-SS-Et-FAS and (B) PGA-SS-Ph-FAS. Data presented as average \pm SD (n = 3).

Overall, the more globular PGA-SS-Ph-FAS micelles may contribute to better internalization in 2D and 3D models than the unimeric conformation of PGA-SS-Et-FAS; however, higher internalization and higher release do not lead to higher cytotoxicity. A possible explanation may lie in the presence of the active FAS-Et-S \cdot metabolite released from PGA-SS-Et-FAS observed in the *in vitro* as well as in our DTT release studies (Figure 5.13), which may result in additional total cytotoxicity of PGA-SS-Et-FAS conjugate. Given the infeasibility of FAS-Et-S \cdot synthesis, we did not evaluate the activity of the metabolite in TNBC models; however, we suggest the use of molecular dynamics and modeling to elucidate if the metabolite binds to the ROCK enzyme.

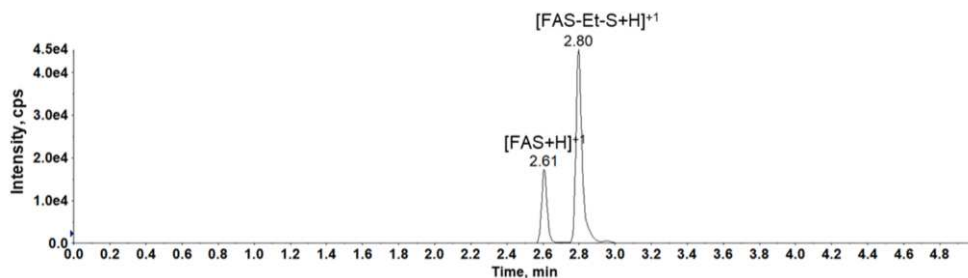


Figure 5.13. LC-MS/MS chromatogram showing the presence of FAS-Et-SH metabolite during *in vitro* drug release studies 72 h after the treatment with PGA-SS-Et-FAS.

Furthermore, the *in vitro* drug release data from PGA-SS-Et-FAS (13.1% FAS released after 72h in 2D and 5.1% in 3D) and PGA-SS-Ph-FAS (55.8% FAS w% released after 72h in 2D and 79.3% in 3D) do not correlate with the DTT-mediated drug release (39.7% FAS released after 72h from FAS-Et-SS, and 82.3% from FAS-Ph-SS), indicating that the carrier adds another level of complexity that influences drug release and the final cytotoxicity profiles in cells. To explore these claims, we performed cell viability studies without PGA by treating 2D cultures of TNBC cells with FAS-Ph-SS and FAS-Et-SS (Figure 5.14). After 72 h, MTS assays revealed the significantly higher cytotoxic activity of the FAS-Ph-SS drug-linker compared to FAS-Et-SS (58% vs. 39%, respectively, $p = 0.00012$) at lower FAS equivalent concentration (Figure 5.14), which agrees well with the DTT drug release studies (82% FAS released from FAS-Ph-SS and 40% FAS released from FAS-Et-SS, Figure 5.2). Moreover, FAS-Et-SS and FAS-Ph-SS linkers exhibited higher cytotoxicity than free FAS and PGA-SS-Et-FAS and PGA-SS-Ph-FAS in the 2D culture of the TNBC model in the 9-107 μM concentration range (FAS eq.).

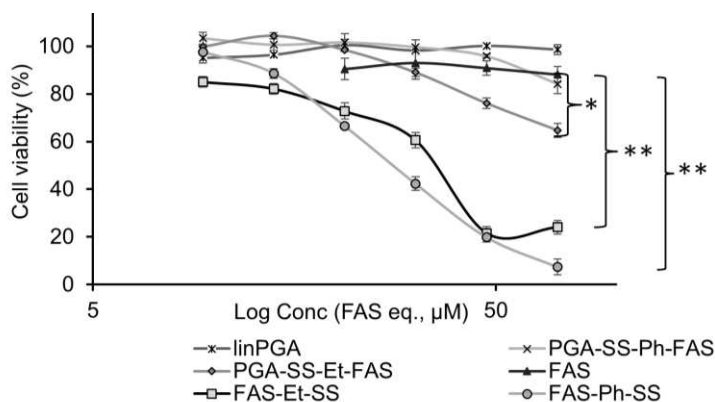


Figure 5.14. Toxicity profiles in the 2D cultures of MBA-MB 231 2D TNBC cells. Data presented as average \pm SD (n = 3). * p <0.05, ** p <0.005. Experiment performed by Esther Masia

The discrepancy between the release and toxicity of PGA-SS-Et-FAS and PGA-SS-Ph-FAS in 2d cultures of TNBC cells suggests that activity depends on more than just release. Other than GSH and GSH/GSSG levels, the presence of other reductive species, such as TRX, GRX, NADPH, NADH, and ROS, may also significantly influence drug release from redox-responsive linkers, especially in the case of Ph-SS linker.^{428–431}

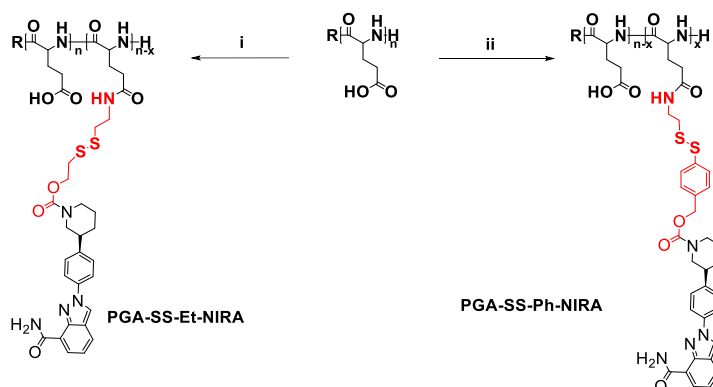
Our data indicates the complexity of designing PDCs with disulfide linkers. Primarily, we conclude that simple DTT drug release studies remain insufficient to elucidate the *in vitro* fate of PDCs and that we require more detailed drug release studies when analyzing *in vitro* models to secure a better *in vitro-in vivo* correlation. Furthermore, by ensuring an appropriate LC-MS/MS method in drug release studies, we can detect and characterize metabolites that add valuable information for cytotoxicity data analysis. Finally, we must consider that PDC conformation, size, intracellular reductive environment, and drug release site and rate within cells all influence the activity of PDCs.

5.2.6 Biological Environment and Carrier Architecture as Essential Factors Influencing the Design of Polypeptide-based Drug Conjugates

The evaluation of PDC activity requires different model systems, ranging from analysis in traditional 2D cell cultures, advanced 3D cell models, patient-derived cell models, and cell cocultures to *in vivo* testing in small and large animal models.³⁷⁴ We evaluated the cytotoxicity profiles of PGA-SS-Et-FAS and PGA-SS-Ph-FAS in 2D and 3D TNBC cell culture models and demonstrated how different levels of GSH influence drug release and, consequently, PDC activity. We next sought to study carrier architecture to understand the influence of another critical parameter in our rational design.

We compared star-shaped PGA (StPGA) and linear-PGA (LinPGA) *in vitro* using 2D cell culture models of TNBC and prostate cancer. In this case, we chose niraparib as a model drug bearing a secondary amino group due to optimal activity as an inhibitor of the enzyme poly ADP ribose polymerase (iPARP) in breast and prostate cancer cells (MBA-MB-231 and PC3 prostate cancer cell lines) compared to fasudil and rucaparib. For this purpose, we conjugated NIRA through Et-SS and Ph-SS linkers (StPGA-SS-Et-NIRA, LinPGA-SS-Et-NIRA, StPGA-SS-Ph-NIRA, and LinPGA-SS-Ph-NIRA, Scheme 5.3) as models to study PGA architecture-dependent drug release and efficacy. We also generated LinPGA-SS-Et-NIRA and StPGA-SS-Et-NIRA at low (α) and high (β) drug loading.

We obtained the desired PDCs with high purity (as shown by the determination of free drug content, Table 5.3.) and yield (70–86%). UV/Vis analysis allowed the determination of TDL, while DLS analysis demonstrated a hydrodynamic radius \approx of 5 nm in 10 mM PB, consistent with unimeric polymer-drug conjugate entities (Table 5.1).



Scheme 5.3. Synthetic scheme of PGA-NIRA design by conjugating niraparib (NIRA) to a polyglutamic acid as a carrier (PGA) through i) ethyl-disulfide (Et-SS) and ii) phenyl-disulfide (Ph-SS) linker. For more detailed reaction conditions, see Section 3.5.3

Table 5.1. Physico-chemical characterization of PDCs determined by UV-Vis* and LC-MS/MS**

Conjugate	TDL (w%)*	FD (w% to TDL)**
StPGA-SS-Et-NIRA_a	0.54 ± 0.11%	< 0.042% (LOQ)
StPGA-SS-Et-NIRA_b	5.35 ± 0.52%	< 0.066% (LOQ)
LinPGA-SS-Et-NIRA_a	0.39 ± 0.32%	< 0.04% (LOQ)
LinPGA-SS-Et-NIRA_b	5.14 ± 0.46%	< 0.004% (LOQ)
StPGA-SS-Ph-NIRA	5.06 ± 0.82%	< 0.004% (LOQ)
LinPGA-SS-Ph-NIRA	1.17 ± 0.14%	< 0.02% (LOQ)

TDL- total drug loading expressed as average value ± SD and n = 3, FD- free drug

Cell viability studies demonstrated the low activity of all niraparib-containing PDCs connected through an SS-Et linker on PC3 prostate cancer cell lines cultured as a 2D monolayer, irrelevant of the TDL or PGA architecture (Figure 5.15A). This result may derive from low niraparib release rates under a redox environment (5 mM DTT, Figure 5.15B). Based on our previous results from drug release kinetics, we synthesized new PDCs implementing the SS-Ph linker (Scheme

5.3), a disulfide moiety cleavable by a redox environment that ensures higher NIRA release compared to the SS-Et linker. We observed significantly greater activity of LinPGA-SS-Ph-NIRA conjugate in the PC3 cell line as opposed to the StPGA and SS-Et counterparts ($p = 1.23E-5$, $p = 2.45E-4$, respectively) and with similar activity to free NIRA (Figure 5.15A). The levels of free NIRA released after 72 h incubation with 5 mM DTT (36.88 w% free NIRA, black squares, Figure 5.15C) and negligible free NIRA released in 10 μ M DTT (grey circles, Figure 5.15C) confirm NIRA release from the SS-Ph linker support the activity results of LinPGA-SS-Ph-NIRA in the PC3 cell model while ensuring the stability extracellularly.

To elucidate the low cytotoxic activity of StPGA-SS-Ph-NIRA in 2D monolayer of PC3 cell line as opposed to its linear counterpart, we performed MTS 72h assay to study the cytotoxic activity of StPGA-SS-Ph-NIRA in 2D monolayer of MDA-MB-231 cells. We observed StPGA-SS-Ph-NIRA cytotoxicity in 2D cultures of MDA-MB-231 cells (Figure 5.15D, grey squares) which we correlated to the higher reductive environment compared to 2D PC3 cell model. The GSH levels of 2D TNBC (25.89 ± 2.39 mM in a single cell) and 2D PC3 cell models (15.57 ± 0.39 mM in a single cell) indicate that the redox environment of the PC3 cell model remains insufficient to support significant niraparib release from StPGA-SS-Ph-NIRA conjugate (5 and 15 w% NIRA detected in PC3 and MDA-MB-231 cell model, respectively, 72 h post-treatment). Moreover, the StPGA carrier conformation may hinder linker accessibility to GSH-mediated cleavage, requiring an extremely high reductive environment for optimal niraparib release and activity. Further conformational and size stability studies with small-angle x-ray scattering, DLS, circular dichroism, and asymmetric flow field flow fractionation are currently being performed to confirm this finding.

Overall, our findings confirm that the implementation of SS-SIL linkers for drug conjugation to its carrier depends greatly on the type of the cancer cell models due to the different levels of GSH and GSH/GSSG.

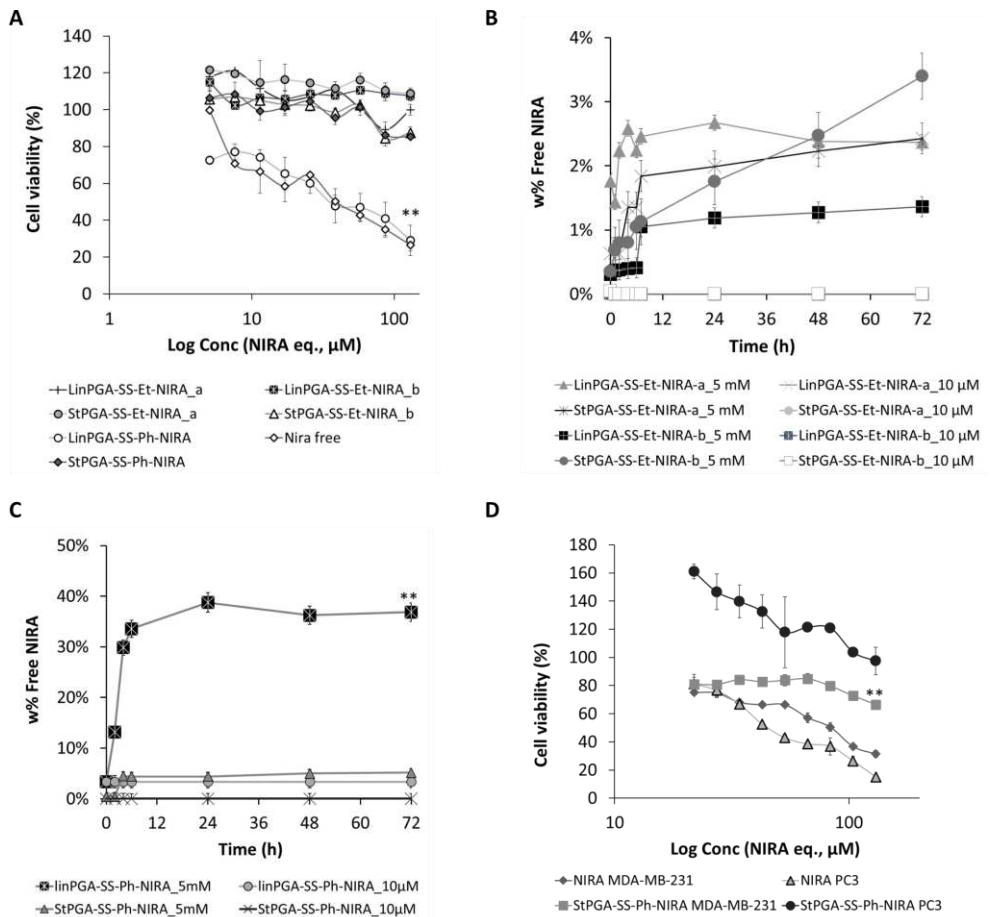


Figure 5.15. PGA-NIRA PDC in vitro toxicity profiles and drug release kinetics under 5 mM DTT and 10 μM DTT. (A) PGA-NIRA PDC toxicity in 2D monolayer of PC3 cells (MTS 72 h data as mean \pm SD (n = 3); **p<0.005). Niraparib release kinetics from **(B)** PGA-SS-Et-NIRA and **(C)** PGA-SS-Ph-NIRA conjugates. Data represented as average value \pm SD and n = 3; **p<0.005. **(D)** StPGA-SS-Ph-NIRA cell viability profiles in 2D Cultures of PC3 and MBA-MB-231 cells (MTS 72 h data as mean \pm SD (n = 3), **p<0.005). In vitro toxicity studies performed by Antonio Serrano Marti.

Of note, the LinPGA-SS-Ph-NIRA conjugate with optimal release and activity in the PC3 *in vitro* cell model is currently being employed as a selected nanoconjugate within Antoni Serrano Martí's Ph.D. project focused on the development of a novel polypeptide-based combination conjugates for the treatment of advanced prostate cancer, where iPARP and docetaxel single and combination nanoconjugates with and without radiotherapy are being explored as efficient therapeutic strategies. Moreover, this Chapter represents a starting point for developing rationally-designed multifunctional nanomedicines such as nanoconjugates to inhibit pancreatic cancer progression with an immunogenic cell death that would synergize with an anticancer nano-vaccine from harnessing the patient's immune system to prevent tumor recurrence (NanoPanTher La Caixa project LCF/PR/HR19/52160021).

5.3 DISCUSSION

Generally, the use of optimal bioresponsive linking moieties within the rational design of PDCs allows for plasma stability as well as for site-specific, efficient and controlled release kinetics under the selected conditions.²⁷ The differential levels of GSH extra- vs. intracellular as well as in normal vs. pathological sites, makes redox-responsiveness one of the preferred strategies to engineer bioresponsiveness within a PDC.¹²⁸

Redox-responsive SS-SIL linkers represent a powerful strategy for intracellular drug delivery; furthermore, they are considered universal linkers as any drug with an amino or hydroxyl group can undergo modification and connection through SS-SIL to a carrier. Of note, the influence of the drug's structural features and the linker-associated spacer on release kinetics remains unexplored.

Therefore, we evaluated the influence of the drugs/spacer's chemical structures, the type of chemical group available for conjugation on drug release, and the biological effect of the designed PDCs.

A mechanistic study of novel mutual prodrugs containing distinct SS-SIL types suggested that structural features of constituent drugs influenced drug release.⁴¹⁹ Nevertheless, the authors of this study failed to investigate the reason behind this finding, and possible intermediate metabolites remain unidentified. In parallel, a study of doxorubicin prodrugs obtained by conjugation through amino and hydroxyl groups demonstrated site-specific drug release from an Et-SS linker.⁴¹⁸ C-14 hydroxyl modification of doxorubicin provided higher anti-tumor efficacy due to a significantly higher release rate than the amino group modification. However, the additional value of our study lies in demonstrating that this phenomenon significantly affects drugs with $-NR_2$ groups with low electronegativity and an inability to form resonance-stabilized structures. We believe this finding remained unreported until now as most drug-Et-SS linkers reported in the literature contain drugs conjugated through the $-OH$ group or through $-NH_2$ with resonance stabilized structures.^{432–436}

Disulfide linkers can be roughly divided into two sub-groups based on their fragmentation mechanism: disulfide linkers with drug release controlled by intramolecular cyclization (SS-Et) and disulfide linkers with drug release controlled by a thioquinone methide cascade (SS-Ph).⁴³⁷ The fragmentation mechanism and, consequently, drug release from SS-Et represents a two-step process where the reductive agent GSH present in the intracellular milieu of mammalian cells (2-10 mM) initially triggers the reduction of a disulfide bond and generates a free thiol group.^{438,439} The second step is initiated by the nucleophilic attack of a deprotonated thiol to a carbonyl group, leading to drug release and the formation of a cyclic side-product.⁴³⁸ Nucleophilic attack represents a fundamental class of chemical reactions in which a leaving group (in the case of a Drug-Et-SS, the drug)

becomes substituted by an electron-rich compound, the nucleophile (a deprotonated thiol in the case of Drug-Et-SS). Faster, more effective nucleophilic substitution generally occurs with an optimal leaving group. Suitable leaving groups are considered weak bases due to their ability to hold a charge, meaning that greater electronegativity signifies a more optimal leaving group.⁴⁴⁰ Since drugs employed as active agents usually possess basic properties and undergo attachment to Et-SS linkers through the amine group, they act as weak leaving groups leading to slow/low drug release; however, the electronegative hydroxyl group (DIN) and the amine group of the drug attached to the Et-SS linker forms part of a structure that can form a resonance stabilized intermediate (RES), resulting in a species less willing to share electrons, which provides better leaving groups and higher drug release.

We provided a PGA-SS-Ph-FAS conjugate with a significantly higher release intracellularly compared to PGA-SS-Et-FAS due to a different drug release mechanism that supports faster and higher release of drugs bearing low electronegative amine group. Nevertheless, our results highlight the importance of the *in vitro* redox environment, its influence on drug release and detailed characterization of PDCs in biological fluids. Adding a phenyl spacer may change the fate of PDCs during the analysis of *in vitro* models due to micelle formation. The influence of size and shape on the penetration profile of PDCs has been reported before.^{441–444} The general trend observed *in vitro* and *in vivo* studies provides robust evidence that diffusion capacity depends on particle size and shape, which may further influence DDS fate in cells.^{445,446} Thus, we must analyze drug release from the disulfide linker in specific cellular compartments. Subcellular fractionation, a method often implemented for this purpose, may lead to false positive or negative results due to cross-contamination.⁴⁴⁷ Therefore, we must choose analytical methodologies with great care and explore new techniques to improve predictions

regarding the intracellular fate of disulfide-containing PDCs, their location, and the extent of disulfide cleavage.

To note, the analysis of identity, structure, TDL, free drug, drug release, and pharmacokinetics (among other parameters) requires multi-step analytical protocols involving method development, sample preparation and analysis, method validation, and data analysis.²⁷ Method development involves obtaining rapid, sensitive, simple, informative, and environmentally sustainable analytical methods.³²⁵ DoE currently represents the most advisable way to optimize any methodology; encouragingly, we have seen a recent increase in studies implementing DoE to optimize related procedures, especially in LC-MS/MS.⁴⁴⁸ The use of an LC-MS/MS method that supports metabolite identification, as opposed to previous implementations of HPLC-UV/Vis that cannot elucidate the fate of SS-SIL in a reducing environment, represents a cardinal point of our study.⁴¹⁹ Herein, implementing DoE allowed us to develop an accurate, specific, and sensitive LC-MS/MS method for determining low drug concentrations in drug release studies. Moreover, we ensured the separation of drug-linkers, intermediate products formed during drug release studies and free drugs, by obtaining the optimal retention factor for each drug, a prerequisite for drug release result interpretation and metabolite identification. Our DoE developed LC-MS/MS method enabled us the identification of FAS-Et-S· intermediate in the *in vitro* drug release studies, for which we hypothesized that influences the *in vitro* cytotoxicity of PGA-SS-Et-FAS conjugate. These hypothesis agrees with previously published data from Giraldo et al. that also reported the presence of FAS-Et-S· intermediate and correlated the prolonged effect of PGA-SS-Et-FAS in the treatment of spinal cord injury also to the presence of FAS-Et-S· intermediate.³²⁶ The generation of FAS-Et-S· is due to the partial disulfide exchange reaction that results from the low pH in endo-lysosomal organelles and protonation of sulfur in a FAS-Et-S· metabolite intermediate, which inhibits the second step of the drug release mechanism.⁴⁴⁹

Our results highlight the complexity of the *in vitro* redox environment and PGA architecture's influence on drug release from the SS-Ph linker. Adding a phenyl spacer may change the fate of PDCs during the analysis of *in vitro* models due to micelle formation. The influence of size and shape on the penetration profile of PDCs has been reported before. Namely, small DDS (from a few to hundred nanometers) enter the cells via pino- or micropinocytosis, the sizes of 120-200nm are usually internalized via caveolin- or clathrin-mediated endocytosis, while bigger particles (250 nm to 3 μ m) by phagocytosis leading to increase in the clearance rate.⁹⁸ The uptake rate and efficiency of smaller (15-30 nm) and large (70-240 nm) particles remain low, while the optimum uptake occurred for 30-50 nm-sized particles. Moreover, a size of about 50 nm leads to a more efficient interaction of particles with cell receptors leading to internalization through receptor-mediated endocytosis.^{99,100} The general trend observed *in vitro* and *in vivo* studies provides robust evidence that diffusion capacity depends on particle size and shape, which may further influence DDS fate in cells.^{445,446} Thus, we must analyze drug release from the disulfide linker in specific cellular compartments. Subcellular fractionation, a method often implemented for this purpose, may lead to false positive or negative results due to cross-contamination.⁴⁴⁷ Therefore, we must choose analytical methodologies with great care and explore new techniques to improve predictions regarding the intracellular fate of disulfide-containing PDCs, their location, and the extent of disulfide cleavage.

5.4 CONCLUSION

To the best of our knowledge, our study represents first to provide evidence and clarify how the structural features of a drug can influence drug release from an Et-SS linker, oppositely to the previous consideration of Et-SS as a universal linker. Hence, we suggest a new SS-Ph linker that would enhance the release

kinetics of the drug with secondary amino groups possessing low electronegativity after conjugation to a polyglutamate.

We achieved significantly higher FAS release from PGA-Ph-SS-FAS than from PGA-Et-SS-FAS in MBA-MD-231 *in vitro* models; however, higher drug release does not always provide the desired higher cytotoxicity for TNBC treatment. Therefore, we must investigate PDC release behavior in cell medium and intracellularly when designing the PDCs on a case-by-case basis instead of mimicking the reductive environment with 5 mM DTT. In the future, we may even explore more sophisticated real-time drug release monitoring methods to accurately evaluate and predict the treatment outcomes *in vivo*.

Elucidating metabolites in drug release studies with fit-for-purpose analytical protocols and exploring the influence of linkers on PDC conformation will prompt a better understanding of their fate in the biological environment.

A better understanding of PDC internalization represents another crucial aspect in carefully tuning drug release and activity profiles to design efficient and safe drug delivery systems.

Ultimately, understanding how varied biological environments influence DDS stability and activity requires thorough investigation and incorporation to establish adequate design criteria for a candidate suitable for further studies.

5.5 EXPERIMENTAL MATERIAL AND METHODS

5.5.1 Materials

Diisopropylethylamine (DIEA), DL-dithiothreitol (DTT), cysteamine hydrochloride, dimethyl sulfoxide (DMSO) anhydrous, ethyl acetate, and methanol (LC-MS grade) were obtained from Sigma-Aldrich (St. Louis, United States). Celite 545, diethyl ether, dichloromethane (DCM), and deuterated solvents such as deuterated oxide (D₂O) were purchased from VWR chemicals (Radnor, US). Silica 60A 20–45-micron, water (LC-MS grade), ammonium formate, triethylamine (TEA), and formic acid (LC-MS grade) were purchased from Fisher Scientific (Pittsburgh, US). Vivaspin 10 kDa was obtained from Sartorius AG (Göttingen, Germany), and Sand 40-100 mesh was provided by ACROS organics (Geel, Belgium). Acetonitrile (ACN), chloroform, dimethylformamide (DMF), and methanol were purchased from Scharlab (Barcelona, Spain). 4-nitrophenyl-2-(pyridine-2yldisulfanyl) ethyl carbonate and 4-nitrophenyl-4-(pyridine-2yldisulfanyl) benzyl carbonate were purchased from Fluorochem (UK). All the drugs (dinaciclib - DIN, resiquimod - RES, niraparib - NIRA, and rucaparib - RUCA) were purchased from MedKoo Biosciences (Morrisville, US) except for fasudil hydrochloride (FAS) that was obtained from Xingcheng Chempharm Co. Ltd (Zhejiang, China). Poly-L-glutamic acid (PGA) and PGA-SS-Et-FAS were kindly provided by Polymer Therapeutic Solutions SL (Valencia, Spain). Acetonitrile (LC-MS grade) was obtained from AppliChem GmbH. 4-dimethyl aminopyridine (DMAP) was obtained from Honeywell Fluka (Pittsburgh, US). 4-(4,6-Dimethoxy-1,3,5-triazin-2-yl)-4-methyl morpholinium (DMTMM) chloride (DMTMM·BF₄) was synthesized according to literature.³⁶⁶

5.5.2 Synthesis and Characterization of Drug-Linkers

All the drug-linker reactions were performed following the same methodology. Table S5.1 details the differences in reagents, amounts, reaction time, and solvents. Each reaction was performed under anhydrous conditions with nitrogen flow and at a defined temperature. First, the drug and the linker were dissolved separately in appropriate solvents under vigorous stirring. Linker solution was added dropwise to the drug solution, and finally, DMAP and/or TEA were added. The reaction was monitored with thin-layer chromatography (TLC) and a direct MS Q1 scan. Liquid-liquid extraction (LLE) and a silica column were implemented in the purification step. If the obtained product was insoluble in ethyl acetate, LLE was not performed, and the product was repeatedly dried in the rotavapor to remove TEA. The mixture was extracted with ethyl acetate and washed with water (x3) and brine (x3). The organic layer was dried with anhydrous magnesium sulfate. The filtrate was then evaporated under a vacuum and purified by column chromatography in DCM:MeOH. Fractions containing the product were joined, and the solvent was evaporated under a vacuum. The identity of the synthesized product was confirmed with a Q1 MS scan.

5.5.3 Synthesis and Characterization of PGA-drug conjugates

Prior to polymer conjugation, the drug-linker product was conjugated to cysteamine. The drug linker (1 eq., 10 mg/ml) was dissolved in DMSO. Then, cysteamine (1.2 eq., dissolved in DMSO and added dropwise over the drug-linker solution). The reaction was left for 3 h at 80°C, precipitated in fresh diethyl ether (1:10), reprecipitated from MeOH to fresh diethyl ether, and dried with the vacuum pump. The identity of the synthesized product was confirmed with a Q1 MS scan.

The drug-linker-cysteamine was then conjugated with poly-L-glutamic acid (PGA) (n = 100). As a general procedure, PGA was dissolved in anhydrous DMSO at 30 mg/ml with stirring, followed by activating the percentage that we want to modify of the acid groups with DMTMM BF₄ (2 eq. with respect to the drug linker) for 30 min. Drug-linker-cysteamine, dissolved in DMSO, was added to the main solution, and the pH was adjusted to 8 with DIEA. The reaction was monitored by TLC and allowed to react for 48 h at room temperature. The product was precipitated twice from fresh diethyl ether (1:10). The total drug load, in all cases, was determined by UV-vis and the free drug content by LC-MS/MS analysis. Milli Q water was added to the solid to obtain the sodium salt of the conjugate for water solubility. A 0.5 M NaHCO₃ solution was added dropwise with vortexing until the complete dissolution of the solid. Using Milli Q water, the solution was purified by a Vivaspin device (3 kDa cutoff). The upper content was lyophilized, and the product was stored at -20°C until further use.

TDL determination by UV-Vis

Fasudil and niraparib solutions in methanol were used as standard stock solutions, while the working standard solutions were obtained by dilution with Milli-Q water. Conjugate total drug loading (TDL) was determined at three concentration levels (0.1, 0.25, and 0.5 mg/ml, in Milli-Q water) by measuring the absorbance at 323 nm (for fasudil) and 259 nm (for dinaciclib). LinPGA water solution in the same concentration as the conjugates was used as a blank. UV-Vis measurements were performed using JASCO V-630 spectrophotometer at 25°C with a 1.0 cm quartz cell and a spectral bandwidth of 0.5 nm.

FD determination by LC-MS/MS

3 mg of the conjugates was suspended in 500 µl MeOH (LC-MS grade), vortexed for 5 min, centrifuged for 10 min at 11.000 rpm to remove the pellet, and the solution was subjected to LC-MS/MS analysis.

NMR spectroscopy

10 mg/ml sample solutions in deuterated water were analyzed at 27°C on a 300 Ultrashield™ spectrometer (Bruker, USA), and data were processed with the software TopSpin and Mestrenova.

5.5.4 Drug release from Drug-linkers and PGA-drug conjugates with DTT

Drug-linkers (1 mg/ml) were incubated at 37 °C, pH 5 (10 mM ammonium formate buffer LC-MS grade), and in the presence of 5 mM DTT (mimicking the lysosomal compartment). 100 µl samples were isolated at various time points (0, 2, 4, 6, 24, 48, 72, and 144 h) and analyzed with LC-MS/MS. A calibration curve for each drug was used to quantify the total drug release from their drug linker. Drug linkers incubated at 37 °C, 10 µM DTT, and pH 7.4 were used as control samples (mimicking the extracellular fluid).

Release studies for PGA-drug conjugates were performed in 5 mM (test sample) and 10 µM DTT (control sample) using three replicates for each sample group. 3 mg/ml conjugate solution was prepared in FA buffer solution (pH 5.5, LC-MS grade) and appropriate concentration of DTT and incubated at 37°C. At defined time points (0, 2, 4, 6, 24, 48, and 72 h), a 100 µl was aliquoted from the primary solution and suspected to the LC-MS/MS analysis.

5.5.5 Fasudil Release from PGA Conjugates in Cell Medium and MBA-231-TNBC Cells

MDA-MB-231 cell lines were seeded in a 96-well plate at 15625 cells/cm² for 2D and 31250 cells/cm² for the 3D model. After 24 h incubation, the cells were incubated with FAS conjugated to PGA through Et-SS and Ph-SS at 200 µM fasudil

equivalence. The cell and cell medium were separated at 72 h and prepared depending on the implemented *in vitro* cell model. The 2D MDA-MB-231-TNBC cells were collected by trypsinization and neutralization with a fresh cell medium. In contrast, in the case of 3D cell models by centrifugation (10 min, 11.000, 4 °C). Cells were lysed by mixing with 400 µl lysis buffer (50 mM Tris HCl, 150 mM NaCl, 0.25% triton-X 100, 0.5% NP40) at 4°C for 30 min. The free and total FAS (free and conjugated to PGA) were quantified in cell medium and lysate. FAS as a free drug was extracted from the cell medium samples with the protocol optimized in the previous step (SI).

In contrast, the cell lysate was first lyophilized, and FAS was extracted with 100 µl methanol. Total FAS was determined by incubating the cell medium and cell lysate samples with 50 mM DTT for 24 h at 37 °C and then preparing the sample accordingly. Before injection in the LC-MS, 20% of 0.1% FA was added in all samples to adjust the amount of water phase and improve the peak shape.

Acknowledgement to Justine Hillaert and Esther Masia for the help in this process.

5.5.6 Direct mass spectrometry scan

All the samples monitored by mass spectrometry (MS) Q1 scan were analyzed by 20 µl direct injection with ACN 50% and H₂O 50% (0.1% formic acid - FA) as mobile phase, and 0.5 ml/min flow rate, while the MS conditions were as follows: curtain gas 20 V, ion source temperature 250 °C, gas 1 45 V, gas 2 45 V, ion source voltage 5500 V, declustering potential 62 v, entrance potential 2 V.

5.5.7 LC-MS/MS for determination of FAS, DIN, NIRA, RUCA, and RES

LC-MS/MS method development was performed by DoE with DesignExpert12 software (see Chapter II). The LC-MS/MS analysis was performed using an ExionLC system comprising a Pump, AC autosampler, AC Column oven, and AB Sciex QTRAP 4500 (all Sciex, Singapore). Eluent A was H₂O with FA 0.1%, and eluent B was ACN. All runs were performed using a Kinetex Biphenyl column (100 mm × 3.0 mm, 2.6 μm, 100 Å) from Phenomenex, USA, with a 20 μL injection volume. The drugs were detected in positive electrospray mode with multiple reaction monitoring scans. The validation parameters evaluated were linearity, the limit of quantification (LOQ), the limit of detection (LOD), and accuracy (Table S5.2.). A low LOQ and a medium LOQ control standard solutions were analyzed each day before analyzing the sample to confirm the quality of LC-MS/MS response. Methanol with 0.1% FA was used as a blank control sample.

5.5.8 Asymmetric flow field flow fractionation for size determination

AF4 method was performed on the Postnova Analytics (Landsberg, Germany) fractionation channel equipped with a regenerative cellulose membrane with a 10 kDa cutoff and a 350 μm spacer. Samples were dissolved in 10 mM sodium phosphate at 2 mg/ml concentration and analyzed with 10 mM sodium phosphate and 0.01% sodium azide as a mobile phase. The fractionation method consisted of a 40 μL injection volume, 5 min injection time, 0.5 ml/min detector flow, 1 ml/min crossflow, and a total run time of 46.5 min. The detectors employed in the method were: a UV detector (280 nm), a refractometer, and a multi-angle light scattering detector.

5.5.9 Protocol optimization for fasudil extraction from cell medium

100 μ l cell medium was spiked with 200 μ M FAS, followed by protein precipitation with 250 μ l ACN and vortex mixing for 3 min. After centrifugation (10 min at 11.000 rpm), the supernatant was collected, and the sample was prepared with six different protocols (the conditions shown in Figure S5.4.) and analyzed by LC-MS/MS. The final extraction protocol was chosen according to the highest fasudil recovery (the ratio between the extracted and the expected amount of fasudil).

5.5.10 Cell culture conditions

We have used the human triple-negative breast cancer cell line MDA-MB-231 (HTB-26™ provided by the ATCC) to evaluate the biological activity of our nanomedicines. The 2D model culture was performed in DMEM/F12 culture medium supplemented with 10% inactivated Fetal Bovine Serum and 1% Penicillin/Streptomycin (Gibco). To develop 3D cell cultures, cells were grown in DMEM/F12 culture medium supplemented with B27 minus vitamin A, EGF, and 1% penicillin/streptomycin. In addition to this, the 3D model was seeded in special ultra-low attachment plates (ULA P96 ref. 3474 from Corning).

5.5.11 *In vitro* cell viability assay

Cell viability assay was performed with CellTiter 96® AQueous Non-Radioactive Cell Proliferation Assay following the manufacturer's protocol (Promega). For the 2D MBA-MB-231 model, cells were seeded in a 96-well plate at

15625 cells/cm², and for the 3D model, 31250 cells/cm². The 2D PC3 model seeded cells at 5.000 cells/cm². All three *in vitro* models were incubated for 24 h before adding treatments. After 72 h, the cells were incubated for 6 h with a mixture of MTS and PMS (ratio 20:1) and measured directly at 490 nm on CLARIOstar multiplate reader (BMG LABTECH).

5.5.12 GSH/GSSG assay

GSH and GSSH levels were detected by GSH/GSSG-Glo™ Assay luminescence kit (V6611, Promega); the kit was used in both 2D and 3D models following the manufacturer's recommendations. 2D model cells were seeded directly in a 96-well white plate for cell culture at 15,625 cells/cm², while 3D model cells were seeded in their corresponding 96-well ULA plate at 31,250 cells/cm². GSH/GSSG assay was performed 24 h after seeding. For the 3D model, the test takes place in the ULA plate; before reading, the volume was transferred to a white plate suitable for luminescence testing. The reading was performed in the CLARIOstar multiplate reader (BMG LABTECH). The absorption levels obtained from GSH/GSSG-Glo™ Assay luminescence kit were used to determine GSH and GSSG concentration in our samples. Notably, the obtained concentration must be recalculated back to the intracellular concentration by implementing the known cell number and independent cell volume for each *in vitro* model. Experiment performed by Esther Masia.

5.6 SUPPLEMENTARY MATERIAL

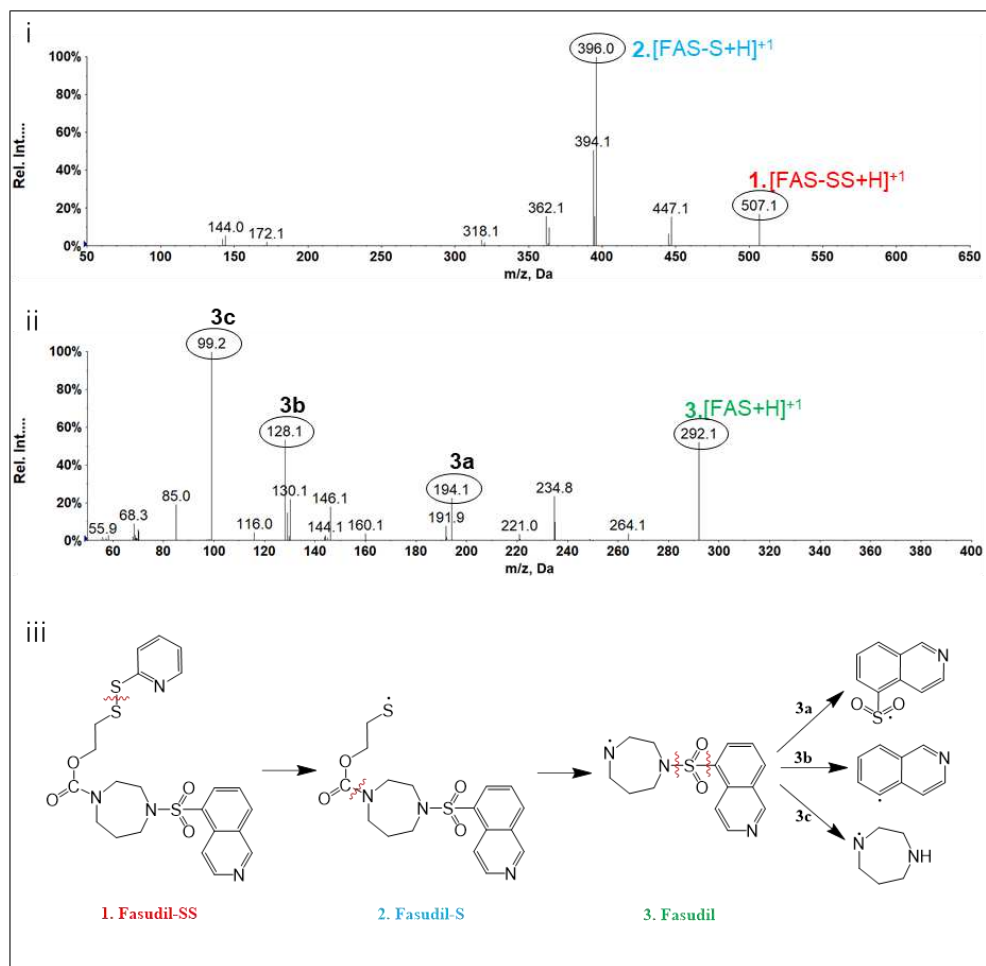


Figure S5.1. Qualitative analysis of fasudil-ethyl-disulfide drug linkers (FAS-Et-SS). Direct MS analysis enabled the identification according to the MS/MS spectra of drug linker (i), drug (ii), and the fragmentation mechanism (iii).

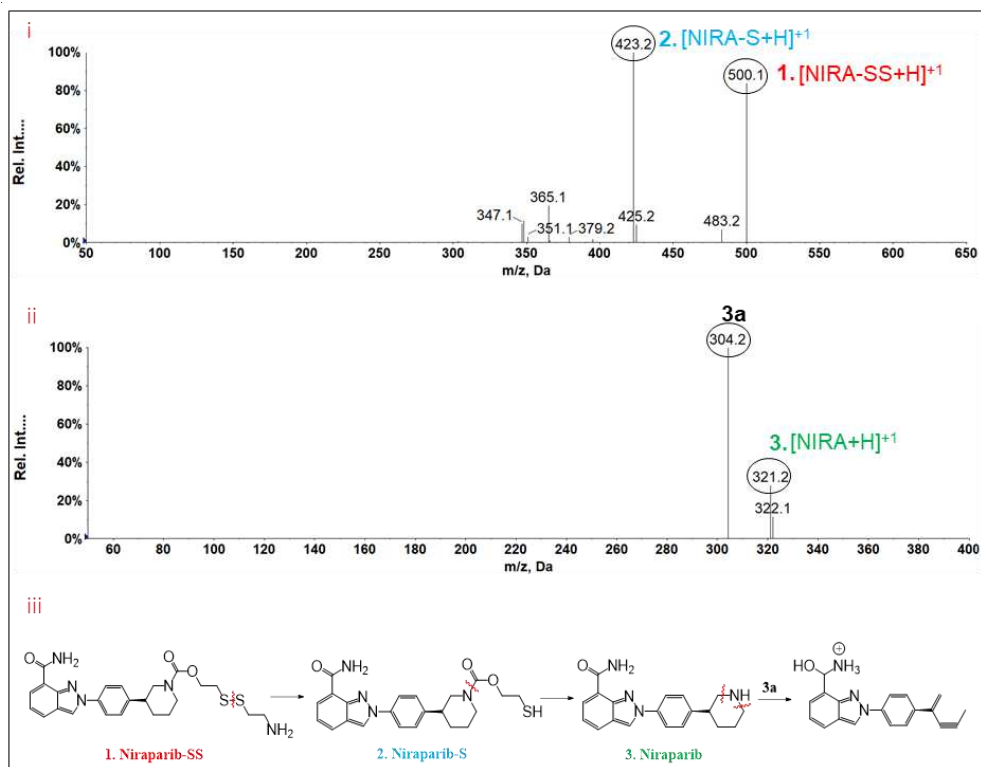


Figure S5.2. Qualitative analysis of niraparib-ethyl-disulfide drug linkers (NIRA-Et-SS). Direct MS analysis enabled the identification according to the MS/MS spectra of drug linker (i), drug (ii), and the fragmentation mechanism (iii).

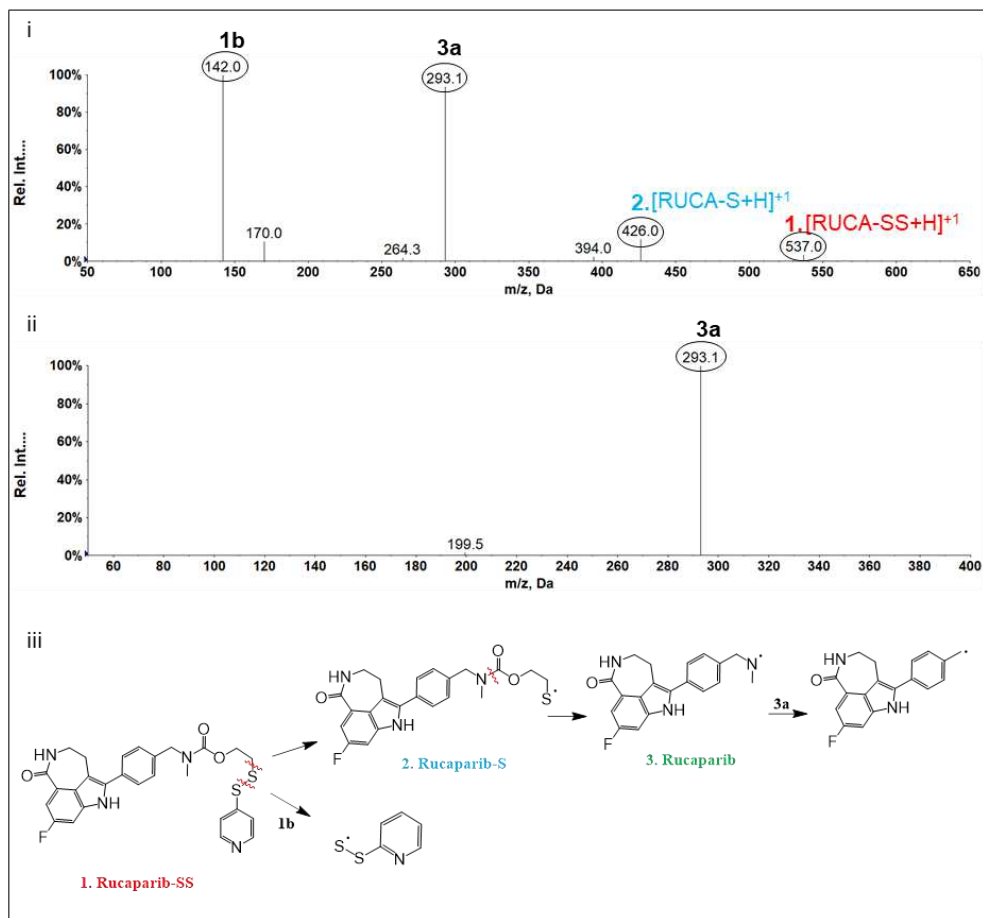


Figure S5.3. Qualitative analysis of rucaparib-ethyl-disulfide drug linkers (RUCA-Et-SS).

Direct MS analysis enabled the identification according to the MS/MS spectra of drug linker (i), drug (ii), and the fragmentation mechanism (iii).

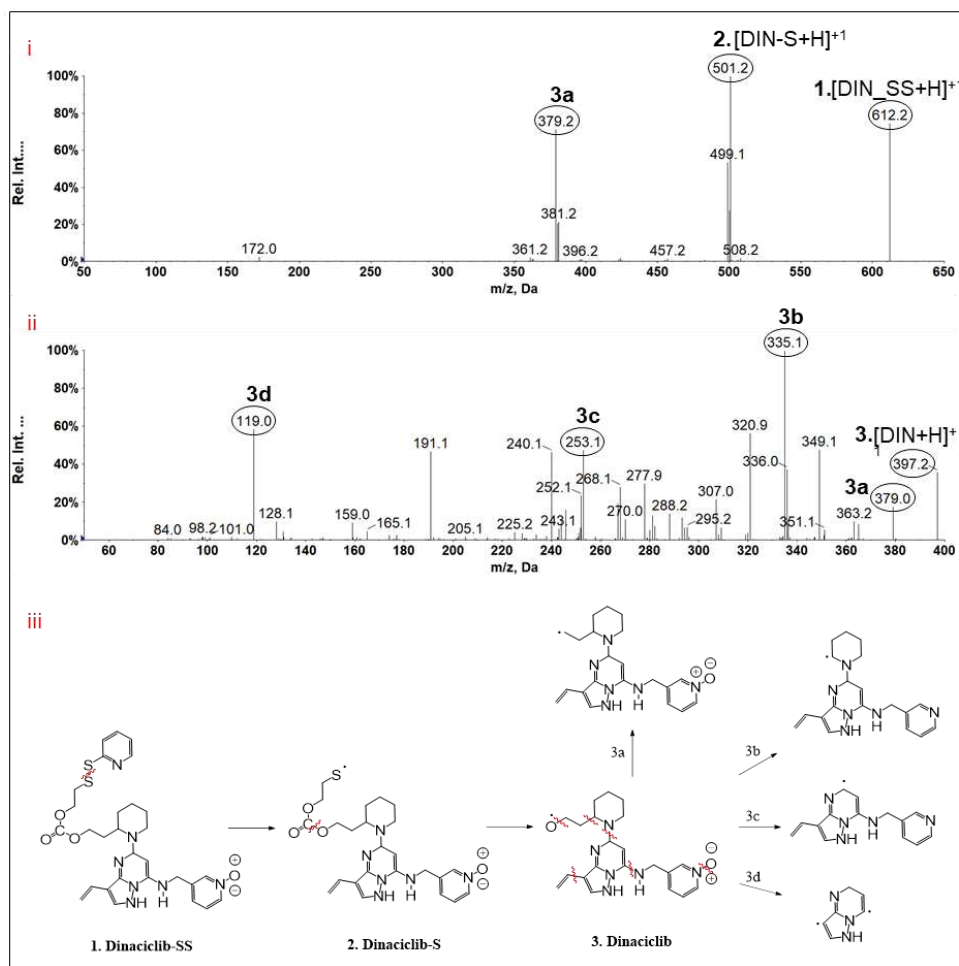


Figure S5.4. Qualitative analysis of dinaciclib-ethyl-disulfide drug linkers (DIN-Et-SS). Direct MS analysis enabled the identification according to the MS/MS spectra of drug linker (i), drug (ii), and the fragmentation mechanism (iii).

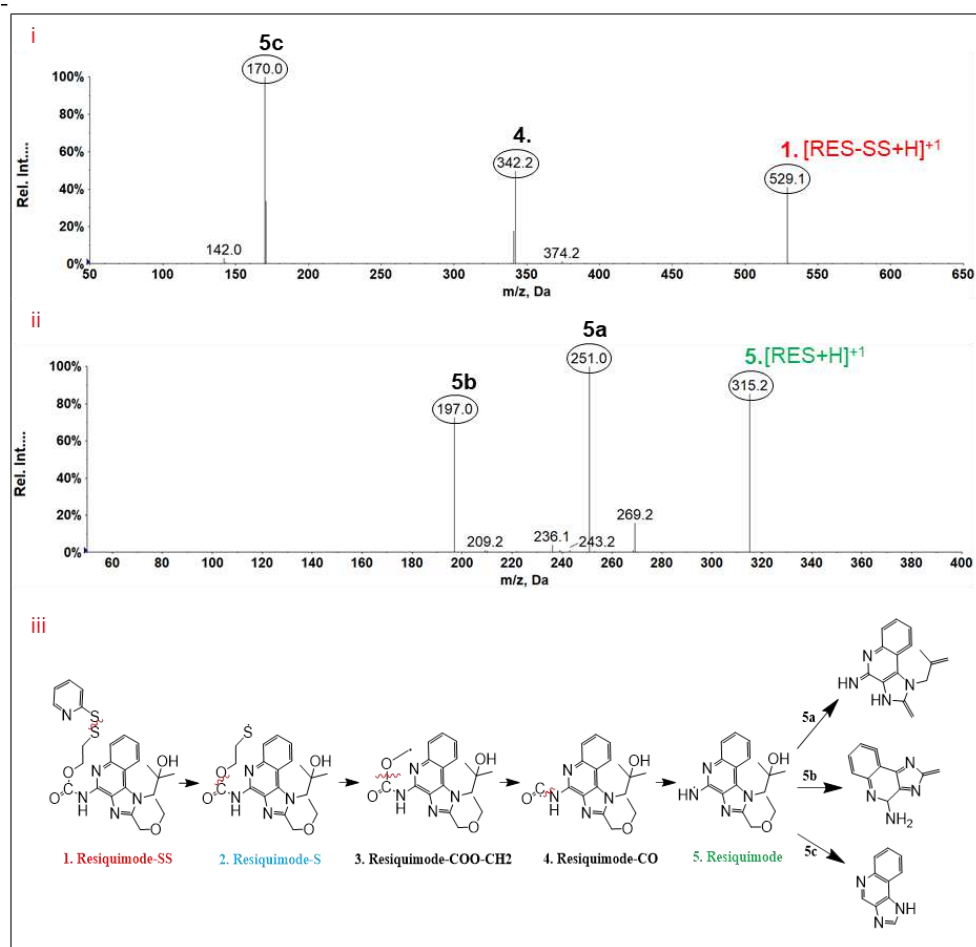


Figure S5.5. Qualitative analysis of resiquimod-ethyl-disulfide drug linkers (RES-Et-SS). Direct MS analysis enabled the identification according to the MS/MS spectra of drug linker (i), drug (ii), and the fragmentation mechanism (iii).

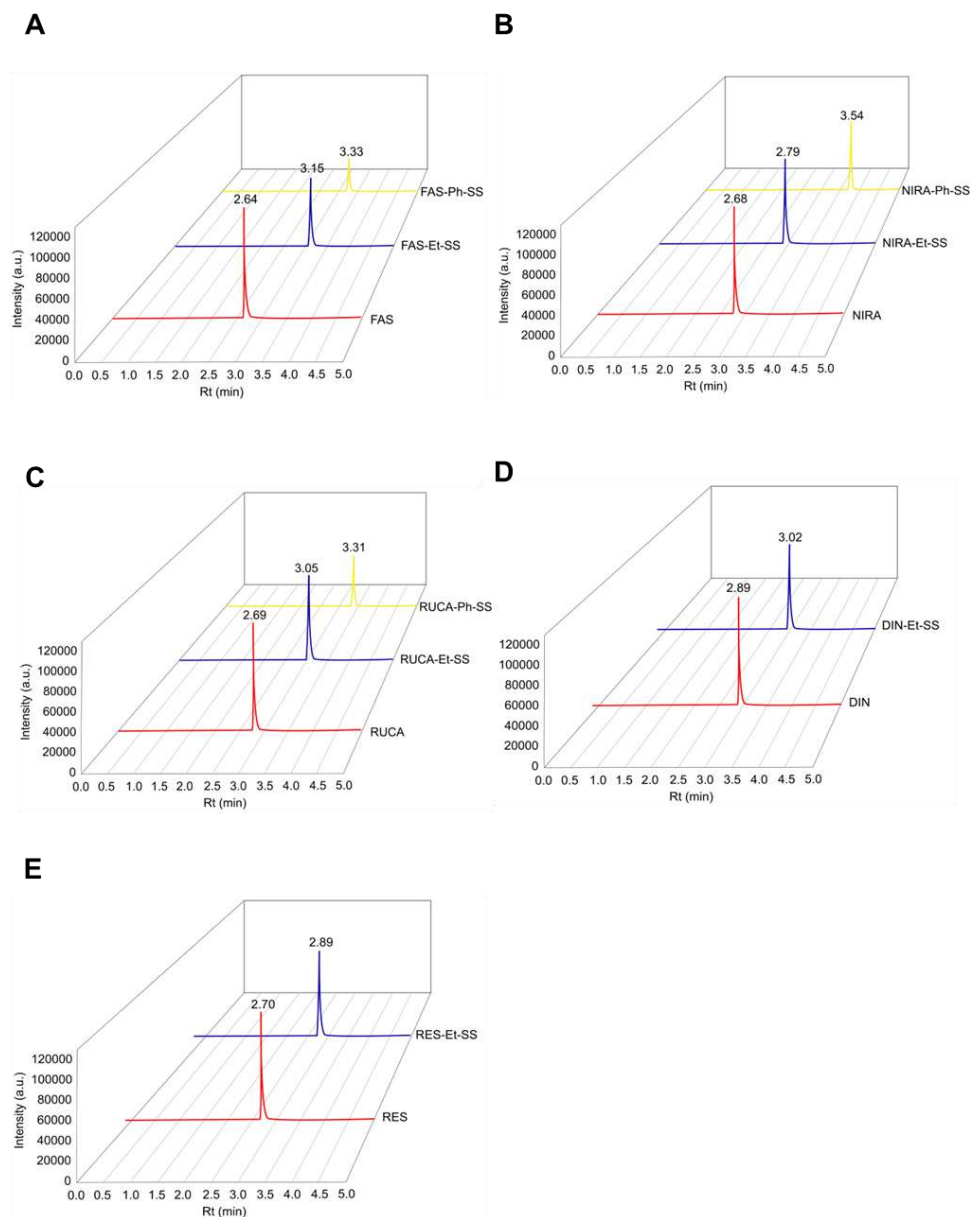


Figure S5.6. LC-MS/MS chromatograms of (A) fasudil - FAS, (B) niraparib - NIRA, (C) rucaparib - RUCA, (D) dinaciclib – DIN, (E) resiquimod – RES, and their corresponding ethyl-disulfide (Et-SS) and phenyl-disulfide (Ph-SS) drug-linkers.

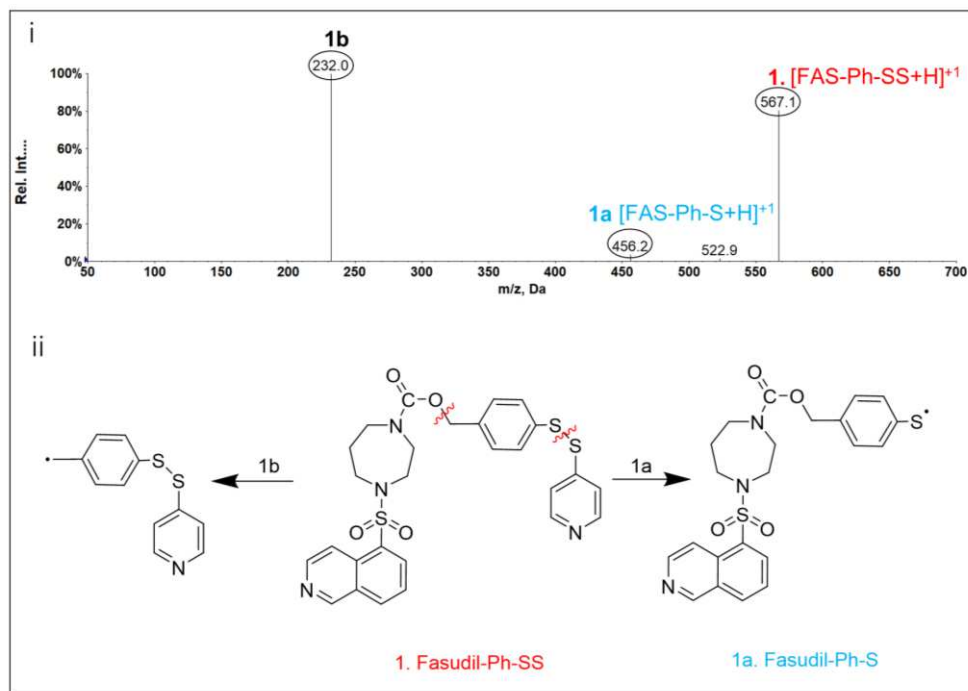


Figure S5.7. Qualitative analysis of fasudil-phenyl-disulfide drug linker (FAS-Ph-SS). Direct MS analysis enabled the identification according to the MS/MS spectra of the drug linker (i) and the fragmentation mechanism (ii).

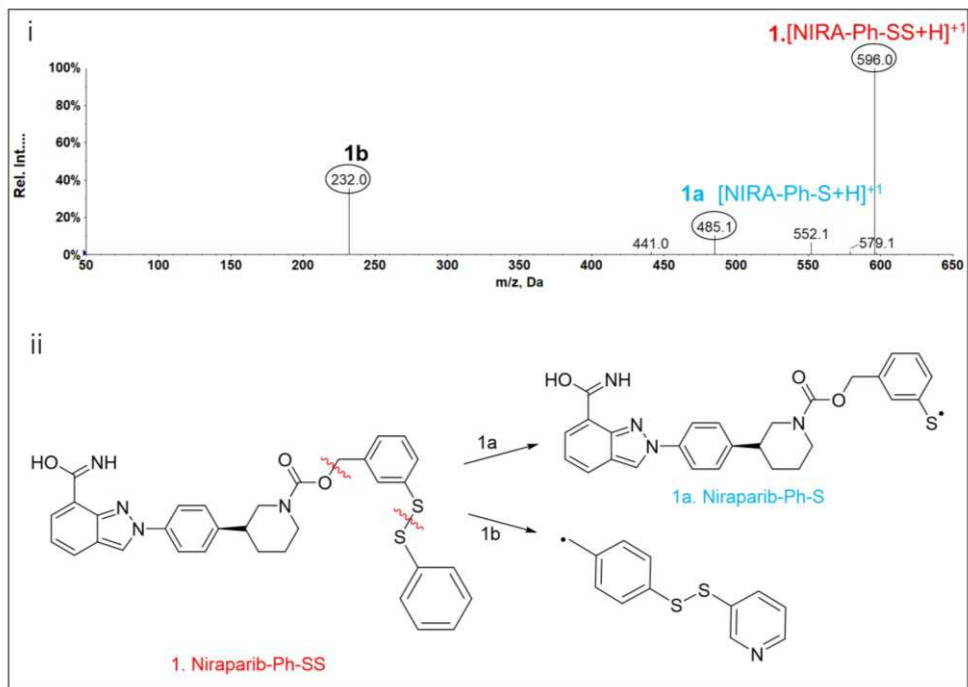


Figure S5.8. Qualitative analysis of niraparib-phenyl-disulfide drug linker (NIRA-Ph-SS).

Direct MS analysis enabled the identification according to the MS/MS spectra of the drug linker (i) and the fragmentation mechanism (ii).

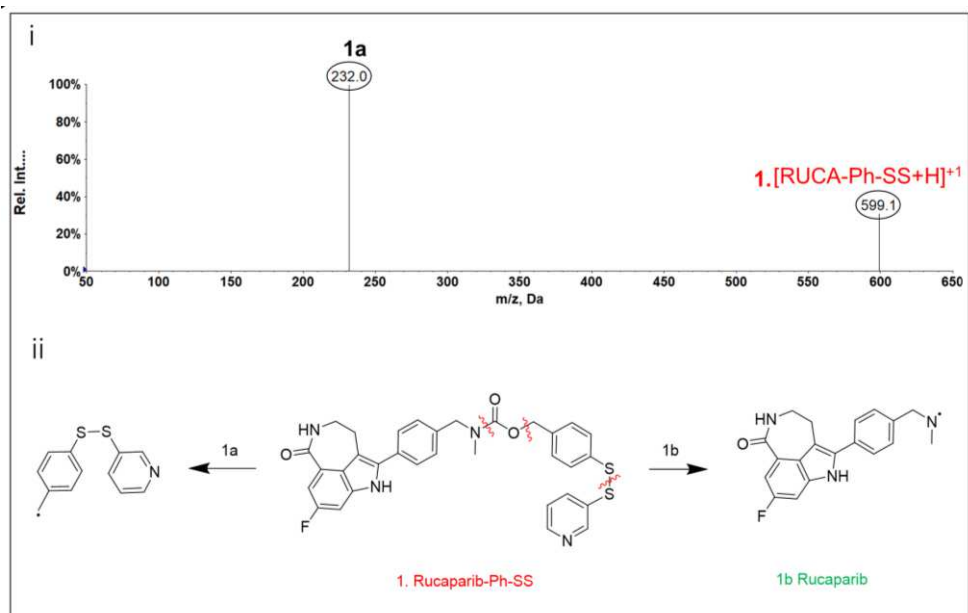
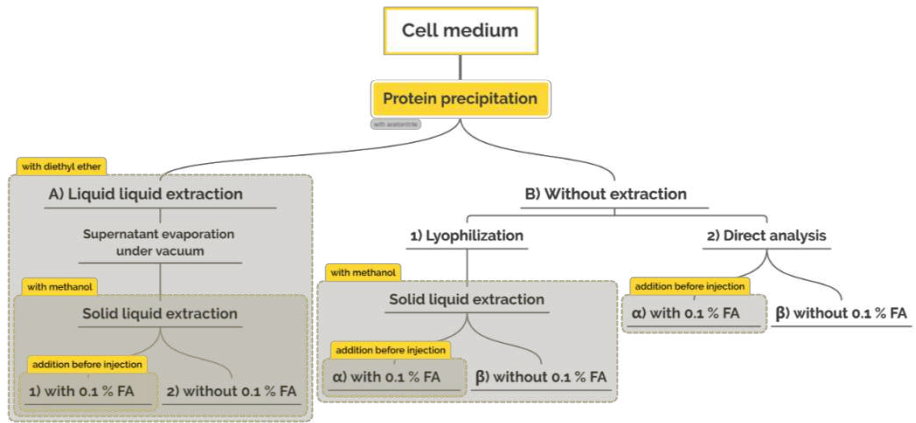


Figure S5.9. Qualitative analysis of rucaparib-phenyl-disulfide drug linker (RUCA-Ph-SS). Direct MS analysis enabled the identification according to the MS/MS spectra of the drug linker (i) and the fragmentation mechanism (ii).

A



B

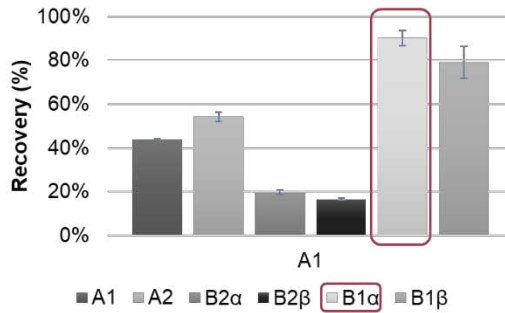


Figure S5.10. Sample preparation optimization protocol (A) Protocol optimization for fasudil extraction from the cell medium (B) FAS/IS peak area ratio for each protocol (the protocol chosen marked in red)

Table S5.1. Reaction conditions for drug linkers synthesis.

Drug-linker	Solvent	Temp	Base	Purification	Reaction time (h)
FAS-Et-SS	DMF	Room	TEA	Column	24 h
NIRA-Et-SS	DMF	Room	TEA	Extraction column	+ 24 h
RUCA-Et-SS	DMF	Room	TEA	Extraction column	+ 24 h
DIN-Et-SS	DMF	50°C	TEA DMAP	Extraction column	+ 24 h
RES-Et-SS	DCM	Room	TEA	Extraction column	+ 48 h
FAS-Ph-SS	DMF	80°C	TEA	Column	24 h
NIRA-Ph-SS	DCM	Room	TEA	Extraction column	+ 24 h
RUCA-Ph-SS	DMF	Room	TEA	Column	48 h

Dimethylformamide (DMF), Dichloromethane (DCM), 4-dimethyl aminopyridine (DMAP), and Triethylamine (TEA). FAS, NIRA, RUCA< DIN, RES, Et, Ph, SS, Temp

Table S5.2. Validation parameters and MS/MS conditions for LC-MS/MS method implemented in the drug release studies for the quantification of drugs

Drug	MRM (m/z)	Collision energy (V)	Linearity				
			C range, µg/ml	R ²	Accuracy, %	LOQ, µg/ml	LOD, µg/ml
Fasudil	292.2 – 99.0	35	0.01 - 0.1	0.998	96.5 – 109.6	0.02	0.01
			0.1 - 0.5	0.997	97.6 – 102.2	0.10	0.03
			0.5 - 1.0	0.996	97.6 – 101.7	0.13	0.04
			1 - 5	0.999	98.7 – 100.8	0.39	0.12
Niraparib	321.2 – 304.2	30	0.05 – 0.4	0.996	94.6 – 106.8	0.07	0.02
			0.4 – 5.0	0.999	95.5 – 111.7	0.67	0.20
			5.0 – 9.0	0.999	98.9 – 101.1	0.76	0.23
Rucaparib	324.3 – 293.0	30	0.05 – 0.4	0.999	96.1 – 105.8	0.03	0.01
			0.4 – 1.0	0.994	96.3 – 101.7	0.25	0.07
			1.0 – 5.0	0.998	94.5 – 104.2	0.73	0.22
Dinaciclib	397.2 – 335.0	40	0.02 – 0.1	0.998	96.5 – 101.4	0.02	0.01
			0.1 – 0.5	0.997	98.7 – 106.1	0.10	0.03
			0.5 – 1.0	0.997	98.7 – 101.6	0.11	0.03
			1.0 – 5.0	0.999	99.4 – 102.1	0.24	0.07
Resiquimod	315.2 – 251.0	30	0.02 – 0.2	0.999	97.4 – 104.1	0.02	0.01
			0.2 – 0.9	0.997	95.5 – 103.0	0.15	0.01
			0.9 – 5.0	0.999	97.8 – 103.5	0.68	0.20

LOD – limit of detection, LOQ – limit of quantification, MRM-multiple reaction monitoring

CHAPTER VI

GENERAL DISCUSSION AND FINAL REMARKS

As a rapidly growing research area and market, nanomedicine offers novel treatment options for various diseases and disorders. While the recent COVID-19 pandemic has dramatically impacted the approval process, the uncertainties and challenges associated with the clinical translation of nanomedicines remain unclear and unconsolidated, as regulatory guidance also remains unclear and unconsolidated. The future improvement/acceleration of the clinical translation process imperatively requires the reinforcement and harmonization of general protocols for pre-clinical development and exhaustive physico-chemical characterization.

Batch-to-batch reproducibility and a complete understanding of the properties that influence interactions occurring with the biological components underlie the efficient design of safe and effective nanomedicines.⁴⁵⁰ Incomplete batch characterization represents an obstacle to their robust clinical assessment, a fact highlighted by the failure of many nanomedicine candidates at the early stages of development.⁴⁵¹ Implementing precise and adequate characterization steps as a standard from the beginning of the PDC design process may avoid many problems encountered in advanced preclinical/clinical stages. Failed clinical trials and recently published meta-analyses have highlighted shortcomings concerning the reproducibility and repeatability of experimental findings.^{94,452} The lack of rigorous characterization, adequate analytical procedures, and systematic reporting for various parameters and analytical and methodological details represents a critical factor that contributes to reproducibility/repeatability issues in academic research principally in nanomedicine and at a more general level.^{453–455} The recent predominant focus of peer review on the significance of the study and the research impact, while neglecting quality control, proper development, and analytical methodology validation, represents a crucial factor contributing to reproducibility

and repeatability problems in nanomedicine (indeed, in most scientific areas). Current literature in nanomedicine gives more attention to rational design and final product synthesis and less to the reproducibility of the synthesis and reproducibility, repeatability and validation of analytical methods employed for characterization (e.g., identification of a final product, determination of free drug, the drug release studies, physical and chemical stability, polydispersity index, and biodistribution studies). There remains much debate regarding the implementation of analytical method validation tools and quality control systems in preclinical research; furthermore, whether the investment of time to this matter when clinical safety and efficacy remain unproven remains an open question.²⁷ Importantly, implementing good manufacturing practices and good laboratory practice standards in academia does not necessarily mean strict control of every process and must not slow innovation in academia; instead, standards and harmonized procedures can establish minimum controls in basic critical processes to ensure the acquisition of reliable data that will, in turn, improve the reproducibility of both preclinical and clinical efficacy studies.

Other than the analytical method employed in characterization, the performance of methods/approaches associated with the task at hand can significantly influence results. For instance, the complexity of drug delivery systems may drive the evaluation of a final product, and not products generated throughout the entire synthetic process, and place importance on those parameters that influence the final characteristics of a synthesized nanomedicine.

The scientific community has shown awareness of such critical issues; recently, a strategy has been proposed to improve data consistency, repeatability, and reproducibility. Faria et al. have suggested MIRIBEL, a scientific reporting checklist that entails the minimal level of information required when reporting bio-

nano experiments, as a requirement for publication.⁴⁵⁶ Unfortunately, four years later, the MIRIBEL checklist has yet to have a significant impact due, in part, to the need for this checklist to cover a broader range of nanomedicine types/subtypes and a lack of guidance regarding the choice, quality, robustness, and validation of employed analytical techniques.

In the context of integrating concepts from analytical chemistry and improving the implementation of rational design within the nanomedicine development process, we aimed to develop fit-for-purpose analytical procedures for the characterization of novel polypeptide-drug conjugates (PDCs) based on polyglutamic acid (PGA) as a carrier.

Given their complexity, heterogeneous nature, and multi-component ionic nature, PDCs represent a significant analytical challenge; furthermore, combination-based drug therapies that employ two (or more) active moieties within the same polymer main chain add further complexity.¹⁶¹ A multidisciplinary approach that integrates know-how from polyelectrolyte characterization^{457,458}, pharmaceuticals^{459,460}, analytical chemistry, and analysis of antibody-drug and other drug-conjugates^{461–463} may provide broad insight into optimized characterization strategies for PDCs.

Based on this rationale, the principal goal of our study was to tackle the reproducibility and repeatability problems in PDCs design and characterization by implementing the fit-for-purpose analytical techniques such as liquid chromatography-mass spectrometry (LC-MS), asymmetric flow field flow fractionation (AF4) and mass spectrometry imaging (MSI).

The characterization of any analyte requires the implementation of adequate method development to meet significant chemical and biological needs. Method development involves obtaining more rapid, sensitive, simple, informative,

and environmentally sustainable analytical methodologies.²¹⁹ Experimental planning, method validation, quality control, multivariate data analysis, and result interpretation can foster more in-depth understanding and higher confidence in obtained results. Thus, we initiated our study with the implementation of a “design of experiments” (DoE), artificial intelligence, and quality-by-design tool for simultaneous optimization of liquid-chromatography-mass spectrometry (LC-MS/MS) method for the quantitative determination of sixteen commonly used anticancer drugs (**Chapter II**). Small-scale scientific experimentation guided by scientific intuition alone creates an illusion of validity and misplaced confidence⁴²⁵; in contrast, DoE permits the mapping and exploration of complex biological and chemical processes. The DoE approach involves statistical software (in our case Design Expert 12) to predict the feasibility of the simultaneous modification of various LC-MS factors, which excludes unnecessary trials and facilitates experimental optimization compared to the conventional one-factor-at-the-time approach. Overall, the implementation of DoE allowed us to obtain an accurate, specific, and sensitive LC-MS/MS method for the determination of sixteen anticancer drugs and to obtain an internal LC-MS/MS method database for the quantitative determination of these drugs employed for the characterization of subsequently synthesized novel single and combination PDCs. This approach will significantly inhibit the possibility of human error due to unfamiliarity with the basics of analytical chemistry terms and practice and increase the reproducibility and accuracy of studies implementing LC-MS/MS methods.

We demonstrated the practical advantages of this approach through the characterization of a PGA-conjugated form of the Rho kinase inhibitor fasudil (FAS) for spinal cord injury (SCI)³²⁶ and TNBC treatment, with the latter as part of a combination regime with the CDK inhibitor dinaciclib (**Chapter IV**), and for the characterization of the noted OximUNO conjugate.³⁴³ Additionally, by achieving the

optimal retention factor for each drug, we employed the developed LC-MS/MS methods in separating drug-linkers metabolites, which supports the accurate interpretation of drug release results and the identification of metabolites (**Chapter V**).

First, exploring the application in SCI, we conjugated FAS to PGA through a glutathione (GSH)-responsive self-immolative disulfide linker (PGA-SS-Et-FAS) to improve solubility, site-specific activity, and bioavailability of this inhibitor.³²⁶ We implemented the DoE-developed LC-MS/MS method to quantitatively determine FAS levels in biological fluids such as plasma and cerebrospinal fluid (CSF). We confirmed i) the plasma stability of PGA-SS-Et-FAS conjugate by demonstrating a low level of FAS release (3% over a 24-h period) and ii) the improved bioavailability of FAS by demonstrating the presence of free FAS in CSF after PGA-SS-Et-FAS administration but the absence of free FAS in CSF after free FAS administration. Moreover, we identified FAS-SH as an intermediate metabolite and FAS as a final product of GSH-triggered release. We then discovered that the conjugation to PGA enhanced the stability and sustained release of FAS, which supported the significant induction of axon growth following the exposure of spinal cord organotypic cultures and neural precursor cells (NPCs) to the conjugate. We also implemented the DoE-developed LC-MS/MS method to characterize a protocol for evaluating an NPCs/PGA-SS-Et-FAS combination treatment for SCI.³⁴² We proved the appropriate development of the *in vitro* NPC sample preparation model for transplantation into the SCI model *in vivo* by demonstrating the cell internalization of the PGA-SS-Et-FAS conjugate. A combination treatment comprising the acute transplantation of NPCs pre-treated with PGA-SS-Et-FAS led to enhanced cell engraftment and reduced cyst formation after SCI in an *in vivo* mouse model. These findings demonstrate how an adequately developed LC-MS/MS method represents an invaluable tool when exploring the fate of PDCs in biological environments, as only a sensitive and

accurate LC-MS/MS method and adequate analytical procedures would allow the detection of the low FAS/metabolite concentrations observed in drug/PDC stability and drug release studies.

We then applied the DoE-developed LC-MS/MS method to characterize the OximUNO conjugate, a star-shaped PGA decorated with a CD206-targeting peptide (mUNO) carrying doxorubicin (DOX) through a pH-responsive hydrazone linker for the treatment of metastatic breast cancer.³⁴³ Upon cellular internalization, DOX becomes released from OximUNO due to the low pH (pH 5) hydrazone linker and the intrinsic biodegradability of St-PGA by cathepsin B (a lysosomal protease highly expressed in breast cancer).³⁴³ Hence, we studied DOX release from OximUNO in the presence of acidic pH (pH 5) and cathepsin B using the LC-MS/MS method developed in **Chapter II**. We aimed to administer OximUNO intraperitoneally, so we also evaluated DOX release in the intraperitoneal fluid. We demonstrated controlled DOX release under lysosomal mimicking conditions but the preservation of OximUNO stability in both physiological conditions – dPBS and intraperitoneal fluid. Overall, these studies further emphasized how the adequate design of bioanalytical studies can allow the proper evaluation of a given PDC's stability in circulation and a controlled release after safely crossing biological barriers and reaching the intended target tissue/cell.

Thus far, DoE developed LC-MS/MS method was an integrated part of analytical platform for the characterization of single PDCs; however, additionally, we aimed to develop the analytical platform for the characterization of polypeptide-based combination conjugates. As described previously, the PDCs combination therapy may be designed by four different strategies with the conjugation of drug combination on the same polymer chain as the most common one owing to the possibility to ensure the delivery of both drugs at the same time

in the same site of action. Additionally, self-assembled structures and crosslinking of single star shaped PDCs at a desired ratio could provide with significant advantages when designing polypeptide-base combination conjugates such as greater versatility and represent an universal tool to control drug ratio in combination therapy.³⁵⁵ Thus, two projects resulted from the combination therapy rationale focusing on the implementation of different analytical methods for their characterization. First, the DoE implementation in the crosslinking combination strategy and the development of AF4 for the size determination of designed crosslinked combination PDCs. Second, the evaluation of new methodology such as MSI in elucidation of the biological fate of FAS and DIN polypeptide-based combination conjugate.

Before moving into the next project of crosslinking PDCs combination design strategy we require a robust and fit-for-purpose analytical method for appropriate size characterization. While traditional approaches used to determine the size and molecular weight of novel PDCs suffer from disadvantages such as shear degradation and interaction with columns in the case of size exclusion chromatography²⁶⁰, low-resolution size and polydispersity analysis due to the discrimination of smaller particles as in batch DLS²⁶⁹, or costs and generally inaccessibility for routine analysis in the case of sophisticated Small Angle Scattering (SAS) techniques; we implemented asymmetric flow field flow fractionation method (AF4) coupled with ultraviolet, refractive index and multi-angle light scattering detector. This approach separates particles over a wide range, from the nanometer scale to several microns in an empty channel eliminating the possibility of sample interactions with the column like in SEC. AF4 also suits the analysis of neutral and charged particles, a clear advantage for PDCs given their polyelectrolyte identity; however, a methodology to evaluate polyelectrolytes such as PGA remained incompletely described, and we lacked a complete understanding

of PGA behavior within the instrument, which would foster the enhanced interpretation of experimental results. Thus, in **Chapter III**, we evaluated the implementation of an AF4-based approach to complement small-angle x-ray scattering (SAXS) for the exhaustive characterization of newly synthesized genipin-crosslinked conjugates. Overall, we demonstrated the primary importance of a detailed knowledge of StPGA behavior within the AF4 separation channel for establishing proper experimental conditions and elucidating fractionation and detection dynamics.

While recent developments have generated significant interest in artificial intelligence and quality-by-design approaches (such as DoE or machine learning), they have rarely been considered in the polymer-drug conjugate design.⁴⁶⁴ Since the first study on DoE application in optimizing drug formulation in 1967, the number of literature reports on the DoE implementation in optimization of the development process for drug delivery technologies has constantly been rising.⁴⁶⁵ The FDA and EMA guidelines that suggest using quality-by-design paradigms have coerced researchers to adopt a rational, efficient, systematized, and cost-efficient strategy, DoE.⁴⁶⁶ Thus, in **Chapter III**, we demonstrated the utility of DoE during the synthesis of genipin-crosslinked StPGA-based combination conjugates, which facilitated the identification of optimized experimental conditions. We illustrated how DoE provides a detailed picture of the genipin-crosslinking process behavior with high efficiency. Finally, we established how DoE determined the contribution of each factor (genipin equivalence, PDC concentration, ionic strength, and hydrophobicity degree), modeled each factor's effect on each response (size, polydispersity index, and crosslinking degree), and resolved factor interactions. While we specifically investigated the use of DoE for optimizing the development of new genipin-crosslinked StPGA-based combination conjugates, we note the insufficiency of the design space (the minimum and maximum levels of tested

factors) to cover a more comprehensive range of nanoconjugate sizes. We suspect that the low PDC concentration in the solution and the genipin equivalents prompted the obtainment of smaller nanoconstructs. Additionally, we plan to implement flow chemistry to improve this approach.

We urgently need quantitative label-free imaging methods to assess drug release and nanomedicine distribution in cells/tissues to contextualize or predict biological outcomes. Current methods require modifications such as fluorescence- or radio-labeling that may not fully represent the clinical behavior of a given nanomedicine. Mass spectrometry imaging (MSI), an increasingly well-known technique in pharmacokinetic studies, may resolve these issues. Thus, in **Chapter IV**, we explored the potential of MSI as a label-free imaging technique to study the pharmacological activity, quantification, the spatial distribution of drugs and evaluate relevant metabolites following treatment with our combination PDC.

MSI has been implemented in studies of drug biodistribution and drug interactions with the tumor microenvironment; however, the potential of MSI in nanomedicine-based research remains incompletely explored. Proof-of-principle studies that demonstrate the appropriate delivery of an active moiety *in vivo* at a required concentration early in translation will minimize the risk of failure in the later stages of drug development. This tenet holds true for novel drug delivery systems such as PDCs.³⁰³ For example, clinical trials of the clinically discontinued polyglutamate-camptothecin conjugate (CT-2106, MAG-CPT) took place before a proof-of-principle pharmacokinetic study revealed that this polymer-based pro-drug did not effectively deliver camptothecin (CPT) to the tumor in patients.⁴⁶⁷ In contrast, phase I trials demonstrated the anticancer activity of capecitabine⁴⁶⁸, even though studies of capecitabine in circulating plasma showed high levels of capecitabine and inactive metabolites but low levels of 5FU (active capecitabine

metabolite). The explanation of the such anticancer activity and, consequently, the desired proof-of-principle came two years later in a pharmacokinetic study of capecitabine, which demonstrated 21-fold higher 5FU levels in the tumor than the plasma and, more importantly, 3-fold higher 5FU levels in the tumor than the surrounding normal tissue explaining the successful clinical results.⁴⁶⁹ The latter represents two clear examples of the importance of adequate analytical techniques to foster clinical approval of PDCs.

MSI offers the unique ability to co-localize drug distribution signals and their metabolites with endogenous compounds as biological markers of therapeutic effect, disease progression, or toxicity. Moreover, current drug release studies of PDCs use experimental protocols (e.g., the presence of dithiothreitol, pH = 5.5, and cathepsin B) that mimic known tumor conditions. Our previous research from **Chapter V** demonstrated a general lack of tumor-mimicking drug release protocols (in dithiothreitol, low pH, or Cathepsin B) and correlation with the *in vivo* physiological results. Thus, we explored the potential of MSI to study drug release from synthesized PDCs administered to preclinically relevant *in vitro* models while also monitoring the spatial localization of drugs and metabolite formation. We evaluated the single drug conjugates and employed the resultant combination conjugate as a model PDC to study drug release, toxicity, and fate in three-dimensional (3D) TNBC spheroid models, mammospheres and matrix embedded (BME)-spheroids by MALDI-MSI during a short research stay at Sheffield Hallam University. We developed and optimized the MALDI-MSI method for detecting FAS and DIN in the 3D TNBC models, ensuring that the matrix and the embedding medium did not interfere with the analysis. We obtained MALDI-MSI images of PDCs treated *in vitro* TNBC models at two resolutions (30 and 10 μm) with lipids such as phosphorylcholine (184.49 m/z) and choline "head" (86.002 m/z) as primary metabolites; however, the conclusive identification and detection of drugs in

biological samples proved problematic due to the MALDI-TOF instrument's high LOD for FAS and DIN. Interestingly, our linker study described in **Chapter V** (performed after MSI experiments) indicated FAS release in 3D TNBC mammospheres from single PGA-SS-Et-FAS at a lower level than in the DTT studies (0.32% and 26%, respectively). Additionally, we only observed ≈40% internalization of PGA-SS-Et-FAS in 3D TNBC mammospheres; thus, we conclude that we induced insufficient drug release in the 3D TNBC *in vitro* models for MALDI-MSI detection.

Leading by the successful implementation of ethyl-disulfide self-immolative linker for the conjugation of FAS and the activity of PGA-SS-FAS for the treatment of spinal-cord injury, we explored the same disulfide linker for the design of PDCs bearing niraparib and rucaparib as active moiety (an iPARP inhibitors for the treatment of pancreatic and prostate cancer). However, we failed to observe any activity of the designed PGA-SS-NIRA and PGA-SS-RUCA in the *in vitro* prostate cancer model (PC3) leading to the conclusion that developing strategies to design next-generation drug delivery systems remains challenging. Despite the technological advancements in the last decade, and despite of previous successful examples we must balance numerous factors in case-by-case design scenario, including controlled drug release and enhanced cellular internalization, through managing rapid immune responses, renal clearance, and off-target toxicities. Moreover, we require novel disease-driven approaches to the rational design of nanomedicines, which necessitate a robust understanding of the relationships between biology and technology, the techniques used to characterize nanomedicines, and the influence of disease pathophysiology on nanomedicine distribution, accumulation, and efficacy.²⁰ Thus, as a part of our **Chapter V** main objective, we performed a systematic study to expand the rational design toolbox for drug delivery systems driven by the chemically controlled drug release that leads to a better understanding of their fate in a biological environment. Generally,

the importance of a proper linking moiety design that allows a controlled drug(s) release at the desired site of action has been extensively studied for single and combination PDCs in different pathological scenarios. Redox-responsive self-immolative linkers bearing disulfide moieties (SS-SIL) represent a powerful strategy for intracellular drug delivery; furthermore, they are considered universal linkers as any drug with an amino or hydroxyl group can undergo modification and connection through SS-SIL to a carrier. Of note, the influence of the drug's structural features and the linker-associated spacer on release kinetics remains unexplored. Therefore, we evaluated the influence of the drugs/spacer's chemical structures, the type of chemical group available for conjugation on drug release, and the biological effect of the PDC. We implemented the LC-MS/MS method developed in **Chapter II** to perform the exhaustive characterization required for this systematic study. The obtained fit-for-purpose analytical protocol enabled the quantification of low drug concentrations in drug release studies and metabolite elucidation. To the best of our knowledge, we are the first to provide evidence and clarify how the drug's structural features influence the drug release from the SS-SIL linker and prove the non-universality of SS-SIL as a linker. We highlighted the importance of a rigorous disulfide linkers characterization in understanding structure-function correlations between linkers, drug chemical functionalities, and *in vitro* release kinetics, the critical information triangle always considered when using the reductive environment as an endogenous drug release trigger.

Ultimately, our findings portray the adequate development of characterization protocols and rational design of efficient personalized polypeptide-based nanoconjugates with a high degree of quality control. In the context of critical self-assessment and limitations of our research findings, we identified several possible research lines to follow the work described within the thesis:

- 1) Expand the implementation of optimized LC-MS/MS methodologies for the characterization of newly developed PDCs.
- 2) Expose academic trainees to the existence of DoE and quality-by-design approaches to contextualize the importance of experimental reproducibility, accuracy, and repeatability.
- 3) Develop an AF4-UV-RI-MALS protocol for the simultaneous determination of total drug loading, free drug, molecular weight, and size of newly developed PDCs.
- 4) Develop an AF4-UV-RI-MALS standard operation protocol combined with LC-MS proteomics for accessing the protein corona of newly developed PDCs.
- 5) Implement the AF4 technique to exosome fractionation to better understand tumor metastasis.
- 6) Expand the design space of the DoE matrix to optimize genipin-crosslinked polypeptide-based combination nanoconjugates.
- 7) Increase the sensitivity of the MSI method for the detection of FAS and DIN by exploring new ionization techniques such as desorption electrospray ionization (DESI), MALDI-2 ionization source, or by implementing sample derivatization processes.
- 8) Undertake a more detailed comparison between 3D mammospheres and spheroid TNBC *in vitro* models to identify which model better recapitulates the *in vivo* scenario.
- 9) Follow-up on the disulfide linker study to evaluate the influence of drug loading on micelle formation and elucidate the internalization mechanisms used by the synthesized conjugates.

FINAL REMARKS

We believe that integrating innovative techniques and properly developed analytical methods will provide for the exhaustive physicochemical characterization of PDCs and foster their enhanced translation into clinical use. Moreover, following this strategy will **increase confidence in results, ensure reproducibility, and reduce risk**; more robust analytical capabilities can accelerate the journey toward the correct answer.

Over the next decade, we remain confident that researchers will begin to appreciate the utility of systematic, rigorous quantitative analysis of structure-function correlations between linker structure/chemistry and bond cleavage and drug release kinetics. Importantly, this will require an adequate LC-MS/MS method. Combining conceptual molecular-level understanding with computational tools such as artificial intelligence approaches (including DoE) will ultimately guide researchers toward a robust and predictive platform for developing next-generation nanomedicines.

Notably, the scientific investigator initiating a new analytical technology (e.g., MSI or AF4) in nanomedicine must understand that successful implementation directly correlates to a candidate's advancement to the clinic. To achieve this goal, we must expand our scientific knowledge by efficiently adjusting to best practices, approaches, and methods to avoid pitfalls and lengthy delays common to a trial-and-error approach. Well-defined objectives, proper experimental design, and project execution represent essential concepts in delivering impactful results and driving the most critical decision-making process – the choice of a candidate for further clinical studies.

REFERENCES

- (1) Pelaz, B et al. *ACS Nano* **2017**, *11* (3), 2313–2381.
- (2) Wolfram, J et al. *Nano Today* **2019**, *25*, 85–98.
- (3) Liz-Marzán, L M et al. *ACS Nano* **2022**, *16* (9), 13257–13259.
- (4) Xie, J et al. *ACS Nano* **2020**, *14* (6), 6729–6742.
- (5) Zhong, W et al. *Nano Res.* **2021**, *14* (7), 2067–2089.
- (6) Davis, G et al. *Curr. Opin. Toxicol.* **2022**, *31*, 100346.
- (7) Neganova, M E et al. *Semin. Cancer Biol.* **2022**, *86*, 805–833.
- (8) Pei, Z et al. *J. Control. Release* **2022**, *352*, 211–241.
- (9) Danquah, M K et al. *Emerg. Nanomedicines Diabetes Mellit. Theranostics* **2022**, 247–260.
- (10) Brusini, R et al. *Adv. Drug Deliv. Rev.* **2020**, *157*, 161–178.
- (11) Ahmar Rauf, M et al. *Drug Discov. Today* **2022**, *27* (11), 103355.
- (12) Xu, R et al. *Semin. Immunol.* **2022**, 61–64, 101664.
- (13) Yang, Y et al. *Adv. Drug Deliv. Rev.* **2021**, *176*, 113898.
- (14) Lee, Y et al. *Adv. Drug Deliv. Rev.* **2021**, *179*, 114021.
- (15) Kou, L et al. *Front. Pharmacol.* **2018**, *9*, 27.
- (16) Blanco, E et al. *Nat. Biotechnol.* **2015**, *33* (9), 941–951.
- (17) Shan, X et al. *Acta Pharm. Sin. B* **2022**, *12* (7).
- (18) Sainz, V et al. *Biochem. Biophys. Res. Commun.* **2015**, *468* (3), 504–510.
- (19) Younis, M A et al. *Adv. Drug Deliv. Rev.* **2022**, *181*, 114083.
- (20) Hare, J I et al. *Adv. Drug Deliv. Rev.* **2017**, *108*, 25–38.
- (21) Metselaar, J M et al. *Drug Deliv. Transl. Res.* **2020**, *10* (3), 721–725.
- (22) Đorđević, S et al. *Drug Deliv. Transl. Res.* **2022**, *12* (3), 500–525.
- (23) Duncan, R et al. *Advanced Drug Delivery Reviews*. 2013, pp 60–70.
- (24) Sibylle, W V H B G et al. *Jt. Res. Cent. JRC46744* **2008**.
- (25) Duncan, R et al. *Nat. Rev. Drug Discov.* **2003**, *2* (5), 347–360.
- (26) Ashford, M B et al. *Adv. Ther.* **2021**, *4* (5), 2000285.
- (27) Melnyk, T et al. *Adv. Drug Deliv. Rev.* **2020**, *160*, 136–169.
- (28) Ekladius, I et al. *Nat. Rev. Drug Discov.* **2019**, *18*, 273–294.
- (29) Duncan, R et al. *J. Control. Release* **2014**, *190*, 371–380.
- (30) Aderibigbe, B A et al. In *Nano- and Microscale Drug Delivery Systems: Design and Fabrication*; Elsevier, 2017; pp 33–48.
- (31) Kopecek, J et al. In *Systematic Aspects of Biocompatibility, Vol. II*; 1981; pp 159–180.
- (32) Kopeček, J et al. *Adv. Drug Deliv. Rev.* **2013**, *65* (1), 49–59.
- (33) Javia, A et al. *Int. J. Pharm.* **2022**, *623*, 121863.
- (34) Duro-Castano, A et al. *Polymers (Basel)*. **2014**, *6*, 515–551.
- (35) Shiah, J G et al. *Eur. J. Cancer* **2001**, *37*, 131–139.

- (36) Zhang, R et al. *Proc. Natl. Acad. Sci. U. S. A.* **2014**, *111*, 12181–12186.
- (37) Fang, J et al. *Adv. Drug Deliv. Rev.* **2020**, *157*, 142–160.
- (38) Vasey, P A et al. *Clin. Cancer Res.* **1999**, *5*, 83–94.
- (39) Vicent, M J et al. *Angew. Chemie - Int. Ed.* **2005**, *44* (26), 4061–4066.
- (40) Schluep, T et al. *Cancer Chemother. Pharmacol.* **2006**, *57* (5), 654–662.
- (41) Minko, T et al. *Int. J. Cancer* **2000**, *86* (1), 108–117.
- (42) Yu, F et al. *J. Control. Release* **2016**, *244* (pt.B), 347–356.
- (43) Nicoletti, S et al. *Int. J. Antimicrob. Agents* **2009**, *33*, 441–448.
- (44) Ward, S M et al. *Mol. Pharm.* **2018**, *15* (11), 5263–5276.
- (45) Zaiden, M et al. *J. Control. Release* **2017**, *257*, 10–20.
- (46) Peng, Z H et al. *ACS Macro Lett.* **2014**, *3*, 1240–1243.
- (47) Armiñán, A et al. *Biomaterials* **2018**, *162*, 144–153.
- (48) Wang, Y et al. *Curr. Pharmacol. Reports* **2016**, *2* (1), 1–10.
- (49) Greco, F et al. *Adv. Drug Deliv. Rev.* **2009**, *61* (13), 1203–1213.
- (50) Ringsdorf, H et al. *J. Polym. Sci.* **1975**, *51*, 135–153.
- (51) Kopeček, J et al. *Adv. Drug Deliv. Rev.* **2020**, *156*, 40–64.
- (52) Vicent, M J et al. *Adv. Drug Deliv. Rev.* **2009**, *61* (13), 1117–1120.
- (53) Duncan, R et al. **2003**, *2*, 347–360.
- (54) Yin, Q et al. *Biomacromolecules* **2013**, *14* (3), 920–929.
- (55) Weinstock-Guttman, B et al. *J. Neurol. Sci.* **2017**, *376*, 255–259.
- (56) Song, J Y et al. *J. Control. Release* **2019**, *293*, 36–47.
- (57) Price, C F et al. *PLoS One* **2011**, *6* (9).
- (58) Zagorodko, O et al. *Macromol. Biosci.* **2017**, *17* (1).
- (59) Nel, A E et al. *Nat. Mater.* **2009**, *8* (7), 543–557.
- (60) Jaradat, D M M et al. *Amino Acids* **2018**, *50* (1), 39–68.
- (61) Varanko, A K et al. *Annu. Rev. Biomed. Eng.* **2020**, *22* (1), 343–369.
- (62) Boyer, C et al. *J. Polym. Sci. Part A Polym. Chem.* **2011**, *49* (3), 551–595.
- (63) Ren, J M et al. *Chem. Rev.* **2016**, *116* (12), 6743–6836.
- (64) Conejos-Sánchez, I et al. *Polym. Chem.* **2013**, *4* (11), 3182–3186.
- (65) Walsh, D J et al. *ACS Catal.* **2019**, *9* (12), 11153–11188.
- (66) Vicent Docón, M.J., Duro Castaño, A., Nebot Carda, V J et al. WO 2017/025298 A1, 2017.
- (67) Jiang, J et al. *ACS Macro Lett.* **2019**, *8* (10), 1216–1221.
- (68) Deming, T J et al. *Prog. Polym. Sci.* **2007**, *32* (8–9), 858–875.
- (69) Deming, T J et al. *Chem. Rev.* **2016**, *116* (3), 786–808.
- (70) Zhang, Y et al. *Commun. Chem.* **2018**, *1* (1), 1–7.
- (71) Holm, R et al. *Macromol. Biosci.* **2020**, *20* (1), 1900152.
- (72) Duro-Castano, A et al. *Biomater. Sci.* **2015**, *3* (10), 1321–1334.
- (73) Cabral, H et al. *Chem. Rev.* **2018**, *118* (14), 6844–6892.
- (74) Kang, H et al. *Adv. Healthc. Mater.* **2020**, *9* (1), 1901223.

- (75) Owens, D E et al. *Int. J. Pharm.* **2006**, *307* (1), 93–102.
- (76) Webster, R et al. *Drug Metab. Dispos.* **2007**, *35* (1), 9–16.
- (77) Thi, T T H et al. *Polymers (Basel)*. **2020**, *12* (2), 298.
- (78) Xu, L et al. *Biomaterials* **2017**, *147*, 1–13.
- (79) Barz, M et al. *Polym. Chem.* **2011**, *2* (9), 1900–1918.
- (80) Birke, A et al. *Prog. Polym. Sci.* **2018**, *81*, 163–208.
- (81) Halamoda-Kenzaoui, B et al. *J. Control. Release* **2021**, *336*, 192–206.
- (82) Buriak, J M et al. *Chem. Mater.* **2017**, *29* (1), 1–2.
- (83) Giannakou, C et al. *Curr. Bionanotechnol.* **2016**, *2* (2), 95–102.
- (84) Dobrovolskaia, M A et al. *J. Control. Release* **2013**, *172* (2), 456–466.
- (85) Maeda, H et al. *J. Control. Release* **2000**.
- (86) Wu, J et al. *J. Pers. Med.* **2021**, *11* (8), 771.
- (87) Park, K et al. *J. Control. Release* **2013**, *172* (1), 391.
- (88) Kwon, I K et al. *J. Control. Release* **2012**, *164* (2), 108–114.
- (89) Nichols, J W et al. *J. Control. Release* **2014**, *190*, 451–464.
- (90) Youn, Y S et al. *Adv. Drug Deliv. Rev.* **2018**, *130*, 3–11.
- (91) Sindhvani, S et al. *Nat. Mater.* **2020**.
- (92) Miller, M A et al. *Nat. Commun.* **2015**, *6* (1), 1–13.
- (93) Miller, M A et al. *Sci. Transl. Med.* **2015**, *7* (314).
- (94) Cheng, Y H et al. *ACS Nano* **2020**, *14* (3), 3075–3095.
- (95) Shi, Y et al. *Theranostics* **2020**, *10* (17), 7921–7924.
- (96) Fang, J et al. *Adv. Drug Deliv. Rev.* **2020**, *157*, 142–160.
- (97) Maeda, H et al. *Int. Immunopharmacol.* **2003**, *3* (3), 319–328.
- (98) Foroozandeh, P et al. *Nanoscale Res. Lett.* **2018**, *13* (1), 1–12.
- (99) Makvandi, P et al. *Nano Today* **2021**, *40*, 101279.
- (100) Jhaveri, A et al. *Expert Opin. Drug Deliv.* **2016**, *13* (1), 49–70.
- (101) Duro-Castano, A et al. *Adv. Mater.* **2017**, *29* (39).
- (102) Zagorodko, O et al. *Macromol. Biosci.* **2017**, *17* (1).
- (103) Kolb, H C et al. *Angew. Chemie Int. Ed.* **2001**, *40* (11), 2004–2021.
- (104) Deforest, C A et al. *Nat. Mater.* **2009**, *8* (8), 659–664.
- (105) Florinas, S et al. *Biomacromolecules* **2016**, *17* (5), 1818–1833.
- (106) Lowe, A B et al. *Polym. Chem.* **2014**, *5* (17), 4820–4870.
- (107) Gao, M et al. *Biomacromolecules* **2017**, *18* (12), 4349–4356.
- (108) Ruttala, H B et al. *Acta Biomater.* **2017**, *63*, 135–149.
- (109) Liu, Q et al. *Biomaterials* **2017**, *114*, 23–33.
- (110) Ren, J et al. *Biomacromolecules* **2013**, *14* (10), 3434–3443.
- (111) Yang, H et al. *Biomacromolecules* **2015**, *16* (4), 1372–1381.
- (112) Li, Y et al. *Biomacromolecules* **2018**, *19* (6), 2062–2071.
- (113) Córdoba-David, G et al. *Sci. Rep.* **2020**, *10* (1).
- (114) Zagorodko, O et al. *Macromol. Biosci.* **2017**, *17* (1), 1–22.

- (115) Conejos-Sánchez, I et al. *Nanoscale* **2020**, *12* (11), 6285–6299.
- (116) Vong, L B et al. *J. Control. Release* **2019**, *310* (June), 74–81.
- (117) Toshiyama, R et al. *Oncogene* **2019**, *38* (2), 244–260.
- (118) Zhang, C et al. *Acta Biomater.* **2017**, *55*, 153–162.
- (119) Ma, D et al. *Biomaterials* **2014**, *35* (14), 4357–4367.
- (120) Han, S S et al. *Small* **2015**, *11* (21), 2543–2554.
- (121) Takeda, K M et al. *Biomaterials* **2017**, *126*, 31–38.
- (122) Kaminskas, L M et al. *J. Control. Release* **2014**, *183*, 18–26.
- (123) Qi, R et al. *Nat. Commun.* **2017**, *8* (1).
- (124) Honary, S et al. *Trop. J. Pharm. Res.* **2013**, *12* (2), 265–273.
- (125) Thomas, S N et al. *Curr. Opin. Chem. Eng.* **2015**, *7*, 65–74.
- (126) Kavand, A et al. *J. Control. Release* **2020**, *321*, 285–311.
- (127) Pisarevsky, E et al. *Adv. Ther.* **2020**, *2000028*, 1–17.
- (128) El-sawy, H S et al. *ACS Nano* **2018**, *12* (11), 10636–10664.
- (129) Chen, B et al. *Theranostics* **2017**, *7* (3), 538–558.
- (130) Milane, L et al. *J. Control. Release* **2011**, *155* (2), 237–247.
- (131) Praveen, K et al. *ACS Appl. Bio Mater.* **2019**, *2* (10), 4162–4172.
- (132) Deirram, N et al. *Macromol. Rapid Commun.* **2019**, *40* (10), 1800917.
- (133) Tsuchikama, K et al. *Protein Cell* **2018**, *9* (1), 33–46.
- (134) Overall, C M et al. *Nat. Rev. Cancer* **2006**, *6* (3), 227–239.
- (135) Murphy, G et al. *Nat. Clin. Pract. Rheumatol.* **2008**, *4* (3), 128–135.
- (136) Aggarwal, N et al. *Proteomics - Clin. Appl.* **2014**, *8* (5–6), 427–437.
- (137) Kirschke, H et al. *Lysosomal Cysteine Proteinases*, 2nd ed.; Oxford University Press, 1998.
- (138) Van Heeswijk, W A R et al. *J. Control. Release* **1985**, *1*, 301–315.
- (139) Pan, H et al. *J. Drug Target.* **2006**, *14* (6), 425–435.
- (140) Bonzi, G et al. *Bioconjug. Chem.* **2015**, *26* (3), 489–501.
- (141) Segal, E et al. *PLoS One* **2009**, *4* (4).
- (142) Mochida, Y et al. *Expert Opin. Drug Deliv.* **2017**, *14* (12), 1423–1438.
- (143) Crommelin, D J A et al. *AAPS Adv. Pharm. Sci. Ser.* **2015**, *20*, 77–106.
- (144) Bekersky, I et al. *Antimicrob. Agents Chemother.* **2002**, *46* (3), 828–833.
- (145) Skoczen, S et al. *J. Control. Release* **2015**, *220* (Pt A), 169–174.
- (146) Mühlebach, S et al. *Adv. Drug Deliv. Rev.* **2018**, *131*, 122–131.
- (147) Melnyk, T et al. *Adv. Drug Deliv. Rev.* **2020**, *160*, 136–169.
- (148) U.S. Department of Health and Human Services Food and Drug Administration et al. *FDA* **2017**, No. December, Stability studies on rFVIII Fc drug substance. 1–14.
- (149) Hadjidemetriou, M et al. *Nat. Nanotechnol.* **2017**, *12* (4), 288–290.
- (150) Becker, G et al. *Nat. Nanotechnol.* **2015**, *11*, 327–377.
- (151) Weber, B et al. *Polymers (Basel)*. **2016**, *8* (12), 427.

- (152) Torrisi, V et al. *Biomacromolecules* **2014**, *15* (8), 3171–3179.
- (153) Papafilippou, L et al. *Nanoscale* **2020**, *12* (18), 10240–10253.
- (154) Wingard, J R et al. *Clin. Infect. Dis.* **2000**, *31* (5), 1155–1163.
- (155) Bertrand, N et al. *Nat. Commun.* **2017**, *8* (1), 777.
- (156) Casals, E et al. *ACS Nano* **2010**, *4* (7), 33623–33632.
- (157) Wang, D et al. *Proc. Natl. Acad. Sci. U. S. A.* **2013**, *110* (8), 2999–3004.
- (158) Mirshafiee, V et al. *Biomaterials* **2016**, *75*, 295–304.
- (159) Liu, Y et al. *Angew. Chemie* **2020**, *132* (12), 4750–4758.
- (160) Souiri, M et al. *Mater. Today Bio* **2022**, *13*, 100208.
- (161) Greco, F et al. *Adv. Drug Deliv. Rev.* **2009**, *61* (13), 1203–1213.
- (162) Arroyo-Crespo, J J et al. *Biomaterials* **2018**, *186*, 8–21.
- (163) Deshantri, A K et al. *J. Control. Release* **2018**, *287*, 194–215.
- (164) Laurencin, C T et al. *Clin. Lab. Med.* **1987**, *7* (2), 301–324.
- (165) Kamaly, N et al. *Chem. Rev.* **2016**, *116* (4), 2602–2663.
- (166) Song, W et al. *J. Control. Release* **2016**, *231*, 94–102.
- (167) Shaffer, S A et al. *Cancer Chemother. Pharmacol.* **2007**, *59* (4), 537–548.
- (168) Dobrovolskaia, M A et al. *J. Control. Release* **2015**, *220* (Pt B), 571–583.
- (169) Shaffer, S A et al. *Cancer Chemother. Pharmacol.* **2007**, *59* (4), 537–548.
- (170) Halamoda-Kenzaoui, B et al. *PLoS One* **2015**, *10* (10), e0141593.
- (171) *Nanotechnology Characterization Laboratory - NCI.*
<https://www.cancer.gov/nano/research/ncl> (accessed 2023-01-22).
- (172) Lorenz, S A et al. *J. Pharm. Sci.* **2002**, *91* (9), 2057–2066.
- (173) Yamada, Y et al. *ACS Omega* **2020**, *5* (51), 33235–33241.
- (174) Stig Pedersen-Bjergaard, B G et al. *Introduction to Pharmaceutical Analytical Chemistry, 2nd Edition | Wiley*, 2nd editio.; 2019.
- (175) Yuan, Y Y et al. *Adv. Mater.* **2012**, *24* (40), 5476–5480.
- (176) Huo, Q et al. *Int. J. Nanomedicine* **2017**, *12*, 8631–8647.
- (177) Alberg, I et al. *Small* **2020**, *16* (18), 1907574.
- (178) Holm, R et al. *Biomacromolecules* **2019**, *20* (1), 375–388.
- (179) Schafer, T et al. *Interactions Between Blood Proteins and Nanoparticles Investigated Using Molecular Dynamics Simulations*; Springer International Publishing: Cham, 2019.
- (180) Frenkel, D et al. *Understanding Molecular Simulation*; 1997.
- (181) MacKerell, A D et al. *J. Phys. Chem. B* **1998**, *102* (18), 3586–3616.
- (182) Moura, L I F et al. *J. Drug Target.* **2017**, *25* (9–10), 873–880.
- (183) Settanni, G et al. *Nanoscale* **2017**, *9* (6), 2138–2144.
- (184) Settanni, G et al. *Comput. Struct. Biotechnol. J.* **2018**, *16*, 543–550.
- (185) Balliu, A et al. *ChemBioChem* **2017**, *18* (14), 1408–1414.
- (186) Wang, H et al. *Eur. J. Pharm. Sci.* **2018**, *119* (2017), 189–199.
- (187) Dabrowiak, J C et al. *Drug Metab. Dispos.* **2002**, *30* (12), 1378–1384.

- (188) Mukherjee, S et al. *RSC Adv.* **2015**, 5 (94), 76987–76999.
- (189) Han, L et al. *AAPS J.* **2019**, 21 (3), 1–11.
- (190) Edwards, K A et al. *Talanta* **2006**, 68 (5), 1432–1441.
- (191) Gómez-Hens, A et al. *TrAC - Trends Anal. Chem.* **2006**, 25 (2), 167–178.
- (192) Chimanuka, B et al. *J. Pharm. Biomed. Anal.* **2002**, 28 (1), 13–22.
- (193) Wu, P C et al. *Int. J. Pharm.* **2004**, 271 (1–2), 31–39.
- (194) Junping, W et al. *Int. J. Pharm.* **2000**, 203 (1–2), 61–69.
- (195) Bellott, R et al. *J. Chromatogr. B Biomed. Sci. Appl.* **2001**, 757 (2), 257–267.
- (196) Maso, K et al. *J. Control. Release* **2020**, 324, 228–237.
- (197) Mehn, D et al. *Int. J. Pharm.* **2017**, 523 (1), 320–326.
- (198) Eldar-Boock, A et al. *J. Drug Target.* **2017**, 32 (15), 3862–3874.
- (199) Segers, K et al. *Bioanalysis* **2019**, 11 (24), 2297–2318.
- (200) Dunn, W B et al. *Nat. Protoc.* **2011**, 6 (7), 1060–1083.
- (201) Tiwari, G et al. *Pharm. Methods* **2010**, 1 (1), 25–38.
- (202) Hooshfar, S et al. *Biomed. Chromatogr.* **2017**, 31 (1).
- (203) Kataoka, H et al. *TrAC - Trends Anal. Chem.* **2003**, 22 (4), 232–244.
- (204) Rebane, R et al. *Eur. J. Mass Spectrom.* **2020**, 26 (1), 46–54.
- (205) Chen, L et al. *J. Chromatogr. Sci.* **2009**, 47 (8), 14–23.
- (206) Domingues, D S et al. *J. Chrom. B An. Techn. Biom. Life Sci* **2015**, 993–994, 26–35.
- (207) Dipe de Faria, H et al. *J. Chromatogr. A* **2017**, 1528, 41–52.
- (208) Wang, M et al. *Talanta* **2016**, 161, 278–287.
- (209) Acquaro, V R et al. *Bioanalysis* **2017**, 9 (6), 555–568.
- (210) Liu, L et al. *J. Chrom B An. Techn. Bio. Life Sci* **2012**, 893–894, 21–28.
- (211) Van den Ouweland, J M W et al. *J. Chromatogr. B Anal. Technol. Biomed. Life Sci.* **2012**, 883 (884), 18–32.
- (212) Mant, C T et al. *Methods Mol. Biol.* **2007**, 386, 3–55.
- (213) Aubry, A F et al. *Bioanalysis* **2011**, 3 (16), 1819–1825.
- (214) Q14 Analytical Procedure Development Guideline. <https://www.ema.europa.eu/en/ich-q14-analytical-procedure-development-scientific-guideline>.
- (215) Zeng, Q et al. *J. Pharm. Biomed. Anal.* **2019**, 169, 215–224.
- (216) Free, T et al. *Biotechniques* **2019**, 67 (5), 204–206.
- (217) Aebersold, R et al. *Nature* **2003**, 422 (6928), 198–207.
- (218) AB Sciex QTRAP 4500 LC-MS/MS instrument et al. .
- (219) Bergquist, J et al. *Anal. Bioanal. Chem.* **2018**, 410 (14), 3235–3237.
- (220) Leardi, R et al. *Anal. Chim. Acta* **2009**, 652 (1–2), 161–172.
- (221) Miller, J N et al. *Chemometrics for Analytical Chemistry*; 2005.
- (222) Politis, S N et al. *Drug Dev. Ind. Pharm.* **2017**, 43 (6), 889–901.
- (223) NIST et al. *Handbook 5. Process Improvement*.

<https://www.itl.nist.gov/div898/handbook/tooluids/pff/pri.pdf> (accessed 2023-01-01).

- (224) Hecht, E S et al. *J. Am. Soc. Mass Spectrom.* **2016**, 27 (5), 767–785.
- (225) Krueve, A et al. *Rapid Commun. Mass Spectrom.* **2010**, 24 (7), 919–926.
- (226) Hu, Y et al. *Anal. Bioanal. Chem.* **2020**, 412 (2), 425–438.
- (227) Alberg, I et al. *Small* **2020**, 16 (1907574).
- (228) Miller, T et al. *Pharm. Res.* **2012**, 29 (2), 448–459.
- (229) Barenholz, Y et al. *J. Control. Release* **2012**, 160 (2), 117–134.
- (230) Delmas, T et al. *J. Colloid Interface Sci.* **2011**, 360 (2), 471–481.
- (231) Caputo, F et al. *J. Control. Release* **2019**, 299, 31–43.
- (232) Gioria, S et al. *Nanomedicine* **2018**, 13 (5), 539–554.
- (233) Mehn, D et al. *EU-NCL Protocol: FFF-MALS Method Development and Measurements of Size and Molecular Weight*; 2016.
- (234) Duro-Castano, A et al. *Adv. Mater.* **2017**, 29 (39).
- (235) Martin, J D et al. *ACS Nano* **2019**, 13 (6), 6396–6408.
- (236) Song, Y et al. *J. Am. Chem. Soc.* **2017**, 139 (12), 4298–4301.
- (237) Yang, C et al. *Int. J. Pharm.* **2018**, 550 (1–2), 79–88.
- (238) Wang, M et al. *Bioconjug. Chem.* **2015**, 26 (4), 725–734.
- (239) Wang, Z et al. *J. Control. Release* **2017**, 264 (June), 66–75.
- (240) Conejos-Sánchez, I et al. *J. Control. Release* **2015**, 198, 80–90.
- (241) Zagorodko, O et al. *Polym. Chem.* **2020**, 11 (6), 1220–1229.
- (242) Quadir, M A et al. *Nanomedicine Nanotechnology, Biol. Med.* **2017**, 13 (5), 1797–1808.
- (243) Niño-Pariente, A et al. *Macromol. Biosci.* **2017**, 17 (10), 1–15.
- (244) Duro-Castano, A et al. *Adv. Mater.* **2017**, 29 (39), 1702888.
- (245) Guilbaud, J B et al. *Chem. Soc. Rev.* **2011**, 40 (3), 1200–1210.
- (246) Saiani, A et al. *Soft Matter* **2009**, 5 (1), 193–202.
- (247) Yu, H et al. *J. Agric. Food Chem.* **2010**, 58 (2), 1290–1295.
- (248) Lai, J et al. *RSC Adv.* **2015**, 5 (60), 48856–48860.
- (249) Arroyo-Crespo, J J et al. *Adv. Funct. Mater.* **2018**, 28 (22), 1800931.
- (250) Nevagi, R J et al. *Bioorganic Med. Chem.* **2019**, 27 (14), 3082–3088.
- (251) Bleher, S et al. *Small* **2019**, 15 (50), 1904716.
- (252) Muhl, C et al. *Eur. Polym. J.* **2019**, 120 (July), 109223.
- (253) Zhang, C et al. *Polym. Chem.* **2014**, 5 (18), 5227–5235.
- (254) Fee, C J et al. *Bioconjug. Chem.* **2004**, 15 (6), 1304–1313.
- (255) Schwiertz, D et al. *Polym. J.* **2020**, 52, 119–132.
- (256) Sui, B et al. *Molecules* **2014**, 19 (8), 11915–11932.
- (257) Song, W et al. *Acta Biomater.* **2014**, 10 (3), 1392–1402.
- (258) Yao, J et al. *Polym. Int.* **2019**, 68 (10), 1817–1825.
- (259) Gu, X et al. *Biomater. Sci.* **2018**, 6, 1526–1534.

- (260) Cölfen, H et al. In *Advances in Polymer Science*; 2000.
- (261) Rebolj, K et al. *Anal. Chem.* **2012**, *84* (17), 7374–7383.
- (262) Williams, P S et al. *Philos. Trans. R. Soc. A* **2010**, *368* (1927), 4419–4437.
- (263) Orita, T et al. *Anal. Sci.* **2013**, *29* (7), 761–764.
- (264) Carpino, F et al. *J. Magn. Magn. Mater.* **2005**, *293* (1), 546–552.
- (265) Williams, P S et al. *Mol. Pharm.* **2009**, *6* (5), 1290–1306.
- (266) Faisant, N et al. *J. Sep. Sci.* **2003**, *26* (15–16), 1407–1416.
- (267) Contado, C et al. *Anal. Bioanal. Chem.* **2013**, *405* (2–3), 703–7011.
- (268) Ratanathanawongs Williams, S K et al. *J. Sep. Sci.* **2006**, *29* (12), 1720–1732.
- (269) Wagner, M et al. *Anal. Chem.* **2014**, *86* (11), 5201–5210.
- (270) Boye, S et al. *Biomacromolecules* **2012**, *13* (12), 4222–4235.
- (271) Kuklenyik, Z et al. *Chromatography* **2015**, *2*, 96–117.
- (272) Zattoni, A et al. *J. Chromatogr. Sci.* **2000**, *38* (3), 122–128.
- (273) Galyean, A A et al. *J. Chromatogr. A* **2016**, *1473*, 122–132.
- (274) Lederer, A et al. *LC GC Eur.* **2011**, *0* (0), 620–628.
- (275) López-Sanz, S et al. *Anal. Chim. Acta* **2019**, *1053*, 178–185.
- (276) Engel, A et al. *Int. J. Pharm.* **2014**, *461* (1–2), 137–144.
- (277) Hadjidemetriou, M et al. *Biomaterials* **2019**, *188*, 118–129.
- (278) Sheibani, S et al. *Nat. Commun.* **2021**, *12* (1), 1–9.
- (279) Wahlund, K G et al. *Anal. Chem.* **1987**, *59* (9), 1332–1339.
- (280) Giddings, J C et al. *Science (80-.)*. **1993**, *260* (5113), 1456–1465.
- (281) Zheng, F et al. *Nanophotonics* **2019**, *8* (3), 391–413.
- (282) Li, T et al. *ACS Nano* **2019**, *13* (3), 3691–3702.
- (283) Cheah, H Y et al. *Mol. Pharm.* **2018**, *15* (7), 2594–2605.
- (284) Córdoba-David, G et al. *Sci. Rep.* **2020**, *10* (1), 1–15.
- (285) Negwer, I et al. *Nat. Commun.* **2018**, *9* (1), 1–9.
- (286) Swales, J G et al. *Int. J. Mass Spectrom.* **2019**, *437*, 99–112.
- (287) Torok, S et al. *Br. J. Pharmacol.* **2015**, *172* (4), 1148–1163.
- (288) Buck, A et al. *Anal. Bioanal. Chem.* **2015**, *407* (8), 2107–2116.
- (289) Liu, X et al. *J. Am. Soc. Mass Spectrom.* **2018**, *29* (3), 516–526.
- (290) Huber, K et al. *Anal. Chem.* **2014**, *86* (21), 10568–10575.
- (291) Liu, X et al. *Anal. Chem.* **2018**, *90* (24), 14156–14164.
- (292) Morosi, L et al. *PLoS One* **2013**, *8* (8), e72532.
- (293) Cesca, M et al. *Mol. Cancer Ther.* **2016**, *15* (1), 125–135.
- (294) Barré, F P Y et al. *Anal. Chem.* **2018**, *90* (24), 14198–14206.
- (295) Paine, M R L et al. *Sci. Rep.* **2019**, *9* (1), 1–10.
- (296) Giordano, S et al. *Sci. Rep.* **2016**, *6* (1), 1–8.
- (297) Yasunaga, M et al. *Sci. Rep.* **2013**, *3* (1), 1–6.
- (298) Ashton, S et al. *Sci. Transl. Med.* **2016**, *8* (325).
- (299) Caprioli, R M et al. *Anal. Chem.* **1997**, *69* (23), 4751–4760.

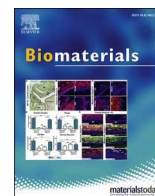
- (300) Kompauer, M et al. *Nat. Methods* **2017**, *14* (1), 90–96.
- (301) Chughtai, K et al. *Chem. Rev.* **2010**, *110* (5), 3237.
- (302) Greer, T et al. *J. Proteomics* **2011**, *74* (12), 2617–2631.
- (303) Jove, M et al. *Crit. Rev. Oncol. Hematol.* **2019**, *141* (2018), 153–162.
- (304) Granborg, J R et al. *TrAC Trends Anal. Chem.* **2022**, *146*, 116482.
- (305) Davoli, E et al. *Mass Spectrom. Rev.* **2021**, *40* (3), 201–214.
- (306) Lamont, L et al. *Anal. Bioanal. Chem.* **2021**, *413* (10), 2779–2791.
- (307) Schwamborn, K et al. *Nat. Rev. Cancer* **2010**, *10* (9), 639–646.
- (308) Goodwin, R J A et al. *J. Proteomics* **2012**, *75* (16), 4893–4911.
- (309) Zhu, X et al. *Front. Chem.* **2022**, *9*, 1076.
- (310) Goodwin, R J A et al. *Proteomics* **2008**, *8* (18), 3801–3808.
- (311) Trim, P J et al. *Methods Mol. Biol.* **2017**, *1618*, 175–189.
- (312) Ly, A et al. *Nat. Protoc.* **2016**, *11* (8), 1428–1443.
- (313) Cobice, D F et al. *Br. J. Pharmacol.* **2015**, *172* (13), 3266–3283.
- (314) Dannhorn, A et al. *Anal. Chem.* **2020**, *92* (16), 11080–11088.
- (315) Diehl, H C et al. *Anal. Bioanal. Chem.* **2015**, *407* (8).
- (316) Cillero-Pastor, B et al. *J. Proteome Res.* **2014**, *13* (2), 325–335.
- (317) Zhou, Q et al. *Anal. Bioanal. Chem.* **2020**, *413* (10), 2599–2617.
- (318) Perry, W J et al. *J. Mass Spectrom.* **2020**, *55* (4), e4491.
- (319) Calvano, C D et al. *Anal. Bioanal. Chem.* **2018**, *410* (17), 4015–4038.
- (320) Bowman, A P et al. *Anal. Chem.* **2020**, *92* (4), 3133–3142.
- (321) Spraggins, J M et al. *Anal. Chem.* **2019**, *91* (22), 14552–14560.
- (322) Soltwisch, J et al. *Anal. Chem.* **2020**, *92* (13), 8697–8703.
- (323) Niehaus, M et al. *Nat. Methods* **2019**, *16* (9), 925–931.
- (324) He, Q et al. *TrAC - Trends Anal. Chem.* **2021**, *136*.
- (325) Bergquist, J et al. *Anal. Bioanal. Chem.* **2018**, *410* (14), 3235–3237.
- (326) Giraldo, E et al. *Biomaterials* **2021**, *276*.
- (327) Kromidas, S et al. *Gradient HPLC for Practitioners - RP, LC-MS, Ion Analytics, Biochromatography, SFC, HILIC*; 2019.
- (328) Raji, M A et al. *Int. J. Mass Spectrom.* **2009**, *279* (2–3), 100–106.
- (329) Charles, L et al. *Eur. J. mass Spectrom.* **2005**, *11* (4), 361–370.
- (330) Leardi, R et al. *Anal. Chim. Acta* **2009**, *652* (1–2), 161–172.
- (331) Priyadarsini, K I et al. *Molecules* **2014**, *19* (12), 20091–20112.
- (332) Wright, J S et al. *J. Mol. Struct.* **2002**, *591* (1–3), 207–217.
- (333) Xu, Y Y et al. *Bioorganic Med. Chem.* **2013**, *21* (2), 388–394.
- (334) Yadav, I S et al. *Gene* **2014**, *539* (1), 82–90.
- (335) Yim-im, W et al. *BMC Bioinformatics* **2014**, *15* (1).
- (336) Davis, B et al. *Pharm. Qual. by Des. A Pract. Approach* **2017**, 1–9.
- (337) Kostic, N et al. *J. Mass Spectrom.* **2013**, *48* (7), 875–884.
- (338) Crommelin, D J A et al. **2015**, *20*.

- (339) Troiano, G et al. *AAPS J.* **2016**, *18* (6), 1354–1365.
- (340) Puri, V et al. *Pharmaceutics* **2022**, *14* (10).
- (341) Abdulla, A et al. *Adv. Ther.* **2020**, *3* (7), 2000034.
- (342) Giraldo, E et al. *Cells* **2022**, *11* (20), 3304.
- (343) Lepland, A et al. *Cancer Res. Commun.* **2022**, *2* (6), 533–551.
- (344) Dai, W et al. *Adv. Drug Deliv. Rev.* **2017**, *115*, 23–45.
- (345) Vogus, D R et al. *Curr. Opin. Colloid Interface Sci.* **2017**, *31*, 75–85.
- (346) Burrell, R A et al. *Nature* **2013**, *501* (7467), 338–345.
- (347) Tolcher, A W et al. *Future Oncol.* **2018**, *14* (13), 1317–1332.
- (348) Ronson, A et al. *Expert Opin. Orphan Drugs* **2017**, *5* (4), 369–374.
- (349) Arroyo-Crespo, J J et al. *Adv. Funct. Mater.* **2018**, *28* (22), 1800931.
- (350) Zagorodko, O et al. *Polym. Chem.* **2021**, *12* (23), 3478–3487.
- (351) Manickam, B et al. *Curr. Drug Deliv.* **2014**, *11* (1), 139–145.
- (352) Yohannes, G et al. *J. Chromatogr. A* **2011**, *1218* (27), 4104–4116.
- (353) Fievet, P et al. *J. Memb. Sci.* **2000**, *168* (1–2), 87–100.
- (354) Zhu, Y et al. *Anal. Biochem.* **2007**, *363* (1), 119–127.
- (355) Duro-Castano, A et al. *Adv. Mater.* **2017**.
- (356) Alasonati, E A et al. *J. Sep. Sci.* **2007**, *30* (14), 2332–2340.
- (357) Benincasa, M-A et al. *J. Chromatogr. A* **2002**, 219–234.
- (358) Alberg, I et al. *Small* **2020**.
- (359) Pitkänen, L et al. *Analyst* **2014**, *139* (22), 5843–5851.
- (360) Quattrini, F et al. *Drug Deliv. Transl. Res.* **2021**, *11* (2), 373.
- (361) Murray, P M et al. *Org. Biomol. Chem* **2016**, *14*, 2373.
- (362) Murray, P M et al. *Org. Process Res. Dev.* **2013**, *17* (1), 40–46.
- (363) Weissman, S A et al. *Org. Process Res. Dev.* **2015**, *19* (11), 1605–1633.
- (364) Arboretti, R et al. *Qual. Reliab. Eng. Int.* **2022**, *38* (2), 1131–1156.
- (365) Hashiba, A et al. *J. Control. Release* **2020**, *327*, 467–476.
- (366) Kunishima, M et al. *Tetrahedron* **1999**, *55* (46), 13159–13170.
- (367) Crown, J et al. *Ann. Oncol.* **2012**, *23*, vi56–vi65.
- (368) Niño-pariente, A et al. *Curr. Pharm. Des.* **2016**, *22*, 1274–1291.
- (369) Arroyo-Crespo, J J et al. *Adv. Funct. Mater.* **2018**, *28* (22).
- (370) Barz, M et al. *Polym. Chem.* **2013**, *4* (10), 2989–2994.
- (371) Vogus, D R et al. *Curr. Opin. Colloid Interface Sci.* **2017**, *31*, 75–85.
- (372) Clevers, H et al. *Cell* **2016**, *165* (7), 1586–1597.
- (373) Sachs, N et al. *Cell* **2018**, *172* (1–2), 373–386.e10.
- (374) Boix-Montesinos, P et al. *Adv. Drug Deliv. Rev.* **2021**, *173*, 306–330.
- (375) Kennedy, L et al. *Biomolecules* **2020**, *10* (10), 1–27.
- (376) Végvári, Á et al. *J. Proteomics* **2010**, *73* (6), 1270–1278.
- (377) Goodwin, R J A et al. *J. Proteomics* **2012**, *75* (16), 4893–4911.
- (378) Mori, N et al. *Front. Oncol.* **2016**, *6*, 262.

- (379) De Molina, A R et al. *Oncogene* **2002**, *21* (27), 4317–4322.
- (380) Cheng, M et al. *Front. Oncol.* **2016**, *6*.
- (381) Pietkiewicz, D et al. *Pharmaceuticals (Basel)*. **2021**, *14* (8).
- (382) Jin, Y et al. *Interational J. Mol. Sci.* **2018**, *19* (907).
- (383) Yang, L et al. *J. Cancer* **2020**, *11* (9), 2540–2551.
- (384) Leij-Halfwerk, S et al. *Am. J. Clin. Nutr.* **2000**, *71* (2), 583–589.
- (385) Tanner, J J et al. *Biochemistry* **2018**, *57* (25), 3433–3444.
- (386) Phang, J M et al. *Antioxidants Redox Signal.* **2019**, *30* (4), 635–649.
- (387) Palka, J et al. *Amino Acids* **2021**, *53* (12), 1917–1925.
- (388) Stewart, D A et al. *J. Proteome Res.* **2016**, *15* (9), 3225.
- (389) Fan, T W M et al. *Pharmacol. Ther.* **2012**, *133* (3), 366–391.
- (390) Lane, A N et al. *OMICS* **2011**, *15* (3), 173.
- (391) Pralea, I E et al. *J. Pers. Med.* **2020**, *10* (4), 1–16.
- (392) Nierode, G et al. *J. Microbiol. Biotechnol.* **2016**, *26* (2), 213.
- (393) Liu, X et al. *Sci. Rep.* **2016**, *6*.
- (394) Lukowski, J K et al. *Anal. Chem.* **2017**, *89* (16), 8453–8458.
- (395) Feist, P E et al. *Anal. Chem.* **2017**, *89* (5), 2773–2781.
- (396) Labonia, G J et al. *Anal. Chem.* **2018**, *90* (2), 1423–1430.
- (397) He, M J et al. *Front. Oncol.* **2022**, *12*, 3485.
- (398) Barré, F P Y et al. *Anal. Chem.* **2019**, *91* (16), 10840–10848.
- (399) Shariatgorji, M et al. *Anal. Chem.* **2012**, *84* (10), 4603–4607.
- (400) Miura, D et al. *J. Proteomics* **2012**, *75* (16), 5052–5060.
- (401) Wishart, D S et al. *Expert Rev. Proteomics* **2014**, *4* (3), 333–335.
- (402) Hanahan, D et al. *Cell* **2011**, *144* (5), 646–674.
- (403) Glunde, K et al. *Nat. Rev. Cancer* **2011**, *11* (12), 835.
- (404) Liesenfeld, D B et al. *Cancer Epidemiol. Biomarkers Prev.* **2013**, *22* (12), 2182.
- (405) Bhatia, S N et al. *Nat. Rev. Cancer* **2022**, *22* (10), 550–556.
- (406) Zhang, Y et al. *Adv. Healthc. Mater.* **2021**, *10* (11), 2001974.
- (407) Aderibigbe, B A et al. *Polymer Therapeutics: Design, Application, and Pharmacokinetics*; Elsevier Inc., 2017.
- (408) Li, C et al. *Adv. Drug Deliv. Rev.* **2008**, *60* (8), 886–898.
- (409) Wang, Q et al. *RSC Adv.* **2020**, *10* (41), 24397–24409.
- (410) Jorgenson, T C et al. *Cancer Res.* **2013**, *73* (20), 6118.
- (411) Brülisauer, L et al. *J. Control. Release* **2014**, *195*, 147–154.
- (412) Blencowe, C A et al. *Polym. Chem.* **2011**, *2* (4), 773–790.
- (413) Bach, R D et al. *J. Org. Chem.* **2008**, *73* (1), 12–21.
- (414) Lee, M H et al. *Acc. Chem. Res.* **2015**, *48* (11), 2935–2946.
- (415) Zhang, D et al. *ACS Med. Chem. Lett.* **2016**, *7* (11), 988–993.
- (416) Guo, X et al. *J. Nanobiotechnology* **2018**, *16* (1), 1–10.
- (417) Zhang, X et al. *Mater. Chem. Front.* **2017**, *1* (5), 807–822.

- (418) Wang, Y et al. *J. Control. Release* **2018**, 279, 136–146.
- (419) Jain, A K et al. *Bioorg. Chem.* **2013**, 49, 40–48.
- (420) Deng, Z et al. *Macromol. Rapid Commun.* **2020**, 41 (1), 1–14.
- (421) Huang, X et al. *J. Control. Release* **2001**, 73 (2–3), 121–136.
- (422) Zheng, Y et al. *ChemMedChem* **2019**, 14 (12), 1196–1203.
- (423) Qian, L et al. *Angew. Chem. Int. Ed. Engl.* **2018**, 57 (6), 1532–1536.
- (424) Sun, T et al. *Chem. Commun.* **2015**, 51 (26), 5721–5724.
- (425) Lendrem, D W et al. *Drug Discov. Today* **2015**, 20 (11), 1365–1371.
- (426) Hsu, C Y et al. *BMC Cancer* **2015**, 15 (1), 1–9.
- (427) Barbosa, M A G et al. *Cancers (Basel)*. **2021**, 14 (1).
- (428) Wu, G et al. *J. Nutr.* **2004**, 134 (3), 489–492.
- (429) Go, Y M et al. *Biochim. Biophys. Acta* **2008**, 1780 (11), 1273–1290.
- (430) Arunachalam, B et al. *Proc. Natl. Acad. Sci. U. S. A.* **2000**, 97 (2), 745–750.
- (431) Adhikari, S et al. *Proc. Natl. Acad. Sci. U. S. A.* **2020**, 117 (31), 18216–18223.
- (432) Tu, J et al. *J. Am. Chem. Soc.* **2018**, 140 (27), 8410–8414.
- (433) Stöckmann, H et al. *Org. Biomol. Chem.* **2011**, 9 (21), 7303–7305.
- (434) Shao, Z et al. *Chem. Commun.* **2018**, 54 (100), 14089–14092.
- (435) Haba, K et al. *Angew. Chemie Int. Ed.* **2005**, 44 (5), 716–720.
- (436) Huvelle, S et al. *Org. Biomol. Chem.* **2017**, 15 (16), 3435–3443.
- (437) Deng, Z et al. *Macromol. Rapid Commun.* **2020**, 41 (1), 1900531.
- (438) Mura, S et al. *Nat. Mater.* **2013**, 12 (11), 991–1003.
- (439) Schafer, F Q et al. *Free Radic. Biol. Med.* **2001**, 30 (11), 1191–1212.
- (440) Vollhardt, P et al. *Organic Chemistry: Structure and Function*, 8th ed.; 2018.
- (441) Ni, D et al. *Small* **2015**, 11 (21), 2518–2526.
- (442) Bugno, J et al. *Mol. Pharm.* **2016**, 13 (7), 2155–2163.
- (443) Goodman, T T et al. *Int. J. Nanomedicine* **2007**, 2 (2), 265.
- (444) Goodman, T T et al. *Biotechnol. Bioeng.* **2008**, 101 (2), 388–399.
- (445) Zhang, C et al. *Biomater. Sci.* **2019**, 7 (11), 4738–4747.
- (446) Lazzari, G et al. *Polym. Chem.* **2017**, 8 (34), 4947–4969.
- (447) Brülisauer, L et al. *J. Control. Release* **2014**, 195, 147–154.
- (448) Hecht, E S et al. *J. Am. Soc. Mass Spectrom.* **2016**, 27 (5), 767–785.
- (449) Bauhuber, S et al. *Adv. Mater.* **2009**, 21 (32–33), 3286–3306.
- (450) Landesman-Milo, D et al. *Bioconjug. Chem.* **2016**, 27 (4), 855–862.
- (451) Coty, J B et al. *J. Control. Release* **2018**, 275, 254–268.
- (452) Brembs, B et al. *Front. Hum. Neurosci.* **2018**, 12, 37.
- (453) Sharifi, S et al. *ACS Nano* **2022**, 17 (1), 4–11.
- (454) Théry, C et al. *J. Extracell. Vesicles* **2018**, 7 (1).
- (455) Richardson, J J et al. *Nano Lett.* **2020**, 20 (3), 1481–1482.
- (456) Faria, M et al. *Nat. Nanotechnol.* **2018**, 13, 777–785.
- (457) Weeks, C A et al. *ACS Biomater. Sci. Eng.* **2016**, 2 (12), 2196–2206.

- (458) Hassan, P A et al. *Functional Materials*; 2012.
- (459) Sinha, S et al. *Pharmaceutical Medicine and Translational Clinical Research*; Elsevier Inc., 2018.
- (460) Gad, S C et al. *Pharmaceutical Sciences Encyclopedia*; 2010.
- (461) Huang, R Y C et al. *Drug Discov. Today* **2016**, 21 (5), 850–855.
- (462) Gorovits, B et al. *Comprehensive Medicinal Chemistry III*, Third Edit.; Elsevier, 2017; Vol. 6.
- (463) Van den Broek, I et al. *J. Chromatogr. B Anal. Technol. Biomed. Life Sci.* **2013**, 929, 161–179.
- (464) Upadhya, R et al. *Adv. Drug Deliv. Rev.* **2021**, 171, 1–28.
- (465) Singh, B et al. *Crit. Rev. Ther. Drug Carrier Syst.* **2005**, 22 (3), 215–293.
- (466) Singh, B et al. *Crit. Rev. Ther. Drug Carrier Syst.* **2020**, 37 (3), 229–269.
- (467) Sarapa, N et al. *Cancer Chemother. Pharmacol.* **2003**, 52 (5), 424–430.
- (468) Mackean, M et al. *J. Clin. Oncol.* **1998**, 16 (9), 2977–2985.
- (469) Schüller, J et al. *Cancer Chemother. Pharmacol.* **2000**, 45 (4), 291–297.



A rationally designed self-immolative linker enhances the synergism between a polymer-rock inhibitor conjugate and neural progenitor cells in the treatment of spinal cord injury

E. Giraldo^{a,b}, V.J. Nebot^{c,d}, S. Đorđević^c, R. Requejo-Aguilar^{a,e}, A. Alastrue-Agudo^a, O. Zagorodko^c, A. Armiñan^c, B. Martinez-Rojas^a, M.J. Vicent^{c,*}, V. Moreno-Manzano^{a,**}

^a Neuronal and Tissue Regeneration Lab. Prince Felipe Research Institute, Valencia, Spain

^b Department of Biotechnology. Universitat Politècnica de València, Valencia, Spain

^c Polymer Therapeutics Lab. Prince Felipe Research Institute, Valencia, Spain

^d PTS S.L., Valencia, Spain

^e Dept. Biochemistry and Molecular Biology, University of Cordoba, Cordoba, Spain. Maimonides Biomedical Research Institute of Córdoba (IMIBIC), Cordoba, Spain

ARTICLE INFO

Keywords:

Polymer therapeutics
Polymer-drug conjugates
Fasudil
Spinal cord injury
Axonal elongation
Neuroprotection
RhoA/ROCK Inhibitor

ABSTRACT

Rho/ROCK signaling induced after spinal cord injury (SCI) contributes to secondary damage by promoting apoptosis, inflammation, and axon growth inhibition. The specific Rho-kinase inhibitor fasudil can contribute to functional regeneration after SCI, although inherent low stability has hampered its use. To improve the therapeutic potential of fasudil, we now describe a family of rationally-designed bioresponsive polymer-fasudil conjugates based on an understanding of the conditions after SCI, such as low pH, enhanced expression of specific proteases, and a reductive environment. Fasudil conjugated to poly-L-glutamate via a self-immolative redox-sensitive linker (PGA-SS-F) displays optimal release kinetics and, consequently, treatment with PGA-SS-F significantly induces neurite elongation and axon growth in dorsal root ganglia explants, spinal cord organotypic cultures, and neural precursor cells (NPCs). The intrathecal administration of PGA-SS-F after SCI in a rat model prevents early apoptosis and induces the expression of axonal growth- and neuroplasticity-associated markers to a higher extent than the free form of fasudil. Moreover, a combination treatment comprising the acute transplantation of NPCs pre-treated with PGA-SS-F leads to enhanced cell engraftment and reduced cyst formation after SCI. In chronic SCI, combinatory treatment increases the preservation of neuronal fibers. Overall, this synergistic combinatorial strategy may represent a potentially efficient clinical approach to SCI treatment.

1. Introduction

The efficient treatment of spinal cord injury (SCI) remains challenging due to the dynamic and progressive nature of the condition conferred by the intrinsic pathological cascades involved. The implementation of complementary neuroprotective and neuroregenerative interventions represents one potential strategy to limit/rescue the neurological deficits induced by the secondary injury phase (previously reviewed by Ahuja and Fehlings [1]). The secondary injury phase involves the necrosis and/or apoptosis of neurons and glia, such as oligodendrocytes, thereby prompting demyelination and a loss of efficient neuronal connectivity. Furthermore, the induction of an ischemic

environment leads to ongoing edema, vessel thrombosis, and vaso-spasms, while persistent inflammatory cell infiltration causes the continuing formation of toxic cystic microcavities. Astrocytes, fibroblasts, and pericytes proliferate and deposit extracellular matrix factors into the perilesional area in the intermediate and chronic phases when damaged axons continue to degenerate (previously reviewed by Bradbury and Burnside [2]). Overall, studies attribute both microenvironmental extrinsic factors and a limited intrinsic axon regrowth capacity to the lack of spontaneous regeneration observed during and after chronic stage injury.

RhoA/ROCK activation represents a major intrinsic inhibitory signal for axonal regrowth [3] by promoting apoptosis, growth cone collapse in

* Corresponding authors.

** Corresponding authors.

E-mail addresses: mjvicent@cipf.es (M.J. Vicent), vmorenom@cipf.es (V. Moreno-Manzano).

<https://doi.org/10.1016/j.biomaterials.2021.121052>

Received 29 January 2021; Received in revised form 4 July 2021; Accepted 24 July 2021

Available online 29 July 2021

0142-9612/© 2021 The Authors.

Published by Elsevier Ltd.

This is an open access article under the CC BY-NC-ND license

(<http://creativecommons.org/licenses/by-nc-nd/4.0/>).

regenerating axons, and subsequent neurite retraction [4]. For these reasons, RhoA/ROCK activation also represents a critical therapeutic target [5]. The RhoA/ROCK inhibitor fasudil (1-(5-isoquinolinesulfonyl)-homopiperazine) can suppress secondary damage by reducing edema, inflammatory cell infiltration, cyst cavitation, and massive apoptosis in acute stage SCI [6]. While the application of fasudil in the treatment of subarachnoid hemorrhage has provided evidence of safety, fasudil displays limited clinical efficacy [7], perhaps due to a short half-life and, of significant note for SCI treatment, a lack of penetration through the blood-brain barrier [8]. These problems, alongside the requirement to improve the site-specific activity and bioavailability, have prompted the exploration of nanocarrier formulations as a potential solution, with the vast majority taking advantage of drug encapsulation [9]. Studies have also provided evidence for the utility of rationally designed polymer-drug conjugates [10,11] as novel therapeutics for SCI using neuroprotectants such as curcumin [12].

Polypeptide-based polymers, particularly poly-L-glutamic acid (PGA), are biocompatible, biodegradable, and multifunctional nanocarriers that allow for high drug loading capacity [13,14]. Polypeptides have been employed as building blocks in the development of polymer-drug conjugates and polymeric micelles for various medical applications [13]. The routine clinical use of Copaxone® [13,14] and the promising clinical results observed with polypeptidic micelles [15] and Opaxio® [13,14,16] have underscored the potential of synthetic polypeptides. Conjugated active agents can be released from PGA thanks to the activity of proteases such as lysosomal protease cathepsin B [17] after engineering polymer side chains [18]. Furthermore, post-polymerization modification reactions provide orthogonal reactive attachment sites for a variety of functionalities for further bioconjugation [19], thereby allowing the conjugation of drugs through rationally-designed bioresponsive linkers that can modify drug release kinetics at sites of injury, such as SCI. Said linkers include those that display pH-responsiveness [12,20] or redox-sensitivity [13,14]. Additional aspects of PGAs that support their application in SCI treatment include an inherently negative z-potential that facilitates the targeting of inflamed areas [21]. Of note, synthetic challenges related to the tight control of PGA properties have been overcome through the development of precise and controlled reactions and characterization steps to yield well-defined polypeptidic architectures [22–24].

In addition to the formation of a permissive platform bridging the extrinsic inhibitory microenvironment in SCI, cell transplantation also affords neuroprotection and prompts immunomodulation [1]. The transplantation of fetal neural progenitor cells (NPCs) [25,26] and induced pluripotent stem cells (iPSCs) [27] have provided promising results in terms of repair and neuronal regeneration [28]. Interestingly, regenerating endogenous axons navigate through NPC grafts to their appropriated sensory and motor targets, indicating that cell transplantation can correctly guide re-innervation without additional exogenous signals [29]. NPCs include multipotent stem cells present in the ependymal region lining the spinal cord's central canal [30], which represent ideal candidates for stem cell therapy due to the functional improvements observed after transplantation and the absence of malignant transformation. We previously established that NPC transplantation in both acute [31–33] and chronic [12] traumatic SCI led to the rescue of voluntary locomotion after one week. Contributing mechanisms induced by NPC transplantation include trophic support, immunomodulation, and the reduction of inhibitory mediators, such as the purinergic receptors associated with neurodegenerative and neuropathic pain. Overall, NPC transplantation can drive the formation of a microenvironment conducive to the preservation of neurons, a reduction in the number of cavities, and the inhibition of scar formation.

Even given these promising results, the limited functional and anatomical improvements obtained in rat models, with poor cell survival as a significant contributor, suggest that NPC transplantation alone will fail to provide sufficient gain of function to foster further clinical development. We have demonstrated that combining a rationally-

designed bioresponsive polyacetal-curcumin conjugate with NPC transplantation significantly enhances therapeutic outcomes via an anti-inflammatory effect and axonal growth via the inhibition of RhoA/ROCK signaling [12]. Herein, we demonstrate that a combination of NPC transplantation and an improved nanoformulation of a Rho kinase inhibitor (fasudil) may represent an efficient alternative treatment for SCI. We developed and optimized a family of bioresponsive PGA-based fasudil conjugates and found that the best candidate, which employed a redox-triggered self-immolative linker, synergized with NPCs to trigger significant levels of axonal regrowth in organotypic cultures, enhanced cell engraftment and a certain locomotor skill recovery in an SCI model after acute administration, and neuronal fiber preservation in a chronic SCI model.

2. Materials and methods

2.1. Synthesis of Poly-L-glutamate (PGA)-Fasudil conjugates

Experimental details for the synthesis of intermediate compounds and final conjugates and the physico-chemical characterization are detailed in the Supporting Information (1. Materials and Experimental Techniques; 2. Synthesis and Physico-chemical Characterization of PGA-X-F Conjugates).

2.2. Fasudil Release Kinetics from conjugates under physiological conditions

2.2.1. pH-dependent drug release kinetics

Specific fasudil release under mildly acidic conditions was demonstrated *in vitro* by incubating the conjugates at 2 mg/mL in phosphate-buffered saline (PBS) at pH 7.4 and pH 5.0, mimicking the blood and tumor (and/or lysosomal) environment, respectively. At determined time points, 100 μ L aliquots were made up to 1 mL with phosphate buffer (PB) pH 7.4 in a 15 mL tube. Liquid-liquid extraction of released fasudil and its quantification by reversed-phase high-performance liquid chromatography (RP-HPLC) was performed employing a Waters instrument equipped with an autosampler (Waters 717), two binary pumps, and a photodiode array detector (Waters 2996). Detection was carried out at $\lambda = 323$ nm (peak characteristic of the drug, mobile phase: H₂O (1 % NH₃)/MeOH (40/60), at a retention time of 6 min) using a column InertSustain C18, 5 μ m, 4.6 \times 250 mm modified with octadecylsilyl groups. The injection volume was 20 μ L, while the flow rate of the mobile phase was set at 1.0 mL/min. The calibration curve was generated using fasudil, showing a linear response within the concentration range employed (1.5–20 μ g/mL).

2.2.2. Cathepsin B-dependent drug release kinetics

Cathepsin B (5 U) was added to a solution of 2 mg of each conjugate in 1 mL of a pH 6 buffer composed of 20 mM sodium acetate, 2 mM ethylenediaminetetraacetic acid (EDTA), and 5 mM dithiothreitol (DTT). The incubation was carried out at 37 °C. Aliquots (100 μ L) were taken at times up to 72 h, immediately frozen in liquid nitrogen, and stored in the absence of light until assayed by HPLC, as described above. The free drug (0.2 mg/mL) was also incubated under the same conditions and later used as the reference control to determine the percentage of release, as was a control solution without cathepsin B.

2.2.3. Redox-dependent drug release kinetics

DTT (100 μ L of 50 mM or 100 μ M solution in PBS) was added to a solution of 2 mg of PGA-SS-F (the equivalent of 0.236 mg/mL of fasudil) in 0.9 mL PBS to obtain a final DTT concentration of 5 mM or 100 μ M. The incubation was carried out at 37 °C. Aliquots (100 μ L) were taken at times up to 72 h and assayed by HPLC, as described above.

2.3. Stability of PGA-SS-F in plasma and cell medium

The stability studies of the PGA-SS-F conjugate was carried out by spiking blank human plasma and cell medium with the appropriate working solutions to achieve concentrations of 400 µg/mL PGA-SS-F and 1 ng/mL ranitidine as an internal standard (IS). Plasma samples were incubated at 37 °C and aliquots taken at 0, 2, 4, 6, and 24 h. Subsequently, 250 µL of acetonitrile was added to 100 µL of collected plasma and cell medium aliquots, followed by vortex-mixing for 30 s and centrifugation at 11,000 rpm for 5 min. Supernatants were then carefully removed, transferred to new tubes, and evaporated under nitrogen. The residue was reconstituted in 100 µL of the mobile phase, followed by vortex-mixing for 1 min. Finally, 20 µL of each solution was injected for liquid chromatography-mass spectrometry (LC-MS/MS) analysis.

2.3.1. LC-MS/MS method for determination of fasudil in plasma and cell medium

Chromatographic analysis was performed using an ExionLC system comprising of a Pump, AC Autosampler, AC Column oven, and AB Sciex QTRAP 4500 (all Sciex, Singapore). The initial mobile phase composition was acetonitrile:formic acid (0.1%) (20:80, v/v). All runs were performed using a Phenomenex Luna®-C18 column (4.6 mm × 30 mm, 5 µm), which was maintained at 40 °C. The injection volume was 10 µL, while the flow rate of the mobile phase was set at 0.4 mL/min. Fasudil and ranitidine as IS were detected in positive electrospray mode, with multiple reactions monitoring scan and by following two mass transitions 292.4 m/z → 99.2 m/z and 292.4 → 129.0 m/z for fasudil, and 315.2 m/z → 101.9 m/z and 315.2 m/z → 130.0 m/z for ranitidine. The LC-MS/MS method was developed using an experimental design approach, where the percentage of acetonitrile, percentage of formic acid, and flow rate from LC conditions and five factors from MS (ion spray voltage (3000–5500 V), the temperature of ion source (300–750 °C), curtain gas pressure (20–40 psi), nebulizer (Gas 1) gas pressure (20–60 psi) and auxiliary (Gas 2) gas pressure (40–80 psi)) were selected as factors that may have a significant effect on ionization efficiency. The influence of collision energy (CE), collision cell exit potential (CXP), entrance potential (EP), and declustering potential (DP) on the fasudil peak area was evaluated using a "One Factor at A Time" approach, as these parameters do not interact with each other. Design of experimental plans and data analysis in the experimental design approach were performed with Design-Expert® 11.0.0 software (Stat-Ease Inc., USA), while data acquisition employed Analyst® software (AB Sciex, Singapore).

Validation of the developed LC-MS method was carried out according to "Guideline on bioanalytical method validation, (July 21, 2011 EMEA/CHMP/EWP/192217/2009 Rev. 1 Corr. 2, Committee for Medicinal Products for Human Use (CHMP))" from the European Medicines Agency. The validation parameters evaluated were linearity, the limit of quantification (LOQ), limit of detection (LOD), recovery, accuracy, precision, stability, and matrix effects. A stock solution (1 mg/mL) and working solutions (10 µg/mL) of fasudil hydrochloride and ranitidine hydrochloride were assessed for storage stability for 48h at -20 °C. Stock solutions were diluted from 1 mg/mL to 10 µg/mL and analyzed together with 10 µg/mL working solutions of fasudil and ranitidine. Linearity was evaluated by constructing a calibration curve obtained by the internal standard method, where fasudil and ranitidine peak area ratios were plotted vs. fasudil and ranitidine concentration ratio. Eight concentrations were used for constructing the calibration curve for fasudil (10, 20, 50, 100, 200, 400, 800, and 1000 ng/mL) with the addition of ranitidine in the concentration of 1 ng/mL. LOD and LOQ values were calculated from the LINEST function, while precision and accuracy were evaluated in two manners - within-run precision/accuracy and between-run precision/accuracy. Three plasma samples were spiked with fasudil and ranitidine at low-quality control level (LLOQ- 10 ng/mL), medium quality control level (medium QC- 500 ng/mL), and upper-quality control level (ULOQ- 1000 ng/mL) and analyzed in a

single run for testing within-run precision/accuracy, while four runs on two different days were performed for between-run precision/accuracy. Matrix effects were tested with two different sample types i) blank plasma/cell medium spiked after sample preparation with fasudil at LLOQ, medium QC, and ULOQ level, and with 1 ng/mL of ranitidine and ii) water solution of fasudil and ranitidine in the same concentration as spiked samples (LLOQ, medium QC and ULOQ level for fasudil and 1 ng/mL for ranitidine). Recovery was assessed on three QC levels by comparing the mass of extracted analyte and analyte in the sample (plasma/cell medium spiked after the sample preparation) and represented as a percentage.

2.4. LC-MS method for the determination of total fasudil content in cerebrospinal fluid

2.4.1. Sample preparation

50 mM DTT was added to 20 µL of cerebrospinal fluid (CSF) samples (collected 48 h after administration of PGA-SS-F [300 µM fasudil equiv.] to animals) to induce the total release of fasudil from the PGA-SS-F conjugate. Then, 50 µL of acetonitrile was added to the sample for protein precipitation, vortex-mixed for 30 s, and centrifuged at 11,000 rpm for 5 min. The supernatant was carefully removed, transferred to fresh tubes, and dried by evaporation. The residue was reconstituted in 20 µL of acetonitrile followed by vortex-mixing for 1 min, and finally, 10 µL of the solution was injected for LC-MS analysis.

2.4.2. LC-MS/MS method for the determination of fasudil in the CSF

The LC-MS/MS conditions employed were identical to those used above for the analysis of fasudil stability in plasma. Nevertheless, the developed LC-MS and extraction methods were re-evaluated for linearity, LOQ, LOD, recovery, and matrix effects. Linearity was evaluated by constructing a calibration curve obtained by the internal standard method, where fasudil and IS peak area ratios were plotted vs. fasudil and IS concentration ratio. Six concentrations were used to construct the calibration curve for fasudil (up to 250 ng/mL) with the addition of ranitidine at a concentration of 2.5 ng/mL. LOD and LOQ values were calculated from the LINEST function. Recovery was assessed by comparing the mass of extracted analyte and analyte in the CSF spiked after the sample preparation, presented as a percentage. Matrix effects were evaluated by comparing two samples - one sample with blank CSF spiked after sample preparation with fasudil at ULOQ (250 ng/mL) and with 2.5 ng/mL of ranitidine, and another sample of a water solution of fasudil and ranitidine in the same concentration as spiked samples.

2.5. NPC isolation, cell culture, and experimental conditions

NPCs or eGFP-NPCs [32] were harvested from neonatal (P4-6) Sprague Dawley-Tg (GFP) 2BalRrc rats. eGFP^{+/+} homozygote rats were used for organocultures and cell transplantation for in vivo experiments, while eGFP^{-/-} rats for all in vitro assays. Spinal cords were dissected after complete laminectomy, and the overlying meninges and blood vessels were removed. The dissected tissue was cut into 1 mm³ segments and mechanically homogenized without enzymatic treatment. NPCs were isolated and cultured as neurosphere-like form in growth medium in low-attachment plates (DMEM/F12 supplemented with 100 U/mL penicillin, 100 µg/mL streptomycin, 2 mM L-glutamine, 5 mM HEPES buffer, 0.125% NaHCO₃, 0.6% glucose, 0.025 mg/mL insulin, 80 µg/mL apotransferrin, 16 nM progesterone, 60 µM putrescine, 24 nM sodium selenite, 4 µg/mL BSA, 0.7 U/mL heparin, 20 ng/mL EGF and 20 ng/mL bFGF, 1 mM N-acetyl-cysteine (NAC)). For adherent conditions, NPCs were cultured on Matrigel® coated coverslips diluted 1/10 in growth medium. To assess spontaneous differentiation of NPCs, neurospheres were dissociated with Accutase following manufacturer instructions and then seeded onto Matrigel® coated coverslips in differentiation media (DMEM/F12 supplemented with 1 mM NAC, 100 U/mL penicillin, 100 µg/mL streptomycin, 2 mM L-glutamine, 5 mM

HEPES buffer, 0.125% NaHCO₃, 0.6% glucose, 0.025 mg/mL insulin, 80 µg/mL apotransferrin, 16 nM progesterone, 60 µM putrescine, 24 nM sodium selenite, 2 % fetal bovine serum) for seven days. Pharmacological treatments (LPA, PGA-SS-F or F) were added at the day three of culture and maintain till cell fixation at day seven.

To determine the effect of fasudil or conjugates on proliferation, cell viability, differentiation and neurite elongation, NPC cultures were treated with 50 or 100 µM of each compound for 24h, 48 h, and 72 h. Neurite length was evaluated using Incucyte NeuroTrack analysis software™ (Cat. 9600–0010) when performed in phase-contrast images (Fig. 3D and Figure S18C) and using the NeuronJ plug-in from ImageJ in Nestin stained cultures (Fig. 6A,D and Figure S19) as previously described [34]. In vitro neurite retraction was induced by adding 10 µM of LPA (L726, Sigma) to the cultures for 24 h after fasudil or PGA-SS-F treatments. For the exploration of the role of 5' adenosine monophosphate-activated protein kinase (AMPK) activation in PGA-SS-F-induced neurite outgrowth, NPCs were treated with an AMPK inhibitor (10 µM Compound C; Merck CAS 866405-64-3) before LPA and/or fasudil or PGA-SS-F treatment (Figure S110).

2.6. Cellular uptake studies

2.6.1. Live-cell confocal imaging

Uptake assays were performed in non-adherent NPC cultures at 37 °C and 4 °C. Cells were seeded in ultra-low attach six-well plates at 1×10^6 cells/cm² and incubated for 24 h. A cathepsin B inhibitor, leupeptin (PanReac AppliChem, VWR, U.E.), was added to each well at 10 µM 30 min before the incubation of conjugates (PGA-F-OG, PGA-O-F-OG, and PGA-SS-F-OG) to avoid degradation. To perform the 4 °C uptake experiment, cells were pre-incubated at 4 °C for 30 min before the addition of the treatments. 12 µg/mL of each polymer were evaluated at different time points (0–300 min). Cell medium was subsequently removed, cells were washed twice with PBS 0.1 wt% BSA (Bovine serum albumin, Sigma-Aldrich, Spain, UE), and then cells were collected in 500 µL of PBS 0.1 wt % BSA and transferred into confocal multiwell plates. Lysotracker-deep red (ThermoFisher) was added, and cells were incubated for 30 min. The percentage of OG-positive cells was evaluated for each treatment after confocal image acquisition in triplicate. Colocalization analysis in the confocal analysis was performed using lysosomes labeled with Dextran-TR (red) co-incubated from time zero in all tested conditions and replicates. Consistent exposures were applied for all images.

2.7. Dorsal root ganglia (DRG) explants and spinal cord (SC) organotypic cultures: experimental conditions, sample preparation, image acquisition, and analysis

DRG explants and SC slices were dissected from five-day-old Sprague-Dawley GFP^{-/-} rats. DRG explants were placed on poly-L-lysine/laminin-coated coverslips and cultured for ten days in neurobasal medium, supplemented with B27, 1 mM N-acetyl cysteine (NAC), 2 mM GlutaMAX, 10 % fetal bovine serum, and 1 % penicillin/streptomycin. Two days after plating DRGs, 50 µM of PGA-SS-F or fasudil were added to the culture media, and the explants were incubated for eight additional days. After fixation, the whole DRG explant and surrounding outgrowth of axons were imaged using a sequential image mapping technique supported by Leica software, in which individual images were stitched together for final analysis. Axonal outgrowth from DRG explants was quantified by beta-III-tubulin staining and the NeuriteJ plug-in from ImageJ as previously described [34]. For GAP43 quantification, images were thresholded and positive area for GAP43 was quantified. Analyses were performed for seven DRG explants from four different experiments.

SC slices were cleaned out from meningeal layers and cut with a McIlwain Tissue Chopper in 350 µm thick slices in the transverse and parasagittal longitudinal plane. Immediately after, the slices were

transferred onto Millicell-CM® (Millipore) inserts and placed into six-well plates with 1 mL of culture medium (50 % Minimum Essential Medium, 25 % Hanks' Balanced Salt Solution, 25 % horse serum, 2 mM GlutaMAX, 1 mM NAC, 0.5 % NaHCO₃ and 1 % penicillin/streptomycin). To generate a gap of damaged and spared axons, mimicking an ex vivo model of SCI, a complete transverse section with a scalpel blade was performed on cultures after five days in vitro, as described previously [35]. After transection, slices were treated with 50 µM fasudil or PGA-SS-F and cultured for seven more days. Then, tissues were fixed with 4 % paraformaldehyde for immunohistochemical analysis (three different slices for at least three animals were used per experimental condition). Consistent exposures were applied for all images. Quantitative analysis of neurofilaments and synaptophysin and PSA-NCAM levels was conducted by quantifying positive area on the maximal intensity projection images from five images per slice.

2.8. Immunocytochemistry

Paraformaldehyde-fixed cells and organotypic cultures were permeabilized with 0.1% Triton X-100 and subsequently blocked with 5% normal goat serum in PBS. The primary antibodies were incubated overnight at 4 °C: nestin (1:500 ab6142, Abcam), anti-beta-III-tubulin (1:500 MO15013, Neuromics), anti-GAP43 (1:500 ab128005, Abcam), synaptophysin (1:400 sc-17750, Santa Cruz), anti-GFP (Abcam), anti-Olig2 (1:500 ab33427, Millipore), anti-MAP2 (1:1000 AB3096, Abcam), anti-GFAP (1:1000 PA1-10004, ThermoFisher), Ki67 (1:500 ab15580, Abcam), and caspase-3 (1:500 9662S, Cell Signaling). After washing, secondary antibodies (anti-mouse, 1:5000 SC-516102, Santa Cruz, or anti-rabbit, 1:5000 SC-2357, Santa Cruz) were incubated for 2 h at R.T. The Phalloidin probe conjugated with Alexafluor647 was used at 1:1000 dilution (P1951 Sigma-Aldrich). All cells were counterstained by incubation with 4,6-diamidino-2-phenylindole dihydrochloride (DAPI; Invitrogen). Apotome Zeiss microscope was used for image acquisition of cell cultures. Confocal microscope SP8 (Leica) was used for image acquisition of DRG explants and organotypic cultures.

2.9. Western blot analysis

Total protein was extracted from spinal cord tissues or cell cultures using a lysis buffer containing 50 mM Tris-HCl, pH 7.5, 150 mM NaCl, 0.02% NaN₃, 0.1% SDS, 1% NP40, 1 mM EDTA, 2 mg/mL leupeptin, 2 mg/mL aprotinin, 1 mM PMSF, and 1 x Protease Inhibitor Cocktail (Roche Diagnostics, San Diego, CA, USA). The protein concentrations of the supernatant were determined using the bicinchoninic acid (BCA) Protein Assay Kit (ThermoFisher Scientific) and stored at –80C. An equal number of proteins (30 µg/well) were separated (10 % SDS-PAGE) and transferred to a polyvinylidene fluoride (PVDF) membrane. The membrane was blocked with 1 % BSA in Tris buffer saline (TBS) with 0.1 % Tween-20 for 1 h at room temperature and incubated at 4 °C overnight with the following primary antibody solutions: pAKT (1:1000 4060, Cell Signaling), Bag-1 (1:1000 sc-376848, Santa Cruz), Bcl-2 (1:1000 2870S, Cell Signaling), BDNF (1:500 sc-655114, Santa Cruz), cAMP (1:500 ab24851, Abcam), caspase-3 (1:1000 9662S Cell Signaling), p-MYPT (1:1000 ABS45 Millipore), and p-mTOR (1:1000 2971 Cell Signaling); AMPK (1:1000 2535 Cell Signaling), LC3I (1:1000 3868 Cell Signaling). To ensure loading with equal amounts of protein lysates, blots were incubated with an antibody against β-tubulin (1:10,000 SIGMA) as a loading control. Signal detection was performed with an enhanced chemiluminescence kit (ECL Plus Western blotting detection reagent - G. E. Healthcare, Piscataway Township, NJ, USA), and bands were developed using Amersham Imager 600. The relative protein expression was quantified by Image Studio Lite software.

2.10. Animals, spinal cord contusion model, and treatments

Female Sprague Dawley rats (~200 g) were bred at the Animal

Experimentation Unit of the Research Institute Príncipe Felipe (Valencia, Spain). The maintenance and use of all animals were in accordance with the National Guide for the Care and Use of Experimental Animals Committee (Animal Care Committee of the Research Institute Príncipe Felipe) (Real Decreto 1201/2005). The rats were housed under standard temperature conditions with controlled 12 h light/dark cycles with ad libitum access to food and water. Severe SCI by contusion at thoracic segment T8 was performed applying 250 kdyn using Infinite Horizon Impactor, as previously described [36]. The experimental groups and the details of the number of animals included for each analysis for acute and chronic SCI models are indicated in Table S1. eGFP-NPCs aliquots for grafting were prepared immediately before injection at a density of 100,000 cells/ μL . 10 μL of an eGFP-NPC suspension were intramedullary transplanted for distribution in rostral and caudal regions at a distance of 2 mm from the lesion at a rate of 2 $\mu\text{L}/\text{min}$ using a silicized pulled glass pipette. In the acute SCI model, PGA-SS-F-pretreated eGFP-NPCs were transplanted immediately after contusion. In the chronic SCI model, the eGFP-NPC and sustained compound delivery were applied five weeks after the SCI.

Intrathecal drug delivery was performed using a catheter introduced immediately below the thoracic injured segment, as previously described [36]. For administration of the compounds, 10 μL of PGA, PGA-SS-F, or free fasudil to reach a final concentration of 300 μM in the CSF was delivered through the catheter. Animals were sacrificed 48 h after SCI and treatments, and CSF and spinal cord tissue were collected for further analysis. For sustained intrathecal drug delivery in the chronic SCI model, the catheter was connected to an osmotic pump Model 1007D filled with 100 μL of 10 mM solution of each of the compounds (PGA, or PGA-SS-F or fasudil) to deliver 1 $\mu\text{L}/\text{h}$ for seven days. After one week, the catheter and the pump were removed. Two months after treatment, all animals were sacrificed.

All animals were subjected to post-surgery care and passive and active rehabilitation protocols, as previously described [36]. Rats received subcutaneous injections of cyclosporin A (10 mg/kg) starting one day before transplantation and administered daily for one month. All animals were sacrificed two months after transplantation. Gait analysis was performed by the CatWalk® (Noldus, Asheville, NC, <http://www.noldus.com>) video-based system for automated gait analysis. Paw contact was quantified by counting high-intensity pixels as the mean of at least three rounds per analysis [37].

2.11. Histological analysis

Rats were overdosed via an intraperitoneal administration of sodium pentobarbital (100 mg/kg) and transcardially perfused with 0.9 % saline followed by 4% paraformaldehyde in PBS. Spinal cord tissue was cryopreserved with 30 % sucrose before inclusion in Tissue-Teck OCT (Sakura Finetek, U.S.A). Coronal (in acute SCI model) or longitudinal (in chronic SCI model) sections at the lesion epicenter were obtained with a cryostat set at 10 μm thickness. For the evaluation of cysts/cavities, every fifth collected section was stained with hematoxylin and eosin in an automatized station (Autostainer XL Leica) and scanned in an Aperio Versa scanner (Leica Biosystems). Images of approximately 12 mm length of the spinal cord (including the epicenter of the lesion) were analyzed with the Image Scope software. The total cyst/cavity area was normalized to the total analyzed spinal cord tissue. Immunofluorescence double staining following the previously detailed methodology was performed using beta-III-tubulin for neuronal fiber detection, GFAP for glial scar analysis, and Olig2 and NeuN for oligodendrocyte and neuron quantification, respectively. All samples were counterstained by incubation with DAPI. All quantified specific signals for each marker were normalized by the total analyzed area at equivalent tissue lengths, including the epicenter of the injury, in all groups using ImageJ software. The glial scar was measured via the lack of GFAP expression. The directionality analysis of beta-III-tubulin positive fibers analysis was performed using ImageJ/Fiji software and the Directionality plug-in.

2.12. Statistical analysis

Data presented as mean \pm standard error of the mean (SEM) and analyzed using Graph Pad Prism Software. The Shapiro-Wilk normality test was performed to ensure normal data distribution. Comparisons between two groups and among multiple groups used unpaired Student's t-test and one-way ANOVA, using Tukey multiple comparison test for post-hoc analysis. If normality was not met, non-parametric tests were used - the Mann-Whitney rank-sum test and the Kruskal-Wallis One-way ANOVA with Dunn's method post hoc correction. P values ≤ 0.05 were considered statistically significant.

3. Results

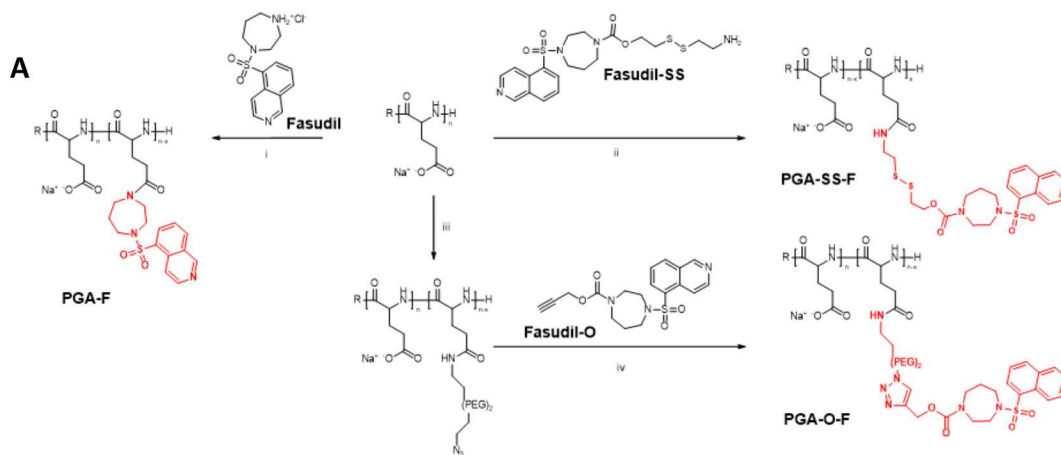
3.1. Rational Design of PGA-Fasudil Conjugates and Polymer-drug Linker Optimization: Synthesis, Characterization, Stability, and Fasudil Release Kinetics in Physiological Media

To overcome the pharmacological limitations of fasudil (low half-life in plasma), we prepared a family of PGA-fasudil conjugates. Fasudil possesses only one accessible functional group - the secondary amine in the diazepane ring; therefore, our synthetic strategy aimed to introduce a range of bioresponsive polymer-drug linkers through this secondary amine to achieve optimized drug release kinetics and maximize the therapeutic value of fasudil with regards to SCI treatment.

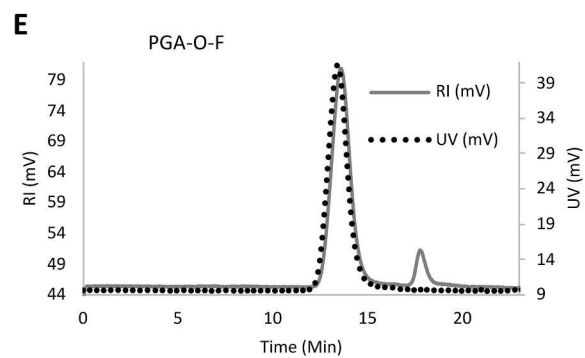
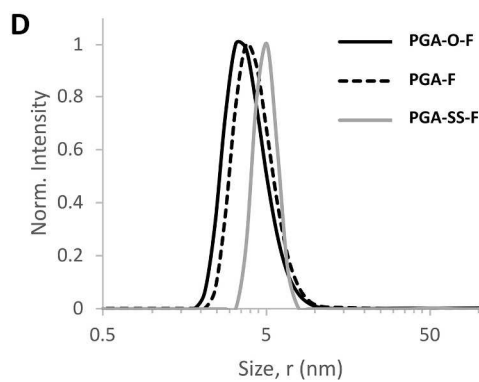
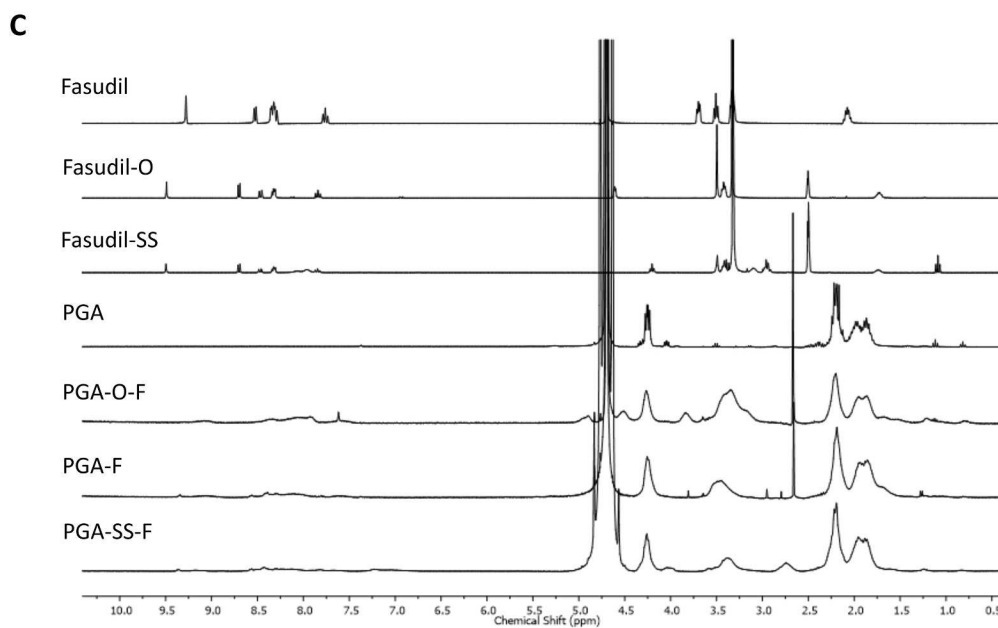
We conjugated fasudil to PGA using three linkers with differing bioresponsiveness - PGA-F employs an amide linker degraded by proteolytic enzymes such as cathepsin B; PGA-O-F employs a hydrolytically-labile carbamate linker; and PGA-SS-F employs a self-immolative disulfide linker susceptible to reducing environments. As shown in Fig. 1A, we prepared the amide-linked conjugate by the direct conjugation of the secondary amide of fasudil to the carboxylic groups of PGA using DMTMM (4-(4,6-dimethoxy-1,3,5-triazin-2-yl)-4-methyl-morpholinium chloride) as a coupling agent [19]. We prepared the carbamate linked conjugate in two steps using a 2-propyn-2-ol carbamate derivative of fasudil conjugated to an azide-modified PGA using a click reaction (see details in Figure S11). We prepared the self-immolative disulfide-linked conjugate in four steps, as shown in Figure S11. The first step comprised the thiol exchange between pyridyl disulfide with mercaptoethanol, while the next two steps involved alcohol activation with *p*-nitrophenyl chloroformate and the consequent reaction with fasudil. The last step comprised the second thiol exchange with cysteamine hydrochloride and compound conjugation to PGA through DMTMM-mediated amide coupling. We observed general instability for product Fas-SS (IC4), with significant degradation after 48 h even at -80°C ; therefore, we performed the last coupling step immediately after compound preparation. Characterization of all intermediates demonstrated high purity and unequivocal assignments of identity (See Figure S12).

We obtained the desired conjugates (Table 1) with high purity, yield, and conjugation efficiency (See full characterization in Fig. 1B–D and Figure S13 and S14). ^1H NMR experiments (Fig. 1B and Figure S13) depict the typical broadening of the signals from the drug for all conjugates consistent with the conjugation of large molecular weight polymer and therefore reduced relaxation times. UV–Vis analysis allowed the determination of total drug loading, which was in a range of 11.5–13.7% (wt) (Figure S13), while HPLC analysis established a free drug content of below 0.1 % wt of total drug loading in all three conjugates. Dynamic light scattering (DLS) analysis demonstrated that all conjugates possessed similar hydrodynamic radius values in PBS (close to 5 nm), which is consistent with unimeric polymer-drug conjugate entities (Fig. 1C and Figure S14). Additionally, we found a z-potential of approximately -40 mV [13,38]. Size exclusion chromatography (SEC) analysis (Figure S14) confirmed the homogeneous conjugation of fasudil throughout the polypeptide molecular weight distribution (by ultraviolet [UV] and refractive index [RI]).

Next, we studied the kinetics of fasudil release in conditions relevant



^aDetermined by UV-Vis. ^bDetermined by HPLC (UV-Vis) and calculated as % of the total drug loading. ^cHydrodynamic radius measured via DLS instrument in PBS expressed as mean Volume value.



(caption on next page)

Fig. 1. Synthesis and Characterization of Polypeptide-based Fasudil Conjugates. A. Synthetic route for the preparation of the PGA-fasudil conjugate family. PGA-fasudil conjugates with amide (PGA-F), carbamate (PGA-O-F), self-immolative disulfide (PGA-SS-F) linking moieties were prepared according to the schematic. Reaction conditions were: i) H₂O, DMTMMCl, fasudil hydrochloride; ii) DMF, DMTMMBF₄, self-immolative disulfide fasudil-derivative; iii) H₂O, DMTMMCl, NH₂-(CH₂)₂-(PEG)₂-N₃; iv) DMF/H₂O, CuSO₄, sodium ascorbate, carbamate fasudil-derivative. B. Chemical identity and purity assessed via ¹H-NMR spectroscopy suggest the successful generation of the desired compounds. Upon conjugation to PGA, a broadening of the bands can be observed, although the characteristic peaks of the parent drug derivative are maintained; C. Size distribution (Rh, volume) of fasudil conjugates by DLS, 3 mg/mL in PBS. D. Size-exclusion chromatograms for all conjugates exhibit narrow molecular weight distribution (UV channel detected at 323 nm) throughout the polypeptide population (RI channel). The PGA-SS-F conjugate is shown as an example.

Table 1

Physico-chemical characterization of PGA-fasudil conjugates.

Conjugate	Linker	Yield, %	Conj. eff., %	TDL, % wt ^a	FD, % wt ^b	R _h , nm ^c
PGA-F	Amide	87	92	13.7	0.01	4.8
PGA-O-F	Carbamate	65	87	12.4	0.1	4.9
PGA-SS-F	Self-immolative disulfide	84	85	11.5	0.1	5.1

^a Determined by UV-Vis.^b Determined by HPLC (UV-Vis) and calculated as % of total drug loading.^c Hydrodynamic radius measured via DLS instrument in PBS expressed as mean volume. TDL – Total drug release.

to the distinct linkers. The protease-sensitive linker of PGA-F and the pH-sensitive linker of PGA-O-F failed to release significant levels of fasudil under appropriate conditions, with only 1.5% release in the presence of cathepsin B (PGA-F) (Figure S15) and 12 % after five days at pH 7.4 (PGA-O-F) observed (Figure S15). We observed more encouraging results for the redox responsive linker employed in PGA-SS-F when evaluating fasudil release in the presence of 5 mM and 10 μM DTT, which we employed to mimic the intracellular and extracellular concentrations of glutathione, respectively. In the presence of 5 mM DTT, we observed rapid drug release with zero-order kinetics during the first 6 h, reaching 80 % of total drug release after 8 h and approximately 100 % after 24 h.

In the presence of 10 μM DTT, we failed to observe any drug release, even after 72 h (Fig. 2A). Figure S16 details the mechanism of fasudil release from the PGA-SS-F conjugate under reductive environment, the intermediates, and the corresponding MS and MS/MS spectra.

To finalize the characterization of the PGA-SS-F conjugate and explore therapeutic potential, we studied stability in plasma and cell medium (Fig. 2B and C, Table 2, and Figure S17) by LC-MS/MS, which provides insight into the fate of PGA-SS-F conjugate after administration. We calculated the concentration of free fasudil in plasma (Fig. 2B) and cell medium (Fig. 2C), sampled at defined time points and presented the values as a percentage of the free drug compared to the total concentration of conjugated fasudil. The percentage of free drug increased to only 3.15% (Figs. 2B) and 3.21 % (Fig. 2C) of total drug release over the 24 h in plasma and cell medium stability studies, respectively, thereby highlighting the high extracellular stability of the PGA-SS-F conjugate afforded by the disulfide linking moiety in agreement with the release studies (Fig. 2A). Conjugates from linear polymers, including those using PGA as a carrier, typically exhibit a blood t_{1/2} lower than 24 h and accumulate rapidly within the lesion site after administration [12, 20, 23]; therefore, a 3 % loss of total drug loading will not significantly impact therapeutic performance. The LC-MS method employed has been fully validated for the determination of fasudil concentration in plasma, evaluating within-run and between-run accuracy, within-run, and between-run precision, matrix effects, and recovery values (Table 2).

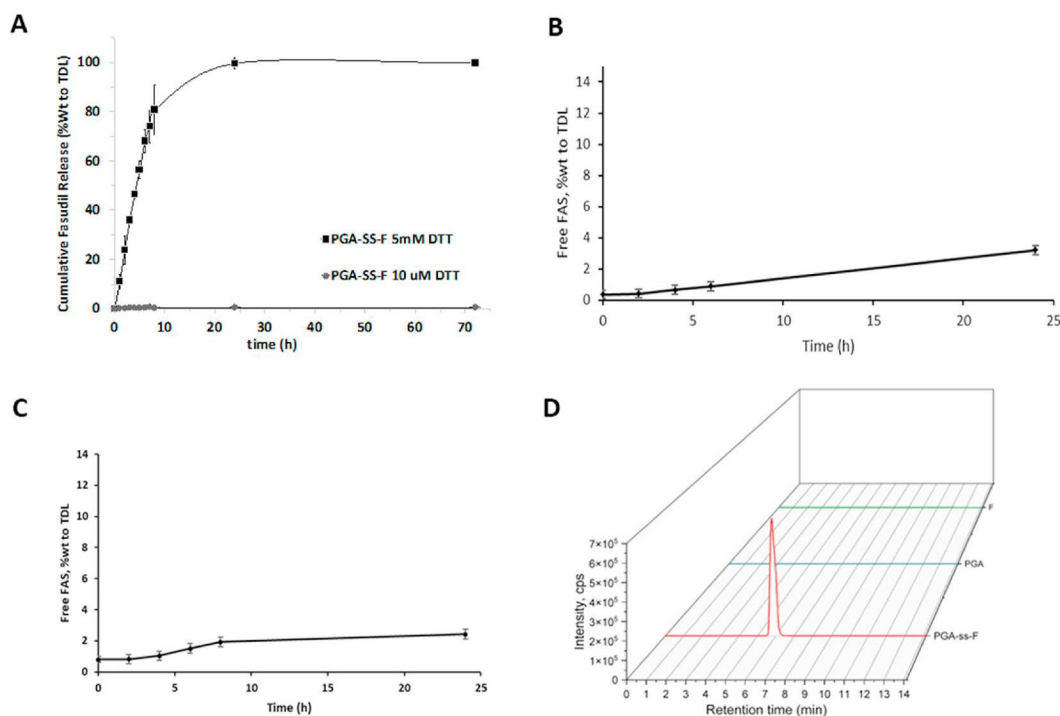


Fig. 2. Evaluation of Fasudil Release Kinetics and PGA-SS-F Conjugate Stability in Physiologically Relevant Media: A. Fasudil release from PGA-SS-F under redox conditions (5 mM [black squares] and 10 μM [grey circles] DTT). Data presented mean ± SEM (n = 3); B. Plasma stability study for the PGA-SS-F conjugate. Values presented as free fasudil % wt to total drug loading. Data presented as mean ± SEM (n = 3). C. Cell medium stability study for the PGA-SS-F conjugate. Values presented as free fasudil % wt to total drug loading. Data presented as mean ± SEM (n = 3). D. LC-MS/MS chromatograms of CSF samples analyzed 24h after the injection of PGA-SS-F and controls (PGA and F).

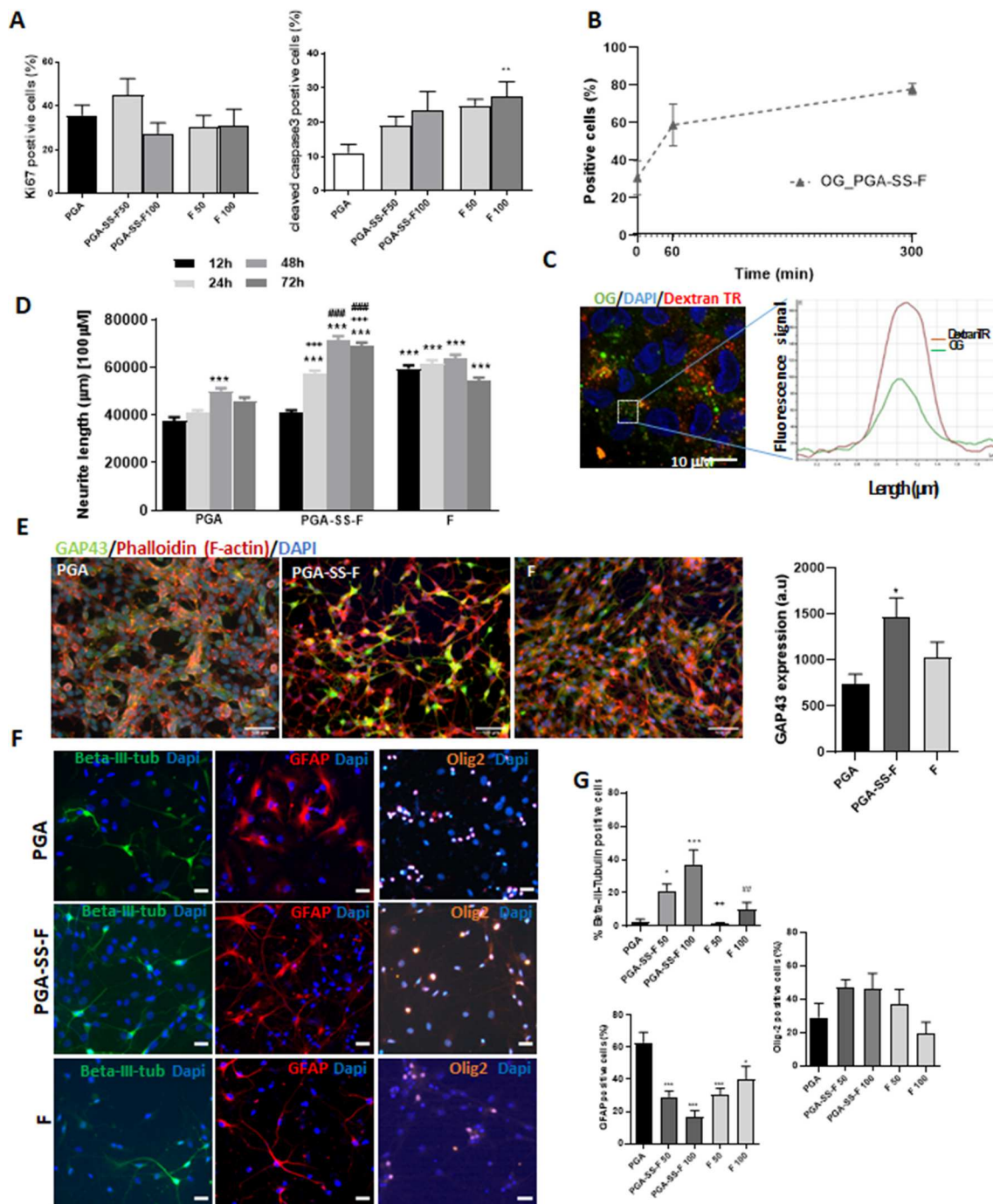


Fig. 3. *In vitro* Effects of PGA-SS-Fasudil Conjugate on NPC Survival, Differentiation, and Neurite Outgrowth. **A.** Quantification of NPCs positive for Ki67 (left panel) and cleaved caspase 3 (right panel) normalized to the total number of cells (DAPI positive, blue) treated for 24 h with 50 or 100 μM of PGA-SS-F or fasudil or the equivalent of PGA. Data expressed as mean ± S.E.M (n = 3 of independent experiments per group). **p < 0.01 vs. PGA, determined by ANOVA multiple comparison test and Tukey's *post hoc* test. **B.** Oregon green (OG) labeled conjugate (PGA-SS-F-OG) internalized into neurospheres-like cultures via an endocytic energy-dependent mechanism. **C.** Quantification of positive cells after confocal images acquisition at 0-, 60-, and 300-min incubation time. **C.** Representative confocal image at 300 min incubation time of PGA-SS-F demonstrates the internalization of the OG-linked compound and the co-localization in the lysosomes labeled with Dextran-TR (red). Data presented as mean ± SEM (n = 3). **D.** Quantification of neurite length of Matrigel-adhered NPCs following exposure to PGA (control) or 50 μM of free fasudil (F) or PGA-SS-F (at 50 μM, fasudil equiv.) for 12, 24, 48, or 72 h. Data presented as mean ± SEM (n = 3 of independent experiments per group) ***p < 0.001 vs. PGA 12h; +++p < 0.001 PGA-SS-F vs. fasudil 48h; ###p < 0.001 PGA-SS-F vs. fasudil 72 h determined by ANOVA multiple comparison test and Tukey's *post hoc* test. **E.** Representative images of immunofluorescent double-staining of GAP43 (green) and phalloidin (red) in NPCs treated as indicated (left panels); Quantification of GAP43 immunofluorescent staining (graph). **F.** Representative images of immunofluorescent staining of beta-III-tubulin (green), GFAP (red), and Olig-2 (orange) in NPCs treated as indicated. **G.** Quantification of immunofluorescent staining. Data presented as mean ± SEM (n = 3 of independent experiments per group) p < 0.05 vs. PGA determined by Kruskal-Wallis multiple comparison test *p < 0.05, **p < 0.05, ***p < 0.001 vs. PGA; ++p < 0.01 vs. PGA-SS-F 50 μM; ##p < 0.01 vs. PGA-SS-F 100 μM, determined by ANOVA multiple comparison test and Tukey's *post hoc* test. Scale bar: 20 μm. (For interpretation of the references to colour in this figure legend, the reader is referred to the Web version of this article.)

Table 2

LC-MS/MS method validation for the determination of fasudil concentration in plasma, evaluating within-run and between-run accuracy, within-run and between-run precision, matrix effects, and recovery values.

Sample	Within-run		Between-run		Matrix effects		Recovery	
	Accuracy (%) ^a	Precision (RSD _{pooled} %)	Accuracy (%) ^a	Precision (RSD _{pooled} %)	MF _{fas} /MF _{ran}	RSD (%)	R, %	RSD, %
LLOQ	-11.49	10.68	-10.10	9.52	0.96	2.83	76.51	3.23
Medium QC	-3.01	5.21	-3.01	5.83	0.99	2.01	78.90	5.14
LLOQ	-2.89	3.18	-2.88	3.15	1.01	1.81	81.34	1.47

^a The difference from nominal value; RSD_{pooled} – pooled relative standard deviation; MF – matrix factor; RSD – relative standard deviation, n = 3; R – recovery.

3.2. PGA-SS-F improves neurogenesis and neuronal differentiation without influencing NPC survival

To evaluate the tolerability of the PGA-SS-F conjugate and the other conjugated forms (PGA-F and PGA-O-F) in rat NPCs, we evaluated cell viability at 50 μ M (non-toxic dose for free fasudil) or 100 μ M (toxic dose for free fasudil) equiv. concentrations for 24 h. While fasudil induced a significant decrease in NPC viability at 100 μ M, the family of PGA-fasudil conjugates failed to induce any significant toxicity at the concentrations tested (Figure S18A).

We next explored the effect of PGA-SS-F treatment on NPC proliferation and apoptosis by immunostaining for Ki67 in neurosphere-like cultures and cleaved caspase 3 in adherent conditions (Matrigel-coated substrate), respectively, at 50 and 100 μ M in comparison with PGA or free fasudil (Fig. 3A). While we failed to encounter significant differences in proliferation in any of the conditions, we did observe a significant increase in apoptosis for 100 μ M fasudil compared to PGA treatment, a finding that agrees with the findings of the cell viability assays (Figure S18A). We employed an additional control condition (NPCs without PGA treatment (control)); however, we did not observe any significant differences in comparison with PGA-treated NPCs in the percentage of Ki67 positive cells (33.1 ± 2.7 for control vs. 35.9 ± 4.6 for PGA) or the percentage of caspase3 positive cells (9.1 ± 1.1 for control vs. 11.2 ± 2.4 for PGA).

Cell internalization studies suggested that the PGA-SS-F conjugate followed an energy-dependent endocytic mechanism with rapid intracellular accumulation (measured by quantifying the percentage of cells containing the Oregon green (OG)-labeled conjugate at 37 °C) (Fig. 3B and Figure S18B). Confocal analysis provided evidence that most of the internalized conjugate moved into the lysosomal compartment (Dextran-TR employed as a lysosomal marker), indicating that fasudil release mainly occurs through a lysosomotropic mechanism [17] (Fig. 3C), in agreement with the release/stability data shown in Fig. 2. To ratify this finding and demonstrate that the presence of a reductive environment triggers fasudil release from PGA-SS-F, we studied the intracellular concentration of GSH in NPCs cells. We determined an intracellular concentration of GSH and GSSG of $7.42 \pm 0.78 \mu$ M and $0.19 \pm 0.03 \mu$ M, respectively, resulting in a GSH:GSSG ratio of 39:1 (experimental details in SI). In cells, the ratio of [GSH]/[GSSG] varies from 30:1 to 100:1, making the intracellular environment highly reducing; therefore, the presence of a disulfide bond is highly unlikely under these conditions. Reported data shows that a GSH:GSSG ratio of $\geq 8:1$ maintains protein disulfide isomerase (PDI) in a fully reduced state, suggesting the presence of only the reduced form of intracellular PDI [39].

We next discovered that NPC treatment with PGA-SS-F induced higher neurite elongation levels than free fasudil after 48 and 72 h of incubation in comparison with PGA-treated NPCs. We failed to encounter any significant differences when comparing PGA-treated NPCs to control (without PGA) (*data not shown*). Fasudil treatment significantly induced neurite outgrowth in NPCs as previously described [40,41]; however, this effect receded after 48 h of incubation. Interestingly, PGA-SS-F maintained neurite elongation for up to 72 h (Fig. 3D and Figure S18C), thereby indicating a sustained long-term effect for fasudil conjugated through a self-immolative linker.

In agreement with the observed longer neurite processes, NPCs displayed significant morphological changes after 48 h of treatment with PGA-SS-F when compared with PGA- or free fasudil-treated NPCs, which exhibited a neuron-like shape (Fig. 3E). PGA-SS-F-treated NPCs exhibited a prominent soma with long and thin cellular projections stained with phalloidin; however, we observed few cell contacts in PGA-treated NPCs. Fasudil-treated NPCs also displayed a neuronal-like shape but with a less prominent soma and thicker projections than those observed for PGA-SS-F. Moreover, PGA-SS-F treatment induced a significant increase in the expression of growth-associated protein 43 (GAP43) in NPCs compared to PGA, free fasudil treatment (Fig. 3E, green), or control (without PGA; *data not shown*). GAP43 expression is classically related to neuronal axon growth and is associated with axon regeneration [42].

Previous studies demonstrated that fasudil promotes NPC differentiation and neurite outgrowth [43]; therefore, we evaluated whether exposure to PGA-SS-F could promote the spontaneous neuronal differentiation of NPCs (Fig. 3F and G). We treated NPCs with PGA, fasudil, or PGA-SS-F at 50 or 100 μ M fasudil equivalents and evaluated beta-III-tubulin, GFAP, and Olig2 expression levels as an indicator of differentiation into a neuronal, astrocytic, or oligodendrocytic fate, respectively (Fig. 3F and G). PGA-SS-F, but not fasudil, induced significant levels of beta-III-tubulin expression when compared to PGA treatment, with the 100 μ M treatment affording a significantly higher increase than the 50 μ M treatment, thereby indicating a possible dose-responsive effect on neuronal differentiation. Control conditions without PGA did not show significant differences when compared with PGA-treated NPCs (*data not shown*). Additionally, treatments with PGA-SS-F or fasudil prompted a highly significant decrease in GFAP expression, suggesting the inhibition of astrocyte differentiation. Finally, we failed to observe any significant alterations in Olig2 expression under any of the experimental conditions.

Overall, these findings suggest that PGA-SS-F treatment induces neuronal differentiation of NPCs at the expense of astrocytic differentiation - an effect that would benefit neuronal reorganization and local circuit re-activation after SCI upon transplantation of NPCs pre-treated with PGA-SS-F.

3.3. PGA-SS-F promotes greater axonal outgrowth in mature neurons from DRG explants

Neonatal rat DRG explants represent a suitable model for the study of axonal elongation, with high survival rates and robust responses to external stimuli. To measure the differential capacity of the various treatments to induce axon outgrowth, we exposed DRG neonatal explants to 50 μ M fasudil-equiv. of free fasudil and PGA-SS-F or PGA (same polymer concentration as used in PGA-SS-F) for eight days and then co-stained with beta-III-tubulin, for further evaluation of neurite outgrowth extension and organization (Fig. 4A and B), and GAP43, whose expression indicates axonal growth (Fig. 4C) [42].

We determined the number of growing axons (beta-III-tubulin-positive) from the explant body and growth distance using NeuriteJ (Image J plug-in [34]) with the following values: i) Sholl critical value (RC), defined as the distance where the maximum number of dendrites intersect (indicating the branching degree), ii) the maximum number of

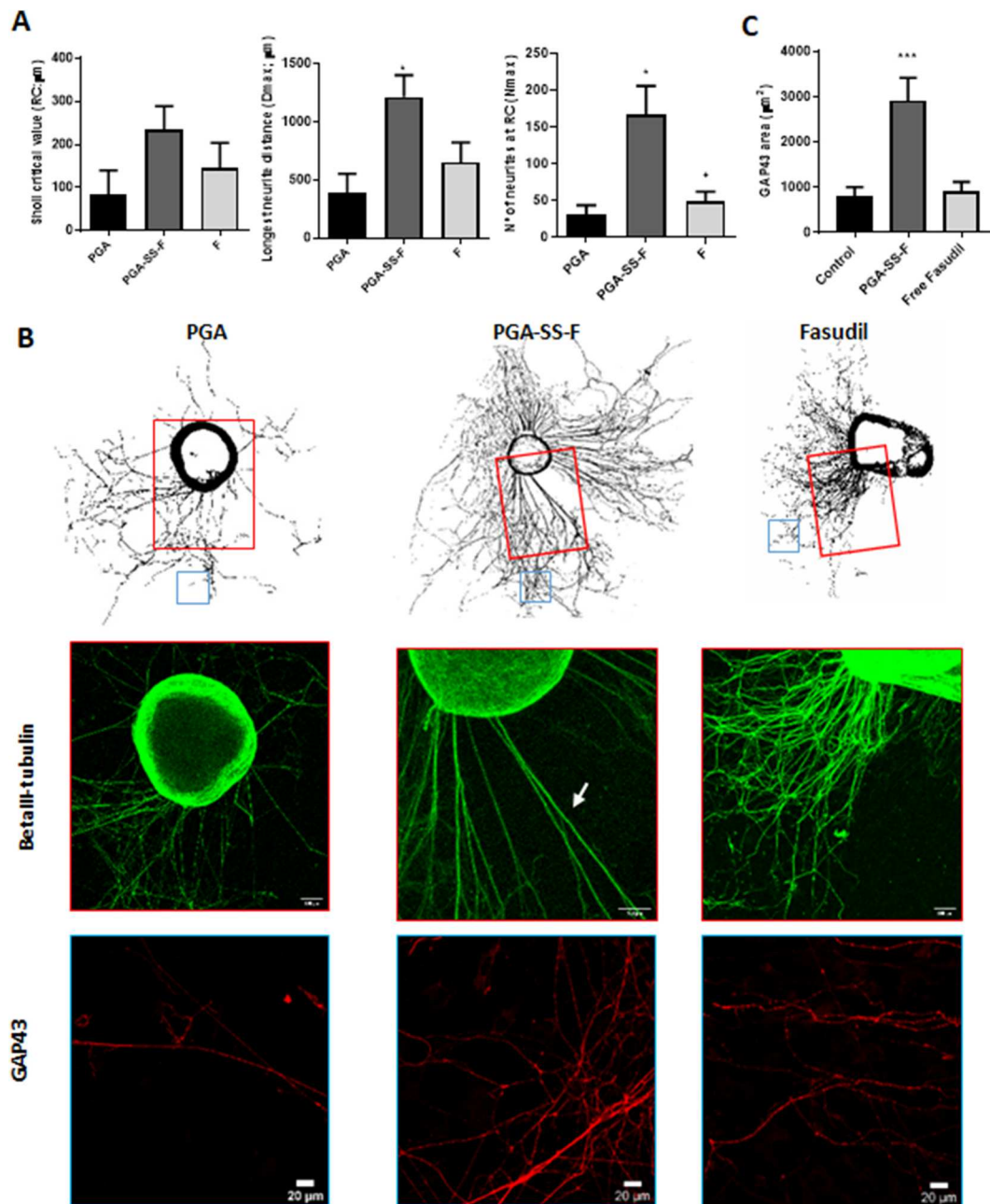


Fig. 4. PGA-SS-F Treatment Promotes Axonal Outgrowth in DRG Explants. A. Quantification of the maximal distance of axonal growth (D_{max}), the distance where the maximum number of axons intersect (Sholl critical value; RC), and the maximum number of axons intersecting at RC distance (N_{max}) in DRG explants using NeuriteJ plug-in. B. Upper panels: Representative image of a panoramic view for beta III-tubulin and GAP43 staining of those employed for axonal outgrowth quantification by NeuriteJ plug-in (quantifications shown in A from beta III-tubulin-stained images) and GAP43; lower panels: Immunofluorescence staining of beta-III-tubulin (green) from the selected area (red square in upper panels) and GAP43 from the selected area (blue square in upper panels) (red) and beta III-tubulin (green). C) Quantification of GAP43 occupied area. Data presented as mean \pm SEM ($n = 4$ of independent experiments and a total of 6 DRGs per group were quantified) * $p < 0.05$, *** $p < 0.001$ vs. PGA and F groups determined by ANOVA multiple comparison test and Tukey's *post hoc* test. Scale bars, 100 μm for whole explants and 20 μm for individual images. (For interpretation of the references to colour in this figure legend, the reader is referred to the Web version of this article.)

neurites at the RC distance (N_{max}), and iii) the distance of the longest neurite (D_{max}). The combination of these three values serves to describe the different growth patterns [34]. As shown in Fig. 4A, we discovered that PGA-SS-F treatment increased the RC value compared to PGA and fasudil treatment although this failed to reach significance; however, we did observe a significant increase in the D_{max} and N_{max} values for PGA-SS-F, but not fasudil, compared to PGA treatment.

PGA-SS-F-treated DRG cultures stained with beta-III-tubulin also displayed significantly higher neurite outgrowth, as evidenced by measuring the total axon length projecting from the soma and the

neuronal projections organized into thick and aligned bundles of fibers positive for beta III-tubulin when compared to PGA or fasudil treatment (as indicated in the PGA-SS-F image by a white arrow - Fig. 4B). In comparison, PGA or fasudil treatment prompted the outgrowth of thinner neuronal projections as randomly oriented processes (Fig. 4B).

PGA-SS-F treatment also prompted significant increases in the GAP43 occupied area compared with PGA and fasudil (Fig. 4B), in agreement with differentiating cultures of NPCs (Fig. 3F), indicating an active axon growth process that would contribute to the development of longer neurites in mature neurons. When compared with either PGA or

free fasudil, PGA-SS-F significantly induced the growth of neurons from DRG explants (Fig. 4A), increasing the maximum number of their neurites and generating the longest projections demonstrating the potential of our newly developed conjugate for axonal outgrowth and neuronal regeneration.

3.4. PGA-SS-F Preserves Neurofilaments and Increases Synaptophysin Expression and Axonal Outgrowth in an Ex Vivo Model of SCI in Organotypic Spinal Cord Slices

To evaluate the effects of PGA-SS-F in neuronal preservation and

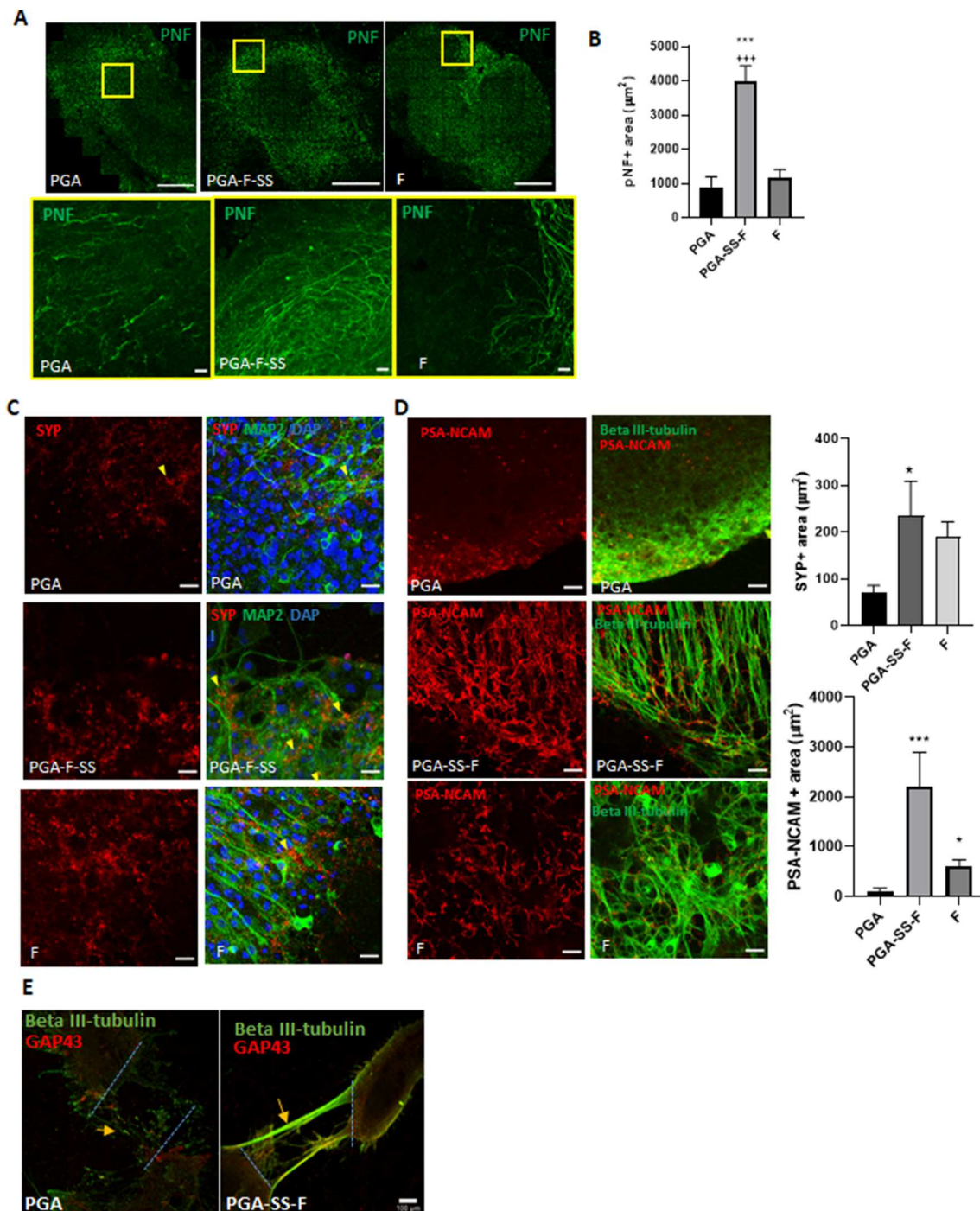


Fig. 5. PGA-SS-F Treatment Preserves a Greater Number of Neurofilaments and Induces Synaptic Features in Spinal Cord Organotypic Ex Vivo Cultures. **A.** Upper panels: Representative panoramic images of organotypic cultures of transversal slices of neonatal spinal cords. Scale bar 500 µm; Lower panels: Zoom images from yellow squares indicated in upper panels; scale 20 µm. **B.** Quantification of the area occupied by pNFs. **C.** Synaptophysin (SYP, red) and MAP-2 (green) stainings; **D.** left panels: PSA-NCAM (red) and beta-III tubulin (green) in organotypic cultures treated with 50 µM of PGA-SS-F or fasudil or PGA (control) for one week. Scale bar 20 µm; right panels: quantification of SYP vesicles and PSA-NCAM protein positive area. Data presented as mean ± SEM (n = 3 per group) *p < 0.05, ***p < 0.001 vs. PGA, +p < 0.05, +++p < 0.001 vs. F group and determined by ANOVA multiple comparison test and Tukey's *post hoc* test. **E.** Confocal image depicts an experiment with the greatest outgrowth and reconnections stained with beta-III-tubulin (green) and GAP43 (red) double immunostaining; n = 4. PGA-SS-F treated slices exhibited bundles of fibers crossing the lesion site, re-connecting both stumps (yellow arrows), positive for both beta-III-tubulin (green) and GAP43 (red). Blue dash lines delimited the lesion site. (For interpretation of the references to colour in this figure legend, the reader is referred to the Web version of this article.)

neuroplasticity in the spinal cord, we employed postnatal rat spinal cord organotypic cultures. We treated transversal spinal cord sections (350 μm) seven days after tissue section and damage with PGA, PGA-SS-F, and fasudil (at 50 μM drug equiv.) and then maintained cultures for five additional days. As the expression of phosphorylated neurofilaments (pNF) constitutes a key event in the regulation of axonal transport and provides stability to mature axons [44], both of relevance for axon regrowth, we evaluated pNF levels under different conditions. Representative images of pNF immunostaining (Fig. 5A) and the quantified data (Fig. 5C) demonstrate that PGA-SS-F treated slices exhibited significantly greater positive area for neuronal phospho-filaments than the PGA or fasudil, indicating that PGA-SS-F promotes active axonal transport on preserved fibers damaged by the sectioning process.

PGA-SS-F-treated injured spinal cord slices also allowed for the preservation of neuronal fibers, which displayed staining for microtubule-associated protein 2 (MAP2) (Fig. 5B; upper panels green). Furthermore, PGA-SS-F-treated injured spinal cord slices displayed significantly higher synaptic vesicle density in MAP2-positive neurons, as evidence by the increased synaptophysin (SYP) positive area (Fig. 5C, red) when compared to PGA or fasudil treatment. These findings suggest enhanced *ex vivo* synaptogenesis in response to PGA-SS-F-treatment.

The brain expresses high levels of polysialylated neuronal cell adhesion molecule (PSA-NCAM) during development, and expression in the adult is linked to functional plasticity [45]; therefore, increasing PSA-NCAM levels have been proposed as a therapeutic mechanism that may promote neuroregeneration following SCI [46]. We explored whether the PGA-SS-F treatment modulates PSA-NCAM expression in spinal cord slices. Representative images of PSA-NCAM immunostaining (Fig. 5D, lower panels; red) and the quantification of expression levels exhibited a significant increase in PSA-NCAM in beta-III tubulin positive neuronal fibers when compared to PGA or fasudil treatment ($***p < 0.001$ vs. PGA & fasudil) (Fig. 5D).

Following a transversally-induced lesion in longitudinal spinal cord slices that generates a gap between both stumps (Fig. 5E, dashed blue line), we evaluated the capacity of PGA-SS-F to re-connect the two sides of the lesion in comparison with PGA. We found that PGA-SS-F efficiently promoted axonal outgrowth in all assayed organocultures (Fig. 5E; the representative image shows the case with the longest reconnection). PGA-SS-F treated slices exhibiting bundles of beta-III-tubulin positive fibers (green) co-expressing GAP43 protein (red) that cross the lesion site and re-connect both stumps five days after lesion and treatment.

3.5. PGA-SS-F increases neurite regrowth following Rho/ROCK activation

Lysophosphatidic acid (LPA), a potent mitogen that activates the Rho/ROCK pathway, induces growth cone retraction and neurite collapse [47,48], and, therefore, mimics the molecular consequences of SCI in model systems. We studied the response of NPCs to LPA-induced Rho/ROCK pathway activation after treatment with PGA-SS-F or fasudil.

We first evaluated the capacity of PGA-SS-F to prevent neurite retraction induced by Rho/ROCK activation induced by LPA by Nestin immunostaining. LPA treatment reduced neurite length by nearly 50 % in NPCs when compared to PGA (Fig. 6A, yellow arrows); however, both PGA-SS-F and fasudil treatment significantly rescued LPA-induced neurite retraction ($***p < 0.001$ vs. LPA). (Fig. 6A, graph). Indeed, PGA-SS-F treatment of NPCs induced increased neurite length to a higher degree than PGA or fasudil treatment, even in the presence of LPA (Fig. 6A).

We also analyzed the effect of Rho/ROCK activation on the spontaneous differentiation of NPCs in the presence of PGA-SS-F. LPA treatment alone limited cell maturation and maintained a significant percentage of NPCs in an undifferentiated stage, as evaluated by the percentage of cells expressing Nestin (Fig. 6B, lower panel). We failed to find any differences in the number of Nestin-positive cells between

control (without PGA) and PGA (46.77 ± 4.3 vs. 59.08 ± 2.14); however, PGA-SS-F in the presence of LPA led to significantly higher levels of beta-III-tubulin when compared to PGA or LPA alone, suggesting a preferential induction of a neuronal fate (Fig. 6B). Indeed, we failed to observe any significant differences in the glial markers Olig2 (early oligodendrocyte marker) and GFAP (astrocytic marker) under any of the studied conditions. As shown in Fig. 6C, we found that both free fasudil and PGA-SS-F efficiently inhibited LPA-induced phosphorylation of myosin phosphatase targeting protein (MYPT), a direct downstream target of Rho/ROCK in NPCs.

Finally, we performed a co-culture of eGFP-NPC (NPCs constitutively expressing eGFP) pre-treated with PGA, PGA-SS-F, or fasudil with the spinal cord organotypic cultures to mimic cell transplantation. PGA-SS-F-treated eGFP-NPCs (50 μM concentration for 24 h) displayed better engraftment when compared to non-pre-treated NPCs and displayed a neuronal-like morphology with an increased percentage of elongated cells (Fig. 6D, white arrow) when compared to NPCs pre-treated with PGA or fasudil, which mostly displayed a more rounded morphology (Fig. 6D, red arrow). We also discovered that PGA-SS-F-treated NPCs resided over long axonal/dendrite processes of the endogenous neurons of the spinal cord slices (Fig. 6D, red); in contrast, PGA- or fasudil-pretreated NPCs displayed lower cell density. This data indicates that NPCs pre-treated with PGA-SS-F exhibit enhanced engraftment abilities upon transplantation into the spinal cord.

3.6. *In vivo* administration of PGA-SS-F enhances neuroprotection and neuroregeneration related-signaling pathways in acute SCI

To investigate the capacity of PGA-SS-F to efficiently mitigate SCI-associated secondary injury at the acute stage after SCI in comparison with the free form of fasudil, we evaluated the consequences of a single local administration of PGA-SS-F or fasudil and PGA (10 $\mu\text{L}/300$ μM fasudil equiv. concentration) after severe experimental SCI. We evaluated protein levels of lysates from T7 to T9 spinal cord segments of at least four different animals, including the epicenter of the lesion induced at T8, 48 h after injury and treatment.

Sample analysis first revealed the significant inhibition of Rho kinase activity after PGA-SS-F treatment compared to PGA, as evidenced by the decreased phosphorylation of MYPT. Western blot images of four tested samples per each group (Fig. 7A) and the corresponding densitometry analysis (Fig. 7A, graph) demonstrate the efficacy of the local administration of the conjugate in reducing Rho kinase activity after SCI. We also collected CSF at the time of animal sacrifice and measured remaining fasudil levels within the intrathecal space via a validated LC-MS method (Fig. 2D and S17). The LC-MS/MS conditions employed were identical to those used above to analyze fasudil stability in plasma. Nevertheless, we re-evaluated the developed LC-MS and extraction methods for linearity, LOQ, LOD, recovery, and matrix effects (Figure S17). We found $1.29 \% \pm 0.08 \%$ ($n = 3$) of total fasudil in the CSF collected 48 h after PGA-SS-F administration, although we failed to detect fasudil in CSF collected 48 h after injection of PGA or fasudil (Fig. 2D). These findings confirm the prolonged bioavailability of fasudil after PGA conjugation, supporting its greater pharmacological activity.

PGA-SS-F treatment significantly activated survival and anti-apoptotic molecular signaling, as evidenced by the significantly decreased the expression of caspase-3 in comparison with PGA or fasudil (Fig. 7B). In addition, PGA-SS-F treatment also significantly increased expression of the anti-apoptotic protein Bcl-2 and reduced the expression of the pro-apoptotic protein Bag1 in comparison with PGA treatment (Figure S11A). This neuroprotective effect could be related to the observed significant increase in p-Akt levels (which can induce pro-survival related-signaling) in addition to the activation of autophagy, as revealed by a significant decrease in the phosphorylation of mTOR and significant increases to AMPK and LC3I levels following PGA-SS-F treatment (Figure S11B).

Interestingly, PGA-SS-F treatment also displayed significant

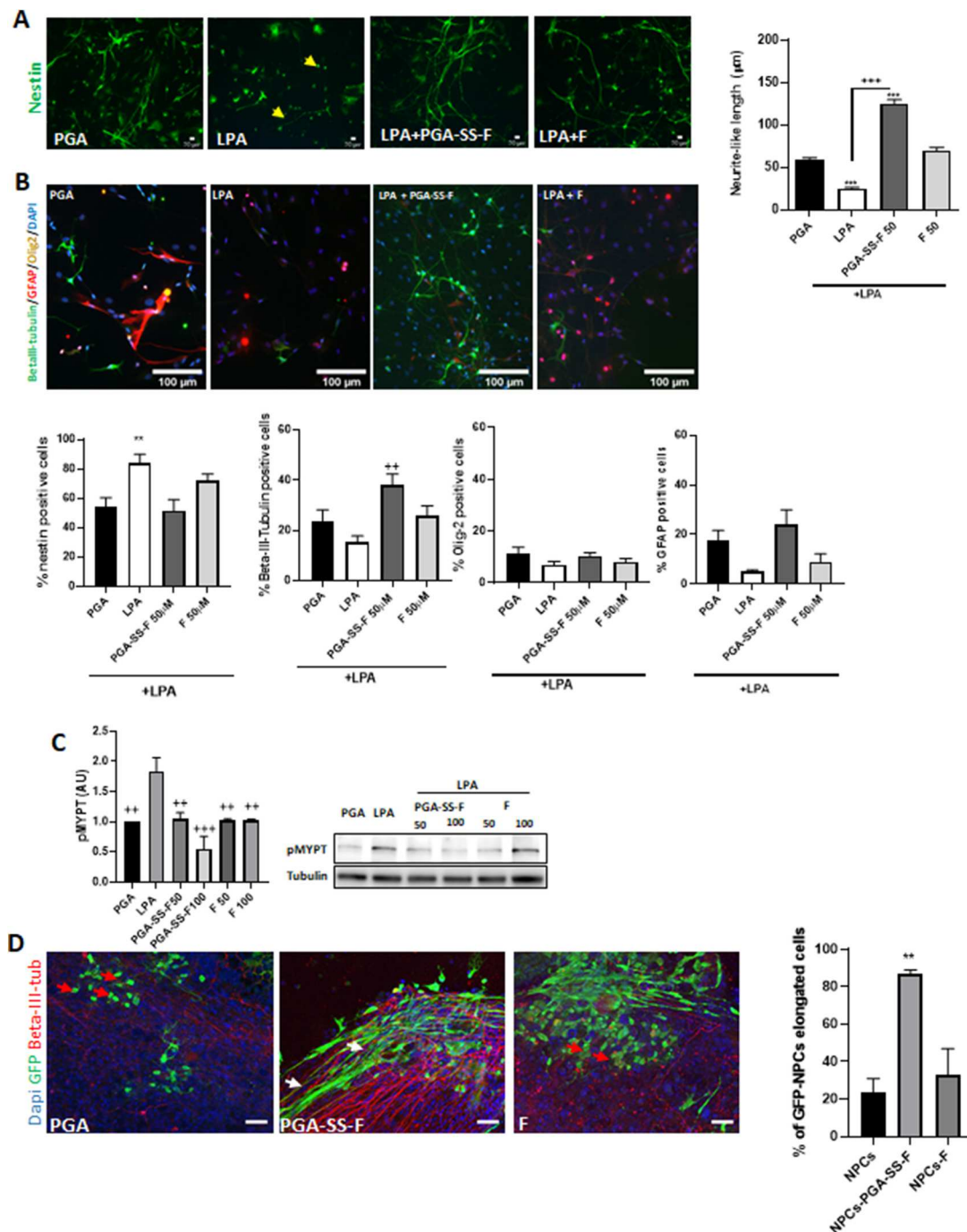


Fig. 6. PGA-SS-F Treatment Counters Neurite Retraction Following Rho/ROCK Activation and Promotes Neuronal Fate, Axonal Growth, and Neuroplasticity following Exposure to LPA in Spinal Cord Organotypic *Ex Vivo* Cultures. **A.** Left panels: NPCs treated with PGA (control) or fasudil/PGA-SS-F (50 μM) in adherent culture with representative immunostaining of Nestin (green). LPA treatment (10 μM) induced neurite retraction (yellow arrows); Right panel: Quantification of the longest neurite from each nestin-positive cell using NeuronJ. Data presented as mean \pm SEM (n = 6 per group) ***p < 0.001 vs. PGA group; +++p < 0.001 vs. LPA group, determined by ANOVA multiple comparison test and Tukey's *post hoc* test. **B.** Upper panels: Representative images of beta-III-tubulin (green), Olig-2 (orange), and GFAP (red) immunostainings after spontaneous differentiation of NPCs treated as indicated. Lower panels: Quantification of the percentage of neurons (beta-III-tubulin positive), oligodendrocytes (Olig-2 positives), astrocytes (GFAP positive) and Nestin following ROCK activation in the presence of fasudil/PGA-SS-F (50 μM). Data presented as mean \pm SEM (n = 3 per group) **p < 0.01 vs. PGA; ++p < 0.01 vs. LPA determined by ANOVA multiple comparison test and Tukey's *post hoc* test. **C.** Quantification of phospho-MYPT levels by Western blotting in NPCs treated with LPA, fasudil, or PGA-SS-F. The relative expression of the protein bands was normalized to tubulin levels. Data presented as mean \pm SEM (n = 3 per group) ++p < 0.01 +++p < 0.001 vs. LPA determined by ANOVA multiple comparison test and Tukey's *post hoc* test. Representative blot is shown. **D.** Co-culture of PGA-SS-F or fasudil pre-treated eGFP-NPCs with organotypic neonatal spinal cord cultures. Left panels: Representative images of beta-III-tubulin (red) and GFP (green) immunostaining; Right panels: Quantification of elongated and engrafted NPCs, expressed as a percentage of total engrafted cells. PGA-SS-F pre-treated NPCs displayed increased neurite-like processes. Data presented as mean \pm SEM (n = 3 per group). **p < 0.01 vs. NPCs and NPCs-F groups determined by ANOVA multiple comparison test and Tukey's *post hoc* test. Scale bar 50 μm . (For interpretation of the references to colour in this figure legend, the reader is referred to the Web version of this article.)

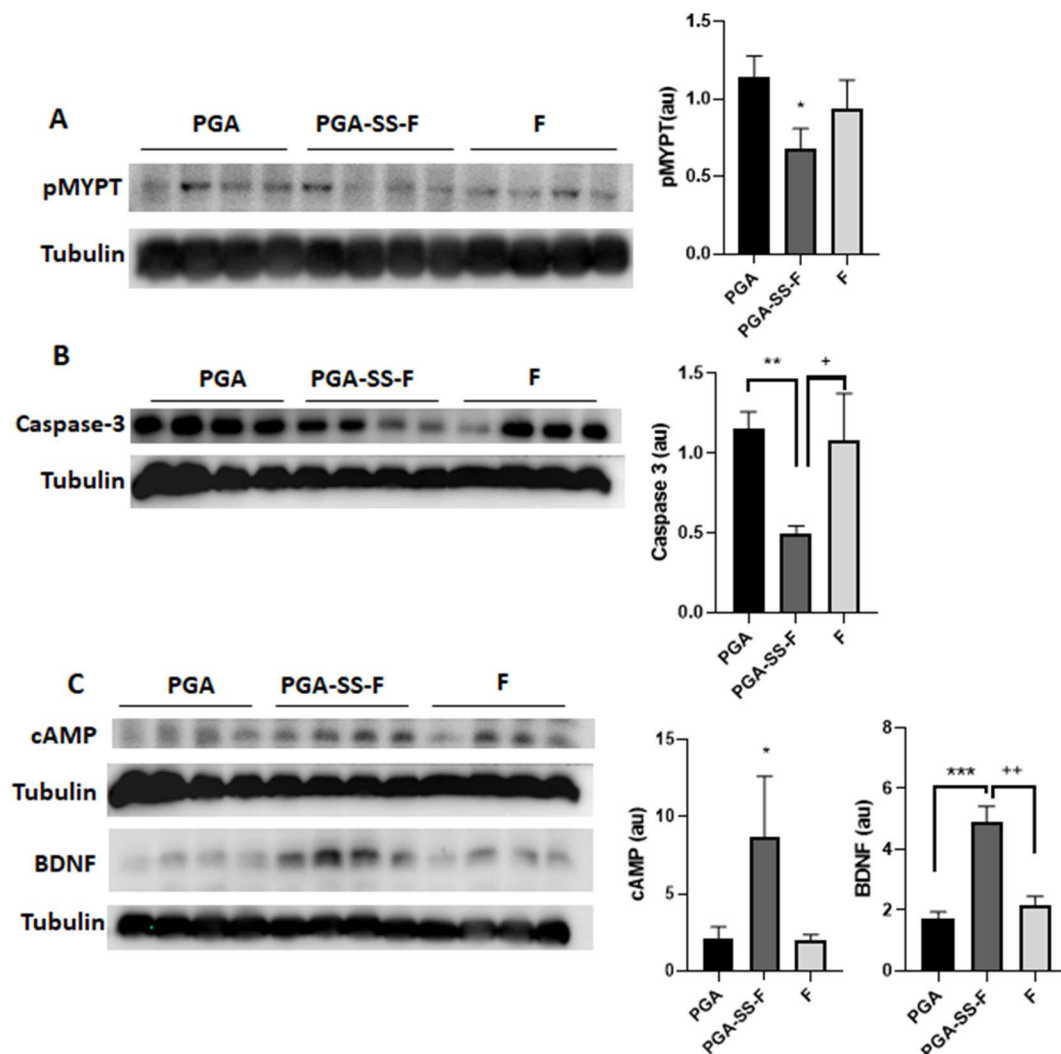


Fig. 7. Intrathecal Administration of PGA-SS-F but not the free form of fasudil Inhibits Rho/Rock Activity and Triggers Neuroprotective and Neuroregenerative Signaling Pathways 48 h after Acute SCI in vivo. **A.** Phospho-MYPT analysis as a proxy for Rho/Rock activation status following SCI. Graph represents the relative expression of the protein bands standardized by densitometry analysis to tubulin levels and presented as mean \pm SEM (PGA and PGA-SS-F groups, $n = 8$; F group, $n = 4$). **B.** Analysis of the pro-apoptosis-related protein levels caspase-3. Graph represents the relative expression of the protein bands standardized by densitometry analysis to tubulin levels and presented as mean \pm SEM. **C.** Analysis of pro-regenerative signaling via the evaluation of cAMP and pro-BDNF protein expression. Graph represents the relative expression of the protein bands standardized by densitometry analysis to tubulin levels and presented as mean \pm SEM. * $p < 0.05$; ** $p < 0.01$; *** $p < 0.001$ vs. PGA group, + $p < 0.05$; ++ $p < 0.01$ vs. F; determined by ANOVA multiple comparison test and Tukey's *post hoc* test.

increases in cyclic (c)AMP and brain-derived neurotrophic factor (BDNF) levels in comparison with PGA or free fasudil treatment (Fig. 7C). BDNF acts as an autocrine factor that maintains neural survival and regulates late axon development, which itself requires the stable elevation of cAMP levels [49].

Together, these data indicates that the in vivo administration of PGA-SS-F, but not free fasudil, activates survival pathways and provides a priming signaling for neuronal regeneration following SCI.

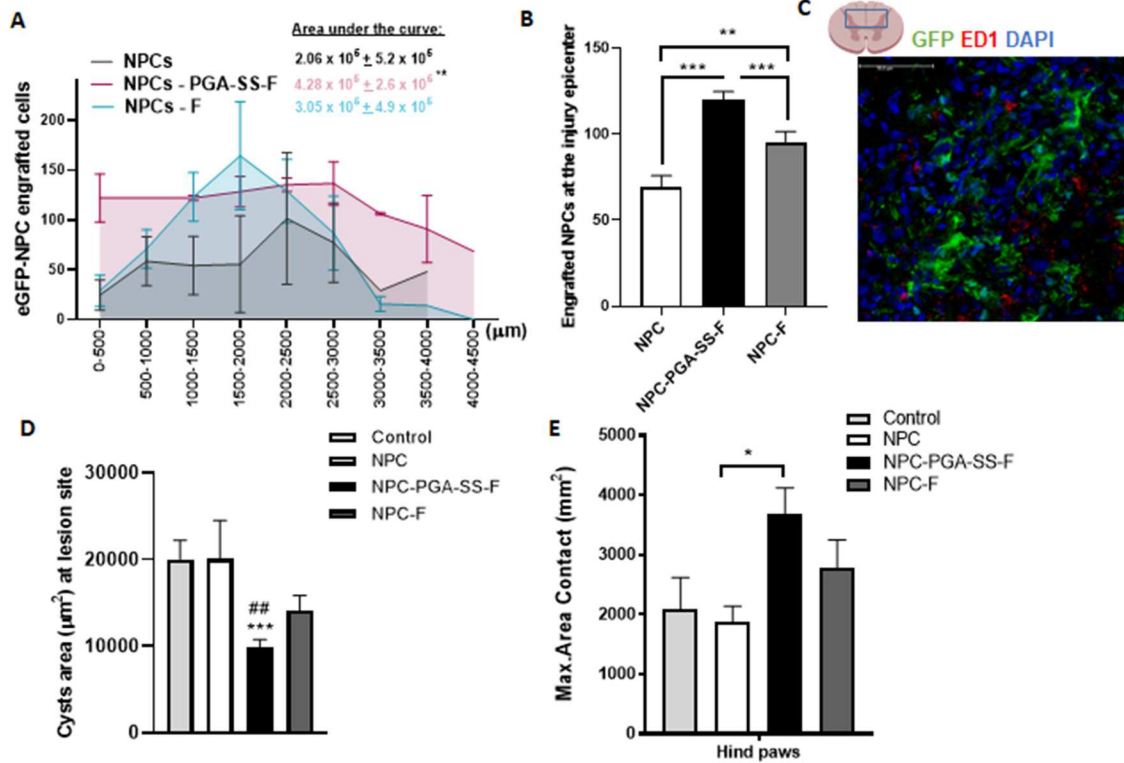
3.7. PGA-SS-F treatment improves NPC transplantation engraftment, survival, and functional locomotor outcomes in a traumatic SCI Rat model

We previously demonstrated the beneficial effects of NPC therapy in acute [32,33] and chronic [12] traumatic SCI; however, low levels of survival and engraftment represent significant limitations associated with NPC transplantation.

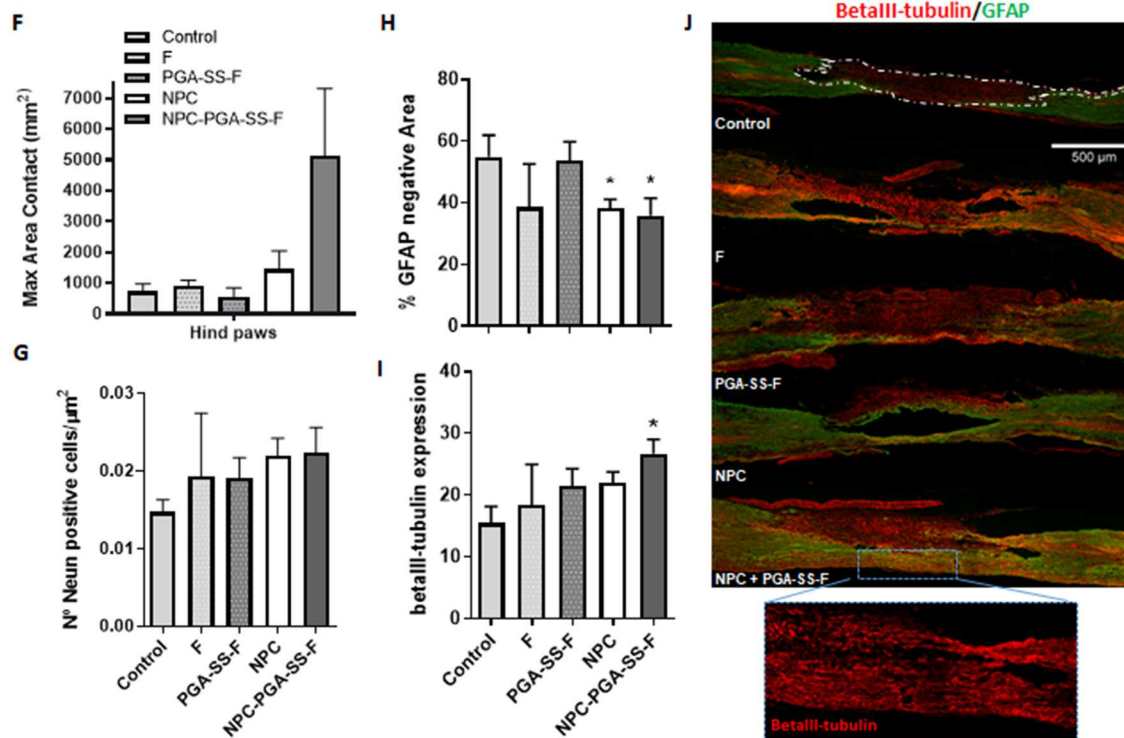
We evaluated whether PGA-SS-F pre-treatment (50 μ M drug equiv., 24 h) could improve the survival and engraftment of transplanted NPCs during in vivo cell transplantation immediately after severe SCI when

compared to fasudil treatment or transplantation of untreated NPCs. We inspected transversal sections of the spinal cord to evaluate the distribution of eGFP-labeled NPCs two months after SCI and transplantation over 4.5 mm length, at the epicenter of the injury as shown in the graphical representation on Fig. 8A. PGA-SS-F-treated eGFP-NPC showed a more extensive distribution from rostral to caudal regions showing a greater area under the curve when compared to untreated eGFP-NPCs (Fig. 8A). The quantification of the total eGFP-NPCs at the epicenter of the injury revealed an increased number of engrafted cells for PGA-SS-F-treated NPCs and fasudil-treated NPCs, compared untreated NPCs. Nevertheless, PGA-SS-F-treated NPCs exhibited increased engraftment compared to fasudil-treated NPCs (Fig. 8B). Representative image of the transversal spinal cord section for GFP and ED-1 co-staining, for eGFP-NPC and macrophages identification respectively, showed that the engrafted eGFP-NPCs (green) co-existed in a non-phagocyte stage with infiltrated macrophages (red) (Fig. 8C). For eGFP-NPC quantification, we discarded ED-1-engulfed cells. We performed cell fate evaluation of the transplanted cells by beta-III tubulin and GFAP double staining; however, we failed to observe positive

Acute transplantation in severe traumatic SCI



Chronic transplantation in severe traumatic SCI



(caption on next page)

Fig. 8. *In vivo* Combination Treatment with PGA-SS-F improves NPCs Engraftment, Preserves Neuronal Fibers, and Promotes Gait Recovery. Panels A-E correspond to the acute SCI model, while Panels F-J correspond to the chronic SCI model. A. Analysis of engrafted eGFP-NPC distribution at the epicenter of the injury via the quantification of cells every 500 μm over 4.5 mm. The area under the curve obtained for each group over the 4.5 mm of the spinal cord is indicated in the corresponding legend. Data presented as mean \pm SEM $^{**}p < 0.01$ vs. NPCs. B. Quantification of engrafted eGFP-NPCs at the epicenter of the injury. Data presented as mean \pm SEM $^{**}p < 0.01$, $^{***}p < 0.001$ as indicated. C. Representative image of GFP (green) and ED1 (red) immunostaining showing non co-localization of transplanted eGFP-NPCs (positive for GFP) and infiltrated macrophages (positive for ED-1). D. Quantification of the cystic area by hematoxylin and eosin staining of spinal cord transversal sections eight weeks after SCI. Data presented as mean \pm SEM. $^{***}p < 0.001$ compared to Conotrol and $^{##}p < 0.01$ compared to NPC. E Gait analysis evaluation showing quantification of maximal area contact. Data presented as mean \pm SEM. $^{*}p < 0.05$ compared as indicated. F. Gait analysis evaluation showing the maximal area contact of hind paws after treatments in the SCI chronic model. G. Quantification of NeuN positive cells per μm^2 . H. Quantification of the GFAP negative area at the lesion site (area delimited in control group with a white dashed line in J). I. Quantification of beta-III-tubulin expression at the epicenter of the injury. J. Representative images of GFAP (green) and beta-III-tubulin (red) immunostainings in longitudinal spinal cord slices two months after treatments. Higher magnification of beta-III-tubulin fibers in NPCs + PGA-SS-F group shown in blue inset square. Data presented as mean \pm SEM. $^{*}p < 0.05$ vs. control group. (For interpretation of the references to colour in this figure legend, the reader is referred to the Web version of this article.)

staining in transplanted eGFP-NPCs (*data not shown*).

We next employed hematoxylin and eosin staining of the spinal cord sections to evaluate cyst/cavity formation. PGA-SS-F-treated NPCs displayed smaller cavities compared to the control and NPC groups (Fig. 8D). Smaller cavities in the PGA-SS-F-treated NPC treated group could indicate tissue preservation, or the decrease in the cystic area could derive from the increased survival of transplanted cells, which, in turn, could fill the cavities.

Finally, *in vivo* functional analysis of gait by using CatWalk system two months after SCI and transplantation demonstrated improvement in certain locomotor skills measured by the increased maximum area of contact of the hind paws (Fig. 8E) in the group of animals transplanted with PGA-SS-F-treated NPCs. No other parameters analyzed in the CatWalk system showed significant differences (*data not shown*).

To evaluate the potential regenerative capacity of PGA-SS-F treatment alone or in combination with NPC transplantation in an extended neuronal degeneration process at the chronic spinal cord injury (five weeks after injury), we evaluated the simultaneous, but separate, application of both NPC transplantation and PGA-SS-F-treatment in chronic SCI. We hypothesized that the constant delivery of PGA-SS-F for one week into the intrathecal space using an osmotic pump would have an influence on both the transplanted eGFP-NPCs and the injured endogenous tissue. While the free form of fasudil demonstrated lower efficiency regarding NPC engraftment, survival, tissue preservation and functional improvement in the acute treatment (Fig. 8A–E), we did not test the combination with fasudil free form in the chronic injuries. None of the tested conditions prompted significant differences during CatWalk gain analysis, which measured the maximum contact area two months after the administration of fasudil or PGA-SS-F alone or after transplantation of NPC alone or in combination with PGA-SS-F (Fig. 8F). While the combination of PGA-SS-F and NPCs increased the maximum contact hind paws area, values failed to reach significance due to the generally high levels of variability in the measurement. The crossing time and stride length index also failed to indicate significant differences between the groups in any of the SCI models (*data not shown*).

We next inspected the spinal cord tissue two months after treatment. The quantification of mature neuronal somas using the NeuN marker at the injury site failed to reveal significant differences between groups (Fig. 8G); however, we did observe a significant reduction in the scar size (Fig. 8H), delimited by the astrocytic barrier, as measured as the percentage of GFAP negative area, following the transplantation of eGFP-NPCs alone or eGFP-NPCs combined with PGA-SS-F. Of note, a single administration of PGA-SS-F treatment failed to influence scar size (Fig. 8H).

Combined PGA-SS-F and eGFP-NPC transplantation prompted the appearance of a significantly higher amount of beta-III-tubulin positive fibers (Fig. 8I–J) within the injured tissue when compared with the PGA treatment as control, indicating a significant neuroprotective effect of the combination treatment in chronic stage SCI. Fig. 8J depicts representative immunostainings of beta-III-tubulin (red) for neuronal fiber detection (a higher magnification of beta-II-tubulin staining is shown for the combinatory treatment from the indicated area; blue square) and

GFAP (green) for astrocytic detection lining the astrocytic barrier (GFAP positive) and delimiting the formed scar (negative for GFAP; Fig. 8J, white dashed line), from one animal per group.

Overall, our data provide evidence that our redox-sensitive conjugated form of fasudil (PGA-SS-F) provides for enhanced NPC survival and integration, which prompted enhanced neuroprotection and repair within the injured SCI.

4. Discussion

Rho kinase signaling rapidly and dramatically activates following SCI [50–52] and contributes to secondary damage by triggering inflammation or apoptosis, among other mechanisms [53]. Rho kinase restrains neuronal polarization and axon growth by inducing myosin-II generated actin arcs to prevent microtubule protrusion in the axonal growth cone [54] and participates in axon tip collapse [4,53,55]. Genetic or pharmacological inhibition of RhoA/ROCK drives axonal regrowth and neuroprotection [50,56,57]; therefore, inhibition of RhoA/ROCK represents a candidate translational strategy to improve functional outcomes after SCI in humans. Several clinical trials of RhoA/ROCK inhibitors have been recently approved [5,58], with fasudil reaching evaluation in a phase III clinical trial, which provided evidence for utility and safety in acute ischemic stroke patients [59]. However, and importantly, the lower than anticipated efficacy of fasudil led to the termination of the trial, with the low stability in circulation and a general lack of penetration through the blood-brain barrier, presumably driving these poor results [8].

To address these limitations and potentiate the benefits of fasudil in SCI treatment, we developed a family of rationally designed polymer-fasudil conjugates based on PGA as a multivalent, biodegradable, and biocompatible carrier [14]. To achieve the site-specific and sustained release of fasudil after intrathecal administration, we explored polymer-drug linking strategies with relevance to the physiological conditions of the SCI lesion, which include the presence of proteases, pH gradients, and reducing environments. Therefore, we synthesized and fully characterized conjugates with a protease labile amide linker (PGA-F), a hydrolytically-labile carbamate linker (PGA-O-F), and a novel disulfide self-immolative (PGA-SS-F) linker susceptible to a reductive environment (Fig. 1) by post-polymerization modification approaches [19].

While we failed to observe toxicity in NPCs for any of the developed conjugates, free fasudil significantly reduced NPC viability at the highest tested concentration, suggesting that polymer conjugation will allow for an increase in the tolerated dose used in patients. Next, we evaluated the capacity of each conjugate to induce neurite elongation from NPCs under adherent conditions, as previously described for fasudil [43], in the hope of improving the integration and neuronal interconnection of NPCs into the damaged spinal cord neural network. Interestingly, PGA-SS-F exhibited a similar capacity to induce neuritogenesis over short periods as free fasudil, but more importantly, only PGA-SS-F prompted long-term neurite elongation (Fig. 3). These results could be explained by drug release kinetics, which demonstrated the higher

bioavailability of fasudil from the PGA-SS-F conjugate under intracellular reductive conditions (Figs. 2 and S1). This neuritogenic effect agrees with the preferential neuronal lineage commitment induced by PGA-SS-F in NPCs (Fig. 3).

Ex vivo experiments provided direct evidence that PGA-SS-F induced axonal outgrowth in both peripheral and central nervous system-derived neurons in neonatal DRG organotypic cultures (Fig. 4), adult dissociated DRGs (S19), or spinal cord slices (Fig. 5) as evidenced by the induced axonal elongation and induced expression of GAP43, a known growth cone marker. Interestingly, the neuronal projections induced by the PGA-SS-F treatment were organized into thick bundles of aligned fibers with larger caliber axons and increased levels of synaptogenesis, as evidenced by the increased expression of synaptophysin in the spinal cord slice neuronal outgrowths. This marked effect on bundle formation could be derived from the increased number of pNFs found following PGA-SS-F treatment. Neurofilaments contribute to an increase in axonal diameter, while larger caliber axons possess more rapid conduction velocities than smaller axons [60]. Neurofilaments undergo phosphorylation to regulate transport and function, increase myelination, and induce stability during axonal growth in vivo [61]. Also, we discovered increased PSA-NCAM expression in the PGA-SS-F treated organotypic slices, indicating a fasciculation process, which contributes to the described bundle formation and, most probably the guiding process, thereby allowing the neuronal projections to re-connect within the spared tissue (Fig. 5F).

LPA treatment induces growth cone retraction and neurite collapse [47,48] in NPCs (Fig. 6). In conditions that mimic the over-activation of the RhoA/ROCK pathway that occurs in vivo after SCI, we demonstrated the enhanced capacity of PGA-SS-F to overcome LPA induced retraction and neural differentiation (Fig. 6) when compared with free fasudil, probably due to the higher Rho inhibitory activity of PGA-SS-F. In vivo, we discovered that a single intrathecal administration of PGA-SS-F immediately after SCI efficiently induced neuroprotection through the inhibition of RhoA/ROCK, a reduction in apoptosis, as evidence by detection of the activated form of caspase 3, and the induction of survival-related signaling factors, such as Bag-1, Bcl2 or, pAKT [62]. AKT phosphorylation could act as a focal point as the critical substrate of axon regeneration related pathways such as PI3K-PDK1, PI3K-mTORC2, mTORC1, or GSK3 β [63]. Therefore, selective activation of the AKT pathway could provide for induced neuroprotection and neuroregeneration. Indeed, brief treatment with PGA-SS-F induced a significant accumulation of cAMP, an axonal growth mediator, and the neurotrophin BDNF but not the free fasudil form, indicating the activation of additional regenerative signals (Fig. 7). Increasing cAMP levels enhances the growth and guidance of axons, opposes the inhibitory signaling exerted by myelin and the glial scar [64], and increases the intrinsic capacity of injured axons to regrow [65] with the aid of BDNF [66]. Also, at early times after injury (48 h), PGA-SS-F significantly reduced the phosphorylation of mTOR (Figure S11). Inhibition of mTOR phosphorylation during the acute phase of SCI can prevent neural cell death by limiting apoptosis [67,68] and reduce secondary damage mediated by microglial activation and migration [69]. Furthermore, the neuroprotective effects of inhibiting mTOR can be achieved by activating autophagy; rapamycin treatment (a specific inhibitor of mTOR) induces autophagy [70] and enhances lysosomal biosynthesis, thereby offering neuroprotection following central nervous system injury [71]. Decreased or blocked autophagic flux has been described in SCI [72], with downregulated autophagic activity related to increased neuronal apoptosis [73], which was more evident in ventral horn motor neurons than in sensory neurons [74]. We also found evidence for the modulation of autophagy by PGA-SS-F treatment by an increase in pAMPK and LC3 levels in vivo (Figure S11), with LC3 and AMPK reported to contribute to autophagosome maturation and lysosomal fusion [75]. We further explored the potential implication of AMPK activation in neurite outgrowth induced by PGA-SS-F (Figure S10). Pre-treatment with the AMPK phosphorylation inhibitor compound C (CC), significantly

reduced neurite elongation from NPCs in culture; however, the inhibition of AMPK activation failed to abolish the neuritogenic effect of PGA-SS-F, thereby arguing against the involvement of the activation of this pathway (Figure S110).

Poor engraftment, low survival, and astrocytic differentiation represent the significant reported limitations of stem cell-based therapies for SCI [76,77]. As PGA-SS-F promotes the survival of NPCs offering a great advantage for cell transplantation, we primed NPCs with PGA-SS-F before transplantation in the hope of overcoming the hostile microenvironment associated with acute-phase SCI. Results revealed that NPCs primed with PGA-SS-F treatment displayed enhanced survival after acute transplantation, with significant higher engraftment extending rostral and caudally to the lesion, significantly greater when compared with the transplanted NPC primed with the free form of fasudil, accompanied by reduced cavitation and increased locomotor skills recovery, as measured as the maximum paw contact area during stepping (Fig. 8A–E). Transplanted cells failed to contribute to astrogliosis; moreover, transplanted NPC failed to show preferential differentiation into a neuronal cell fate since no co-localization with either GFAP or beta-III-tubulin, respectively. These findings indicate that the dedifferentiation of NPCs into an immature stage occurs independently of the PGA-SS-F treatment. We previously reported that spinal cord-derived NPCs transplanted after SCI express Olig2 [31], a marker of undifferentiated oligodendrocytes, indicating a preferential oligodendroglia rather than neuronal or astroglial cell fate.

In the chronic SCI scenario, we previously reported that spinal cord-derived NPCs in combination with a polymer-curcumin conjugate prompted a significant improvement in functional locomotor recovery after transplantation. While conjugate treatment failed to induce any significant effect when administered alone, the combination with NPCs led to improvements above and beyond those observed with the transplantation of NPCs alone [12]. We employed a similar approach by combining PGA-SS-F and NPC transplantation in severe chronic SCI by direct administration into the injured area (Fig. 8F–J). The combination of treatments, PGA-SS-F delivered within an osmotic pump for a week, and the NPCs, intramedullary injected rostral and caudal to the lesion, prompted a more significant amount of beta III-tubulin fibers at the lesion site two months after treatment, as previously shown for the combination of the polymer-curcumin conjugate and NPC [12]. Furthermore, a significant number of these fibers possessing a straightened, organized pattern indicating an anatomical guided preservation suggesting protection of the ultrastructural organization of the long tracts. Although gait performance analysis showed non-significant differences among the groups and variability between the samples, the combination treatment group displayed a better gait response in the SCI chronic model.

5. Conclusion

Herein, we report on the transplantation of spinal cord-derived NPCs in combination with a polymer conjugated form of the Rho kinase inhibitor fasudil for the treatment of SCI. We improved the therapeutic potential of fasudil, with a short serum half-life, through conjugation to a polypeptidic carrier via an optimized redox-dependent self-immolative linker. PGA conjugation enhanced stability, sustained fasudil release, and improved neuroprotective and regenerative activity in acute and chronic in vivo models of SCI. Furthermore, PGA-SS-F treatment of transplanted NPCs improved tissue engraftment and cell survival, and so, this may represent an important approach towards the development of successful cell transplantation strategies.

Declaration of competing interest

The authors declare the following financial interests/personal relationships which may be considered as potential competing interests: Patent application filed for PGA-SS-F conjugate (PCT/EP2020/058940)

co-inventors EG, VJN, OZ, RRA, AA, AA, SD, MJV, and VMR. No other commercial conflicts of interest are present.

Acknowledgments

This research was funded by FEDER/Ministerio de Ciencia e Innovación – Agencia Estatal de Investigación [RTI2018-095872-B-C21/ERDF], Ministerio de Ciencia e Innovación [SAF2016-80427-R, PID2019-108806RB-I00], Fundació Marató TV3 [20172230, 20172231 and 20172110] Fundación Step by Step, Agencia Valenciana de Innovación (AVI) [INNVAl10/19/047] and MINECO/FEDER, UE; Fondo Europeo de Desarrollo Regional (FEDER) incluido en el Programa Operativo FEDER de la Comunidad Valenciana 2014–2020.

Appendix A. Supplementary data

Supplementary data to this article can be found online at <https://doi.org/10.1016/j.biomaterials.2021.121052>.

Authors contribution

E. Giraldo: Conceptualization; Data curation; Formal analysis; Investigation; Methodology; Roles/Writing – original draft; Writing – review & editing. V.J. Nebot: Conceptualization; Data curation; Formal analysis; Investigation; Methodology. S. Dorđević: Data curation; Formal analysis; Investigation; Methodology; Writing – review & editing. Raquel Requejo-Aguilar: Conceptualization; Data curation; Formal analysis; Investigation; Methodology. A. Alastrue-Agudo: Investigation; Methodology. O. Zagorodko: Data curation; Formal analysis; Investigation; Methodology; Writing – review & editing. A. Armiñan: Data curation; Formal analysis; Investigation; Methodology; B. Martínez-Rojas: Investigation; Methodology. M.J. Vicent: Conceptualization; Data curation; Formal analysis; Roles/Writing – original draft; Writing – review & editing; Funding acquisition; Project administration. Moreno-Manzano: Conceptualization; Data curation; Formal analysis; Roles/Writing – original draft; Writing – review & editing; Funding acquisition; Project administration.

Data availability

The data that support the findings of this study are available on request from the corresponding author. The data are not publicly available due to privacy or ethical restrictions.

References

- C.S. Ahuja, M. Fehlings, Concise review: bridging the gap: novel neuroregenerative and neuroprotective strategies in spinal cord injury, *Stem cells translational medicine* 5 (2016) 914–924.
- E.J. Bradbury, E.R. Burnside, Moving beyond the glial scar for spinal cord repair, *Nat. Commun.* 10 (2019) 3879.
- T. Madura, T. Yamashita, T. Kubo, M. Fujitani, K. Hosokawa, M. Tohyama, Activation of Rho in the injured axons following spinal cord injury, *EMBO Rep.* 5 (2004) 412–417.
- Y. Fujita, T. Yamashita, Axon growth inhibition by RhoA/ROCK in the central nervous system, *Front. Neurosci.* 8 (2014) 338.
- R. Watzlawick, E.S. Sena, U. Dirnagl, B. Brommer, M.A. Kopp, M.R. Macleod, et al., Effect and reporting bias of RhoA/ROCK-blockade intervention on locomotor recovery after spinal cord injury: a systematic review and meta-analysis, *JAMA Neurol.* 71 (2014) 91–99.
- D. Impellizzeri, E. Mazzon, I. Paterniti, E. Esposito, S. Cuzzocrea, Effect of fasudil, a selective inhibitor of Rho kinase activity, in the secondary injury associated with the experimental model of spinal cord trauma, *J. Pharmacol. Exp. Therapeut.* 343 (2012) 21–33.
- S. Hasegawa, Y. Hasegawa, M. Miura, Current therapeutic drugs against cerebral vasospasm after subarachnoid hemorrhage: a comprehensive review of basic and clinical studies, *Curr. Drug Deliv.* 14 (2017) 843–852.
- B.K. Mueller, H. Mack, N. Teusch, Rho kinase, a promising drug target for neurological disorders, *Nat. Rev. Drug Discov.* 4 (2005) 387–398.
- V. Gupta, N. Gupta, I.H. Shaik, R. Mehvar, I.F. McMurtry, M. Oka, et al., Liposomal fasudil, a rho-kinase inhibitor, for prolonged pulmonary preferential vasodilation in pulmonary arterial hypertension, *J. Contr. Release* 167 (2013) 189–199.
- I. Ekladius, Y.L. Colson, M.W. Grinstaff, Polymer-drug conjugate therapeutics: advances, insights and prospects, *Nat. Rev. Drug Discov.* 18 (2019) 273–294.
- K. Maso, A. Grigoletto, M.J. Vicent, G. Pasut, Molecular platforms for targeted drug delivery, *Int Rev Cell Mol Biol.* 346 (2019) 1–50.
- R. Requejo-Aguilar, A. Alastrue Agudo, M. Cases Villar, E. Lopez-Mocholi, R. England, M.J. Vicent, et al., Combined polymer-curcumin conjugate and ependymal progenitor/stem cell treatment enhances spinal cord injury functional recovery, *Biomaterials* 113 (2017) 18–30.
- O. Zagorodko, J.J. Arroyo-Crespo, V.J. Nebot, M.J. Vicent, Polypeptide-Based Conjugates as Therapeutics: Opportunities and Challenges, *Macromol Biosci* (2017) 17.
- A. Duro-Castano, I. Conejos-Sánchez, M.J. Vicent, Peptide-based polymer therapeutics, *Polymers* 6 (2014) 515–551.
- A. Varela-Moreira, Y. Shi, M.H.A.M. Fens, T. Lammers, W.E. Hennin, R. M. Schifferlers, Clinical application of polymeric micelles for the treatment of cancer, *Materials Chemistry Frontiers* 1 (2017) 16.
- R. Duncan, Polymer therapeutics at a crossroads? Finding the path for improved translation in the twenty-first century, *J. Drug Target.* 25 (2017) 759–780.
- J.J. Arroyo-Crespo, C. Deladriere, V.J. Nebot, D. Charbonnier, E. Masía, A. Paul, et al., Anticancer activity driven by drug linker modification in a polyglutamic acid-based combination-drug conjugate, *Adv. Funct. Mater.* 28 (2018) 18.
- A. Duro-Castano, N.H. Lim, I. Tranchant, M. Amoura, F. Beau, H. Wieland, et al., Vivo imaging of MMP-13 activity using a specific polymer-FRET peptide conjugate detects early osteoarthritis and inhibitor efficacy, *Adv. Funct. Mater.* (2018) 28.
- M. Barz, A. Duro-Castano, M.J. Vicent, A versatile post-polymerization modification method for polyglutamic acid: synthesis of orthogonal reactive polyglutamates and their use in “click chemistry”, *Polym. Chem.* 4 (2013) 2989–2994.
- J.J. Arroyo-Crespo, A. Arminan, D. Charbonnier, L. Balzano-Nogueira, F. Huertas-Lopez, C. Marti, et al., Tumor microenvironment-targeted poly-L-glutamic acid-based combination conjugate for enhanced triple negative breast cancer treatment, *Biomaterials* 186 (2018) 8–21.
- N.L. Trevasakis, L.M. Kaminskas, C.J. Porter, From sewer to saviour - targeting the lymphatic system to promote drug exposure and activity, *Nat. Rev. Drug Discov.* 14 (2015) 781–803.
- A. Duro-Castano, V.J. Nebot, A. Nino-Pariente, A. Arminan, J.J. Arroyo-Crespo, A. Paul, et al., Capturing “extraordinary” soft-assembled charge-like polypeptides as a strategy for nanocarrier design, *Adv. Mater.* (2017) 29.
- A. Duro-Castano, R.M. England, D. Razola, E. Romero, M. Oteo-Vives, M. A. Morcillo, et al., Well-defined star-shaped polyglutamates with improved pharmacokinetic profiles as excellent candidates for biomedical applications, *Mol. Pharm.* 12 (2015) 3639–3649.
- I. Conejos-Sánchez, A. Duro-Castano, A. Birke, M. Barz, M.J. Vicent, A controlled and versatile NCA polymerization method for the synthesis of polypeptides, *Polym. Chem.* 4 (2013) 3182–3186.
- E.S. Rosenzweig, J.H. Brock, P. Lu, H. Kumamaru, E.A. Salegio, K. Kadoya, et al., Restorative effects of human neural stem cell grafts on the primate spinal cord, *Nat. Med.* 24 (2018) 484–490.
- E. Curtis, J.R. Martin, B. Gabel, N. Sidhu, T.K. Rzesiewicz, R. Mandeville, et al., A first-in-human, phase I study of neural stem cell transplantation for chronic spinal cord injury, *Cell Stem Cell.* 22 (2018) 941–950, e6.
- H. Kumamaru, K. Kadoya, A.F. Adler, Y. Takashima, L. Graham, G. Coppola, et al., Generation and post-injury integration of human spinal cord neural stem cells, *Nat. Methods* 15 (2018) 723–731.
- P. Assinck, G.J. Duncan, B.J. Hilton, J.R. Plemel, W. Tetzlaff, Cell transplantation therapy for spinal cord injury, *Nat. Neurosci.* 20 (2017) 637–647.
- H. Kumamaru, P. Lu, E.S. Rosenzweig, K. Kadoya, M.H. Tuszynski, Regenerating corticospinal axons innervate phenotypically appropriate neurons within neural stem cell grafts, *Cell Rep.* 26 (2019) 2329–2339, e4.
- F. Barnabe-Heider, C. Goritz, H. Sabelstrom, H. Takebayashi, F.W. Pfrieger, K. Meletis, et al., Origin of new glial cells in intact and injured adult spinal cord, *Cell Stem Cell.* 7 (2010) 470–482.
- V. Moreno-Manzano, F.J. Rodriguez-Jimenez, M. Garcia-Rosello, S. Lainez, S. Erceg, M.T. Calvo, et al., Activated spinal cord ependymal stem cells rescue neurological function, *Stem Cell.* 27 (2009) 733–743.
- A. Alastrue-Agudo, F.J. Rodriguez-Jimenez, E.L. Mocholi, F. De Giorgio, S. Erceg, V. Moreno-Manzano, FM19G11 and ependymal progenitor/stem cell combinatory treatment enhances neuronal preservation and oligodendrogenesis after severe spinal cord injury, *Int. J. Mol. Sci.* (2018) 19.
- R. Gomez-Villafuertes, F.J. Rodriguez-Jimenez, A. Alastrue-Agudo, M. Stojkovic, M.T. Miras-Portugal, V. Moreno-Manzano, Purinergic receptors in spinal cord-derived ependymal stem/progenitor cells and their potential role in cell-based therapy for spinal cord injury, *Cell Transplant.* 24 (2015) 1493–1509.
- A. Torres-Espín, D. Santos, F. González-Pérez, J. del Valle, X. Navarro, Neurite-J: an image-J plug-in for axonal growth analysis in organotypic cultures, *J. Neurosci. Methods* 236 (2014) 26–39.
- B. Bonnici, J.P. Kapfhammer, Spontaneous regeneration of intrinsic spinal cord axons in a novel spinal cord slice culture model, *Eur. J. Neurosci.* 27 (2008) 2483–2492.
- A. Alastrue-Agudo, S. Erceg, M. Cases Villar, V. Bisbal-Velasco, R.J. Griffith, F. J. Rodriguez Jimenez, et al., Experimental cell transplantation for traumatic spinal cord injury regeneration: intramedullary or intrathecal administration, *Methods Mol. Biol.* 1210 (2014) 23–35.
- F. Hamers, A. Lankhorst, T. Van Laar, W. Veldhuis, W. Gispen, Automated quantitative gait analysis during overground locomotion in the rat: its application

- to spinal cord contusion and transection injuries, *J. Neurotrauma* 18 (2001) 187–201.
- [38] L.B. Vong, Y. Ibayashi, Y. Lee, D.N. Ngo, Y. Nishikawa, Y. Nagasaki, Poly (ornithine)-based self-assembling drug for recovery of hyperammonemia and damage in acute liver injury, *J. Contr. Release* 310 (2019) 74–81.
- [39] A. Raturi, B. Mutus, Characterization of redox state and reductase activity of protein disulfide isomerase under different redox environments using a sensitive fluorescent assay, *Free Radic. Biol. Med.* 43 (2007) 62–70.
- [40] S. Chen, M. Luo, Y. Zhao, Y. Zhang, M. He, W. Cai, et al., Fasudil stimulates neurite outgrowth and promotes differentiation in C17.2 neural stem cells by modulating notch signalling but not autophagy, *Cell. Physiol. Biochem.* 36 (2015) 531–541.
- [41] Z.A. Nizamudeen, L. Chakrabarti, V. Sottile, Exposure to the ROCK inhibitor fasudil promotes gliogenesis of neural stem cells in vitro, *Stem Cell Res.* 28 (2018) 75–86.
- [42] S.K. Doster, A.M. Lozano, A.J. Aguayo, M.B. Willard, Expression of the growth-associated protein GAP-43 in adult rat retinal ganglion cells following axon injury, *Neuron* 6 (1991) 635–647.
- [43] S. Chen, M. Luo, Y. Zhao, Y. Zhang, M. He, W. Cai, et al., Fasudil stimulates neurite outgrowth and promotes differentiation in C17.2 neural stem cells by modulating notch signalling but not autophagy, *Cell. Physiol. Biochem.* 36 (2015) 531–541.
- [44] T.B. Shea, C. Jung, H.C. Pant, Does neurofilament phosphorylation regulate axonal transport? *Trends Neurosci.* 26 (2003) 397–400.
- [45] J.Z. Kiss, D. Muller, Contribution of the neural cell adhesion molecule to neuronal and synaptic plasticity, *Rev. Neurosci.* 12 (2001) 297–310.
- [46] A. El Maarouf, A.K. Petridis, U. Rutishauser, Use of polysialic acid in repair of the central nervous system, *Proc. Natl. Acad. Sci. U.S.A.* 103 (2006) 16989–16994.
- [47] K. Jalink, E.J. van Corven, T. Hengeveld, N. Morii, S. Narumiya, W.H. Moolenaar, Inhibition of lysophosphatidate- and thrombin-induced neurite retraction and neuronal cell rounding by ADP ribosylation of the small GTP-binding protein Rho, *J. Cell Biol.* 126 (1994) 801–810.
- [48] O. Kranenburg, M. Poland, F.P. van Horck, D. Drechsel, A. Hall, W.H. Moolenaar, Activation of RhoA by lysophosphatidic acid and Galpha12/13 subunits in neuronal cells: induction of neurite retraction, *Mol. Biol. Cell* 10 (1999) 1851–1857.
- [49] P.L. Cheng, A.H. Song, Y.H. Wong, S. Wang, X. Zhang, M.M. Poo, Self-amplifying autocrine actions of BDNF in axon development, *Proc. Natl. Acad. Sci. U. S. A.* 108 (2011) 18430–18435.
- [50] C.I. Dubreuil, M.J. Winton, L. McKerracher, Rho activation patterns after spinal cord injury and the role of activated Rho in apoptosis in the central nervous system, *J. Cell Biol.* 162 (2003) 233–243.
- [51] M.K. Erschbamer, C.P. Hofstetter, L. Olson, RhoA, RhoB, RhoC, Rac1, Cdc42, and Tc10 mRNA levels in spinal cord, sensory ganglia, and corticospinal tract neurons and long-lasting specific changes following spinal cord injury, *J. Comp. Neurol.* 484 (2005) 224–233.
- [52] W.J. Wei, Z.Y. Yu, H.J. Yang, M.J. Xie, W. Wang, X. Luo, Cellular expression profile of RhoA in rats with spinal cord injury, *J. Huazhong Univ Sci Technolog Med Sci.* 34 (2014) 657–662.
- [53] X. Wu, X.M. Xu, RhoA/Rho kinase in spinal cord injury, *Neural Regen Res.* 11 (2016) 23–27.
- [54] S. Dupraz, B.J. Hilton, A. Husch, T.E. Santos, C.H. Coles, S. Stern, et al., RhoA controls axon extension independent of specification in the developing brain, *Curr. Biol.* 29 (2019) 3874–3886, e9.
- [55] J.C. Koch, L. Tatenhorst, A.E. Roser, K.A. Saal, L. Tönges, P. Lingor, ROCK inhibition in models of neurodegeneration and its potential for clinical translation, *Pharmacol. Ther.* 189 (2018) 1–21.
- [56] P. Dergham, B. Ellezam, C. Essagian, H. Avedissian, W.D. Lubell, L. McKerracher, Rho signaling pathway targeted to promote spinal cord repair, *J. Neurosci.* 22 (2002) 6570–6577.
- [57] F. Boato, S. Hendrix, S.C. Huelsenbeck, F. Hofmann, G. Grosse, S. Djalali, et al., C3 peptide enhances recovery from spinal cord injury by improved regenerative growth of descending fiber tracts, *J. Cell Sci.* 123 (2010) 1652–1662.
- [58] M.G. Fehlings, K.D. Kim, B. Aarabi, M. Rizzo, L.M. Bond, L. McKerracher, et al., Rho inhibitor VX-210 in acute traumatic subaxial cervical spinal cord injury: design of the SPinal cord injury rho INhibition InvestiGation (SPRING) clinical trial, *J. Neurotrauma* 35 (2018) 1049–1056.
- [59] M. Shibuya, S. Hirai, M. Seto, S. Satoh, E. Ohtomo, Fasudil Ischemic Stroke Study G. Effects of fasudil in acute ischemic stroke: results of a prospective placebo-controlled double-blind trial, *J. Neurol. Sci.* 238 (2005) 31–39.
- [60] R.L. Friede, T. Samorajski, Axon caliber related to neurofilaments and microtubules in sciatic nerve fibers of rats and mice, *Anat. Rec.* 167 (1970) 379–387.
- [61] R. Starr, B. Attema, G.H. DeVries, M.J. Monteiro, Neurofilament phosphorylation is modulated by myelination, *J. Neurosci. Res.* 44 (1996) 328–337.
- [62] M.S. Song, L. Salmena, P.P. Pandolfi, The functions and regulation of the PTEN tumour suppressor, *Nat. Rev. Mol. Cell Biol.* 13 (2012) 283–296.
- [63] L. Miao, L. Yang, H. Huang, F. Liang, C. Ling, Y. Hu, mTORC1 is necessary but mTORC2 and GSK3beta are inhibitory for AKT3-induced axon regeneration in the central nervous system, *Elife* 5 (2016) e14908.
- [64] C. Aglah, T. Gordon, Posse de Chaves EL. cAMP promotes neurite outgrowth and extension through protein kinase A but independently of Erk activation in cultured rat motoneurons, *Neuropharmacology* 55 (2008) 8–17.
- [65] S. Neumann, F. Bradke, M. Tessier-Lavigne, A.I. Basbaum, Regeneration of sensory axons within the injured spinal cord induced by intraganglionic cAMP elevation, *Neuron* 34 (2002) 885–893.
- [66] Y. Ji, P.T. Pang, L. Feng, B. Lu, Cyclic AMP controls BDNF-induced TrkB phosphorylation and dendritic spine formation in mature hippocampal neurons, *Nat. Neurosci.* 8 (2005) 164–172.
- [67] Z. Wang, L. Zhou, X. Zheng, G. Chen, R. Pan, J. Li, et al., Autophagy protects against PI3K/Akt/mTOR-mediated apoptosis of spinal cord neurons after mechanical injury, *Neurosci. Lett.* 656 (2017) 158–164.
- [68] P. Tang, H. Hou, L. Zhang, X. Lan, Z. Mao, D. Liu, et al., Autophagy reduces neuronal damage and promotes locomotor recovery via inhibition of apoptosis after spinal cord injury in rats, *Mol. Neurobiol.* 49 (2014) 276–287.
- [69] L. Xie, F. Sun, J. Wang, X. Mao, L. Xie, S.H. Yang, et al., mTOR signaling inhibition modulates macrophage/microglia-mediated neuroinflammation and secondary injury via regulatory T cells after focal ischemia, *J. Immunol.* 192 (2014) 6009–6019.
- [70] X. Lin, L. Han, J. Weng, K. Wang, T. Chen, Rapamycin inhibits proliferation and induces autophagy in human neuroblastoma cells, *Biosci. Rep.* (2018) 38.
- [71] S. Peña-Llopis, S. Vega-Rubin-de-Celis, J.C. Schwartz, N.C. Wolff, T.A. Tran, L. Zou, et al., Regulation of TFE3 and V-ATPases by mTORC1, *EMBO J.* 30 (2011) 3242–3258.
- [72] M.M. Lipinski, J. Wu, A.I. Faden, C. Sarkar, Function and mechanisms of autophagy in brain and spinal cord trauma, *Antioxidants Redox Signal.* 23 (2015) 565–577.
- [73] S. Liu, C. Sarkar, M. Dinizo, A.I. Faden, E.Y. Koh, M.M. Lipinski, et al., Disrupted autophagy after spinal cord injury is associated with ER stress and neuronal cell death, *Cell Death Dis.* 6 (2015) e1582.
- [74] T. Muñoz-Galdeano, D. Reigada, Velez I. Del Águila Á, M.J. Caballero-López, R. M. Maza, et al., Cell specific changes of autophagy in a mouse model of contusive spinal cord injury, *Front. Cell. Neurosci.* 12 (2018) 164.
- [75] M. Jang, R. Park, H. Kim, S. Namkoong, D. Jo, Y.H. Huh, et al., AMPK contributes to autophagosomal maturation and lysosomal fusion, *Sci. Rep.* 8 (2018) 12637.
- [76] P. Lu, L. Graham, Y. Wang, D. Wu, M. Tuszynski, Promotion of survival and differentiation of neural stem cells with fibrin and growth factor cocktails after severe spinal cord injury, *J. Vis. Exp.* 89 (2014), e50641, <https://doi.org/10.3791/50641>.
- [77] Y. Li, W.M. Zhang, T.H. Wang, Optimal location and time for neural stem cell transplantation into transected rat spinal cord, *Cell. Mol. Neurobiol.* 31 (2011) 407–414.

Article

Transplantation of Human-Fetal-Spinal-Cord-Derived NPCs Primed with a Polyglutamate-Conjugated Rho/Rock Inhibitor in Acute Spinal Cord Injury

Esther Giraldo ^{1,2,3,†}, Pablo Bonilla ^{1,†}, Mara Mellado ¹ , Pablo Garcia-Manau ⁴ , Carlota Rodo ⁴ , Ana Alastrue ¹ , Eric Lopez ¹, Elena Carreras Moratonas ⁴, Ferran Pellise ⁵ , Snežana Đorđević ⁶ , María J. Vicent ⁶  and Victoria Moreno Manzano ^{1,*} 

- ¹ Neuronal and Tissue Regeneration Laboratory, Centro de Investigación Príncipe Felipe, E-46012 Valencia, Spain
- ² Department of Biotechnology, Universitat Politècnica de València, E-46022 Valencia, Spain
- ³ UPV-CIPF Joint Research Unit Disease Mechanisms and Nanomedicine, Centro de Investigación Príncipe Felipe, E-46012 Valencia, Spain
- ⁴ Maternal-Foetal Medicine Unit, Vall d'Hebron Hospital Campus, E-08035 Barcelona, Spain
- ⁵ Spine Surgery Unit, Hospital Universitari Vall d'Hebron, E-08035 Barcelona, Spain
- ⁶ Polymer Therapeutics Laboratory, Centro de Investigación Príncipe Felipe, E-46012, Valencia, Spain
- * Correspondence: vmorenom@cipf.es
- † These authors contributed equally to this work.



Citation: Giraldo, E.; Bonilla, P.; Mellado, M.; Garcia-Manau, P.; Rodo, C.; Alastrue, A.; Lopez, E.; Moratonas, E.C.; Pellise, F.; Đorđević, S.; et al. Transplantation of Human-Fetal-Spinal-Cord-Derived NPCs Primed with a Polyglutamate-Conjugated Rho/Rock Inhibitor in Acute Spinal Cord Injury. *Cells* **2022**, *11*, 3304. <https://doi.org/10.3390/cells11203304>

Academic Editors: Kee D. Kim, Julius O. Ebinu and Alexander V. Ljubimov

Received: 23 August 2022
Accepted: 19 October 2022
Published: 20 October 2022

Publisher's Note: MDPI stays neutral with regard to jurisdictional claims in published maps and institutional affiliations.



Copyright: © 2022 by the authors. Licensee MDPI, Basel, Switzerland. This article is an open access article distributed under the terms and conditions of the Creative Commons Attribution (CC BY) license (<https://creativecommons.org/licenses/by/4.0/>).

Abstract: Neural precursor cell (NPC) transplantation represents a promising therapy for treating spinal cord injuries (SCIs); however, despite successful results obtained in preclinical models, the clinical translation of this approach remains challenging due, in part, to the lack of consensus on an optimal cell source for human neuronal cells. Depending on the cell source, additional limitations to NPC-based therapies include high tumorigenic potential, alongside poor graft survival and engraftment into host spinal tissue. We previously demonstrated that NPCs derived from rat fetal spinal cords primed with a polyglutamate (PGA)-conjugated form of the Rho/Rock inhibitor fasudil (PGA-SS-FAS) displayed enhanced neuronal differentiation and graft survival when compared to non-primed NPCs. We now conducted a similar study of human-fetal-spinal-cord-derived NPCs (hfNPCs) from legal gestational interruptions at the late gestational stage, at 19–21.6 weeks. In vitro, expanded hfNPCs retained neural features, multipotency, and self-renewal, which supported the development of a cell banking strategy. Before transplantation, we established a simple procedure to prime hfNPCs by overnight incubation with PGA-SS-FAS (at 50 μ M FAS equiv.), which improved neuronal differentiation and overcame neurite-like retraction after lysophosphatidic-acid-induced Rho/Rock activation. The transplantation of primed hfNPCs into immune-deficient mice (NU(NCr)-Foxn1^{nu}) immediately after the eighth thoracic segment compression prompted enhanced migration of grafted cells from the dorsal to the ventral spinal cord, increased preservation of GABAergic inhibitory Lbx1-expressing and glutamatergic excitatory Tlx3-expressing somatosensory interneurons, and elevated the numbers of preserved, c-Fos-expressing, activated neurons surrounding the injury epicenter, all in a low percentage. Overall, the priming procedure using PGA-SS-FAS could represent an alternative methodology to improve the capabilities of the hfNPC lines for a translational approach for acute SCI treatment.

Keywords: human fetal neural precursor; NPC transplantation; Rho/ROCK kinase inhibition; cell priming; spinal cord injury

1. Introduction

Spinal cord injury (SCI) following severe physical trauma triggers a series of complex multicellular and molecular responses, resulting in a diverse degree of permanent motor,

sensory, and/or autonomic dysfunctions. Despite the promising results obtained from intense research efforts in preclinical models over the past decade, no effective therapy has been efficiently translated into the clinic. Cell transplantation and advanced cell engineering have provided hope for treatment strategies with translational potential [1,2]. Neural progenitor cell (NPC) transplantation prompts neuroprotection and induces neuroregeneration by providing neurotrophic support, attenuating secondary damage, supplying a permissive substrate for axon regrowth [3,4], replacing lost neurons and establishing novel synaptic connections with host axons [5,6], and enhancing remyelination [7,8], which ultimately promote functional recovery in rodents [9,10]. The features and origin of NPCs represent crucial aspects of developing translatable cell therapies. Primary self-renewing NPCs isolated from fetal tissue display *in vitro* expansion potential, thereby providing an optimal cell source, which avoids inherent variations associated with the use of different fetal donors and the cell heterogeneity, which can elevate the risk of immune rejection and/or tissue contamination.

Standard procedures have been proposed to obtain “clinical-grade” NPCs from fetal neural tissue with minimal manipulation and in compliance with pharmaceutical good manufacturing practice (GMP) guidelines to ensure the production of advanced therapies for safe clinical use [11]. The transplantation of *in vitro*-expanded human fetal NPCs (hfNPCs) obtained from the lower cervical and upper thoracic spinal cord of an eight-week-old fetus prevented cyst expansion in an adult rat model of chronic SCI and post-traumatic syringomyelia [12]; however, current clinical trials with fetal tissue have employed immortalized cell lines derived from early fetal spinal cord [13] or brain tissue [14,15]. Alternative clinical approaches have employed NPCs derived from pluripotent stem cells; for example, Kumamaru et al. developed a xeno-free methodology to culture human spinal neural stem cells (NSCs) differentiated from embryonic stem cells (ESCs), thereby providing a scalable source for clinical translation [16]. These NSCs integrated into host tissue, induced the regeneration of the injured corticospinal tract, and enabled the extension of prolonged and persistent axonal projections, resulting in improved motor function in nude rats [16]. In non-human primates, these NSCs survived for nine months after transplantation and extended hundreds of thousands of human axons through monkey white matter, which established synapses and improved forelimb function, overcoming the immune graft rejection of the exogenous human cells [9]. Sugai et al. recently reported on the first clinical trial using NPCs derived from human induced pluripotent stem cells (iPSCs) as an SCI treatment [17]. Of note, while immortalized cell lines and pluripotent-cell-derived NPCs provide an inexhaustible source of cells, their application entails a high risk of tumorigenesis [18].

Here, we propose *in vitro*-amplified hfNPCs derived from the spinal cords of electively aborted fetuses at 19–21.6 weeks of gestation as an innovative approach for SCI treatment. As we recently demonstrated that priming fetal rat NPCs with PGA-SS-FAS, a polyglutamic acid (PGA)-conjugated form of the Rho/Rock inhibitor fasudil (FAS), which provides improved stability and controlled release, enhanced graft survival and improved cell migration through the injured spinal cord [19], we also evaluated the impact of PGA-SS-FAS priming on hfNPCs. Transplantation of PGA-SS-FAS-primed hfNPCs in the acute stage of compressive SCI promoted host neuron preservation and the increased expression of *c-fos*, a hallmark for cell activation, without any sign of tumorigenesis.

2. Materials and Methods

2.1. Isolation and Expansion of hfNPCs

hfNPCs were isolated and expanded from human fetal spinal cord tissue obtained from five fetuses from legally elective abortions induced by vaginal Misoprostol administration after being diagnosed with severe congenital malformations at 19.0–21.6 gestational weeks of gestation at the maternal–fetal medicine department at Vall d’Hebron Hospital Campus (Barcelona, Spain). The experimental procedures were evaluated and accepted by the clinical ethical committee at the Vall d’Hebron Hospital with the approved protocol

PR(AMI)120/2017. Written informed consent for anonymized tissue collection was signed by each donor. Samples with an identified central-nervous-system-associated anomaly during the ultrasound examination were excluded. Negative serology for hepatitis and AIDS from donors was confirmed.

Human fetal spinal cords were dissected with sterile gloves and dissecting tools during the first hour after delivery. Each spinal cord, from cervical to lumbar segments, was transferred and maintained in 4 °C Hibernate™-E CTS™ Medium (Gibco™, Waltham, MA, USA) supplemented with 2% CTS™ B-27™ Supplement (Gibco™) in a hermetic sterile tube on ice for up to 5 h. In biosafe flow hoods, the spinal cords were washed twice with fresh hibernation media, and the meninges, dura, and pia mater were carefully removed, cut into ~1 mm³ pieces, and mechanically dissociated by repeated pipetting. The obtained cell suspension was centrifuge, and the cell pellet plated on ultra-low attachment plates in proliferation culture media—CTS™ Neurobasal™ Medium (Gibco™) supplemented with CTS™ GlutaMAX™-I Supplement (Gibco™), CTS™ B-27™ XenoFree Supplement, 100 µg/mL penicillin–streptomycin (Sigma-Aldrich; Darmstadt, Germany), 0.7 U/mL heparin (Sigma-Aldrich), 20 ng/mL human recombinant epidermal growth factor (hEGF; Peprotech, London, U.K.), 20 ng/mL basic human recombinant fibroblast growth factor (hbFGF; Peprotech), and 10 ng/mL human recombinant leukemia inhibitory factor (hLIF; Peprotech). Plates were incubated in 5% CO₂ at 37 °C for two to three days until neurospheres formed. hfNPCs effectively formed neurospheres, which supported selection, clonal division, and cell proliferation. Neurospheres were enzymatically and mechanically dissociated using Accutase (STEMCELL™, Vancouver, Canada), and individualized cells were seeded at a density of 2.6×10^4 cells/cm² in six-well culture plates coated with human recombinant Laminin 521 (BioLamina, Sundbyberg, Sweden). Subsequential sub-cultivation and expansion were performed for up to an additional nine passages. hfNPC cryopreservation as neurospheres or adherent growing cultures was performed using CryoStor® (Merck, Darmstadt, Germany). hfNPCs were then stored in liquid nitrogen.

2.2. Priming hfNPCs with PGA-SS-FAS Prior to Transplantation

Passage 5–7 hfNPCs were thawed and cultured in neurosphere-forming conditions in ultra-low attachment plates for 24 h and then incubated with PGA-SS-FAS (50 µM FAS-equiv.) for an additional 24 h in 5% CO₂ and 37 °C. PGA-SS-FAS was synthesized and fully characterized as previously reported [19] following ICH guidelines to achieve an endotoxin-free nanoconjugate with a reliable impurity profile. The guidelines for good manufacturing practices (GMP) manufacturers were provided by PTS S.L. (Valencia, Spain). In general, PGA-SS-FAS was highly pure, with no significant impurities of residual solvents or ionic impurities. Before transplantation, hfNPCs were harvested and centrifuged at 200 × g for 5 min and washed twice with culture media. The cell media discarded at every wash step was collected for inspection of the extracellular content of fasudil by liquid chromatography-tandem mass spectrometry (LC-MS/MS). The sample preparation and LC-MS/MS method for fasudil quantification were previously developed and described in Giraldo et al. [19]. Nevertheless, the developed LC-MS/MS method and extraction protocol were re-evaluated for linearity, the limit of quantification (LOQ), the limit of detection (LOD), recovery, and matrix effects to ensure its status as fit for purpose. Linearity was evaluated by constructing a calibration curve obtained by the internal standard method (ranitidine as an internal standard). LOD and LOQ values were calculated from the LINEST function. At the same time, matrix effects were evaluated by analyzing two different sample types: (i) blank cell medium spiked after sample preparation with fasudil as three quality control (QC) samples (low, medium, and upper) and with 1 ng/mL of ranitidine and (ii) water solution of fasudil and ranitidine in the same concentration as spiked samples. Recovery was assessed at the three QC levels by comparing the mass of extracted analyte and analyte in the sample (plasma spiked after the sample preparation) and represented as a percentage. Fasudil was not encountered in any cell washing media, suggesting that hfNPCs did not secrete fasudil or PGA-SS-FAS during washing and confirming that

the cell preparation will not deliver fasudil or PGA-SS-FAS to the extracellular space or surrounding cells after transplantation into the spinal cord tissue.

2.3. hfNPC Proliferation Assay

The doubling time, in hours, of hfNPCs was studied by subculturing passage 1 cells in adherent conditions at a density of 1.5×10^4 cells/cm² until confluency, according to the following formula, $t = t \times \log 2 / (\log N_t - \log N_0)$, where t is the culture time in hours, N_0 is the initial cell number, and N_t is the harvested cell number.

The number of individual proliferating cells in the cell population was assayed by adding 10 μ M 5'-Br-2'-deoxyuridine (BrdU, Sigma-Aldrich) 24 h before analysis. Cells were fixed with 2% paraformaldehyde (PFA) for 10 min, washed with phosphate buffer solution (PBS), treated with 2M HCl for 20 min at room temperature, and then stopped with 0.1 M Na₂B₄O₇ for 30 min. The expression of Ki67 was assayed by immunocytochemistry in the same cultures to evaluate the number of cells undergoing the G1 to mitosis transition. Cells were blocked for 1 h in Tris-buffered saline (TBS) containing 0.2% Triton-X-100 and 5% normal goat serum and then incubated with anti-BrdU (1:400; Sigma-Aldrich) and anti-Ki67 (1:400; GTX16667, GeneTex) antibodies diluted in blocking solution overnight at 4 °C. Cells were subsequently incubated with Alexa-Fluor-conjugated antibodies for 2 h at room temperature, washed twice with PBS, and finally, incubated with DAPI for nuclear staining.

2.4. Spontaneous hfNPC Differentiation Assay

Neurosphere hfNPC cultures at passage 1 were dissociated with Accutase and seeded onto human recombinant Laminin 521-coated (BioLamina, Sundbyberg, Sweden) coverslips in DMEM/F12 supplemented with 100 U/mL penicillin, 100 μ g/mL streptomycin, 2 mM L-glutamine, 5 mM HEPES buffer, 0.125% NaHCO₃, 0.6% glucose, 0.025 mg/mL insulin, 80 μ g/mL apotransferrin, 16 nM progesterone, 60 μ M putrescine, 24 nM sodium selenite, and 2% of human serum for seven days. hfNPCs were then treated with 50 μ M of PGA-SS-FAS on Day 3 to determine any effect of PGA-SS-FAS on cell differentiation. Cells were fixed on Day 7, and the neuronal, astrocytic, and oligodendroglia identity of the cells were evaluated by immunostaining with beta-III tubulin, GFAP, and OLIG2 antibodies, respectively.

2.5. Neurite Elongation Assays

hfNPCs in growth media were pre-treated with or without 50 μ M of PGA-SS-FAS for 24 h. 10 μ M lysophosphatidic acid, a pharmacological activator of the Rho/ROCK pathway (LPA; Sigma-Aldrich), was added for an additional 24 h to induce neurite retraction. Cultures were then fixed and immunolabeled with Nestin, and neurite outgrowth was quantified using the NeuronJ plug-in from ImageJ v1.48 [20].

2.6. Immunostaining

Cells were fixed with 4% PFA in PBS for 10 min, then permeabilized and blocked with 5% normal goat serum (NGS; Thermo Fisher) and 0.2% Triton X-100 (Sigma) and incubated overnight at 4 °C with primary antibodies. Fixed spinal cord tissues were first cryoprotected in 30% sucrose overnight at 4 °C before inclusion in Tissue-Teck OCT (Sakura Finetek Europe BV, Flemingsweg, Netherlands) and then cryo-sectioned to provide 20 μ m-thick sections. Tissue sections were permeabilized and blocked in PBS containing 0.1% Triton X-100, 5% horse serum, and 10% fetal bovine serum for 1 h at room temperature and then incubated overnight at 4 °C with primary antibodies.

The employed primary antibodies were: chicken anti-GFAP (1:1000; PA1-10004, Thermo Fisher), guinea pig anti-DCX (1:400; ab5910, Chemicon, Temecula, California, United States), anti-PAX6 (1:400; PRB-278P, Biolegend, San Diego, California, USA), rabbit anti-SOX2 (1:400; MAB5326, Abcam), rabbit anti-Ki67 (1:400; GTX16667, GeneTex), mouse anti-Nestin (1:400; MAB5326, Sigma Aldrich), mouse anti-Notch-1 (1:400; AF1057, R&D System, Minneapolis,

Minnesota, USA), mouse anti-Olig2 (1:400; AB9610, Sigma-Aldrich), mouse anti-FOXJ1 (1:300; 14-9965-82, Thermo Fisher), mouse anti-Neurogenin1 (1:400; sc-100332, Santa Cruz), chicken anti-NeuN (1:400; ABN91, Sigma-Aldrich), rabbit anti-Tlx3 (1:5,000 gift of C. Birchmeier), guinea pig anti-Lbx1 (1:10,000 gift of C. Birchmeier), rabbit anti-c-Fos (1:400; ab190289, Abcam), and chicken anti-GFP (1:400; ab13970, Abcam).

After three washes with PBS, cells or tissues were incubated with AlexaFluor-488, -555, or -647 (1:400, Invitrogen) secondary antibodies for 2 h at room temperature. Nuclei staining was performed by incubation with DAPI (1:1000, Sigma).

Fluorescent images were acquired using an apotome fluorescent microscope (Zeiss) or confocal microscope SP8 (Leica) as indicated. Consistent exposures were applied, and images were visualized and quantified with ImageJ/Fiji software v1.48.

Grafted cells found along the spinal cord were enumerated to analyze hfNPC survival, with the figure normalized to the microns of tissue thickness analyzed. The quantification of activated hfNPCs (double-positive for GFP and c-Fos) and the percentage of hfNPCs positive for c-Fos used a similar procedure. The neuroprotective properties of cell grafts were determined by analyzing neuronal preservation and activation 2 mm rostral and caudal to the lesion site and the lesion site (corresponding to the transplanted and injured area). Neuronal preservation was measured by enumerating the number of NeuN⁺ neurons, while neuronal activation used the number of neurons double-positive for NeuN and c-Fos normalized to the total analyzed area. All stainings and cell quantifications were performed from every fifth horizontal section of 20 mm in thickness in 3 animals per group. Cell number quantifications were then normalized to the analyzed summed tissue thickness (from ventral to dorsal sections) and expressed in mm².

Further analysis of neuroprotective effects on specific dorsal horn somatosensory interneuron populations measured the preservation of GABAergic Ladybird homeobox 1 (Lbx1)-expressing inhibitory and glutamatergic T cell leukemia homeobox 3 (Tlx3)-expressing excitatory interneurons 2 mm rostral and 2 mm caudal to the lesion site and in the lesion site normalized to the total analyzed area.

2.7. Spinal Cord Injury, hfNPC Transplantation, and Tissue Processing

All experimental procedures were approved by the Animal Care Committee of the Research Institute Principe Felipe (Valencia, 2020/VSC/PEA/0119, Spain) in accordance with the National Guide to the Care and Use of Experimental Animals (Real Decreto 53/2013).

Immune-deficient female NU (*NCr*)-*Foxn1*tm mice (Charles River, France) weighing ≈20 g were housed under controlled light and temperature conditions. For surgical interventions, mice received subcutaneous morphine (5 mg/kg) 30 min prior to surgery and were anesthetized with 2% isoflurane in a continuous oxygen flow of 1 L/min. Laminectomy was performed at the T8-T9 level, exposing the dorsal surface of the dura matter. Using Bonn Micro Forceps (11083-07, Fine Science Tool, Heidelberg, Germany) (0.3 mm wide), a one-second compressive spinal cord injury was performed at the T8 thoracic level, as previously described [21]. Immediately after compression, 2 μL containing 2.5×10^5 hfNPCs (previously infected with pII3.1-eGFP lentivirus for eGFP ectopic expression) primed with PGA-SS-Fas (hfNPCs + PGA-SS-FAS group), vehicle (hfNPCs group), or culture medium (control group) were intramedullary injected at the epicenter of the lesion in one single point to a 1 mm depth from the dorsal side. All animals were subjected to post-surgery care consisting of manual drainage of bladders twice a day until vesical reflex was recovered and subcutaneous administration of 5 mg/kg of enrofloxacin for seven days and 0.1 mg/kg of buprenorphine twice a day for four days. One month after injury and transplantation, animals were overdosed with an intraperitoneal administration of pentobarbital and transcardially perfused with PBS, followed by 4% of PFA in 0.1 M phosphate buffer (PB, pH = 7.4). Spinal cords were collected and maintained in 0.1M PB for further cryopreservation and histological analysis.

Hind limb motor function was evaluated for up to four weeks using the Basso Mouse Scale (BMS) locomotor rating scale [22] by videotaping the animals in an open field twice a

week using a high-definition camera. Two individuals blinded to the treatment of the mice then examined and scored motor function. We did not find significant differences at any analyzed point between the three compared groups.

In addition, 2.5×10^5 hfNPCs primed with PGA-SS-Fas or vehicle were transplanted into non-injured mice at the T8 segment to evaluate tumorigenic/invasive potential one month after transplantation. hfNPCs were monitored by semiquantitative PCR for the eGFP gene expressed by transplanted hfNPCs in brain, heart, and liver samples using specific primers (fw_AAGTCGTGCTGCTTCAATGTG; rv_GACGTAAACGGCCACAAGTT). Total RNA was isolated using TRIzolTM Reagent (Invitrogen), and cDNA was synthesized from 1 µg RNA using the high-capacity RNA-to-cDNATM kit (4368814, Applied Biosystems) following the manufacturer's instructions. For PCR reactions, 50 ng of cDNA was amplified using GoTaq[®] DNA Polymerase (Promega, Madison, Wisconsin, EEUU), using 55 °C for primer annealing. Mouse GAPDH amplification was used as a housekeeping gene (fw_CGGTGCTGAGTATGTCGTGGAGT; rv_CGTGGTTCACACCCATCACAAA).

2.8. Transmission Electron Microscopy

For electron microscopy studies, human spinal cords were fixed in 4% PFA overnight at 4 °C. After washing steps in 0.1 M PB, 200 µm coronal sections were cut on a Leica VT-1000 vibratome (Leica, Heidelberg, Germany). Sections were post-fixed with 2% osmium, rinsed, dehydrated, and embedded in Durcupan resin (Fluka, Sigma-Aldrich, St. Louis, USA). Semithin sections (1.5 µm) were cut with an Ultracut UC-6 (Leica microsystems, Wetzlar, Germany) and stained lightly with 1% toluidine blue. Finally, ultrathin sections (70–90 nm) were cut with a diamond knife, stained with lead citrate (Reynolds solution), and examined under an FEI Tecnai G2 Spirit BioTwin transmission electron microscope (ThermoFisher Scientific, Oregon, USA) using a Morada digital camera (Olympus Soft Image Solutions GmbH, Münster, Germany).

2.9. Statistical Analysis

Data are graphically represented as the mean ± standard error mean (SEM) and analyzed using Graph Pad Prism software. The Shapiro–Wilk normality test was performed to evaluate each dataset's Gaussian distribution. For comparisons between the two groups, a one-tailed *t*-test with a confidence level of 95% was used. If normality was not met, the non-parametric Mann–Whitney rank sum test was used.

3. Results

3.1. Human Fetal Spinal Cord NPCs Reside in the Ependymal Central Canal and the Spinal Parenchyma

Rodents maintain proliferative NSCs in the ependymal central canal, representing an endogenous source of cells for the repair of lesions [23–25]; however, we currently lack a detailed study of the human fetal spinal cord canal. Transmission electron microscopy (TEM) images (Figure 1A) demonstrated the organization of ependymal cells at a gestational stage corresponding to 20 weeks—a tight alignment of ependymal cells with a radial morphology organized as a pseudostratified epithelium forming the central canal. We observed features previously described in fetal mice spinal cord [26]—highly polarized and multiciliated ependymal cells with a large number of cilia in the apical zone facing the lumen of the central canal (white arrow), nuclei with condensed chromatin (*), and long large junction complexes (white arrowheads).

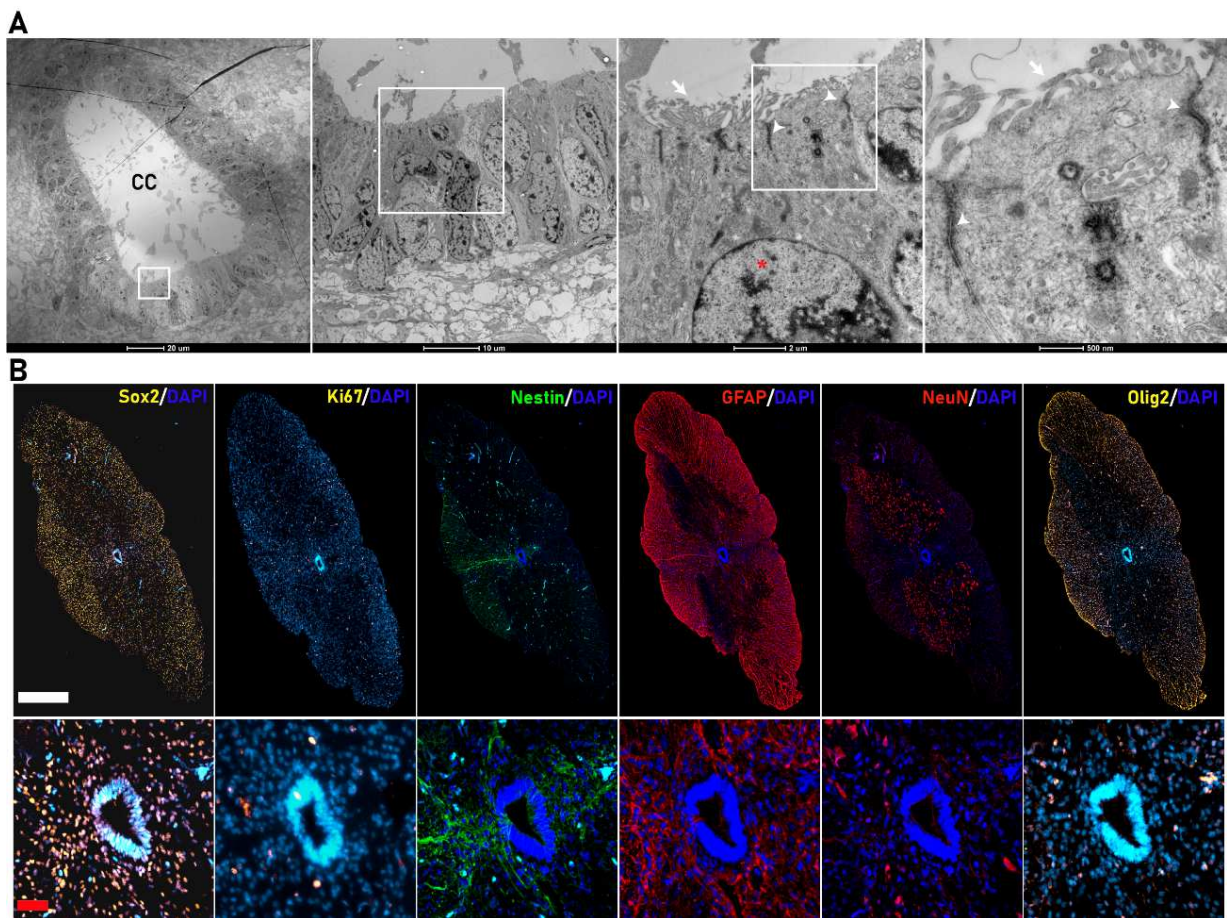


Figure 1. Cytoarchitecture of the human fetal spinal cord. **(A)** Transmission electron microscopy (TEM) images of the central canal of the human fetal spinal cord (scale bar (from left to right) = 20 μ m, 10 μ m, 2 μ m, and 500 nm). The central canal is formed by ependymal cells organized as a pseudostratified epithelium with a large number of cilia in the apical zone (white arrow), nuclei with condensed chromatin (*), and large apical junction complexes (white arrowheads). **(B)** Representative coronal immunostaining images (complete coronal sections in upper panels and magnified view of the corresponding CC area in the lower panels) of human fetal spinal cords for SOX2 (yellow), Ki67 (yellow), Nestin (green), Gfap (red), NeuN (red), and Olig2 (yellow) (white bar scale= 500 μ m; red bar scale = 50 μ m).

We explored the expression of sex determining region Y (SRY)-box 2 (SOX2), the earliest transcription factor expressed in neural stem/progenitor cells [27], which controls the specification of early neural lineages and brain and spinal cord development [28] as a means to identify spinal-cord-resident NPCs in fetal samples at the late gestational stage of 19–21.6 weeks. We found abundant positive nuclear staining for SOX2 in the spinal cord parenchyma and the cells of the central canal (Figure 1B). We also observed double-SOX2-/Ki67-positive cells in the central canal and distributed throughout the spinal cord parenchyma contributing to the active proliferative NPC population [29]. As the cell constituting the central canal migrate towards the dorsal and ventral regions of the spinal cord, they differentiate, specialize, and determine the spinal cord cytoarchitecture. In our samples, we identified elongating processes from both NESTIN- and GFAP-expressing cells from the roof plate of the central canal (Figure 1B), which may help to determine the dorso-ventral regionalization of the spinal cord, as previously reported in rodents [30,31]. We also observed neurons, oligodendrocytic precursors, and astrocytes positive for NEUN (red), OLIG2 (yellow), or GFAP (red), respectively, distributed through the spinal cord parenchyma, allowing the determination of dorso-ventral regionalization (Figure 1B).

3.2. hfNPCs Proliferate and Express Canonical Neural Markers in Vitro

NPCs self-renew, proliferate, and differentiate into the three neural lineages [32]; therefore, we evaluated the isolation and expansion of NPCs from whole human fetal spinal cord homogenates in neurosphere-like-forming cultures that support the self-renewal and clonal-like growth of NPCs [33]. Dissociation and culture of a human fetal spinal cord supported the efficient generation of neurospheres in free-floating conditions after two days of in vitro culture in the presence of the human recombinant mitotic factors bFGF, EGF, and LIF. After three days of culture, we observed an enrichment of primary (white arrow) and secondary (black arrow) neurospheres (Figure 2A).

After three days of culture, we expanded hfNPCs in adherent conditions in laminin-coated wells, retaining their morphology during the long-term expansion of subcultures (Figure 2B) as previously described for adult human NPCs [34]. Following subculture and reaching 80% confluency, we calculated the cell doubling time in hours (t) for hfNPCs for four passages (Figure 2C, black line). The t of rat NPCs derived from E15.5 spinal cords was also evaluated as a reference sample (Figure 2C, red line). Although we observed more significant heterogeneity in the results during the first two passages, cell doubling times during four passages did not significantly differ, ranging from 75.68 ± 10.87 to 103.1 ± 16.23 h, more than three-times the time needed for the rat fetal cells to duplicate in culture (Figure 2C). Nevertheless, hfNPCs at passage 4 continued to proliferate, with $21.4 \pm 3.3\%$ of cells incorporating BrdU at the S phase and $37.5 \pm 4.7\%$ displaying positive staining for the Ki67 mitotic marker (Figure 2E).

Previous studies of the subventricular zone of adult brain tissue revealed a pinwheel structure, which corresponds to the adult neurogenic niche [35]; furthermore, this structure also represents a hallmark of stemness in mouse-spinal-cord-derived neurospheres [36]. To study if hfNPCs from late gestational stages also form neurogenic niche-like structures, we immunostained for γ -tubulin to indicate microtubule-organizing centers, centrosomes, basal bodies, and β -catenin to delineate cell borders for the identification of pinwheel structures. For the first time, we revealed that in vitro cultures of spinal cord hfNPC-derived neurospheres adopt a pinwheel structure and display the neural features of fetal developmental stages (Figure 2D).

To ascertain whether amplified hfNPCs expressed canonical neural markers at passages 2 to 3, we immunoassayed samples for neurogenic locus notch homolog protein 1 (NOTCH1), paired-box protein 6 (PAX6), NESTIN, SOX2, Forkhead Box J1 (FoxJ1), doublecortin (DCX), and Neurogenin1 (Figure 2F). hfNPCs expressed high levels of nuclear NOTCH1 and PAX6 ($90.5 \pm 13.8\%$ and $91.7 \pm 4.4\%$ positive cells, respectively)—activated NOTCH translocates to the nucleus to support stemness [37], while Pax6 regulates NPC proliferation and self-renewal [30]. hfNPCs also stained positive for NESTIN ($83.4 \pm 2\%$ positive cells) and SOX2 ($79.7 \pm 2.2\%$ positive cells), which are expressed in late NPCs [38,39]. Additionally, $65 \pm 6.4\%$ of hfNPCs stained positive for FOXJ1, which is expressed in ciliated cells such as the ependymal cells [40], while hfNPCs also expressed DCX ($56.4 \pm 7.4\%$) and Neurogenin1 ($45.8 \pm 9.5\%$), with both proteins involved in neurogenesis [41,42] (Figure 2F).

3.3. PGA-SS-FAS Priming Enhances the Neuronal and Oligodendroglial Differentiation of hfNPCs

We next assessed the multipotent differentiation potential of hfNPCs after mitogen withdrawal and serum supplementation in the absence and presence of PGA-SS-FAS priming via immunofluorescence analysis for β -III-tubulin (pan-neuronal marker; green), GFAP (astrocyte marker; red), OLIG2 (oligodendrocyte marker, green), and NEUN (mature neuronal marker, red) (Figure 3A). Immunofluorescence quantitative analysis demonstrated that hfNPCs gave rise to neurons (9.85 ± 1.91 of cells positive for β -III-tubulin), astrocytes ($17.78 \pm 3.49\%$ of cells positive for GFAP), and oligodendrocytes ($15.54 \pm 2.54\%$ of cells positive for OLIG2) (Figure 3B), revealing the multipotency of the hfNPCs after in vitro amplification. Interestingly, PGA-SS-FAS priming significantly increased neuronal differentiation (up to four-times the number of β -III-tubulin-positive neurons in comparison with non-primed control hfNPCs; $43.61 \pm 4.92\%$ vs. 9.85 ± 1.91) and promoted mature neuronal

differentiation ($4.75 \pm 1.11\%$ NeuN-positive cells compared to non-primed hfNPCs, which lacked mature neurons) (Figure 3B). PGA-SS-FAS priming also significantly increased oligodendrocyte differentiation ($30.11 \pm 3.78\%$ OLIG2-positive cells compared to non-treated hfNPCs), although we observed no differences regarding astrocyte differentiation (Figure 3B).

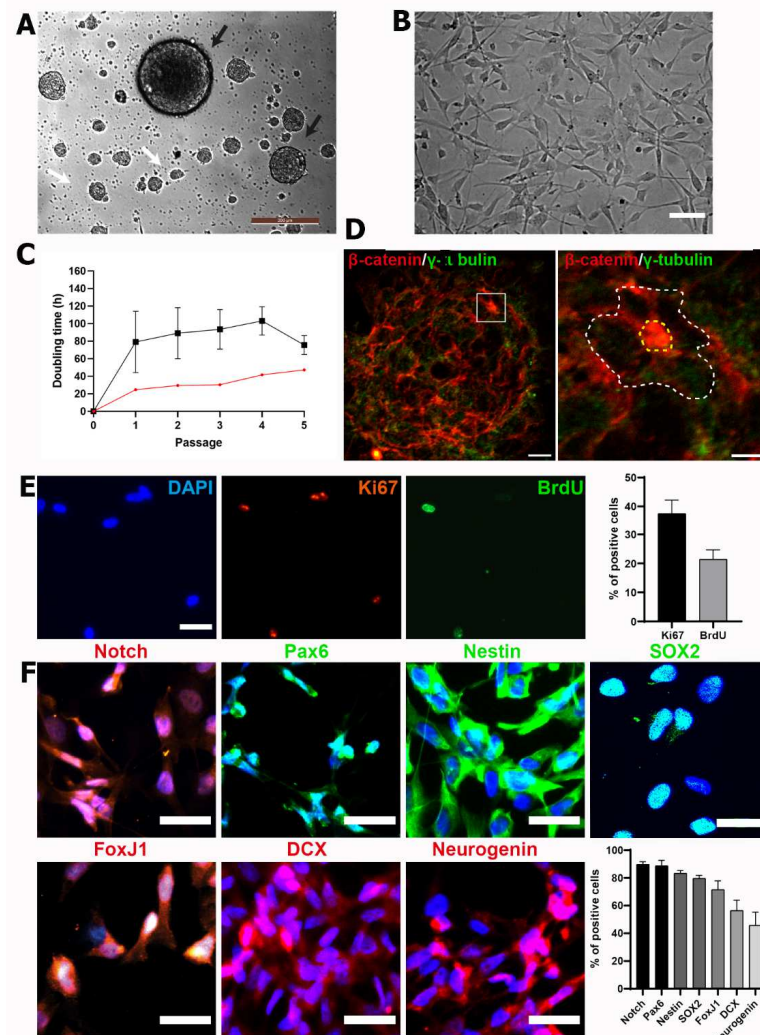


Figure 2. hfNPCs display proliferative potential and express canonical NPC markers in vitro. (A) Phase contrast image from hfNPCs as neurospheres-like cultures forming primary (black arrows) and secondary (white arrows) neurospheres as a hallmark of self-renewal in the presence of mitogens at passage 1. Scale bar = 200 μ m. (B) Representative phase contrast image of hfNPC culture in adherent conditions in laminin-coated wells when cultured at passages 2–5 (Scale bar = 20 μ m). (C) Doubling time (t) analysis of hfNPCs (black line; data presented as the mean \pm SEM ($n = 5$ samples)) and one rat fetal NPC sample (red line) growing in adherent conditions over five passages. (D) The pin-wheel cytoarchitecture (indicated with a white dotted line) of hfNPC at passage 1 from neurosphere-like cultures is highlighted after β -catenin (red; delimiting the cell perimeter) and γ -tubulin (green; for cilia detection) staining (scale bar = 20 μ m (left panel) and 10 μ m (right panel)). (E) Representative images from nuclear staining of DAPI (blue), Ki67 (red), and BrdU (green) of hfNPCs in adherent conditions (scale bar = 10 μ m). Right panel: Quantification of the percentage of positive cells for BrdU and Ki67. Data presented as the mean \pm SEM ($n = 3$ samples). (F) Left panel: Representative images of immunofluorescent staining for Notch, Pax6, Nestin, Sox2, FoxJ1, DCX, and neurogenin (scale bar = 20 μ m). Right panel: Quantification of the percentage of positive cells for each canonical neural progenitor cell marker. Data presented as the mean \pm SEM ($n = 5$ samples).

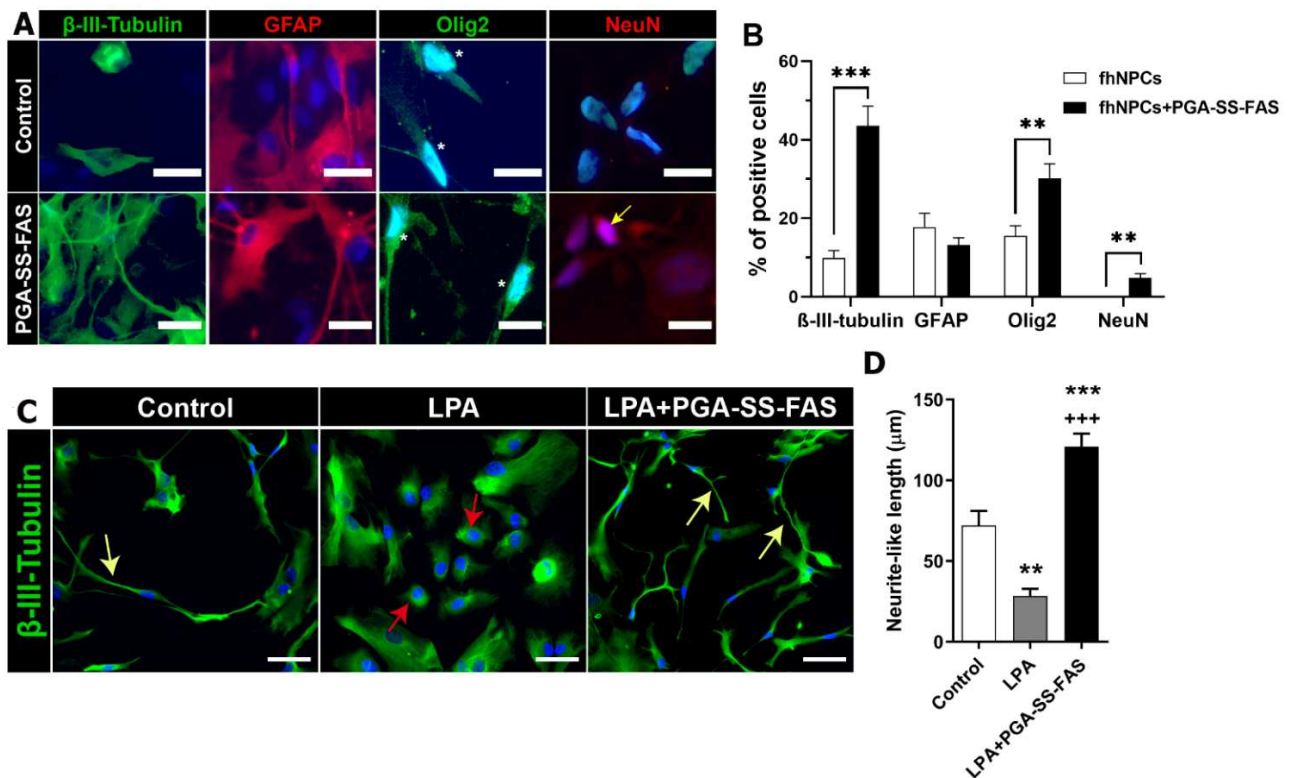


Figure 3. PGA-SS-FAS priming process enhances neuronal and oligodendrocyte differentiation and induces neurite outgrowth in a model of neurite retraction. (A) Representative immunofluorescence images of hfNPCs using β -III-tubulin for immature neurons (green), GFAP for astrocytes (red), Olig2 for oligodendrocytes (green), NeuN for mature neurons (red), and DAPI (blue) (scale bar = 20 μ m) (positive nuclear staining is indicated with an arrow) in the presence of the PGA-SS-FAS compound for inducing the priming process (PGA-SS-FAS) or its vehicle (control). (B) Quantification of the percentage of positive cells for each of the indicated cell markers with (black bars) or without (white bars) 24 h PGA-SS-FAS priming. Data presented as the mean \pm SEM determined by Student's unpaired t-test ($n = 3$). ** $p < 0.01$, *** $p < 0.001$ vs. hfNPCs. (C) Representative immunofluorescence images of β -III-tubulin (green) and DAPI (blue) staining during the in vitro neurite retraction assay induced by lysophosphatidic acid (LPA) treatment during 24 h in hfNPC adherent cultures. Yellow arrows indicate neurite-like processes emanating from neuronal progenitors in the control condition (in the absence of LPA) and in co-treated cultures (LPA + PGA-SS-FAS); red arrows indicate rounded cells 24 h after LPA treatment and induced neurite-like retraction (scale bar = 50 μ m). (D) Neurite length quantification presented as the mean \pm SEM determined by one-way ANOVA with the Tukey multiple comparison test ($n = 3$). ** $p < 0.01$, *** $p < 0.001$ vs. control; +++ $p < 0.001$ vs. control.

SCI activates the Rho/ROCK pathway, constituting one of axonal regrowth's most significant inhibitory signals [43]. We activated the Rho/ROCK pathway by culturing hfNPCs in the presence of 10 μ M LPA, a potent mitogen that induces neurite collapse [44], for 24 h, mimicking the intrinsic mechanism that blocks axon regeneration following SCI (Figure 3C,D). LPA induced a significant retraction of neurite-like processes in hfNPCs compared to control non-primed hfNPCs ($28.45 \pm 4.41\%$ vs. $72.07 \pm 8.96\%$; Figure 3C, red arrows); however, PGA-SS-FAS priming of hfNPCs efficiently inhibited neurite-like retraction after LPA exposure (120.8 ± 8.16 vs. $28.45 \pm 4.41\%$; Figure 3D, yellow arrows). These data suggest that priming with PGA-SS-FAS would prevent neuronal-like retraction of hfNPCs at the injury site following Rho/ROCK signaling activation.

3.4. PGA-SS-FAS Priming Enhances the Ventral Engraftment of hfNPCs, Endogenous Neuronal Activation, and Neuronal Survival After Transplantation into the Injured Spinal Cord

We next performed an intramedullary transplant of hfNPCs primed with PGA-SS-FAS (hfNPCs + PGA-SS-FAS) or vehicle (hfNPCs) immediately after compressive injury to the eighth thoracic vertebrae segments in nude mice to evaluate their therapeutic potential (Figure 4). We did not observe significant differences in the total number of surviving hfNPCs when comparing hfNPCs and hfNPCs + PGA-SS-FAS (Figure 4A–C), in both cases with a low survival rate (with an estimated percentage for the total cells of 2.7 ± 1.1 for hfNPCs + PGA-SS-FAS and 2.6 ± 0.5 for the hfNPC group), as shown in the representative images of GFP-positive grafted cells (Figure 4A). hfNPCs primed with PGA-SS-FAS (hfNPCs + PGA-SS-FAS) possessed enhanced grafting and migratory capacities and were encountered from the ventral to the dorsal areas of the spinal cord, while non-primed cells were restricted to the dorsal and injected areas (Figure 4D). In addition, hfNPCs + PGA-SS-FAS grafts possessed increased expression of c-Fos (Figure 4E,F) (a marker associated with neuronal activity [45]) when compared to non-primed hfNPCs, thereby suggesting that PGA-SS-FAS priming enhances the activation of transplanted hfNPCs. To determine the safety of the hfNPC transplantation and the priming process, we evaluated the potential invasiveness of grafted cells for both groups outside the spinal cord. Four weeks after transplantation, we evaluated the expression of eGFP by transplanted hfNPCs in the brain, heart, and liver by semiquantitative PCR. We failed to detect GFP expression in any of the analyzed tissues (data not shown). GABAergic inhibitory Lbx1 and glutamatergic excitatory Tlx3 are transcription factors involved in neuronal fate determination of somatosensory interneuron populations located in the dorsal horns of the spinal cord, which modulate and integrate peripheral somatosensory inputs [46]. A low percentage of hfNPCs displayed Lbx1 and Tlx3 expression in the grafts, while priming with PGA-SS-FAS did not influence this cell fate determination, as we failed to find any significant differences between the groups (Figure 4G–I).

Quantifying neuron survival at the injury site demonstrated no significant differences between primed and non-primed hfNPCs rostral or caudal to the injury and at the lesion epicenter (Figure 4J–L). Nevertheless, PGA-SS-FAS-primed hfNPCs showed a modest, but significant number of c-Fos⁺/NeuN⁺ cells at the injury site (Figure 4M), indicating a potential effect of the primed grafts on the subrounded neuronal activation. Furthermore, a modest increase in Lbx1 and Tlx3 interneurons surrounding the graft was found in the hfNPCs + PGA-SS-FAS group at the dorsal horn compared with the hfNPC group (Figure 4N–P).

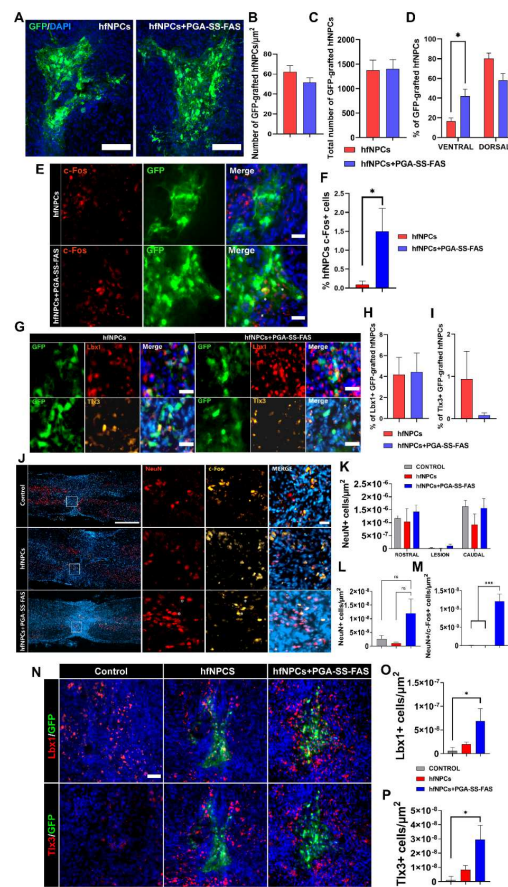


Figure 4. Quantification, distribution, and phenotypic characterization of non-primed and primed hfNPCs post-transplantation. (A) Representative images of GFP staining for hfNPC-grafted cells in spinal cord horizontal sections for the indicated groups (green) (scale bar = 50 μm). (B) Quantification of GFP-positive transplanted cells normalized to the total measured thickness in μm^2 . (C) quantification of GFP-positive transplanted cells in absolute numbers every 5th 20 mm section. (D) Quantification of the dorso-ventral distribution of the GFP-positive cells expressed in percentage of the total number of quantified cells. (E) representative images of c-Fos+ (red) and GFP (green) and the merged image including DAPI (blue) -positive immunostaining of grafted GFP-positive hfNPCs. (F) Quantification of the percentage of c-Fos-positive hfNPCs in the primed or non-primed groups, presented as the mean \pm SEM and determined by Student's unpaired t-test ($n = 3$). (* $p < 0.05$). (G) Representative images of immunofluorescent staining for GFP- (green), Lbx1- (red), and Tlx3- (yellow) positive grafted cells and merged images with DAPI (blue) of both experimental groups (scale bar = 25 μm). (H) Quantification of the percentage of Lbx1. (I) Tlx3-positive hfNPCs presented as the mean \pm SEM and determined by Student's unpaired t-test ($n = 3$). (J) Representative immunostainings of c-Fos (yellow), NeuN (red), and DAPI (blue) (white scale bar = 500 μm ; red scale bar = 25 μm). (K) Quantification of NeuN-positive cells in the rostral, lesion normalized to the total measured thickness in μm^2 , and caudal sites. (L) Quantification of NeuN-positive cells in the lesion site; data presented as the mean \pm SEM determined by one-way ANOVA with Tukey's multiple comparison test ($n = 3$). (M) Quantification of NeuN/c-Fos-double-positive cells in the lesion site normalized to the total measured thickness in μm^2 . Data presented as the mean \pm SEM determined by one-way ANOVA with Tukey's multiple comparison test ($n = 3$). (N) Representative immunostainings of (top panel) Lbx1 (red), GFP (green), and DAPI (blue) and (bottom panel) Tlx3 (red), GFP (green), and DAPI (blue) (scale bar = 50 μm) for the indicated experimental groups. (O) Quantification of Lbx1. (P) Tlx3-positive cells in the area surrounding the graft and lesion normalized to the total measured thickness in μm^2 . Data presented as the mean \pm SEM and determined by one-way ANOVA with Tukey's multiple comparison test ($n = 3$) (* $p < 0.05$, *** $p < 0.001$ (* $p < 0.05$, *** $p < 0.001$, ns = non-significant).

4. Discussion

The inflammatory and secondary damage milieu of SCI, which causes poor cell survival and grafting and improper differentiation, has been attributed as the factor limiting the therapeutic potential of cell therapy [47]. Survival rates and sufficient engraftment and integration into spinal cord circuits represent critical factors for successful cell transplantation and functional improvements [2]. In addition, aberrant neuronal connections induced by SCI can prompt allodynia, among other undesired effects [48]. Despite their multipotency, NPC transplants lack consistent neuronal motor differentiation [9,49], with differentiation generally driven towards the generation of glia by the SCI milieu. Combination therapies with varying levels of success have been developed to overcome these limitations—as reviewed by Griffin and Bradke [50]—with strategies including the combination of Notch inhibitors, to induce neuronal differentiation [51], with biocompatible matrices [52] or exogenous neurotrophic factors [53,54].

The origin and properties of NPCs have enormous significance in regenerating damaged spinal circuits [53]. Kadoya et al. recently demonstrated that rat fetal NPCs with spinal cord features (and not brain-derived NPCs) promoted regeneration of the corticospinal tract and functional motor improvement [53]. Moreover, Dulin et al. revealed that NPCs retain their features and differentiate towards specific phenotypes after transplantation into homologous regions of the host tissue, depending on their dorsal or ventral origin. [55].

Currently, translational strategies under investigation employ ESC- [16] or iPSC- [17] derived NSCs or immortalized fetal NPC lines [13] that have undergone significant manipulation prior to transplantation (e.g., reprogramming, long differentiation processes, or cell cycle manipulation for cell immortalization). We wanted to propose an alternative source for NPCs with minimal manipulation in the present study. To adhere to clinical-grade conditions, we isolated and *in vitro* expanded hfNPCs from 19.0–21.6 weeks of gestation human fetal spinal cords under xeno-free conditions. We found that the isolated hfNPCs retained canonical neural features and multipotency *in vitro*, making them suitable as a clinical translational approach for SCI. In addition, we evaluated a combinatorial strategy by priming hfNPCs with an in-house-developed polymer-conjugate of the Rho/ROCK inhibitor fasudil (PGA-SS-FAS), which previously demonstrated neurogenerative properties in an immunocompetent rat model of SCI [19]. This approach allowed for the standardized culture of spinal-cord-derived hfNPCs and the generation of a procedure for improved combinatorial therapy suitable for cell replacement therapy in the injured spinal cord.

We encountered SOX2-expressing proliferative NPCs densely packed within the central canal, but also occupying most of the spinal cord, giving rise to a heterogeneous population of progenitors at the primary culture expanded from the whole fetal spinal cord. Nevertheless, the heterogeneous hfNPC population possesses a homogeneous-like cell morphology in culture with a consistent cell fate profile when comparing different samples. hfNPCs retained stemness, with more than 80% of cells expressing SOX2 over several passages *in vitro*; however, we uncovered an important barrier for cell banking: hfNPCs possessed a low amplification efficiency, with a PD time more than three-times the time needed for cell duplication when compared with other cell populations derived from earlier gestational stages [12]. Although hfNPCs retained their proliferative capacity under the evaluated conditions, the employed growth-factor-enriched formulation (supplemented with bFGF, EGF, and LIF) requires further improvement to promote higher *in vitro* proliferative rates and cell expansion to make cell banking more feasible since rat-derived NPCs, also from late gestational stages, displayed a significant lower doubling time in the same cell culture conditions. Direct comparative analyses between different gestational ages for NPC isolation, expansion, and banking production will be required.

In vitro priming with PGA-SS-FAS promoted faster cell maturation, favoring neuronal and oligodendroglial differentiation without interference with astroglial differentiation within 24 h of incubation. Poor neuronal differentiation has been reported as a significant limitation of NPC transplantation approaches; we now report a one-step priming procedure to partially overcome this problem, avoid *in vivo* application of PGA-SS-FAS, and reduce

the potential side effects on host tissue. The convergence RhoA/ROCK pathway becomes activated by inhibitory molecules within the SCI milieu and plays a central role in inflammation, apoptosis, neuronal degeneration, and axon retraction [56]. Given the importance of these processes to SCI pathogenesis and the impairment of functional recovery, several pharmacological strategies have been developed to prevent cell death and promote axonal regeneration and functional recovery after SCI [57,58]. We previously described that NPCs derived from fetal rat spinal cords displayed improved neurite regrowth *in vitro* following treatment with PGA-SS-FAS, which also enhanced engraftment, induced a neuronal-like morphology, and elongated neurons from NPCs *in vitro* and *in vivo* [19]. Conversely, Stern et al. reported that RhoA inhibition had opposing roles in neurons and astrocytes, with RhoA activation limiting astrogliosis and RhoA ablation enhancing axon regeneration in neurons [59]. Considering these results, selective cell-specific approaches will be required to avoid side effects in host tissues.

Following SCI, axonal disruption and neuron death cause irreversible functional losses; therefore, preserving neuronal circuits, replacing lost neurons, and providing a regenerating environment to enhance plasticity after injury represent critical objectives for SCI therapeutics. We found that primed hfNPCs significantly preserved Tlx3- and Lbx1-expressing neuronal cells, which could be supported by the higher percentage of oligodendrocyte precursors induced by the treatment with PGA-SS-FAS prior to transplantation demonstrated *in vitro*. The Tlx3 homeobox gene functions as a developmental regulator of excitatory neurons, promoting glutamatergic excitatory specification and suppressing GABAergic specification in dorsal spinal cord neurons [60]. Lbx1 is required for the correct specification of early dorsal interneuron populations and plays a critical role in developing the spinal cord sensory pathways that transmit pain and touch [61]. Furthermore, grafted hfNPCs without the influence of the PGA-SS-FAS priming differentiated into Tlx3 and Lbx1 interneurons, showing phenotypically appropriate host target regions in the dorsal area of the spinal cord.

PGA-SS-FAS-primed hfNPCs induced the *in vivo* expression of c-Fos, a classical marker of neuronal activity [62], which is also related to synaptic plasticity and learning [63]. We observed a double effect: First, PGA-SS-FAS priming activated grafted hfNPCs, which could influence the differential migratory profile encountered compared with the non-primed hfNPCs. Fasudil-induced migration has been previously described via activation of the MAPK signaling pathway in mesenchymal stem cells [64] and the ERK signaling pathway in microglia [65]. Further analysis of the mechanism of action involved in hfNPC migration needs further investigation. Second, the transplantation of PGA-SS-FAS-primed hfNPCs induced the increased activation of endogenous neurons surrounding the graft (measured by the increased expression of c-Fos in host neurons), which has been related to synaptic plasticity and learning in other systems [63]. Nonetheless, despite the identified histological signs showing modest, but significant, improved neural preservation capabilities on the hfNPCs + PGA-SS-FAS group, we did not find differences on the locomotion recovery by the BMS test weekly analysis (data not shown).

5. Conclusions

Overall, our results provide evidence that PGA-SS-FAS-primed hfNPCs exert modest, but significant improved neuroprotective and a more migratory engraftment capability with an increased activation of surrounding endogenous neurons, which could provide a new combinatorial approach in a single formulation, which may serve as an improved cell therapy for SCI. However, since the differences reported here, employing PGA-SS-FAS-primed hfNPCs, did not improve graft survival and did not improve functional regeneration, we expect that PGA-SS-FAS-primed hfNPCs from earlier fetal stages would provide better results. In addition, since an immune-deprived mouse model was employed hosting the exogenously transplanted human cells, further evaluation in an immune competent model will be needed to address the important limitation of the immune rejection prior to clinical application.

Author Contributions: Conceptualization, V.M.M. and E.G.; methodology, V.M.M., E.G., P.B., S.Đ., M.J.V., M.M., A.A., E.L., P.G.-M. and C.R.; investigation, V.M.M., E.G., P.B., S.Đ., M.J.V., M.M., A.A., E.L., P.G.-M., C.R., F.P. and E.C.M.; resources, V.M.M.; data curation, V.M.M., E.G., P.B., S.Đ., M.M., A.A. and E.L.; writing—original draft preparation, V.M.M., E.G. and P.B.; writing—review and editing, V.M.M., E.G., P.B., M.J.V., S.Đ., F.P. and P.G.-M.; project administration, V.M.M.; funding acquisition, V.M.M. All authors have read and agreed to the published version of the manuscript.

Funding: This research was funded by Fundació Marató TV3 2017/refs.20172230, 20172231, Agencia Valenciana de Innovación (AVI) (INNVAL10/19/047 and Grants RTI2018-095872-B-C21 and PDI2021-1243590B-I00/ERDF funded by MCIN/AEI//10.13039/501100011033 and by ERDF A way of making Europe). This project was also funded by Project 964562 (RISEUP), H2020 FetOpen program.

Institutional Review Board Statement: The study was conducted in accordance with the Declaration of Helsinki and approved by the Institutional Clinical Ethics Committee of Vall de Hebron Hospital (Protocol Code PR(AMI)120/2017, approved in 2017). The animal study protocol was approved by the Ethical Animal Experimentation Committee of Centro de Investigación Príncipe Felipe (Protocol Code 2020/VSC/PEA/0119, approved in 2020).

Informed Consent Statement: Informed consent was obtained from all subjects involved in the study. Written informed consent was obtained from sample donors to publish this paper.

Data Availability Statement: Not applicable.

Acknowledgments: We would like to thank Fundació Step by Step for its support during the project, providing critical feedback from patients and clinical needs. We thank Marta Gutiérrez Delgado for her support in the project dissemination and sample recruitment. We thank the Banco de sangre y tejidos de Cataluña (BST), especially Joaquim Vives, for accepting their participation and contributing to the project with sub-contracting services for evaluating the cell banking capabilities for potential clinical use. We thank Francisco Javier Rodriguez for helping us on the pinwheel-like structures' analysis. We also thank Stuart P. Atkinson for his detailed English editing of this manuscript.

Conflicts of Interest: The authors declare no conflict of interest.

References

1. Dalamagkas, K.; Tsintou, M.; Seifalian, A.; Seifalian, A.M. Translational Regenerative Therapies for Chronic Spinal Cord Injury. *Int. J. Mol. Sci.* **2018**, *19*, 1776. [[CrossRef](#)] [[PubMed](#)]
2. Assinck, P.; Duncan, G.J.; Hilton, B.J.; Plemel, J.R.; Tetzlaff, W. Cell transplantation therapy for spinal cord injury. *Nat. Neurosci.* **2017**, *20*, 637–647. [[CrossRef](#)] [[PubMed](#)]
3. Kumamaru, H.; Ohkawa, Y.; Saiwai, H.; Yamada, H.; Kubota, K.; Kobayakawa, K.; Akashi, K.; Okano, H.; Iwamoto, Y.; Okada, S. Direct isolation and RNA-seq reveal environment-dependent properties of engrafted neural stem/progenitor cells. *Nat. Commun.* **2012**, *3*, 1140. [[CrossRef](#)] [[PubMed](#)]
4. Nishimura, S.; Yasuda, A.; Iwai, H.; Takano, M.; Kobayashi, Y.; Nori, S.; Tsuji, O.; Fujiyoshi, K.; Ebise, H.; Toyama, Y.; et al. Time-dependent changes in the microenvironment of injured spinal cord affects the therapeutic potential of neural stem cell transplantation for spinal cord injury. *Mol. Brain* **2013**, *6*, 3. [[CrossRef](#)]
5. Abematsu, M.; Tsujimura, K.; Yamano, M.; Saito, M.; Kohno, K.; Kohyama, J.; Namihira, M.; Komiya, S.; Nakashima, K. Neurons derived from transplanted neural stem cells restore disrupted neuronal circuitry in a mouse model of spinal cord injury. *J. Clin. Invest.* **2010**, *120*, 3255–3266. [[CrossRef](#)]
6. Cummings, B.J.; Uchida, N.; Tamaki, S.J.; Salazar, D.L.; Hooshmand, M.; Summers, R.; Gage, F.H.; Anderson, A.J. Human neural stem cells differentiate and promote locomotor recovery in spinal cord-injured mice. *Proc. Natl. Acad. Sci. USA* **2005**, *102*, 14069–14074. [[CrossRef](#)]
7. Karimi-Abdolrezaee, S.; Eftekharpour, E.; Wang, J.; Morshead, C.M.; Fehlings, M.G. Delayed transplantation of adult neural precursor cells promotes remyelination and functional neurological recovery after spinal cord injury. *J. Neurosci.* **2006**, *26*, 3377–3389. [[CrossRef](#)]
8. Kawabata, S.; Takano, M.; Numasawa-Kuroiwa, Y.; Itakura, G.; Kobayashi, Y.; Nishiyama, Y.; Sugai, K.; Nishimura, S.; Iwai, H.; Isoda, M.; et al. Grafted Human iPS Cell-Derived Oligodendrocyte Precursor Cells Contribute to Robust Remyelination of Demyelinated Axons after Spinal Cord Injury. *Stem Cell Rep.* **2016**, *6*, 1–8. [[CrossRef](#)]
9. Rosenzweig, E.S.; Brock, J.H.; Lu, P.; Kumamaru, H.; Salegio, E.A.; Kadoya, K.; Weber, J.L.; Liang, J.J.; Moseanko, R.; Hawbecker, S.; et al. Restorative effects of human neural stem cell grafts on the primate spinal cord. *Nat. Med.* **2018**, *24*, 484–490. [[CrossRef](#)]
10. Requejo-Aguilar, R.; Alastrue-Agudo, A.; Cases-Villar, M.; Lopez-Mocholi, E.; England, R.; Vicent, M.J.; Moreno-Manzano, V. Combined polymer-curcumin conjugate and endymal progenitor/stem cell treatment enhances spinal cord injury functional recovery. *Biomaterials* **2017**, *113*, 18–30. [[CrossRef](#)]

11. Ferrari, D.; Gelati, M.; Profico, D.C.; Vescovi, A.L. Human fetal neural stem cells for neurodegenerative disease treatment. In *Human Neural Stem Cells*; Springer: Berlin/Heidelberg, Germany, 2018; pp. 307–329.
12. Xu, N.; Xu, T.; Mirasol, R.; Holmberg, L.; Vincent, P.H.; Li, X.; Falk, A.; Benedikz, E.; Rotstein, E.; Seiger, A.; et al. Transplantation of Human Neural Precursor Cells Reverses Syring Growth in a Rat Model of Post-Traumatic Syringomyelia. *Neurotherapeutics* **2021**, *18*, 1257–1272. [[CrossRef](#)] [[PubMed](#)]
13. Curtis, E.; Martin, J.R.; Gabel, B.; Sidhu, N.; Rzesiewicz, T.K.; Mandeville, R.; Van Gorp, S.; Leerink, M.; Tadokoro, T.; Marsala, S.; et al. A First-in-Human, Phase I Study of Neural Stem Cell Transplantation for Chronic Spinal Cord Injury. *Cell Stem Cell* **2018**, *22*, 941–950. [[CrossRef](#)] [[PubMed](#)]
14. Shin, J.C.; Kim, K.N.; Yoo, J.; Kim, I.S.; Yun, S.; Lee, H.; Jung, K.; Hwang, K.; Kim, M.; Lee, I.S.; et al. Clinical Trial of Human Fetal Brain-Derived Neural Stem/Progenitor Cell Transplantation in Patients with Traumatic Cervical Spinal Cord Injury. *Neural. Plast.* **2015**, *2015*, 630932. [[CrossRef](#)] [[PubMed](#)]
15. Levi, A.D.; Anderson, K.D.; Okonkwo, D.O.; Park, P.; Bryce, T.N.; Kurpad, S.N.; Aarabi, B.; Hsieh, J.; Gant, K. Clinical Outcomes from a Multi-Center Study of Human Neural Stem Cell Transplantation in Chronic Cervical Spinal Cord Injury. *J. Neurotrauma* **2019**, *36*, 891–902. [[CrossRef](#)]
16. Kumamaru, H.; Kadoya, K.; Adler, A.F.; Takashima, Y.; Graham, L.; Coppola, G.; Tuszynski, M.H. Generation and post-injury integration of human spinal cord neural stem cells. *Nat. Methods* **2018**, *15*, 723–731. [[CrossRef](#)]
17. Sugai, K.; Sumida, M.; Shofuda, T.; Yamaguchi, R.; Tamura, T.; Kohzuki, T.; Abe, T.; Shibata, R.; Kamata, Y.; Ito, S.; et al. First-in-human clinical trial of transplantation of iPSC-derived NS/PCs in subacute complete spinal cord injury: Study protocol. *Regen. Ther.* **2021**, *18*, 321–333. [[CrossRef](#)]
18. Deng, J.; Zhang, Y.; Xie, Y.; Zhang, L.; Tang, P. Cell Transplantation for Spinal Cord Injury: Tumorigenicity of Induced Pluripotent Stem Cell-Derived Neural Stem/Progenitor Cells. *Stem Cells Int.* **2018**, *2018*, 5653787. [[CrossRef](#)]
19. Giraldo, E.; Nebot, V.J.; Dordevic, S.; Requejo-Aguilar, R.; Alastrue-Agudo, A.; Zagorodko, O.; Arminan, A.; Martinez-Rojas, B.; Vicent, M.J.; Moreno-Manzano, V. A rationally designed self-immolative linker enhances the synergism between a polymer-rock inhibitor conjugate and neural progenitor cells in the treatment of spinal cord injury. *Biomaterials* **2021**, *276*, 121052. [[CrossRef](#)]
20. Torres-Espin, A.; Santos, D.; Gonzalez-Perez, F.; del Valle, J.; Navarro, X. Neurite-J: An image-J plug-in for axonal growth analysis in organotypic cultures. *J. Neurosci. Methods* **2014**, *236*, 26–39. [[CrossRef](#)]
21. Boulland, J.L.; Lambert, F.M.; Zuchner, M.; Strom, S.; Glover, J.C. A neonatal mouse spinal cord injury model for assessing post-injury adaptive plasticity and human stem cell integration. *PLoS ONE* **2013**, *8*, e71701. [[CrossRef](#)]
22. Basso, D.M.; Fisher, L.C.; Anderson, A.J.; Jakeman, L.B.; McTigue, D.M.; Popovich, P.G. Basso Mouse Scale for locomotion detects differences in recovery after spinal cord injury in five common mouse strains. *J. Neurotrauma* **2006**, *23*, 635–659. [[CrossRef](#)] [[PubMed](#)]
23. Namiki, J.; Tator, C.H. Cell proliferation and nestin expression in the ependyma of the adult rat spinal cord after injury. *J. Neuropathol. Exp. Neurol.* **1999**, *58*, 489–498. [[CrossRef](#)] [[PubMed](#)]
24. Moreno-Manzano, V.; Rodriguez-Jimenez, F.J.; Garcia-Rosello, M.; Lainez, S.; Erceg, S.; Calvo, M.T.; Ronaghi, M.; Lloret, M.; Planells-Cases, R.; Sanchez-Puelles, J.M.; et al. Activated spinal cord ependymal stem cells rescue neurological function. *Stem Cells* **2009**, *27*, 733–743. [[CrossRef](#)] [[PubMed](#)]
25. Moreno-Manzano, V. Ependymal cells in the spinal cord as neuronal progenitors. *Curr. Opin. Pharmacol.* **2020**, *50*, 82–87. [[CrossRef](#)] [[PubMed](#)]
26. Alfaro-Cervello, C.; Soriano-Navarro, M.; Mirzadeh, Z.; Alvarez-Buylla, A.; Garcia-Verdugo, J.M. Biciliated ependymal cell proliferation contributes to spinal cord growth. *J. Comp. Neurol.* **2012**, *520*, 3528–3552. [[CrossRef](#)] [[PubMed](#)]
27. Avilion, A.A.; Nicolis, S.K.; Pevny, L.H.; Perez, L.; Vivian, N.; Lovell-Badge, R. Multipotent cell lineages in early mouse development depend on SOX2 function. *Genes Dev.* **2003**, *17*, 126–140. [[CrossRef](#)]
28. Bylund, M.; Andersson, E.; Novitsch, B.G.; Muhr, J. Vertebrate neurogenesis is counteracted by Sox1-3 activity. *Nat. Neurosci.* **2003**, *6*, 1162–1168. [[CrossRef](#)]
29. Silbereis, J.C.; Pochareddy, S.; Zhu, Y.; Li, M.; Sestan, N. The Cellular and Molecular Landscapes of the Developing Human Central Nervous System. *Neuron* **2016**, *89*, 248–268. [[CrossRef](#)]
30. Sansom, S.N.; Griffiths, D.S.; Faedo, A.; Kleinjan, D.J.; Ruan, Y.; Smith, J.; van Heyningen, V.; Rubenstein, J.L.; Livesey, F.J. The level of the transcription factor Pax6 is essential for controlling the balance between neural stem cell self-renewal and neurogenesis. *PLoS Genet.* **2009**, *5*, e1000511. [[CrossRef](#)]
31. Canizares, M.A.; Albors, A.R.; Singer, G.; Suttie, N.; Gorkic, M.; Felts, P.; Storey, K.G. Multiple steps characterise ventricular layer attrition to form the ependymal cell lining of the adult mouse spinal cord central canal. *J. Anat.* **2020**, *236*, 334–350. [[CrossRef](#)]
32. Shimada, I.S.; LeComte, M.D.; Granger, J.C.; Quinlan, N.J.; Spees, J.L. Self-renewal and differentiation of reactive astrocyte-derived neural stem/progenitor cells isolated from the cortical peri-infarct area after stroke. *J. Neurosci.* **2012**, *32*, 7926–7940. [[CrossRef](#)] [[PubMed](#)]
33. Reynolds, B.A.; Rietze, R.L. Neural stem cells and neurospheres—re-evaluating the relationship. *Nat. Methods* **2005**, *2*, 333–336. [[CrossRef](#)] [[PubMed](#)]
34. Mothe, A.J.; Zahir, T.; Santaguida, C.; Cook, D.; Tator, C.H. Neural stem/progenitor cells from the adult human spinal cord are multipotent and self-renewing and differentiate after transplantation. *PLoS ONE* **2011**, *6*, e27079. [[CrossRef](#)] [[PubMed](#)]

35. Mirzadeh, Z.; Merkle, F.T.; Soriano-Navarro, M.; Garcia-Verdugo, J.M.; Alvarez-Buylla, A. Neural stem cells confer unique pinwheel architecture to the ventricular surface in neurogenic regions of the adult brain. *Cell Stem Cell* **2008**, *3*, 265–278. [[CrossRef](#)] [[PubMed](#)]
36. Rodriguez-Jimenez, F.J.; Clemente, E.; Moreno-Manzano, V.; Erceg, S. Organized Neurogenic-Niche-Like Pinwheel Structures Discovered in Spinal Cord Tissue-Derived Neurospheres. *Front. Cell Dev. Biol.* **2019**, *7*, 334. [[CrossRef](#)]
37. Imayoshi, I.; Sakamoto, M.; Yamaguchi, M.; Mori, K.; Kageyama, R. Essential roles of Notch signaling in maintenance of neural stem cells in developing and adult brains. *J. Neurosci.* **2010**, *30*, 3489–3498. [[CrossRef](#)]
38. Lendahl, U.; Zimmerman, L.B.; McKay, R.D. CNS stem cells express a new class of intermediate filament protein. *Cell* **1990**, *60*, 585–595. [[CrossRef](#)]
39. Collignon, J.; Sockanathan, S.; Hacker, A.; Cohen-Tannoudji, M.; Norris, D.; Rastan, S.; Stevanovic, M.; Goodfellow, P.N.; Lovell-Badge, R. A comparison of the properties of Sox-3 with Sry and two related genes, Sox-1 and Sox-2. *Development* **1996**, *122*, 509–520. [[CrossRef](#)]
40. Li, X.; Floriddia, E.M.; Toskas, K.; Chalfouh, C.; Honore, A.; Aumont, A.; Vallieres, N.; Lacroix, S.; Fernandes, K.J.L.; Guerout, N.; et al. FoxJ1 regulates spinal cord development and is required for the maintenance of spinal cord stem cell potential. *Exp. Cell Res.* **2018**, *368*, 84–100. [[CrossRef](#)]
41. Sun, Y.; Nadal-Vicens, M.; Misono, S.; Lin, M.Z.; Zubiaga, A.; Hua, X.; Fan, G.; Greenberg, M.E. Neurogenin promotes neurogenesis and inhibits glial differentiation by independent mechanisms. *Cell* **2001**, *104*, 365–376. [[CrossRef](#)]
42. Brown, J.P.; Couillard-Despres, S.; Cooper-Kuhn, C.M.; Winkler, J.; Aigner, L.; Kuhn, H.G. Transient expression of doublecortin during adult neurogenesis. *J. Comp. Neurol.* **2003**, *467*, 1–10. [[CrossRef](#)] [[PubMed](#)]
43. Madura, T.; Yamashita, T.; Kubo, T.; Fujitani, M.; Hosokawa, K.; Tohyama, M. Activation of Rho in the injured axons following spinal cord injury. *EMBO Rep.* **2004**, *5*, 412–417. [[CrossRef](#)] [[PubMed](#)]
44. Kranenburg, O.; Poland, M.; van Horck, F.P.; Drechsel, D.; Hall, A.; Moolenaar, W.H. Activation of RhoA by lysophosphatidic acid and Galphai2/13 subunits in neuronal cells: Induction of neurite retraction. *Mol. Biol. Cell* **1999**, *10*, 1851–1857. [[CrossRef](#)] [[PubMed](#)]
45. Hudson, A.E. Genetic Reporters of Neuronal Activity: C-Fos and G-CaMP6. *Methods Enzymol.* **2018**, *603*, 197–220. [[CrossRef](#)] [[PubMed](#)]
46. Monteiro, F.A.; Miranda, R.M.; Samina, M.C.; Dias, A.F.; Raposo, A.; Oliveira, P.; Reguenga, C.; Castro, D.S.; Lima, D. Tlx3 Exerts Direct Control in Specifying Excitatory Over Inhibitory Neurons in the Dorsal Spinal Cord. *Front. Cell Dev. Biol.* **2021**, *9*, 642697. [[CrossRef](#)] [[PubMed](#)]
47. Stern, S.; Knoll, B. CNS axon regeneration inhibitors stimulate an immediate early gene response via MAP kinase-SRF signaling. *Mol. Brain* **2014**, *7*, 86. [[CrossRef](#)]
48. Hofstetter, C.P.; Holmstrom, N.A.; Lilja, J.A.; Schweinhardt, P.; Hao, J.; Spenger, C.; Wiesenfeld-Hallin, Z.; Kurpad, S.N.; Frisen, J.; Olson, L. Allodynia limits the usefulness of intraspinal neural stem cell grafts; directed differentiation improves outcome. *Nat. Neurosci.* **2005**, *8*, 346–353. [[CrossRef](#)]
49. Lu, P.; Woodruff, G.; Wang, Y.; Graham, L.; Hunt, M.; Wu, D.; Boehle, E.; Ahmad, R.; Poplawski, G.; Brock, J.; et al. Long-distance axonal growth from human induced pluripotent stem cells after spinal cord injury. *Neuron* **2014**, *83*, 789–796. [[CrossRef](#)]
50. Griffin, J.M.; Bradke, F. Therapeutic repair for spinal cord injury: Combinatory approaches to address a multifaceted problem. *EMBO Mol. Med.* **2020**, *12*, e11505. [[CrossRef](#)]
51. Okubo, T.; Nagoshi, N.; Kohyama, J.; Tsuji, O.; Shinozaki, M.; Shibata, S.; Kase, Y.; Matsumoto, M.; Nakamura, M.; Okano, H. Treatment with a Gamma-Secretase Inhibitor Promotes Functional Recovery in Human iPSC-Derived Transplants for Chronic Spinal Cord Injury. *Stem Cell Rep.* **2018**, *11*, 1416–1432. [[CrossRef](#)]
52. Elkhenany, H.; Bonilla, P.; Giraldo, E.; Alastrue Agudo, A.; Edel, M.J.; Vicent, M.J.; Roca, F.G.; Ramos, C.M.; Doblado, L.R.; Pradas, M.M.; et al. A Hyaluronic Acid Demilune Scaffold and Polypyrrole-Coated Fibers Carrying Embedded Human Neural Precursor Cells and Curcumin for Surface Capping of Spinal Cord Injuries. *Biomedicines* **2021**, *9*, 1928. [[CrossRef](#)] [[PubMed](#)]
53. Kadoya, K.; Lu, P.; Nguyen, K.; Lee-Kubli, C.; Kumamaru, H.; Yao, L.; Knackert, J.; Poplawski, G.; Dulin, J.N.; Strobl, H.; et al. Spinal cord reconstitution with homologous neural grafts enables robust corticospinal regeneration. *Nat. Med.* **2016**, *22*, 479–487. [[CrossRef](#)] [[PubMed](#)]
54. Fu, E.; Wallace, K.; Grayden, K.; Kaplan, M. A Review of Neural Stem Cell Transplant Therapy for Traumatic Spinal Cord Injury. *SN Compr. Clin. Med.* **2021**, *3*, 1586–1592. [[CrossRef](#)]
55. Dulin, J.N.; Adler, A.F.; Kumamaru, H.; Poplawski, G.H.D.; Lee-Kubli, C.; Strobl, H.; Gibbs, D.; Kadoya, K.; Fawcett, J.W.; Lu, P.; et al. Injured adult motor and sensory axons regenerate into appropriate organotypic domains of neural progenitor grafts. *Nat. Commun.* **2018**, *9*, 84. [[CrossRef](#)]
56. Roy, A.; Pathak, Z.; Kumar, H. Strategies to neutralize RhoA/ROCK pathway after spinal cord injury. *Exp. Neurol.* **2021**, *343*, 113794. [[CrossRef](#)]
57. Boato, F.; Hendrix, S.; Huelsenbeck, S.C.; Hofmann, F.; Grosse, G.; Djalali, S.; Klimaschewski, L.; Auer, M.; Just, I.; Ahnert-Hilger, G.; et al. C3 peptide enhances recovery from spinal cord injury by improved regenerative growth of descending fiber tracts. *J. Cell Sci.* **2010**, *123*, 1652–1662. [[CrossRef](#)]

58. Otsuka, S.; Adamson, C.; Sankar, V.; Gibbs, K.M.; Kane-Goldsmith, N.; Ayer, J.; Babiarz, J.; Kalinski, H.; Ashush, H.; Alpert, E.; et al. Delayed intrathecal delivery of RhoA siRNA to the contused spinal cord inhibits allodynia, preserves white matter, and increases serotonergic fiber growth. *J. Neurotrauma* **2011**, *28*, 1063–1076. [[CrossRef](#)]
59. Stern, S.; Hilton, B.J.; Burnside, E.R.; Dupraz, S.; Handley, E.E.; Gonyer, J.M.; Brakebusch, C.; Bradke, F. RhoA drives actin compaction to restrict axon regeneration and astrocyte reactivity after CNS injury. *Neuron* **2021**, *109*, 3436–3455. [[CrossRef](#)]
60. Shimomura, A.; Patel, D.; Wilson, S.M.; Koehler, K.R.; Khanna, R.; Hashino, E. Tlx3 promotes glutamatergic neuronal subtype specification through direct interactions with the chromatin modifier CBP. *PLoS ONE* **2015**, *10*, e0135060. [[CrossRef](#)]
61. Gross, M.K.; Dottori, M.; Goulding, M. Lbx1 specifies somatosensory association interneurons in the dorsal spinal cord. *Neuron* **2002**, *34*, 535–549. [[CrossRef](#)]
62. Gao, Y.J.; Ji, R.R. c-Fos and pERK, which is a better marker for neuronal activation and central sensitization after noxious stimulation and tissue injury? *Open Pain J.* **2009**, *2*, 11–17. [[CrossRef](#)] [[PubMed](#)]
63. Jaworski, J.; Kalita, K.; Knapska, E. c-Fos and neuronal plasticity: The aftermath of Kaczmarek’s theory. *Acta Neurobiol. Exp.* **2018**, *78*, 287–296. [[CrossRef](#)]
64. Li, Z.; Hu, X.; Zhong, J.F. Mesenchymal Stem Cells: Characteristics, Function, and Application. *Stem Cells Int.* **2019**, *2019*, 8106818. [[CrossRef](#)]
65. Fu, P.C.; Tang, R.H.; Yu, Z.Y.; Xie, M.J.; Wang, W.; Luo, X. The Rho-associated kinase inhibitors Y27632 and fasudil promote microglial migration in the spinal cord via the ERK signaling pathway. *Neural. Regen. Res.* **2018**, *13*, 677–683. [[CrossRef](#)] [[PubMed](#)]



Depletion of Mannose Receptor-Positive Tumor-associated Macrophages via a Peptide-targeted Star-shaped Polyglutamate Inhibits Breast Cancer Progression in Mice

Anni Lepland¹, Alessio Malfanti², Uku Haljasorg³, Eliana K. Ascitutto⁴, Monica Pickholz^{5,6}, Mauro Bringas^{7,8}, Snežana Đorđević², Liis Salumäe⁹, Pärt Peterson³, Tambet Teesalu^{1,10}, María J. Vicent², and Pablo Scodeller^{1,11}

ABSTRACT

Although many studies have explored the depletion of tumor-associated macrophages (TAM) as a therapeutic strategy for solid tumors, currently available compounds suffer from poor efficacy and dose-limiting side effects. Here, we developed a novel TAM-depleting agent (“OximUNO”) that specifically targets CD206⁺ TAMs and demonstrated efficacy in a triple-negative breast cancer (TNBC) mouse model. OximUNO comprises a star-shaped polyglutamate (St-PGA) decorated with the CD206-targeting peptide mUNO that carries the chemotherapeutic drug doxorubicin (DOX). In the TNBC model, a fluorescently labeled mUNO-decorated St-PGA homed to CD206⁺ TAMs within primary lesions and metastases. OximUNO exhibited no acute liver or kidney toxicity *in vivo*. Treatment

with OximUNO reduced the progression of primary tumor lesions and pulmonary metastases, significantly diminished the number of CD206⁺ TAMs and increased the CD8/FOXP3 expression ratio (indicating immunomodulation). Our findings suggest the potential benefit of OximUNO as a TAM-depleting agent for TNBC treatment. Importantly, our studies also represent a novel design of a peptide-targeted St-PGA as a targeted therapeutic nanoconjugate.

Significance: A peptide-targeted nanoformulation of DOX exclusively eliminates mannose receptor⁺ TAMs in breast cancer models, generating response without off-target effects (a drawback of many TAM-depleting agents under clinical study).

Introduction

Triple-negative breast cancer (TNBC), defined by the lack of the expression of the estrogen receptor, progesterone receptor, and HER2 (1, 2), represents an aggressive breast cancer subtype with poor prognosis (3) that comprises up to 20% of all breast cancer cases (3, 4). Interfering with immune checkpoints signaling [e.g., through the modulation of programmed cell death 1 (PD-1) and its ligand (PD-L1)] represents an alternative treatment strategy for several cancers and is currently being employed in combination with chemotherapy as a

neoadjuvant or adjuvant treatment (5–8). The FDA recently granted accelerated approval for a combination of a PD-L1-blocking antibody (atezolizumab, Tecentriq) and nab-paclitaxel (Abraxane; ref. 9) as a first-line treatment for unresectable locally advanced or metastatic TNBC (10). While promising clinical results have resulted, this combinatorial treatment approach suffers from significant obstacles, including the problematic identification and heterogeneity of PD-L1 expression in patients (11), the limited applicability to patients with PD-L1-positive TNBC (only 20%–42% of cases; refs. 12, 13), and the induction of severe side effects (e.g., neutropenia, peripheral neuropathy, and

¹Laboratory of Precision and Nanomedicine, Institute of Biomedicine and Translational Medicine, University of Tartu, Tartu, Estonia. ²Polymer Therapeutics Laboratory, Prince Felipe Research Centre, Valencia, Spain. ³Molecular Pathology Research Group, Institute of Biomedicine and Translational Medicine, University of Tartu, Tartu, Estonia. ⁴School of Science and Technology, National University of San Martín (UNSAM) ICIFI and CONICET, Buenos Aires, Argentina. ⁵Departamento de Física, Facultad de Ciencias Exactas y Naturales, Universidad de Buenos Aires, Buenos Aires, Argentina. ⁶Instituto de Física de Buenos Aires (IFIBA), CONICET-Universidad de Buenos Aires, Buenos Aires, Argentina. ⁷Departamento de Química Inorgánica, Analítica y Química Física, Facultad de Ciencias Exactas y Naturales, Universidad de Buenos Aires, Buenos Aires, Argentina. ⁸Fundación Instituto Leloir, Instituto de Investigaciones Bioquímicas de Buenos Aires (IIBBA-CONICET), C1405BWE Ciudad Autónoma de Buenos Aires, Buenos Aires, Argentina. ⁹Pathology Department, Tartu University Hospital, Tartu, Estonia.

¹⁰Centre for Nanomedicine and Department of Cell, Molecular and Developmental Biology, University of California, Santa Barbara, California. ¹¹Department of Immunology and Oncology, Centro Nacional de Biotecnología (CNB-CSIC), Madrid, Spain.

A. Lepland, A. Malfanti, T. Teesalu, M.J. Vicent, and P. Scodeller contributed equally to this article.

Corresponding Author: Pablo Scodeller, Department of Biomedicine, University of Tartu, Tartu 50411, Estonia. Phone: 372-737-4268; E-mail: pablo.david.scodeller@ut.ee

doi: 10.1158/2767-9764.CRC-22-0043

This open access article is distributed under the Creative Commons Attribution 4.0 International (CC BY 4.0) license.

© 2022 The Authors; Published by the American Association for Cancer Research

colitis; refs. 10, 14, 15). Other immune checkpoint inhibitors (ICI), including the CTL-associated antigen 4 (CTLA-4) blockers ipilimumab and tremelimumab, are currently under evaluation for TNBC treatment in combination with other drugs (clinical trial identifiers: NCT03606967, NCT02983045); however, anti-CTLA-4 treatments induce severe side effects such as endocrinopathies, myopathy, enterocolitis, and hepatitis (16–19), which narrow their use. Overall, the limited success of alternative treatment options for TNBC has maintained chemotherapy as the standard of care for most patients (20).

The anthracycline drug doxorubicin (DOX), which presents high off-target effects such as cardiotoxicity (21, 22), represents a frequently employed chemotherapeutic for TNBC; however, disease relapse and metastatic development have also been associated with DOX treatment (23). M2 (anti-inflammatory)-polarized tumor-associated macrophages (TAM; ref. 24) found within both primary and metastatic tumor lesions mediate both events (25); furthermore, TAMs represent the main executioners of tumor progression, immunosuppression, and invasion (24–29), and their presence correlates with inadequate therapeutic response and poor prognosis (25). Recent efforts have focused on eliminating TAMs, and several ongoing clinical trials are currently evaluating TAM depletion in combination with treatments such as ICIs (30). The current clinical-stage gold standard for TAM depletion relies on agents that block colony stimulating factor 1 (CSF1) or its receptor CSF1R, such as the small-molecule CSF1R inhibitor PLX3397 (31); however, microglia also expresses CSF1R (32), the inhibition of CSF1R with PLX5622 impacts M1 macrophages (33), and PLX3397 treatment causes edema (34). Clinical data suggest that anti-CSF1R antibodies induce a modest effect (35, 36) and cause severe side effects that include hematologic toxicities (35) and hepatotoxicity by targeting Kupffer cells (35, 36). Overall, these findings highlight the overwhelming need for new TAM depletion strategies.

Notably, both perivascular TAMs associated with disease relapse and therapeutic resistance (24) and metastasis-associated macrophages (37) express the mannose receptor (CD206/MRC1). Perivascular TAMs employ CD206 to navigate the surrounding collagen-dense stroma (38), which favors tumor progression (39, 40).

For the first time, we report the effects of depleting the CD206⁺ subpopulation of TAMs in a metastatic TNBC mouse model through the use of a targeting agent (the mUNO peptide) for a CD206 site different from the mannose-binding site (41–44). Previous studies have employed mannose to target CD206; however, mannose has other receptors besides CD206 (45, 46).

We decorated a three-arm branched biodegradable multivalent polyanion with a defined negative charge and nanometer-size hydrodynamic radius (star-shaped polyglutamate or St-PGA) with mUNO peptide to function as a targeted delivery platform for a chemotherapeutic agent (DOX) conjugated through a bioresponsive linker. St-PGA-DOX-mUNO (referred to as OximUNO) efficiently depleted CD206⁺ TAMs, relieved immunosuppression in the tumor microenvironment (TME) and limited metastasis/tumor growth, thereby supporting OximUNO as an alternative TAM depletion strategy.

Most importantly, this study represents the first described combination of two reported technologies—the St-PGA nanocarrier and the mUNO-targeting peptide. Overall, this OximUNO proof of concept demonstrates the potential of the peptide-targeted St-PGA nanosystem. Our studies lay a foundation for future work using this nanosystem to target other receptors efficiently by changing the targeting peptide.

Materials and Methods

Reagents and Solutions

The peptides mUNO (sequence: CSPGAK-COOH) and FAM-mUNO (FAM-Ahx-CSPGAK-COOH) were purchased from TAG Copenhagen and DOX from Sigma-Aldrich. St-PGA was kindly provided by Polypeptide Therapeutic Solution S.L. (PTS). See the Supplementary Data for information on all other reagents and solutions.

Mayer's hematoxylin solution was prepared by dissolving 5 g of aluminium potassium sulphate dodecahydrate (Merck Millipore, catalog no. 1010421000) in 100 mL of water, and adding 1 g of hematoxylin (Merck, catalog no. H9627). After complete dissolution, 0.02 g of sodium iodide (Merck, catalog no. 1065230100) was added and completely dissolved. Then, 2 mL of acetic acid (Sigma-Aldrich, catalog no. 33209) was added, and then the solution was boiled and then cooled. Once ready to use, the solution was filtered using a 0.45- μ m filter.

Eosin (5%) solution was prepared by dissolving 0.5 g of Eosin Y (Sigma-Aldrich, catalog no. 230251) in 99 mL water/1 mL acetic acid.

Cell Culture and Experimental Animals

4T1 cells were purchased from ATCC, and 4T1-GFP cells were a gift from Ruoslahti laboratory (Sanford Burnham Prebys Medical Discovery Institute, La Jolla, CA). 4T1 and 4T1-GFP cells were cultured in RPMI1640 medium (Gibco by Life Technologies, catalog no. 72400-021) supplemented with 10% volume for volume (v/v) FBS (Capricorn Scientific, catalog no. FBS-IIA) and 100 IU/mL penicillin/streptomycin (Capricorn Scientific, catalog no. PS-B) at 37°C in the presence of 5% CO₂. For all animal experiments, 8–12 weeks old female Balb/c mice were used. Animal experiment protocols were approved by the Estonian Ministry of Agriculture (Project #159). All methods were performed in accordance with existing guidelines and regulations.

Tumor Models

Two tumor models were used for homing studies: the orthotopic TNBC model, where 1×10^6 4T1 cells in 50 μ L of PBS (Lonza, catalog no. 17-512F) were subcutaneously injected into the fourth mammary fat pad, and the experimental metastasis of TNBC model, where 5×10^5 4T1 cells in 100 μ L of PBS were injected intravenously into Balb/c mice.

Two tumor models were used for treatment studies: the orthotopic TNBC model where 5×10^4 4T1 cells in 50 μ L of PBS were injected subcutaneously into fourth mammary fat pad; and the experimental metastasis of TNBC model where 2×10^5 4T1-GFP cells in 100 μ L of PBS were intravenously injected.

Nanoconjugate Synthesis and Characterization

In vivo homing studies used St-PGA-OG (Oregon Green) and St-PGA-OG-mUNO, while *in vitro* cytotoxicity and *in vivo* treatment studies used St-PGA-DOX and St-PGA-DOX-mUNO (“OximUNO”). Detailed synthetic procedures for single nanoconjugates can be found in Supplementary Data.

Physicochemical Characterization Methods

Nuclear Magnetic Resonance Spectroscopy

Nuclear magnetic resonance (NMR) spectra were recorded at 27°C (300 K) on a 300 Ultrashield from Bruker. Data were processed with Mestrenova software. Sample solutions were prepared at the desired concentration in D₂O or D₂O supplemented with NaHCO₃ (0.5 mol/L).

UV-visible Analysis

UV-visible (UV-Vis) measurements were performed using JASCO V-630 spectrophotometer at 25°C with 1-cm quartz cells and a spectral bandwidth of 0.5 nm. Spectra analysis was recorded three times in the range of 200–700 nm.

Fluorescence Analysis

Fluorescence analysis was performed using a JASCO FP-6500 spectrofluorimeter at 25°C with 1-cm quartz cells.

Dynamic Light Scattering

Size measurements were performed using a Malvern ZetasizerNano ZS instrument, supported by a 532 nm laser at a fixed scattering angle of 173°. Nanoconjugate solutions (0.1 mg/mL) were freshly prepared in PBS (10 mmol/L phosphate, 150 mmol/L NaCl), filtered through a 0.45- μ m cellulose membrane filter, and measured. Size distribution was measured (diameter, nm) for each polymer in triplicate. Automatic optimization of beam focusing and attenuation was applied for each sample.

Zeta Potential Measurements

Zeta potential measurements were performed at 25°C using a Malvern ZetasizerNano ZS instrument, equipped with a 532 nm laser using disposable folded capillary cells, provided by Malvern Instruments Ltd. Nanoconjugate solutions (0.1 mg/mL) were freshly prepared in 1 mmol/L KCl. Solutions were filtered through a 0.45- μ m cellulose membrane filter. Zeta potential was measured for each sample per triplicate.

Molecular Dynamics Simulations

Molecular dynamics (MD) simulations of PGA chains, and mUNO peptide were carried out using the ff19SB force field (47) in the Amber20 MD engine (<https://sbgrid.org/software/titles/ambertools>). The nanoconjugate system was neutralized using Na⁺ ions and hydrated to account for a total of approximately 920,000 atoms (~300,000 TIP3P water molecules) in a truncated octahedral box. A hydrogen mass repartitioning strategy was applied on the resulting topology, allowing us a 4 fs integration time step (48). Standard minimization and equilibration protocols were used to reach 300 K and 1 atm., followed by 50 ns of production MD run. The simulations were run under the NVT ensemble [constant number of particles, volume, and temperature through Berendsen thermostat (49)], considering periodic boundary conditions. The SHAKE algorithm was used to fix hydrogen atoms (50). The nonbound cut-off value was set to Angstrom. The central moiety was parameterized using the recommended protocol for the Amber force field. It was necessary to introduce amide bond, angle, and dihedral terms using the ParmEd module to establish the bond of the central molecule to the PGA chains.

Tumor Homing Studies

Tumors were induced as described in the tumor model section. Tumor homing studies were performed on mice bearing orthotopic TNBC or experimental metastasis of TNBC. Ten days post-induction (p.i) of the orthotopic TNBC or the experimental metastasis of TNBC model, mice were intraperitoneally injected with St-PGA-OG-mUNO (0.41 mg/0.5 mL of PBS) or St-PGA-OG (0.35 mg/0.5 mL of PBS; corresponding to 15 nanomoles of OG, absorbance measured by UV-Vis). The homing of a higher dose of St-PGA-OG (0.82 mg/0.5 mL of PBS) or St-PGA-OG (0.7 mg/0.5 mL of PBS; corresponding to 30 nanomoles of OG) was also analyzed and compared with the homing of FAM-mUNO (30 nanomoles/0.5 mL of PBS). In every case, nanoconjugates or

free peptide were circulated for 6 hours, after which time, mice were sacrificed by anesthetic overdose followed by cervical dislocation. Organs and tumors were collected and fixed in cold 4% w/v paraformaldehyde (PFA) in PBS at +4°C for 24 hours, washed in PBS at room temperature for 1 hour and cryoprotected in 15% w/v sucrose (Sigma Life Science, catalog no. S9378) followed by 30% w/v sucrose at 4°C overnight. Cryoprotected and fixed tissues were frozen in optimal cutting temperature (OCT; Leica, catalog no. 14020108926), cryosectioned at 10- μ m thickness on Superfrost+ slides (Thermo Fisher Scientific, catalog no. J1800AMNZ) and stored at –20°C. Immunofluorescence staining was performed as described earlier (42). OG was detected using rabbit anti-FITC/Oregon Green (dilution 1/100, Invitrogen by Thermo Fisher Scientific, catalog no. A889) and Alexa Fluor 647 goat anti-rabbit antibody (dilution 1/250, Invitrogen by Thermo Fisher Scientific, catalog no. A21245). CD206 was detected using rat anti-mouse CD206 (dilution 1/150, Bio-Rad, catalog no. MCA2235GA) and Alexa Fluor 546 goat anti-rat antibody (dilution 1/250, Life Technologies, catalog no. A11081). CD86 was detected using rat anti-mouse CD86 (dilution 1/100, BioLegend, catalog no. 105001) and Alexa Fluor 546 goat anti-rat secondary antibody (dilution 1/250). CD11c was detected using hamster anti-mouse CD11c antibody (dilution 1/75, BioLegend, catalog no. 117301) and Alexa Fluor 546 goat anti-hamster secondary antibody (dilution 1/200, Life Technologies, catalog no. A21111). CD31 was detected with rat anti-mouse CD31 (dilution 1/100, BD Biosciences, catalog no. 553370) as primary antibody and with Alexa Fluor 546 goat anti-rat (dilution 1/200, Invitrogen, catalog no. A11081) as secondary antibody. Slides were counterstained using 4',6-diamidino-2-phenylindole (DAPI, 1 μ g/mL in PBS, Sigma-Aldrich, catalog no. D9542-5MG). Coverslips were mounted using mounting medium (Fluoromount-G Electron Microscopy Sciences, catalog no. 17984-25), and sections were imaged using Zeiss confocal microscope (Zeiss LSM-710) and 20 \times objective. The colocalization analysis between the FAM or OG channel and the CD206 channel was carried out using the “Coloc2” plugin in the Fiji program and selecting the “Pearson *R* value (no threshold)” coefficient. The colocalization values were obtained from at least three representative images per mouse per group and their average and SE were plotted. The OG/FAM mean signal per CD206⁺ cell analysis was measured using ImageJ, taking the mean OG/FAM signal, and dividing it with the number of CD206⁺ cells. Average values were obtained from four images per mouse. *N* = 3 for orthotopic TNBC and *N* = 2 for the homing in experimental metastasis of TNBC.

Analysis of Tumor and Liver Leakiness

Endogenous IgG immunostaining of orthotopic 4T1 tumors and livers was performed following the same Immunofluorescence (IF) protocol as described above to assess leakiness. Endogenous IgG was detected using Alexa Fluor 647 goat anti-mouse antibody (dilution 1/200, Invitrogen by Thermo Fisher Scientific, catalog no. A21235) and slides were counterstained with DAPI (1 μ g/mL in PBS). The coverslips were mounted, and sections were imaged using Zeiss confocal microscope and 20 \times objective (*N* = 3 tumors).

PDL1 Expression Analysis in Orthotopic TNBC Tumors

The assessment of PDL1 expression in orthotopic 4T1 tumors followed the IF protocol described above. PDL1 was detected using rat anti-mouse PDL1 (dilution 1/100, BioLegend, catalog no. 124302) as primary antibody and Alexa Fluor 647 goat anti-rat (dilution 1/200, Invitrogen, catalog no. A21247) as the secondary antibody. Slides were counterstained with DAPI (1 μ g/mL in PBS), mounted, and imaged using a Zeiss confocal microscope.

Tumor Homing of Anti-PDL1 in Orthotopic TNBC Tumors

For the homing analysis with anti-PDL1, we injected 1×10^6 4T1 cells in 50 μ L of PBS subcutaneously and 10 days p.i., PD-L1 antibody (5 mg/kg, rat anti-mouse, BioXcell, catalog no. BE0101) was injected intravenously, circulated for 24 hours after which time, mice were sacrificed, organs collected and fixed with PFA. Ten-micron-thick tissue sections were stained with Alexa Fluor 647 goat anti-rat antibody (dilution 1/200), counterstained with DAPI (1 μ g/mL in PBS), mounted, and imaged with a Zeiss confocal microscope.

Plasma Half-life Evaluation for St-PGA-OG-mUNO

Plasma half-life studies were performed as described previously (42). Briefly, healthy female Balb/c mice ($N = 3$) were intraperitoneally injected with St-PGA-OG-mUNO (0.41 mg/0.5 mL of PBS, corresponding to 15 nanomoles OG). Ten microliters of blood was sampled at different timepoints (0, 5, 10, 15, 30, 60, 180, 360, and 1,440 minutes) and mixed with 50 μ L of PBS-Heparin solution. Blood samples were centrifuged to obtain plasma ($300 \times g$ for 5 minutes at room temperature) and OG fluorescence was read with a plate reader (FlexStation II Molecular Devices) at 480 nm excitation/520 nm emission.

DOX Release Studies

LC/MS was implemented to determine free drug levels, stability, and drug release with OximUNO. The LC/MS system consisted of an ExionLC LC system and AB Sciex QTRAP 4500, a triple quadrupole ion trap hybrid equipped with a Turbo VTM electrospray ionization source. DOX was detected with an internal standard method: 1 μ g/mL of daunorubicin (DAU) was used as internal standard, where three calibration curves (in a range from 0.5 to 50 μ g/mL DOX) were prepared and used for accurate analysis of DOX in the samples. Both DOX and DAU were detected with positive electrospray ionization mode by following two mass transitions (544.2 m/z \rightarrow 397 m/z and 544.2 m/z \rightarrow 379 m/z for DOX, and 528 m/z \rightarrow 363.1 m/z and 528 m/z \rightarrow 321.3 m/z for DAU). The obtained LC/MS optimal conditions were as follows: flow rate 0.5 mL/minute; mobile phase – 0.05% trifluoroacetic acid with 70% of acetonitrile; LiChrospher 100 C18 column (125 \times 4.0 mm; Merck); column temperature 40°C, 10 μ L injection volume.

Stability Study of OximUNO Conjugate in PBS, pH 7.4

OximUNO was incubated in 10 mmol/L dPBS (Dulbecco's phosphate-buffered saline) at 37°C at the concentration of 3 mg/mL and with 3 μ g/mL of DAU. A total of 100 μ L aliquots were collected at defined timepoints (0, 1, 2, 5, 24, 48, 72 hours), extracted with 3 \times 250 μ L chloroform, and mixed by vortexing for 5 minutes. Organic phases from all three chloroform extracts were collected in one tube, evaporated using speed vacuum, and stored at -20°C . On the day of analysis, dried samples were reconstituted in 300 μ L of methanol (LC/MS grade), vortexed for 5 minutes, and centrifuged for 5 minutes at $30,437 \times g$. Supernatants were filtered through a 0.45- μ m filter and subjected to LC/MS analysis.

Stability Study of OximUNO in the Intraperitoneal Fluid

Intraperitoneal fluid was collected from healthy 8–12 weeks old Balb/c female mice as performed in ref. 51 by collecting the supernatant and discarding the pellet after the centrifugation step. A working solution containing 3 mg/mL of OximUNO and 3 μ g/mL of DAU in intraperitoneal fluid was incubated at 37°C. A total of 50 μ L aliquots were collected at scheduled timepoints (0, 2, 5, 7, and 24 hours). Samples were then diluted with 100 μ L of methanol,

sonicated to dissolve DOX, and injected into the LC/MS after filtration through a 0.45- μ m filter.

Cathepsin B Release Kinetic Studies

Cathepsin B (5 IU) was activated in 2 mmol/L EDTA (Ethylenediaminetetraacetic acid), 5 mmol/L DTT (Dithiothreitol), and 20 mmol/L CH_3COONa buffer and incubated at 37°C for 15 minutes. In a separate tube, a solution containing 3 mg/mL OximUNO and 3 μ g/mL of DAU was prepared with 20 mmol/L CH_3COONa and incubated at 37°C for 15 minutes. The two solutions were then combined to produce a reaction solution that was incubated at 37°C. A total of 100 μ L aliquots were collected at scheduled timepoints (0, 1, 2, 5, 8, 24, 48, 72 hours), and after the addition of 900 μ L of dPBS (to adjust the pH level to 7.4), free DOX and DAU were extracted with 2.5 mL of CHCl_3 three times. Samples were processed as described under "Stability Study of OximUNO conjugate in PBS, pH 7.4". After CHCl_3 evaporation, samples were reconstituted with 300 μ L of methanol, filtered through a 0.45- μ m filter, and subjected to LC/MS analysis. A blank solution was prepared with the same components as the sample solution but without cathepsin B and used as a control sample.

In Vitro Cytotoxicity Assay

Human peripheral blood mononuclear cells (PBMC) were purified from human blood buffy coat using Ficoll Paque Plus (GE Healthcare, catalog no. 17-1440-02) reagent and CD14^+ microbeads (MACS Miltenyi Biotec, catalog no. 130-050-201) as described previously (42). A total of 1.2×10^5 cells in 50 μ L of RPMI1640 medium were seeded on an FBS-coated 96-well plate. To obtain optimal macrophage attachment and M2 resembling, 50 μ L of IL4 (50 ng/mL, BioLegend, catalog no. 574002) and MCSF (50 ng/mL, BioLegend, catalog no. 574802) mixture was added to the wells. The medium was replenished by substituting half of the medium with fresh medium containing IL4 and MCSF every other day for 6 days. To obtain M1-resembling macrophages, monocytes were incubated with M-CSF (50 ng/mL) for 6 days, replenishing every other day with fresh medium containing MCSF and on day 6, 50 μ L of MCSF, lipopolysaccharide (LPS, 100 ng/mL, Sigma-Aldrich, catalog no. L4391) and $\text{IFN}\gamma$ (20 ng/mL, BioLegend, catalog no. 570202) was added and incubated overnight. On day 7, cells were incubated for 15 minutes at 37°C with OximUNO, St-PGA-DOX, DOX in medium, or free medium as a control ($N = 3$ wells/group). Concentrations used were calculated on the basis of DOX: 33 and 100 μ mol/L. (Of note, the dose of OximUNO used for the 33 μ mol/L DOX *in vitro* experiments corresponds to the same dose of OximUNO used for both *in vivo* treatment studies). *In vivo*, all treated groups received injections containing 2 mg/kg of DOX, which, assuming the dilution in mouse blood, corresponds to a DOX concentration of 33 μ mol/L. After incubation, wells were washed, fresh medium added, and cells incubated for 48 hours at 37°C. After 48 hours, 10 μ L of 3-(4,5-dimethylthiazol-2-yl)-2,5-diphenyltetrazolium bromide (MTT, concentration 5 mg/mL, Invitrogen, catalog no. M6494) in PBS was added to each well containing culture medium and incubated for 2.5 hours at 37°C. Medium containing MTT was then removed without removing formed crystals, and 100 μ L of isopropanol was added to each well to dissolve crystals. Absorbance was read at 580 nm using a plate reader (Tecan Sunrise) and the corresponding Magellan 7 program. To analyze the CD206 expression of M2-resembling and M1-resembling macrophages, cells were lifted from 24-well plate using cell scraper, washed 2 \times with full RPMI and once with PBS, seeded on a 96-well plate with conical bottom at a concentration of 1×10^5 cells in 100 μ L of RB ["running buffer": 4 mL 0.5 mol/L EDTA, 100 mL 5% (w/v) BSA in 1 L of PBS] per well, blocked with 0.5 μ L of human TruStain FcX (BioLegend, 422302)

in 100 μ L of RB at +4°C for 30 minutes after which cells were washed with 100 μ L of RB and incubated with 0.5 μ L of APC anti-human CD206 (BioLegend, 321109) in 100 μ L of RB containing 0.25 μ L of human TruStain FcX for 25–45 minutes at +4°C in the dark. After that, cells were washed 2 \times with 200 μ L of RB and read using BD Accuri 6 plus (BD Biosciences). As an isotype control, APC mouse IgG (BioLegend, catalog no. 400119) was used. For washing, plate was centrifuged at 350 \times g for 7 minutes at +4°C.

In Vivo Liver and Kidney Toxicology Studies with OximUNO

Three healthy 12-week-old female Balb/c mice were intraperitoneally injected once with OximUNO (0.704 mg/0.5 mL PBS or 1.408 mg/0.5 mL) and circulated for 48 hours. Then, mice were anesthetized, and blood collected through retro-orbital bleeding into Lithium Heparin tubes (BD Vacutainer, catalog no. 368494). Blood samples were centrifuged at 1,800 \times g for 15 minutes at +4°C and 400 μ L of plasma was collected for analysis. Samples were analyzed in Tartu University Hospital using a Cobas 6000 IT-MW (Roche Diagnostics GmbH) machine and reagents for creatinine (CREP2, catalog no. 03263991) and alanine aminotransferase (ALTLP, catalog no. 04467388).

For histologic analysis of livers and kidneys, after sacrificing animals, tissues were frozen into block, sectioned at 10- μ m thickness and kept at room temperature for approximately 30 minutes before fixing them with ice-cold methanol for 2 minutes at room temperature followed by hematoxylin and eosin (H&E) staining as described under “H&E staining on PFA-fixed cryosections.” Slides were scanned using Leica DM6 B microscope and Leica Aperio Versa 8 slides scanner with 20 \times zoom and images were analyzed using the ImageScope (version 12.3.3). Slides were then analyzed by pathologists.

To analyze IFN γ in tissues after OximUNO injection, after sacrificing, tissues were fixed with 4% PFA and cryoprotected. Ten-micron-thick tissue sections were stained with rat anti-mouse IFN γ (dilution 1/50, BioLegend, catalog no. 505701) and Alexa Fluor 647 goat anti-rat antibody (dilution 1/200), counterstained with DAPI (1 μ g/mL in PBS), mounted, and imaged with a Zeiss confocal microscope and 10 \times objective.

OximUNO Treatment of Orthotopic TNBC

A total of 5 \times 10⁴ 4T1 cells in 50 μ L of PBS were subcutaneously injected into the fourth mammary fat pad of 8–12 weeks old female Balb/c mice. On day 7, mice were sorted into four groups by tumor volume measured using a digital caliper (Mitutoyo). Tumor volume was calculated on the basis of the formula ($W^2 \times L$)/2, where W is the tumor's width and L is the tumor's length. The starting volume for each group was approximately 25 mm³, and the number of mice in each group was five. The first intraperitoneal injection of compounds was carried out on day 7, followed by an intraperitoneal injection every other day; nine injections were performed in total. The dose of nanoconjugates was calculated on the basis of DOX, 2 mg/kg per injection (DOX: 39.5 μ g/0.5 mL PBS; St-PGA-DOX: 476 μ g/0.5 mL PBS; OximUNO: 341 μ g/0.5 mL PBS) giving a cumulative dose of DOX of 18 mg/kg. Mouse bodyweight and tumor volumes were monitored every other day. The final injection was on day 25 and all mice were sacrificed on day 28. Tumor tissues were processed as described under “*In vivo* biodistribution studies,” and the lungs and hearts were embedded in paraffin and processed for H&E staining (described below). Tumors were immunostained as described above. CD206 was detected using rat anti-mouse CD206 (dilution 1/200), CD8 using rat anti-mouse CD8 (dilution 1/75 BioLegend, catalog no. 100701), FOXP3 using rat anti-mouse FOXP3 (dilution 1/75, BioLegend, catalog

no. 126401) as primary antibodies, Alexa Fluor goat anti-rat 647 (dilution 1/300 for CD206 and 1/200 for CD8, FOXP3,) was used as a secondary antibody for all markers. Slides were counterstained with DAPI (1 μ g/mL in PBS) and imaged using a Zeiss confocal microscope with a 10 \times objective. All five tumors from each group were included in the IF analysis and at least three images per mouse per group were included. Fluorescent signal intensity was calculated using the ImageJ; to account for different amounts of tissue in the different images, only the area containing tissue was selected and the “mean signal intensity” given by the program taken (total integrated intensity divided by the selected area). For this analysis, at least three images per tumor were included.

Survival Analysis Following OximUNO Treatment of Orthotopic TNBC

For survival analysis, treatment was performed the same way as described above, with $N = 5$ mice in each group. Mice were sacrificed when their tumors reached 1,500 mm³. Survival was analyzed using GraphPad Prism (version 9.3.1) to plot Kaplan–Meier survival curves and to perform Mantel–Cox test for statistical analysis.

H&E Staining in Paraffin-embedded Formalin-fixed Tissues

For H&E staining, 2- μ m-thick sections were cut from paraffin-embedded blocks. Slides were warmed at 60°C for 2 minutes before deparaffinizing using xylene (3 \times 2 minutes, 1 \times 1 minute) followed by 100% ethanol washes (3 \times 1 minute), 80% ethanol wash (1 \times 1 minute) followed by 1-minute wash in water. Slides were first incubated with ST-1 HemaLast for 30 seconds, followed by ST-2 hematoxylin for 5 minutes after which time, slides were washed in water for 2 minutes. Then, ST-3 differentiator was added for 45 seconds, and slides were washed in water for 1 minute. Next, ST-4 Bluing Agent was added (1 minute), washed for 1 minute in water followed by 1-minute incubation in 80% ethanol, after which time, ST-5 eosin was added and incubated for 1 minute. For rehydration, incubations in 100% ethanol (2 \times 30 seconds, 1 \times 2 minutes) were carried out and finished with incubations in xylene (2 \times 2 minutes). All washes were carried out in tap water. H&E staining was performed in Tartu University Hospital by pathologists using Leica staining automat and ST Infinity H&E Staining System (Leica, catalog no. 38016998). Stained lung sections were scanned using a slide scanner (Leica SCN400) and 20 \times zoom. Images were analyzed using the QuPath program (version 0.1.2; ref. 52). Five levels approximately 1 mm apart were used for each mouse to obtain comprehensive pulmonary metastases profile. Stained heart sections were also scanned using a slide scanner and analysed with the QuPath program. Tartu University Hospital pathologists assessed cardiotoxicity in hearts and pulmonary metastases.

Analysis of CD31 Expression and Blood Vessel Count

CD31 expression after treating orthotopic TNBC tumors with OximUNO, St-PGA-DOX, or DOX was detected using rat anti-mouse CD31 (dilution 1/100) and Alexa Fluor 546 goat anti-rat (dilution 1/200) was used as the secondary antibody. Slides were counterstained with DAPI (1 μ g/mL in PBS) and imaged using Zeiss confocal microscope with a 10 \times objective. CD31 expression was calculated using ImageJ and mean signal per field as described under “OximUNO therapy in orthotopic TNBC,” including at least five images per mouse per group, $N = 5$ mice per group. The blood vessel count was calculated from the same images using ImageJ as follows: the image was changed to an 8-bit image, threshold (Triangle algorithm with modifications to account for as

much actual CD31 signal as possible) was added, and particles analyzed. At least three images per mouse per group were included in the analysis, $N = 5$ mice per group. Field size was 1.42 mm \times 1.42 mm for all images.

OximUNO Treatment of Experimental Metastasis of TNBC

A total of 2×10^5 4T1 cells in 100 μ L of PBS were intravenously injected into the tail vein of 8–12 week old female Balb/c mice. Treatment with OximUNO, St-PGA-DOX, or DOX began on day 4 p.i.; each group comprised 6 mice. Doses of different compounds were calculated on the basis of DOX (2 mg/kg): DOX: 39.5 μ g/0.5 mL PBS; St-PGA-DOX: 774.5 μ g/0.5 mL PBS; OximUNO: 704 μ g/0.5 mL PBS. Mouse bodyweight was monitored every other day. A total of six injections were carried out every other day. The final injection was on day 12, and all animals were sacrificed on day 18 using anesthetic overdose and perfusion with PBS. Three right lungs from each group were analyzed with flow cytometry (FC), and three full lungs and three left lungs from each group were frozen into blocks using OCT. Frozen lung tissues were cryosectioned as described earlier, fixed for 10 minutes with cold 4% PFA (CD206) or acetone (for CD8 and FOXP3), and stained as described in the following section. Immunofluorescence staining was performed using the same markers and antibodies as shown in the “OximUNO treatment in orthotopic TNBC” section.

GFP Staining and Imaging

Six lungs from each group were frozen in OCT. Ten-micron-thick sections were cut and slides were kept at -20°C until ready to use. Slides were taken out of the freezer at least 30 minutes before staining. For staining, slides were fixed with 4% PFA for 10 minutes at room temperature, washed with PBS for 10 minutes at room temperature, counterstained using DAPI (1 μ g/mL in PBS) for 5 minutes at room temperature, washed 3 \times 4 minutes with PBS and finally mounted using mounting medium. Permeabilization was not used in this step to improve GFP visualization. GFP was visualized using its native fluorescence. Slides were imaged using Olympus confocal microscope (FV1200MPE) with a 10 \times objective.

Macroscopic Analysis of GFP Signal

Lungs from each group were imaged using Illumatool Bright Light System LT-9900 (LightTool's Research) in the green channel to visualize the fluorescent

signal macroscopically, and a photograph of each lung was taken. The total GFP signal of each lung was quantified by ImageJ using the “IntDen” value.

FC Analysis

Three mice were sacrificed using anesthetic overdose, perfused with PBS and right lung tissues were placed in cold RPMI1640 medium supplemented with 2% v/v FBS. Lungs were cut into small pieces on ice in a solution containing collagenase IV (160 U/mL, Gibco, catalog no.17104019)/dispase (0.6 U/mL, Gibco, catalog no. 17105-041)/DNase I (15 U/mL; AppliChem, catalog no. A3778) mixture. To obtain a single-cell suspension, lung pieces were incubated in 10 mL of the same mixture at 37°C on a rotating platform for 45–60 minutes, pipetting every 10 minutes to improve digestion. The cells were washed with 5 mL of RB, centrifuged (350 \times g, 7 minutes, 4°C), and red blood cells were lysed with 3 mL of ammonium-chloride-potassium lysing buffer at room temperature. A total of 10 mL of RB was added; cells were centrifuged and filtered using a 100- μ m cell strainer (Falcon, catalog no. 352360). Cells were counted using the bright-field mode of LUNA Automated Cell counter (Logos Biosystems). Cells were collected in RB at a concentration of $5 \times 10^6/100 \mu\text{L}$, placed on a 96-well plate with conical bottom and incubated for 30 minutes in FcR-blocking 2.4G2 hybridoma medium at 4°C . The cells were then stained for either macrophage or T-cell markers for 25–45 minutes in the dark at $+4^\circ\text{C}$, centrifuged and washed twice with RB. The antibodies used are listed in Table 1. For intracellular staining of T cells, cells were fixed using eBioscience FOXP3/Transcription Factor Staining Buffer Set (Thermo Fisher Scientific, catalog no. 00-5523-00) according to the protocol provided. Cells were stained for 25–45 minutes in the dark at room temperature following permeabilization and washed twice using RB. All cells were collected in 150 μ L of RB, filtered through a 70- μ m filter (Share Group Limited) and 150 μ L of RB was used to wash the filter. BD LSR-Fortessa Flow Cytometer and FCS Express 7 Flow (De Novo Software) were used for analysis.

H&E Staining on PFA-fixed Cryosections

Ten-micron-thick sections were cut from unfixed tissues in a frozen block; sections were stored at -20°C until ready to use. When ready, slides were taken out of the freezer 30 minutes before staining and stained within an hour for optimal results. Room temperature slides were fixed with cold 4% PFA for 10 minutes at room temperature followed by washing in PBS for 10 minutes at room

TABLE 1 Antibodies used in FC analysis: macrophage and T-cell markers

	Antibody	Dilution, Company
Macrophage markers	PerCP/Cyanine5.5 anti-mouse CD206 (MMR)	1/200, BioLegend, clone C068C2, catalog no. 141715
	PE anti-mouse CD86	1/400, BioLegend, clone PO3, catalog no. 105105
	PE/Cyanine7 anti-mouse F4/80	1/200, BioLegend, clone BM8, catalog no. 123114
	PE/Dazzle 594 anti-mouse/human CD11b	1/ 800, BioLegend, clone M1/70, catalog no. 101255
	eBioscience Fixable Viability Due eFluor 506	1/800, Thermo Fisher Scientific, catalog no. 65-0866-18
T-cell markers	Brilliant Violet 570 anti-mouse CD4	1/400, BioLegend, clone RM4-5, catalog no. 100542
	Brilliant Violet 605 anti-mouse CD8a	1/400, BioLegend, clone 53-6.7, catalog no. 100744
	PE/Dazzle 594 anti-mouse CD279 (PD-1)	1/200, BioLegend, clone 29F.1A12, catalog no. 135228
	Alexa Fluor 488 anti-mouse FOXP3	1/100, BioLegend, clone MF-14, catalog no. 126406
	PerCP/Cyanine5.5 anti-mouse CD3 ϵ	1/200, BioLegend, clone 145-2C11, catalog no. 100328
	Brilliant Violet 421 anti-mouse CD152 (CTLA4)	1/200, BioLegend, clone UC10-4B9, catalog no. 106312
	eBioscience Fixable Viability Due eFluor 506	1/800, Thermo Fisher Scientific, catalog no. 65-0866-18

temperature. After washing, slides were dipped into Mayer's hematoxylin solution (see preparation under "Reagents and Solutions") for 10 seconds, followed by washing in running tap water for 5 minutes. Then, slides were dipped into Eosin (5%) solution (see preparation under "Reagents and Solutions") for 20 seconds, followed by washing in running tap water for 5 minutes. For rehydration, slides were placed first in 96% ethanol (2×2 minutes) followed by 100% ethanol (2×2 minutes). For clearance, slides were placed in RotiClear solution (Roth, catalog no. A538.5) for two times 5 minutes, after which time, slides were mounted using Eukitt quick-hardening mounting medium (Merck, catalog no. 03989). Slides were scanned using Leica DM6 B microscope and Leica Aperio Versa 8 slides scanner with $20\times$ zoom and images were analyzed using the ImageScope program (version 12.3.3). QuPath was used to analyze the pulmonary tumor area coverage by dividing the tumor area per whole lung area and multiplying with 100. $N = 6$ lungs per group were analyzed.

Statistical Analysis

All statistical analysis was carried out using one-way ANOVA and Fisher LSD (Least Significant Difference) tests, using the Statistica program (release 7),

except for survival analysis, where GraphPad Prism (version 9.3.1) was used to perform Kaplan–Meier survival curves and Mantel–Cox for statistical analysis.

Data Availability

All data needed to evaluate the conclusions on the article are presented in the article and/or the Supplementary Data. Additional data related to the findings of this study are available from the corresponding author.

Results

Design and Structural Modeling of St-PGA-OG-mUNO

To characterize and explore the function of OximUNO, we first developed an mUNO-targeted St-PGA labeled with the OG fluorescent dye (referred to as St-PGA-OG-mUNO; Fig. 1A; Supplementary Scheme S1). We conjugated OG to St-PGA using an amide linker to allow *in vitro* or *in vivo* tracking and coupled mUNO through a disulphide bond formed between the free cysteine of mUNO and a pyridyldithiol linker on St-PGA. We previously demonstrated that mUNO conjugated to polymeric nanostructures through the cysteine thiol group preserves CD206 binding (42). To evaluate the structure and dye

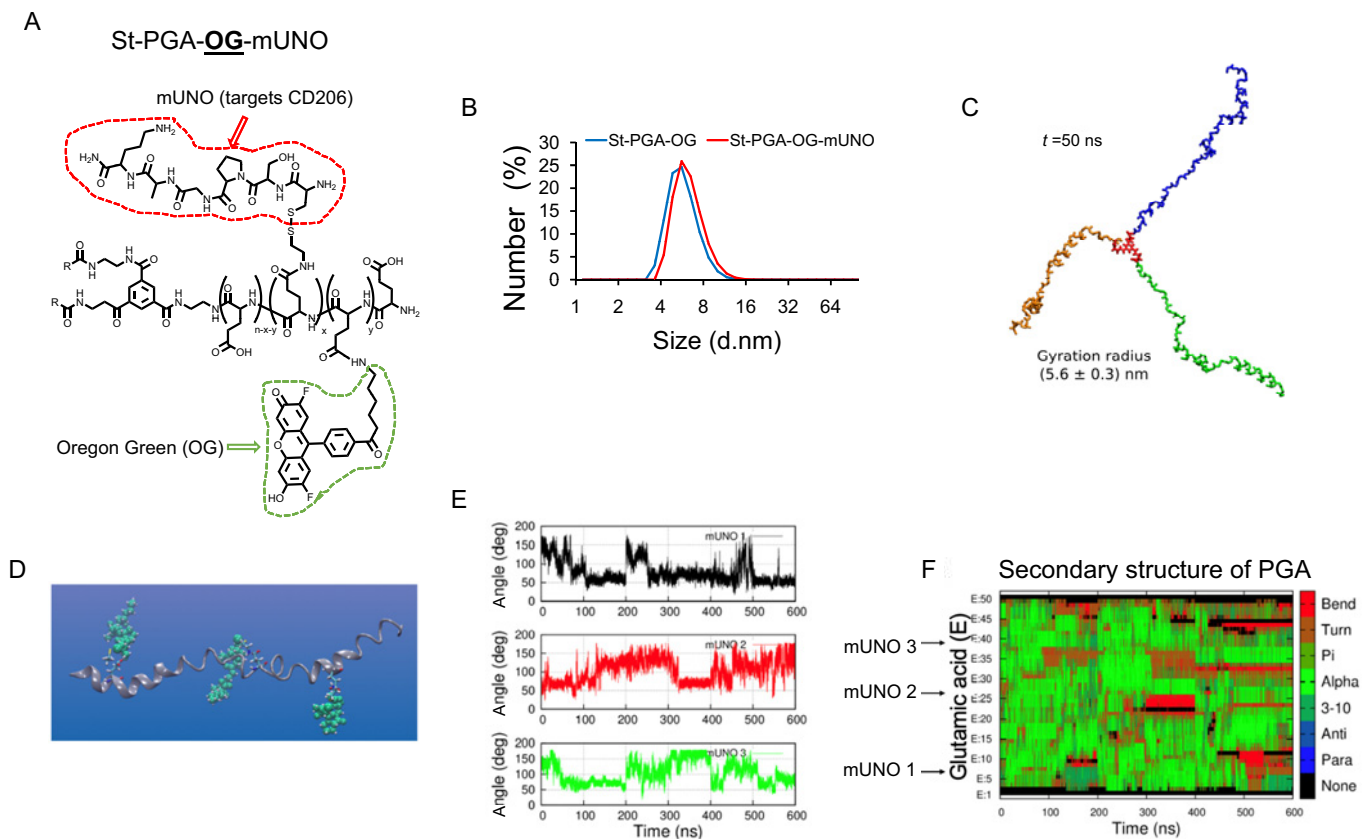


FIGURE 1 Design and analysis of mUNO-targeted St-PGA. **A**, Representative structure of St-PGA decorated with mUNO peptides (red) and OG (green). **B**, DLS graph demonstrating uniform size for both St-PGA-OG-mUNO and St-PGA-OG. **C**, A snapshot of modeled St-PGA structure in water and Na^+ counterions at the last stage of the simulation (50 ns), displaying the three arms in different colors for visual clarity. The average gyration radius was 5.6 ± 0.3 nm, t shows time in ns. **D**, Representative MD snapshot of a single St-PGA-mUNO branch containing three equidistant mUNO peptides. Green spheres represent mUNO and a Licorice representation shows the linker. **E**, mUNO rotation around the PGA chain for each of the three peptides (black, red, and green lines). **F**, PGA chain secondary structure evolution, where red and brown regions show how mUNO perturbs the chain structure, turning alpha helices into random coils.

loading, we analyzed St-PGA-OG-mUNO and St-PGA-OG using NMR and UV-Vis analyses (Supplementary Fig. S1).

Dynamic light scattering (DLS) analysis demonstrated that St-PGA-OG-mUNO and St-PGA-OG displayed similar hydrodynamic diameters of 6.8 and 5.9 nm, respectively (Supplementary Table S1; Fig. 1B), while both nanoconjugates exhibited highly negative charges (-42 and -48 mV, respectively) as shown by Zeta potential analysis (Supplementary Table S1); an expected result given the glutamic acid nature of the polymer carrier. Analysis of mUNO loading (Supplementary Table S1) indicated the presence of approximately seven mUNO peptides in St-PGA-mUNO nanoconjugate, which would allow multivalent receptor binding.

We next assessed the structure of unlabeled and untargeted St-PGA in water using MD simulations to access information at the atomic scale. We assumed an initial helical conformation for the three PGA chains. The studied system consisted of a fully hydrated St-PGA and the Na^+ counterions ($\sim 920,000$ atoms) and was built after initial minimization under vacuum conditions. We simulated 50 ns of the entire St-PGA macromolecule, with Fig. 1C displaying a snapshot corresponding to the last step of the simulation. Averaging the gyration radius over the last 25 ns of the simulation run provided a value of 5.6 ± 0.3 nm, which lies in the same order of magnitude as the results from DLS analysis and suggests a lack of aggregation of both St-PGA-OG-mUNO and St-PGA-OG in PBS. A video simulation (Supplementary Video S1) suggested that the three PGA chains remain in an extended conformation throughout the simulation and do not show any intramolecular or intermolecular interaction, suggesting that the mUNO peptides linked to St-PGA will not interfere with each other.

To investigate whether mUNO can engage with the CD206 receptor when grafted onto St-PGA, we modeled the structure and mobility of St-PGA-mUNO using computational analysis. To attain a computationally feasible system, we simulated only single branches of St-PGA-mUNO. We placed three equidistant mUNO peptides on a PGA single branch and fully solvated the system. We observed that three mUNO peptides remained exposed to the solution available for receptor binding (Fig. 1D). The rotation of mUNO around PGA, tracked by the angle formed by a proline aromatic carbon within mUNO (Supplementary Fig. S2, green sphere), a pyridyldithiol linker nitrogen (Supplementary Fig. S2, blue sphere), and a glutamic acid aromatic carbon (Supplementary Fig. S2, light blue sphere) revealed angles between 50° and 180° (Fig. 1E). This value supports the ability of mUNO peptides to interact with their receptor (43). Comparisons with an undecorated PGA branch demonstrated the minimal alterations of secondary structure dynamics in the presence of mUNO peptides—turning alpha helices (Fig. 1F, green) into random coils (Fig. 1F, brown) at regions where they are placed; however, the PGA chain structure remained mainly helical except in the middle, where a slight kink formed (Fig. 1F).

Altogether, St-PGA-OG-mUNO and St-PGA-OG nanoconjugates possessed similar sizes by DLS, highly negative charges, and, according to simulations, displayed their three arms in an extended open structure. Our simulation analyses demonstrated that mUNO peptides induced a minimal effect on PGA structure and rotated around the PGA chain with considerable freedom. Overall, these findings suggest St-PGA-mUNO as a suitable platform for CD206 targeting.

St-PGA-OG-mUNO targets CD206⁺ TAMs and Displays Low Hepatic Accumulation

We next evaluated the potential of St-PGA-OG-mUNO to target CD206⁺ TAMs in a TNBC model—induced by orthotopic inoculation (referred to as

“orthotopic TNBC”) or by intravenous inoculation (referred to as “experimental metastasis of TNBC”) of 4T1 cells. We administered St-PGA-OG-mUNO or St-PGA-OG intraperitoneally, allowed circulation for 6 hours, and then analyzed tumor homing using confocal fluorescence microscopy. Our previous study provided the rationale for the intraperitoneal administration route, where we demonstrated that the intraperitoneally administered mUNO peptide exhibited a substantially longer half-life than intravenously administered mUNO in the same mice (same strain, sex, and age) used in this study (42).

In the orthotopic TNBC, we observed a high colocalization of OG/CD206 (Fig. 2A, yellow signal) with St-PGA-OG-mUNO but a much lower colocalization of OG/CD206 with nontargeted St-PGA-OG (Fig. 2B) [0.57 and 0.21, respectively (Fig. 2C)]. We observed a low level of accumulation of St-PGA-OG-mUNO or St-PGA-OG in the liver (Supplementary Fig. S3A and S3B). We employed confocal image acquisition parameters throughout this study to visualize CD206 in the tumor without signal saturation. Given the higher levels of CD206 in the tumor, imaging with associated settings provides low CD206 visualization in the liver. Using a higher image intensity, we observed the expected CD206 signal in the liver (as expected from Kupffer cells and sinusoid vessels; Supplementary Fig. S4A) and a saturated CD206 signal in the tumor (Supplementary Fig. S4B).

Immunostaining for endogenous mouse IgG in the tumor and the liver indicated the leaky nature of the tumor vasculature (Supplementary Fig. S5A) compared with the liver vasculature (Supplementary Fig. S5B) in the 4T1 model. A leaky tumor vasculature favors the hypothesis that St-PGA-OG-mUNO has a more extended (both in time and space) access to CD206 in the tumor than in the liver. We speculate that the leaky tumor vasculature combined with lower CD206 expression in the liver than the tumor explains the low hepatic accumulation of St-PGA-OG-mUNO. St-PGA-OG-mUNO did not accumulate in the lungs (Supplementary Fig. S6A) or spleen (Supplementary Fig. S6B); however, we did observe some accumulation in the sentinel lymph node (Supplementary Fig. S6C) and the kidneys (Supplementary Fig. S6D). Of note, the observed kidney signal agrees with our prior studies that demonstrated the renal excretion of St-PGA (53).

Importantly, we did not detect homing to M1 macrophages (CD86⁺) or dendritic cells (CD11c⁺, DC) with St-PGA-OG-mUNO or with St-PGA-OG (Fig. 2D–G). In the experimental metastasis of TNBC, most of the cellular signal of St-PGA-OG-mUNO associated with CD206⁺ TAMs (Fig. 2H, yellow signal) when compared with St-PGA-OG (Fig. 2I; OG/CD206 colocalization 0.42 and 0.14, respectively, Fig. 2J). Here, we also observed no colocalization between OG and CD86 (M1 macrophages; Fig. 2K and L) or OG and CD11c (DCs; Fig. 2M and N) and the observed hepatic accumulation of St-PGA-OG-mUNO or St-PGA-OG was low (Supplementary Fig. S7).

One of the rationales behind the design of OximUNO was to increase mUNO targeting through increased avidity and plasma half-life. To evaluate these aspects, we compared the homing of St-PGA-OG-mUNO with a monomeric, carboxyfluorescein-labeled mUNO peptide (FAM-mUNO). We note that even given the different nature of the fluorescent labels (OG on St-PGA-OG-mUNO and fluorescein on FAM-mUNO), we did not use their native fluorescence as a readout; instead, we used an antibody that recognizes both FAM and OG; therefore, we do not expect biases from potential differences in FAM and OG emissions.

We discovered that St-PGA-OG-mUNO (Supplementary Fig. S8A) displayed significantly higher OG/CD206 colocalization than for FAM/CD206 with

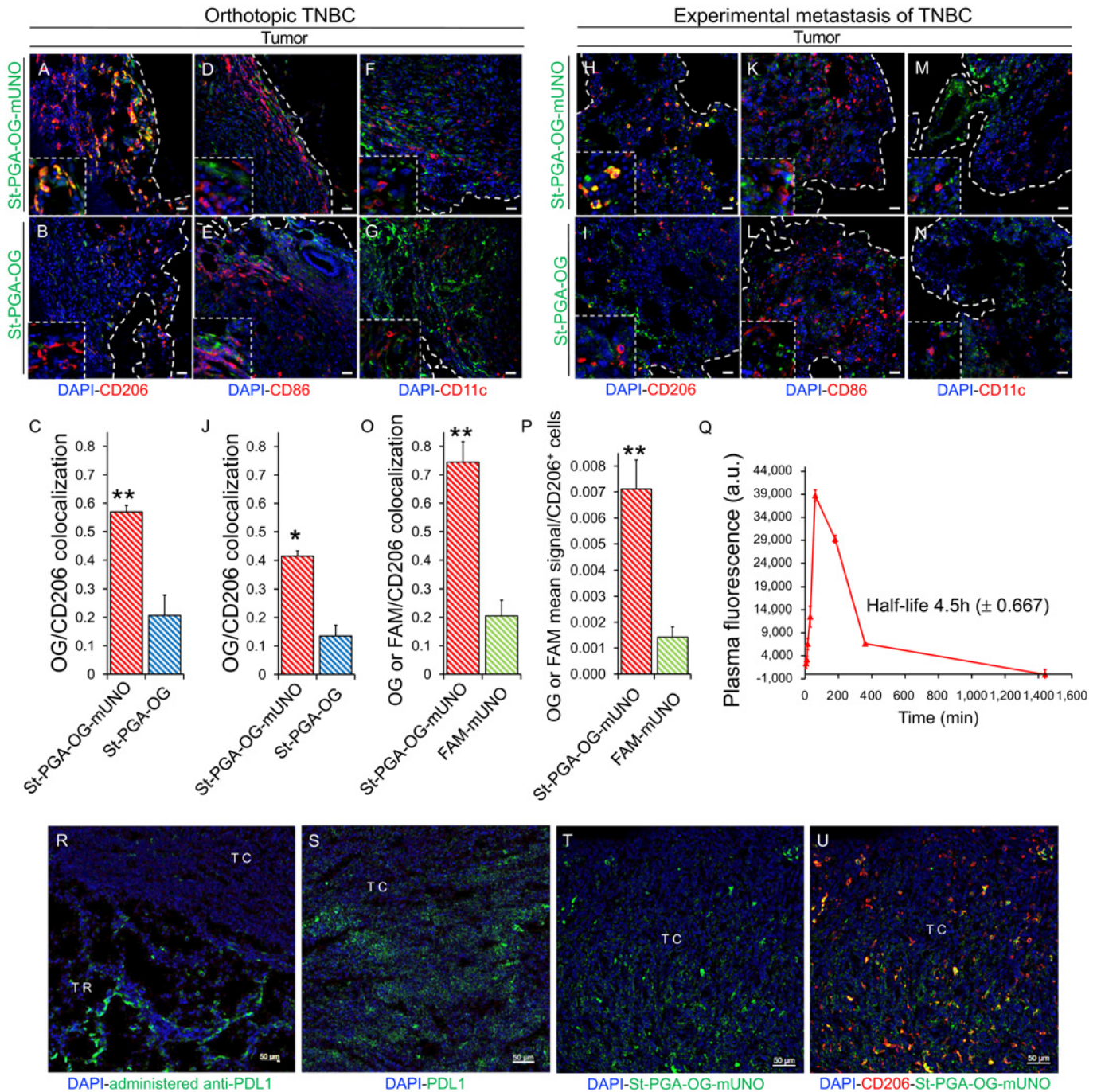


FIGURE 2 St-PGA-OG-mUNO targets CD206⁺ TAMs in models of orthotopic TNBC and experimental metastasis of TNBC and displays an extended plasma half-life. Homing studies with intraperitoneally administered St-PGA-OG-mUNO (0.41 mg/0.5 mL of PBS) or St-PGA-OG (0.35 mg/0.5 mL of PBS), after 6 hours of circulation. *N* = 3 for orthotopic TNBC and *N* = 2 for experimental metastasis of TNBC. **A–G**, Homing in orthotopic TNBC. **A**, St-PGA-OG-mUNO displayed high colocalization between OG and CD206 (yellow signal), whereas St-PGA-OG displayed minimal colocalization (**B**). **C**, Graph depicting the quantification of CD206 and OG colocalization in the orthotopic TNBC. St-PGA-OG-mUNO and St-PGA-OG did not show any homing to CD86⁺ cells (M1 macrophages; **D** and **E**) nor CD11c⁺ cells (DCs; **F** and **G**). **H–N**, Homing study in the experimental metastasis of TNBC. St-PGA-OG-mUNO displayed high colocalization with OG and CD206 (yellow signal; **H**), whereas St-PGA-OG showed minimal colocalization (**I**). **J**, Graph depicting the quantification of CD206 and OG colocalization in the experimental metastasis of TNBC. St-PGA-OG-mUNO and St-PGA-OG did not show any homing to CD86⁺ cells (M1 macrophages; **K** and **L**) or CD11c⁺ cells (DCs; **M** and **N**). Scale bars = 20 μm. **O**, Quantification of colocalization analysis for St-PGA-OG-mUNO or FAM-mUNO with CD206 homing after 6 hours of circulation, *N* = 2 (30 nanomoles in OG and FAM, respectively). Colocalization was quantified using the Fiji program and Pearson coefficient (for more information, see Materials and Methods). **P**, Mean OG/FAM signal per CD206⁺ cell analyzed using the ImageJ program. **Q**, Plasma fluorescence (in the green channel) (Continued on the following page.)

(Continued) of intraperitoneally administered St-PGA-OG-mUNO (dose 15 nanomoles in OG) in healthy Balb/c mice ($N = 3$). **R**, Rat anti-mouse PD-L1 was intravenously injected 10 days after tumor induction (p.i.) and circulated for 24 hours after which time, mice were sacrificed, tumors collected, fixed, and stained for rat IgG. **S**, PDL1 expression was detected in noninjected subcutaneous 4T1 tumors by staining with rat anti-mouse PDL1. **T** and **U**, Representative images showing St-PGA-OG-mUNO (0.41 mg/0.5 mL) intraperitoneally injected 10 days after tumor induction and circulated for 6 hours after which time, mice were sacrificed, tumors fixed, and then stained for OG and CD206. The OG channel is shown separately in **T**, and the colocalization with CD206 for the same image is shown in **U**. Scale bars = 50 μm . Error bars represent SEM. *, $P \leq 0.05$; **, $P \leq 0.01$.

FAM-mUNO (Supplementary Fig. S8B) at 6 hours [0.74 vs. 0.21, respectively (Fig. 2O)]. In addition, we found that the OG/FAM mean signal per CD206⁺ cell was five times higher for St-PGA-OG-mUNO than FAM-mUNO (Fig. 2P). These findings suggest that conjugating mUNO to the St-PGA backbone greatly improved receptor binding.

Plasma half-life analysis for intraperitoneally administered St-PGA-OG-mUNO revealed a 4.5-hour half-life (Fig. 2Q), a value over two times longer than that observed after the intraperitoneal administration of FAM-mUNO in our previous study (42). We previously showed that the plasma half-life of systemically administered St-PGA is approximately 12 hours (53), that negligible degradation of FAM coupled to mUNO through an amide bond (FAM-mUNO) occurs in serum (42), and that the fluorescence of FAM-UNO was not affected by serum from mice bearing 4T1 tumors (41). On the basis of these antecedents, we here attributed the plasma fluorescence of Fig 2Q, to St-PGA-OG-mUNO.

Overall, this finding suggests that conjugating mUNO to St-PGA increased the plasma half-life of mUNO peptide, a desirable feature that will improve *in vivo* ligand targeting.

We next compared tumor homing of St-PGA-OG-mUNO with that of a therapeutic mAb by intravenously injecting anti-PDL1 in orthotopic 4T1 tumor-bearing mice and allowing circulation for 24 hours. We observed that administered anti-PDL1 accumulated in the tumor rim (Fig. 2R, TR) but not in the tumor core (Fig. 2R, TC) even given expression of the receptor (PDL1) in the tumor core (Fig. 2S, TC). The observed accumulation of St-PGA-OG-mUNO in the tumor core (Fig. 2T, TC) and receptor colocalization (Fig. 2U), supported the implementation of our platform as an efficient alternative to antibody-based therapies such as anti-PDL1 or antibody–drug conjugates.

Administration of a higher dose of nanoconjugate (0.82 mg/0.5 mL St-PGA-OG-mUNO and 0.7 mg/0.5 mL St-PGA-OG) resulted in high CD206⁺ TAM targeting for St-PGA-OG-mUNO (Supplementary Fig. S9A) albeit at the expense of higher hepatic accumulation (Supplementary Fig. S9B). Tumor and hepatic accumulation of St-PGA-OG are shown in Supplementary Fig. S9C and S9D. For this reason, we employed lower nanoconjugate doses (0.41 mg/0.5 mL and 0.35 mg/0.5 mL) for subsequent studies. As St-PGA-OG-mUNO did not target the lung, liver, or spleen (Supplementary Fig. S6), at this dose we expect OximUNO not to affect the macrophage populations of those organs.

Overall, we demonstrated that St-PGA-OG-mUNO homes to CD206⁺ TAMs in the orthotopic TNBC and in experimental metastasis of TNBC, with no significant hepatic accumulation. We also established that St-PGA-OG-mUNO does not target M1 macrophages or DCs in the tumor, thereby providing evidence of high specificity for CD206⁺ TAMs.

OximUNO Enhances the *In Vitro* Cytotoxicity of DOX on M2-resembling Macrophages

St-PGA displays a large surface with multiple sites available for the conjugation of proapoptotic or cytotoxic cargoes via bioresponsive polymer–drug linkers

(54, 55). To selectively deplete CD206⁺ TAMs, we conjugated an apoptotic chemotherapeutic agent (DOX) to St-PGA-mUNO to form St-PGA-DOX-mUNO (designated “OximUNO”; Fig. 3A, Scheme S2). We conjugated DOX to St-PGA-mUNO using a hydrazone bond (54) to allow for site-specific drug release in the acidic milieu of the endosomes or lysosomes (54, 56).

To evaluate the effect of mUNO targeting, we included St-PGA-DOX as an untargeted control. We employed ¹H NMR and UV-Vis analyses to evaluate the chemical identity of nanoconjugates (Supplementary Fig. S10A and S10B).

OximUNO displayed DOX and mUNO loadings of approximately 10% and approximately 4% in weight, respectively, corresponding to around four DOX and seven mUNO molecules for every OximUNO. OximUNO exhibited a size of approximately 40 nm and a highly negative surface charge of -40 mV (Supplementary Table S2; Fig. 3B). We obtained similar DOX loading, size by DLS, and surface charge values for St-PGA-DOX (Supplementary Table S2; Fig. 3B).

The pH-sensitive hydrazone linker and the intrinsic biodegradability of St-PGA by lysosomal protease cathepsin B are expected to secure DOX release from OximUNO after cell internalization (57). Hence, we studied DOX release kinetics from OximUNO in the presence of acidic pH (pH 5) and cathepsin B using LC/MS (Supplementary Fig. S11A–S11G). As we aimed for the intraperitoneal administration of OximUNO, we assessed DOX release in intraperitoneal fluid (Fig. 3C). At pH 5, we observed a sustained DOX release in the first 8 hours (reaching a plateau at 15%), thereby demonstrating the suitability for endosomal-lysosomal drug delivery. DOX release in the presence of cathepsin B displayed comparable values in the first 8 hours ($\sim 13\%$), followed by a plateau and a reduced rate in the following hours ($\sim 13\%$ cumulative release at 72 hours). Importantly, OximUNO exhibited negligible drug release in both physiologic conditions evaluated (PBS and intraperitoneal fluid; Fig. 3C).

We next evaluated the *in vitro* cytotoxicity of OximUNO and St-PGA-DOX in primary human macrophages derived from PBMCs, polarized with different cytokines to resemble M2 (MCSF + IL4) and M1 (MCSF + IFN γ + LPS) macrophages. Under these conditions, macrophages polarized with MCSF + IFN γ + LPS expressed nonnegligible CD206 levels, albeit at levels lower than for macrophages polarized with MCSF + IL4 (Fig. 3D). Bertani and colleagues (58) observed the same pattern of CD206 expression in PBMC-derived macrophages polarized under similar conditions.

Because the *in vivo* concentration that provided optimal CD206⁺ TAM targeting with minimal hepatic accumulation was 30 $\mu\text{mol/L}$ in OG, here we focused our interest on conjugates at 33 $\mu\text{mol/L}$ of DOX. Our previous studies comparing other mUNO-targeted versus untargeted polymeric nanosystems (44) demonstrated that the highest targeted uptake in primary MCSF + IL4 polarized macrophages occurred after an interval of 10 to 30 minutes. For this reason, we used an incubation time of 15 minutes for these experiments.

Importantly, in MCSF + IL4 polarized macrophages, OximUNO displayed a significantly higher toxicity than DOX and St-PGA-DOX (Fig. 3E). St-PGA-DOX showed its highest toxicity in MCSF + IFN γ + LPS polarized

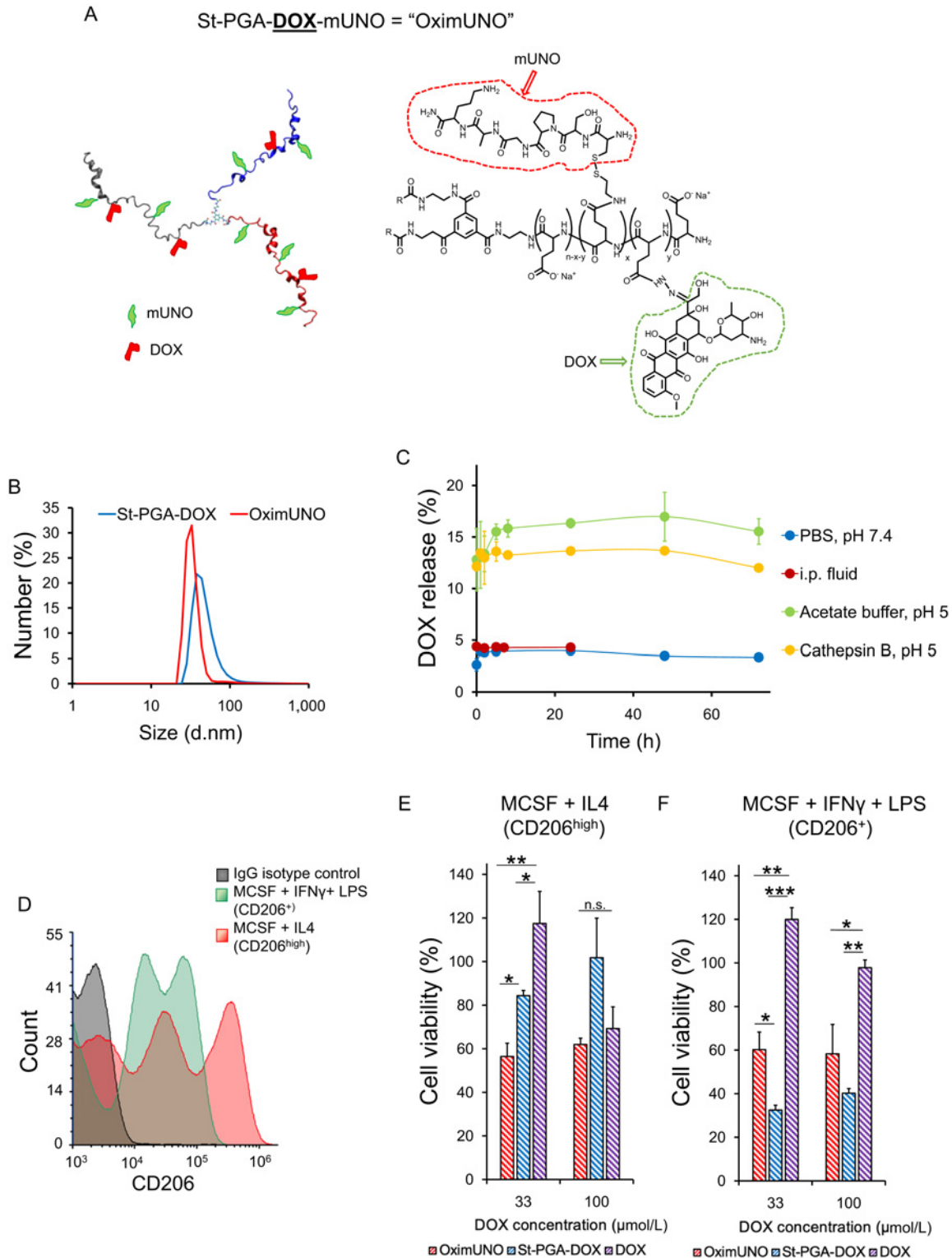


FIGURE 3 OximUNO enhances the *in vitro* efficacy of DOX on M2-resembling macrophages. **A**, Simplified form of OximUNO (left) and molecular structure (right) showing St-PGA decorated with mUNO (red) and DOX (green). **B**, A DLS graph for measurements shown in Supplementary Table S2, indicating the uniform size of OximUNO and St-PGA-DOX. **C**, DOX release from OximUNO showing the drug release in PBS, intraperitoneal fluid, acetate buffer or in the presence of cathepsin B. **D**, CD206 expression by M1-resembling (green) and M2-resembling (red) macrophages using FC. *In vitro* cytotoxicity in primary human M2-resembling (MCSF + IL4 polarized; **E**), M1-resembling (MCSF + IFN γ + LPS polarized; **F**) macrophages after treatment with OximUNO (red bars), St-PGA-DOX (blue bars), and DOX (purple bars) following a 15-minute incubation, washed, cultured for additional 48 hours, and then analyzed for cell viability as evaluated by MTT assay. Error bars represent SEM. *, $P \leq 0.05$; **, $P \leq 0.01$; ***, $P \leq 0.001$.

Downloaded from <http://aacrjournals.org/cancerrescommun/article-pdf/2/6/533/3165324/crc-22-0043.pdf> by guest on 08 January 2023

macrophages (Fig. 3F). We speculate that here, the phagocytic activity, known to be highest for MCSF + IFN γ + LPS polarized macrophages (59, 60), governs the uptake of St-PGA-DOX. Here, the 60% cell viability observed for OximUNO (Fig. 3F) is consistent with the fact that under these conditions, MCSF + IFN γ + LPS polarized macrophages also expressed CD206 (Fig. 3D). *In vivo*, St-PGA-OG-mUNO did not target M1 TAMs (Fig. 2D and K); hence, we do not expect OximUNO to affect this population. Free DOX only displayed toxicity in MCSF + IL4 polarized macrophages at 100 μ mol/L (Fig. 3E).

These results provide evidence that OximUNO displayed increased toxicity toward M2-resembling macrophages when compared with St-PGA-DOX or DOX alone.

We also evaluated the hepatic and renal safety profile of a single administration of OximUNO (at doses corresponding to 2 and 4 mg/kg of DOX) by analyzing creatinine (Crea) and alanine aminotransferase (ALAT) levels 48 hours after intraperitoneal administration in healthy mice (Supplementary Table S3). These doses did not induce toxic levels of Crea or ALAT compared with the values reported in the literature (61) or the reference values for the female Balb/c reported in the Mouse Phenome Database by The Jackson Laboratory (<https://phenome.jax.org/search/details/ssmeasures?searchterm=alanine+aminotransferase+&ontavail=2>) or Charles River facilities (<https://www.criver.com/products-services/find-model/balbc-mouse?region=3616>). However, increased ALAT levels with the higher dose prompted the selection of the OximUNO dose corresponding to 2 mg/kg of DOX for further *in vivo* studies. Administration of OximUNO at 2 mg/kg of DOX showed no histologic changes indicative of hepatic and renal toxicity, as evaluated by a pathologist (Supplementary Fig. S12A), and IFN γ IF did not detect a clear increase that would indicate inflammatory changes (Supplementary Fig. S12B).

In summary, the conjugation of mUNO and DOX to the St-PGA backbone to yield OximUNO, enhanced the *in vitro* efficacy of DOX toward M2-resembling macrophages with no *in vivo* renal or hepatic toxicity observed.

OximUNO Treatment of Orthotopic TNBC Depletes CD206⁺ TAMs, Inhibits Tumor Progression, and Attenuates Immunosuppression

The findings of the *in vivo* homing and *in vitro* cytotoxicity studies supported the subsequent evaluation of OximUNO in the orthotopic TNBC. When tumors reached 25 mm³, we treated mice with intraperitoneal injections of OximUNO, St-PGA-DOX, or DOX, at 2 mg/kg of DOX every other day for 18 days. Encouragingly, OximUNO treatment significantly reduced primary tumor volume growth kinetics (Fig. 4A, red line) compared with DOX, St-PGA-DOX, and PBS. Furthermore, only the OximUNO treatment significantly reduced final tumor weight (Fig. 4B) compared with the untreated group. We assigned this encouraging therapeutic effect to mUNO-mediated targeting, as mice treated with the untargeted St-PGA-DOX possessed tumor volumes (Fig. 4A, blue line) similar to the PBS group (Fig. 4A, black line). Furthermore, OximUNO treatment did not affect mouse bodyweight, whereas treatment with DOX induced a significant decrease in mouse bodyweight starting from day 21 p.i. until the end of the treatment (Fig. 4C).

Histologic analysis of lungs from treated mice (Supplementary Fig. S13 shows an H&E stain from a healthy lung for comparison) revealed that OximUNO showed a decreasing trend in the metastatic lung area and nodule number (Fig. 4D–F). Meanwhile, IF microscopy revealed no significant changes in CD31 expression in tumors (Fig. 4G and H), but significantly fewer CD31⁺ structures

in the OximUNO-treated mice compared with DOX-treated mice (Fig. 4G and I), suggesting that the reduction in nodule number in the OximUNO group (of Fig. 4F) may be mediated by the lower vascularization in the primary tumor. We suggest that partial vascular homing of St-PGA-DOX in the tumor (as suggested by the tumor homing of its OG equivalent; Supplementary Fig. S14) contributes to the blood vessel reduction observed in this group. Importantly, histologic analysis revealed no cardiotoxicity in any treatment groups (Supplementary Fig. S15). IF analysis revealed that only OximUNO significantly reduced the CD206 expression (assigned to CD206⁺ TAMs), compared with PBS (Fig. 4J and K). Interestingly, treatment with DOX upregulated CD206 expression (Fig. 4J and K), which agrees with previous reports that demonstrated an increase in the number of CD206⁺ TAMs following chemotherapy (24).

Notably, only OximUNO treatment significantly increased CD8 expression [a marker of cytotoxic T lymphocyte (CTL)] compared with PBS and DOX treatment (Fig. 4L and M). Unexpectedly, St-PGA-DOX treatment increased the expression of FOXP3, a marker for regulatory T cells (Treg; Fig. 4N and O). Analysis of the CD8/FOXP3 expression ratio revealed that OximUNO treatment resulted in a 5-fold increase compared with St-PGA-DOX or DOX treatment (Fig. 4P), suggesting that OximUNO stimulated a shift in the immune landscape toward immunostimulation. Of note, in all cases, we normalized the quantification of marker expression using immunofluorescent images to the tissue area to account for different amounts of tissue in different images.

A repetition of this treatment study, monitoring primary tumor growth and survival, showed the slowest tumor growth kinetics in the OximUNO group (Supplementary Fig. S16A) and Kaplan–Meier curves showed a significantly prolonged survival for OximUNO-treated mice compared with untreated mice (Supplementary Fig. S16B–S16D).

By targeting CD206⁺ TAMs with DOX via OximUNO treatment, we increased the efficacy and reduced the toxicity of DOX in the orthotopic TNBC. Our results also suggest that the depletion of CD206⁺ TAMs by OximUNO elicited an immunostimulatory shift.

OximUNO Treatment of Experimental Metastasis of TNBC Reduces CD206⁺ TAMs Number, Tumor Burden and Attenuates Immunosuppression

We next evaluated the effect of OximUNO on experimental metastasis of TNBC using GFP-labeled 4T1 cells. We treated mice every other day with intraperitoneal injections of OximUNO, St-PGA-DOX, or DOX, starting from day 4 p.i. and sacrificed mice on day 18 p.i. Analysis of whole lung fluorescence in the green channel revealed that OximUNO treatment induced the lowest GFP fluorescence, indicating a lower level of pulmonary metastases (Fig. 5A). Representative macroscopic images also provided evidence for a reduction in metastases (Fig. 5B). Confocal fluorescence microscopy of lungs confirmed the trend observed with whole lung fluorescence, showing fewer GFP fluorescent nodules in the OximUNO-treated group (Fig. 5C). Furthermore, histologic analysis of lungs displayed the lowest number of pulmonary nodules for OximUNO-treated mice (Fig. 5D and E). Mice treated with the untargeted St-PGA-DOX and free DOX showed a significant decrease in bodyweight, resulting in a 19% (Fig. 5F, blue line) and 17% loss (Fig. 5F, purple line), respectively; meanwhile, OximUNO-treated mice displayed lower bodyweight loss (Fig. 5F, red line).

We next employed FC to analyze the effect of different treatments on the immune cell populations in whole lungs. This analysis demonstrated that

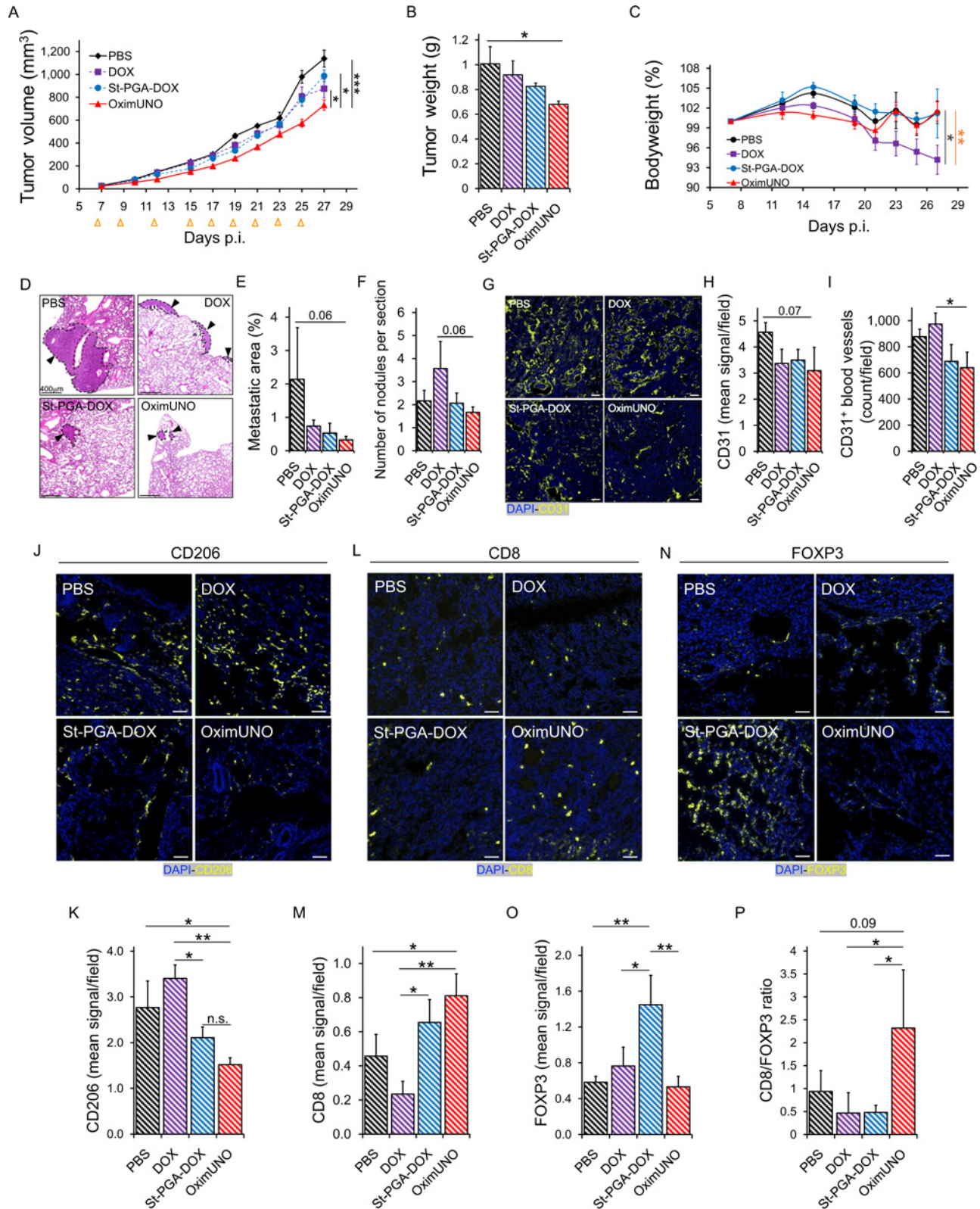


FIGURE 4 OximUNO treatment reduces primary tumor growth and pulmonary metastases and alleviates immunosuppression. Treatment with OximUNO, St-PGA-DOX, or DOX at 2 mg/kg of DOX in mice bearing orthotopic TNBC tumors ($N = 5$). Intraperitoneal injections began when tumors reached 25 mm³ and were performed every other day to give a total of nine injections. **A**, Primary tumor volume progression during treatment. Orange arrows indicate injection days. **B**, Primary tumor weight at the experimental endpoint, demonstrating a significantly smaller weight for OximUNO-treated mice (red bar) than other groups. **C**, Mouse bodyweight analysis suggests the safety (Continued on the following page.)

(Continued) of OximUNO treatment (red line); meanwhile, DOX treatment induced a significant reduction in bodyweight by the experimental endpoint (purple line). Dark gray * DOX versus PBS, orange * DOX versus St-PGA-DOX. **D**, Representative H&E images showing spontaneous pulmonary metastases for all groups (scale bars = 400 μm); OximUNO treatment associated with the smallest metastatic area (**E**) and the lowest number of average nodules per lung (**F**). **G**, Representative images showing the expression of CD31 and blood vessels in primary tumors. **H**, Graph depicting the expression of CD31 in primary tumors. **I**, Graph depicting the CD31⁺ blood vessel count in primary tumors. CD31 expression and blood vessel count were calculated using ImageJ and five images per mouse per group for expression analysis and at least three images per mouse per group for blood vessel count. Representative confocal microscopy images and quantification graphs of primary tumors demonstrating the expression of CD206 (**J** and **K**), CD8 (**L** and **M**), and FOXP3 (**N** and **O**). Scale bars = 50 μm . **P**, Graph of CD8/FOXP3 expression ratio showing a shift in the immune profile. Quantification was performed using the ImageJ from at least three images per mouse and 5 mice per group. Error bars represent SEM. *, $P \leq 0.05$; **, $P \leq 0.01$; ***, $P \leq 0.001$; n.s., > 0.05 .

OximUNO treatment significantly lowered the percentage of M2 TAMs (CD206⁺; Fig. 5G) but did not significantly impact the percentage of M1 TAMs, CTLs, or Tregs (Fig. 5H–J). We observed the same trend when we expressed these populations as total cell counts (Supplementary Fig. S17–S20).

To evaluate whether OximUNO affected CD206⁺ macrophages other than M2 TAMs, we analyzed the state of splenic macrophages from this treatment study using FC. This analysis revealed no significant differences in the CD206/CD86 populations between the OximUNO-treated mice and PBS-treated mice (Supplementary Fig. S21A–S21C).

While FC analysis informs on the immune status of the whole lung, it does not provide specific information regarding the TME. To characterize the immune landscape of the TME, we next analyzed the expression of markers for TAMs, CTLs, and Tregs in pulmonary nodules using IF. This analysis revealed significantly lower CD206 expression in OximUNO-treated mice than PBS-treated mice (Fig. 5K and L), providing evidence for a robust reduction in the number of CD206⁺ TAMs in the TME. Importantly, and similarly to OximUNO treatment in the orthotopic TNBC, OximUNO elicited the highest expression of CD8 (Fig. 5M and N). OximUNO-treated and St-PGA-DOX-treated mice demonstrated significantly lower lung FOXP3 expression than PBS- and DOX-treated mice (Fig. 5O and P). OximUNO-treated mice displayed between a two and three times higher CD8/FOXP3 expression ratio than St-PGA-DOX and DOX, and nearly seven times higher than PBS (Fig. 5Q). Therefore, our IF analysis in the pulmonary tumor nodules suggested that OximUNO triggered a shift in the immune profile of the TME toward immunostimulation.

By targeting DOX to CD206⁺ TAMs in experimental metastasis of TNBC, we increased the efficacy and reduced the toxicity of DOX, as OximUNO treatment associated with the presence of fewer pulmonary tumor lesions and less bodyweight loss when compared with treatment with untargeted St-PGA-DOX and DOX. Our results suggest that the observed therapeutic effect derived from CD206⁺ TAM depletion, which elicited an immunologic shift in the TME.

Discussion

To date, TNBC remains an aggressive breast cancer subtype (3) with few treatment options, with conventional chemotherapy representing the current standard of care (20). ICIs for TNBC have provided only modest improvements in complete response and progression-free survival in a small subset of patients with TNBC (9, 12, 15, 16). Targeting TAMs can potentiate ICIs and other modalities and, therefore, represents an intense area of study (62–66); however, TAMs represent a diverse population (67–69), and which TAM subtype to target remains under investigation.

Promising TAM-focused interventions under clinical evaluation include antibody-mediated depletion of TREM2-expressing TAMs (clinical trial identifier: NCT04691375). Antibody blockade of Clever-1 on M2 TAMs stimulated an M2→M1 switch in TNBC models (4T1) and synergized with the PD-1 blockade (70). Appealing studies have used anti-CD163 antibodies to target TAMs (71) by decorating DOX-carrying liposomes with anti-CD163, to deplete TAMs and potentiate ICIs in melanoma. Given our data comparing the tumor penetration of an anti-PDL1 antibody versus St-PGA-OG-mUNO, anti-CD163 systems may also display lower tumor accumulation than St-PGA-OG-mUNO and OximUNO. Strategies targeting generic TAM markers such as CSF1R and CCR2 have shown side effects and limited efficacy.

Motivated by the preponderance of the mannose receptor in tumorigenic/metastatic TAMs in breast cancer (72–74), here, we set out to deplete CD206⁺ TAMs in an aggressive TNBC model and study the consequences on the progression and immunosuppressive state of the tumor. To target CD206, a CD206-binding nanobody was developed by Ginderachter and colleagues (75) which showed homing to CD206⁺ TAMs in *in vivo* models of lung and breast cancers (75). Navidea Inc. engineered a mannosylated compound (ref. 76; Manocept), that forms part of the FDA-approved contrast agent Lymphoseek. Unfortunately, mannose-based ligands have other binding partners besides CD206, including CD209 in intestinal and genital tissues (45), and can target dendritic cells (46). Riptide Inc. also designed a peptide (RP-182) that binds to CD206; however, the peptide also binds to RelB, Sirp- α , and CD47 (77).

We recently identified and described a short peptide called mUNO (sequence: CSPGAK) that targets mouse (41) and human CD206 (43) at a different binding site than for mannose on CD206 (43). We identified mUNO from an *in vivo* screen using a peptide library in mice bearing metastatic breast cancer; we subsequently described how mUNO homed to CD206⁺ TAMs in other solid tumor models (41, 78) and in early-stage models of TNBC (42) displaying low hepatic accumulation.

We envisioned that conjugating mUNO to St-PGA would significantly enhance targeting through the avidity effect and increased plasma half-life (79).

Compared with synthetic polymers such as N-(2-hydroxypropyl) methacrylamide, polypeptide-based nanocarriers show several benefits, including biodegradability, lower immunogenicity, and a lack of long-term accumulation, and the number of polypeptide-based constructs reaching clinical evaluation has significantly increased in recent years (80–82). We employed St-PGA-based nanoconjugates with three linear chains (~50 glutamic acids each) linked to a central core. Overall, the safety, lack of toxicity, and biodegradability of St-PGA meet FDA approval criteria (83). A previous screen of PGA structures suggested that larger architectures enhanced plasma half-life and increased bioavailability

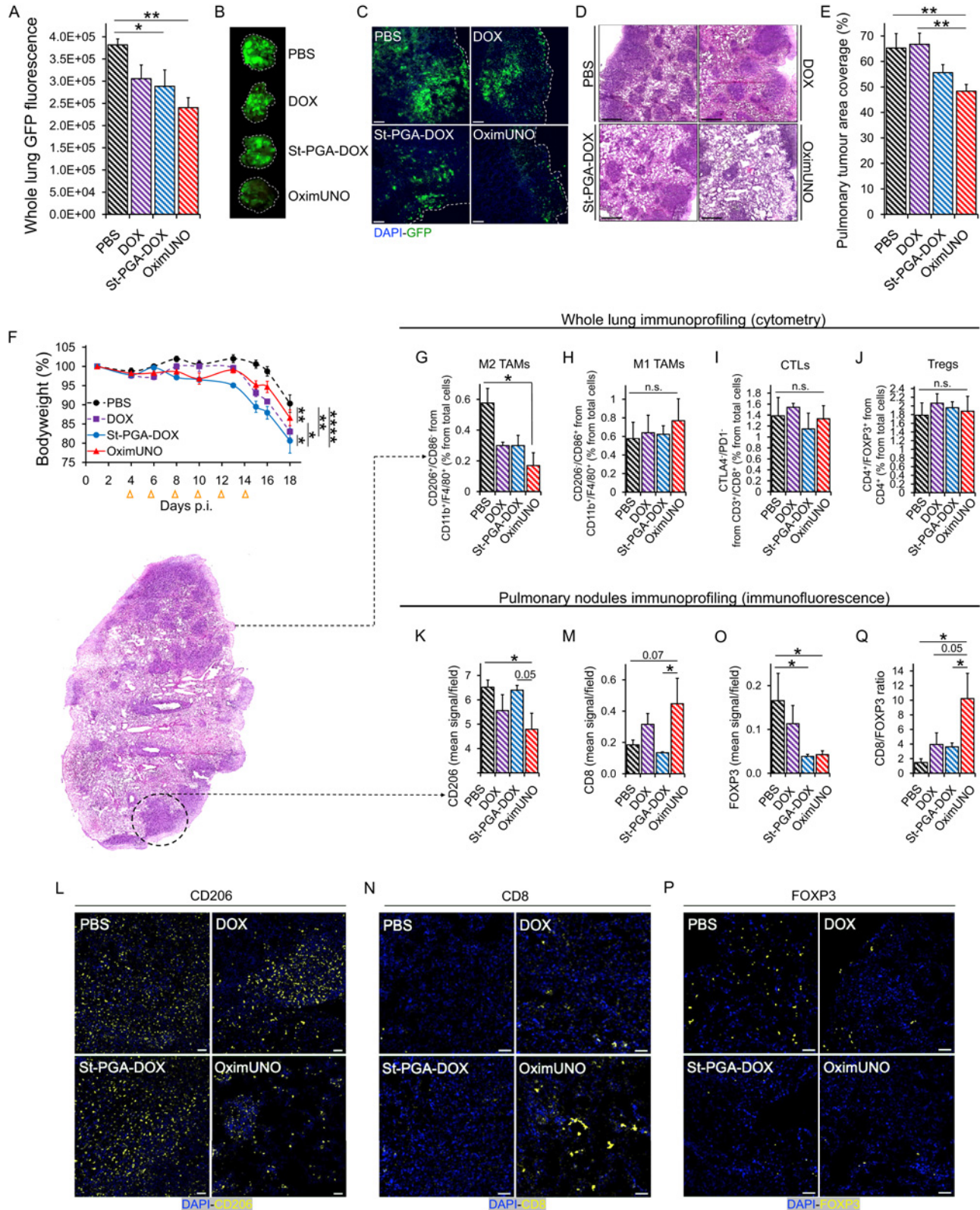


FIGURE 5 OximUNO treatment in experimental metastasis of TNBC significantly reduces CD206⁺ TAM number and tumor burden and alleviates immunosuppression. Treatment with OximUNO, St-PGA-DOX, or DOX at 2 mg/kg of DOX in the experimental metastasis of TNBC model, created using GFP-labeled 4T1 cells ($N = 6$). Intraperitoneal injections began on day 4 p.i. and were performed every other day to give a total of six injections. **A**, Quantification of whole lung GFP fluorescence at the experimental endpoint using the ImageJ ($N = 6$). **B**, Representative macroscopic photographs of GFP fluorescence in the lungs. **C**, Representative confocal microscopy images of GFP expression, scale (Continued on the following page.)

(Continued) bars = 100 μm . **D**, Representative H&E images showing pulmonary metastases for all groups (scale bars = 900 μm). **E**, Quantification of pulmonary metastases from H&E images, expressed as percentual area of whole lung section. **F**, Mouse bodyweight analysis, demonstrating significantly lower bodyweight lost with OximUNO (red line) compared with St-PGA-DOX-treated mice (blue line) and DOX-treated mice (purple dotted line). Orange arrows indicate injection days. **G–J**, FC analysis on three right lungs per group. M2 TAMs (CD206⁺; **G**), M1 TAMs (**H**), CTLs (**I**) and Tregs (**J**). Representative IF images and analysis on the pulmonary tumor nodules to detect the expression of CD206 (**K** and **L**), CD8 (**M** and **N**), and FOXP3 (**O** and **P**). **Q**, Graph showing CD8/FOXP3 expression ratio. IF images quantified using the ImageJ from at least five images per mouse and 3 mice per group. Scale bars = 50 μm . Error bars represent SEM. *, $P \leq 0.05$; **, $P \leq 0.01$; ****, $P \leq 0.0001$; n.s., > 0.05 .

through a higher hydrodynamic volume that reduces rapid renal clearance (53, 84). Of note, an extended plasma half-life will be advantageous when targeting the continuously replenished TAM cell type (85, 86).

St-PGA-OG-mUNO, a fluorescent counterpart of OximUNO, can be easily monitored by immunostaining for OG or detecting native OG fluorescence (as for the half-life study). Given weak DOX fluorescence and the inability to detect DOX with an antibody, we first designed St-PGA-OG-mUNO for validation purposes. We then exchanged OG for DOX to generate St-PGA-DOX-mUNO, referred to as “OximUNO.” Our studies demonstrated that St-PGA-OG-mUNO displayed a far greater plasma half-life and specificity to CD206⁺ TAMs than free mUNO and avoided CD86⁺ M1 TAMs and CD11c⁺ DCs, an important fact because M1 TAMs display antitumorogenic activity (25), and CD11c⁺ DCs participate in antigen presentation (87). In line with these observations, the computational analysis indicated that mUNO peptides are available to a receptor and sweep a vast space (130°) around PGA. Altogether these data demonstrate the benefit of conjugating mUNO to St-PGA. While previous studies have reported the St-PGA nanocarrier (53, 83) and the mUNO-targeting peptide (42), this work represents a novel design of a peptide-targeted St-PGA nanosystem. Regarding the administration route of peptide-guided St-PGA nanosystems, in the future we also wish to evaluate the intravenous route, which, barring the case of intraperitoneal chemotherapy, represents a more clinically translatable route to deliver cancer therapies.

In the OximUNO system, drug release studies revealed only 15% DOX release, which agrees with our previous studies (54, 56) but suggests room for improvement, which may come from using longer polymer-drug linkers such as EMCH (N- ϵ -maleimidocaproic acid hydrazide) moiety (54, 56) or from the use of external triggers (88–90). Unexpectedly, we failed to observe a significant increase in DOX release in the presence of cathepsin B with respect to the hydrolytic conditions; we hypothesize that the nanoconjugate conformation slows down proteolytic degradation, hampering *in vitro* quantification within the studied timeframe (53).

Our *in vivo* efficacy studies showed that, strikingly, the sole depletion of CD206⁺ TAMs with OximUNO alleviated tumoral immunosuppression and reduced dissemination and growth, confirming the protumoral and immunosuppressive roles assigned to CD206⁺ TAMs in the literature and reaffirming the importance of targeting this particular TAM subset. In addition, the observed reduction in the number of CD206⁺ TAMs and CD31⁺ structures for OximUNO agrees with the established angiogenic role of CD206⁺ TAMs (24).

From a safety point of view, we found that the OximUNO nanoformulation of DOX had the least negative impact on mouse bodyweight compared with free DOX or the untargeted nanoformulation St-PGA-DOX. In addition, OximUNO did not alter Crea or ALAT levels, indicating the absence

of acute hepatic or renal toxicity. Our data suggest that the signal observed in the kidneys for St-PGA-OG-mUNO [consistent with the previously reported excretion of St-PGA (53, 83)] did not translate into acute renal toxicity for OximUNO. These are relevant findings as DOX induces cell death and tissue damage not only in the heart but also in the liver and kidneys (91). OximUNO did not affect or alter the macrophage populations of the spleen *in vivo*, in agreement with the absence of spleen targeting we observed for St-PGA-OG-mUNO.

Most preclinical studies evaluating the effect of M2 TAM targeted monotherapy in the 4T1 mouse model have either not shown efficacy on secondary tumors (92, 93), a lack of efficacy in primary tumors or metastases in the case of anti-CLEVER-1 (70), or a prometastatic effect in the case of anti-CSFIR (94). Hence, along with anti-MARCO therapy (95), OximUNO constitutes one of the few reports of an M2 TAM-targeted monotherapy affecting both primary and secondary tumors in the 4T1 mouse model.

Beyond TAM depletion, we show that St-PGA-mUNO represents an attractive platform to carry additional therapeutic payloads other than DOX, which could include M2→M1 polarizing agents such as TLR7 agonists (44, 96), beta-emitting radiotherapeutic agents such as dodecanetetraacetic acid-chelated ¹⁷⁷Lu (97), or photosensitizers used in photodynamic therapy (88–90). We also envisage the combination of TAM depletion via OximUNO administration together with current chemotherapy regimens to prevent dissemination and relapse, or the use of OximUNO prior to surgery, that is, as neoadjuvant chemotherapy.

Taking OximUNO as a proof of concept, our data support the peptide-targeted St-PGA design reported here as a new targeted nanosystem that could target other receptors by exchanging the targeting peptide.

Authors' Disclosures

A. Lepland reports a patent to Compositions that target tumor-associated macrophages and methods of use therefor pending and licensed; and P. Scodeller and T. Teesalu are inventors of patents on the mUNO peptide. M.J. Vicent is an inventor of a patent on BTA-core branched polypeptides (including St-PGA) licensed to PTS SL. In addition, T. Teesalu is an inventor of iRGD and CendR peptides and a shareholder of Cend Therapeutics Inc., a company that holds a license for the mUNO, iRGD, and CendR peptides. M. Bringas reports other from Centro de Computo de Alto Rendimiento (CECAR) FCEN UBA during the conduct of the study. S. D. N. UBA reports grants from European research Council during the conduct of the study. P. Peterson reports grants from University of Tartu during the conduct of the study. T. Teesalu reports a patent to US201762565356P pending; and T. Teesalu is a founder and shareholder of Cend Therapeutics Inc. that develops iRGD peptide for

precision targeting of solid tumors. P. Scodeller reports a patent to Compositions that target tumor-associated macrophages and methods of use therefor pending and licensed. No disclosures were reported by the other authors.

Authors' Contributions

A. Lepland: Conceptualization, data curation, formal analysis, investigation, visualization, methodology, writing-original draft, writing-review and editing. **A. Malfanti:** Conceptualization, data curation, formal analysis, investigation, methodology, writing-review and editing. **U. Haljasorg:** Data curation, formal analysis, methodology. **E.K. Ascitutto:** Data curation, software, formal analysis, writing-review and editing. **M. Pickholz:** Data curation, software, formal analysis, writing-review and editing. **M. Bringas:** Data curation, software, formal analysis, writing-review and editing. **S. Đorđević:** Data curation, formal analysis, methodology. **L. Salumäe:** Formal analysis, methodology. **P. Peterson:** Resources, writing-review and editing. **T. Teesalu:** Conceptualization, resources, supervision, funding acquisition, investigation, project administration, writing-review and editing. **M.J. Vicent:** Conceptualization, resources, supervision, funding acquisition, investigation, project administration, writing-review and editing. **P. Scodeller:** Conceptualization, resources, supervision, funding acquisition, investigation, project administration, writing-review and editing.

Acknowledgments

We would like to thank Stuart P. Atkinson for English editing, Merje Jakobson for performing H&E studies on paraffin-embedded formalin-fixed tissues, Dr. Aivar Orav for *in vivo* toxicity study analysis and Dr. Mario Plaas and Toomas Jagomäe, MSc, for the help with the slide scanner. P. Scodeller acknowledges support from the Estonian Research Council (grant: PUT PSG38, to P. Scodeller), a Feasibility fund of the University of Tartu (grant: ARENG51, to P. Scodeller) and from the Spanish Ministry of Science and Innovation (grant: Ramón y Cajal RYC2020-028754-I, to P. Scodeller). A. Lepland acknowledges a PhD fellowship from the Estonian government. M.J. Vicent acknowledges the support by European Research Council grants (ERC-CoG-2014-648831 “My-Nano” and ERC-PoC-2018-825798 “Polymune”). Part of the equipment employed in this work has been funded by Generalitat Valenciana and cofinanced with FEDER funds (PO FEDER of Comunitat Valenciana 2014–2020). U. Haljasorg acknowledges the support by EsRC Mobilitas+ grant MOBTP185. T. Teesalu acknowledges the support by UT EIK grant, European Regional Development Fund (project no. 2014-2020.4.01.15-0012), EuroanomedII projects ECM-CART and iNanoGun, and by Estonian Research Council (grant PRG230 and EAG79).

Received January 25, 2022; revised May 03, 2022; accepted June 03, 2022; published first June 28, 2022.

References

- Rivenbark AG, O'Connor SM, Coleman WB. Molecular and cellular heterogeneity in breast cancer: challenges for personalized medicine. *Am J Pathol* 2013;183: 1113-24.
- Foulkes WD, Smith IE, Reis-Filho JS. Triple-negative breast cancer. *N Engl J Med* 2010;363: 1938-48.
- Lehmann BD, Bauer JA, Chen X, Sanders ME, Chakravarthy AB, Shyr Y, et al. Identification of human triple-negative breast cancer subtypes and preclinical models for selection of targeted therapies. *J Clin Invest* 2011;121: 2750-67.
- Garrido-Castro AC, Lin NU, Polyak K. Insights into molecular classifications of triple-negative breast cancer: improving patient selection for treatment. *Cancer Discov* 2019;9: 176-98.
- Pardoll DM. The blockade of immune checkpoints in cancer immunotherapy. *Nat Rev Cancer* 2012;12: 252-64.
- Esfahani K, Roudaia L, Buhlaiga N, Del Rincon SV, Papneja N, Miller WH Jr. A review of cancer immunotherapy: from the past, to the present, to the future. *Curr Oncol* 2020;27: S87-S97.
- Adams S, Gatti-Mays ME, Kalinsky K, Korde LA, Sharon E, Amiri-Kordestani L, et al. Current landscape of immunotherapy in breast cancer: a review. *JAMA Oncol* 2019;5: 1205-14.
- Gong J, Chehrizi-Raffle A, Reddi S, Salgia R. Development of PD-1 and PD-L1 inhibitors as a form of cancer immunotherapy: a comprehensive review of registration trials and future considerations. *J Immunother Cancer* 2018;6: 8.
- Schmid P, Adams S, Rugo HS, Schneeweiss A, Barrios CH, Iwata H, et al. Atezolizumab and nab-paclitaxel in advanced triple-negative breast cancer. *N Engl J Med* 2018;379: 2108-21.
- Schmid P, Rugo HS, Adams S, Schneeweiss A, Barrios CH, Iwata H, et al. Atezolizumab plus nab-paclitaxel as first-line treatment for unresectable, locally advanced or metastatic triple-negative breast cancer (IMpassion130): updated efficacy results from a randomised, double-blind, placebo-controlled, phase 3 trial. *Lancet Oncol* 2020;21: 44-59.
- Marra A, Viale G, Curigliano G. Recent advances in triple negative breast cancer: the immunotherapy era. *BMC Med* 2019;17: 90.
- Mori H, Kubo M, Yamaguchi R, Nishimura R, Osako T, Arima N, et al. The combination of PD-L1 expression and decreased tumor-infiltrating lymphocytes is associated with a poor prognosis in triple-negative breast cancer. *Oncotarget* 2017;8: 15584-92.
- Mittendorf EA, Philips AV, Meric-Bernstam F, Qiao N, Wu Y, Harrington S, et al. PD-L1 expression in triple-negative breast cancer. *Cancer Immunol Res* 2014;2: 361-70.
- Socinski MA, Jotte RM, Cappuzzo F, Orlandi F, Stroyakovskiy D, Nogami N, et al. Atezolizumab for first-line treatment of metastatic nonsquamous NSCLC. *N Engl J Med* 2018;378: 2288-301.
- Adams S, Diéras V, Barrios CH, Winer EP, Schneeweiss A, Iwata H, et al. Patient-reported outcomes from the phase III IMpassion130 trial of atezolizumab plus nab-paclitaxel in metastatic triple-negative breast cancer. *Ann Oncol* 2020;31: 582-9.
- Fecher LA, Agarwala SS, Hodi FS, Weber JS. Ipilimumab and its toxicities: a multidisciplinary approach. *Oncologist* 2013;18: 733-43.
- Hunter G, Voll C, Robinson CA. Autoimmune inflammatory myopathy after treatment with ipilimumab. *Can J Neurol Sci* 2009;36: 518-20.
- Maker AV, Phan GQ, Attia P, Yang JC, Sherry RM, Topalian SL, et al. Tumor regression and autoimmunity in patients treated with cytotoxic T lymphocyte-associated antigen 4 blockade and interleukin 2: a phase I/II study. *Ann Surg Oncol* 2005;12: 1005-16.
- Phan GQ, Yang JC, Sherry RM, Hwu P, Topalian SL, Schwartzentruber DJ, et al. Cancer regression and autoimmunity induced by cytotoxic T lymphocyte-associated antigen 4 blockade in patients with metastatic melanoma. *Proc Natl Acad Sci U S A* 2003;100: 8372-7.
- Cretella D, Fumarola C, Bonelli M, Alfieri R, La Monica S, Digiacomio G, et al. Pre-treatment with the CDK4/6 inhibitor palbociclib improves the efficacy of paclitaxel in TNBC cells. *Sci Rep* 2019;9: 13014.
- Arola OJ, Saraste A, Pulkki K, Kallajoki M, Parvinen M, Voipio-Pulkki LM. Acute doxorubicin cardiotoxicity involves cardiomyocyte apoptosis. *Cancer Res* 2000;60: 1789-92.

22. Zhang S, Liu X, Bawa-Khalfe T, Lu LS, Lyu YL, Liu LF, et al. Identification of the molecular basis of doxorubicin-induced cardiotoxicity. *Nat Med* 2012;18: 1639-42.
23. Keklikoglou I, Cianciaruso C, Güç E, Squadrito ML, Spring LM, Tazzyman S, et al. Chemotherapy elicits pro-metastatic extracellular vesicles in breast cancer models. *Nat Cell Biol* 2019;21: 190-202.
24. Hughes R, Qian BZ, Rowan C, Muthana M, Keklikoglou I, Olson OC, et al. Perivascular M2 macrophages stimulate tumor relapse after chemotherapy. *Cancer Res* 2015;75: 3479-91.
25. Lewis CE, Pollard JW. Distinct role of macrophages in different tumor microenvironments. *Cancer Res* 2006;66: 605-12.
26. Peranzoni E, Lemoine J, Vimeux L, Feuillet V, Barrin S, Kantari-Mimoun C, et al. Macrophages impede CD8 T cells from reaching tumor cells and limit the efficacy of anti-PD-1 treatment. *Proc Natl Acad Sci U S A* 2018;115: E4041-50.
27. Neubert NJ, Schmittnaegel M, Bordry N, Nassiri S, Wald N, Martignier C, et al. T cell-induced CSF1 promotes melanoma resistance to PD1 blockade. *Sci Transl Med* 2018;10: eaan3311.
28. Daurkin I, Eruslanov E, Stoffs T, Perrin GQ, Algood C, Gilbert SM, et al. Tumor-associated macrophages mediate immunosuppression in the renal cancer microenvironment by activating the 15-lipoxygenase-2 pathway. *Cancer Res* 2011;71: 6400-9.
29. Gok Yavuz B, Gunaydin G, Gedik ME, Kosemehmetoglu K, Karakoc D, Ozgur F, et al. Cancer associated fibroblasts sculpt tumour microenvironment by recruiting monocytes and inducing immunosuppressive PD-1 + TAMs. *Sci Rep* 2019;9: 3172.
30. Pathria P, Louis TL, Varner JA. Targeting tumor-associated macrophages in cancer. *Trends Immunol* 2019;40: 310-27.
31. DeNardo DG, Brennan DJ, Rexhepaj E, Ruffell B, Shiao SL, Madden SF, et al. Leukocyte complexity predicts breast cancer survival and functionally regulates response to chemotherapy. *Cancer Discov* 2011;1: 54-67.
32. Mancini VSBW, Pasquini JM, Correale JD, Pasquini LA. Microglial modulation through colony-stimulating factor-1 receptor inhibition attenuates demyelination. *Glia* 2019;67: 291-308.
33. Lee S, Shi XQ, Fan A, West B, Zhang J. Targeting macrophage and microglia activation with colony stimulating factor 1 receptor inhibitor is an effective strategy to treat injury-triggered neuropathic pain. *Mol Pain* 2018;14: 1744806918764979.
34. Bissinger S, Hage C, Wagner V, Maser IP, Brand V, Schmittnaegel M, et al. Macrophage depletion induces edema through release of matrix-degrading proteases and proteoglycan deposition. *Sci Transl Med* 2021;13: eab44550.
35. Wesolowski R, Sharma N, Reebel L, Rodal MB, Peck A, West BL, et al. Phase Ib study of the combination of pexidartinib (PLX3397), a CSF-1R inhibitor, and paclitaxel in patients with advanced solid tumors. *Ther Adv Med Oncol* 2019;11: 1758835919854238.
36. Papadopoulos KP, Gluck L, Martin LP, Olszanski AJ, Tolcher AW, Ngarmchammanrith G, et al. First-in-human study of AMG 820, a monoclonal anti-colony-stimulating factor 1 receptor antibody, in patients with advanced solid tumors. *Clin Cancer Res* 2017;23: 5703-10.
37. Kitamura T, Doughty-Shenton D, Cassetta L, Fraggogianni S, Brownlie D, Kato Y, et al. Monocytes differentiate to immune suppressive precursors of metastasis-associated macrophages in mouse models of metastatic breast cancer. *Front Immunol* 2018;8: 2004.
38. Madsen DH, Jürgensen HJ, Siersbæk MS, Kuczek DE, Grey Cloud L, Liu S, et al. Tumor-associated macrophages derived from circulating inflammatory monocytes degrade collagen through cellular uptake. *Cell Rep* 2017;21: 3662-71.
39. Ishihara D, Dovas A, Hernandez L, Pozzuto M, Wyckoff J, Segall JE, et al. Wiskott-aldrich syndrome protein regulates leukocyte-dependent breast cancer metastasis. *Cell Rep* 2013;4: 429-36.
40. Karousou E, D'Angelo ML, Kouvidi K, Vigezzi D, Viola M, Nikitovic D, et al. Collagen VI and hyaluronan: the common role in breast cancer. *Biomed Res Int* 2014;2014: 606458.
41. Scodeller P, Simón-Gracia L, Kopanchuk S, Tobi A, Kilik K, Säälk P, et al. Precision targeting of tumor macrophages with a CD206 binding peptide. *Sci Rep* 2017;7: 14655.
42. Lepland A, Asciutto EK, Malfanti A, Simón-Gracia L, Sidorenko V, Vicent MJ, et al. Targeting pro-tumoral macrophages in early primary and metastatic breast tumors with the CD206-binding mUNO peptide. *Mol Pharm* 2020;17: 2518-31.
43. Asciutto EK, Kopanchuk S, Lepland A, Simón-Gracia L, Aleman C, Teesalu T, et al. Phage-display-derived peptide binds to human CD206 and modeling reveals a new binding site on the receptor. *J Phys Chem B* 2019;123: 1973-82.
44. Figueiredo P, Lepland A, Scodeller P, Fontana F, Torrieri G, Tiboni M, et al. Peptide-guided resiquimod-loaded lignin nanoparticles convert tumor-associated macrophages from M2 to M1 phenotype for enhanced chemotherapy. *Acta Biomater* 2021;133: 231-43.
45. Jameson B, Baribaud F, Pöhlmann S, Ghavimi D, Mortari F, Doms RW, et al. Expression of DC-SIGN by dendritic cells of intestinal and genital mucosae in humans and rhesus macaques. *J Virol* 2002;76: 1866-75.
46. Connot J, Scomparin A, Peres C, Yeini E, Pozzi S, Matos AI, et al. Immunization with mannosylated nanovaccines and inhibition of the immune-suppressing microenvironment sensitizes melanoma to immune checkpoint modulators. *Nat Nanotechnol* 2019;14: 891-901.
47. Tian C, Kasavajhala K, Belfon KAA, Raguette L, Huang H, Migues AN, et al. ff19SB: amino-acid-specific protein backbone parameters trained against quantum mechanics energy surfaces in solution. *J Chem Theory Comput* 2020;16: 528-52.
48. Hopkins CW, Le Grand S, Walker RC, Roitberg AE. Long-time-step molecular dynamics through hydrogen mass repartitioning. *J Chem Theory Comput* 2015;11: 1864-74.
49. Berendsen HJC, Postma JPM, van Gunsteren WF, DiNola A, Haak JR. Molecular dynamics with coupling to an external bath. *J Chem Phys* 1984;81: 3684-90.
50. Ryckaert JP, Ciccotti G, Berendsen HJC. Numerical integration of the cartesian equations of motion of a system with constraints: molecular dynamics of n-alkanes. *J Comput Phys* 1977;23: 327-41.
51. Ray A, Dittel BN. Isolation of mouse peritoneal cavity cells. *J Vis Exp* 2010: 1488.
52. Bankhead P, Loughrey MB, Fernández JA, Dombrowski Y, McArt DG, Dunne PD, et al. QuPath: open source software for digital pathology image analysis. *Sci Rep* 2017;7: 16878.
53. Duro-Castano A, England RM, Razola D, Romero E, Oteo-Vives M, Morcillo MA, et al. Well-defined star-shaped polyglutamates with improved pharmacokinetic profiles as excellent candidates for biomedical applications. *Mol Pharm* 2015;12: 3639-49.
54. Arroyo-Crespo JJ, Armiñán A, Charbonnier D, Balzano-Nogueira L, Huertas-López F, Martí C, et al. Tumor microenvironment-targeted poly-L-glutamic acid-based combination conjugate for enhanced triple negative breast cancer treatment. *Biomaterials* 2018;186: 8-21.
55. Duro-Castano A, Sousa-Herves A, Armiñán A, Charbonnier D, Arroyo-Crespo JJ, Wedepohl S, et al. Polyglutamic acid-based crosslinked doxorubicin nanogels as an anti-metastatic treatment for triple negative breast cancer. *J Control Release* 2021;332: 10-20.
56. Arroyo-Crespo JJ, Deladriere C, Nebot VJ, Charbonnier D, Masiá E, Paul A, et al. Anticancer activity driven by drug linker modification in a polyglutamic acid-based combination-drug conjugate. *Adv Funct Mater* 2018;28: 1800931.
57. Shaffer SA, Baker-Lee C, Kennedy J, Lai MS, de Vries P, Buhler K, et al. *In vitro* and *in vivo* metabolism of paclitaxel polyglumex: identification of metabolites and active proteases. *Cancer Chemother Pharmacol* 2007;59: 537-48.
58. Bertani FR, Mozetic P, Fioramonti M, Iuliani M, Ribelli G, Pantano F, et al. Classification of M1/M2-polarized human macrophages by label-free hyperspectral reflectance confocal microscopy and multivariate analysis. *Sci Rep* 2017;7: 8965.
59. Gordon SR, Maute RL, Dulken BW, Hutter G, George BM, McCracken MN, et al. PD-1 expression by tumour-associated macrophages inhibits phagocytosis and tumour immunity. *Nature* 2017;545: 495-9.
60. Zhang M, Hutter G, Kahn SA, Azad TD, Gholamin S, Xu CY, et al. Anti-CD47 treatment stimulates phagocytosis of glioblastoma by M1 and M2 polarized macrophages and promotes M1 polarized macrophages *in vivo*. *PLoS One* 2016;11: e0153550.
61. Simon-Gracia L, Savier E, Parizot C, Brossas JY, Loisel S, Teesalu T, et al. Bifunctional therapeutic peptides for targeting malignant B cells and hepatocytes: proof of concept in chronic lymphocytic leukemia. *Adv Ther* 2020;3: 2000131.

62. Cassetta L, Kitamura T. Targeting tumor-associated macrophages as a potential strategy to enhance the response to immune checkpoint inhibitors. *Front Cell Dev Biol* 2018;6: 38.
63. Santoni M, Romagnoli E, Saladino T, Foghini L, Guarino S, Capponi M, et al. Triple negative breast cancer: key role of tumor-associated Macrophages in regulating the activity of anti-PD-1/PD-L1 agents. *Biochim Biophys Acta Rev Cancer* 2018;1869: 78-84.
64. Rodell CB, Arlauckas SP, Cuccarese MF, Garris CS, Li R, Ahmed MS, et al. TLR7/8-agonist-loaded nanoparticles promote the polarization of tumour-associated macrophages to enhance cancer immunotherapy. *Nat Biomed Eng* 2018;2: 578-88.
65. Loeuillard E, Yang J, Buckarma E, Wang J, Liu Y, Conboy C, et al. Targeting tumor-associated macrophages and granulocytic myeloid-derived suppressor cells augments PD-1 blockade in cholangiocarcinoma. *J Clin Invest* 2020;130: 5380-96.
66. Choo YW, Kang M, Kim HY, Han J, Kang S, Lee JR, et al. M1 macrophage-derived nanovesicles potentiate the anticancer efficacy of immune checkpoint inhibitors. *ACS Nano* 2018;12: 8977-93.
67. Arlauckas SP, Garren SB, Garris CS, Kohler RH, Oh J, Pittet MJ, et al. Arg1 expression defines immunosuppressive subsets of tumor-associated macrophages. *Theranostics* 2018;8: 5842-54.
68. Landry AP, Balas M, Alli S, Spears J, Zador Z. Distinct regional ontogeny and activation of tumor associated macrophages in human glioblastoma. *Sci Rep* 2020;10: 19542.
69. Zheng X, Weigert A, Reu S, Guenther S, Mansouri S, Bassaly B, et al. Spatial density and distribution of tumor-associated macrophages predict survival in non-small cell lung carcinoma. *Cancer Res* 2020;80: 4414-25.
70. Viitala M, Virtakoivu R, Tadayon S, Rannikko J, Jalkanen S, Hollmén M. Immunotherapeutic blockade of macrophage clever-1 reactivates the CD8 + T-cell response against immunosuppressive tumors. *Clin Cancer Res* 2019;25: 3289-303.
71. Etzerodt A, Tsalkitzi K, Maniecki M, Damsky W, Delfini M, Baudoin E, et al. Specific targeting of CD163 + TAMs mobilizes inflammatory monocytes and promotes T cell-mediated tumor regression. *J Exp Med* 2019;216: 2394-411.
72. Linde N, Casanova-Acebes M, Sosa MS, Mortha A, Rahman A, Farias E, et al. Macrophages orchestrate breast cancer early dissemination and metastasis. *Nat Commun* 2018;9: 21.
73. Witschen PM, Chaffee TS, Brady NJ, Huggins DN, Knutson TP, LaRue RS, et al. Tumor cell associated hyaluronan-CD44 signaling promotes pro-tumor inflammation in breast cancer. *Cancers* 2020;12: 1325.
74. Guo C, Chen Y, Gao W, Chang A, Ye Y, Shen W, et al. Liposomal nanoparticles carrying anti-IL6R antibody to the tumour microenvironment inhibit metastasis in two molecular subtypes of breast cancer mouse models. *Theranostics* 2017;7: 775-88.
75. Movahedi K, Schoonoghe S, Laoui D, Houbracken I, Waelput W, Breckpot K, et al. Nanobody-based targeting of the macrophage mannose receptor for effective *in vivo* imaging of tumor-associated macrophages. *Cancer Res* 2012;72: 4165-77.
76. Azad AK, Rajaram MVS, Metz WL, Cope FO, Blue MS, Vera DR, et al. γ -tilmanocept, a new radiopharmaceutical tracer for cancer sentinel lymph nodes, binds to the mannose receptor (CD206). *J Immunol* 2015;195: 2019-29.
77. Jaynes JM, Lopez HW, Martin GR, YATES C, Garvin CE. Peptides having anti-inflammatory properties, US9492499B2; 2016.
78. Scodeller P, Asciutto EK. Targeting tumors using peptides. *Molecules* 2020;25: 808.
79. Ekladius I, Colson YL, Grinstaff MW. Polymer-drug conjugate therapeutics: advances, insights and prospects. *Nat Rev Drug Discov* 2019;18: 273-94.
80. Duro-Castano A, Conejos-Sánchez I, Vicent MJ. Peptide-based polymer therapeutics. *Polymers* 2014;6: 515-51.
81. Moura LIF, Malfanti A, Peres C, Matos AI, Guegain E, Sainz V, et al. Functionalized branched polymers: promising immunomodulatory tools for the treatment of cancer and immune disorders. *Mater Horiz* 2019;6: 1956-73.
82. Melnyk T, Dordević S, Conejos-Sánchez I, Vicent MJ. Therapeutic potential of polypeptide-based conjugates: rational design and analytical tools that can boost clinical translation. *Adv Drug Deliv Rev* 2020;160: 136-69.
83. Duro-Castano A, Nebot VJ, Niño-Pariente A, Armiñán A, Arroyo-Crespo JJ, Paul A, et al. Capturing "extraordinary" soft-assembled charge-like polypeptides as a strategy for nanocarrier design. *Adv Mater* 2017;29.
84. Duro-Castano A, Movellan J, Vicent MJ. Smart branched polymer drug conjugates as nano-sized drug delivery systems. *Biomater Sci* 2015;3: 1321-34.
85. Cortez-Retamozo V, Etzrodt M, Newton A, Rauch PJ, Chudnovskiy A, Berger C, et al. Origins of tumor-associated macrophages and neutrophils. *Proc Natl Acad Sci U S A* 2012;109: 2491-6.
86. Kurashige M, Kohara M, Ohshima K, Tahara S, Hori Y, Nojima S, et al. Origin of cancer-associated fibroblasts and tumor-associated macrophages in humans after sex-mismatched bone marrow transplantation. *Commun Biol* 2018;1: 131.
87. Veglia F, Gabrilovich DI. Dendritic cells in cancer: the role revisited. *Curr Opin Immunol* 2017;45: 43-51.
88. Agostinis P, Berg K, Cengel KA, Foster TH, Girotti AW, Gollnick SO, et al. Photodynamic therapy of cancer: an update. *CA Cancer J Clin* 2011;61: 250-81.
89. Cheah HY, Gallon E, Dumoulin F, Hoe SZ, Japundžić-Žigon N, Glumac S, et al. Near-infrared activatable phthalocyanine-poly-L-glutamic acid conjugate: enhanced *in vivo* safety and antitumor efficacy toward an effective photodynamic cancer therapy. *Mol Pharm* 2018;15: 2594-605.
90. Nguyen VN, Yan Y, Zhao J, Yoon J. Heavy-atom-free photosensitizers: from molecular design to applications in the photodynamic therapy of cancer. *Acc Chem Res* 2021;54: 207-20.
91. Tacar O, Sriamornsak P, Dass CR. Doxorubicin: an update on anticancer molecular action, toxicity and novel drug delivery systems. *J Pharm Pharmacol* 2013;65: 157-70.
92. Shan H, Dou W, Zhang Y, Qi M. Targeted ferritin nanoparticle encapsulating CpG oligodeoxynucleotides induces tumor-associated macrophage M2 phenotype polarization into M1 phenotype and inhibits tumor growth. *Nanoscale* 2020;12: 22268-80.
93. Ramesh A, Brouillard A, Kumar S, Nandi D, Kulkarni A. Dual inhibition of CSF1R and MAPK pathways using supramolecular nanoparticles enhances macrophage immunotherapy. *Biomaterials* 2020;227: 119559.
94. Hollmén M, Karaman S, Schwager S, Lisibach A, Christiansen AJ, Maksimov M, et al. G-CSF regulates macrophage phenotype and associates with poor overall survival in human triple-negative breast cancer. *Oncol Immunology* 2015;5: e1115177.
95. Georgoudaki AM, Prokopec KE, Boura VF, Hellqvist E, Sohn S, Östling J, et al. Reprogramming tumor-associated macrophages by antibody targeting inhibits cancer progression and metastasis. *Cell Rep* 2016;15: 2000-11.
96. Zhang F, Ayaub EA, Wang B, Puchulu-Campanella E, Li YH, Hettiarachchi SU, et al. Reprogramming of profibrotic macrophages for treatment of bleomycin-induced pulmonary fibrosis. *EMBO Mol Med* 2020;12: e12034.
97. Sartor O, de Bono J, Chi KN, Fizazi K, Herrmann K, Rahbar K, et al. Lutetium-177-PSMA-617 for metastatic castration-resistant prostate cancer. *N Engl J Med* 2021;385: 1091-1103.

Critical Design Strategies Supporting Optimized Drug Release from Polymer-Drug Conjugates.

Snežana Đorđević, María Medel, Justine Hillaert, Esther Masià, Inmaculada Conejos-Sánchez*, María J. Vicent*.

Polymer Therapeutics Laboratory, Centro de Investigación Príncipe Felipe (CIPF) and CIBERONC, Valencia, Spain.

KEYWORDS redox-responsive self-immolative linkers, polymer-drug conjugates, drug release kinetics, drug delivery, structure-activity relationship, design of experiment.

ABSTRACT: The importance of an adequate linking moiety design that allows controlled drug(s) release at the desired site of action has been extensively studied for single and combination polymer-drug conjugates (PDCs) under different pathological scenarios. Redox-responsive self-immolative linkers bearing disulfide moieties (SS-SIL) represent a powerful strategy for intracellular drug delivery; however, the influence of drug structural features and linker-associated spacers on release kinetics remains relatively unexplored. We evaluated the influence of drug/spacer chemical structure and the chemical group available for conjugation on drug release and the biological effect of resultant PDCs. We implemented an artificial intelligence tool ("design of experiments") to develop a liquid chromatography-mass spectrometry method to perform the exhaustive characterization required for this systematic study. The obtained fit-for-purpose analytical protocol enabled the quantification of low drug concentrations in drug release studies and the elucidation of metabolite presence and provided the first data (to the best of our knowledge) that clarifies how drug structural features influence the drug release from SS-SIL and demonstrates the non-universal nature of the SS-SIL. We highlight the importance of rigorous linker characterization in understanding structure-function correlations between linkers, drug chemical functionalities, and in vitro release kinetics, a critical strategic crafting methodology that should remain under consideration when using a reductive environment as an endogenous drug release trigger.

INTRODUCTION

Specificity, adequate potency, toxicity in a therapeutic range, and availability at the site of action represent essential attributes when selecting a lead compound for drug delivery research and development. Recent research in the anti-cancer nanomedicine field has underlined the importance of vascularization, macrophage populations, patient-specific tumor stroma, and patient-specific tissue morphology in selecting a candidate for clinical translation.^{1,2} These findings suggest the need for a disease-driven approach to the rational design of nanomedicine, which requires a robust understanding of the relationships between biology and technology, the techniques used to characterize nanomedicines, and the influence of disease pathophysiology on nanomedicine distribution, accumulation, and efficacy.³

Among other capabilities, polymer-drug conjugates (PDCs)⁴⁻⁶ enable a therapeutic cargo to reach a desired site of action through passive (due to enhanced permeability and retention) and/or active targeting (by including targeting moieties).⁷ Controlled drug release from PDCs supports bioavailability in the target tissue, cell, or subcellular compartment, which can be achieved by designing a linking moiety between the drug and the polymeric carrier for cleavage in the presence of endogenous or exogenous triggers.^{8,9}

Redox-responsive self-immolative linkers bearing a disulfide moiety (SS-SIL) represent a powerful approach for intracellular drug delivery by PDCs.¹⁰ High levels of the reducing agent glutathione (GSH) in the endosomal compartment and the presence of a specific reducing enzyme (gamma-interferon-inducible lysosomal thiol reductase or GILT) can trigger drug release from SS-SILs.^{11,12} The implementation of disulfide linkers remained limited to thiol-containing drugs until recently; now, novel universal linking strategies have been developed to modify thiol-free drugs and allow conjugation to a suitable carrier.¹³

The most prevalent SS-SILs use a cyclization elimination mechanism where drug release occurs through nucleophilic substitution-elimination – the so-called "thiol-disulfide interchange reaction."^{10,14} Importantly, disulfide linker stability can be easily tuned by introducing distinct spacers between the disulfide bond and the drug (e.g., methyl-disulfide or ethyl-disulfide [Et-SS]); however, the rate of linker self-immolation via the intramolecular cyclization mechanism of drug release can slow under acidic conditions, such as those present in the endosomal and lysosomal compartments and the tumor microenvironment (TME).^{15,16} This obstacle has prompted the development of alternative spacers for SS-SIL design, with phenyl-disulfide linkers (Ph-SS) as one potential alternative.

Multiple studies have sought to explore drug release mechanisms and fine-tune the activity of SS-SILs.^{17,18} Previous studies reported site-specific drug release from an Et-SS linker¹⁹ and the influence of drug structural features on drug release.²⁰ Nevertheless, these studies failed to explain or investigate the reason behind these findings; thus, possible intermediate metabolites remain unidentified and the influence of drug structural features on release kinetics remains unexplored.

To investigate the drug-dependent release from Et-SS linkers and to improve the reproducibility of preclinical studies of PDCs, we designed a robust analytical procedure required to meet the major chemical and biological needs. Herein, we implemented an artificial intelligence tool – design-of-experiments or DoE – to simultaneously optimize a liquid chromatography–tandem mass spectrometry (LC-MS/MS) method to quantitatively determine the presence of various active agents. Unlike traditional approaches such as auto-tuning or "one factor at a time," which remain helpful in the low method sensitivity setting, DoE considers interactions between variables, minimizes uncontrolled effects, and evaluates their impact on the analysis.^{21,22}

Overall, we aimed to evaluate the impact of the chemical group of the drug used for conjugation (i.e., electronegativity, basicity, and ability to form resonance stabilized intermediates) on drug release kinetics. Importantly, we validated drug release kinetics by directly analyzing the resulting metabolites in preclinically relevant cell models to achieve a better theoretical and *in vitro* drug release correlation. Finally, we report on the critical strategies that must be considered when rationally designing PDCs to gain optimized biological output.

RESULTS

Drug-Et-SS synthesis and their characterization using an accurate LC-MS/MS platform. We first synthesized five drug-ethyl-disulfides (Drug-Et-SS) formed using varying functional sites on different drugs as a first step to understanding the influence of drug chemical functionality on release kinetics (Figure 1A). As model drugs, we chose fasudil (FAS), niraparib (NIRA), and rucaparib (RUCA), which each bear a secondary amino group (a chemical group with low electronegativity), dinaciclib (DIN), which bears a primary alcohol group, and resiquimod (RES), which bears a primary amino group that forms part of a resonance stabilized structure (Figure 1B). We synthesized individual Drug-Et-SS by reacting each drug with the *p*-nitrophenyl chloroformate-activated alcohol group of an SS-Et linker (see Table S1 and the Materials and Methods for more details on the synthetic process). We hypothesized that drugs bearing an amino group that forms part of resonance stabilized structure or a primary alcohol group (with higher electronegativity than the amino group) would support the highest drug release rate.

To identify the synthesized Drug-Et-SS compounds, we reported the molecular ions ($[H^+]$) and/or sodium adduct ions ($[Na^+]$): FAS-Et-SS (Figure 1C), RUCA-Et-SS (Figure 1D), NIRA-Et-SS (Figure 1E), DIN-Et-SS (Figure 1F), and

RES-Et-SS (Figure 1G) obtained by a Q1 MS direct scan; nevertheless, we also matched the MS/MS fingerprint spectra with their fragmentation mechanism to confirm the identity of Drug-Et-SS products and the success of each chemical reaction (Figures S1-5). We determined the most abundant fragment of each drug (Table S2) and Drug-Et-SS (Table S3) from the MS/MS fingerprint spectra and employed this data to form the multiple-reaction-monitoring (MRM) scan necessary for the LC-MS/MS method employed in the release studies.

In addition of implementing the Q1 MS scan for identification purposes we also used it to examine our hypothesis of higher drug release in DIN-Et-SS and RES-Et-SS. The Q1 MS scan of RES-Et-SS and DIN-Et-SS demonstrated higher susceptibility of the product to MS in-source fragmentation when compared to other Drug-Et-SS compounds (Figure 1C-E), as shown by the presence of fragments such as $[DIN+H]^+$ and $[DIN-Et-S+H]^+$ in the DIN-Et-SS Q1 MS scan (Figure 1F) and $[RES+H]^+$ and $[RES-Et-S+H]^+$ in the RES-Et-SS Q1 MS scan (Figure 1G). These results suggest the lower stability and higher drug release of RES-Et-SS and DIN-Et-SS compared to other Drug-Et-SS.

We developed a highly sensitive LC-MS/MS method utilizing DoE, which we initiated by first optimizing LC conditions. We performed MRM scans following one mass transition for each drug (Table S2) and Drug-Et-SS (Table S3) in positive electrospray ionization (ESI) mode. Values for MS parameters such as ion spray voltage (5500 V), temperature (250 °C), curtain gas (20 V), nebulizer (45 V) and auxiliary gas (45 V), declustering potential (62 V), entrance potential (2 V), exit potential (8 V) were defined by system auto-tuning to allow LC parameter optimization.

We used the Box-Behnken design to optimize seven LC gradient parameters: the acetonitrile (ACN) content in the mobile phase at the beginning (A) and end of gradient (B), flow rate (C), the 0.1 % formic acid (FA) content in sample (D), column temperature (E), gradient time (F), and plateau time (G) (Table S4). Moreover, we confirmed the robust predictive capacity of our DoE model through the analysis of variance (ANOVA), where the model *p* and *F* values for each output model displayed significance (Table S5).

We chose optimal LC conditions according to the desirability graph (Figure 1H), an objective function that ranges from a value of 0 outside the limits to 1 at the goal. The goal characteristics may be altered by adjusting the importance of each response and factor, and final optimization finds a point with maximized desirability. We selected suitable ranges for LC-MS/MS system responses: analyte response maximization (signal-to-noise ratio – S/N) and minimization of total run time (by minimizing retention time) but with simultaneous optimal retention factor (2-5), optimal tailing factor range (0.9-1.3), and optimal range for the peak width at 10% of its height (0.1-0.3).²³ Encountering a robust set of LC conditions that meet all goals for each active agent represents the purpose of optimization with the desirability function. We chose the final optimal LC conditions as A: 5% ACN, B: 89% ACN, C: 0.48 ml/min, D: 18.5%, E: 45.8 °C, F: 2 min, and G: 2.1 min (Figure 1H). We then performed a confirmation run to analyze the accuracy of output prediction

and validate the DoE model for LC-MS/MS method development (Figure 1I). We found that model prediction accuracy lay in a generally acceptable range ($\pm 20\%$). Among the parameters evaluated, peak width and tailing factor suffered

from a less accurate prediction due to the change in reproducibility of Gaussian smoothing for each chromatogram.

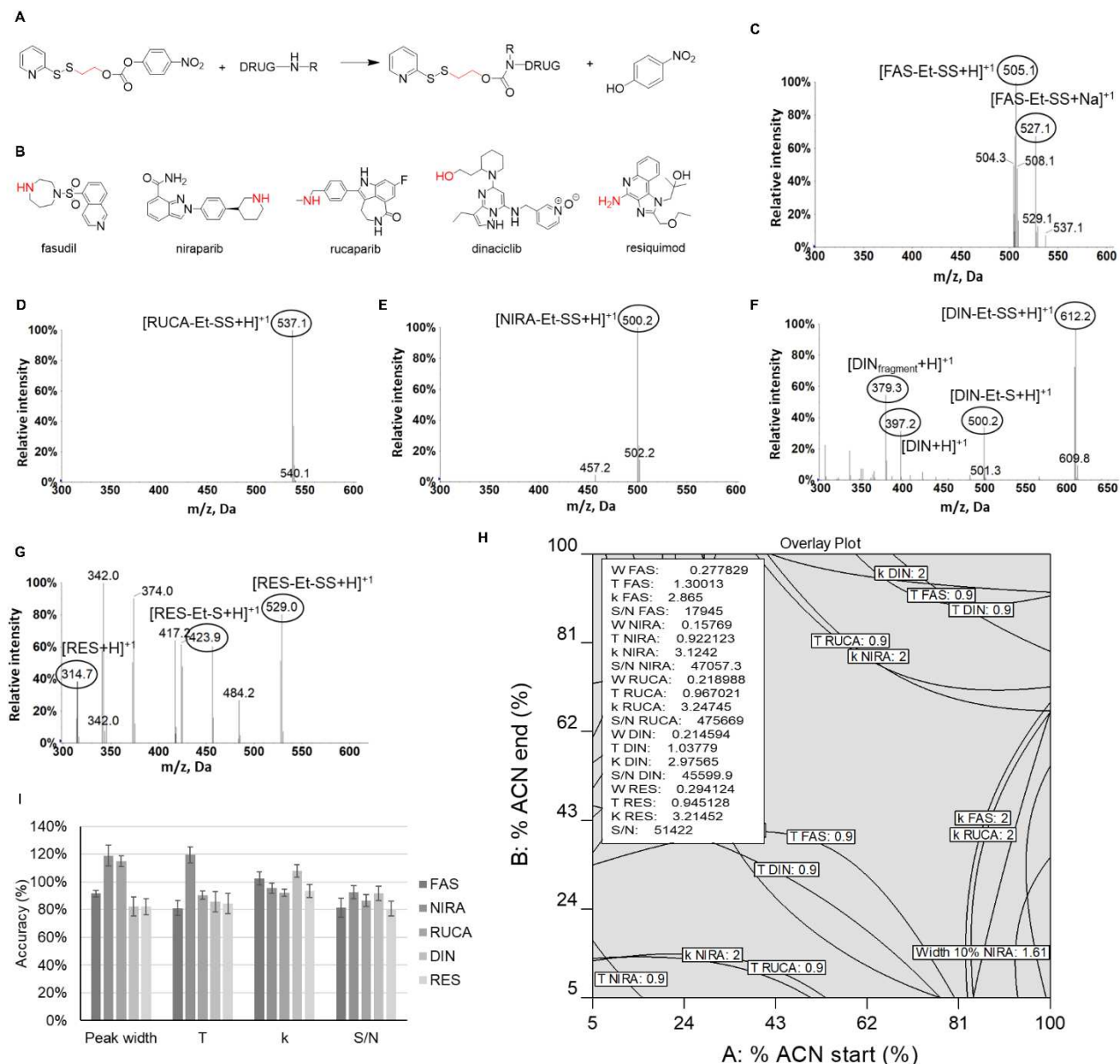


Figure 1. Synthesis and qualitative analysis of Drug-Et-SS and DoE-optimized quantitative analysis of drugs. (A) Drug-Et-SS synthetic scheme (B) Chemical structures of implemented drugs bearing different chemical groups available for the attachment with Et-SS linker (marked in red): fasudil (FAS), niraparib (NIRA), rucaparib (RUCA), dinaciclib (DIN), and resiquimod (RES). (C-I) Q1 MS scans proving the identity of individual Drug-Et-SS (C) fasudil-ethyl-disulfide (FAS-Et-SS), (D) rucaparib-ethyl-disulfide (RUCA-Et-SS), (E) niraparib-ethyl-disulfide (NIRA-Et-SS), (F) dinaciclib-ethyl-disulfide (DIN-Et-SS), and (G) resiquimod-ethyl-disulfide (RES-Et-SS). (H) Desirability graph to optimize LC parameters for the quantitative determination of FAS, NIRA, RUCA, DIN, and RES with optimal factor levels and predicted values presented in the inset box. (I) DoE prediction accuracy of LC outputs for each drug. (W-peak width at 10% height, T-tailing factor, k-retention factor, S/N- signal-to-noise ratio).

Drug Release from Individual Drug-Et-SS Depends on Drug Structural Features. We then implemented this fit-for-purpose LC-MS/MS method to finalize Drug-Et-SS characterization and perform drug release studies by quantifying the cumulative amount of drug released from the Drug-Et-SS at specific times over a total period of 144 h (six days) in the presence of 5 mM dithiothreitol (DTT), which provides a reductive environment (mimicking lysosomal conditions). In agreement with our hypothesis, we found that DIN-Et-SS (with a primary alcohol group) released a significantly higher cumulative amount of drug (63.8% of DIN) compared to FAS-Et-SS (39.7% of FAS, $p = 6.27E-05$), NIRA-

Et-SS (42.8% of NIRA, $p = 0.00040$), and RUCA-Et-SS (24.08% of RUCA, $p = 1.72E-05$), which all bear secondary amino groups (Figure 2A, empty squares). Additionally, we obtained significantly higher cumulative drug release from RES-Et-SS (with an amino group that forms part of resonance stabilized structure) (77.01% of RES) compared to FAS-Et-SS ($p = 1.48E-05$), NIRA-Et-SS ($p = 6.66E-05$), and RUCA-Et-SS ($p = 6.40E-06$) (Figure 2A, empty diamonds). These data suggest that drug release from Drug-Et-SS under a reductive environment depends on drug structural features.

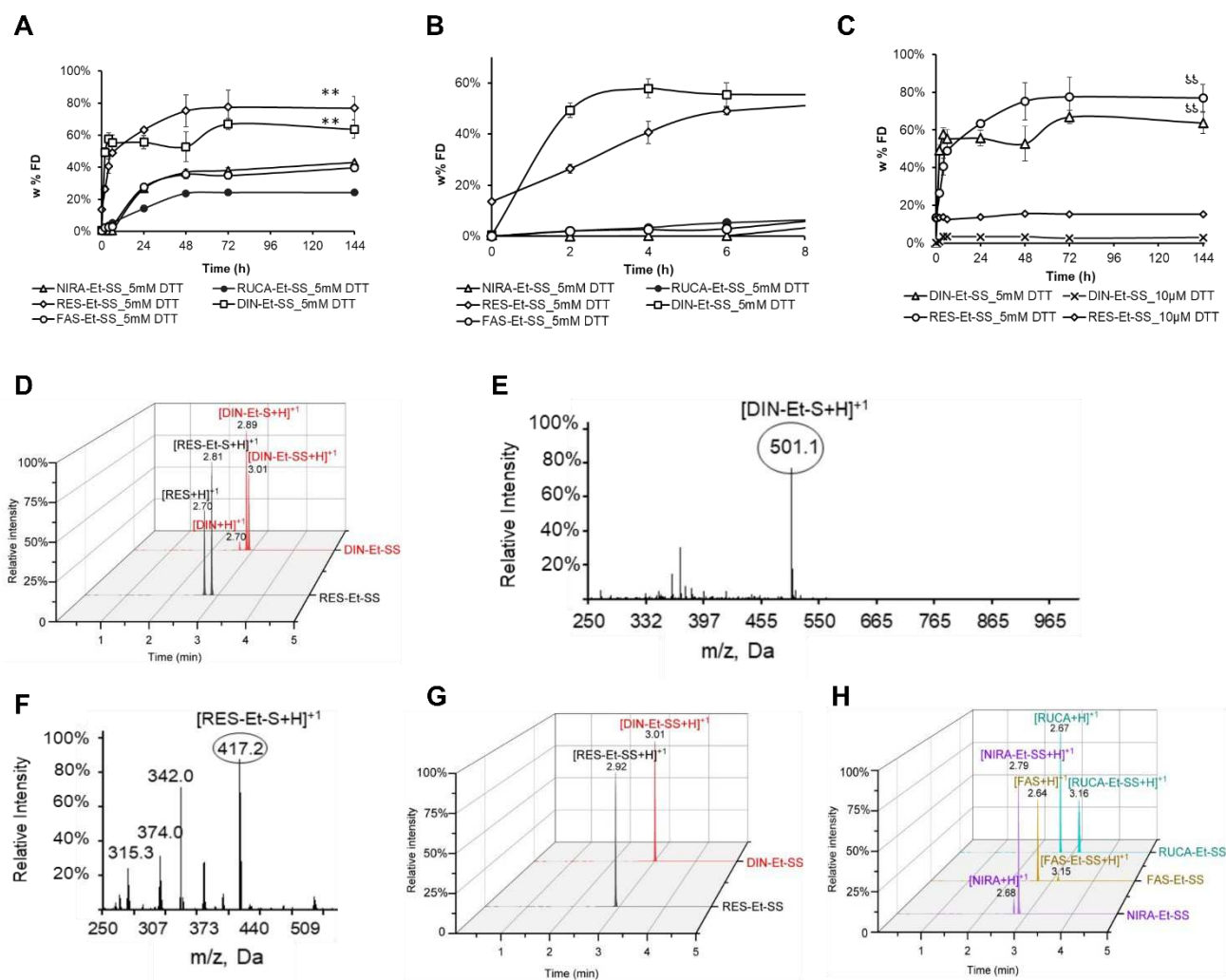


Figure 2. Drug release studies of Drug-Et-SS compounds. Drug release over (A) 0-144 h and (B) 0-8 h in the presence of 5 mM DTT. (C) Dinaciclib (DIN) and resiquimod (RES) release from dinaciclib-ethyl-disulfide (DIN-Et-SS) and resiquimod-ethyl-disulfide (RES-Et-SS) in the presence of 5 mM DTT and 10 µM DTT. (D) RES-Et-SS and DIN-Et-SS LC-MS/MS chromatograms at 0 h (in 5 mM DTT) showing the presence of intermediates (RES-Et-S-H and DIN-Et-S-H) and free drugs (RES, and DIN). (E) Q1 MS scan at 2.81 min showing the intermediate product RES-Et-S-H and (F) Q1 MS scan at 2.89 min showing the intermediate product DIN-Et-S-H. (G) LC-MS/MS chromatograms of the blank samples (without DTT) indicate the presence of a peak for only RES-Et-SS and DIN-Et-SS. (H) Last time point indicative of Drug-Et-SS detection in LC-MS/MS chromatograms: 6h for niraparib-ethyl-disulfide (NIRA-Et-SS), 24h for fasudil-ethyl-disulfide (FAS-Et-SS), and 144h for rucaparib-ethyl-disulfide (RUCA-Et-SS).

The 13.6% of RES release observed at the 0 h time point under a reductive environment (5 mM DTT) combined with the low/negligible drug release from other Drug-Et-SS (< 0.41%, < 0.52%, < 0.45% corresponding to the LC-MS/MS limit of quantification (LOQ) for FAS, NIRA, and RUCA, respectively) demonstrates how the capacity of drugs to form resonance-stabilized structures could prompt a rapid and initial burst release (Figure 2B – drug release over the initial 8 h). Interestingly, the incubation of RES-Et-SS with 10 μ M DTT (mimicking extracellular conditions) triggered a 12.8% and 15.3% RES release at 0 h and 144 h, respectively, indicating that even a low reductive environment suffice to support the initial burst RES release observed from RES-Et-SS (Figure 2C), the highly significant difference between 144 h cumulative drug release values in the presence of 5 mM DTT and 10 μ M DTT for RES-Et-SS ($p = 1.28616E-06$) highlights the need for a highly reductive environment (such as that present in the lysosome) to support complete RES release.

We failed to observe any significant DIN release from DIN-Et-SS during a 144 h incubation with 10 μ M DTT (0.002 % to 0.03 % DIN released from 0 h to 144 h), confirming extracellular stability; however, the presence of 5 mM DTT, DIN-Et-SS provided a comparatively significantly higher level of drug release ($p = 2.42E-05$, Figure 2C), demonstrating its ability to support site-specific release.

Interestingly, the LC-MS/MS chromatogram obtained from DIN-Et-SS and RES-Et-SS drug release studies with 5 mM DTT at 0 h provided proof of a rapid first step of DIN and RES release through the presence of the free drugs (DIN and RES) and intermediate products (DIN-Et-SH and RES-Et-SH) (Figures 2D). Via a Q1 MS scan, we confirmed the presence of DIN-Et-SH (Figure 2E) and RES-Et-SH (Figure 2F) intermediates eluting at retention times of 2.81 min and 2.89 min, respectively. The presence of only DIN-Et-SS and RES-Et-SS in samples analyzed after incubation in the absence of DTT (Figure 2G) confirmed the DTT-specific release of DIN and RES; thus, findings at the 0 h time point in the presence of 5 mM DTT do not represent synthesis artifacts or indicate DIN-Et-SS and RES-Et-SS storage instability.

The disappearance time of Drug-Et-SS compounds peaks from the LC-MS/MS chromatograms when incubated in the presence of 5 mM DTT (highly reductive environment) may represent the final indicator of the rapid nature of the first step of drug release. The absence of the RES-Et-SS peak and the presence of both free RES [RES+H]⁺ and intermediate [RES-Et-S+H]⁺ peaks at 0 h in the LC-MS/MS chromatogram indicates an immediate reduction of the -SS- bond when exposed to 5 mM DTT (Figure 2D). Analysis of LC-MS/MS chromatograms over 144 h demonstrated the final presence of Drug-Et-SS peaks at varying times for NIRA-Et-SS (at 6 h) and FAS-Et-SS (at 24 h), with the RUCA-Et-SS peak still evident at 144 h (Figure 2H), suggesting a difference in the speed (shown in descending order) of the first step of drug release from Drug-Et-SS. These data provide further evidence that drug release from individual Drug-Et-SS depends on the chemical group employed for the attachment of each drug to the linker.

Of note, the burst release obtained with RES-Et-SS represents a drug release phenomenon commonly observed in drug delivery systems of different forms and compositions, mainly when encapsulating rather than conjugating drugs. Nevertheless, this drug release mode involves some negative impacts, such as short in vivo drug half-lives and shortened release profiles, which require more frequent dosing and may induce local or systemic toxicity.²⁴ The influence of burst RES from Drug-Et-SS on the therapeutic effect of their corresponding PDCs remains outside the scope of our study.

Ph-SS as a Substitute for the Et-SS Linker. The low levels of FAS, NIRA, and RUCA release (drugs bearing secondary amino groups) from Drug-Et-SS impede the use of the Et-SS linker in the design of PDCs. To provide for more significant FAS, NIRA, and RUCA release levels, we implemented a disulfide-modified linker using a phenyl spacer instead of an ethyl spacer between the disulfide bond and the drug. Instead of the intramolecular cyclization in the case of Et-SS (Figure 3A), the drug release mechanism from Drug-Ph-SS is based on the 1,6-elimination (pDTB-dithiobenzyl) after disulfide bond reduction (Figure 3B); thus, the second step of drug release will not depend on drug structural features since pDTB elimination occurs through the thioquinone methide cascade.²⁵

Following the drug release results observed for the Drug-Et-SS, we aimed to enhance the drug release rate from FAS-Et-SS, NIRA-Et-SS, and RUCA-Et-SS by synthesizing counterparts that carried a Ph-SS, which displays increased hydrophobicity, instead of an Et-SS linker. We synthesized each Drug-Ph-SS by reacting each drug with the *p*-nitrophenyl chloroformate-activated alcohol group of Ph-SS (Figure 3C, Table S1). We confirmed the identity of each Drug-Ph-SS by reporting the molecular ions ([H⁺]), sodium adduct ions ([Na⁺]), and potassium adduct ions ([K⁺]) in a Q1 MS scan for FAS-Ph-SS, NIRA-Ph-SS, and RUCA-Ph-SS (Figure 3D-F) and matching the fragmentation mechanism for each Drug-Ph-SS product to the MS/MS scan (Figures S6-8).

Encouragingly, the implementation of Ph-SS enabled a significantly higher release of NIRA (76.7%, $p = 0.00029$, Figure 3G), FAS (82.3%, $p = 5.53E-06$, Figure 3H), and RUCA (86.7%, $p = 7.064E-06$, Figure 3I) from their corresponding Drug-Ph-SS when compared to release from Et-SS drug linkers (39.7%, 42.8%, and 24.08%, respectively) in the presence of 5 mM DTT. The Ph-SS linker has not been implemented to a high degree for drug conjugation since the literature had suggested low stability and, consequently, low specificity for intracellular drug release;²⁶ however, the negligible drug release from the Drug-Ph-SS products in the presence of 10 μ M DTT (a weaker reductive environment) (< 0.41%, < 0.52%, < 0.45% corresponding to the LC-MS/MS limit of quantification (LOQ) for FAS, NIRA, and RUCA, respectively) indicates extracellular stability and that Ph-SS may represent a stable option for drugs containing secondary amino groups.

We next confirmed the one-step drug release from Drug-Ph-SS when we failed to detect the presence of any intermediates in the chromatograms obtained from drug release studies in the presence of 5 mM DTT (Figures 3J-L). Additionally, we observed only the peak associated with the free

drug (FAS, NIRA, and RUCA) at the last time point in the drug release studies (144 h), suggesting the complete degradation of each Drug-Et-SS.

Overall, we provide evidence that implementing a Ph-SS linker offers significantly higher drug release than the Et-SS linker under a reductive environment and thereby

represents a robust option for the attachment of drugs with secondary amino groups displaying low electronegativity. In this case, drug release did not significantly depend on drug structural features since the drug release relied on the thioquinone methide cascade and not cyclization (as in the case of Et-SS).²⁶⁻²⁸

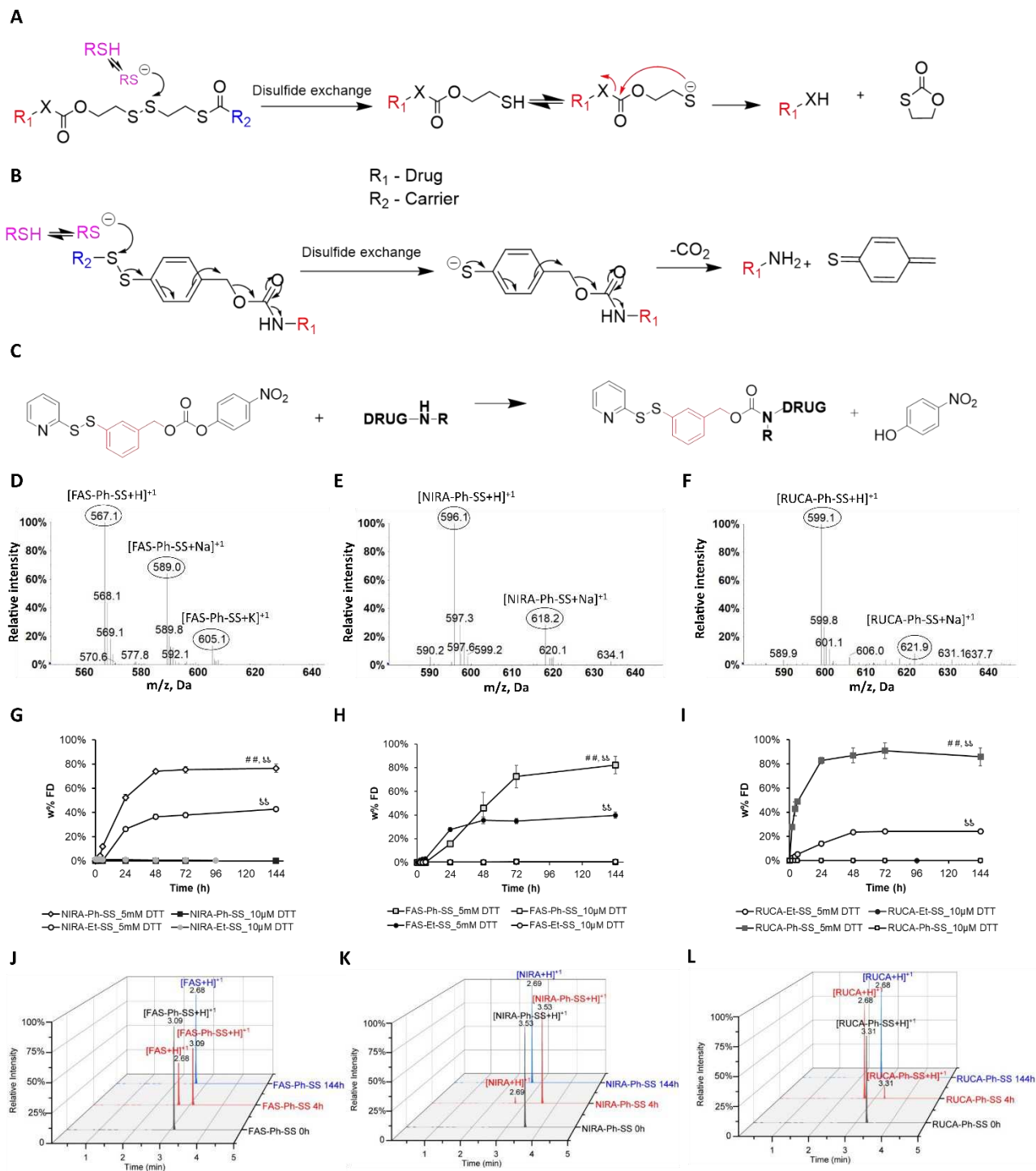


Figure 3. Synthesis, qualitative analysis, and drug release studies of Drug-Ph-SS. Drug release mechanism from (A) Drug-Et-SS via intramolecular cyclization and (B) Drug-Ph-SS via the thioquinone methide cascade (adapted from Wang et al.10). (C) Drug-Ph-SS synthetic scheme. (D-F) Q1 MS scans showing the identity of (D) fasudil-phenyl-disulfide (FAS-Ph-SS), (E) niraparib-phenyl-disulfide (NIRA-Ph-SS), and (F) rucaparib-phenyl-disulfide (RUCA-Ph-SS). (G-I) Evaluation of drug release over 0-144 h in the presence of 5

mM DTT or 10 μ M DTT from (G) niraparib-ethyl-disulfide (NIRA-Et-SS) and NIRA-Ph-SS, (H) fasudil-ethyl-disulfide (FAS-Et-SS) and FAS-Ph-SS, (I) rucaparib-ethyl-disulfide (RUCA-Et-SS) and RUCA-Ph-SS. (J-L) LC-MS/MS chromatogram at 0, 4, and 144 h after the addition of 5 mM DTT to (J) FAS-Ph-SS, (K) NIRA-Ph-SS, and (L) RUCA-Ph-SS. (data from G, H, and I presented as the cumulative weight percentage of free drug (w% FD) compared to the total drug amount in the Drug-Ph/Et-SS \pm SD (n=3). ##p<0.005 indicates statistically significant differences between drug release from each Drug-Ph-SS compared to the corresponding Drug-Et-SS. \$\$p<0.005 indicates statistically significant differences between drug release at 5 mM DTT and 10 μ M DTT.)

Synthesis and Characterization of Polypeptide-based Fasudil Conjugates with Optimized Linkers. Given this success, we then moved to the next level of complexity, which entailed the conjugation of the Drug-Et/Ph-SS to a polypeptide carrier to explore the possible transfer of the identified behavior at the small molecular weight scale to the rational design of PDCs. Studies of PDCs have underscored the importance of linking moieties to the tightly controlled release of drugs at the desired site of action.²⁹ Here,

we chose FAS as a representative of drugs bearing a low electronegative -NR₂ group and a polyglutamate (PGA)-based polypeptide carrier, which displays biocompatibility, biodegradability, and multivalency and allows high drug loading.³⁰ We conjugated FAS to PGA using both Et-SS and Ph-SS and used the resultant PDCs (PGA-SS-Et-FAS and PGA-SS-Ph-FAS) as model PDCs to study drug release and efficacy in treating triple-negative breast cancer (TNBC) using in vitro models (Figure 4A).

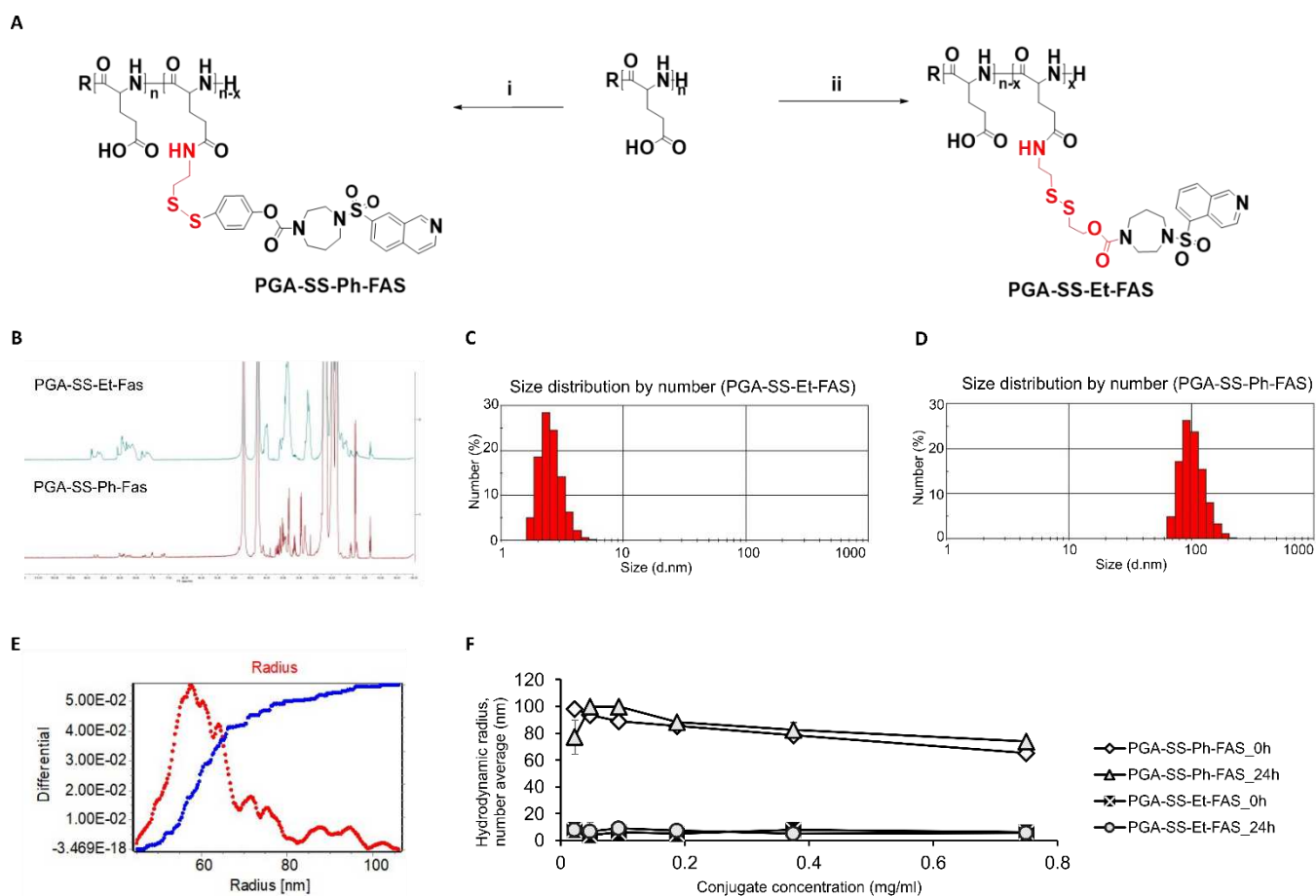


Figure 4. Synthesis and Characterization of PGA-SS-Et-FAS and PGA-SS-Ph-FAS. (A) The synthetic route used to prepare PGA-SS-Et-FAS and PGA-SS-Ph-FAS (B) Chemical identity and purity of PGA-SS-Et-FAS and PGA-SS-Ph-FAS assessed via 1H-NMR spectroscopy. (C) DLS hydrodynamic radius determination of PGA-SS-Et-FAS, (D) DLS hydrodynamic radius determination of PGA-SS-Ph-FAS, (E) Asymmetric flow field flow fractionation - UV/Vis - multi-angle light scattering determination of the PGA-SS-Ph-FAS radius of gyration. (F) size stability studies of PGA-SS-Et-FAS and PGA-SS-Ph-FAS in dPBS.

We obtained PGA-SS-Et-FAS and PGA-SS-Ph-FAS with high purity (shown by ^1H NMR experiments, Figure 4B) and high yield (79.5–83.7%). UV/Vis analysis allowed the determination of total drug loading (TDL) in a range of 11.6 ± 0.04 w% for PGA-SS-Et-FAS and 7.2 ± 0.02 w% for PGA-SS-Ph-FAS (representing high loading); meanwhile, LC-MS/MS analysis established a free drug content of below 0.02 w% (compared to TDL) for both conjugates, which lies under the generally accepted limits for designed PDCs ($<2\text{wt}\%$ of TDL)^{31,32}.

Dynamic light scattering (DLS) analysis demonstrated a hydrodynamic radius ≈ 5 nm in Dulbecco's phosphate-buffered saline (dPBS, pH 7.4) for PGA-SS-Et-FAS, which agrees well with the presence of unimeric PDC entities (Figure 4C). Meanwhile, the addition of the phenyl group as a hydrophobic spacer in PGA-SS-Ph-FAS led to the formation of micelles with a hydrodynamic radius of 99.2 nm (as determined by DLS – Figure 4D) and a radius of gyration of 63.7 nm (determined by asymmetric flow field flow fractionation – UV/Vis – multi-angle light scattering [AF4-UV/Vis-MALS] – Figure 4E). We then performed a DLS analysis of PGA-SS-Et-FAS and PGA-SS-Ph-FAS at the highest and lowest active concentrations (200 μM and 80 μM FAS equivalents) typically used in *in vitro* cell viability evaluations. The sizes remained unchanged for PGA-SS-Et-FAS (5.7 ± 1.2 nm) and PGA-SS-Ph-FAS (99.2 ± 3.6 nm), ensuring the presence of unimers or micelles, respectively, for subsequent studies. Moreover, initial critical micellar concentration (CMC) studies of PGA-SS-Et-FAS and PGA-SS-Ph-FAS in dPBS (pH 7.4) confirmed the formation of particles by PGA-SS-Ph-FAS at a concentration >80 μM FAS equivalents (but not for PGA-SS-Et-FAS) and the stability of PGA-SS-Ph-FAS micelles after 24 h at 4°C (Figure 4F). Overall, the addition of phenyl spacer increases the hydrophobicity of the FAS-Ph-SS linker (logP 4.17, calculated in ChemDraw) compared to the FAS-Et-SS linker (logP 2.73, calculated in ChemDraw), leading to the formation of stable micelles with higher hydrodynamic radius triggered by π - π stacking at concentration >80 μM FAS equivalents.

In vitro Cell Viability in Response to PDC Treatment Depends on Variables Other Than Drug Release. Previous studies have reported significantly higher levels of the Rho-associated protein kinases (ROCK1 and ROCK2) in TNBC; therefore, these aggressive cancer cells should display a higher sensitivity to ROCK inhibitors such as fasudil.³³ Thus, to understand the biological implications of the different linking chemistries, we evaluated the toxicity of PGA-SS-Et-FAS and PGA-SS-Ph-FAS using the MDA-MB-231 TNBC cell line cultured as a traditional two-dimensional cell monolayer (2D). Moreover, we also evaluated PGA-SS-Et-FAS and PGA-SS-Ph-FAS in advanced three-dimensional (3D) culture models (mammospheres), which better mimic *in vivo* tumor features. We expected to observe differences in cellular trafficking with the 3D models; furthermore, diffusion rates through mammospheres (influenced by size, shape, and deformability) could represent another parameter considered in the rational design of PDCs.³⁴

We performed cell viability studies by MTS assay 72 h post-treatment with PGA-SS-Et-FAS and PGA-SS-Ph-FAS.

Compared with free FAS, PGA-SS-Et-FAS and PGA-SS-Ph-FAS displayed significantly greater cytotoxicity at concentrations lower than 150 μM FAS equivalents in the 2D model (Figure 5A). On the contrary, we failed to observe the increased toxicity of PGA-SS-Et-FAS and PGA-SS-Ph-FAS compared to free FAS in the 3D model (Figure 5B). Comparisons using 200 μM FAS equivalents between 2D and 3D TNBC models for PGA-SS-Et-FAS and PGA-SS-Ph-FAS indicated that both conjugates exhibited more significant cytotoxicity under 2D than 3D conditions (Figure 5C) ($p=0.0013$ and $p=1.56\text{E}-6$, respectively). To ensure that the cytotoxicity levels observed from PGA-SS-Et-FAS and PGA-SS-Ph-FAS arise from the FAS and not from the PGA carrier, we introduced linear PGA as a control. As expected, we did not observe any significant toxicity associated with control PGA (Figure 5A-B).

Two reasons may lie behind the differential toxicity of PGA-SS-Et-FAS and PGA-SS-Ph-FAS in 2D and 3D models. First, the more significant internalization of PGA-SS-Et-FAS and PGA-SS-Ph-FAS in the 2D monolayer than in 3D mammospheres, and second, a significant difference in drug release caused by distinct intracellular GSH levels. To evaluate these two hypotheses, we needed to optimize the sample preparation process for quantification of free FAS amount in the *in vitro* models treated with PGA-SS-Et-FAS and PGA-SS-Ph-FAS (See Figure S9 and Experimental Section for more details).

To explore potential differences in internalization rates, we determined the level of internalized PGA-SS-Et-FAS and PGA-SS-Ph-FAS in 2D vs. 3D models by quantifying the levels of total FAS present within cells and in the cell medium 72 h post-treatment (total FAS = free FAS + conjugated FAS, quantified after sample incubation with 50 mM DTT to ensure complete FAS release). We obtained significantly higher levels of total FAS internalized in the 2D model treated with PGA-SS-Et-FAS (53%, 69%, and 61%) compared to the 3D model (34%, 48%, and 33%) at all concentrations tested (the lowest - 20 μM , $p = 0.00012$; medium - 80 μM , $p = 0.00057$; and the highest - 200 μM , $p = 0.00026$, respectively) (Figure 5D), thereby confirming the variability of PGA-SS-Et-FAS internalization between the two models. Meanwhile, the PGA-SS-Ph-FAS internalization rate remained similar between models (Figure 5E) but with a significantly higher percentage of internalization at all three concentrations compared to PGA-SS-Et-FAS in the 2D (83%, $p = 0.00027$; 93%, $p = 0.0011$; 90%, $p = 0.001$; Figure 5F) and 3D models (81%, $p = 3.60\text{E}-05$; 89%, $p = 0.00045$; 91%, $p = 1.51\text{E}-05$; Figure 5G). We suggest that the larger size and, most probably, the more globular conformation of PGA-SS-Ph-FAS facilitates internalization in the *in vitro* models due to better fluidity and diffusion capacity than the unimolecular form of PGA-SS-Et-FAS.

Next, we sought to explore our second hypothesis for the difference observed in relation to *in vitro* cytotoxicity between models by evaluating drug release efficiency and intracellular GSH levels. Instead of performing drug release studies with DTT, we employed a more realistic scenario and directly quantified FAS released after the exposure of *in vitro* TNBC models to PGA-SS-Et-FAS and PGA-SS-Ph-FAS

for 72 h at three FAS equivalents (20, 80, and 200 μM ; the minimum, medium and maximum dose in the FAS cytotoxicity curve). We subsequently determined the w% of FAS released in cells and represented it as the percentage of free FAS compared to the total internalized FAS. We found

significantly higher levels of FAS released from PGA-SS-Et-FAS (Figure 5H) and PGA-SS-Ph-FAS conjugates (Figure 5I) in the 2D model compared to the 3D model, correlating with the observed activity (Figures 5A and 5B).

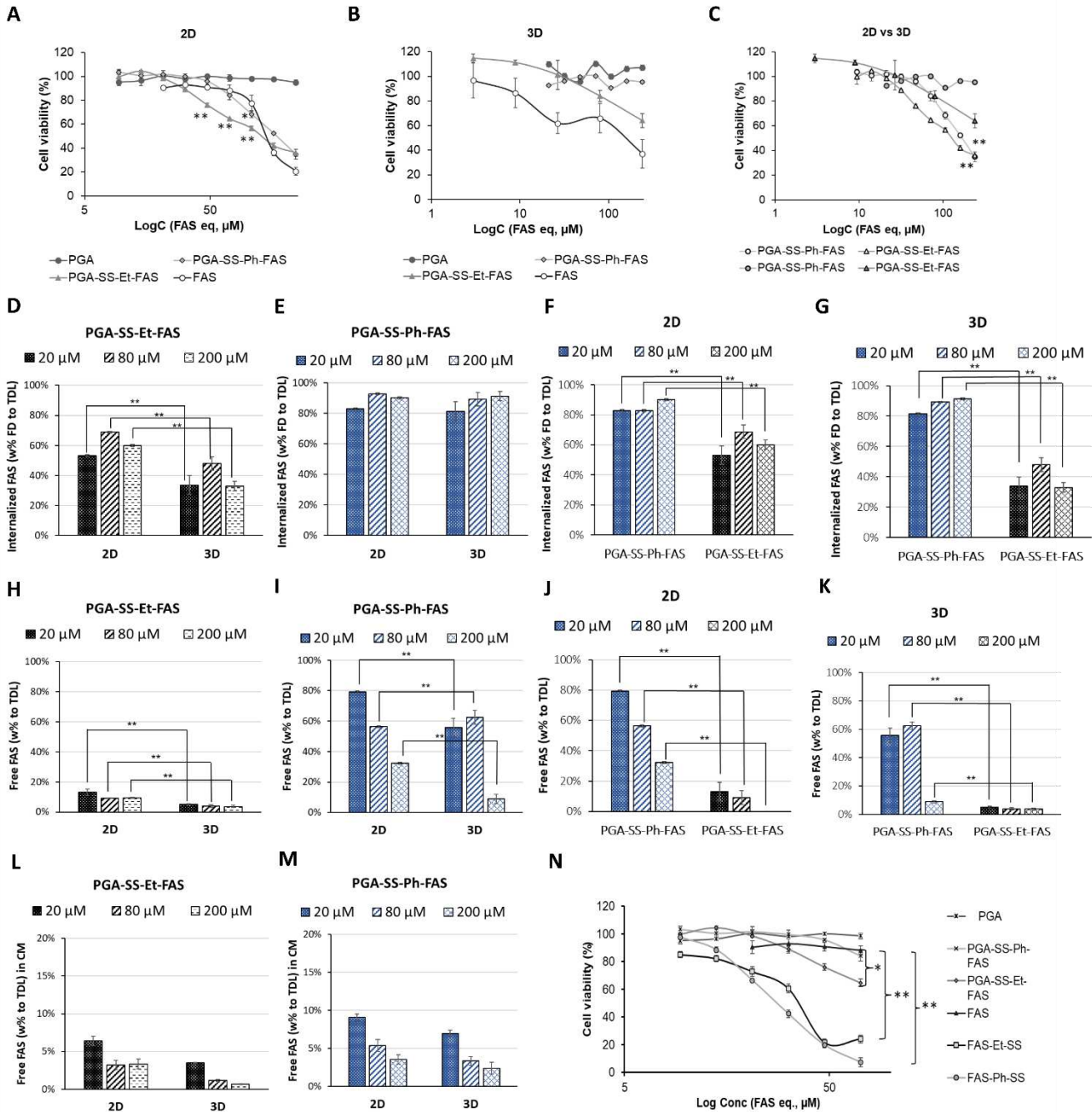


Figure 5. In vitro viability and drug release studies in cells and cell medium. (A-B) Toxicity profiles comparison of PGA-SS-Et-FAS and PGA-SS-Ph-FAS with free FAS in two MBA-MB 231 TNBC cell models (A) 2D monolayers and (B) 3D mammospheres. (C) Toxicity profiles comparison of PGA-FAS conjugates between 2D and 3D models. (D-E) Comparison of total FAS w% between 2D and 3D in vitro models internalized with (D) PGA-SS-Et-FAS and (E) PGA-SS-Ph-FAS. (F-G) Comparison of total internalized FAS w% between PGA-FAS conjugates in (F) 2D and (G) 3D in vitro models. (H-I) Comparison of free FAS w% released inside the cells from the internalized (H) PGA-SS-Et-FAS and (I) PGA-SS-Ph-FAS between the in vitro models. (J-K) Comparison of free FAS w% released inside the

cells of (J) 2D and (K) 3D *in vitro* model. (L-M) Free FAS w% detected in cell medium (CM) of 2D and 3D *in vitro* cell models 72 h after the treatment with (L) PGA-SS-Et-FAS and (M) PGA-SS-Ph-FAS. (N) Toxicity profiles of PGA-SS-Et-FAS, PGA-SS-Ph-FAS and FAS-Et-SS and FAS-Ph-SS in the MBA-MB 231 2D TNBC *in vitro* model (* $p < 0.05$, ** $p < 0.005$; all data presented as average \pm SD ($n=3$); in A, B, and N, PGA was used as control).

The *in vitro* drug release study and the cell viability data obtained from PGA-SS-Et-FAS and PGA-SS-Ph-FAS in the 2D and 3D TNBC models also correlated with GSH and GSH/GSSG levels: the significantly higher values present in the 2D model (25.89 ± 0.39 mM GSH, and 16.76 ± 1.99 GSH/GSSG) compared to 3D model (13.40 ± 0.59 mM GSH, and 3.45 ± 0.22 GSH/GSSG) indicate a higher reductive environment, which prompts more significant FAS release and cytotoxicity ($p = 0.001$ for GSH and $p=0.0003$ for GSH/GSSG). The decreased levels of GSH/GSSG in 3D cell models indicate more significant levels of oxidative stress, possibly due to the hypoxia in the center of relatively large, compact 3D mammospheres (Figure S10).

Finally, we confirmed that PGA-SS-Ph-FAS provided significantly higher FAS release intracellularly at all concentrations and in both 2D (Figure 5J) and 3D models (Figure 5K) compared to PGA-SS-Et-FAS via drug release studies using *in vitro* models. Thus, we provided evidence that the SS-Ph linker acts as a substitute for the SS-Et linker in designing PDCs with a higher release of drugs bearing a low electro-negative amine group. Interestingly, from the drug release data in both models, we observed a lower trend for FAS release in cells with increasing doses, indicating a limitation on the reductive capacity for -SS- bond cleavage inside cells due to a possible conformational impediment to the S-S moiety upon increased concentration and subsequent PDC accumulation in the lysosome (Figures 5H-5K). We mostly observed concentration-dependent release in the 2D and 3D models for PGA-SS-Ph-FAS and the 2D model for PGA-SS-Et-FAS since the release of FAS is sufficient for the differences between different concentrations to be detected. Additionally, the low amount of free FAS quantified in the cell medium after 72 h treatment with PGA-SS-Et-FAS and PGA-SS-Ph-FAS in both *in vitro* models suggests the predominantly intracellular release of FAS (Figures 5L and 5M); however, we cannot conclude from our study if the quantified amount of FAS in the cell medium derives from the extracellular release of FAS from PGA-SS-Et-FAS and PGA-SS-Ph-FAS or the efflux of intracellular FAS.

Overall, the more globular PGA-SS-Ph-FAS micelles may contribute to better internalization in 2D and 3D models than the unimeric conformation of PGA-SS-Et-FAS; however, higher internalization and higher release do not lead to higher cytotoxicity. A possible explanation may lie in the presence of the active FAS-Et-S \cdot metabolite released from PGA-SS-Et-FAS observed *in vitro* and in our DTT release studies (Figure S11), which may result in additional total cytotoxicity of PGA-SS-Et-FAS conjugate. Due to the unfeasible synthesis, we could not evaluate the cytotoxic activity of FAS-Et-S \cdot in TNBC models; however, molecular dynamics and modeling may elucidate whether the metabolite binds the ROCK enzyme, a hypothesis that may be evaluated in the future studies.

The *in vitro* drug release data from PGA-SS-Et-FAS (13.1% FAS released after 72h in 2D and 5.1% in 3D) and PGA-SS-Ph-FAS (55.8% FAS w% released after 72h in 2D and 79.3% in 3D) do not correlate with the DTT-mediated drug release (39.7% FAS released after 72h from FAS-Et-SS, and 82.3% from FAS-Ph-SS), indicating that the carrier adds another level of complexity that influences drug release and the final cytotoxicity profiles in cells. To explore these claims, we performed cell viability studies without PGA by treating the 2D *in vitro* TNBC cell model with FAS-Ph-SS and FAS-Et-SS (Figure 5N). After 72 h, MTS assays revealed the significantly higher cytotoxic activity of the FAS-Ph-SS drug-linker compared to FAS-Et-SS (58% vs. 39%, respectively, $p=0.00012$) at lower FAS equivalent concentrations (Figure 5N), which agrees well with the DTT-mediated drug release studies (82% FAS released from FAS-Ph-SS and 40% FAS released from FAS-Et-SS, Figure 3F). Moreover, FAS-Et-SS and FAS-Ph-SS linkers exhibited higher cytotoxicity than free FAS and PGA-SS-Et-FAS and PGA-SS-Ph-FAS in the 2D TNBC model in the 9-107 μ M concentration range (FAS eq) (Figure 5N), which may lead to a further investigation of FAS-Et-SS and FAS-Ph-SS as FAS prodrugs in the treatment of TNBC.

DISCUSSION

Despite the technological advancements made in the last decade, the design of next-generation drug delivery systems remains a challenging task. We must balance numerous factors, from controlled drug release and enhanced cellular internalization to managing rapid immune responses, renal clearance, and off-target toxicities. We performed a systematic study to expand the rational design toolbox for drug delivery systems (focusing on PDCs) that employ stimuli-controlled drug release to gain a better understanding of PDC fate in a biological environment.

Implementing optimal bioresponsive linking moieties within the rational design of PDCs generally allows for plasma stability and efficient, site-specific, controlled drug release under the conditions of the targeted site.⁹ The differential levels of GSH observed between extra- vs. intracellular sites and between normal and pathological sites make the use of redox-sensitive linkers a preferred strategy to engineer a bioresponsiveness PDC.⁸

Redox-responsive SS-SIL linkers represent a powerful strategy for intracellular drug delivery; furthermore, they are considered universal linkers as any drug with an amino or hydroxyl group can undergo modification and connection through SS-SIL to a carrier molecule. Of note, the influence of the drug's structural features and the linker-associated spacer on release kinetics remains unexplored. Therefore, we evaluated the influence of the drugs/spacer's chemical structures, the type of chemical group available for

conjugation on drug release, and the biological effect of the developed PDCs.

A mechanistic study of novel mutual prodrugs containing distinct SS-SIL types suggested that structural features of constituent drugs influenced drug release.²⁰ Nevertheless, the authors of this study failed to investigate the reason behind this finding, and possible intermediate metabolites remain unidentified. In parallel, a study of doxorubicin prodrugs obtained by conjugation through amino and hydroxyl groups demonstrated site-specific drug release from an Et-SS linker.¹⁹ C-14 hydroxyl modification of doxorubicin provided higher anti-tumor efficacy due to a significantly higher release rate than the amino group modification; however, the additional value of our study lies in demonstrating that this phenomenon significantly affects drugs with -NR₂ groups with low electronegativity and an inability to form resonance-stabilized structures. We believe this finding remained unreported until now as most drug-Et-SS linkers reported in the literature contain drugs conjugated through the alcohol group or the amino group with resonance-stabilized structures.^{35–39}

Disulfide linkers can be roughly divided into two subgroups based on their fragmentation mechanism: disulfide linkers with drug release controlled by intramolecular cyclization (SS-Et) and disulfide linkers with drug release controlled by a thioquinone methide cascade (SS-Ph).⁴⁰ The fragmentation mechanism and, consequently, drug release from SS-Et represents a two-step process where the reductive agent GSH present in the intracellular milieu of mammalian cells (2–10 mM) initially triggers the reduction of a disulfide bond and generates a free thiol group.^{41,42} The second step is initiated by the nucleophilic attack of a deprotonated thiol to a carbonyl group, leading to drug release and the formation of a cyclic side-product.⁴¹ Nucleophilic attack represents a fundamental class of chemical reactions in which a leaving group (in the case of a Drug-Et-SS, the drug) becomes substituted by an electron-rich compound, the nucleophile (a deprotonated thiol in the case of Drug-Et-SS). More rapid and more effective nucleophilic substitution generally occurs with an optimal leaving group. Suitable leaving groups are considered weak bases due to their ability to hold a charge, meaning that greater electronegativity signifies a more optimal leaving group.⁴³ Since drugs employed as active agents usually possess basic properties and undergo attachment to Et-SS linkers through the amine group, they act as weak leaving groups leading to slow/low drug release; however, the electronegative hydroxyl group (DIN) and the amine group of the drug attached to the Et-SS linker forms part of a resonance stabilized structure (RES), resulting in a species less willing to share electrons, which provides better leaving groups and higher drug release.

The PGA-SS-Ph-FAS conjugate displayed a significantly higher intracellular release than PGA-SS-Et-FAS due to a different drug release mechanism that supports the faster and higher release of drugs bearing a low electronegative amine group. Nevertheless, our results highlight the importance of the *in vitro* redox environment, its influence on drug release, and the detailed characterization of PDCs in biological fluids. Adding a phenyl spacer may change the fate of PDCs

during the analysis of *in vitro* models due to micelle formation. The influence of size and shape on the penetration profile of PDCs has been reported before.^{44–47} The general trend observed *in vitro* and *in vivo* studies provides evidence that diffusion capacity depends on particle size and shape, which may further influence DDS fate in cells.^{48,49} Thus, we must analyze drug release from the disulfide linker in specific cellular compartments. Subcellular fractionation, a method often implemented for this purpose, may lead to false positive or negative results due to cross-contamination.⁵⁰ Therefore, we must choose analytical methodologies with great care and explore new techniques to improve predictions regarding the intracellular fate of disulfide-containing PDCs, their location, and the extent of disulfide cleavage.

To note, the analysis of identity, structure, TDL, free drug, drug release, and pharmacokinetics (among other parameters) requires multi-step analytical protocols involving method development, sample preparation and analysis, method validation, and data analysis.⁹ Method development involves obtaining rapid, sensitive, simple, informative, and environmentally sustainable analytical methods.⁵¹ DoE currently represents the most advisable way to optimize any methodology; encouragingly, we have seen a recent increase in studies implementing DoE to optimize related procedures, especially in LC-MS/MS.⁵² The use of an LC-MS/MS method that supports metabolite identification, as opposed to previous implementations of HPLC-UV/Vis that cannot elucidate the fate of SS-SIL in a reductive environment, represents a cardinal point of our study.²⁰ Herein, implementing DoE allowed us to develop an accurate, specific, and sensitive LC-MS/MS method for determining low drug concentrations in drug release studies. Moreover, we ensured the separation of drug linkers, intermediate products formed during drug release studies, and free drugs by obtaining the optimal retention factor for each drug, a prerequisite for drug release result interpretation and metabolite identification. Our DoE-developed LC-MS/MS method enabled us the identification of FAS-Et-S[•] intermediate in the *in vitro* drug release studies, for which we hypothesized that influences the *in vitro* cytotoxicity of PGA-SS-Et-FAS conjugate. This hypothesis agrees with previously published data from Giraldo et al., that also reported the presence of FAS-Et-S[•] intermediate and correlated the prolonged effect of PGA-SS-Et-FAS in the treatment of spinal cord injury to the presence of FAS-Et-S[•] intermediate.⁵³ The generation of FAS-Et-S[•] derives from the partial disulfide exchange reaction that occurs as a result of the low pH present in endo-lysosomal organelles and the protonation of sulfur in a FAS-Et-S[•] metabolite intermediate, which inhibits the second step of the drug release mechanism.⁵⁴

Our data suggest the overall complexity of designing PDCs with disulfide linkers. We conclude that simple DTT-mediated drug release studies remain insufficient to elucidate the *in vitro* fate of PDCs and that more detailed drug release studies must be performed when analyzing *in vitro* models to secure better *in vitro-in vivo* correlations. By ensuring the adequate construction of an LC-MS/MS methodology for drug release studies, we can detect and

characterize metabolites that add valuable information for cytotoxicity data analysis. Finally, we must consider that not only the conformation and the size of PDCs may influence internalization but also the intracellular reductive environment and, consequently, the drug release site and rate within cells.

CONCLUSION

To the best of our knowledge, our study represents the first to provide evidence and clarify how the structural features of a drug can influence drug release from an Et-SS linker, repudiating the previous consideration of Et-SS as a universal linker. Hence, we suggest a new SS-Ph linker for conjugating drugs with secondary amino groups possessing low electronegativity.

We achieved significantly higher FAS release from PGA-Ph-SS-FAS than from PGA-Et-SS-FAS in MBA-MD-231 *in vitro* models; however, higher drug release does not always provide the higher toxicity needed for TNBC treatment. Therefore, the release behavior of PDCs should be investigated both in the cell medium and intracellularly when designing the PDCs on a case-by-case basis instead of mimicking the reductive environment with 5 mM DTT. In the future, we hope to explore more sophisticated real-time drug release monitoring methods to accurately evaluate and predict the treatment outcomes *in vivo*.

Notably, the elucidation of metabolites in the drug release studies with fit-for-purpose analytical protocols and an exploration of the influence of linkers on the PDCs conformation must be implemented to better understand PDC fate in the biological environment as well as a better understanding of PDC internalization, which represents another crucial aspect in carefully tuning drug release and activity profiles to design efficient and safe drug delivery systems. Understanding how varied biological environments influence PDC stability and activity must also be thoroughly investigated and incorporated to establish adequate design criteria for a candidate suitable for further studies.

Ultimately, our findings portray how adequate experimental planning, development of characterization protocols, and multivariate analysis could foster a better rational design of personalized PDCs with a high degree of quality control that supports higher confidence in obtained results.

EXPERIMENTAL SECTION

Materials. Diisopropylethylamine (DIEA), DL-dithiothreitol (DTT), cysteamine hydrochloride, dimethyl sulfoxide (DMSO) anhydrous, ethyl acetate, and methanol (LC-MS grade) were obtained from Sigma-Aldrich (St. Louis, United States). Celite 545, diethyl ether, dichloromethane (DCM), and deuterated solvents such as deuterated oxide (D₂O) were purchased from VWR chemicals (Radnor, US). Silica 60A 20–45-micron, water (LC-MS grade), ammonium formate, triethylamine (TEA), and formic acid (LC-MS grade) were purchased from Fisher Scientific (Pittsburgh, US). Vivaspin 10 kDa was obtained from Sartorius AG (Göttingen, Germany). Sand 40-100 mesh was provided by

ACROS organics (Geel, Belgium). Acetonitrile (ACN), chloroform, dimethylformamide (DMF), and methanol were purchased from Scharlab (Barcelona, Spain). 4-nitrophenyl-2-(pyridine-yl)disulfanyl ethyl carbonate and 4-nitrophenyl-4-(pyridine-2yl)disulfanyl benzyl carbonate were purchased from Fluorochem (UK). All the drugs (dinaciclib - DIN, resiquimod - RES, niraparib - NIRA, and rucaparib - RUCA) were purchased from MedKoo Biosciences (Morrisville, US) except for fasudil hydrochloride (FAS) that was obtained from Xingcheng Chempharm Co. Ltd (Zhejiang, China). Poly-L-glutamic acid (PGA) and PGA-SS-Et-FAS were kindly provided by Polymer Therapeutic Solutions SL (Valencia, Spain). Acetonitrile (LC-MS grade) was obtained from AppliChem GmbH. 4-dimethylaminopyridine (DMAP) was obtained from Honeywell Fluka (Pittsburgh, US). 4-(4,6-Dimethoxy-1,3,5-triazin-2-yl)-4-methyl morpholinium (DMTMM) chloride (DMTMM·BF₄) was synthesized according to literature.⁵⁵

Synthesis and Characterization of Drug-Linkers. All drug-linker synthetic reactions were performed following the same methodology. Differences in reagents, amounts, reaction time, and solvents are detailed in Table S1. Each reaction was performed under anhydrous conditions with nitrogen flow at a defined temperature. First, the drug and the linker were dissolved separately in appropriate solvents under vigorous stirring. The linker solution was added dropwise to the drug solution, and finally, DMAP and/or TEA were added. The reaction was monitored with thin-layer chromatography and a direct MS Q1 scan. Liquid-liquid extraction (LLE) and a silica column were implemented in the purification step. If the obtained product was not soluble in ethyl acetate, LLE was not performed, and the product was repeatedly dried in the rotavapor to remove TEA. The mixture was extracted with ethyl acetate and washed with water (three times) and brine (three times). The organic layer was dried with anhydrous magnesium sulfate. The filtrate was then evaporated under a vacuum and purified by column chromatography in DCM:MeOH. Fractions containing the product were joined, and the solvent was evaporated under a vacuum. The identity of the synthesized product was confirmed with a Q1 MS scan.

Synthesis and Characterization of PDCs. Prior to polymer conjugation, the drug-linker product was conjugated to cysteamine. The drug linker (1 equivalent, 10 mg/ml) was dissolved in DMSO. Then, cysteamine (1.2 equivalents, dissolved in dimethyl sulfoxide (DMSO) and added dropwise over the drug-linker solution). The reaction was left for three hours at 80°C, precipitated in fresh diethyl ether (1:10), reprecipitated from methanol (MeOH) to fresh diethyl ether, and dried with the vacuum pump. The identity of the synthesized product was confirmed with a Q1 MS scan.

The drug-linker-cysteamine was then conjugated with poly-L-glutamic acid (PGA) (n=100). In general, PGA was dissolved in anhydrous DMSO at 30 mg/ml with stirring, followed by activating the percentage required of the acid groups with DMTMM BF₄ (2 equivalents with respect to the drug linker) for 30 min. Drug-linker-cysteamine, dissolved in DMSO, was added to the main solution, and the pH was

adjusted to 8 with DIEA. The reaction was monitored by thin-layer chromatography and allowed to react for 48 h at room temperature. The product was precipitated twice from fresh diethyl ether (1:10). The total drug loading, in all cases, was determined by UV-vis and the free drug content by LC-MS/MS analysis. Milli-Q water was added to the solid to obtain the sodium salt of the conjugate for water solubility. A 0.5 M NaHCO₃ solution was added dropwise with vortexing until the complete dissolution of the solid. Using Milli-Q water, the solution was purified by a Vivaspin device (3 kDa cutoff). The upper content was lyophilized, and the product was stored at -20°C until further use.

TDL determination by UV-Vis. Fasudil solutions in MeOH were used as standard stock solutions, while the working standard solutions were obtained by dilution with Milli-Q water. The total drug loading of the conjugates was determined at three concentration levels (0.1 mg/ml, 0.25 mg/ml, and 0.5 mg/ml in Milli-Q water) by measuring the absorbance at 323 nm (for fasudil). A solution of linear PGA in water at the same concentration as the conjugates was used as a blank. UV-Vis measurements were performed using JASCO V-630 spectrophotometer at 25°C with a 1.0 cm quartz cell and a spectral bandwidth of 0.5 nm.

FD determination by LC-MS/MS. 3 mg of PDCs were suspended in 500 µl MeOH (LC-MS grade), vortexed for 5 min, centrifuged for 10 min at 11,000 rpm to remove the pellet, and then the solution was subjected to LC-MS/MS analysis.

NMR spectroscopy. 10 mg/ml PDCs solutions in deuterated water were analyzed at 27°C on a 300 Ultrashield™ spectrometer (Bruker, USA), and data were processed with the software TopSpin and Mestrenova.

Drug release from Drug-linkers with DTT. Drug-linkers (1 mg/ml) were incubated at 37 °C, pH 5 (10 mM ammonium formate buffer LC-MS grade), and in the presence of 5 mM DTT (mimicking lysosomal conditions). 100 µl samples were isolated at various time points (0, 2, 4, 6, 24, 48, 72, and 144 h) and analyzed with LC-MS/MS. A calibration curve for each drug was used to quantify the total drug release from their drug linker. Drug linkers incubated at 37 °C, 10 µM DTT, and pH 7.4 were used as control samples (mimicking extracellular conditions).

Fasudil Release from PDCs in Cell Medium and MBA-231-TNBC Cells. MDA-MB-231 cell lines were seeded in a 96-well plate at 15,625 cells/cm² for 2D and 31,250 cells/cm² for the 3D model. After 24 h incubation, the cells were incubated with FAS conjugated to PGA through Et-SS and Ph-SS at 200 µM fasudil equivalents. The cell and cell medium were separated at 72 h and prepared depending on the implemented in vitro cell model. The 2D MDA-MB-231 cells were collected by trypsinization and neutralization with a fresh cell medium, while 3D cell models were collected by centrifugation (10 min, 11,000, 4 °C). Cells were lysed by mixing with 400 µl lysis buffer (50 mM Tris HCl, 150 mM NaCl, 0.25 % triton-X 100, 0.5 % NP40) at 4°C for 30 min. The free and total FAS (free and conjugated to PGA) were quantified in cell medium and lysate. FAS as a free drug was extracted from the cell medium samples with the protocol optimized in the previous step (SI). In contrast, the

cell lysate was first lyophilized, and FAS was extracted with 100 µl methanol. Total FAS was determined by incubating the cell medium and cell lysate samples with 50 mM DTT for 24 h at 37 °C and then preparing the sample accordingly. Before injection in the LC-MS, 20% of 0.1 % FA was added in all samples to adjust the amount of water phase and improve the peak shape.

Data analysis. Design of experiment data analysis was performed in Design-Expert 12, the LC-MS/MS analysis in Analyst software, and the 3D graphics in Origin 8.0.

ASSOCIATED CONTENT

Supporting Information

Supporting Information is available free of charge containing additional data, including materials synthesis and characterizations, design of experiment, and LC-MS/MS method.

AUTHOR INFORMATION

Corresponding Authors

***Inmaculada Conejos Sanchez** - Polymer Therapeutics Laboratory, Centro de Investigación Príncipe Felipe (CIPF), CIBERONC, Eduardo Primo Yufera 3, 46012 Valencia – Spain; e-mail: iconijos@cipf.es, ORCID: 0000-0002-4196-0855

***María J. Vicent** - Polymer Therapeutics Laboratory, Centro de Investigación Príncipe Felipe (CIPF), CIBERONC, Eduardo Primo Yufera 3, 46012 Valencia – Spain, e-mail: mjvicent@cipf.es, ORCID: 0000-0001-7771-3373

Authors

Snežana Đorđević - Polymer Therapeutics Laboratory, Centro de Investigación Príncipe Felipe (CIPF), CIBERONC, Eduardo Primo Yufera 3, 46012 Valencia – Spain; e-mail: iconijos@cipf.es, ORCID: 0000-0002-4196-0855

Maria Medel - Polymer Therapeutics Laboratory, Centro de Investigación Príncipe Felipe (CIPF), CIBERONC, Eduardo Primo Yufera 3, 46012 Valencia – Spain; e-mail: iconijos@cipf.es, ORCID: 0000-0002-4196-0855

Justine Hillaert - Polymer Therapeutics Laboratory, Centro de Investigación Príncipe Felipe (CIPF), CIBERONC, Eduardo Primo Yufera 3, 46012 Valencia – Spain; e-mail: iconijos@cipf.es, ORCID: 0000-0002-4196-0855

Esther Masià - Polymer Therapeutics Laboratory, Centro de Investigación Príncipe Felipe (CIPF), CIBERONC, Eduardo Primo Yufera 3, 46012 Valencia – Spain; e-mail: iconijos@cipf.es, ORCID: 0000-0002-4196-0855

Author Contributions

Conceptualization S.Đ., I.C.J., M.M.; methodology S.Đ., I.C.J., M.M.; investigation S.Đ., I.C.J., M.M., J.H., and E.M.; data curation S.Đ.; writing—original draft preparation S.Đ.; writing—review and editing I.C.J., M.J.V.; work supervision and funding acquisition, M.J.V. All authors have read and agreed to the published version of the manuscript.

Funding Sources

A This work was supported by the Fundació La Caixa Health Research Grant (LCF/PR/HR19/52160021- NanoPanTher)

and the Spanish Ministry of Economy and Competitiveness (grant PID2019-108806RB-I00). ICS is funded by AECC Junior Grant Ref INVES211323CONE. Part of the equipment employed was funded by the Generalitat Valenciana and co-financed with FEDER funds (PO FEDER of Comunitat Valenciana 2014–2020).

ACKNOWLEDGMENT

The authors thank Stuart P. Atkinson for English editing and aid in manuscript construction.

ABBREVIATIONS

2D- two-dimensional; 3D- three-dimensional; ACN- acetonitrile; ANOVA- analysis of variance; AF4-UV/Vis-MALS asymmetric flow field flow fractionation – UV/Vis – multi-angle light scattering; CMS- critical micellar concentration; PDCs- polymer-drug conjugates; DIEA- Diisopropylethylamine; DCM- dichloromethane; DoE- design of experiment; DMF- dimethyl formamide; DMSO- dimethyl sulfoxide; DIN-dinacilib; DTT-dithiothreitol; dPBS- Dulbecco's phosphate-buffered saline; ESI- electrospray ionization; Et-SS – ethyl disulfide; FD- free drug; FAS- fasudil; FA- formic acid; GSSG- glutathione disulfide; GSH – glutathione; LLE- liquid-liquid extraction; LC-MS/MS liquid chromatography – mass spectrometry, MeOH- methanol; MRM- multiple reaction monitoring; NMR- nuclear magnetic resonance; NIRA- niraparib; pDTB- para dithiobenzyl; Ph-SS- phenyl disulfide; PGA- poly-L-glutamic acid; RUCA- rucaparib; RES- resiquimod; SS-SIL – disulphide self immolative linkers; S/N- signal-to-noise ratio; SD- standard deviation; TDL-total drug loading; TNBC- triple negative breast cancer; TEA- triethylamine; TLC- thin-layer chromatography; UV/Vis – ultraviolet visible.

REFERENCES

(1) Metselaar, J. M.; Lammers, T. Challenges in Nanomedicine Clinical Translation. *Drug Deliv. Transl. Res.* **2020**, *10* (3), 721–725.

(2) Bhatia, S. N.; Chen, X.; Dobrovolskaia, M. A.; Lammers, T. Cancer Nanomedicine. *Nat. Rev. Cancer* **2022**, *22* (10), 550–556.

(3) Hare, J. I.; Lammers, T.; Ashford, M. B.; Puri, S.; Storm, G.; Barry, S. T. Challenges and Strategies in Anti-Cancer Nanomedicine Development: An Industry Perspective. *Adv. Drug Deliv. Rev.* **2017**, *108*, 25–38.

(4) Zhang, Y.; He, P.; Zhang, P.; Yi, X.; Xiao, C.; Chen, X. Polypeptides-Drug Conjugates for Anticancer Therapy. *Adv. Healthc. Mater.* **2021**, *10* (11), 2001974.

(5) Aderibigbe, B. A.; Mukaya, H. E. *Polymer Therapeutics: Design, Application, and Pharmacokinetics*; Elsevier Inc., 2017.

(6) Li, C.; Wallace, S. Polymer-Drug Conjugates: Recent Development in Clinical Oncology. *Adv. Drug Deliv. Rev.* **2008**, *60* (8), 886–898.

(7) Fang, J.; Islam, W.; Maeda, H. Exploiting the Dynamics of the EPR Effect and Strategies to Improve the Therapeutic Effects of Nanomedicines by Using EPR Effect Enhancers. *Adv. Drug Deliv. Rev.* **2020**, *157*, 142–160.

(8) El-sawy, H. S.; Al-abd, A.; Ahmed, T.; El-say, K. M.; Torchilin, V. P. Stimuli-Responsive Nano-Architectures Drug Delivery Systems to Solid Tumor Microenvironment: Past, Present and Future Perspectives Stimuli-Responsive Nano-Architectures Drug Delivery Systems to Solid Tumor Department of Pharmaceutics and Pharmaceutical Techn. *ACS Nano* **2018**, *12* (11), 10636–10664.

(9) Melnyk, T.; Đorđević, S.; Conejos-Sánchez, I.; Vicent, M. J. Therapeutic Potential of Polypeptide-Based Conjugates: Rational Design and Analytical Tools That Can Boost Clinical Translation. *Adv. Drug Deliv. Rev.* **2020**, *160*, 136–169.

(10) Wang, Q.; Guan, J.; Wan, J.; Li, Z. Disulfide Based Prodrugs for Cancer Therapy. *RSC Adv.* **2020**, *10* (41), 24397–24409.

(11) Jorgenson, T. C.; Zhong, W.; Oberley, T. D. Redox Imbalance and Biochemical Changes in Cancer. *Cancer Res.* **2013**, *73* (20), 6118.

(12) Brülisauer, L.; Gauthier, M. A.; Leroux, J. C. Disulfide-Containing Parenteral Delivery Systems and Their Redox-Biological Fate. *J. Control. Release* **2014**, *195*, 147–154.

(13) Blencowe, C. A.; Russell, A. T.; Greco, F.; Hayes, W.; Thornthwaite, D. W. Self-Immolative Linkers in Polymeric Delivery Systems. *Polym. Chem.* **2011**, *2* (4), 773–790.

(14) Bach, R. D.; Dmitrenko, O.; Thorpe, C. Mechanism of Thiolate-Disulfide Interchange Reactions in Biochemistry. *J. Org. Chem.* **2008**, *73* (1), 12–21.

(15) Lee, M. H.; Sessler, J. L.; Kim, J. S. Disulfide-Based Multifunctional Conjugates for Targeted Theranostic Drug Delivery. *Acc. Chem. Res.* **2015**, *48* (11), 2935–2946.

(16) Zhang, D.; Pillow, T. H.; Ma, Y.; Cruz-Chuh, J. Dela; Kozak, K. R.; Sadowsky, J. D.; Lewis Phillips, G. D.; Guo, J.; Darwish, M.; Fan, P.; Chen, J.; He, C.; Wang, T.; Yao, H.; Xu, Z.; Chen, J.; Wai, J.; Pei, Z.; Hop, C. E. C. A.; Khojasteh, S. C.; Dragovich, P. S. Linker Immolation Determines Cell Killing Activity of Disulfide-Linked Pyrrolonebenzodiazepine Antibody-Drug Conjugates. *ACS Med. Chem. Lett.* **2016**, *7* (11), 988–993.

(17) Guo, X.; Cheng, Y.; Zhao, X.; Luo, Y.; Chen, J.; Yuan, W. E. Advances in Redox-Responsive Drug Delivery Systems of Tumor Microenvironment. *J. Nanobiotechnology* **2018**, *16* (1), 1–10.

(18) Zhang, X.; Han, L.; Liu, M.; Wang, K.; Tao, L.; Wan, Q.; Wei, Y. Recent Progress and Advances in Redox-Responsive Polymers as Controlled Delivery Nanoplatfoms. *Mater. Chem. Front.* **2017**, *1* (5), 807–822.

(19) Wang, Y.; Wang, X.; Deng, F.; Zheng, N.; Liang, Y.; Zhang, H.; He, B.; Dai, W.; Wang, X.; Zhang, Q. The Effect of Linkers on the Self-Assembling and Anti-Tumor Efficacy of Disulfide-Linked Doxorubicin Drug-Drug Conjugate Nanoparticles. *J. Control. Release* **2018**, *279*, 136–146.

(20) Jain, A. K.; Gund, M. G.; Desai, D. C.; Borhade, N.; Senthilkumar, S. P.; Dhiman, M.; Mangu, N. K.; Mali, S. V.; Dubash, N. P.; Halder, S.; Satyam, A. Mutual Prodrugs Containing Bio-Cleavable and Drug Releasable Disulfide Linkers. *Bioorg. Chem.* **2013**, *49*, 40–48.

(21) Leardi, R. Experimental Design in Chemistry: A Tutorial. *Anal. Chim. Acta* **2009**, *652* (1–2), 161–172.

(22) Miller, J. N.; Miller, J. C. *Chemometrics for Analytical Chemistry*; 2005.

(23) Kromidas, S. *Gradient HPLC for Practitioners - RP, LC-MS, Ion Analytics, Biochromatography, SFC, HILIC*; 2019.

(24) Huang, X.; Brazel, C. S. On the Importance and Mechanisms of Burst Release in Matrix-Controlled Drug Delivery Systems. *J. Control. Release* **2001**, *73* (2–3), 121–136.

(25) Deng, Z.; Hu, J.; Liu, S. Disulfide-Based Self-Immolative Linkers and Functional Bioconjugates for Biological Applications. *Macromol. Rapid Commun.* **2020**, *41* (1), 1–14.

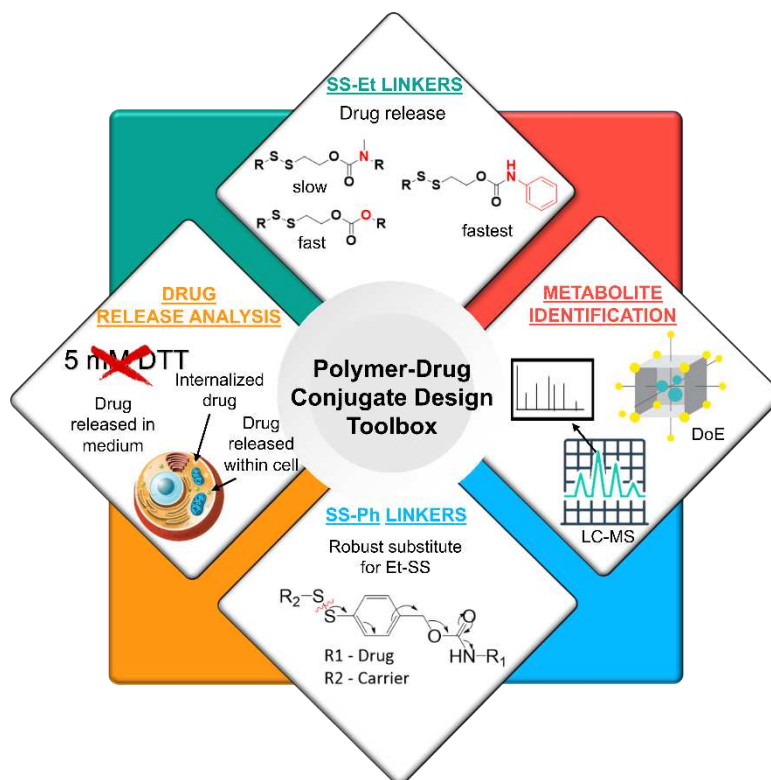
(26) Zheng, Y.; Shen, Y.; Meng, X.; Wu, Y.; Zhao, Y.; Wu, C. Stabilizing P-Dithiobenzyl Urethane Linkers without Rate-Limiting Self-Immolation for Traceless Drug Release. *ChemMedChem* **2019**, *14* (12), 1196–1203.

(27) Qian, L.; Fu, J.; Yuan, P.; Du, S.; Huang, W.; Li, L.; Yao, S. Q. Intracellular Delivery of Native Proteins Facilitated by Cell-Penetrating Poly(Disulfide)s. *Angew. Chem. Int. Ed. Engl.* **2018**, *57* (6), 1532–1536.

(28) Sun, T.; Morger, A.; Castagner, B.; Leroux, J. C. An Oral Redox-Sensitive Self-Immolating Prodrug Strategy. *Chem. Commun.* **2015**, *51* (26), 5721–5724.

(29) Kamaly, N.; Yameen, B.; Wu, J.; Farokhzad, O. C. Degradable Controlled-Release Polymers and Polymeric

- Nanoparticles: Mechanisms of Controlling Drug Release. *Chem. Rev.* **2016**, *116* (4), 2602–2663.
- (30) Duro-Castano, A.; Conejos-Sánchez, I.; Vicent, M. J. Peptide-Based Polymer Therapeutics. *Polymers (Basel)*. **2014**, *6*, 515–551.
- (31) Lendrem, D. W.; Lendrem, B. C.; Woods, D.; Rowland-Jones, R.; Burke, M.; Chatfield, M.; Isaacs, J. D.; Owen, M. R. Lost in Space: Design of Experiments and Scientific Exploration in a Hogarth Universe. *Drug Discov. Today* **2015**, *20* (11), 1365–1371.
- (32) Zagorodko, O.; Arroyo-Crespo, J. J.; Nebot, V. J.; Vicent, M. J. Polypeptide-Based Conjugates as Therapeutics: Opportunities and Challenges. *Macromol. Biosci.* **2017**, *17* (1).
- (33) Hsu, C. Y.; Chang, Z. F.; Lee, H. H. Immunohistochemical Evaluation of ROCK Activation in Invasive Breast Cancer. *BMC Cancer* **2015**, *15* (1), 1–9.
- (34) Barbosa, M. A. G.; Xavier, C. P. R.; Pereira, R. F.; Petrikaitė, V.; Vasconcelos, M. H. 3D Cell Culture Models as Recapitulators of the Tumor Microenvironment for the Screening of Anti-Cancer Drugs. *Cancers (Basel)*. **2021**, *14* (1).
- (35) Tu, J.; Xu, M.; Parvez, S.; Peterson, R. T.; Franzini, R. M. Bioorthogonal Removal of 3-Isoocyanopropyl Groups Enables the Controlled Release of Fluorophores and Drugs in Vivo. *J. Am. Chem. Soc.* **2018**, *140* (27), 8410–8414.
- (36) Stöckmann, H.; Neves, A. A.; Stairs, S.; Brindle, K. M.; Leeper, F. J. Exploring Isonitrile-Based Click Chemistry for Ligation with Biomolecules. *Org. Biomol. Chem.* **2011**, *9* (21), 7303–7305.
- (37) Shao, Z.; Liu, W.; Tao, H.; Liu, F.; Zeng, R.; Champagne, P. A.; Cao, Y.; Houk, K. N.; Liang, Y. Bioorthogonal Release of Sulfonamides and Mutually Orthogonal Liberation of Two Drugs. *Chem. Commun.* **2018**, *54* (100), 14089–14092.
- (38) Haba, K.; Popkov, M.; Shamis, M.; Lerner, R. A.; Barbas, C. F.; Shabat, D. Single-Triggered Trimeric Prodrugs. *Angew. Chemie Int. Ed.* **2005**, *44* (5), 716–720.
- (39) Huvelle, S.; Alouane, A.; Le Saux, T.; Jullien, L.; Schmidt, F. Syntheses and Kinetic Studies of Cyclisation-Based Self-Immolative Spacers. *Org. Biomol. Chem.* **2017**, *15* (16), 3435–3443.
- (40) Deng, Z.; Hu, J.; Liu, S. Disulfide-Based Self-Immolative Linkers and Functional Bioconjugates for Biological Applications. *Macromol. Rapid Commun.* **2020**, *41* (1), 1900531.
- (41) Mura, S.; Nicolas, J.; Couvreur, P. Stimuli-Responsive Nanocarriers for Drug Delivery. *Nat. Mater.* **2013**, *12* (11), 991–1003.
- (42) Schafer, F. Q.; Buettner, G. R. Redox Environment of the Cell as Viewed through the Redox State of the Glutathione Disulfide/Glutathione Couple. *Free Radic. Biol. Med.* **2001**, *30* (11), 1191–1212.
- (43) Vollhardt, P.; Schore, N. *Organic Chemistry: Structure and Function*, 8th ed.; 2018.
- (44) Ni, D.; Ding, H.; Liu, S.; Yue, H.; Bao, Y.; Wang, Z.; Su, Z.; Wei, W.; Ma, G. Superior Intratumoral Penetration of Paclitaxel Nanodots Strengthens Tumor Restriction and Metastasis Prevention. *Small* **2015**, *11* (21), 2518–2526.
- (45) Bugno, J.; Hsu, H. J.; Pearson, R. M.; Noh, H.; Hong, S. Size and Surface Charge of Engineered Poly(Amidoamine) Dendrimers Modulate Tumor Accumulation and Penetration: A Model Study Using Multicellular Tumor Spheroids. *Mol. Pharm.* **2016**, *13* (7), 2155–2163.
- (46) Goodman, T. T.; Olive, P. L.; Pun, S. H. Increased Nanoparticle Penetration in Collagenase-Treated Multicellular Spheroids. *Int. J. Nanomedicine* **2007**, *2* (2), 265.
- (47) Goodman, T. T.; Chen, J.; Matveev, K.; Pun, S. H. Spatio-Temporal Modeling of Nanoparticle Delivery to Multicellular Tumor Spheroids. *Biotechnol. Bioeng.* **2008**, *101* (2), 388–399.
- (48) Zhang, C.; Gau, E.; Sun, W.; Zhu, J.; Schmidt, B. M.; Pich, A.; Shi, X. Influence of Size, Crosslinking Degree and Surface Structure of Poly(ϵ -N-Vinylcaprolactam)-Based Microgels on Their Penetration into Multicellular Tumor Spheroids. *Biomater. Sci.* **2019**, *7* (11), 4738–4747.
- (49) Lazzari, G.; Couvreur, P.; Mura, S. Multicellular Tumor Spheroids: A Relevant 3D Model for the in Vitro Preclinical Investigation of Polymer Nanomedicines. *Polym. Chem.* **2017**, *8* (34), 4947–4969.
- (50) Brülisauer, L.; Gauthier, M. A.; Leroux, J. C. Disulfide-Containing Parenteral Delivery Systems and Their Redox-Biological Fate. *J. Control. Release* **2014**, *195*, 147–154.
- (51) Bergquist, J.; Turner, C. Analytical Chemistry for a Sustainable Society – Trends and Implications. *Anal. Bioanal. Chem.* **2018**, *410* (14), 3235–3237.
- (52) Hecht, E. S.; Oberg, A. L.; Muddiman, D. C. Optimizing Mass Spectrometry Analyses: A Tailored Review on the Utility of Design of Experiments. *J. Am. Soc. Mass Spectrom.* **2016**, *27* (5), 767–785.
- (53) Giraldo, E.; Nebot, V. J.; Đorđević, S.; Requejo-Aguilar, R.; Alastrue-Agudo, A.; Zagorodko, O.; Armiñan, A.; Martínez-Rojas, B.; Vicent, M. J.; Moreno-Manzano, V. A Rationally Designed Self-Immolative Linker Enhances the Synergism between a Polymer-Rock Inhibitor Conjugate and Neural Progenitor Cells in the Treatment of Spinal Cord Injury. *Biomaterials* **2021**, 276.
- (54) Bauhuber, S.; Hozsa, C.; Breunig, M.; Göpferich, A. Delivery of Nucleic Acids via Disulfide-Based Carrier Systems. *Adv. Mater.* **2009**, *21* (32–33), 3286–3306.
- (55) Kunishima, M.; Kawachi, C.; Morita, J.; Terao, K.; Iwasaki, F.; Tani, S. 4-(4,6-Dimethoxy-1,3,5-Triazin-2-Yl)-4-Methyl-Morpholinium Chloride: An Efficient Condensing Agent Leading to the Formation of Amides and Esters. *Tetrahedron* **1999**, *55* (46), 13159–13170.



Graphical abstract

Supplementary Information

Critical Design Strategies Supporting Optimized Drug Release from Polymer-Drug Conjugates

Snežana Đorđević, María Medel, Justine Hillaert, Esther Masià, Inmaculada Conejos-

Sánchez, María J. Vicent**

Polymer Therapeutics Laboratory, Centro de Investigación Príncipe Felipe (CIPF) and
CIBERONC, Valencia, Spain

Direct mass spectrometry scan. All samples monitored by mass spectrometry (MS) Q1 scan were analyzed by 20 μ l direct injection with 50 % ACN and 50 % H₂O (0.1 % formic acid - FA) as mobile phase, and 0.5 ml/min flow rate, while the MS conditions were as follows: curtain gas 20 V, ion source temperature 250 °C, gas 1 45 V, gas 2 45 V, ion source voltage 5500 V, declustering potential 62 V, and entrance potential 2 V.

LC-MS/MS for the determination of FAS, DIN, NIRA, RUCA, and RES. The development of the LC-MS/MS method was performed using the Design of Experiments (DoE) approach through the DesignExpert12 software. The LC-MS/MS analysis was performed using an ExionLC system comprising a pump, AC autosampler, AC Column oven, and AB Sciex QTRAP 4500 (all Sciex, Singapore). Eluent A was H₂O with 0.1 % FA, and eluent B was ACN. All runs were performed using a Kinetex Byphenyl column (100 mm \times 3.0 mm, 2.6 μ m, 100 Å) (Phenomenex, USA) with a 20 μ L injection volume. The drugs were detected in positive electrospray mode with multiple reaction monitoring scans. The validation parameters evaluated were linearity, the limit of quantification (LOQ), the limit of detection (LOD), and accuracy (Table S2). A low LOQ and a medium LOQ control standard solutions were analyzed each day before analyzing the sample to confirm the quality of LC-MS/MS response. Methanol with 0.1% FA was used as a blank control sample.

Asymmetric flow field flow fractionation for size determination. The AF4 methodology was performed on the Postnova Analytics (Landsberg, Germany) fractionation channel equipped with a regenerative cellulose membrane with a 10 kDa cut-off and a 350 μ m spacer. Samples were dissolved in 10 mM sodium phosphate at 2 mg/ml concentration and analyzed with 10 mM sodium phosphate and 0.01 % sodium azide as a mobile phase. The fractionation method consisted of a 40 μ l injection volume, 5 min injection time, 0.5 ml/min detector flow, 1 ml/min cross-flow, and a total run time

of 46.5 min. The detectors employed in the method were: a UV detector (280 nm), a refractometer, and a multi-angle light scattering detector.

Protocol optimization for fasudil extraction from cell medium. 100 μ l cell medium was spiked with 200 μ M FAS, followed by protein precipitation with 250 μ l ACN and vortex mixing for 3 min. After centrifugation (10 min at 11,000 rpm), the supernatant was collected, and the sample was prepared with six different protocols (the conditions shown in Figure S10) and analyzed by LC-MS/MS. The final extraction protocol was chosen according to the highest fasudil recovery (the ratio between the extracted and the expected amount of fasudil).

Cell culture conditions

The human triple-negative breast cancer cell line MDA-MB-231 (HTB-26™ provided by the ATCC) was used to evaluate the biological activity of PDCs and related compounds. The conventional 2D cell culture model was performed in DMEN/F12 culture medium supplemented with 10% inactivated fetal bovine serum and 1% penicillin/streptomycin (Gibco). To develop the 3D cell culture, cells were grown in DMEN/F12 culture medium supplemented with B27 minus vitamin A, EGF, and 1% penicillin/streptomycin after seeding in ultra-low attachment plates (ULA P96 ref. 3474, Corning).

In vitro cytotoxicity assay

Cell viability assays were performed with CellTiter 96® AQueous Non-Radioactive Cell Proliferation Assay following the manufacturer's protocol (Promega). For the 2D model, cells were seeded in a 96-well plate at 15,625 cells/cm²; for the 3D model, 31,250 cells/cm² were incubated for 24 h before adding treatments. After 72 h, the cells were incubated for 6 h with a mixture of MTS and PMS (ratio 20:1) and measured directly at 490 nm on CLARIOstar multiplate reader (BMG LABTECH).

GSH/GSSG assay

GSH and GSSH were detected by GSH/GSSG-Glo™ Assay luminescence kit (V6611, Promega), which was used in both 2D and 3D models following the manufacturer's recommendations. 2D cultured cells were seeded directly onto a 96-well white plate for cell culture at 15,625 cells/cm², while 3D model cells were seeded in their corresponding 96-well ULA plate at 31,250 cells/cm². The GSH/GSSG assay was performed 24 h after seeding. For the 3D model, the test was performed on the ULA plate itself and just before reading the sample was transferred to a white plate suitable for luminescence testing. Readings were performed using a CLARIOstar multiplate reader (BMG LABTECH). The absorption levels obtained from GSH/GSSG-Glo™ Assay luminescence kit were used for the determination of GSH and GSSG concentration in our samples. Notably, the obtained concentration needs to be recalculated back to the intracellular concentration by implementing the known cell number and independent cell volume for each in vitro model.

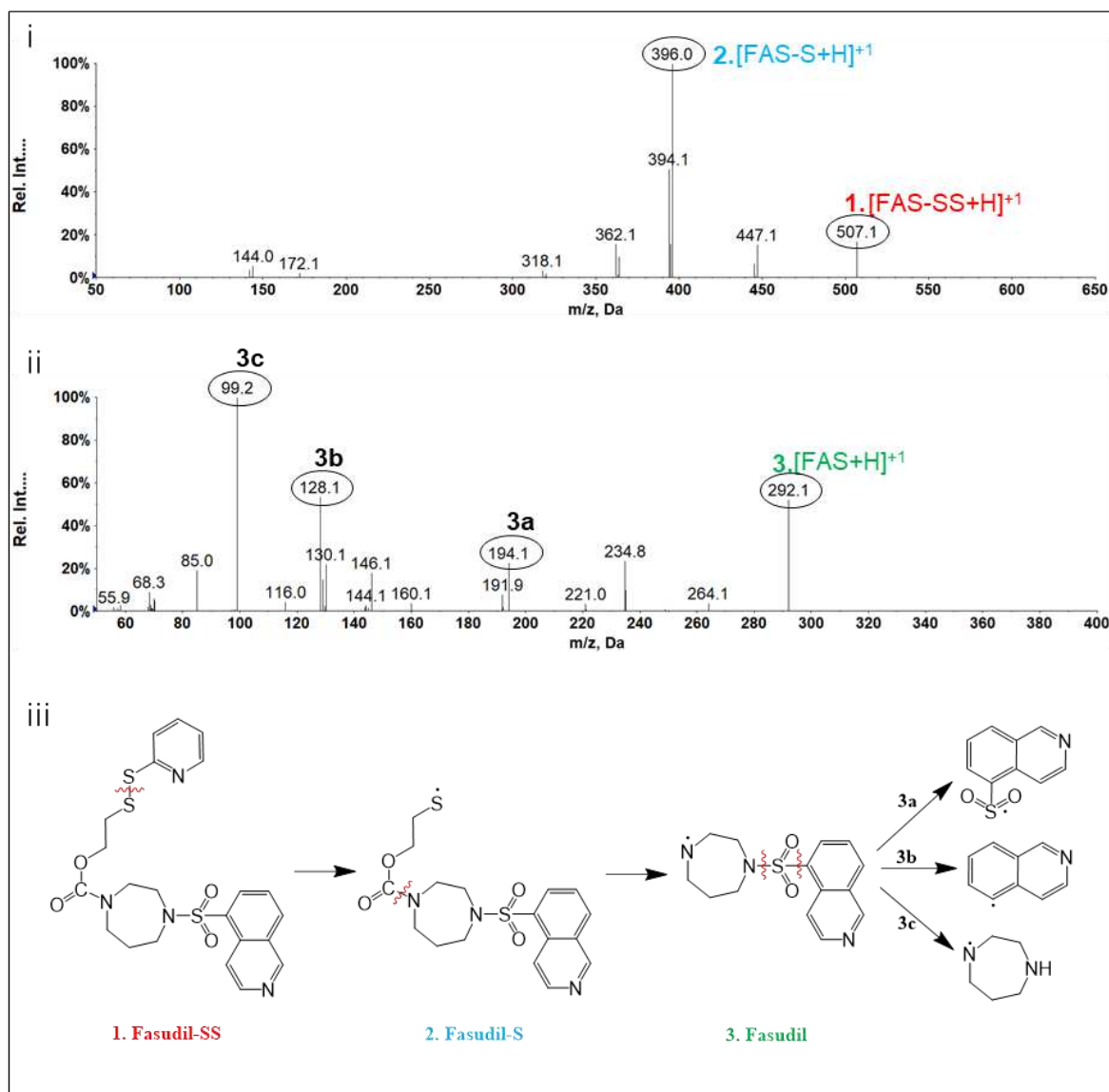


Figure S1. Qualitative analysis of fasudil-ethyl-disulfide drug linkers (FAS-Et-SS). Direct MS analysis enabled the identification according to the MS/MS spectra of (i) drug linker, (ii) drug, and (iii) the fragmentation mechanism.

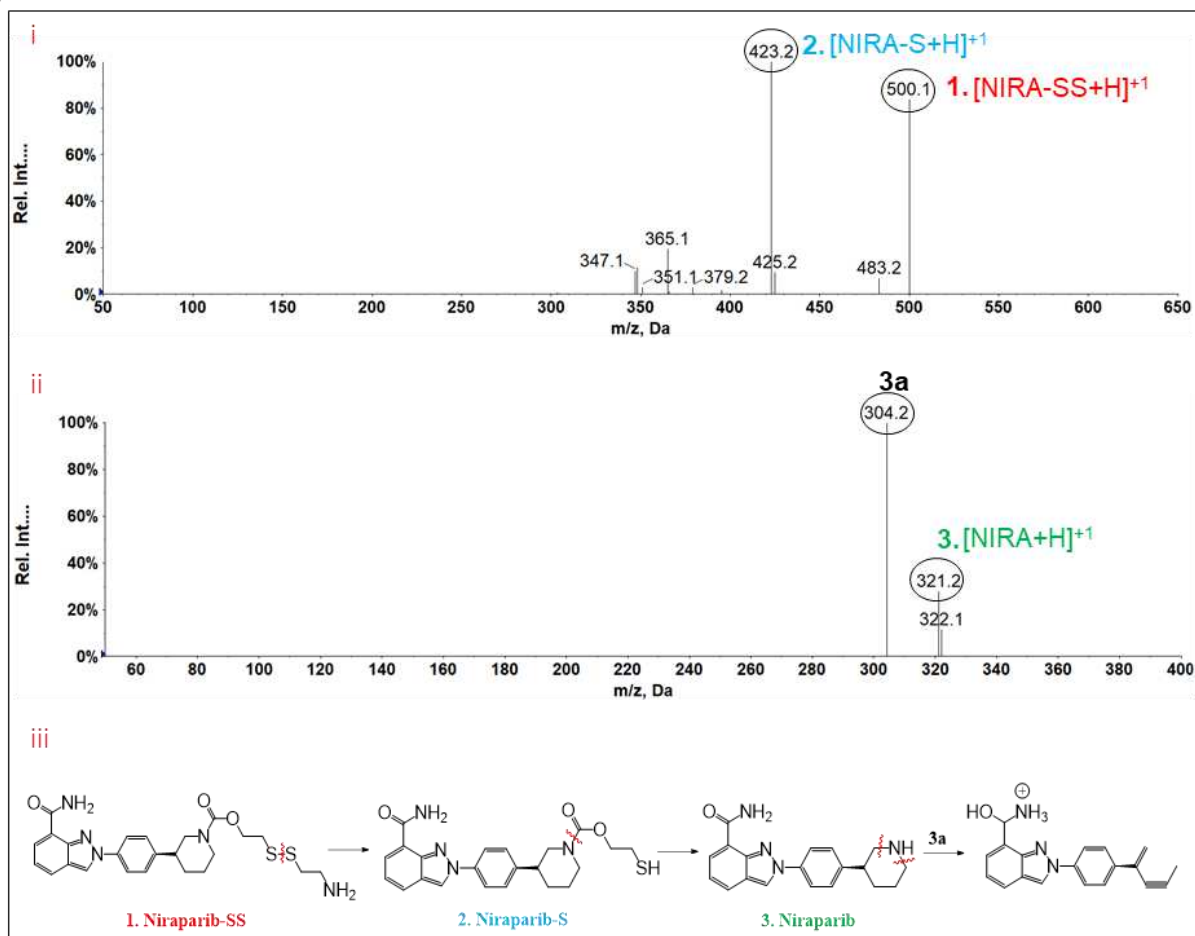


Figure S2. Qualitative analysis of niraparib-ethyl-disulfide drug linkers (NIRA-Et-SS). Direct MS analysis enabled the identification according to the MS/MS spectra of (i) drug linker, (ii) drug, and (iii) the fragmentation mechanism.

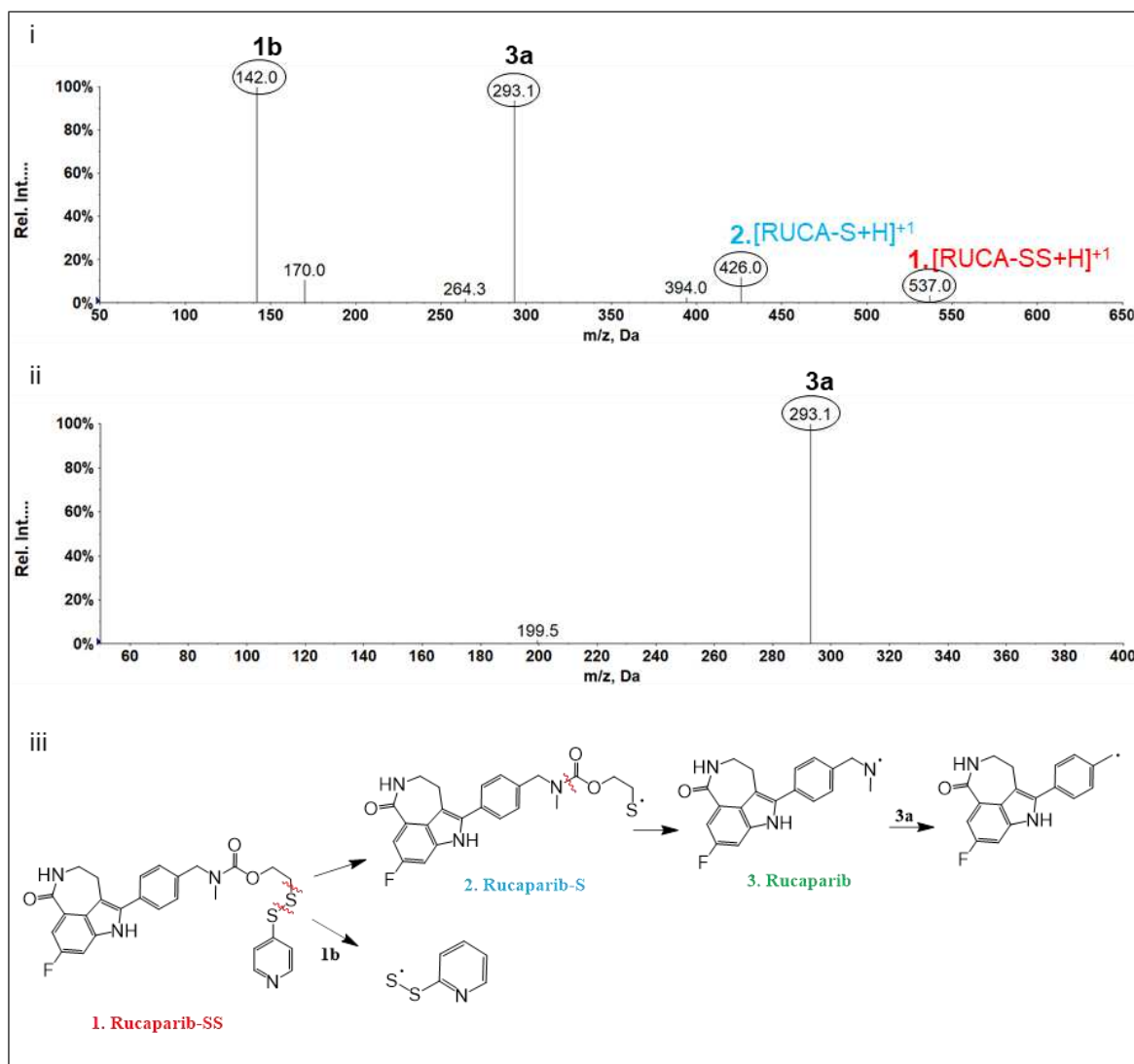


Figure S3. Qualitative analysis of rucaparib-ethyl-disulfide drug linkers (RUCA-Et-SS). Direct MS analysis enabled the identification according to the MS/MS spectra of (i) drug linker, (ii) drug, and (iii) the fragmentation mechanism.

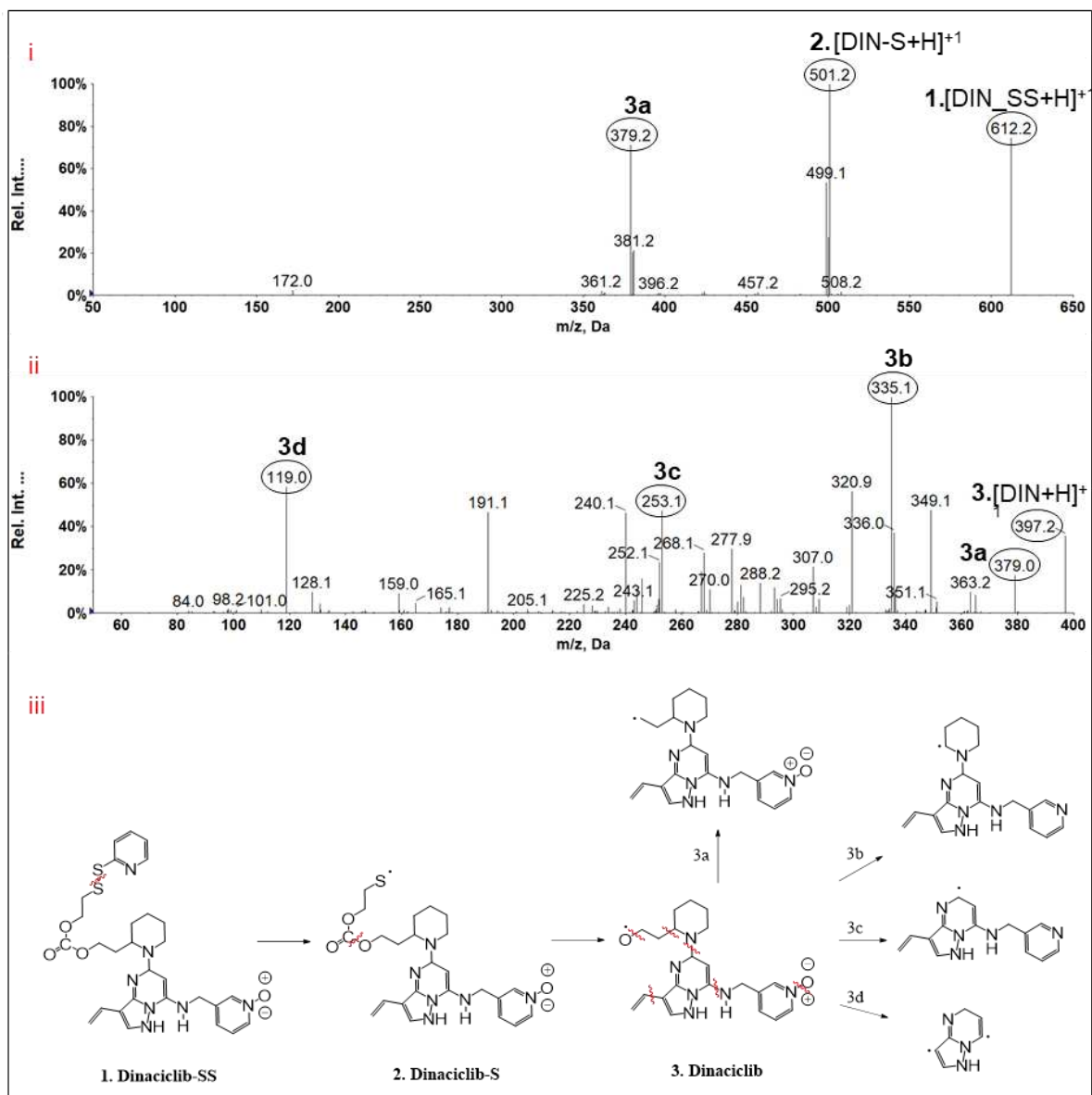


Figure S4. Qualitative analysis of dinacilib-ethyl-disulfide drug linkers (DIN-Et-SS).

Direct MS analysis enabled the identification according to the MS/MS spectra of (i) drug linker, (ii) drug, and (iii) the fragmentation mechanism.

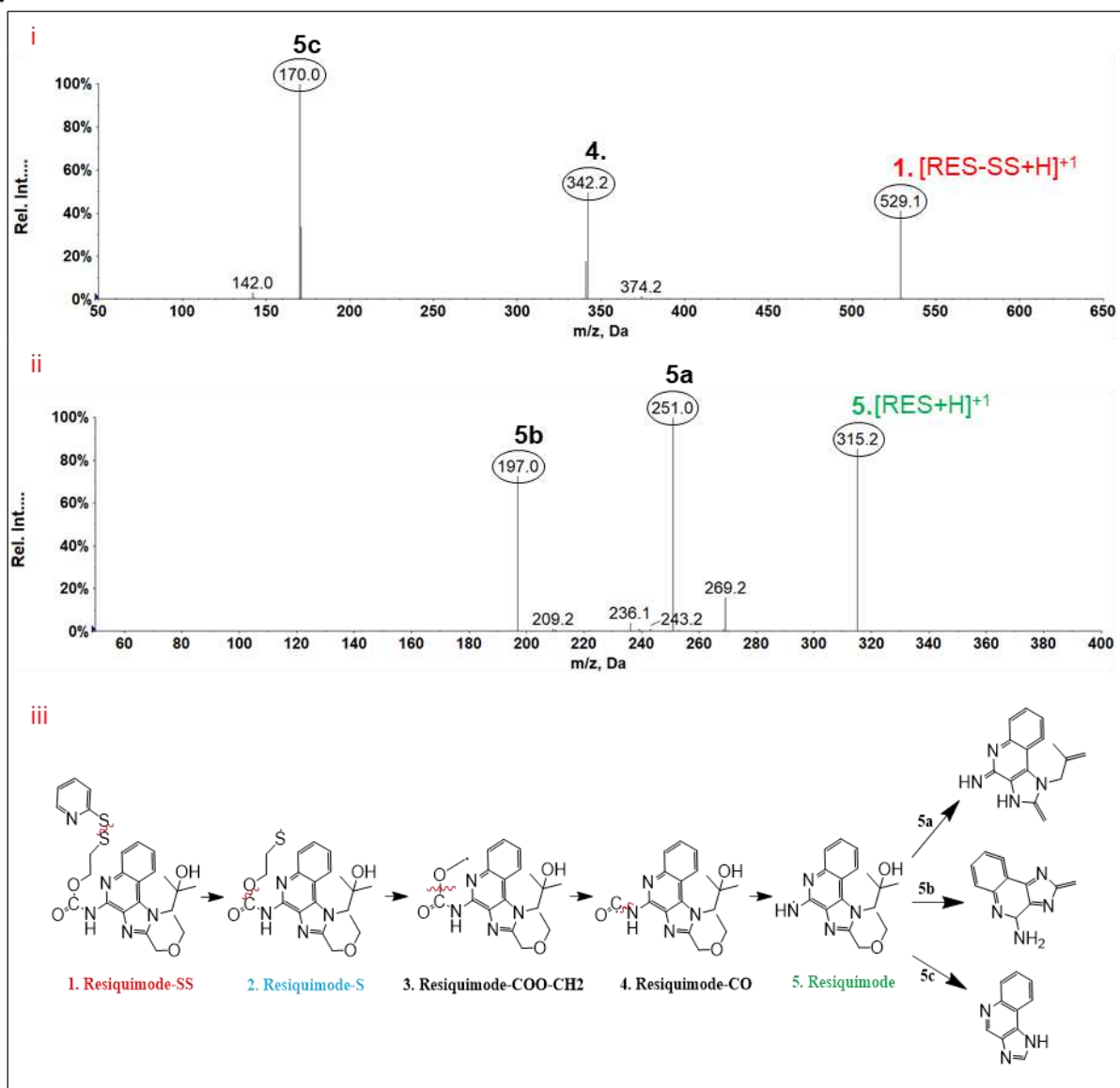


Figure S5. Qualitative analysis of resiquimod-ethyl-disulfide drug linkers (RES-Et-SS). Direct MS analysis enabled the identification according to the MS/MS spectra of (i) drug linker, (ii) drug, and (iii) the fragmentation mechanism.

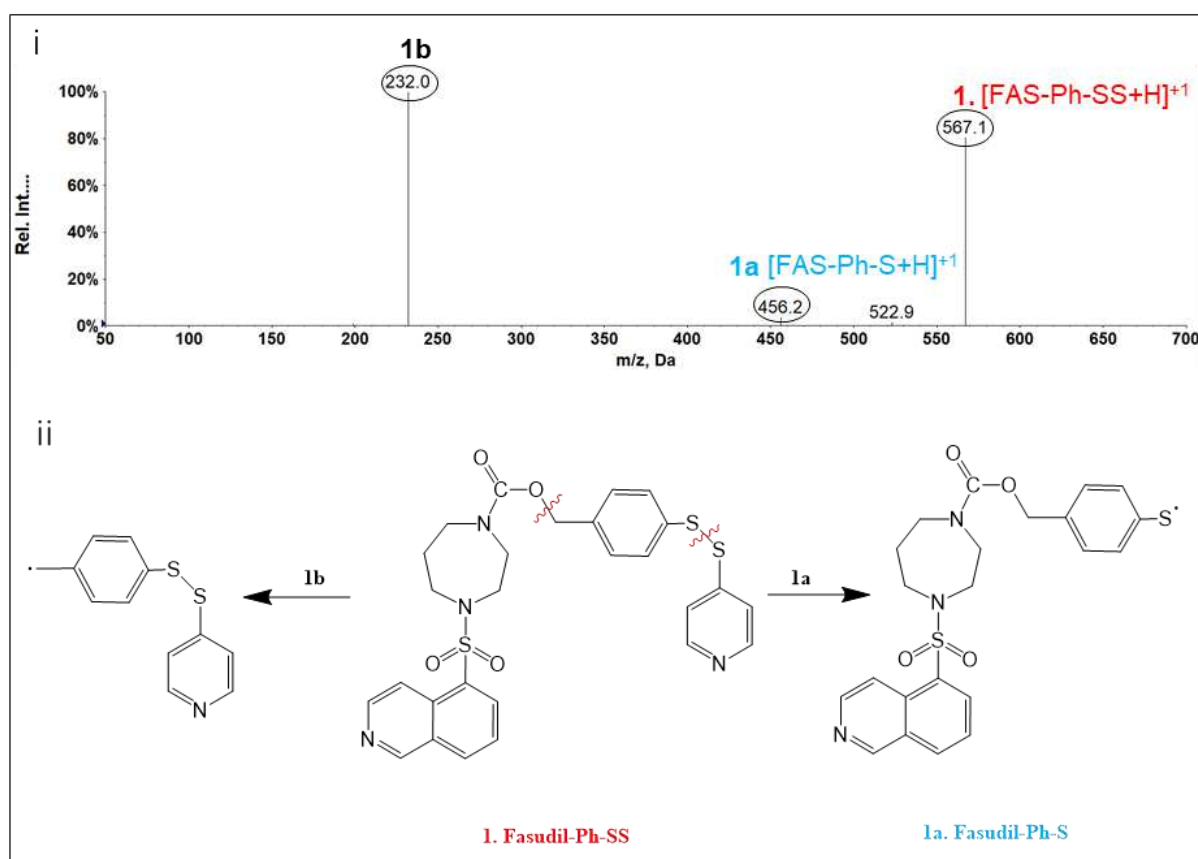


Figure S6. Qualitative analysis of fasudil-phenyl-disulfide drug linker (FAS-Ph-SS). Direct MS analysis enabled the identification according to the MS/MS spectra of (i) drug linker, (ii) drug, and (iii) the fragmentation mechanism.

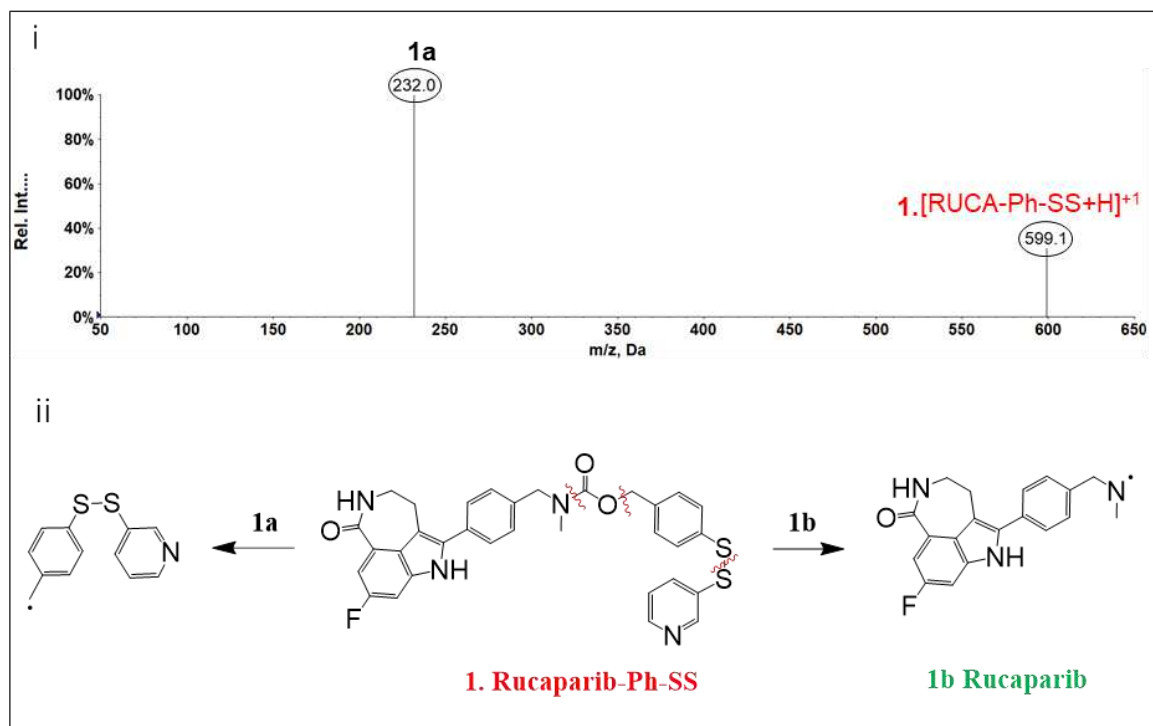


Figure S8. Qualitative analysis of rucaparib-phenyl-disulfide drug linker (RUCA-Ph-SS). Direct MS analysis enabled the identification according to the MS/MS spectra of (i) drug linker, (ii) drug, and (iii) the fragmentation mechanism.

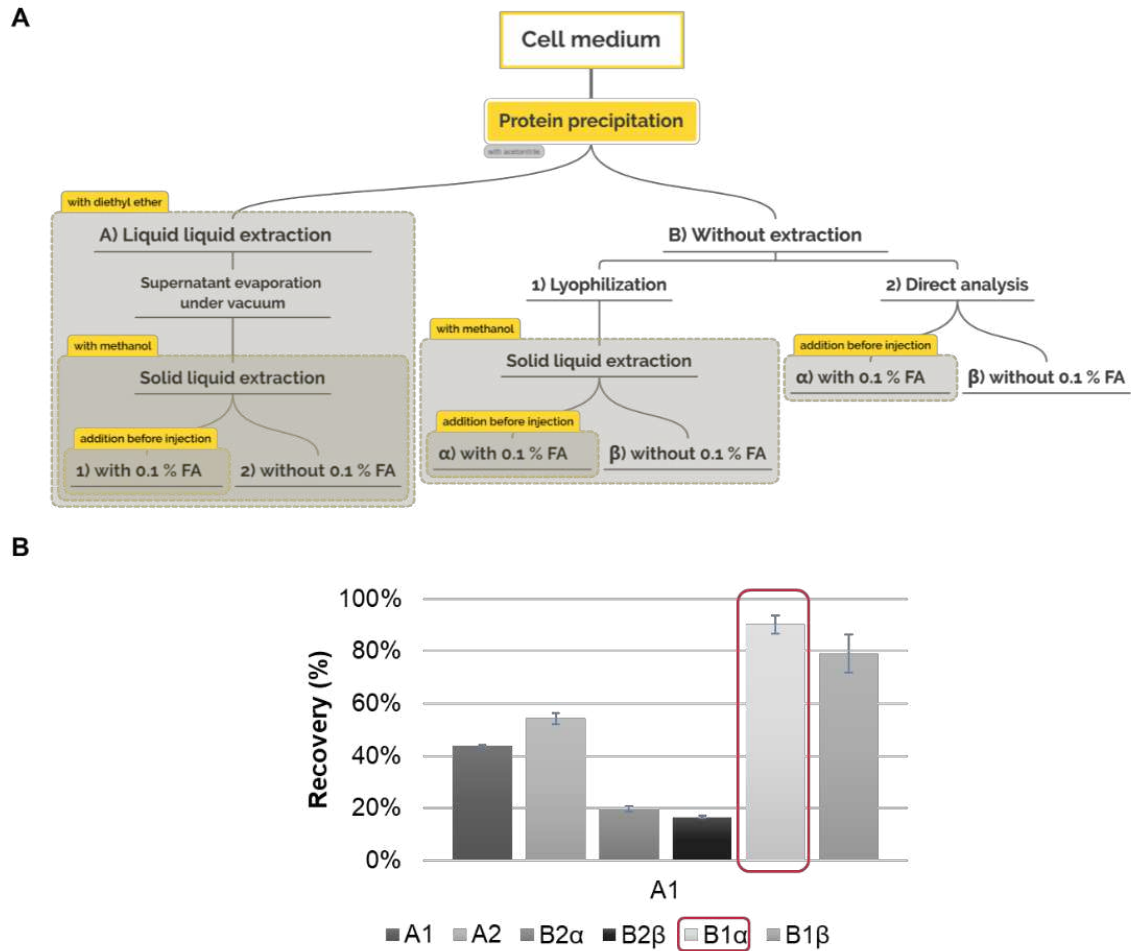


Figure S9. Protocol optimization for fasudil extraction from the cell medium. (A) extraction protocol scheme, (B) FAS/IS peak area ratio for each protocol (the protocol chosen is marked in red).

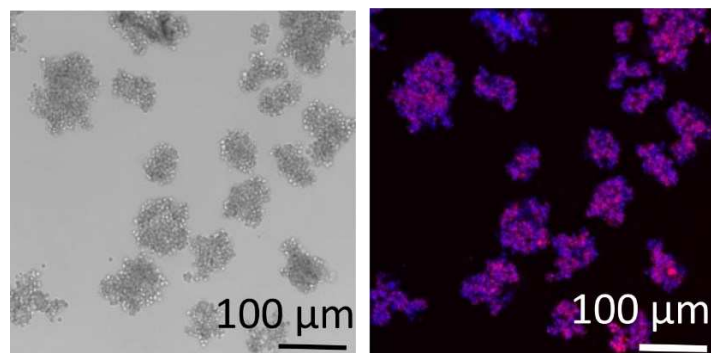


Figure S10. Mammospheres visualization by microscopy (left), and fluorescence (right; Hoechst blue – nucleus, purple – cell membrane)

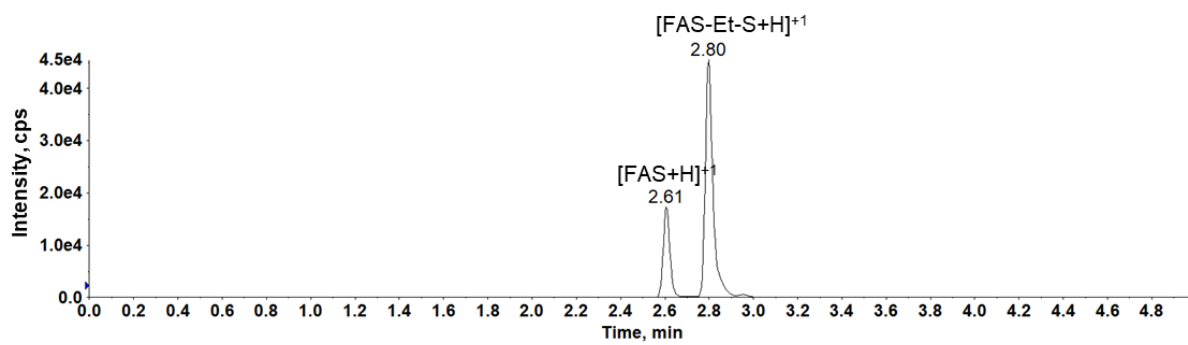


Figure S11. LC-MS/MS chromatogram showing the presence of FAS-Et-S· metabolite in *in vitro* drug release studies 72 h after the treatment with PGA-SS-Et-FAS.

Table S1. Reaction conditions for drug linker synthesis

Drug-linker	Solvent	Temperature	TEA/DMAP	Purification	Reaction time (h)
FAS-Et-SS	DMF	Room	TEA	Column	24 h
NIRA-Et-SS	DCM	Room	TEA	Extraction + column	24 h
RUCA-Et-SS	DMF	Room	TEA	Extraction + column	24 h
DIN-Et-SS	DMF	50°C	TEA + DMAP	Extraction + column	24 h
RES-Et-SS	DCM	Room	TEA	Extraction + column	48 h
FAS-Ph-SS	DMF	80°C	TEA	Column	24 h
NIRA-Ph-SS	DCM	Room	TEA	Extraction + column	24 h
RUCA-Ph-SS	DMF	Room	TEA	Column	48 h

(DMF- dimethylformamide, DCM - dichloromethane, DMAP - 4-dimethylaminopyridine, TEA – triethylamine, FAS-Et-SS - fasudil-ethyl-disulphide, NIRA-Et-SS - niraparib-ethyl-disulphide, RUCA-Et-SS - rucaparib-Et-SS, DIN-Et-SS - dinaciclib-ethyl-disulphide, RES-Et-SS - resiquimod-ethyl-disulphide, FAS-Ph-SS - fasudil-phenyl-disulphide, NIRA-Ph-SS - niraparib-phenyl-disulphide, RUCA-Ph-SS - rucaparib-phenyl-disulphide)

Table S2. Validation parameters and MS/MS conditions for LC-MS/MS method implemented in the drug release studies for the quantification of drugs

Drug	MRM (m/z)	Collision energy (V)	Linearity				
			C range, µg/ml	R ²	Accuracy, %	LOQ, µg/ml	LOD, µg/ml
Fasudil	292.2 – 99.0	35	0.01 - 0.1	0.998	96.5 – 109.6	0.02	0.01
			0.1 - 0.5	0.997	97.6 – 102.2	0.10	0.03
			0.5 - 1.0	0.996	97.6 – 101.7	0.13	0.04
			1 - 5	0.999	98.7 – 100.8	0.39	0.12
Niraparib	321.2 – 304.2	30	0.05 – 0.4	0.996	94.6 – 106.8	0.07	0.02
			0.4 – 5.0	0.999	95.5 – 111.7	0.67	0.20
			5.0 – 9.0	0.999	98.9 – 101.1	0.76	0.23
Rucaparib	324.3 – 293.0	30	0.05 – 0.4	0.999	96.1 – 105.8	0.03	0.01
			0.4 – 1.0	0.994	96.3 – 101.7	0.25	0.07
			1.0 – 5.0	0.998	94.5 – 104.2	0.73	0.22
Dinaciclib	397.2 – 335.0	40	0.02 – 0.1	0.998	96.5 – 101.4	0.02	0.01
			0.1 – 0.5	0.997	98.7 – 106.1	0.10	0.03
			0.5 – 1.0	0.997	98.7 – 101.6	0.11	0.03
			1.0 – 5.0	0.999	99.4 – 102.1	0.24	0.07
Resiquimod	315.2 – 251.0	30	0.02 – 0.2	0.999	97.4 – 104.1	0.02	0.01
			0.2 – 0.9	0.997	95.5 – 103.0	0.15	0.01
			0.9 – 5.0	0.999	97.8 – 103.5	0.68	0.20

(*LOD – limit of detection, LOQ – limit of quantification, MRM-multiple reaction monitoring, C-concentration)

Table S3. MS/MS conditions for LC-MS/MS method implemented in detection of Drug-Et-SS compounds. MRM – multiple reaction monitoring

Compound	MRM scan (m/z)	Collision energy (V)
FAS-Et-SS	505.1 - 396.0	30
NIRA-Et-SS	500.2 - 423.2	30
RUCA-Et-SS	537.1 - 293.1/142.0	30
DIN-Et-SS	612.2 - 501.2	30
RES-Et-SS	529.9 - 170.0	20

Table S4. Experimental design matrix table for optimization of LC-MS/MS method

Run	% ACN start	% ACN end	Flow (ml/min)	% Aq phase*	Column temp (°C)	Gradient time (min)	Plateau time (min)
1	52.5	100	0.2	10	45	1	6
2	52.5	5	0.5	10	45	1	6
3	100	100	0.35	20	45	4.5	6
4	52.5	52.5	0.35	20	60	1	6
5	52.5	52.5	0.5	0	45	4.5	9
6	52.5	5	0.35	10	60	4.5	9
7	52.5	52.5	0.5	20	45	4.5	9
8	52.5	52.5	0.35	10	45	4.5	6
9	100	52.5	0.5	10	60	4.5	6
10	52.5	52.5	0.2	0	45	4.5	3
11	100	52.5	0.35	10	45	8	3
12	100	5	0.35	0	45	4.5	6
13	52.5	100	0.35	10	30	4.5	3
14	52.5	5	0.35	10	30	4.5	3
15	52.5	100	0.5	10	45	1	6
16	100	100	0.35	0	45	4.5	6
17	52.5	52.5	0.35	10	45	4.5	6
18	52.5	100	0.35	10	30	4.5	9
19	5	52.5	0.5	10	30	4.5	6
20	5	52.5	0.2	10	30	4.5	6
21	100	52.5	0.5	10	30	4.5	6
22	52.5	100	0.2	10	45	8	6
23	100	5	0.35	20	45	4.5	6
24	52.5	52.5	0.35	0	30	1	6
25	52.5	52.5	0.2	20	45	4.5	9

Run	% ACN start	% ACN end	Flow (ml/min)	% Aq phase*	Column temp (°C)	Gradient time (min)	Plateau time (min)
26	52.5	52.5	0.35	20	30	1	6
27	5	52.5	0.5	10	60	4.5	6
28	52.5	5	0.35	10	60	4.5	3
29	5	52.5	0.35	10	45	1	3
30	100	52.5	0.35	10	45	8	9
31	52.5	52.5	0.35	0	30	8	6
32	52.5	52.5	0.5	0	45	4.5	3
33	100	52.5	0.2	10	30	4.5	6
34	5	5	0.35	0	45	4.5	6
35	52.5	5	0.2	10	45	8	6
36	52.5	100	0.5	10	45	8	6
37	52.5	5	0.5	10	45	8	6
38	52.5	52.5	0.35	10	45	4.5	6
39	5	52.5	0.35	10	45	8	3
40	52.5	52.5	0.5	20	45	4.5	3
41	52.5	52.5	0.35	10	45	4.5	6
42	52.5	52.5	0.35	10	45	4.5	6
43	5	5	0.35	20	45	4.5	6
44	100	52.5	0.35	10	45	1	3
45	5	52.5	0.2	10	60	4.5	6
46	5	52.5	0.35	10	45	1	9
47	100	52.5	0.35	10	45	1	9
48	52.5	52.5	0.35	0	60	1	6
49	52.5	52.5	0.2	0	45	4.5	9
50	52.5	5	0.35	10	30	4.5	9
51	52.5	5	0.2	10	45	1	6
52	52.5	52.5	0.35	20	30	8	6

Run	% ACN start	% ACN end	Flow (ml/min)	% Aq phase*	Column temp (°C)	Gradient time (min)	Plateau time (min)
53	100	52.5	0.2	10	60	4.5	6
54	52.5	52.5	0.35	10	45	4.5	6
55	5	100	0.35	0	45	4.5	6
56	5	52.5	0.35	10	45	8	9
57	52.5	100	0.35	10	60	4.5	3
58	5	100	0.35	20	45	4.5	6
59	52.5	52.5	0.35	20	60	8	6
60	52.5	52.5	0.35	0	60	8	6
61	52.5	52.5	0.35	10	45	4.5	6
62	52.5	52.5	0.2	20	45	4.5	3
63	52.5	100	0.35	10	60	4.5	9

(ACN- acetonitrile;Aq- aquatic *0.1 % formic acid in the sample)

Table S5. Important LC factors and factor interactions for system outputs and data transformation used for each prediction model.

Drug	System output	Data transformation	Prediction model	P-value/F-value	Important factors
Rucaparib	S/N	Natural log	Quadratic	<0.0001/5.83	A, AB, E ² , G ²
	k	Square root	Quadratic	<0.0001/5.19	AB, A ² , B ² , D ²
	Peak width	Inverse	Quadratic	<0.0001/5.46	A, C, E, AB, AD, A ² , B ² , D ² , F ²
	T	None	Quadratic	0.0005/3.73	A, B, AB, A ² , B ² , E ² , F ²
Niraparib	S/N	Square root	Quadratic	0.0196/2.18	A, B, C, AB, A ² , B ²
	k	Square root	Quadratic	0.0011/3.26	A, F, AB, A ² , B ² , D ² , E ² , G ²
	Peak width	Inverse	Quadratic	<0.0001/7.76	A, B, C, AD, BE, C ² , E ² , F ² , G ²
	T	Square root	Quadratic	0.0002/4.28	A, B, AF, BE, BF, B ² , F ² , G ²
Fasudil	S/N	Square root	Quadratic	<0.001/3.61	A, C, A ²
	k	Square root	Quadratic	<0.0001/5.47	AB, A ² , B ² , D ² , F ² , G ²
	Peak width	Square root	Quadratic	<0.0001/4.39	A, C, AB, AC, AE, B ² , C ² , D ² , E ²
	T	None	Quadratic	<0.001/3.36	AB, A ² , B ²
Dinaciclib	S/N	Square root	Linear	<0.0001/6.41	A, C, E
	k	Power	2FI	<0.0001/2.43	AB, AD, A ² , B ² , C ² , D ² , E ² , F ² , G ²
	Peak width	Square root	Quadratic	<0.0001/8.82	A, C, D, AB, BD, A ² , B ² , C ² , D ²
	T	None	Quadratic	<0.0001/4.34	A, C, E, AB, AC, AE, BD, B ² , C ² , E ²
Resiquimod	S/N	Square root	Quadratic	<0.0001/4.21	A, C, E, AB
	k	Square root	Linear	<0.0001/2.16	A, AB, A ² , B ² , D ²
	Peak width	Square root	Quadratic	<0.0001/3.78	A, C, AB, BD, A ² , B ²
	T	Square root	Quadratic	<0.0001/4.11	A, B, C, AB, AC, BC, B ² , C ²

S/N – signal-to-noise; k- retention factor; T- tailing factor; A- % ACN start; B- % ACN end; C- flow (ml/min); D- % Aq phase; E- Column temp (°C); F- Gradient time (min); G- Plateau time (min)